Direct and Indirect Effects of Flood Basalt Volcanism on Reservoir Quality Sandstone

CLAYTON GROVE

DURHAM UNIVERSITY

Direct and Indirect Effects of Flood Basalt Volcanism on Reservoir Quality Sandstone

Clayton Grove

2014

Abstract

This thesis describes the direct diagenetic effects on porous clean sand substrate due to the emplacement of basalt lava flows. The thesis also describes the effects of the emplacement of basaltic dykes and sills into clean porous sandstone. The primary dataset comes from the Cretaceous Etendeka Group, NW Namibia, where the Etendeka Flood Basalts (and associated subsurface plumbing system) interacted with the aeolian Twyfelfontein Formation sandstone. Secondary datasets from the recent Rekjanes Peninsular basalts, Iceland; the Miocene Columbia River Flood Basalt province and the Miocene Snake River Basalts, NW USA are used to constrain the direct effects of lava on substrates in a variety of palaeoenvironmental conditions.

The thesis makes use of a number of analytical techniques including: petrography, scanning electron microscopy, image analysis, X-ray diffraction, X-Ray fluorescence, stable isotope spectroscopy (δ^{18} O and δ^{13} C) and gas permeability (Hasler and probe).

The findings of this work constrain the degree of porosity reduction in clean sandstones due to intrusion emplacement over a complete range of thermal regimes, controlled by the magma flow pathways and duration. The effects range from mild hydrothermal activity and compaction through to intense pyrometamorphism, sediment melting and segregation. Beneath lava flows, the degree of porosity loss is determined by palaeoenvironment (specifically the availability of free water), the lava thickness and the substrate composition. Together the geometries of the igneous components (intrusions and extrusive flows) of the Etendeka Group compartmentalise the sedimentary components (Twyfelfontein Formation), which can be traced due to their effects on hydrothermal activity. The main compartment forming lithologies are vertical-subvertical intrusions, with the lava flows being a minor contributor. The diagenesis during hydrothermal activity was found to be a natural sequestration mechanism of CO_2 derived from igneous activity as well as a highly compartmentalised porosity degradation mechanism.

Direct and Indirect Effects of Flood Basalt Volcanism on Reservoir Quality Sandstone

---

Clayton Grove

2014

This thesis is submitted in accordance with the regulations for the degree of Doctor of Philosophy in the University of Durham Department of Earth Sciences

Dedicated to

George F. Grove

1928-2010

Table of Contents

1. Introduction and Thesis Outline

2. Geological background and a review of direct and indirect effects of igneous rocks on porous sediments

3. Methods

8. Conclusions

9. Supporting Publications

10. References

Appendices

List of Figures

List of Tables

Abbreviations

Photomicrographs and XRD spectra are labelled thus:

alb albite
anal analcite
an anorthite
bö böhmite
calc calcite
chlor/chl chlorite
cpx clinopyroxene
Fe-calc ferroan calcite
fluo fluorite
frac fracture
g glass
goe goethite
haem haematite
i-g porosity intergranular porosity
Il ilmenite
kao kaolinite
K-f potassium feldspar
opx orthopyroxene
or orthoclase
plag plagioclase
PmFm feldspar matrix crystallised from partial melt
ps- pressure solution
prep section preparation induced feature
q quartz
q-og quartz overgrowth
sid siderite
tr/ tr-inv quartz paramorph after tridymite
zeo zeolite

*Other minerals are labelled in full

Rock unit abbreviations are detailed in Chapter 2 and are consistent throughout the thesis. Units are as per the American Association of Petroleum Geologists (AAPG) guidelines.

Declaration

No part of this degree has previously been submitted for a degree at any other university. The work described is entirely the work of the author, except where previously published work has been cited, for which due reference has been made.

CLAYTON GROVE Date:

Department of Earth Sciences

University of Durham

DH1 3LE

Acknowledgements

I acknowledge the Volcanic Margins Research Consortium (VMRC), founded by Dougal Jerram and One Northeast, supported by Rick Smith for providing funds for this project. I also thank DougalEarth for providing valued financial support for fieldwork and conferences.

Without the support of Nick Schofield I wouldn't have considered applying for a PhD position. Nick has been a true mentor over the past eight years. Secondly I thank my supervisory team, who have helped me through ups and downs and have continually placed their trust in me. Dougal Jerram conceived the PhD, acquired funding and has been a mentor and friend throughout, his good will, trust and generosity stands out above all. I thank Dougal for setting up the VMRC. Richard Brown and Jon Gluyas stood in as Durham supervisors in 2011, taking over the administration of the project. I thank them for patience, allowing me to develop the project to what it is now, scientific guidance and friendship.

My fieldwork companion, Tim Watton has been a constant scientific buddy and the two way transfer of ideas had greatly influenced this thesis. I thank him for inviting me on all of his field seasons and assisting me on mine in Namibia. Fieldwork assistance was also provided by Sam Clark and Victoria Gee, with supervision by R. Brown and D. Jerram. In Iceland, Thor Thordarson helped by providing his Toyota to TW and I. In the USA, Terry Tolan suggested the Rock Creek outcrop and useful guidance was given by Dennis Geist, Bill Bonnichsen and Marty Godchaux. Hindrance was in the form of strong ale consumed by TW in Portland. Three trips to Namibia were made possible by Dougal Jerram. For the first trip I thank Bob Trumbull and his team from Germany, who are fondly remembered. The second trip was supervised by RB, and assisted by TW, VG and SC in Namibia and Dougal on the satphone from the Huab! The third trip was made possible by Breno Waichel and his Brazilian team who are thanked and will be remembered for their sophisticated scientific teamwork, good company and eccentricities matching my own. In Namibia, The Geological Survey of Namibia (Gabi Schneider), Branco Corner, Ansgar Wanke and the Steiner family are gratefully acknowledged for their help and company.

Lab work in Durham has been supported by Ian Chaplin and Dave Sales (thin sections), Alan Carr (microscopes, everything), Jo Peterkin (isotopes) and Chris Ottley (mineral staining, good company). Useful scientific conversation and guidance has been provided by Richard Hobbs and Henry Emeleus. Henry is particularly thanked for his untiring enthusiasm and assistance in microscopy, geological curiosity, good company and the donation to my custodianship of his ~ 50 years' worth of *National Geographic* magazines. Lab work has also been in collaboration with Andrew Hurst and Colin Taylor at Aberdeen University, who are thanked for their help, scientific advice and impartial advice during the more difficult times of this project. In Durham, I particularly want to thank Paula Elliott who has supported my fieldwork and travel from the office with utmost professionalism and competency, sometimes I feel Paula has been the keystone holding the world together!

My family and friends are thanked for suffering the expressions of my mind and continuing to support me. I thank everyone who has contributed to geological discussion, and defended open conversation and open mindedness. I especially thank my late Grandfather, George Grove for advising me to 'work hard' and instilling in me good frugal principles.

Colleagues at OMV (U.K.) are thanked for encouragement during the final stages of this work that was completed while juggling other work commitments. Gia Pendred, Frances Gibb, Mike Hawkins and Martin Smith deserve special thanks.

My final acknowledgement is to Vincent Curinier (and the rest of the Geosciences office at TOTAL E&P UK) for taking me on for 7 months and showing me the applied side of my research. The industry exposure has greatly improved the PhD, even though it is not directly included.

1

Introduction and Thesis Outline

1.1 Project motivation: the problems

The existence of hydrocarbons in and around igneous rocks is well documented (Schutter, 2003a, b) and as such, the requirement of knowledge regarding the impact that igneous rocks have on reservoir lithologies (e.g. sandstone) is required for an effective petroleum exploration and production strategy. The importance of this understanding is highlighted below, in a selection of known petroleum basins globally, for both igneous sills and dykes and extrusive lava flows.

1.1.1 Lava flows in regions prospective for petroleum

Faroe-Shetland Basin

Palaeocene–Eocene lava flows were erupted into the Faroe-Shetland basin (Andersen, 1988; Underhill, 2003; Smallwood et al., 2004) in both subaerial and submarine environments (e.g. White, 1988; Lamers & Charmichael, 1999; Ellis et al., 2002). The lavas are often interbedded with siliciclastic sands in the Faroe-Shetland basin (e.g. Rosebank (213/27-1z) (Helland-Hansen, 2009), 214/4-1 (Passey, 2004), 214/9-1 (UK Discovery Digest, 2013).

The Rosebank field operated by Chevron was discovered in 2004 in an anticlinal structure with ~ 100 m of sediments interbedded with lava flows and volcaniclastic sediments (Fig. 1.1, Fig. 1.2.) (Helland-Hansen, 2009). The Rosebank discovery appraisal is challenging due to the interfingering volcanic system introducing uncertainty due to poor geological knowledge of such systems (Helland-

Hansen, 2009). Two of the problems identified by Helland-Hansen is the possibility of 'Reservoir sands being degraded by "cooking" of hot volcanic material (lava flows and sills)' and 'Volcanic material seeping into and decreasing reservoir quality through diagenetic processes'. These could be termed *DIRECT* and *INDIRECT* diagenetic processes. It is the understanding of these uncertainties that this thesis seeks to address.

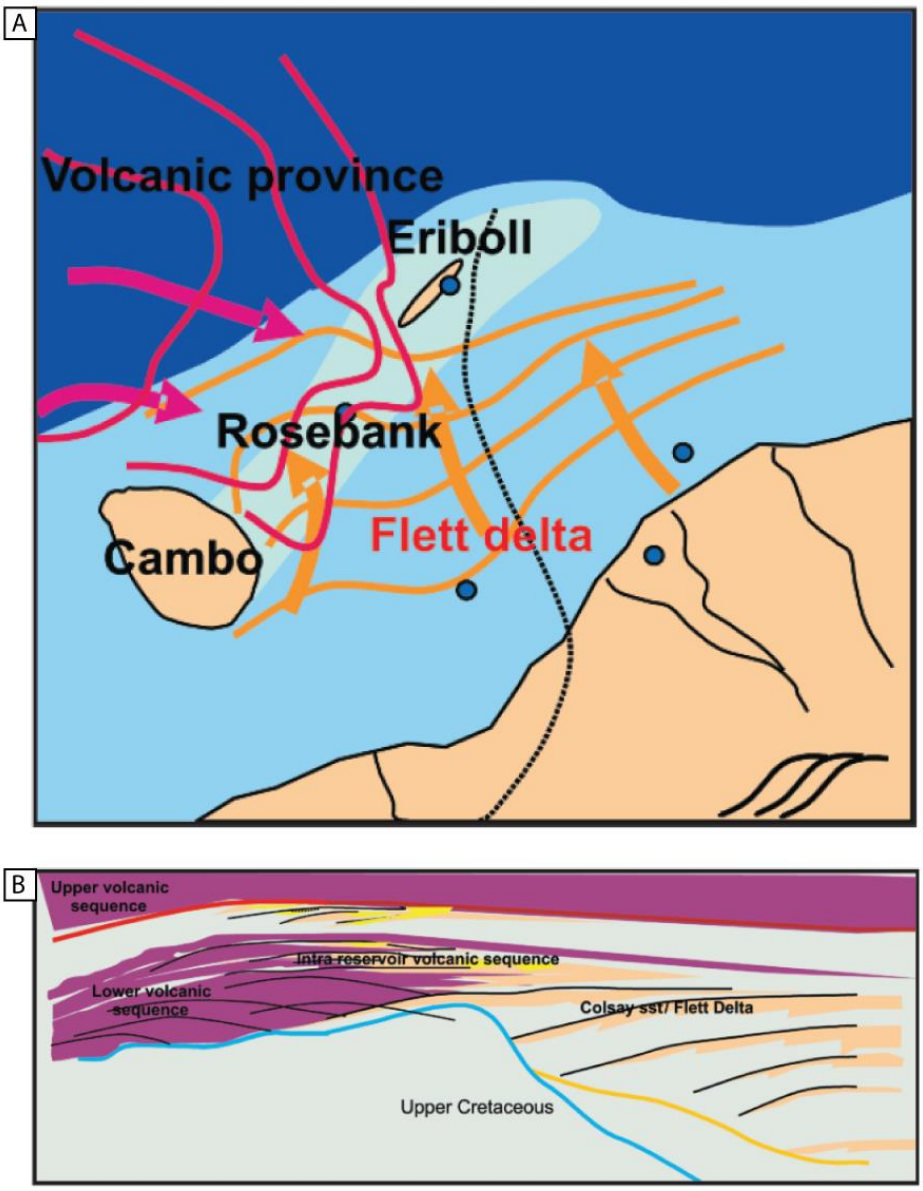

Fig. 1.1 (A) Vertical view of the depositional nature of the Rosebank sediments and volcanic rocks. The section shows the interfingering between siliciclastic sandstone (Colsay reservoir units in the Flett Formation) and the volcanic rocks comprising lava flows, sills, hyaloclastites and volcaniclastics. (B) Schematic section of the interfingering lava flows and siliciclastic sediments. Figure modified from Helland-Hansen (2009).

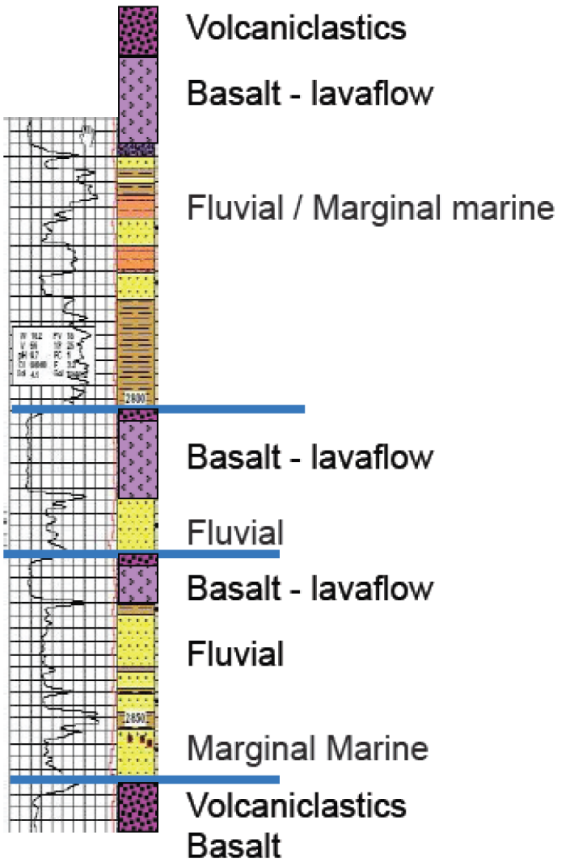

Fig. 1.2 Composite well log through part of well 213/27-1z showing lava flows and siliciclastic sediments intersected by the Rosebank discovery well (Figure modified from Duncan et al., 2009.

Kudu, Offshore Namibia

The Kudu gas field was discovered in 1974 and later appraised in 1987–1988 by Seokor, Chevron and Regent. Results were initially promising, but the reserve estimates have fallen from 15 TCF to a current figure of 1.38 TCF proved (Tullow Oil, 2006). The Kudu gas field is composed of two reservoir intervals: The Lower Gas sand and the Upper Gas sand. The Lower Gas sand is the major reservoir interval as the Upper Gas sand is tight having low porosity (0-9 %_ and low permeability (0.01 md) (Rijswijk & Steyn, 1990). The Lower Gas sand comprises of sedimentary interlayers from 12 to 38 m in thickness between basalt flows (Wickens

& McLachlan, 1990; Stanistreet & Stollhofen, 1999). The sandstone consists of siliciclastic and volcaniclastic components and thin calcareous layers containing bivalves (Fig. 1.3.). Evaporites are common in the sand layers (Stainistreet & Stollhofen, 1999). The Lower Gas sand were tentatively assigned to a coastal dune complex (Wickens & McLachlan, 1990; Stanistreet & Stollhofen, 1999). The Upper Gas sand is shallow marine (Wickens & McLachlan, 1990).

The Twyfelfontein Formation (Etjo at the time) was initially proposed as a lithological and chronological analogue for the Kudu field by Horsthemke et al. (1990) and an assumption of an Early Cretaceous age was made for the Lower Gas sand (Horsthemke et al., 1990; Stanistreet & Stollhofen, 1999), despite the Lower Gas sand not providing biostratigraphical data or radiometric dating to support the Cretaceous age (McMillan, 1990). Later work by Stanistreet & Stollhofen (1999) suggested an Early Jurassic age for the Lower Gas sand, and correlation with Karoo age Kalkrand flood basalts of southern Namibia.

Despite the direct correlation with the Twyfelfontein Formation being less likely than originally thought (Horsthemke et al., 1990), the Twyfelfontein Formation is still a valuable analogue for the study of the diagenesis at lava-sediment contacts. Further, Cretaceous sandstones, directly equivalent to the Twyfelfontein Formation probably exist offshore, further north than the Kudu field that are interbedded with (probable) Etendeka Group lavas and are affected by igneous intrusions (e.g. in the region of the Tapir South Prospect of Chariot Oil, Chariot Oil & Gas presentation, www.chariotoilandgas.com accessed March 2013, un-interpreted seismic line).

The existence of igneous geology in proximity to potential reservoir units provides an additional level of uncertainty, akin to the Rosebank field and highlights the uncertainties being addressed in this thesis have application to multiple basins.

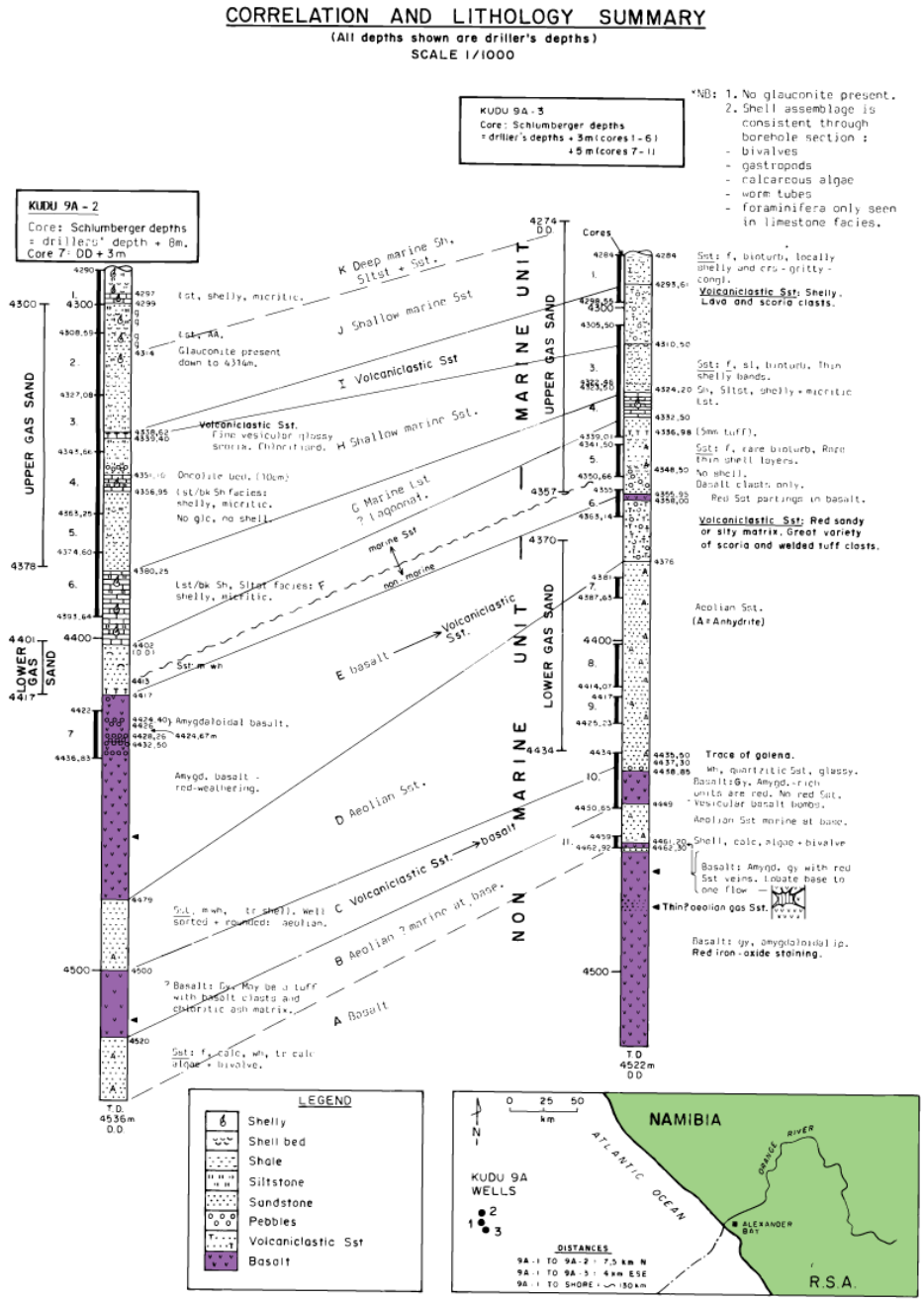

Fig. 1.3 Correlation and lithological summary of Kudu 9A-2 and Kudu 9A-3 wells (1987 and 1988). The lower gas sand is interbedded with lava flows (modified from Wickens & McLachlan, 1990). The Lower Gas Sand is aeolian and marine sandstone and the Upper Gas Sand is marine, there being a transgressive episode between the two sands.

1.1.2 Igneous intrusions in regions prospective for petroleum

Faroe-Shetland Basin

The Faroe-Shetland basin is prospective from the Devonian to the Eocene (Scotchman et al., 1998; Sircar, 2004; Smallwood & Kirk, 2005), indeed prospectivity even exists in fractured Precambrian basement (Sircar, 2004). Igneous intrusions exist in all of the prospective stratigraphy (e.g. Bell & Butcher, 2002; Ellis et al., 2002; Ellefsen et al., 2010; Schofield et al., 2012; Grove, 2013). Fig. 1.4 shows a seismic line approximately through the middle of the basin illustrating the intensity of sill intrusion (the high amplitude reflectors labelled). Clearly it is instructive to determine the effects that these kind of intrusions have on reservoir quality sandstone. This thesis addresses this in Chapter 6 and Chapter 7 using the Twyfelfontein Formation as an analogue. Verification of this as a suitable analogue has been performed using oil industry data (Grove & Curinier, PETEX 2012, award winning oral presentation) but is not included within this thesis.

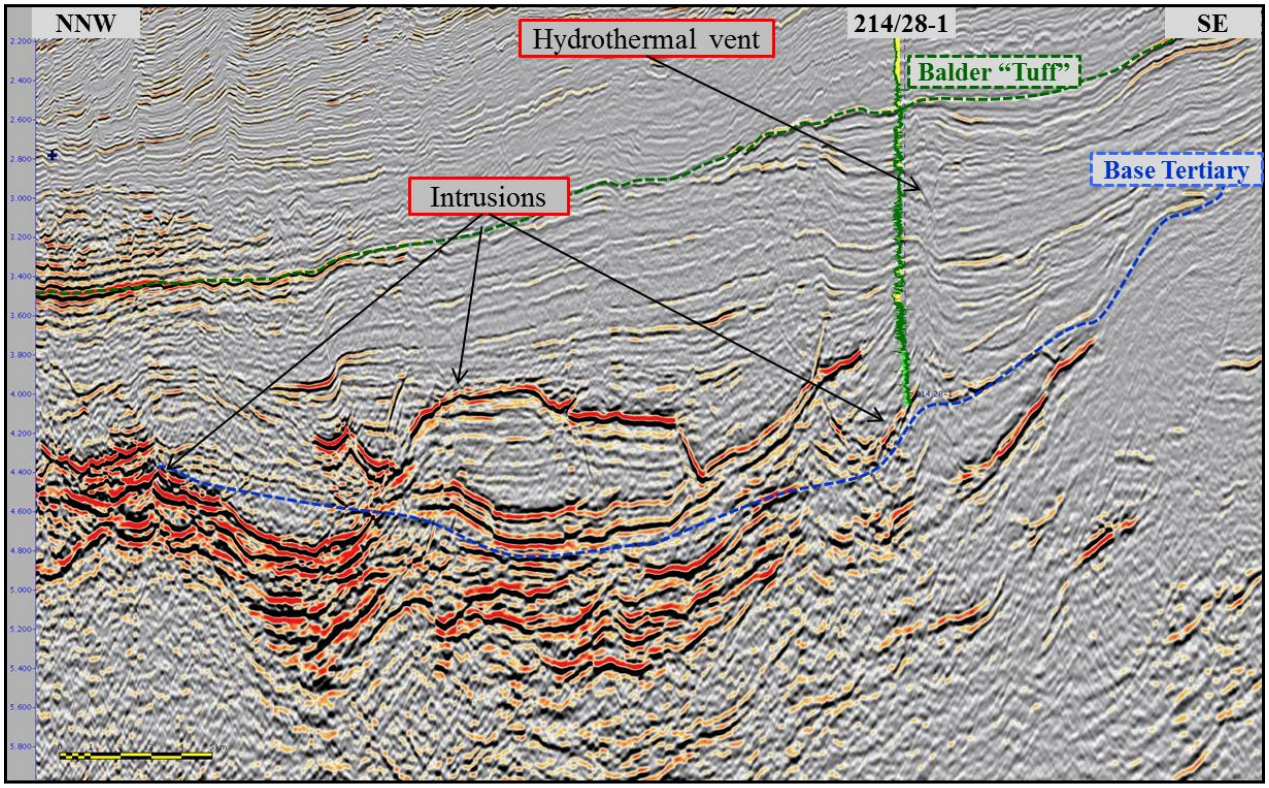

PSTM Data provided courtesy of PGS

Fig. 1.4 Seismic line showing igneous intrusions in the Faroe-Shetland basin, sill intrusions exist in stratigraphy from the Jurassic to the late Palaeocene, which includes all of the major reservoir containing stratigraphy (From presentation given at PETEX 2012 in collaboration with Vincent Curinier, Total E & P UK).

Offshore Australia

The passive margins surrounding Australia are prospective for petroleum exploration and are frequently intruded by sills and contain lava flows (Holford et al., 2012; Magee et al., 2013) e.g. the Bight, Otway, Bass, Gippsland, Ceduna (Fig. 1.5.) and Sorel basins (Holford et al., 2012). These Australian occurrences of igneous rocks within petroleum basins highlight the requirement of field analogue based data, constraining the degree of potential reservoir degradation to be expected. The increasing quality and availability of 2D and 3D seismic data covering such basins makes this especially important as these data are opening up new prospects in association with the igneous rocks (Holford et al., 2012).

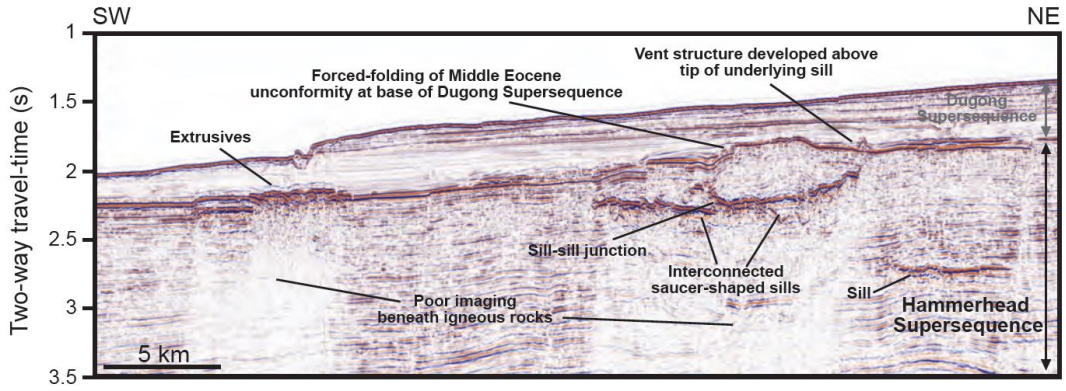

Fig. 1.5 Seismic line from the Ceduna sub-basin (from Holford et al., 2012). This seismic line illustrates a variety of igneous features found offshore Australia including numerous intrusions.

1.2 Thesis Aims

The examples presented above have identified that the mapping and emplacement mechanisms of igneous rocks in petroleum basins is well understood compared to the effects the igneous rocks have on reservoir development. Igneous rocks are present in many regions with petroleum prospectively (e.g. The Faroe-Shetland Basin (Bell & Butcher, 2002; Smallwood et al., 2004; Grove, 2013), Southern Atlantic passive volcanic margins (Jungslager, 1999; Stainistreet and Stollhofen, 1999; Davison, 1999), Australian passive volcanic margin basins (Holford et al., 2012)). These areas have traditionally avoided or overlooked due to difficulties associated with seismic imaging and the detrimental short-term and long-term impacts on petroleum systems, such as reservoir degradation and compartmentalisation (Holford et al., 2012). The direct and indirect effects of igneous activity (extrusive and intrusive) on potential reservoir development are the topics investigated in this thesis and can be split into the following aims:

- To characterise the direct diagenetic effects of basaltic lava flows on reservoir quality sand substrate.
- To characterise the direct diagenetic effects of basaltic igneous intrusions on reservoir quality sandstone country rocks. Can conventional reservoirs exist in proximity to igneous intrusions?
- To find evidence of compartmentalisation of reservoir quality sandstone by igneous intrusions and characterise the effects of the compartmentalisation on the development of reservoir quality.
- To provide evidence of how different igneous lithologies (lava flows, sills and dykes) control the hydraulic regime in the compartmentalised sandstone.

1.3 Hydrothermal Sediment Volcanism

Sill intrusion can cause host rock fluidisation and the mobilisation of the fluidised sediment from the subsurface to the surface. This results in an extrusive complex at the palaeosurface composed of material transported through a hydrothermal conduit. Such features are present in the Faroe-Shetland basin. One such feature is described in Chapter. 9, where a published paper (Grove, 2013) is attached in lieu.

1.4 Thesis Outline

Chapter 1

Introduction to igneous provinces within regions prospective for petroleum and motivation, thesis aims and thesis outline

Chapter 2

Introduction to the geology of NW Namibia and the Huab Basin, including the basin development and pre-Cretaceous stratigraphy. Detailed description of the Lower Cretaceous Twyfelfontein Formation which is the main clastic unit described in the thesis. Detailed new work on the burial of the Twyfelfontein Formation. Review of previous work on the direct and indirect effects of basaltic igneous intrusions on country rock and the effects of lava flows on their substrates.

Chapter 3

Overview of methods used in the thesis and the fieldwork undertaken.

Chapter 4

Detailed descriptions of the direct effects of the Etendeka basaltic lavas on the siliciclastic Twyfelfontein Formation; a substrate in an arid desert palaeoenvironment.

Chapter 5

Detailed descriptions of the direct effects of lava flows on sediments in wet palaeoenvironments. Comparison between the effects in different palaeoenvironments and the controls of the effects (e.g. lava flow thickness and water).

Chapter 6

Detailed description of the full range of direct contact effects in the Twyfelfontein Formation as a result of the emplacement and cooling of basaltic dykes and sills. Effects span compaction and mild hydrothermal activity to partial melting and melt segregation within the sandstone.

Chapter 7

Reports work on indirect effects of igneous intrusions in the Twyfelfontein Formation. This chapter uses fossil hydrothermal activity within the sandstone to trace fluid flow during cooling of the igneous intrusions and therefore the compartmentalisation of the formation. The chapter describes the reservoir degradation as a result of hydrothermal activity within the sandstone.

Chapter 8

Conclusions and recommendations for future work

Chapter 9

Attached article published in *Geology* on hydrothermal sediment volcanism in the Faroe-Shetland Basin.

Attached article published in *Computers & Geosciences* on digital image analysis and point counting.

Appendices

Papers published in support of the thesis. Map of the Huab Outliers field area showing geology and other relevant information. Data tables. Logistical information.

2

Geological background and a review of direct and indirect effects of igneous rocks on porous sediments.

2. GEOLOGICAL BACKGROUND AND A REVIEW OF DIRECT AND INDIRECT EFFECTS OF IGNEOUS ROCKS ON POROUS SEDIMENTS 17

2. Geological background and a review of direct and indirect effects of igneous rocks on porous sediments

2.1 Chapter summary

This chapter describes the pre-Cretaceous geology and Cretaceous Etendeka Group geology of the Huab Basin, NW Namibia. New petrographical work is presented classifying the background sandstone of the Twyfelfontein Formation, which includes new calculations of potential burial; this sets a benchmark for comparison of the direct effects of igneous intrusions & lava flows and the indirect hydrothermal effects reported.

The direct effects of sills and dykes on country rocks intruded are reviewed, concentrating on sandstone. The range of effects reported varies from pyrometamorphism (Grapes, 2010) where partial melt occurs, through to the more common, but less thoroughly studied non-pyrometamorphic contact metamorphism, which is essentially a compaction and hydrothermal process, controlled by the cooling effect of the sandstone aquifer.

The direct effects of lava flows on substrate are reviewed. This subject has a paucity of previous studies. The references to sandstone being affected by lava flows are usually 'throw away' comments with little or no background given or justification.

Sandstone bleaching is loosely reviewed as Chapter 7 provides a more thorough explanation of the processes involved; many of the indirect effects appear unique to the Huab Basin in style as currently reported.

2.2 Geology of the Huab Basin, NW Namibia.

2.2.1 Overview

The Huab Basin was introduced by Horsthemke et al (1990) to encompass the Karoo deposits and Etendeka Group deposits (extrusive volcanic rocks and sediments) to the north and south of the Huab River (Jerram et al., 1999a). The deposits to the south of the Huab River are known as the Huab Outliers. The preserved stratigraphy in the Huab Basin records the geological evolution of the region from the end of the Damara orogeny (500-600 Ma), with the basement recording deposition and tectonic activity prior to the Damara orogeny (Gray et al., 2008). The deposition in the Huab Basin records the Carboniferous to Cretaceous progressive break-up of Gondwana (Mountney et al., 1998; Stollhofen et al., 1998; Mountney et al., 1999a; Jerram et al., 1999a; Jerram et al., 1999b; Faure et al., 1999; Stollhofen et al., 2000a). Cretaceous stratigraphy is characterised by the emergence of the Etendeka Igneous Province, which forms the eastern most extent of the larger Paraná- Etendeka Flood Basalt Province (Peate, 1997; Jerram et al., 1999a, b; Waichel et al., 2011). The Etendeka Igneous Province in the Huab Basin occurs as intrusive basic dykes and sills (Erlank et al., 1984; Duncan et al., 1989; Marsh et al., 1991; Thompson et al., 2001) and laccoliths, extrusive basic lava flows (Ewart et al., 1998a; Jerram et al., 1999a, b; Marsh et al., 2001; Marsh & Milner, 2003; Ewart et al., 2004a) and extrusive silicic quartz latite units (Milner et al., 1992; Milner et al., 1995; Ewart et al., 1998b; Marsh et al., 2001; Ewart et al., 2002; Ewart et al., 2004b; Bryan et al., 2010).

2.2.2 Assembly of Gondwana and the genesis of the Damara basement rocks.

The oldest rocks cropping out belong to the Damara Sequence (considered basement). These Damara basement rocks were initially deposited in a passive margin and deep water setting as carbonates and turbidites spanning the Neoproterozoic (770 Ma– 600 Ma) (Gray et al., 2008). Subsequently the Damara deposits were involved in continental collision between the Kalahari, Congo and Río de la Plata Cratons during the Pan-African Damara orogenic sequence with peak deformation and regional metamorphism at 530–500 Ma (Gray et al., 2008). Thrusting onto the Kalahari Craton occurred from 495 Ma to 480 Ma (Gray et al., 2008). In the field area, these basement rocks consist of meta-greywacke, marble and pelite cropping out as NNW trending folds (Fig. 2.5A.) and 10 km diameter granitic intrusions. It can be observed that later Cretaceous igneous intrusions are associated with the basement structure; the Doros Crater gabbroic pluton is on the SE margin of a Damaran syntectonic granitic intrusion (the Doros Pluton, Passchier et al., 2007) and the major Cretaceous dyke trend matches the basement structural trend; Mesozoic rift geometry is also thought to be controlled by Pan-African basement fabrics (Clemson et al., 1997). Fig. 2.1 shows the basement structure and timings for the orogenic assembly of Gondwana in the late Neo-proterozoic and earliest Palaeozoic.

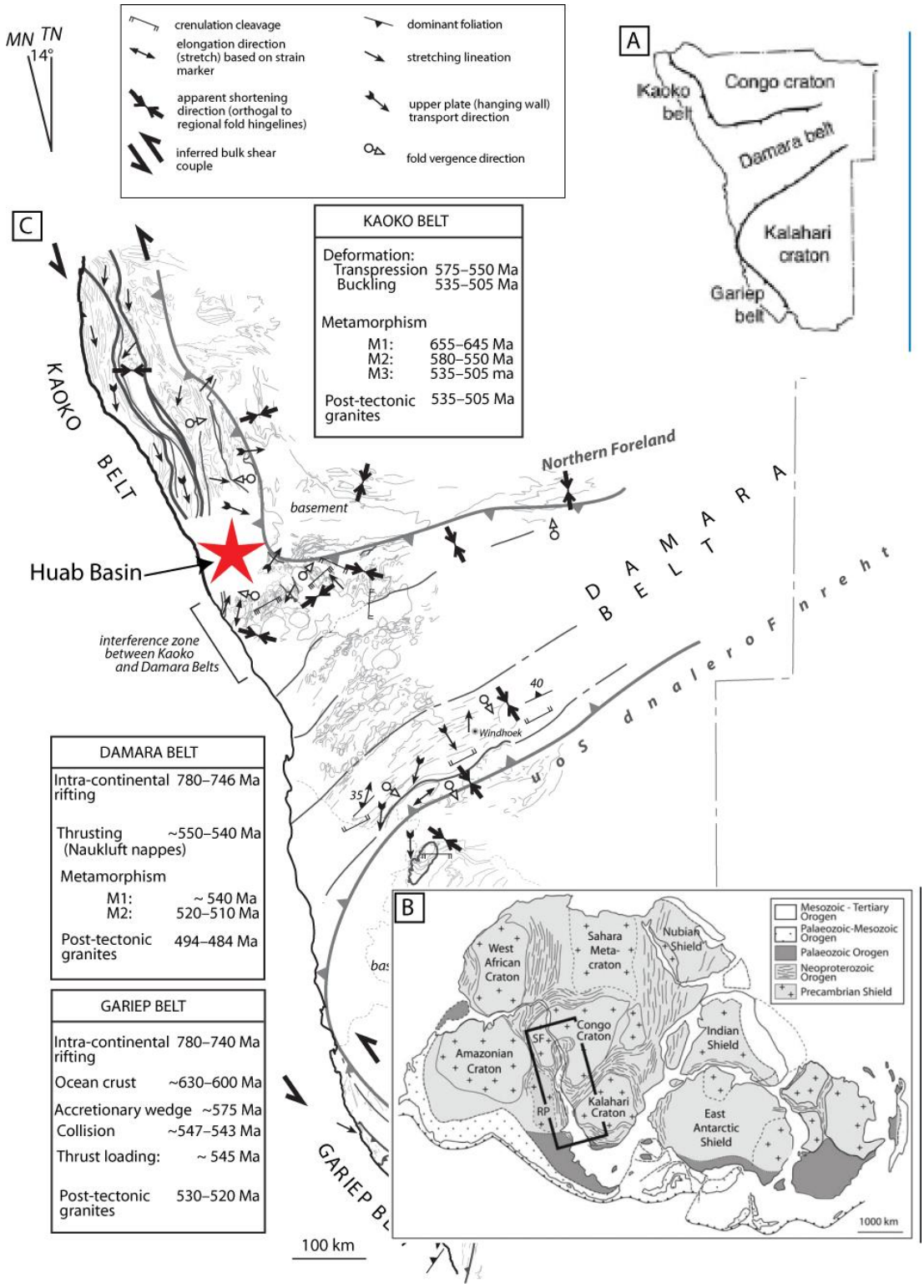

Fig. 2.1. (A) Sketch map of locations of the major cratonic basement zones in Namibia. (B) Map of Gondwana showing the locations of the cratonic belts that were created during the amalgamation of the constituents. (C) Map showing summary of the deformation and kinematic data for the Damara orogeny. Insets provide summary of geological timing of geological processes for the key fold belts. Location of the Huab Basin is indicated with a red star. Figure modified from those in Gray et al (2008).

2.2.3 The Karoo Supergroup- early intra-continental rift-fill and synrift sediments

The pre-Etendeka development of the Huab Basin is important, as to understand the long term extension (Stollhofen et al., 2000a) from the Carboniferous to the Cretaceous that preceded the eventual separation of Gondwana, into South America and Africa, to form the South Atlantic Ocean. The sedimentary fill and erosional hiatuses preserve the palaeoenvironmental and tectonic evolution of the area that led to the deposition of the Cretaceous sequence of interest in this thesis. The pre-Etendeka Group rocks comprise a Karoo succession that formed in a Karoo sub-basin; separate from the main Karoo foredeep related to the Cape Fold Belt (Wanke et al., 2000; Stollhofen et al., 2000a). Undifferentiated Karoo Supergroup is mapped as **PzKA**.

Basal Karoo deposits in the Huab Basin are the Dwyka Group (**CDw,** Fig. 2.2.) which comprise rare diamictites and thin turbidite units which accumulated in periglacial lakes (Jerram et al., 1999a). They preserve a maximum thickness of 15 m. Their deposition records the disintegration of the ice sheets covering southern Gondwana during the end of the Carboniferous (Stollhofen et al., 2000a). In Namibia the Dwyka Group was deposited in newly formed extensional fault systems comprising NW-NE trending grabens and half grabens regarded as early intracratonic rifts and in glacial topography, such as U-shaped valleys (Stollhofen et al., 2000a). The Dwyka Group formed during successive periods of glacial retreat, preserving four sequences, which are all preserved in southern Namibia (Visser, 1997; Stollhofen et al., 2000a). Palaeo-U-shaped valleys reflect the shape of the developing intracratonic basins, and define a depocentre which reflects the embryonic stages of a rift valley depression in Namibia during the latest

Carboniferous (~ 302 Ma) (Stollhofen et al., 2000a) (Fig. 2.3.). The mapping of the palaeoglacial features such as incised valleys and striations delineates Carboniferous rift axes (Fig. 2.3) that suggest the rifting in Namibia was approximately parallel to the Cretaceous rifting that opened the Atlantic (Stollhofen et al., 2000a). In the Huab Basin, Dwyka Group occurrences are confined to these incised glacial valleys (Jerram et al., 1999a).

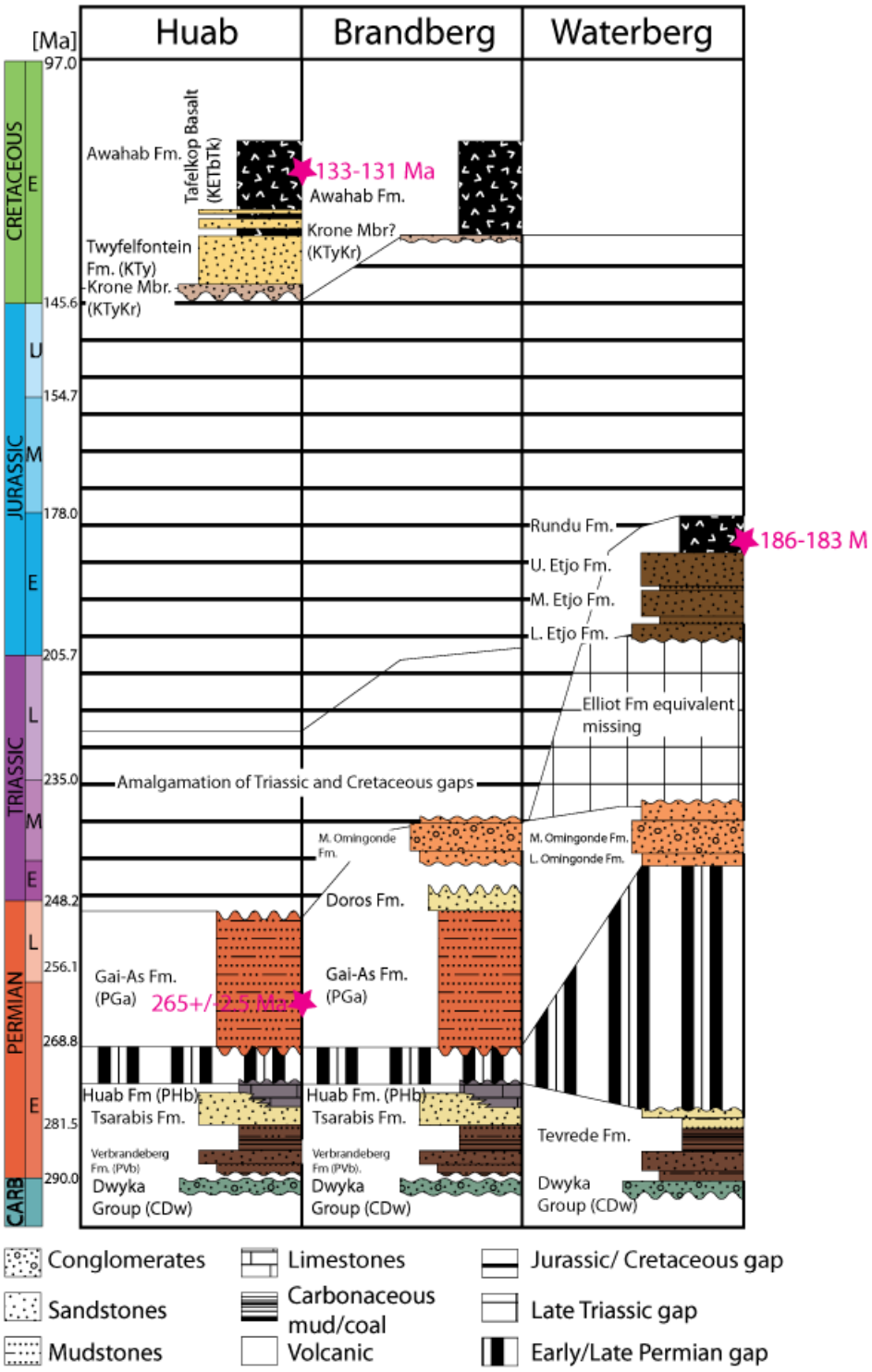

Fig. 2.2. Stratigraphy of the Karoo sequence in the Huab Basin and the Karoo at Brandberg (65 km from Huab) and Waterberg (270 km from Huab) adapted from Wanke et al (2000). Note major stratigraphical gaps and the absence of the Jurassic Etjo Formation in the Huab and Brandberg sections. Dates are shown in pink and are from Wanke et al (2000) and Stollhofen et al (2000a).

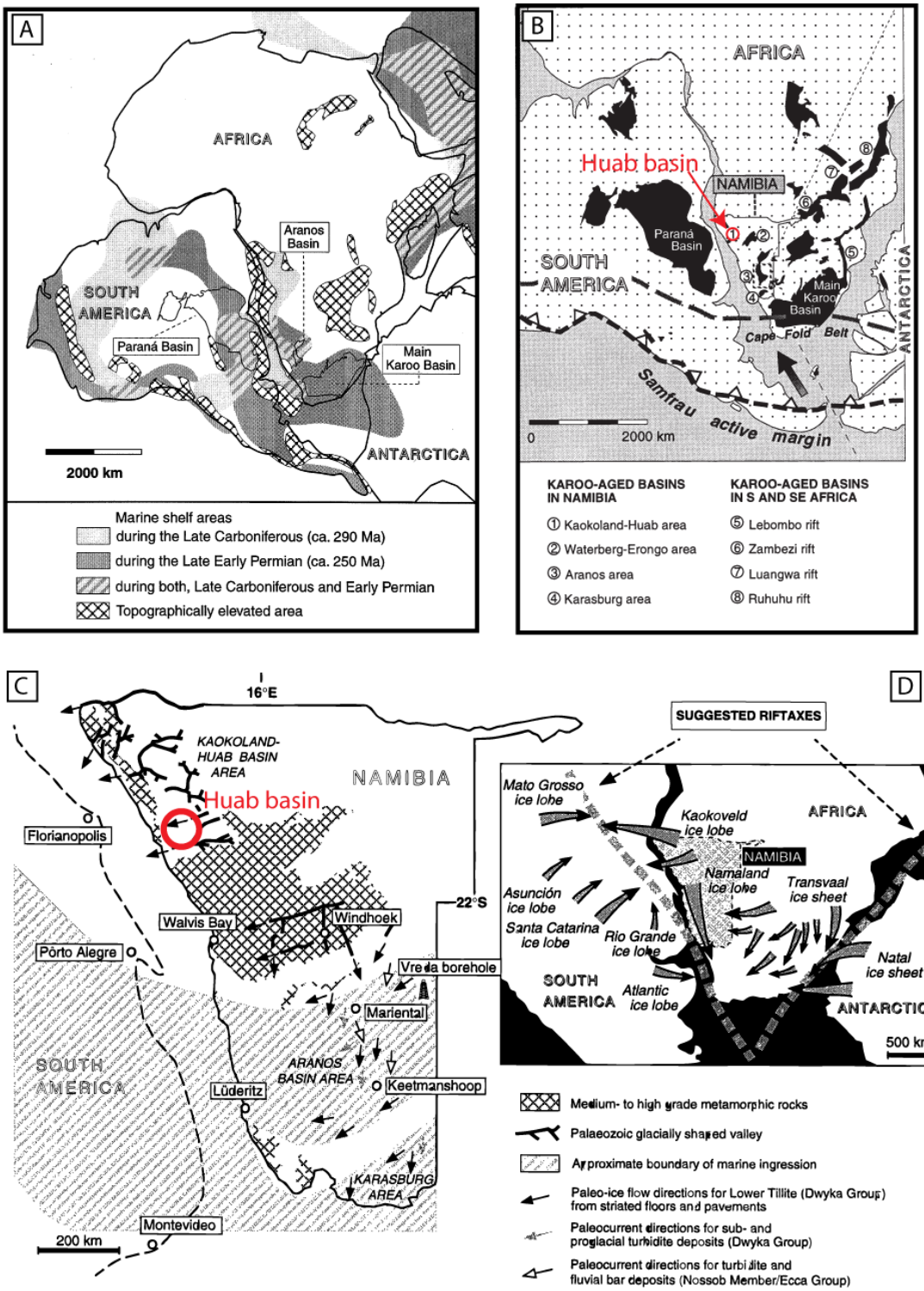

Fig. 2.3. Figures showing the distribution and palaeogeography of the Permo-Carboniferous Dwyka Formation and the development of the Karoo basins. (A) Map showing palaeogeography of Gondwana illustrating the Carboniferous transgression and the Permian transgressions. (B) Palaeogeographic reconstruction of south-western Gondwana at ~ 250 Ma. Surface outcrops of Karoo-aged rocks are in black and the Huab Basin (1) is highlighted. (C) Overview of evidence for a glaciated Gondwana, incised glacially shaped valleys exists in the Huab Basin. (D) Compilation of ice flow directions suggesting the existence of a rift valley depression (indicated). Figures modified from Stollhofen et al (2000a).

The Early Permian Verbrandeberg Formation (**PVb**) is dominated by carbonaceous mudstones, fine sandstones and thin, laterally restricted coal seams and is up to 70 m thick in the Huab Basin (Jerram et al., 1999a). The Verbrandeberg Formation covers the entire Huab Basin and is also present in the Waterberg area (Jerram et al., 1999a; Stollhofen et al., 2000a; Wanke et al., 2000). The Verbrandeberg Formation was deposited in cool-temperate post-glacial climates (Horsthemke et al., 1990) in a swampy flood basin environment with meandering rivers (Wanke et al., 2000). A single thin scoriaceous basaltic lava, up to 1.5 m thick is interleaved with the fluvial sediments and forma the only known Permian in-situ effusives in Namibia, possibly related to the widespread extensional activity at the time (Jerram et al., 1999a; Stollhofen et al., 2000a).

The cool-temperate, fluvial and swamp depositional system gradually changed during the deposition of the Tsarabis Formation which involves an upward transition from fluvio-deltaic to shallow marine near shore environments (Wanke et al., 2000) The unit represents two stacked transgressive cycles. The first cycle is meandering fluvial sandstones that grade upwards into plane bedded foreshore sandstones containing marine trace fossil *Siphonichnus*. The second cycle is a thin widespread unit of laterally amalgamated fluvial sandstone rapidly interfingering with foreshore sands (Jerram et al., 1999a). In the eastern part of the Huab Basin the Tsarabis Formation is condensed, exclusively comprising fluvial channel sandstones deposited in westward flowing rivers (Fig. 2.4.) (Jerram et al., 1999a). Silicified wood (Fig. 2.5.) is abundant in the Tsarabis Formation (Bamford, 2000) and based on known Main Karoo Basin biozones, the formation is equivalent to the Ecca and Beaufort Groups (Permian *Prototaxoxylon africanum, Araucarioxylon africanum* and *Araucarioxylon karooensis*).

The succeeding stromatolitic carbonates and shales of the Huab Formation (**PHb**)record a continuation of the transgression preserved in the Tsarabis Formation, and the establishment of warm Mediterranean climates (Wanke et al., 2000). The Huab Formation contains evidence for vast microbial blooms (Faure & Cole, 1999). A widespread bone bed (Fig. 2.5C.) containing abraded bones and teeth of *Mesosaurus tenuidens* esists in one maximum flooding surface in the formation (Jerram et al., 1999a; Wanke et al., 2000; Warren et al., 2001). The Huab Formation is the equivalent to the Upper Beaufort Formation bases on terrigenous plant remains (Bamford, 2000). Extension was ongoing at the time of deposition, evident in north trending synsedimentary normal faults and stromatolite drapes over growth faults (Jerram et al., 1999a).

Following the deposition of the Huab Formation was a significant hiatus (Jerram et al., 1999a; Wanke et al., 2000). Field evidence for the hiatus is in the abrupt change from marine dominated conditions (Huab Formation) to continental red beds of the predominantly lacustrine Late Permian/ earliest Triassic Gia-As Formation (Jerram et al., 1999a; Wanke et al., 2000; Stollhofen et al., 2000b). No angular unconformity is developed, but non-deposition and erosion are indicated by abundant pedogenic features (Wanke et al., 2000). The mudstone-dominated red beds contain an endemic bivalve association which provide the basis for a correlation with the Serrinha Member of the Rio do Rasto Formation in the Paraná Basin (Jerram et al., 1999a; Stollhofen et al., 2000b; David et al., 2011) (Fig. 2.4.). Up to five fallout tuff beds contained in the Gai-As Formation (**PGa**) preserve evidence of a distal volcanic province, possibly formed by a magmatic event fringing the southern margin of Gondwana (Fig. 2.4.) (Jerram et al., 1999a). The Tuff beds have been dated using U/ Pb zircon ages of 265 +/- 2.5 Ma (Wanke et al., 2000). The Gai-As

Formation has fossil woods of the Upper Beaufort in the Main Karoo Basin (Bamford, 2000). As in the older Karoo strata, northerly trending extensional faults are recorded by thickness and facies changes within the formation (Jerram et al., 1999a).

The Doros Formation conformably overlies the Gai-As Formation in part of the Huab Basin (Fig. 2.2.) and is composed of sheet-like fluvial sandstone with thin lacustrine mudstones and microbial limestones, including drying out features (mudcracks and evaporite replacement crystals (Jerram et al., 1999a).

A major stratigraphic gap is developed between the Karoo Supergroup and the overlying Cretaceous Etendeka Group in the Huab Basin (Wanke et al., 2000). The unconformity varies considerably in the Huab Basin, most commonly the basal Krone Member of the Twyfelfontein Formation incises into the Karoo sediments (Wanke et al., 2000). Deflation surfaces are also observed, particularly west of Gai-As (see Fig. 2.6. map and detailed map in the Appendix) (Wanke et al., 2000). The stratigraphic gap is thought to represent early stages of thermal uplift related to the early Cretaceous rifting phase (Jerram et al., 1999a).

The Karoo Supergroup in the Huab Basin, therefore records the episodes of extension and deposition and erosion related to the long-term rifting of Gondwana along a N-S axis from the Carboniferous to the earliest Cretaceous. The lattermost expression led to the Cretaceous rifting, igneous activity and later opening of the Atlantic. The Cretaceous sediments and igneous rocks are recorded in the Etendeka Group.

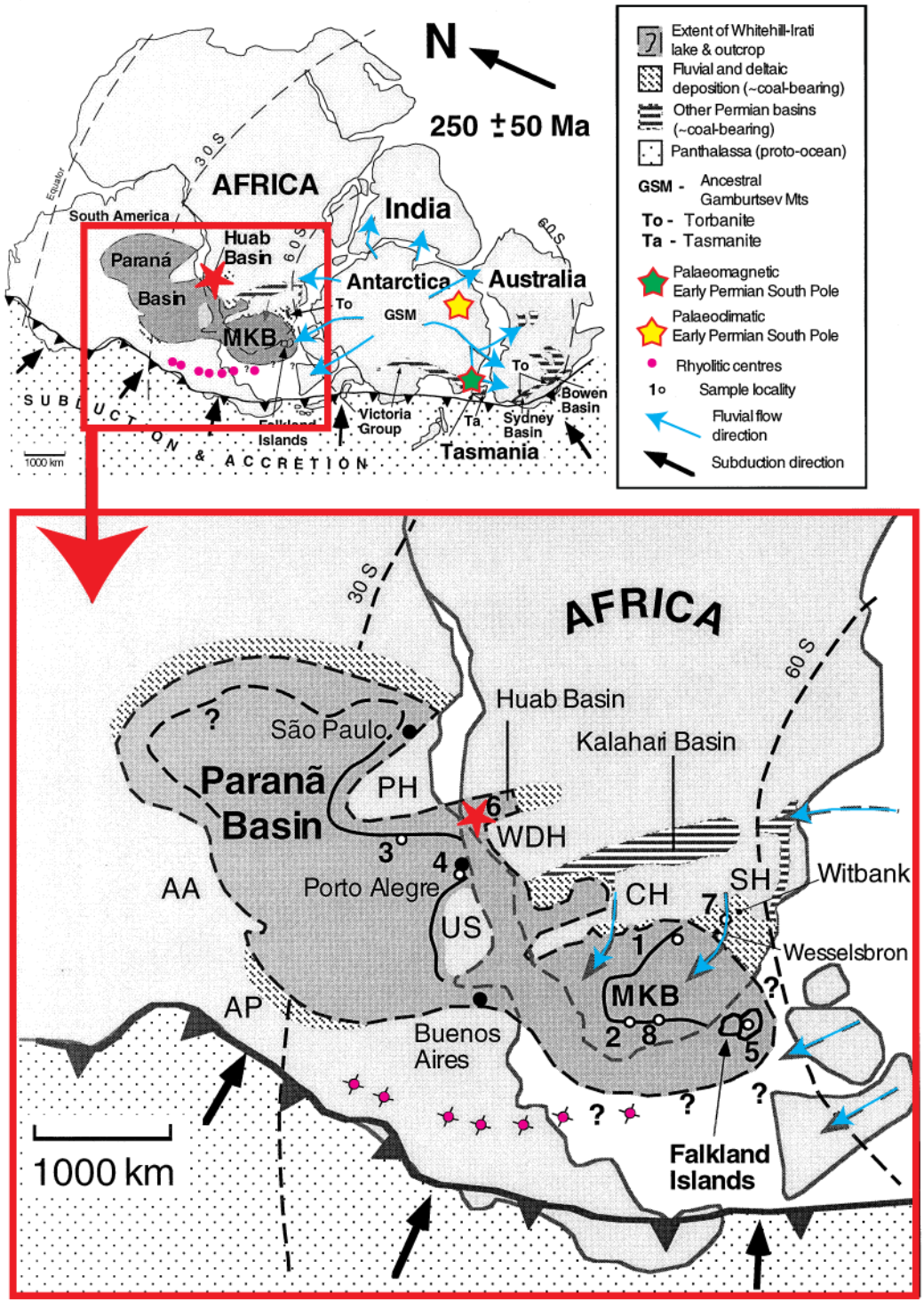

Fig. 2.4. Maps showing the extent of the Paraná, Main Karoo (MKB) and Huab basins in south-western Gondwana, in a 250 +/- 50 Ma palinspastic position. The maps show the Huab Basin, indicated by a red star. Blue arrows show the main fluvial flow direction. Maps modified from Faure & Cole (1999).

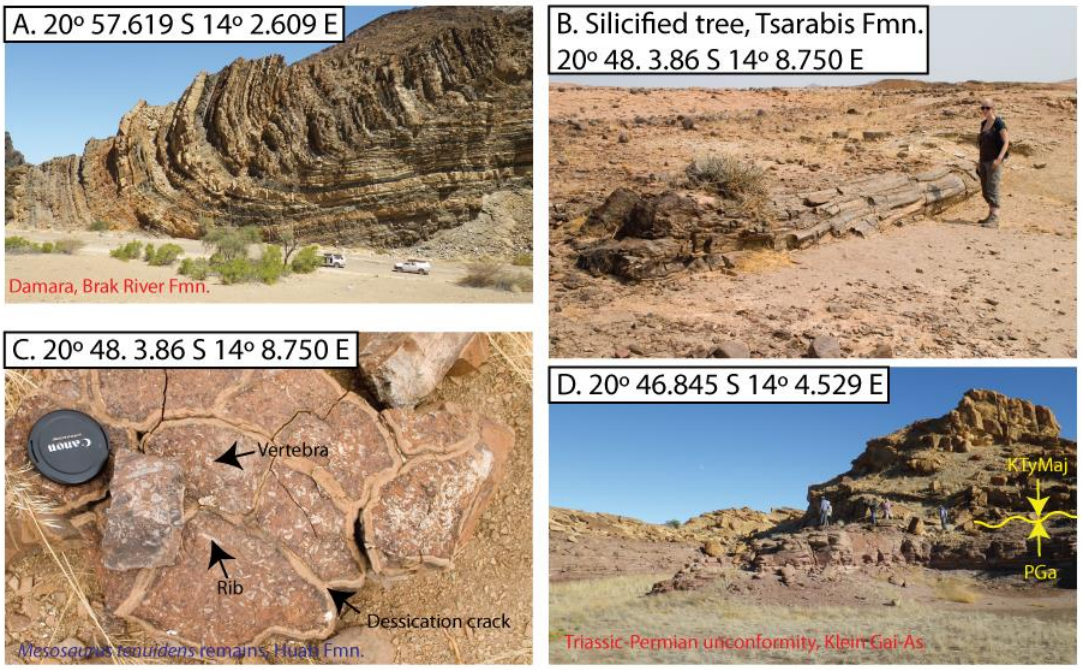

Fig. 2.5. Photographs showing the main pre-Cretaceous geology in the Huab Basin. (A) Neoproterozoic Damara Brak River Formation metamorphic rocks characteristic of the basement beneath the Huab Basin. (B) Silicified tree in the Permian Tsarabis Formation. (C) Remains of *Mesosaurus tenuidens* in the Permian Huab Formation within calcareous siltstones displaying prominent desiccation cracks. (D) Angular contact between the Permian Gai-As Formation (265 +/- 2.5 Ma) and the Major Erg unit of the Twyfelfontein Formation (132-133 Ma).

2.2.4 The Etendeka Group

The Lower Cretaceous Etendeka Group comprises fluvial and aeolian units of the Twyfelfontein Formation (**KTy**) (see below for naming of this formation) and the igneous rocks of the Etendeka Igneous Province (Peate, 1997; Jerram et al., 1999a). The basal sedimentary rocks of the Etendeka rest unconformably on the Karoo sequence (Fig. 2.2; Fig 2.5D.) with the stratigraphic gap representing c. 120 Ma (Wanke et al., 2000). The subaerial volcanic sequence interfingers and then overlies the sediments and is comprised of the eroded remnants of a thick sequence of basalts and rheoignimbrites (quartz latites) the entire sequence dated at 132 +/- 1 Ma (Renne et al., 1996; Marsh et al., 2001). Eight mafic magma types and 17 silicic magma types have been recognised in the province (Marsh et al., 2001). The Etendeka

Igneous province forms the eastern part of the Paraná-Etendeka continental flood basalt province (Hawkesworth et al., 1992; Milner et al., 1995a, b; Peate, 1997) and the basal sediments are equivalent to the same lithostratigraphical facies in Brazil (Scherer & Goldberg, 2007; Petry et al., 2007). Intrusive igneous rocks within the Etendeka Igneous Province (132 +/-1 Ma) are horizontal and subhorizontal dolerite sills (e.g. the Huab Sill Complex (Duncan et al., 1989)), vertical and subvertical dolerite dykes (Marsh et al., 1991; Thompson et al., 2001; Marsh et al., 2001) and large felsic to mafic subvolcanic ring intrusions (Marsh et al., 2001).

The Twyfelfontein Formation

The Twyfelfontein Formation is mapped and labelled in figures as **KTy** and subdivisions are labelled first according to stratigraphic position and second according to colour (see Fig. 2.6. and Fig. 2.7.).

For the gestation of the current name- the 'Twyfelfontein Formation' for the basal Etendeka Group sediments in the Huab Basin please read below. The Twyfelfontein Formation has been well studied from the sedimentological and stratigraphical perspectives (Horsthemke et al., 1990; Dickinson & Milliken, 1995; Mountney et al., 1998; Mountney et al., 1999a, b; Jerram et al., 1999a, b; Stanistreet & Stollhofen, 1999; Jerram et al., 2000a; Howell & Mountney, 2001; Jerram et al., 2002a, b).

The Twyfelfontein Formation is the lowest formation in the Etendeka Group and lies unconformably on the Karoo Supergroup in the Huab Basin (e.g. at Klein Gai-As, Fig. 2.5D.) and directly onto Damara basement at the basin edges (Jerram et al., 1999a).

The basal 10 to 15 m of the Twyfelfontein Formation comprises a poorly to moderately sorted pebble and cobble conglomerate termed the Krone Member (**KTyKr**) (Mountney et al., 1998; Mountney et al., 1999a). The Krone is well exposed west of Krone Farm (20° 29.183' S 14° 01.919' E, Fig 2.7. photo 1.) and south of the RYD outcrop (see Chapter 6 and 7) at (20° 37.365' S 14° 04.379' E), a small exposure also exists west of the RYD outcrop. The Krone Member is spatially restricted, being confined along the axis of the present-day Huab River and the region immediately to the north and south with tributary streams flowing north-westward into the major system (Mountney et al., 1998). For instance, the Krone Member is absent as far south as Klein Gai-As, where the later Major Erg (**KTyMaj**, see below) aeolian deposits rest directly on the Permian Gai-As Formation (Fig. 2.5D.). The Krone Member often has an erosive base that cuts down into the underlying Gai-As Formation and along the Huab River axis, further into the Tsarabis Formation (Mountney et al., 1998). The Krone Member was deposited by flash floods and ephemeral streams with drying out common, with material possibly derived from eroding scarps fringing the Huab Basin (Mountney et al., 1998).

The Krone Member conglomerates are overlain conformably by up to 30 m of mixed fluvial and aeolian sandstones (**KTyMix**) which record a transition from pebble dominated deposition to pure sand deposition (Mountney et al., 1998; Mountney et al., 1999a; Jerram et al., 1999a) which includes reworked aeolian material. Preserved aeolian bedforms within the mixed unit rarely exceed 2 m in thickness (Jerram et al., 1999a). This unit represents the transition from fluvial to aeolian facies and the aridification or falling water tables in the region (Mountney et al., 1998). A good outcrop of the mixed unit is at 20° 42.520' S 14° 06.160' E.

Above the mixed unit there is an abrupt transition to large-scale cross-bedded sandstones that dominate the Twyfelfontein Formation (Mountney et al., 1999a). This first aeolian unit has been termed the 'Main aeolian unit' by Mountney et al. (1998), Jerram et al. (1999a) and Mountney et al. (1999a), while Jerram et al. (1999b) terms the unit the 'Major Erg', which is adopted here (KTyMaj). The Major Erg deposition and sedimentology is described in detail be Mountney et al. (1998), Mountney et al. (1999a), and Mountney et al. (1999b). The Major Erg obtains a thickness of up to 150 m and consists of rounded fine to medium-grained red, yellow and white quartz rich sandstones showing high degrees of maturity (see below and Mountney et al., 1998; Mountney et al., 1999a). Individual bed-sets are typically 10 m thick, although single beds can reach 52 m thick in the basin centre (Mountney et al., 1999a). Individual transverse dunes preserved have heights up to 100 m with wavelengths of < 1 km (Mountney et al., 1999b). The thickness variation of the Major Erg is apparent when transecting from Klein Gai-As, via the main S-N track to the Huab River. At Klein Gia-As, the erg rests on the Karoo Gai-As Formation and is thin (~20-30 m), before being covered by the first basalts; this is towards the edge of the basin. At the RYD locality, the Major Erg rests on a pebbly Krone Member and is ~ 90-100 m thick and further north, it thickens further to the maximum thickness. These thickness variations and the onlapping relationship onto the Karoo at the basin margins delineate the Huab Basin. Within the erg, foresets consist of grainflow/grainfall cross-strata, with wind rippled sand deposits in the basal parts of sets (Mountney et al., 1999a). The onset of flood basalt volcanism uniquely preserved the dune forms, including topset beds, from which important information regarding aeolian bounding surfaces in the rock record in relationship to the bed forms that generated them have been studied (Mountney et al., 1999b; Jerram et al.,

2000). Palaeowind direction is common throughout the formation suggesting winds blowing from the SW to the NE (Mountney et al., 1998) common to the South American Botucatu Formation of the Paraná Basin, which is thought to be the source of the sand (Mountney et al., 1999b; Scherer & Goldberg, 2007).

The Major Erg deposits represent large-scale aeolian sand sea in a sand saturated system, with little control from water tables on dune geometry (Mountney et al., 1998). In this thesis, the diagenesis at the contact between Etendeka lavas from the Tafelkop type and the Tafelberg type and the Major Erg is investigated (Chapter 4.). The diagenesis and 'contact metamorphism' at the contacts between dolerite dykes and sills and the Major Erg is also investigated (Chapter 6.). Indirect diagenetic effects of the volcanic province on the Major erg are investigated in Chapter 7.

The Major Erg unit deposition was interrupted by the onset of flood basalt volcanism in the area. The Major Erg was progressively flooded with lava, which led to the unique preservation of the dune-forms in the Major Erg (Mountney et al., 1999b; Jerram et al., 2000; Jerram et al., 2002a). Aeolian deposition onto the surfaces of the first lava flows that is preserved has been termed the 'Upper Aeolian Unit' by Mountney et al. (1998), Mountney et al. (1999a), Jerram et al. (1999a) and the 'Minor Erg' by Jerram et al. (1999b). The latter nomenclature of Minor Erg (**KTyMin**) is adopted here. The Minor Erg comprises of laterally continuous major units of aeolian sand dunes occurring directly above the Major Erg in the succession (Jerram et al., 1999b) (see Fig. 2.7. for dune drowning sequence). The Minor Erg is distinct from the Major Erg because it occurs after the first period of flood basalt volcanism, which significantly altered the sediment mobility in the region, such that a bounding surface exists between the Major and Minor Ergs even where no basalt

exists (Jerram et al., 1999b). The first lavas were laterally discontinuous, which allows the Minor Erg to lay either directly on Major Erg *or* lava flow surfaces. The Minor Erg may be up to 60 m thick (e.g. north of the Awahab camp, see Appendix map). Palaeowinds for the Minor Erg are towards the NE, as in the Major Erg (Jerram et al., 1999b). The diagenesis and 'contact metamorphism' at the contacts between dolerite dykes and the Minor Erg is investigated in this thesis as well as indirect diagenetic effects (Chapter 6 and Chapter 7.).

Continued flood basalt emplacement dramatically reduced the amount of mobile sand in the basin (Mountney et al., 1998; Jerram et al., 2000), possibly also by restricting sand migration (the extrabasinal sediment source) from the Botucatu Formation in the west. The consequence was the cessation of large scale dune formation was: switching to discontinuous sand pockets in lava topography (Lava topography infill, Jerram et al., 1999b); bypass surfaces, where evidence of sand migration is preserved within shallow and deep cracks in the basalt lava flows (Jerram et al., 1999b) but no with overlying dune preserved between lava flows and; isolated barchanoid dunes (Isolated Dunes, Fig. 2.8.) resting on the lava surface, which can be single or multiple (i.e. 2 or more barchans linked) (Mountney et al., 1998; Jerram et al., 1999b).

The Isolated Dunes (**KTyId**) were transported towards the SE, markedly different to the Major Erg (Mountney et al., 1998; Jerram et al., 1999b). The change in direction may represent a regional change in dominant wind direction or restriction of sediment supply from upwind (SW), by lava flooding the erg to the west (i.e. flooding of the Botucatu Formation by Paraná lava flows) (Jerram et al., 1999b) in favour of a lower sediment yielding wind from the NW (Mountney et al., 1998). Isolated Dunes are well preserved throughout the Huab Outliers, within the

Tafelkop type lava, but are most spectacularly preserved in ‘Dune Valley to the SW of Mount Awahab (Fig. 2.6, Fig. 2.7.). In this thesis, Isolated Dunes are used to study the contact effects of lava emplacement (Chapter 4.), the diagenetic effects of dyke emplacement (Chapter 6.) and the indirect hydrothermal effects of the flood basalt on the sandstones (Chapter 7.).

The Twyfelfontein Formation records the aridification of the Lower Cretaceous palaeoclimate and the establishment of a large erg system (Jerram et al., 1999a). Contemporary and subsequent flood basalt volcanism and intrusive activity make it the ideal natural analogue for the study of the effects of igneous rocks on clean, reservoir quality sediment. The petrography and burial of the aeolian component of the Twyfelfontein Formation is discussed below, followed by a brief overview of the volcanology of the Etendeka igneous province.

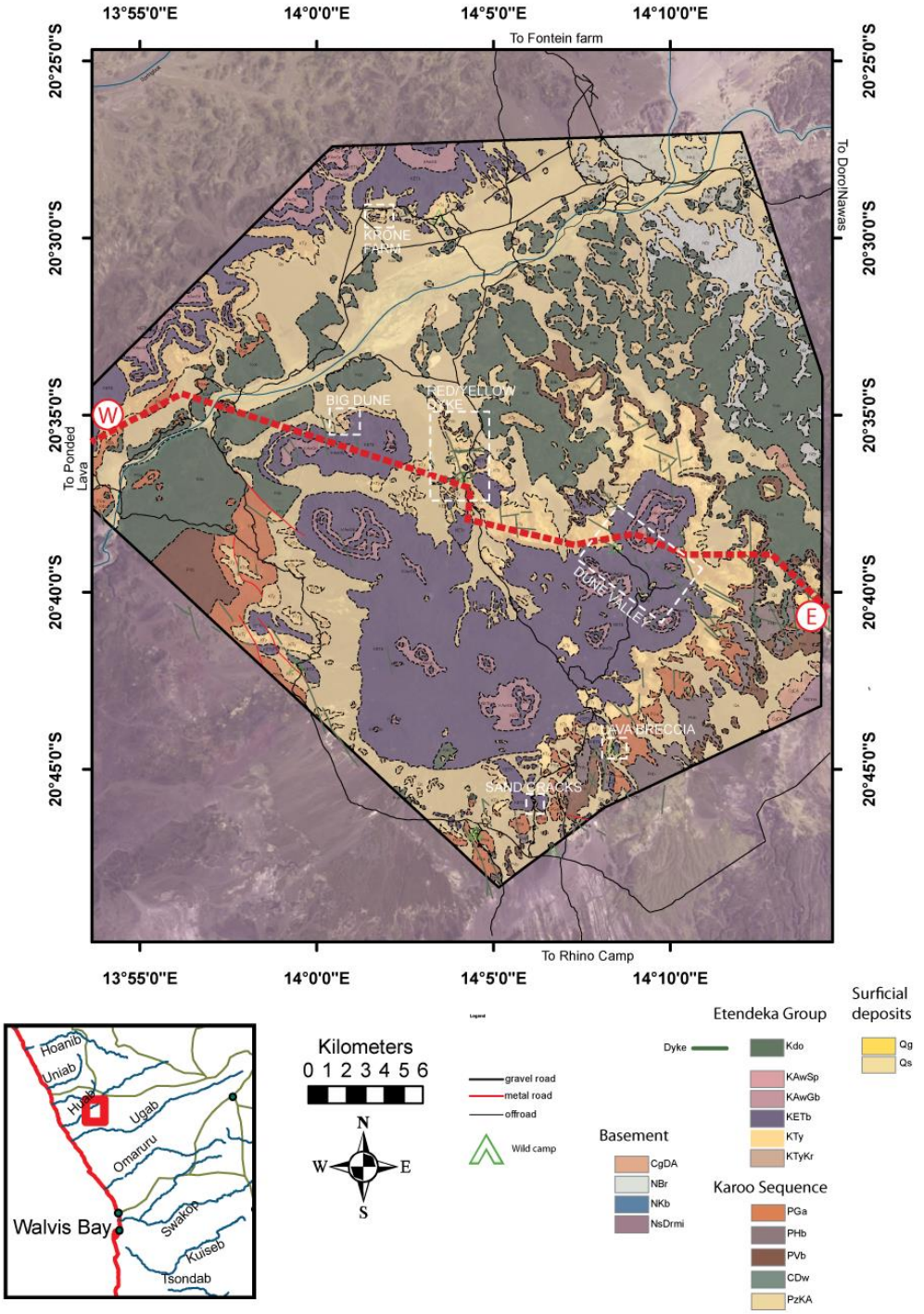

Fig. 2.6. 1:250 k geological map of the Huab Basin field area highlighting the key localities focussed on in this thesis. Correlation panel in Fig. 2.7. Is indicated. Geology is overlain on a Landsat 7 ETM+ image, bands 3, 4 and 1. For full map at 1: 50 k see the appendix.

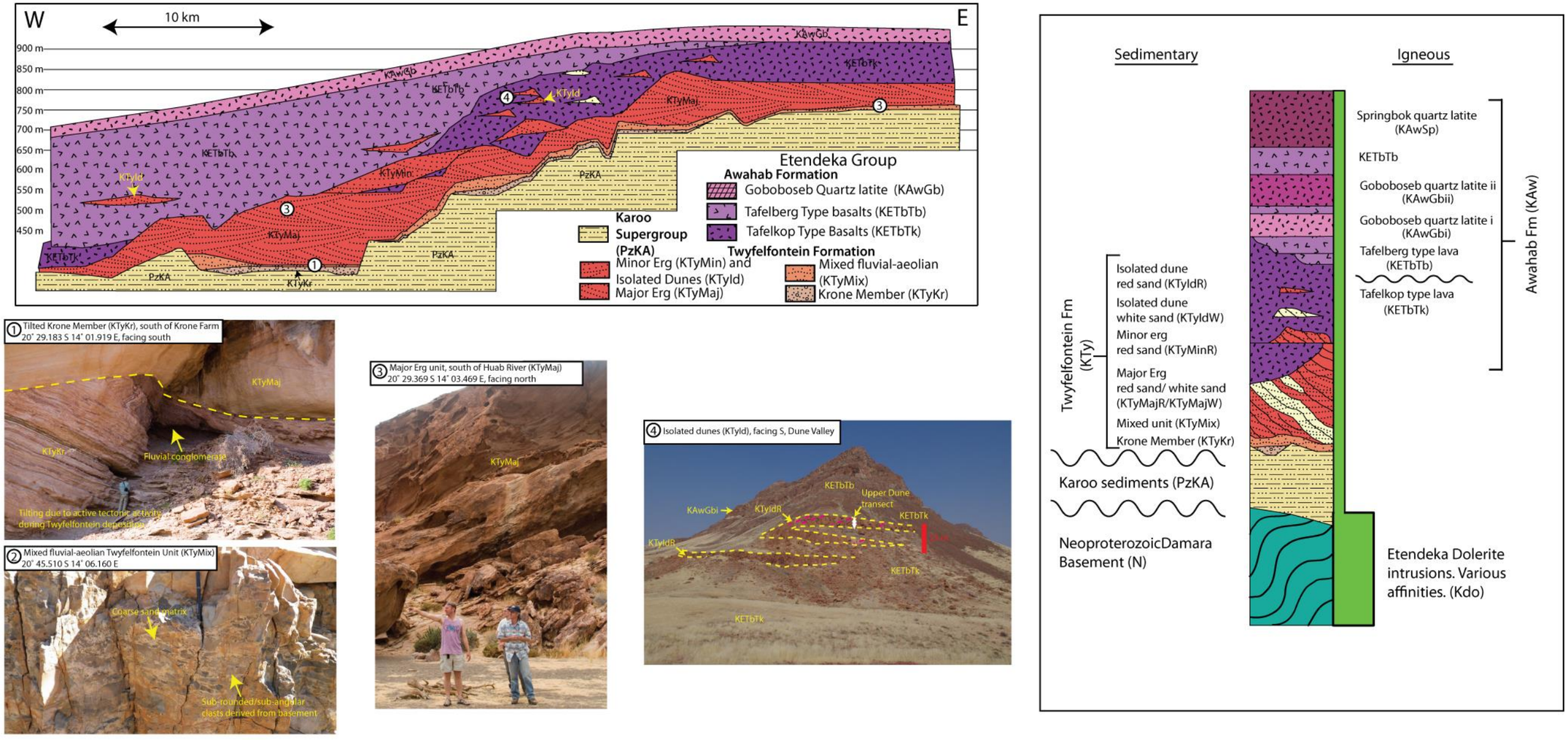

Fig. 2.7. Stratigraphical column with detail directed to the Cretaceous Twyfelfontein Formation and Awahab Formation applicable to the Huab Basin field area. Correlation panel adapted from Jerram et al (1999a) showing the distribution of the Krone Member, Mixed fluvial-aeolian unit, the Major Erg and the Isolated Dunes. The interaction with the Etendeka Lavas is also apparent, the Tafelkop basalt predominates in the ease and is earlier than the Tafelberg type basalt that onlaps the Tafelkop lava field from the west. Photographs of the key Twyfelfontein Formation units: (1) The Krone Member, here with a neotectonically induced angular unconformity under the Major Erg unit. (2) A fluvial bed from the mixed unit. (C) The major Erg unit showing large-scale dipping foresets. (4) Isolated dunes within Tafelkop basalt, which is onlapped further up the succession by the Tafelberg basalts.

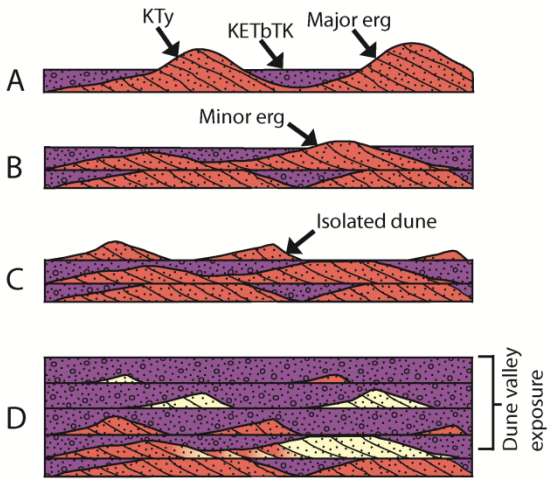

Fig. 2.8. Schematic diagram of passive drowning of Twyfelfontein erg system in the Huab Basin by Lower Cretaceous Basalts (mainly Tafelkop type basalts in Huab Outliers south of Huab River and a mix of Tafelkop & Tefelberg type basalts along the main river sections). The transverse draa dominated major erg is first drowned (A) which restricts sediment mobility. Remaining unburied sediment reworks to form minor erg (B) and bypass surfaces where sand infiltrates basalt cooling cracks but does not form dunes. The minor erg is then drowned by lava. Further lava drowning isolates more sediment from the active aeolian system creating a sediment poor aeolian system of isolated barchanoid dunes (C) which are themselves drowned by lava. Successive drowning locks up more sediment until no more dunes are formed on lava surfaces (D). This is followed by differential diagenesis to form red and white sandstone. Drowning sequence modified from Jerram et al., (1999a & 2000).

Naming of the Twyfelfontein Formation

The Twyfelfontein Formation is the current name applied to the Lower Cretaceous fluvial to aeolian sequence in the Huab Basin Area. The formation has undergone recent name changes and has only recently been universally accepted as the Twyfelfontein Formation. The current name, the Twyfelfontein Formation was proposed by Stanistreet & Stollhofen (1999) based on the compilation of accurate biostratigraphic dating of the (true) Early Jurassic Etjo sandstone at Mount Etjo and Waterberg, which does not correlate to the Huab Basin sandstones that are associated with the radiometrically dated Etendeka basalts (~133-132 Ma, Renne et al., 1996; Wanke et al., 2000). The name was subsequently recommended to be incorporated

into the Etendeka Group by Marsh et al. (2003). Twyfelfontein Formation is the name used on the latest Namibia Geological Survey map (Schreiber, 2006).

The Twyfelfontein was formerly included within the upper Karoo Sequence as the Etjo Formation, which also crops out at Waterberg and Mount Etjo (Dickinson & Milliken, 1995). The Etjo is correlated with the Cave Sandstone of eastern South Africa (Fig. 2.11.)(Stanistreet & Stollhofen, 1999). Horsthemke et al, (1990) assigned an uncertain age of uppermost Triassic to lowermost Cretaceous in the Huab Basin and recognised the interfingering with the Etendeka lavas, which at the time were 'believed' to be Lower Cretaceous, further they recognised the potential correlation with the Botucatu Sandstone in Brazil based on palaeo wind directions. The Botucatu Sandstone is Lower Cretaceous (e.g. Scherer, 2000). Milner et al. (1994) upgraded the Etendeka succession to group status and assigned the Etjo Sandstone Formation as the basal formation of the Etendeka Group.

In the late 1990's reliable dating of the igneous rocks interbedded with the (at the time) Etjo Formation produced Lower Cretaceous ages. The first reported reliable dating produced ages of 137–124 Ma (Milner et al., 1995b) (Rb-Sr and $^{40}Ar/Ar^{39}$), which was further refined by Renne et al, (1996) using $^{40}Ar/^{39}Ar$ dating to 131.7 +/- 0.7 to 132 +/- 0.7 Ma. The intimate relationship between the Major Erg and Isolated Dune units of the aeolian sandstone and the basalts clearly demonstrated that the Etjo formation in the Huab Basin was of Cretaceous age and not, as formerly thought, Jurassic (186-183 Ma).

Research on the deposition of the Etjo Formation in the Huab Basin in the late 1990's continued to use the name Etjo Formation (Mountney et al., 1999a; Jerram et al., 1999b) or the Cretaceous Etjo Formation (Mountney et al., 1998; Mountney et al., 1999b; Jerram et al., 1999a); these contributions recognising the

Lower Cretaceous age. The Stanistreet & Stollhofen (1999) proposal of the new name of the Twyfelfontein Formation was published prior to Jerram et al., 1999a, but the continued use of the old name was justified, as the name Twyfelfontein Formation was not widely known; this is understandable considering the contemporary use of the Etjo Formation name in the spate of research on-going at the time. Jerram & Stollhofen (2002) were the first, after the initial suggestion by Stanistreet & Stollhofen (1999) to formally adopt the new name of Twyfelfontein Formation. The use of Twyfelfontein Formation removes all confusion with the Jurassic Etjo Formation of the Karoo in Namibia and is therefore the current name in use (e.g. Schreiber, 2006).

Petrography and non-volcanic-related diagenesis of the Twyfelfontein Formation

This is a description of the petrography of the aeolian units of the Twyfelfontein Formation, where the sandstone is not affected by direct or indirect diagenesis resulting from igneous activity. This is taken to be sandstones with a porosity of > 8 %, where the detrital grains are fully or partially coated with haematite, giving the sandstone a red appearance.

Of the 123 Twyfelfontein Formation sandstone samples analysed, 14 were >8 % porosity and red from the Isolated Dunes and 27 were >8 % porosity from the Major Erg and the Minor Erg. The remaining 83 samples (+ some oddities, basalt, dolerite etc.,) were either white sandstone, or indurated as a result of igneous activity (lava flows or intrusions).

The Twyfelfontein Formation is a highly mature sandstone. Mica is absent as a detrital component and lithic grains are rare, typically forming < 1 %, with a maximum of 1.8 % and several samples returning zero lithic grains. Fig 2.9 and Fig.

2.10 show ternary plots of the Twyfelfontein Sandstone with detrital modal percentages plotted (as % of detrital grains). All feldspar in the red sandstone > 8 % porosity (n= 41) is 25.8%, with a 1σ of 4.5. The background red sandstone therefore plots as a borderline subarkose-arkose (after Pettijohn et al., 1973; Tucker, 2001). This classification is in contrast with Mountney et al. (1998) and Dickinson & Milliken (1995) who classified the unit as a litharenite-sublitharenite, which would require 25 % lithic fragments (Tucker, 2001), which is inconceivable based on these data presented in this thesis. True litharenite-sublitharenite sandstones are quite rare, with most sands that contain large numbers of lithic clasts also containing significant proportions of feldspar, making a feldspathic litharenite (e.g. Taylor et al., 2010). Further litharenite-sublitharenites do not commonly exist in the tectonic and geological situation here, instead being characteristic of back-arc or fore-arc settings (Tucker, 2001). The subarkose-arkose composition reported here, for the red samples >8 % porosity, is consistent with the passive margin, transitional continental setting (Tucker, 2001). The detrital composition reported in this thesis is also approximately equal to the Botucatu Formation, Brazil (personal communication, Claiton Scherer, 2012).

It can be seen in Fig. 2.9 that the variability in the detrital composition of sandstone with >8 % porosity is less than the variability of sandstone with <8 % porosity. This is due to the lower porosity sandstone being affected by the flood basalts preferentially consuming detrital phases. Similarly in Fig 2.10, a more sophisticated analysis of the full dataset including samples affected by sill emplacement (pyrometamorphism- see below). This also shows that samples affected by flood basalt related diagenesis have more variability. The average values for red and white sandstones are plotted for >8 % porosity and <8 % porosity. Both

red and white >8 % porosity have a larger proportion of quartz, reflecting the dissolution of feldspar in these samples and the formation of diagenetic quartz arenite and diagenetic subarkose from more feldspar rich protolith. The final population that stands out in Fig. 2.10 is the red dots representing the pyrometamorphic buchite formed where detrital feldspar has melted, leaving a diagenetic quartzite (e.g. Grapes, 2010). **Buchite**- a vitreous metamorphic rock produced by the contact metamorphism of basaltic magma.

Most heavy minerals are rare in the Twyfelfontein Formation. Detrital zircons, amphibole and epidote were encountered during petrographic analysis, with epidote being the most common. Detrital epidote was point counted in five of the 123 Twyfelfontein Formation samples analysed. Detrital amphibole was encountered in two samples. Zircon was not encountered under examination with conventional light microscopy, but was encountered during SEM analysis, where a perfect euhedral crystal was confirmed using EDS. The most common heavy minerals in the formation is ilmenite and magnetite, which make up the bulk of detrital opaque grains. Ilmenite was confirmed in XRD in some samples and is thought to be deposited into placer deposits within dunes. Both ilmenite and magnetite can be observed behaving in this way in the modern Namib Desert south of Swakopmund (22º 41' S 14º 32' E).

The observed heavy mineral assemblage suggests the source rocks for the Twyfelfontein Formation were granitic basement rocks, with some influence from basic igneous rocks (ilmenite) (cf. Tucker, 2001).

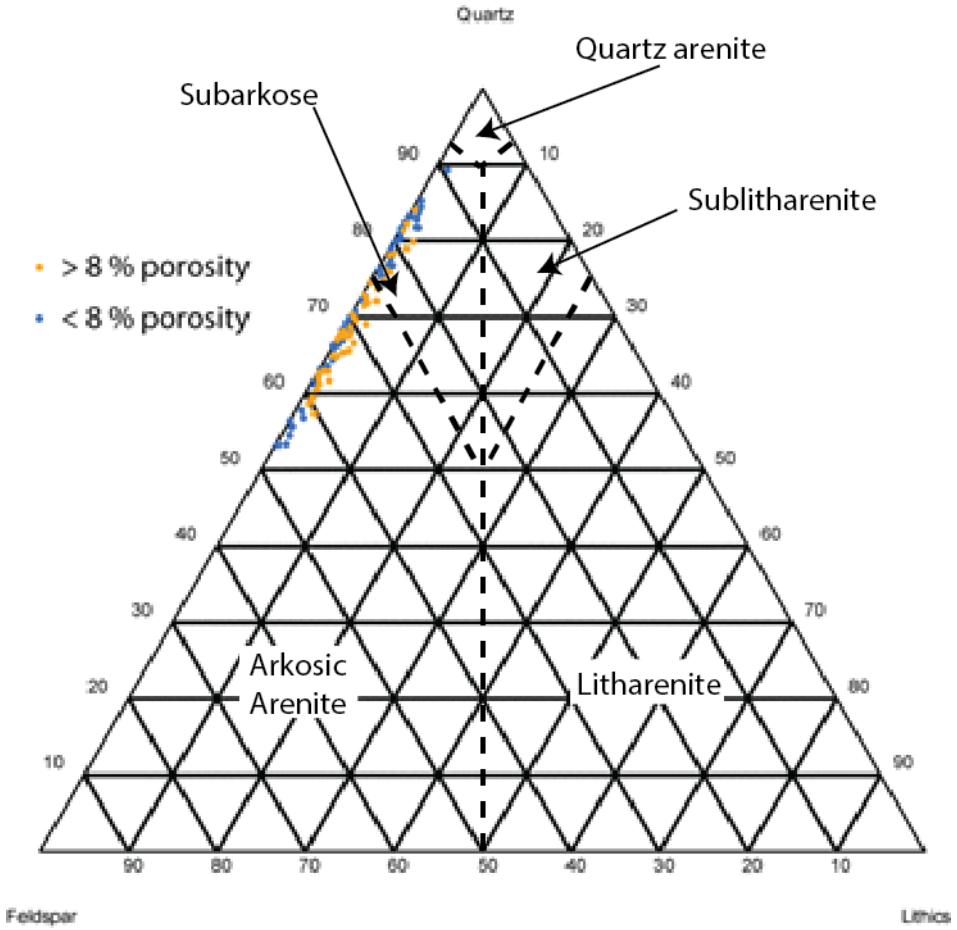

Fig. 2.9. Ternary plot of the quartz, feldspar and lithic components of all sedimentary samples collected (except for pyrometamorphic samples) separated into > 8 % porosity and < 8 % porosity. Lower porosity sandstones show more feldspar variation due to diagenetic processes, whereas the high porosity sandstones show less variation. Most samples plotting as subarkose arenites, with some as diagenetic quartz arenites and more the feldspathic as arkose.

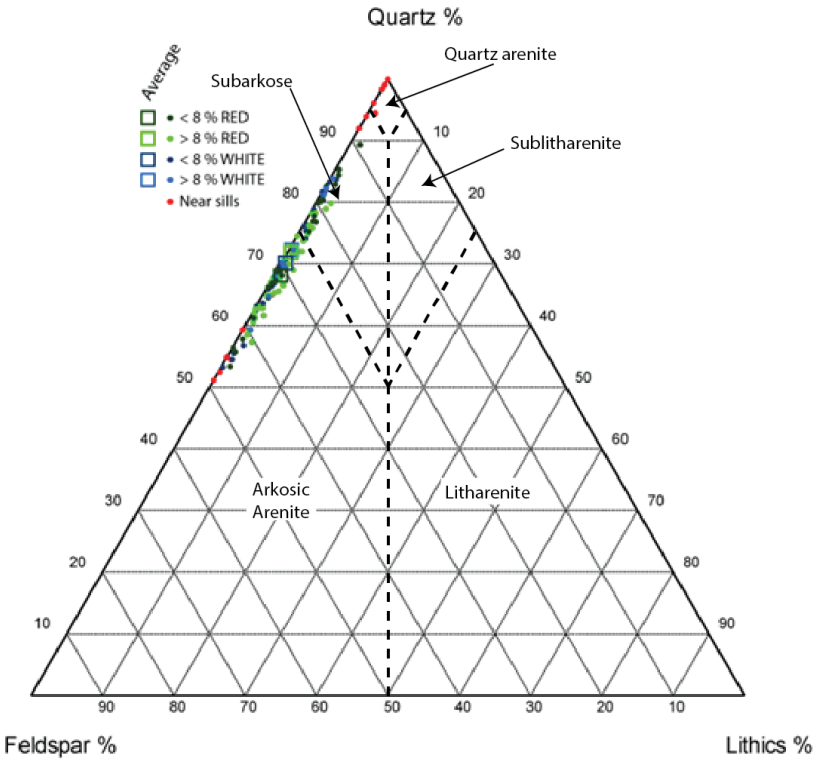

Fig. 2.10. Ternary diagram of the detrital composition of the Twyfelfontein Formation samples, separated by porosity and by diagenesis (red or white). White sandstones affected by hydrothermal fluids show slightly more variation but the average values are all clustered in the arkose–sub-arkose border. Red sandstones are more arkosic than the diagenetic white sandstones due to feldspar dissolution affecting the white sandstones during hydrothermal activity.

In the red sandstones (>8 % porosity), the record of early diagenesis is minimal, due to the arid palaeoenvironment and minimal organic activity, not favouring early authigenic cementation. This compares with the sandstone affected by lava emplacement, which is characterised by early diagenesis (Chapter 4, Chapter 5). The red porous sandstone diagenesis is characterised by processes that occurred during burial. The most important process recorded is compaction, which has been quantified based on the equations in Lundegard (1992). The average compaction component of porosity loss (COPL) in the red porous sandstones is 37.6 % for the porous red isolated dunes (KTyIdR) and 39.4 % for the Major Erg. The assumed depositional porosity of 49 % is taken from Lundegard (1992) and is based on

reported field measurements. The compaction observed is accommodated by mechanical reorganisation of framework grains, resulting in closer packing, pressure solution (cf. Renton et al., 1969; Rutter, 1983; Houseknecht, 1984, 1988; Tada & Siever, 1989) between quartz grains (feldspar grains almost always penetrate quartz) and brittle deformation compaction (reported in the Twyfelfontein by Dickinson & Milliken, 1995). The brittle compaction is evident in both quartz and feldspar detrital grains, but is particularly evident in feldspar grains, where fracturing accommodating compaction occurs along cleavage planes (Fig. 2.11B,E, G.). Pressure solution is evident as the large number of sutured grains present (Fig. 2.11.) and through cuspate embayments that are common.

Mineral authigenesis within the red sandstones in minor and is quantified as a component of porosity loss using Lundegard's (1992) cementational porosity loss (CEPL). Average CEPL for the red porous Major Erg is 1.9 % and for the red porous Isolated Dunes is 2.9 %. The most important authigenic mineral is quartz in the form of syntaxial overgrowths on detrital quartz grains (Fig. 2.11G.) which probably formed during pressure solution compaction (e.g. Tada & Siever, 1989). Calcite is present in some samples as minor replacement of plagioclase, but rarely growing into pore space (cf. Chapter 4, Chapter 6 and Chapter 7.). Clay mineralisation is minor and is usually confined to within detrital feldspar grains, where it is impossible to state whether the clay authigenesis was prior or after deposition. Very rare albite overgrowths exist on detrital plagioclase, where extinction and twinning is syntaxial with the detrital grain.

The relatively simple diagenesis of the porous red Twyfelfontein Formation sandstone makes it ideal for the study of the indirect and direct effects of flood basalt volcanism.

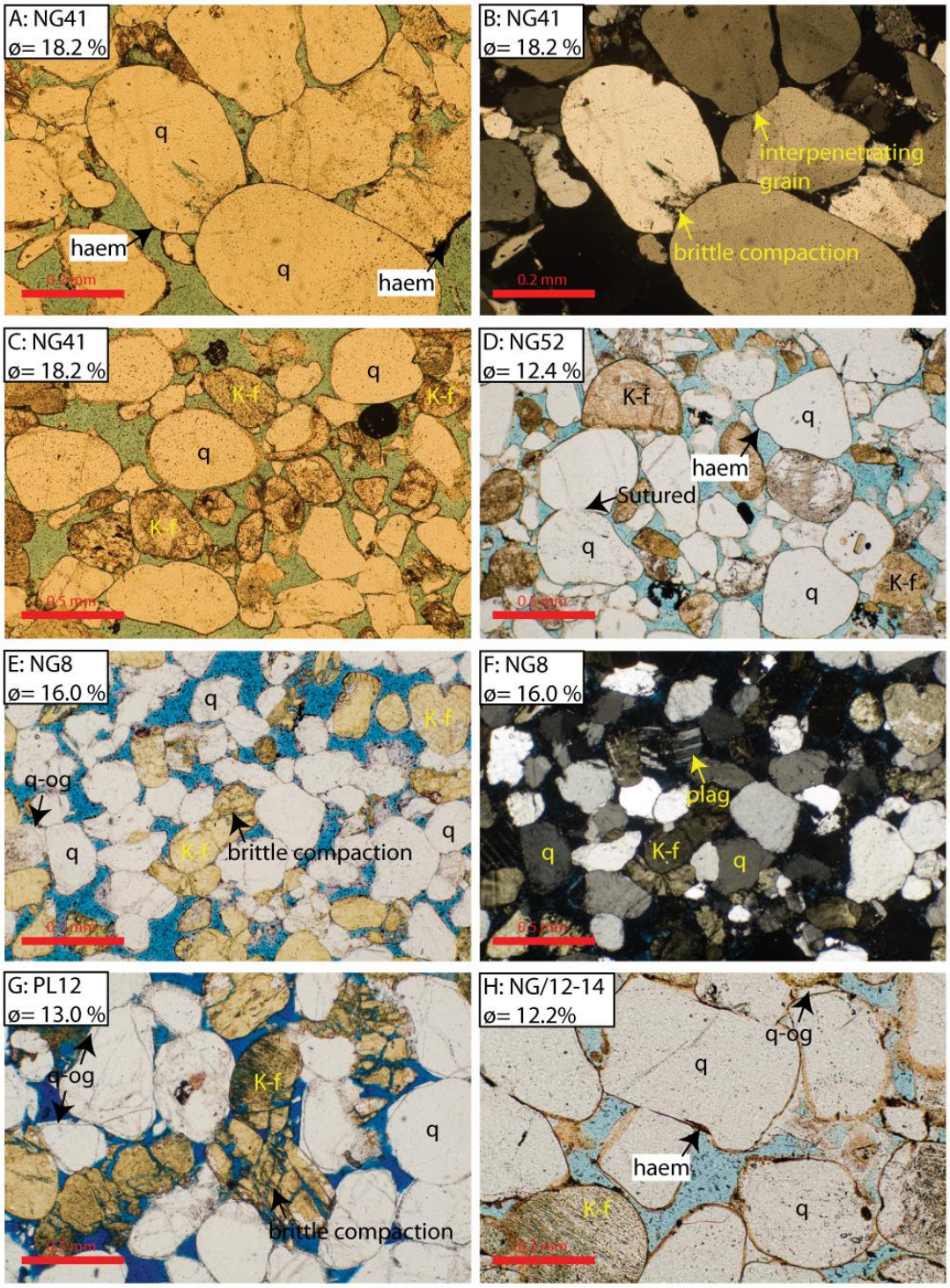

Fig. 2.11. Photomicrographs of Twyfelfontein Formation sandstone away from the influence of igneous rocks, which can be taken as 'normal' Twyfelfontein Formation. (A PPL, B XPL, C PPL) 18.2 % porosity sandstone displaying many of the features typical for the formation: rounded detrital grains coated with haematite that interpenetrate

and show evidence of brittle compaction. (D PPL) Sample NG52, which is used throughout the thesis as a 'normal' sandstone for comparison. (E PPL) Sandstone showing a finer grain fall layer, containing both plagioclase and potassium feldspar. Quarts overgrowths are occasionally present. (F XPL) same as E in XPL. (G PPL) 13.0 % porosity sandstone showing compaction by brittle deformation of feldspar component, grain interpenetrations of quartz. Porosity loss is also through quartz authigenesis. (H PPL) Sample showing haematite grain coatings and occasional quartz overgrowths in a 12.2 % porosity sandstone.

2.2.5 Burial and exhumation of the Twyfelfontein Formation

There are four methods in which the burial depth of the Twyfelfontein Formation can *easily* be estimated. The first two: (A) correlation with exposed stratigraphy to give an overburden thickness, and (B) apatite fission track analyses from the literature (e.g. Raab et al, 2005). The final two, come from data collected in this study. (C) Porosity (or Porosity minus cement (Pmc) where cements are present) values can be directly compared to trends from large porosity-depth datasets (e.g. Gluyas & Cade, 1997). Secondly, compaction calculations at vertically separate locations within the same formation can be compared to the same parameters from larger datasets (in this case calculated from Gluyas & Cade, 1997) and back calculated to the surface.

Figure 2.12A Shows the hydrostatically pressured, uncemented, rigid-grain sandstones from Gluyas & Cade (1997) and the average porosities from the isolated dune and the Major Erg units of the Twyfelfontein (with 1σ error bars) not directly or indirectly affected by igneous activity (porosity > 8 %). The isolated dune plots at 4.91 km deep and the Major Erg at 5.15 km deep, showing a difference in burial depth based on porosity of 240 m. The difference (240 m) is slightly less than field observations of outcrops in the Huab area (536 m). The disparity may be due to not taking into account that some of the samples have low abundances of authigenic cements. This discrepancy is within the plotted 1σ error. Some of the samples have minor authigenic quartz cements, generally less than 1 %. A more sophisticated technique is therefore to factor in this cement by adding the cement volume to the porosity to get the uncemented pore volume (Pmc) (Fig. 2.12B.). When compared to the sandstones presented in Gluyas & Cade (1997) the Isolated Dunes give a depth of

4.24 km and the Major Erg, 3.61 km. This produces a vertical separation of 630 m, which is closer to the observed value of 536 m than simply comparing porosities. Simply using Pmc does not account for bulk volume changes during compaction; using COPL (Lundegard, 1992) (See Chapter 3 also), which accounts for bulk volume loss goes a way towards solving this problem.

Figure 2.12C shows Compactional Component of Porosity Loss (COPL) calculated for the hydrostatically pressured, uncemented, rigid-grain sandstones from Gluyas & Cade (1997). The COPL calculation has been made according to Lundegard (1992) assuming an initial depositional porosity of 44.75 % (also from Lundegard, 1992). When the average COPL for the isolated dunes is plotted, the burial depth is estimated as 4.66 km. The Major Erg burial depth is estimated as 5.20 km, giving a difference of 541 m, approximately equal to the vertical difference between the isolated dunes sampled in 'Dune Valley' and the RYD lava pond case study at the top of the Major Erg, south of the Huab River (536 m). The close match between the calculated difference and the field measured difference, when using COPL (compared to just using Pmc or porosity) is probably due to COPL taking into account volume loss and cement component of porosity loss. Such a close match gives great confidence in the use of the COPL technique throughout this thesis.

Observed porosity, Pmc and COPL values have also been compared to the porosity–depth curve for uncemented quartz arenite by Emery & Robinson (1993) (Table. 2.2.), which universally overestimates the burial depth compared to all other methods.

So how deep was the Twyfelfontein Formation buried? Comparisons with the dataset for hydrostatically pressured, uncemented, rigid grain sandstones from Gluyas & Cade (1997), with COPL calculated appear to best match the apatite

fission track analyses data of Raab et al (2005), and best match the observed vertical separation between the Isolated Dunes and Major Erg. The likely average maximum burial depth is therefore ~4.6 km for the Isolated Dunes and ~5.2 km for the Major Erg unit. The close match between the calculated separation between the Isolated Dunes and the Major Erg unit using COPL and the Gluyas & Cade curve gives confidence in the burial estimate by this method.

Method	Isolated Dune depth	Major Erg depth
Apatite Fission Track (base of Brandberg at land surface today) (Raab et al., 2005)	5 km	
Stratigraphy Based on total Etendeka lava thickness (e.g. Peate, 1997; Jerram, 2000b; Jerram *personal communication*).	3 km to 4 km	
Porosity cf. Gluyas & Cade, 1997	4.91 km	5.15 m
Porosity Robinson & Gluyas, 1992	9.16 km	10.37 km
COPL cf. Gluyas & Cade, 1997	4.66 km	5.20 km
Pmc cf. Gluyas & Cade, 1997	3.61 km	4.24 km
Pmc Emery & Robinson, 1993	4.91 km	6.59 km

Table. 2.1. Summary of burial depths from 2.5.2.

This approximate depth of 5 km is more than can be estimated by using the thickness of Etendeka stratigraphy, suggesting there has been erosion of rock units deposited in the Cretaceous (uplift and erosion began between 60 Ma and 80 Ma, Raab et al., 2005) that are not preserved anywhere in the Etendeka. The Etendeka

lava pile could have been much thicker than is currently preserved (by about 1 km to 2 km).

It should be mentioned that basalt (i.e. the Etendeka overburden) is denser than a siliciclastic overburden, so the observed compaction for a given burial depth is likely to be overestimated compared to the equivalent siliciclastic overburden. For this reason the figure of ~ 5 km is probably a slight overestimate; although the close match between COPL calculated vertical separation and the true vertical separation between the Isolated Dunes and the Major Erg may show that the increased density of basalt does not make as significant difference in this regard. This new information may be of importance for petroleum exploration offshore Namibia.

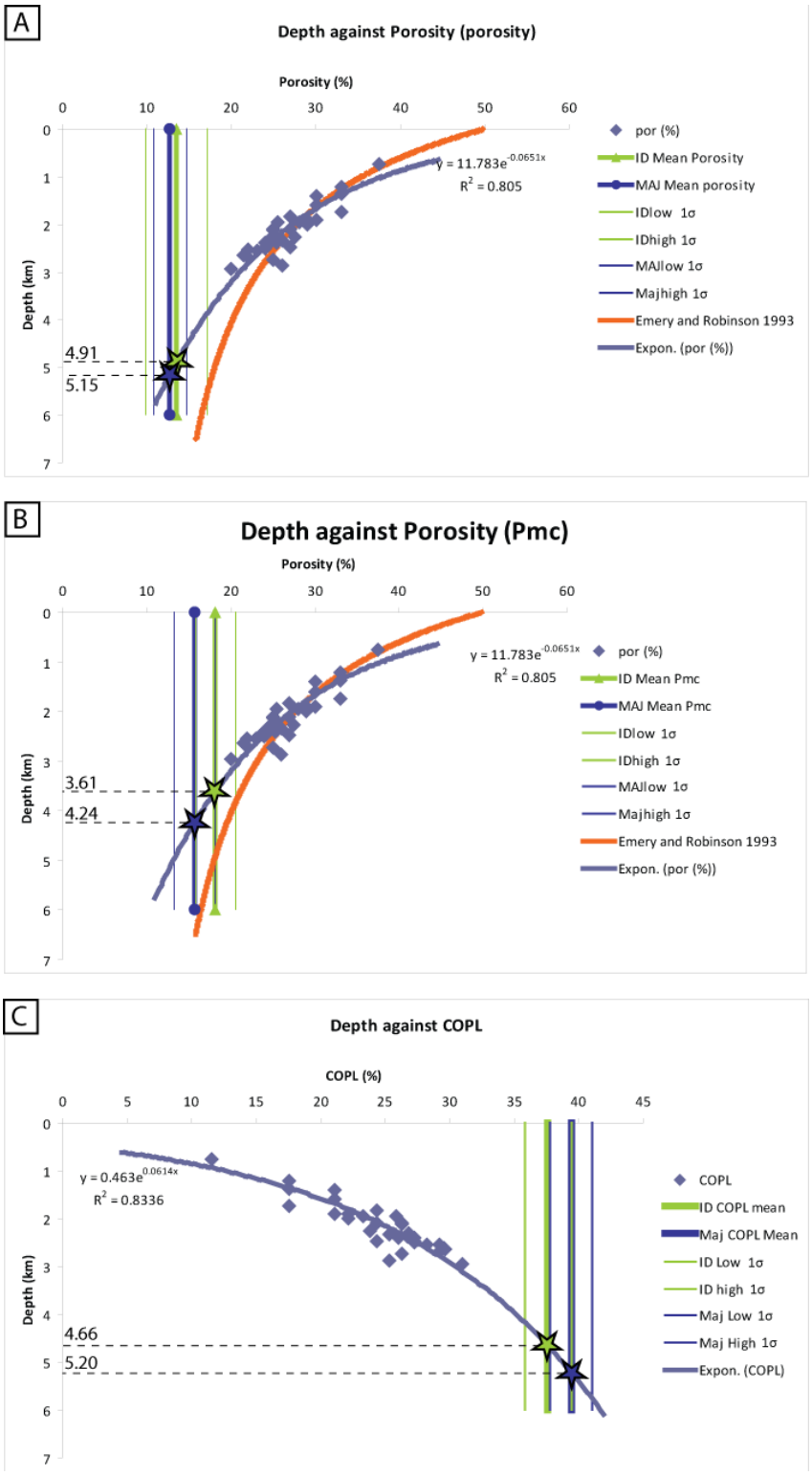

Fig. 2.12. (A, B) Graphs showing porosity–depth data from Gluyas & Cade (1997) (blue trendline) and porosity-depth curve from Emery & Robinson (1993) (orange trendline) with (A) average porosity of red sandstone away from igneous effects (B) Pmc of red sandstone away from igneous effects. 1σ error bars are shown on porosity and Pmc values (C) COPL calculated for the Gluyas & Cade (1998) dataset compared to average COPL of red sandstone away from igneous influence.

2.3 Volcanology of the Etendeka Large Igneous Province

Most geological work on the Phanreozoic of the Huab region in Namibia has focussed on the igneous geology that makes up the Etendeka Large Igneous Province (LIP). The Etendeka LIP and the Paraná LIP once formed a single magmatic province prior to the opening of the Atlantic (Hawkesworth et al., 1992; Milner et al., 1995; Peate, 1997). Together the Paraná-Etendeka province ranks as one of the largest continental LIPs, with an estimated volume of > $1x10^6$ km^3 (Peate, 1997) or > $3.62x10^6$ km^3 (Gladczenko et al., 1998). The Paraná province will not be further discussed in detail, but suggested reading includes: Hawkesworth et al. (1992); Milner et al. (1995b); Renne et al. (1996); Renne et al. (1997); Ernesto et al. (1999); Gilg et al. (2003); Waichel et al. (2006); Petry et al. (2007); Waichel et al. (2008); Duarte et al. (2009); Waichel et al. (2011). It is important to recognise the significance of the two igneous provinces sharing a common origin during the break-up of Gondwana and that the consideration of both provinces as one is scientifically advantageous. The Etendeka LIP formed ~ 5 % of the overall Paraná-Etendeka (Jerram et al., 1999a).

Igneous rocks, considered part of the Etendeka LIP were formed between 137 Ma and 124 Ma (Milner et al., 1995), with most of the volcanic activity between 135 Ma and 130 Ma (Renne at al., 1996; Jerram et al., 1999a). The flood basalt volcanism was however relatively short lived, probably lasting about 2-3 Ma from 135–132 Ma (Milner et al., 1995). Renne et al. (1996) showed that the duration was shorter, probably within the resolution of the $^{40}Ar/^{39}Ar$ method, giving a duration of 0.6 +/- 1.0 Ma from 131 +/- 0.7 Ma to 132.3 +/- 0.7 Ma (see discussion in 'Naming of the Twyfelfontein Formation for the relationship between the flood basalt age and

the Twyfelfontein Formation). Magmatic activity lingered on past the flood basalts for approximately 5 to 10 Ma, during the formation of the Damaraland igneous complexes (e.g. Messum, Brandberg, Spitzkuppe, Erongo, Okenyenya) (Watkins et al., 1994; Renne et al., 1996). The most reliable dating of the flood basalts seems to be that of Renne et al. 1996 (personal communication, Dougal Jerram). Overall, the dating is becoming more reliable as better lab techniques are developed or refined and the trend is for the duration of magmatism to be reducing to a short period of ~ 2 Ma (e.g. Wigand et al., 2004).

The initiation of magmatism is often cited to be attributable to decompression melting of the lithosphere (Hawkesworth et al., 1999), melting of the asthenosphere or depleted lithosphere under the influence of the Tristan Plume plume, a combination of both (some units showing plume signatures, others less so) (e.g. O'Connor & Duncan, 1990; Ewart et al., 1998a; Thompson et al., 2001; Trumbull et al., 2003) or melt related to a plume with crustal contamination (e.g. Ewart et al., 1998a). Initial continental rifting preceded volcanism is apparent in that the pre-flood basalt sediments show syn-rift sedimentation (e.g. the Krone Member) and that the magma flow trends show that faults exerted control (Glen et al., 1997; Franke, 2012). The initial magmatism was followed 15 Ma later by the initiation of sea floor spreading (Milner et al., 1995). The Etendeka is clearly spatially associated with both the Tristan Plume hot spot trace and regional extension at the time (Hawkesworth et al., 1999).

The Etendeka LIP embraces a wide variety of alkaline and tholeitic, mafic to felsic igneous rocks (Marsh et al., 2001). The subaerially emplaced part of the province is made up of the eroded remnants of a thick sequence of basalts (e.g. Tafelkop type and Tafelberg type, Jerram et al., 1999a; Ewart et al., 2004a) and

silicic rheoignimbrite sheets (the quartz latites, Milner & Duncan, 1987; Ewart et al., 1998b), carbonatite is also present (e.g. Ernst & Bell, 2010). The intrusive component is made up of subhorizontal, often transgressive dolerite sills (e.g. the Huab Sill complex, Duncan et al., 1989), dolerite dyke swarms (Marsh et al., 1991; Marsh et al., 2001; Thompson et al., 2001; Trumbull et al., 2004) and a number of large subvolcanic ring complexes and Damaraland complexes (e.g. Marsh et al., 2001; Ewart et al., 2002; Trumbull et al., 2003). The Doros igneous centre in the SE of the field area is a basic layered complex (Owen-Smith et al., 2012) thought to feed the Tafelkop basalts (Jerram et al., 1999a; Marsh et al., 2001). A comprehensive review of the magma types can be found in Marsh et al. (2001). Of the intrusive rocks, the effects of the dolerite dykes and sills on the Twyfelfontein Formation are presented in this thesis (Chapter 6 and Chapter 7), the occurrence and morphology is therefore detailed further below. The effects of the Tafelkop type and Tafelberg type basalts are also considered in the thesis (Chapter 4) so are also detailed below. Other types such as the quartz latites and the Damara complexes are not further considered.

2.3.1 Intrusive Igneous Rocks

Intrusive dolerites (dykes and sills) in the Huab Basin are referred to as **Kdo** on figures and maps consistent with the 2006 geological map (Schreiber, 2006).

Dykes

Dolerite dykes occur throughout the Huab Basin field area, and can be geochemically grouped into at least seven magma types by composition (Marsh et al., 2001). Some of the dykes are compositional equivalents of extrusive magmas found in the Etendeka (e.g. Tafelberg, Albin, Esmerelda and Khumib types, Marsh et al., 1991; Marsh et al., 2001; Thompson et al., 2001) but three have no extrusive

equivalent discovered as of 2001 (Horingbaai, Huab-1 and Huab-2, Marsh et al., 2001). Evidence for a feeder dyke from the Doros crater is presented by Jerram et al. (1999a). The petrography of the dykes is described by Marsh et al. (1991), who remark on the widespread presence on olivine compared to the basaltic lavas (except the Tafelkop, which is olivine phyric).

Most dykes in the Huab outliers strike between NNW and NNE (e.g. Lord et al., 1996), although dykes exist striking in all directions (e.g. Trumbull et al., 2004). The thickest and longest dykes tend to strike NNW. The dykes follow older Damara Belt structures within 100 km of the coast (Trumbull et al., 2004). The dykes range from 45 cm thick (e.g. the small dyke north of the main RYD outcrop, Chapter 6 and Fig. 2.14G.) up to > 10 m and crosscut all stratigraphy exposed in the Huab Basin (e.g. Fig. 2.14.). Some dykes terminate in the exposed stratigraphy, most are discontinuous both horizontally and vertically. The discontinuous nature supports the mode of intrusion being through propagating, then coalescing fingers (cf. Hutton, 2009) that intrude vertically or sub-vertically (see Fig. 2.14F showing a dyke broken bridge illustrating sub vertical emplacement). The consequence of the emplacement mechanism is that 'holes' exist in dykes, filled with the country rock (sediment or lava depending on stratigraphic position). Dykes can be traced up to ~ 20 km, although most disappear after > 5 km as traced through discontinuous exposure. Duncan et al. (1989) found little geochemical relationship between dykes and sills in the Huab Basin, but outcrops clearly illustrate Huab Sills branching into dykes (Fig. 2.15A.). The dykes weather more readily than the surrounding sediments or basement, making observation of internal structure difficult, where dykes are well preserved, columnar jointing is sometimes observed perpendicular to the margin (Fig. 2. 14B.) suggesting emplacement into an aquifer that cooled the dyke. No dyke

has been found with visible displacement attributable to pre-intrusion extensional faulting or syn-emplacement extensional faulting; observed displacement is purely due to inflation (see Fig 2.15A.). Nevertheless, well developed mineral lineations have been found adjacent to dykes (Fig. 2.14C.), where sediments show no offset; these can only be attributed to magma flow within the dyke (cf. Varga et al., 1998; Correa-Gomes et al., 2001; Muirhead et al., 2012).

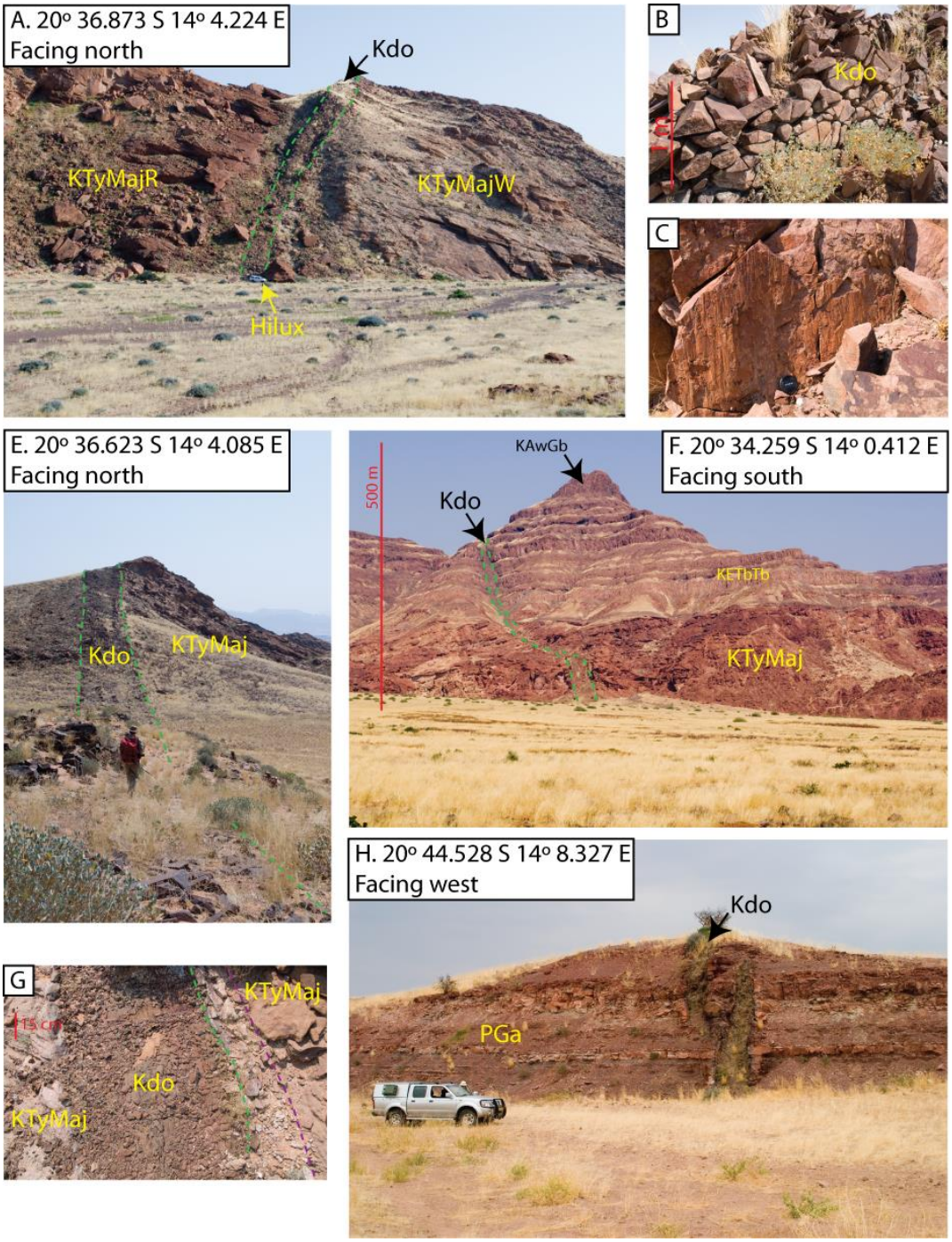

Fig. 2.13. Photographs of dykes in the Huab Basin. (A) The Red Yellow Dyke (RYD) locality, where a ~ 5 m thick dolerite dyke cuts the Major Erg, the sand to the east is white and the sand to the west is red. (B) The RYD dyke to the north of the cliff showing crude columnar fractures perpendicular to the cooling surface. (C) 'Hot Slickensides' on the eastern contact of the RYD dyke from the top of the cliff exposure, not no apparent offset of the Twyfelfontein Formation is evident, so the slicks must be magmatic in origin. (E) RYD exposure trending north. (F) Dyke cutting all Cretaceous stratigraphy exposed in Huab Basin, from the Krone Member to the Goboboseb Quartz Latite. (G) The thinnest dyke found, calcite induration at the contacts is clearly identified. (H) dyke within the Permian Gai-As Formation illustrating two offset segments of the same dyke forming a bridge structure meaning the dyke propagated sub-vertically (e.g. Magee et al, 2012; Hutton, 2009).

Sills

The sills within the Huab Basin form part of the Huab Sill complex (Duncan et al., 1989), which extends from the Huab Basin westwards to the Atlantic coast. The Huab Sill complex consists of at least four different compositional groups (distinguished by incompatible element ratios) that form a number of sills that have intruded at approximately the same stratigraphic level (the Karoo–basal Etendeka Group) (Duncan et al., 1989). The compositions are termed Huab-1 to Huab-4, which Huab-1 being the most common and Huab-4 the least common (Duncan et al., 1989). All of the sills are tholeiitic in composition with normative hypersthene and olivine and are rather primitive in character (High MgO, Ni, Cr, Duncan et al., 1989). None of the sills are compositional equivalents of extrusive volcanic rocks in the area (Duncan et al., 1989). The sills appear to favour intruding the argillaceous Karoo rocks (Fig. 2.15A.) or into the lowermost Twyfelfontein Formation (Fig. 2.15B, D.), although a thin (<<5 m thickness) sill does transgress into the Tafelberg lava south of Krone Farm (Fig. 2.15F.). In the northeast of the Huab Basin, sills are typically intrusive into the Damara schists (Duncan et al., 1989). The sills are up to 130 m thick and are formed into broad saucer shapes, although not as pronounced as saucers in the Karoo (e.g. Schofield et al., 2010), which is probably related to host sediment thickness being much less in the Huab (i.e. less space to develop saucer-shaped morphology in non-crystalline rock). Fig. 2.15C shows the sill complex viewed from the NW, south of the Huab River, where it is extensive and flat lying, although some dipping edges can be seen suggesting a flattened saucer. Fig. 2.15E shows a clearly transgressive saucer edge north of the Huab River, where the Twyfelfontein Formation is intruded. The sills probably emplaced as propagating magma fingers,

like the Golden Valley Sill in the Karoo (cf. Schofield et al., 2010; Schofield et al., 2012) although no evidence of significant host rock fluidisation was found. At transgressive tips, complex morphologies are preserved, showing apophasis preceding the sill inflation, often sill tips become steepened to sub-vertical orientations (i.e. dykes) (Fig. 2.15D, Chapter 6). Sills also 'spawn' dykes along their top surfaces not at sill-tips (fig. 2.15A.). Duncan et al. (1989) were only able to link two dykes based on geochemistry to type-1 Huab Sill composition. The Huab Sill complex jacks up the overburden south of the Huab River by ~150 m (consistent with 3D seismic reflection observations elsewhere e.g. Holford et al., 2012), which together with other evidence presented in Duncan et al. (1989) strongly suggests the sill complex postdates exposed lavas in the region.

This thesis describes the effects of the Huab Sills on the Twyfelfontein Formation sandstone in Chapter 6.

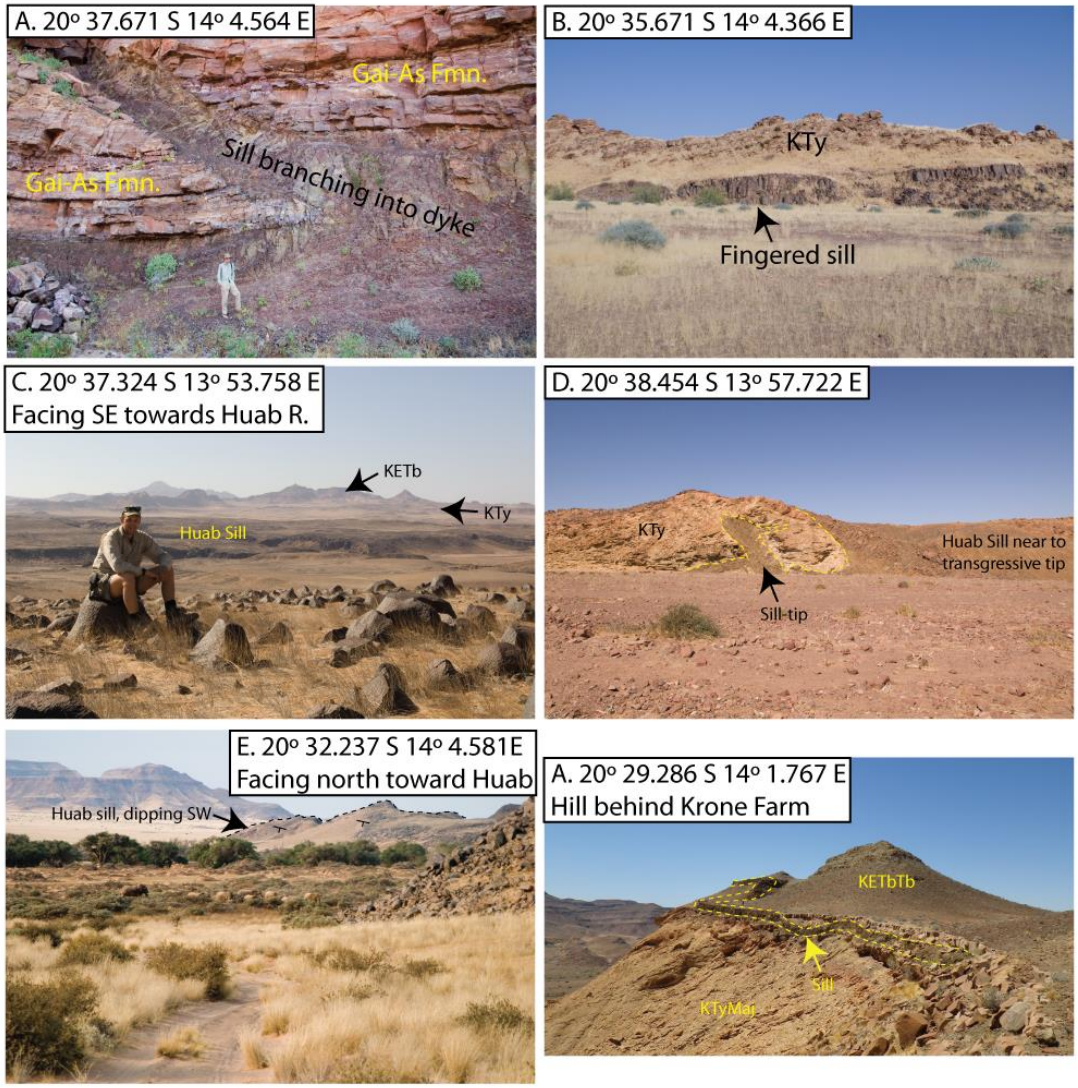

Fig. 2.14. Photographs of Etendeka sills in the Huab Basin. (A) Dolerite sill within the Permian Gai-As Formation, where a dyke is branching from the sill, note preservation of angular country rock. (B) Dolerite sill in contact with the Major Erg unit. The sill is showing a typical, magma finger morphology (e.g. Schofield et al., 2010). (C) Photograph to illustrate the large extent of the Huab Sill complex and the flat geometry compared to sill complexes in thicker sedimentary basins, saucer shapes in the Huab are poorly developed and transgression tends to be abrupt. (D) Transgressive sill tip, multiple apophasis extend from the transgressing sill tip. (E) Dipping limb of a Huab Sill, where it is beginning to develop a saucer-like morphology. (F) Thin sill intruding along the base of a basalt lava flow at the Major Erg contact (probably at the rheological boundary created by the lava induration of the sand), this sill transgresses into the lava and is the highest sill (stratigraphically) found.

2.3.2 Extrusive Igneous Rocks

Etendeka mafic magmas (**KETb**) have been grouped into HTZ and LTZ groups based on high and low Ti and Zr concentrations (Marsh et al., 2001). The HTZ basalts are confined to the northern Etendeka and the Paraná so will not be discussed further. The LTZ (low-Ti suite) basalts in the Goboboseb area are further geochemically subdivided based on Ti/Zr ratio into the LTZ.H (higher Ti/Zr) and LTZ.L (lower Ti/Zr) series (Ewart et al., 1998a). The LTZ.H basalts reported by Ewart et al. (1998a) are geochemically the same as the Tafelkop type basalts (Milner et al., 1994) in the Goboboseb area and the Tafelkop-type (Tafelkop interdune member, Jerram et al., 1999a) of the Awahab Formation in the Huab Outliers (Fig. 2.17.). The Tafelkop type basalts are more primitive being more magnesian than the later Tafelberg type basalts (LTZ, Ewart et al., 1998a). The Tafelkop type basalts have been identified as dominantly mantle plume derived melts (Ewart et al., 1998a). The common LTZ basalts of Ewart et al. (1998a) are the most extensive basalts in the Etendeka and are also known as the Tafelberg type basalts (Erlank et al., 1984; Jerram et al., 1999a; Marsh et al., 2001). The Tafelberg type basalts vary from tholeiitic basalt to tholeiitic andesite (Marsh et al., 2001). Tafelberg type basalts/andesites will be referred to as Tafelberg type basalts in this thesis. The extrusive igneous rocks in the Huab Outliers mostly belong to the Awahab Formation (Fig. 2.7.). Both the Tafelkop type basalt and the Tafelberg basalt crop out in the study area and are in contact with Twyfelfontein Formation sandstone. The lavas are subdivided based on geochemistry, but also have clear morphological differences visible in the field (see Jerram 1999a; 1999b, for detailed descriptions):

(1) The oldest lavas in the study area are Tafelkop type basalts (**KETbTk**). In the Huab Basin (Awahab Formation) these are olivine-phyric basalts often with associated interleaved sediments. The basalts were low viscosity compound type (*senso* Walker, 1971) pahoehoe flows. Evidence for the type of flow comes from the complex internal morphology (where weathering is minimal, Fig. 2.15B.) and preserved pahoehoe prints on overlying lithified sandstone (Fig. 2.15E. Image published as front cover of *Geology* Jan 2013). The Tafelkop Type basalt crops out extensively south of the Huab River and is interbedded with the Twyfelfontein Sandstone. Complex interactions often result, where the basalt flows have been active during dune migration, for example the fractured and inflated dome in Fig 2.17C where sand was blown over a hot, inflating basalt tumulus (possibly similar to the ridges reported by Ibrahim & Al-Malabeh (2006) in similar arid conditions of recent volcanism in Jordan). The Tafelkop type flows weather readily and are poorly exposed. The flows weather to a grey talus, which often obscures outcrops. The unit is better preserved where it has ponded between sand dunes. The Tafelkop type lavas in the study area most likely erupted from a shield centred on the Doros complex which may have acted as a sub-volcanic magma reservoir (Jerram et al., 1999a; Jerram & Robbe, 2001; Marsh et al., 2001). Evidence for this is in the thickening of the Tafelkop basalt towards Doros (Jerram & Robbe, 2001) and a feeder dyke linking to Doros (Jerram et al., 1999a; personal communication, Dougal Jerram). The Tafelkop type lavas in the field area were therefore likely erupted from a large shield volcano centred about 18 km SE of the Awahab Camp (Fig. 2.6; Appendix map).

Tafelkop type lavas that are in contact with Twyfelfontein Formation sandstone are described in Chapter 4 and Chapter 5 and are mainly studied where they crop out in Dune Valley (Chapter 7).

A disconformity exists above the Tafelkop type lava flows in Dune Valley (Fig. 2.7) which is apparent where the shallow gradient of the northward dipping Tafelkop type Doros shield volcano is onlapped by Tafelberg type basalt (**KETbTb**). This surface also has a patchy, poorly developed volcaniclastic sediment beds, suggesting a time gap. This time gap may be ~ 100 ka (personal communication, Dougal Jerram). Desert environments existed throughout this time gap, as evident in sand filled cracks in the vicinity of the volcaniclastic beds. Both the Tafelkop type lava and the Tafelberg type lava in area interact with active erg. Fig. 2.15 shows a panoramic view of Dune Valley, where the lower Tafelkop type basalts are overlain by the later Tafelberg type basalts and Awahab Formation quartz latites (**KAwGbi, KAwGbii, KAwSp**).

(2) The Tafelkop type basalts that onlap the Doros shield volcano are more voluminous and laterally extensive lava flows (Jerram et al., 1999a). These flows form well exposed outcrops (Fig. 2.15A,E.) (in contrast with the weathered Tafelkop type basalt). The Tafelkop type flows in this region are up to 60 m thick where ponded and have rubbly, vesicular flow tops, the middle parts of the flows are massive. A flow front is visible in the east cliff of the mountain to the west of Awahab/Mikberg in Dune Valley, suggesting flow from the north, consistent with the onlap model (Jerram et al., 1999a) (Fig. 2.7). In the cliffs surrounding Dune Valley, the Tafelberg type basalts are interbedded with the Awahab Formation quartz latites (Jerram et al., 1999a; Ewart et al., 1998b; Marsh et al., 2001), which were possibly sourced from Messum (Milner & Ewart, 1989; Ewart et al., 1998b) where intrusive geochemical equivalents occur. The Awahab Formation Quartz latites are not present to the north, at the Tafelberg type section (cf. Marsh & Milner, 2003) where different quartz latites are present. This suggests there is a volcanic

disconformity between the Awahab Formation (this study, Dune Valley) and the Tafelberg type section, where the *geochemical type* of the Tafelberg basalt is the same as in the Awahab Formation, but the lava flows are separate (Jerram et al., 1999a). As a result of this disconformity, Jerram et al., 1999a used the term 'Tsuhasis Member' basalts for the Tafelkop type basalts in the Awahab Formation, here Tafelberg type basalt is used. It can be seen in Fig. 2.17 that the Awahab Formation Tafelberg type basalts (Tsuhasis Member) plot in the Tafelberg field (Erlank et al., 1984; Ewart et al., 1998a).

Tafelkop type basalts are directly in contact with aeolian dunes to the north and west of the Huab Basin and sediment interlayers are less abundant than in the Tafelkop type basalts (Jerram et al., 1999a). The direct diagenetic effects of the Tafelberg type basalts on the Twyfelfontein Formation is described in Chapter 4 and summarised in Chapter 5.

(3) The Tafelberg type basalts in the Awahab Formation are interbedded with large volume quartz latite units (Fig. 2.7; Fig. 2.15A). Three quartz latite units are present in the Awahab Formation: Goboboseb quartz latite (units I and II; KAwGbi, KAwGbii) and the thicker Springbok quartz latite (KAwSp). The Goboboseb I quartz latite overlies both the older Tafelkop type basalts (in the SE of the Huab Basin) and the younger Tafelberg type basalts elsewhere, providing important chronostratigraphic information (Jerram et al., 1999a). The quartz latite units are important stratigraphical markers (Milner et al., 1995; Peate, 1997; Ewart et al., 1998b; Jerram et al., 1999a; Marsh et al., 2001; Marsh & Milner, 2003) in the Etendeka and are the main cliff-forming units (Fig. 2.15A.). One example of the Goboboseb quartz latite in contact with the Twyfelfontein Formation has been reported (Jerram et al., 1999a) but was not studied as part of this thesis.

Fig. 2.15. Photographs of key outcrops illustrating the Tafelkop type basalt and the Tafelberg type basalt. (A) Panorama of Dune Valley facing north with Mikberg to the east. Relationship between the lower Tafelkop basalts (Tafelkop Interdune Member basalts, Jerram et al (1999a) and the onlapping Tafelberg type basalts is clear in the west. (B) Close up of a typical Tafelkop type outcrop, showing the weathered basalt, an indurated sand lens, the compound nature of the flows can just be discerned. This kind of weathering is typical of the olivine phyric vesicular Tafelkop flows in Dune Valley. (C) An inflated lava dome in the Tafelkop type basalt that has cracked, where sand has fallen into the cracks it has been cemented with calcite (typical of hot contacts) proving the dome was active during sedimentation. (D) Tafelberg type flow is a tabular classic lava, with a thick crystalline core with few vesicles. (E) Pahoehoe mould preserved in an overlying sand bed, proving the Tafelkop basalts were pahoehoe.

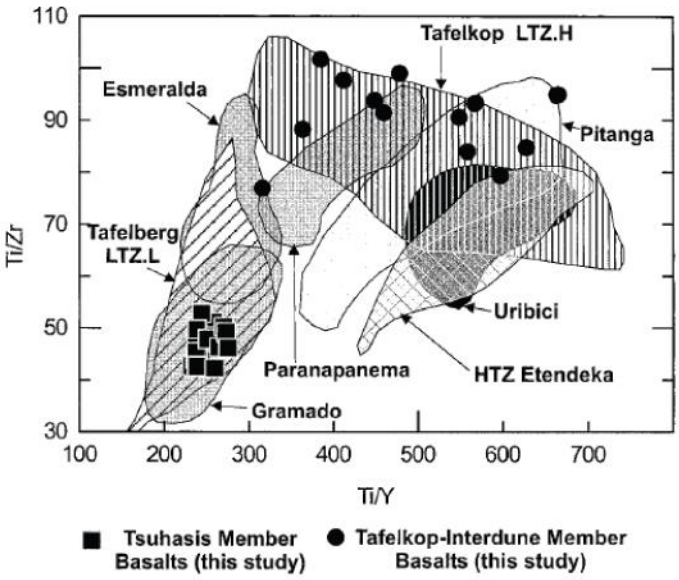

Fig. 2.16. Geochemical discrimination of the Tafelkop type and the Tafelberg type basalts in the Huab Basin from Jerram et al (1999a). Squares are for the Tafelberg type basalts of the Tsuhasis Member and circles are for Tafelkop type lavas.

2.4 A review of previous work regarding 'contact metamorphism' adjacent to basaltic dykes and sills

The effects of the emplacement and cooling of dykes and sills on host rocks have been well studied in the literature, seldom focussing on clean reservoir sandstones. Studies generally concern protolith material favouring diagnostic mineral reactions, such as fine grained aluminium rich (clay rich, mica rich) protoliths such as shale (e.g. Smith, 1969; Brauckmann and Füchtbauer, 1983; Barker et al., 1998; Dutrow et al., 2001; Suchy et al., 2004; Aarnes et al., 2011a; Aarnes et al., 2011b; Wang et al., 2012; Hudson and Andrews, 1987). Studies of organic rich rocks such as coal or shale in proximity to intrusions have the benefit of the vitrinite-reflectance geothermometer (Barker et al., 1998; Suchy et al., 2004; Cooper et al., 2007; Stewart

et al., 2005). Other studies on organic rich rocks are concerned with the maturation and volatile (CO_2 and CH_4) release with relevance to petroleum sources and global warming events (Summer and Verosub, 1992; Suchý et al., 2004; Aarnes et al., 2011a; Aarnes et al., 2011b). Basaltic intrusions into metamorphic basement (comparatively mica rich and low porosity compared to clean reservoir sands) have also yielded successful studies, particularly in constraining mineral reaction texture and chemistry (e.g. Smith, 1969; Nawaz, 1977; Wartho et al., 2001; Holness & Watt, 2002; Holness & Humphreys, 2003; Holness et al., 2005).

Work on siliciclastic sandstones in contact with basaltic intrusions has had a variety of focusses, spanning a complete range of alteration. Of the studies into the effects of igneous intrusions on sandstone country rocks, there has been little emphasis on (A) the modification of petroleum reservoir properties and (B) the normal effects as opposed to the exceptional. Many studies focus on the most intense (and rarest) effects leading to pyrometamorphism (Grapes, 2010; Butcher & Grapes 2011) where sufficient heat has been transferred to the intrusion wall rocks to cause partial melting and the formation of a buchite (e.g. Reynolds, 1940; Frankel, 1949; Ackermann & Walker, 1960; Wyllie, 1961; Wilson, 1964; Spry & Solomon, 1964; Kitchen, 1984; Krynauw et al., 1988; Philpotts & Asher, 1992; Merguerian & Saunders, 1995; Balance & Waiters, 2002; Holness, 1999; Holness et al., 2012). Contacts that do not lead to melting are *more* common in the field, but *not so well* documented; effects are hydrothermal, leading to metasomatism and mineral authigenesis (e.g. Brauckmann & Füchtbauer, 1983; Summer & Ayalon, 1995; Barker et al., 1998; Balance & Waiters, 2002) , often recorded by clay mineralogy (e.g. McKinley et al., 2001; Ahmed, 2003, Balance & Waiters, 2002). The common minor effects on red Triassic marls and sandstones have been documented in brief by

Walker (1959) along dykes in Antrim, Northern Ireland and comprise bleaching and poikilitic calcite cementation, similar to described in Chapter 6.

The most intense alteration of sandstone due to intense heating by the intrusion is the best understood. As the hot intrusion is neared, characteristic mineral transformations occur within the sandstone. These mineral reactions rely on there being the appropriate detrital assemblage. The rocks created by the contact metamorphism near to igneous intrusions are commonly termed pyrometamorphic, which appears to have been used since 1969 (Smith, 1969) and reviewed by Grapes (2010). The first description of rocks falling into the Pyrometamorphic facies is believed to be by Reynolds (1940) who analysed Triassic sandstone adjacent to a bifurcating dyke. Nearly all reported instances of pyrometamorphism occur adjacent to sills (e.g. Frankel, 1949; Ackermann & Walker, 1960; Wyllie, 1961; Krynauw et al., 1988; Wartho et al., 2001; Balance & Waiters, 2002; Holness & Watt, 2002), 'plugs/ necks' (e.g. Spry & Solomon, 1964; Smith, 1969; Nawaz, 1977; Kitchen, 1984; Holness, 1999; Holness et al., 2012), with reports rare from adjacent to dykes (e.g. Reynolds, 1940). The dykes in Reynolds (1940) evidently were the location of flow localisation and increased heat transfer. Plugs and necks are usually inferred to be feeders for magma flow localisation over time (Holness, 1999; Holness et al., 2012) possibly as shallow sub-volcanic feeder conduits.

At typical pyrometamorphic thermal aureole is first noticed by the breakdown of muscovite (if present) into biotite, potassium feldspar, spinel, corundum and aggregates of mullite needles (Holness, 1999; Holness & Humphries, 1993; Holness et al., 2005; Holness et al., 2012). Wyllie (1961) noted the disappearance of sericite as the first evidence of pyrometamorphism, which is consistent with above. Outside of this zone (cooler), the effects are generally hydrothermal, caused by the

convection of fluids cooling the intrusion and aureole. The hydrothermal fluids tend to be reducing (e.g. Holness, 1999; Young, 2008; Holness et al., 2012). Haematite is often reduced to magnetite (Holness, 1999) and sandstones are often bleached (e.g. Holness et al., 2012), this zone may be mineralised with calcite or zeolite (Smith, 1969; Balance & Waiters, 2002). Chlorite is then replaced by biotite (Holness, 1999) and muscovite if Fe/Mg is low. Biotite is subsequently replaced by an aggregate of oxide minerals. As the intrusion is approached, potassium feldspar begins to invert to sanidine (e.g. Ackermann & Walker, 1960; Grapes, 2010; Holness et al., 2012). The inversion of potassium feldspars to sanidine is soon accompanied by incipient melting of the sanidine along cleavages (Ackermann & Walker, 1960), rims of quartz and feldspar intergrown along grain boundaries (Holness et al., 2005). The melt at this point frequently vitrifies into a brown-green-clear glass (Frankel, 1949; Spry & Solomon, 1964; Kitchen, 1984; Holness et al., 2005), which sometimes subsequently devitrifies to a potassium feldspar mantle (Ackermann & Walker, 1960). This melt reaction is Qtz+Ab+Or+H_2O→melt (after Holness 2012), with possible H_2O sources being muscovite or chlorite present in the protolith, magmatic H_2O or groundwater. The four phase sanidine-quartz-liquid-gas curve is described by Shaw (1963). As the temperature increases, melt proportion increases, frequently sanidine is completely resorbed before quartz and plagioclase which are more refractory (e.g. Ackermann & Walker, 1960). The melt is often preserved as granophyric rims and matrix (e.g. Kitchen, 1984; Holness et al., 2012). Closer to the intrusion, where temperature is higher still, tridymite needles and plates appear (Reynolds, 1940; Frankel, 1949; Spry & Solomon, 1964;Wyllie, 1961; Ackermann & Walker, 1960; Holness, 1999; Balance & Waiters, 2002; Holness & Humphries, 2003, Holness et al., 2005; Holness et al., 2012). Over time the tridymite inverts to quartz paramorphs, which are the

mineral observed today. The tridymite frequently mantles restic detrital quartz grains (e.g. Frankel, 1949; Wyllie, 1961; Holness et al., 2012) and float freely in the granophyric matrix (e.g. Spry & Solomon, 1964; Ballance & Waiters, 2002; Holness et al., 2012). Quartz grains are often fractured as a result of shock heating (Holness et al., 2005). The tridymite stability field is presented in Grapes (2010) and partially by Shaw (1963). Orthopyroxene also frequently occurs at the higher end of the pyrometamorphic temperatures (e.g. Holness et al., 2012). At any point in the pyrometamorphic gradient, of increasing temperature, the rock can cool to below the solidus of the melt, which depending on the rate of cooling can either vitrify the melt+ crystals (Tridymite and possibly pyroxene) or crystallise (quartz-K-feldspar granophyre containing crystals). Often glasses produced during vitrification devitrify over time to spherulitic masses of potassium feldspar (e.g. Ackermann & Walker, 1960). Pyrometamorphic sediments adjacent to igneous intrusions have frequently been reported to display columnar jointing (Spry & Solomon, 1964; Buist, 1980; Philpotts & Asher, 1993; Summer & Ayalon, 1995; Young, 2008), suggesting fracturing during cooling, possibly by water (e.g. the hydrothermal aquifer).

Pyrometamorphism of an arkosic sandstone is not as useful as that of a pelitic protolith in the formation of mineral geothermometers (cf. Smith, 1969; Holness & Watt, 2002), but nevertheless, up to five isograds can be determined, depending on protolith composition, to derive simple thermal models:

(1) (< 5 kbar) Muscovite + quartz = Al_2SiO_5 + K-feldspar + H_2O + biotite

(2) Fe/Al biotite = Mg/Al biotite + K-feldspar/ melt + magnetite + hercynitic spinel + H_2O

or

Biotite+ quartz + plagioclase = orthopyroxene +/- K-feldspar + melt

(3) Quartz + Albite + Orthoclase + H_2O = melt

(4) The quartz-tridymite inversion

(5) The orthopyroxene thermometer

References: (1, 2, 3, 4, 5) Holness et al., 2005, Grapes, 2010 (3) Shaw (1963), (5) Brey & Kohler, (1990)

Of these geothermometers only the Quartz + Albite + Orthoclase + H_2O = melt and the quartz-tridymite inversion were apparent in the sandstones sampled in this thesis. Previous studies of pyrometamorphism (e.g. Balance & Waiters, 2002; Holness et al., 2012) usually show at least these two of these reactions, whereas the other mineral reactions are highly dependent on protolith (1, 2, 5).

Beyond the pyrometamorphic zone (if present) the recorded mineral assemblage is hydrothermal or metasomatic (Walker, 1959; Barker et al., 1998; McKinley et al., 2001; Ahmed, 2002). Dykes do not commonly show evidence of pyrometamorphism, and the direct effects due to emplacement are usually only recorded by a hydrothermal assemblage (Summer & Ayalon, 1995; Barker et al., 1998; McKinley et al., 2001; Ahmed, 2002). In addition to potential

pyrometamorphism and hydrothermal mineralisation, dyke intrusion contacts have been reported to be compacted (Summer & Ayalon, 1995; Balance & Waiters, 2002).

Hydrothermal systems existing outside of the zone of pyrometamorphism have been documented by Spry & Solomon (1964) and Balance & Waiters (2002). Holness et al. (2012) also presented observations consistent with a hydrothermal system outside of the pyrometamorphic zone (sand bleaching). Hydrothermal effects in the Beacon Sandstone, Antarctica, noted by Balance & Waiters (2002) include: matrix compaction, potassium feldspar overgrowths on potassium feldspar grains, pore filling secondary micas and clay (chlorite and rare smectite), rare pore-filling laumontite, and calcite. The calcite occurred as: intergranular pore-filling cement (poikilitic), isolated patches replacing all other minerals and replacement of quartz, isolated euhedral grains and as thin lenses within detrital grain cleavage planes (biotite and feldspar).

Hydrothermal effects adjacent to igneous intrusions into sandstone, not associated with pyrometamorphism reported are limited to dykes (Summer & Ayalon, 1995; Barker et al., 1998; McKinley et al., 2001; Ahmed, 2002). Studies on Permo-Triassic sandstones in the United Kingdom (McKinley et al., 2001; Ahmed, 2002) have found variable effects. McKinlley et al. (2001) found that the Triassic Sherwood Sandstone (cf. Burley, 1984) had a diagenetic transition towards the dyke contact, where the background diagenetic minerals (smectite, quartz and dolomite) reacted to first form talc at temperatures of 130–180 °C. Closer to the dyke the talc reacted with calcite to form actinolite amphibole. Potassium feldsapar was not observed to be involved with mineral reactions and no net porosity or permeability reduction towards the dyke was observed. In contrast, Ahmed (2002) (also studying the Permo-Triassic sandstones in Northern Ireland, indeed one outcrop (Scrabo

Quarry) was used in both studies), found different results. Ahmed (2002) found that there was no effect on pre-existing quartz and feldspar overgrowths with proximity to the dyke intrusions. Pre-existing authigenic illite/smectite mixed layer clays reacted to form illite and chlorite approaching the dykes, where actinolite, albite and laumontite were found to be major phases. Ahmed (2002) also studied the sandstones of the Hartford Basin, USA for comparison. It was found that sandstone near to dykes had modified quartz and feldspar overgrowths which formed microcrystalline mosaics near to intrusions (cited as 'not common'). Abundant albite and quartz overgrowths increased in quantity away from the intrusions. Chlorite 'clumps' and laumontite were also documented. Heamatite is absent near to the intrusions in the Hartford Basin, and the sandstone is assumed to have been bleached by the hot fluids (Ahmed, 2002). For both examples studied by Ahmed (2002), porosity and permeability decreased towards the dyke from 5.4 % to 27.4 % and 1350 md, to 0 to 1.2 % porosity and 1 md within 5 m of the intrusion. Ahmed (2002) concludes that the observed authigenic minerals are due to hydrothermal activity and heat flow form the igneous intrusions.

Summer & Ayalon (1995) studied the effects of emplacement of dykes into the Inmar sandstone, Makhtesh Ramon, Israel. They found that authigenic quartz, vermicular kaolinite and iron oxides increased towards dyke contacts. Importantly they recognised that compaction adjacent to the dyke was an important process (Fig. 2.15A.). Calcite existing as grain coatings, fracture fills and as pore-filling cement was noted near to the dyke contacts. Porosity and permeability were found to decrease from ~ 20 % and 2500 md 6 m from the contact to < 5 % and negligible permeability at the contact. Tensile strength and density were found to increase

towards the contact. Mild hydrothermal conditions of an acidified meteoric water are suggested to have existed.

The most thorough study of the diagenetic effects of dyke intrusion on sandstone, where no pyrometamorphic effects were observed is on nine basalt dykes from the Upper Jurassic–Lower Cretaceous Strzelecki Group, onshore Gippsland Basin, Australia (Barker et al., 1998). The study uses petrography, fluid inclusions (FI), vitrinite reflectance ($R_{v\text{-}r}$) and stable isotopes ($\delta^{13}C$ and $\delta^{18}O$) and heat flow modelling to characterise the diagenetic chemistry and conditions caused by the dykes. In contrast to the pyrometamorphic studies (e.g. Holness, 2012), Barker at al. (1998) approach the contact rocks from the petroleum geoscience and sedimentary diagenesis point of view. The $R_{v\text{-}r}$ revealed a zone of elevated temperatures caused by a hydrothermal convection cell heated by the dyke adjacent to the largest dykes (c. 40 m) and evidence for the rise of heated fluids along smaller dykes but no fully developed hydrothermal convection. Temperature profiles away from dykes are presented for ideal cooling scenarios: simple conductive, complex conductive, incipient convection and convection cell (Fig. 2.15B.). Oxygen stable isotope values of carbonate cements were found to negatively correlate with $R_{v\text{-}r}$ values suggesting carbonates precipitating in the hydrothermal system also recorded the heat transfer from the dyke to the aquifer. Barker et al. (1998) important conclusions were: (1) Post depositional FI homogenization temperatures approach the maximum temperature reached during contact metamorphism. (2) Heat-flow models based on simple conductive cooling in a closed system do not adequately describe temperatures reached, the conditions need to be established for each dyke, especially system closure (hydrogeological conditions) before making temperature predictions.

(3) $R_{v\text{-}r}$ increases towards dykes and the profile can be used to determine the cooling mechanism of the dyke.

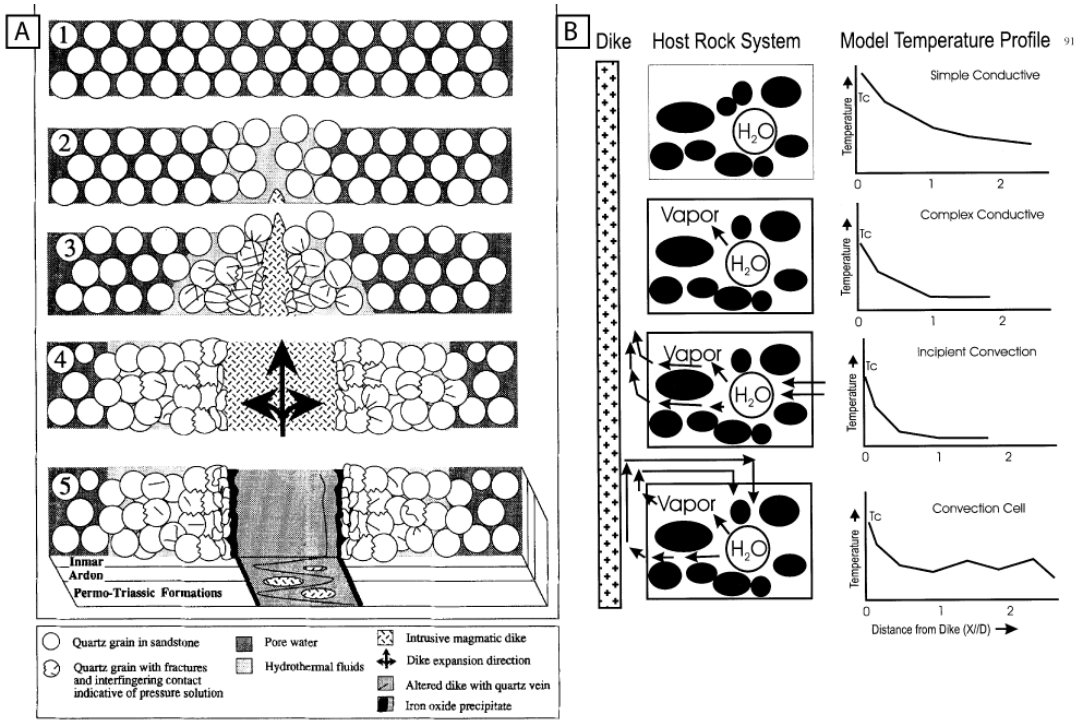

Fig. 12. Cartoon of the overall model for the dike/sandstone interaction. (1) The country sandstone prior to intrusion. (2) Hydraulic fracturing of the sandstone ahead of the dike tip. (3) Dike tip enters fracture, wedging through the sandstone and repacking and fracturing quartz grains. (4) As this wedging continues, or as the dike dilates, the sandstone on each side of the dike is compressed and heated with fracture healing and pressure solution. Thus the sandstone is indurated to a quartzite in the contact zone. (5) As the dike cools it is partially altered to a clay-rich matrix. Veins are emplaced in the altering dike. Iron oxides precipitate between the altering dike and quartzite, and within the quartzite along fractures and adjacent microporosity.

Fig. 2.17. (A) Diagram showing dyke intrusion and compaction modified from Summer & Ayalon (1995), see figure for caption. (B) Figure modified from Barker at al. (1995) showing four models for dyke and wall rock cooling: Four models of cooling in a host rock after intrusion of a dike. The host rock system shown initially consists of framework grains (solid spots) with pore water H_2O. After intrusion the pore water may vaporize (indicated as 'vapor') or convect forming additional heat sinks. This system shows four cooling modes: (1) simple conductive model—after intrusion of the dike, pore water does not vaporize and is assumed to have a negligible effect as a heat sink; (2) complex conductive model—after intrusion of the dike, pore water is assumed to absorb heat and vaporize; (3) incipient convection model—rapid cooling of the dike after intrusion causes rise of heated fluid near the dike without the development of a recharge system; and (4) convection cell model—after intrusion, a convection cell featuring the buoyant rise of heated fluids next to dike and recharge to the cooled fluids away from the dike. The temperature profiles for each model, shown as a function of position (X) from the contact divided by dike thickness (D), by shows the different responses conjectured to result from the different cooling models. A contact aureole that consists of an extended zone of general temperature decrease extending to over X/D=2 and a $T_{contact} >> T_{magma}+T_{host})/2$ appears to be a signature of simple conductive cooling. Incipient convection is indicated by a T_{max} profile that generally decreases to background levels at X/D<1. A convection cell is indicated by a wave-like form of the T_{max} profile and relatively high temperatures that may not decrease to background

levels until beyond distances of X/D>1.5. Because of T_{max} sets R_{v-r}, a similar profile to that shown for temperature is expected for vitrinite-reflectance data measured next to a dike (caption from Barker et al., 1995, p91.)

Many studies in both pyrometamorphism of sandstone and other rocks, non-pyrometamorphic contact metamorphism of sandstones, argillaceous rocks and organic rich rocks have attempted to model the temperature profiles away from the intrusions (e.g. Brauckmann & Fuchtbauer, 1983; Krynauw et al., 1988; Barker et al., 1998; Holness 1999; Svensen et al., 2004; Aarnes et al., 2011a; Aarnes et al., 2011b; Holness et al., 2012; Wang et al., 2013). The modelling of such temperatures can be useful in predicting temperature dependent processes such as the maturation and expulsion of hydrocarbons from source rocks (Svensen et al., 2004; Stewart et al., 2005; Cooper et al., 2007; Aarnes et al., 2011a, b; Wang et al., 2013) or temperature dependent reservoir reducing authigenic mineralisation (e.g. quartz overgrowths cf. Houseknecht, 1984). Most numerical models in previous studies overestimate temperature compared to observed geothermometers (e.g. Brauckmann & Fuchtbauer, 1983; Krynauw et al., 1988; Barker et al., 1995; Wang et al., 2013); the earlier studies not taking into account the role of pore-water. Notable is Archer et al., (2005), who noticed that their modelled temperatures around sills *underestimated* the vitrinite reflectance temperatures in UKCS well 164/7-1, this could be due to a deep seated large intrusion also increasing the regional geotherm (personal communication. Stuart Archer, 2013).

In reviewing the literature on both pyrometamorphism and non-pyrometamorphic contact metamorphism (hydrothermal) it is apparent that water exerts a dominant control on the cooling regimes and mineralisation around cooling igneous intrusions (cf. Barker et al., 1995). Indeed, Barker et al. (1995) state that the degree of system closure [to groundwater and hydrothermal cooling] seems to be

more important than heating duration in determining the $R_{v\text{-}r}$ resulting from contact metamorphism.

This thesis will explore these ideas in Chapter 6 where a number of sill and dyke intrusions into sandstone are studied. Chapter 6 shows the importance of water and shows instances where the magma flow regime within dykes and sills can cause intense pyrometamorphic effects, therefore overwhelming the cooling capacity of the aquifer. The indirect hydrothermal effects on sandstone are studied in Chapter 7.

2.5 A review of previous work regarding the direct effects of basaltic lava flows on substrate sediments

There is a marked scarcity of literature regarding the direct effects of basalt emplacement on sediment substrates. Most references to the process are short observations concerning 'baking' of sediments, often without follow-up work (e.g. Skinner & Ricker, 1968; Waichel et al., 2008; Jerram et al., 1999b; Jerram et al., 2000a). It appears that 'baking' is the assumed process for any field observation of colour or hardness change proximal to lava flows. Where follow-up work has been conducted, reports are confined to a sentence or two (Petry et al., 2007; Waichel et al., 2008), with the most thorough report reaching to a few paragraphs within a broader study (Jerram & Stollhofen, 2002). Ghosh et al (2006) examined 'bole' like substrates in the Deccan Traps and found no evidence of metasomatism (i.e. no direct diagenetic effects from the basalt); similarly Sheldon (2003) made the same conclusion in the Columbia River Basalts. Smith & McAlister (1995) made detailed examinations of clay rich sediments beneath Tertiary Antrim basalts in Northern

Ireland, often making references to ‘baking’ in the top 10 to 30 cm but not clarifying the definition. Sheldon (2003) cites Smith & McAlister (1995) as ‘… suggested that baking of the underlying palaeosols [*sic*] was restricted to the upper few decimetres of the profiles’. Cooper et al (2011) have developed a new zircon and apatite (U-THz)/He geochronology method based on ‘baking’, where based on a simple one dimensional heat conduction model suggested that temperatures may reach in excess of 1000 ℃ 10 cm below a 7 m lava flow. Their simple model is clearly flawed as will be demonstrated throughout this thesis using both previous work (including direct temperature measurements (e.g. Keszthelyi, 1995), vitrinite reflectance geothermometers (Sheldon, 2003) and numerous original petrographic observations in this study. The simple thermal diffusivity model presented does not take into account the ‘thermal shielding’ developed at the base of a lava flow or realistic basalt flow regimes. Cooper et al (2011) present no petrographic evidence (e.g. melting, fusing of grains, dehydration reactions) of such high temperatures being attained in their baked sediment, and the provided field photograph does not resemble outcrops where true baking has occurred adjacent to sill intrusions studied as part of this study. Lava flows have been observed flowing on top of snow in Iceland without immediate melting, illustrating on decimetre scale the effective thermal insulation between incandescent lava and substrate (Edwards et al., 2012).

This thesis is limited to basaltic volcanism typical of flood basalt provinces. It is pertinent to mention that other magma compositions and eruptive/intrusive styles not considered here have been reported to have measureable effects on substrates. For instance, komatiite lava can transfer significant heat (Williams et al., 2000) and unusually hot silicic ignimbrites have been reported having clear thermal influence

(development of columnar cooling joints in substrate) (Branney et al., 2008) although 'baking' was not defined petrographically.

As far as I am aware, all previous work, more detailed than a cursory sentence has concentrated either on the 'baking' (or lack of) of palaeosols (Sheldon, 2003; Ghosh et al., 2006) or on the Cretaceous sandstones in the Parana-Etendeka region (e.g. Jerram & Stollhofen, 2002).

Palaeosol 'baking'

Sheldon (2003) states 'Reddened zones between lava flows have often been characterized [*sic*] as 'baked zones' and all visible alteration attributed to heating by the overlying flow'. No citations are given for this 'often' characterisation. The lack of citations mirrors my own findings in the literature. Researchers often refer to these 'baked' zones, without particular evidence to support the interpretation. It appears the existence of these 'baked zones' is an established geological paradigm, that has been poorly investigated.

The palaeosols in the Picture Gorge subgroup, Columbia River Group have been analysed by Sheldon (2003) using vitrinite reflectance, the results found elevated values (R_o 1.14) within 3 cm of the hot contact, declining to the normal diagenetic value (R_o 0.32) by 10 cm concluding that the upper 6 cm was heated to 160–180 °C, declining to no more than 60–80 °C at a depth of 10 cm. These temperatures are certainly not sufficient to produce contact metamorphic or pyrometamorphic reactions at surface pressures (cf. Grapes, 2010) or match the modelled values of Cooper et al (2011). In addition ceramicization of the clay component of the palaeosols was not found, thus the process of 'baking' was

rejected, and it was suggested that no or limited heating occurred below the lava flow studied (Sheldon, 2003).

Sand 'baking'

Of the numerous references to 'baking' of substrates below basaltic lava flows (Skinner & Ricker, 1968; Smith & McAlister, 1995; Jerram et al., 1999b; Jerram et al 2000a; Jerram & Stollhofen, 2002; Petry et al., 2007; Waichel et al., 2007; Waichel et al., 2008; Cooper et al., 2011), only Jerram & Stollhofen (2002) stands out, even then, petrographic detail is minimal and description reaches a paragraph. Common observations between each of the papers are, in the field, observation a 'baked' contact (usually without further elaboration). Petry et al (2007) observed very rare dissolution and recrystallization of the sand matrix, inferring high temperatures, but did not discuss the nature of the observation or present supporting petrographical data.

2.6 Indirect effects- sandstone bleaching

Chemical bleaching of sandstones is not rare; it has been documented as a result of hydrocarbon migration and other reducing fluid flow through sandstone (Moulton, 1926; Surdam et al., 1993; Kirkland et al., 1995; Beitler et al., 2003; Parry et al., 2004; Beitler et al., 2005; Schöner & Gaupp, 2005; Ma et al., 2007). Bleached zones have been used to indicate migration pathways of hydrocarbons and to infer the existence of emptied reservoirs (Kirkland et al., 1995; Beitler et al., 2003).

Where hydrocarbons have migrated through red coloured sandstones, the bleaching has been attributed to acidic, reducing conditions (e.g. Ma et al., 2007; Surdam et al., 1993). These conditions can be achieved by biologically mediated oxidation of CH_4 to produce CO_2 and simultaneous reduction of SO_4^{2-} to H_2S (Kirkland et al., 1995). In such a reaction the CO_2 and H_2S are achieved in conditions where dissolved H_2S (present as HS^-) reacts with ferric iron oxide (haematite) to form soluble ferrous iron. The HCO^{3-} reacts with Ca^{2+} and Mg^{2+} to form carbonate (Surdam et al., 1993; Kirkland et al., 1995). Dissolved ferrous iron and H_2S would not necessarily react immediately to precipitate as iron minerals (e.g. pyrite) and can migrate in pore waters (Kirkland et al., 1995). These conditions could also be achieved without contemporary biological mediation, as many hydrocarbons are associated with H_2S and CO_2. Petrographic study of bleached sandstones has documented alteration of feldspars to clay (kaolinite) in these settings (Ma et al., 2007).

Sandstone bleaching has also been noticed adjacent to igneous intrusions or pyrometamorphic zones (Walker, 1959; Ahmed, 2002; Holness et al., 2012), where reducing conditions existed.

The essential conditions for bleaching must be capable of removing haematite grain coatings (typically $< <1$ weight %). Haematite is insoluble in water, so must be reduced to Fe^{2+}. Such conditions are reducing.

2.7 Chapter Conclusion

This review chapter leads into Chapter 4, Chapter 6 and Chapter 7 and to a lesser extent Chapter 3 (Geology of the Columbia River Basalts, Snake River Basalts and the Rekjanes Peninsular is summarised in the chapter). The background geology of the Huab Basin given is sufficient to understand the pre-Cretaceous geology. The Cretaceous geology (Etendeka Group) has been summarised in more detail, especially the Twyfelfontein Formation, where new data concerning 'background' diagenesis, burial and compaction has been presented.

Reviews have been given on pyrometamorphism of sandstone, and hydrothermal effects related to igneous intrusion. The review of pyrometamorphism of sandstone is comprehensive; further information on different kinds of pyrometamorphism of a range of substrates and further detail of metastable mineral reactions not required for the Twyfelfontein Formation can be found in Grapes (2010). The review of the contact effects of lava flows on substrate is also comprehensive, if bare. This is due to the paucity of literature on the area. The bleaching of sandstones is not rare, and there is a plethora of literature on the subject. Important references have been given in this chapter and the processes are further discussed in Chapter 7.

3

Methods

3.1 Chapter summary

This chapter describes the analytical methods used in this thesis. It covers each method in sufficient detail to (A) justify its use and (B) provide enough information for further reading or complete clarification. The chapter is not an encyclopaedic instruction into each method used. Errors are discussed for each method.

The second part outlines the five overseas fieldtrips during which data were gathered for this thesis (Namibia x3, USA and Iceland). The Appendix contains additional information regarding the undertaking of fieldwork, logistics and contacts.

3.2 Petrography

All of the chapters make use of quantitative petrographic analyses of thin-sections using a polarising light microscope.

Most of the analyses were carried out on cover-slipped 30 μm thick thin-sections that were stained for carbonate and potassium feldspar identification. Some work has been undertaken on 30 μm thick polished thin-sections which were not stained. The polished thin-sections were also analysed using the Hitachi TM-1000 bench top SEM. Rock chips cleaved from hand specimens not made into polished thin-sections were also analysed using the SEM.

3.2.1 Thin section preparation

3.2.1.1 Technicians and labs used

The thin sections used in this thesis were prepared by a total of three thin-section technicians at two laboratories (Dave Sales and Ian Chaplin at Durham University and John Coundon).. Ian Chaplin's initial sections suffered from poor staining due to the resins available. These sections were suitable for microscopy, but not for image analysis. In all cases, pre-cut rock samples of appropriate size were presented to the technician, who followed the usual procedures for modern thin section production using epoxy resins (e.g. Allman & Lawrence, 1972). A list of commercial thin-section laboratories is contained in the Appendix.

3.2.1.2 Staining

Detrital feldspar crystals are often difficult to differentiate in thin-section. Potassium feldspar is often cleaved along twins such that a simple twin is destroyed during erosion and transportation. Both potassium feldspar and plagioclase are frequently hydrolysed (Tucker, 2001) and sericitised, giving a dusty appearance that makes identification difficult. Most plagioclase feldspars show a characteristic polysynthetic twinning, but some do not and show simple Manebach or Carlsbad twins (Deer et al., 1996). For these reasons staining is desired.

The method followed for staining was that of Wilson & Sedeora (1978). The sections were washed with acetone and rinsed with water to remove grease and finger prints. The sections were then etched over concentrated HF vapour (49–51 %) for 45 seconds. The etching time was chosen based on preliminary tests. The acid

was contained within a plastic petri dish, with a hole cut into the lid of the dimensions of the area on the thin-section to be etched. The section was then immediately immersed in a saturated solution of sodium cobalinitrite for 45 seconds. The section was then removed from the sodium cobalinitrite solution and rinsed three times in three water baths, the final bath being under a running tap. The sections were then dried. The entire procedure was carried out in a fume cupboard using standard departmental safety procedures. This process stains potassium feldspar yellow.

Carbonate staining followed the Dickson method (Allman & Lawrence, 1972). Thin sections without cover-slips that had already been stained for potassium feldspar were etched in 1.5 % HCl for 10–15 seconds. The sections were then immersed in the first staining solution (50 ml of Alizarin red S + 1 g of potassium ferricyanide in 50 ml 1.5 % HCl) for 30–45 seconds. Following the first solution the sections were immersed in the second solution (100 ml of Alizarin red S) for 10 seconds. Following this, the slides were washed in a series of water baths and dried on the hot plate at 50 °C. The Dickson method results in an overall thinning of the calcite component of the thin section, from 30 μm to ~ 15 μm. Overzealous etching can thin calcite such that under XPL, interference colours can be significantly lower than the characteristic 4^{th} order pastel colours (Allman & Lawrence, 1972). See Table 3.1 for stain results.

Mineral Type	Colour after treatment
Calcite	Varying through very pale pink to red
Ferroan calcite	Varying through mauve, purple to royal blue
Dolomite	No colour
Ferroan dolomite	Pale to deep turquoise

Table. 3.1. Summary of the colours produced by Dickson's staining method (from Allman & Lawrence, 1972).

3.2.2 Microscopy and petrographical techniques

3.2.2.1 Point counting

Much use of point counting has been made in this thesis, largely due to the ability to measure a range of phases (feature classes) using the same method so that like-for-like comparisons can be made. Point counting was carried out using a Swift Model F automated point counting stage on a Nikon Optiphot T2-POL polarising microscope using the procedure in Galehouse (1971). It is a standard tool in petrographic studies (e.g. Purvis, 1992; Galehouse, 1971), however, it is slow, laborious, error-prone and requires specialised equipment (Grove & Jerram, 2011). Nevertheless it is a standard tool for the petrographer (e.g. Purvis, 1992; Galehouse, 1971). Much use of point counting has been made in this thesis, largely due to the ability to measure a range of phases (feature classes) using the same method so that like for like comparisons can be made. Point counting also requires a high degree of

operator control and associated decision-making, which allows the occasional poorly impregnated section to be quantified with no less accuracy than the well impregnated sections (with a time penalty, however). Analysis of the less well impregnated sections was not possible using digital image analysis techniques.

Point counting was carried out using a Swift Model F automated point counting stage on a Nikon Optiphot T2-POL polarising microscope using the procedure in Galehouse (1971).

When point counting, both mineral and porosity phases can be considered as a mineral phase for the purpose of area fraction measurements (Ehrlich et al., 1984). Sources of error during point counting are: (1) Errors as a result of taking systematic observations of a thin section and using for areal analysis (Chayes, 1949; Demirmen, 1971; Galehouse, 1971), this is termed 'counting error' or 'analytical error' (Chayes and Fairbairn, 1951) and is inversely related to the number of points counted. In this study, we counted 500 points for each slide, 300 points were recommended as sufficient by sedimentologists regularly using point counts (Stuart Jones, Personal Communication, 2010), which agrees with the 300 or fewer points that are routinely used by other workers in sedimentology (e.g., Purvis, 1992). Therefore 500 points comfortably exceeds the general practice, making my data robust. (2) The error encountered when using a 2D slice to estimate volume percentage in the hand sample, generally termed 'specimen error'. It arises due to heterogeneity in the hand sample that are often not sampled in the thin section (Murphy, 1983) and to stereological considerations in converting 2D data to 3D data, where variations in the pore size distribution can affect the reproducibility of true 3D from 2D data (e.g., Jerram et al., 2009; Mock and Jerram, 2005; Morgan and Jerram, 2006). (3) The user-introduced variability commonly termed as 'operator error' (Demirmen, 1971)

or ‘inter-operator differences’ (Chayes and Fairbairn, 1951). Results obtained by multiple operators may disagree due to misidentification of feature classes (mineral phases, including porosity), skill of researcher, experience, degree of fatigue, psychological state and physical conditions (Griffiths and Rosenfeld, 1954; Demirmen, 1972). Data depicting the inter-operator variability in point counting has been sourced from the literature (Chayes and Fairbairn, 1951; Griffiths and Rosenfeld, 1954; Demirmen, 1972).

	Point Counting (Area %)	**jPOR (Area %)**	**Reason for error**
Counting Error (2σ)	2.5[1] 2.6[3]	0.039[1]	Result of counting observations being an estimate of the true area and not the true fraction.
Operator Error (σ)	3.1[2] 1.2[3] 2.9[4]	1.2[1]	Misidentification, inconsistent identification, mistakes.

[1]This study (Grove & Jerram, 2010) (ten operators, 14 thin sections, porosity), [2]Griffiths and Rosenfeld (1954) (five operators, three thin sections, quartz area), [3]Chayes and Fairbairn (1951) (five operators, ten thin sections, quartz area), [4]Demirmen (1972) (eight operators, five thin sections, limestone constituent)

Table. 3.2. Comparison of errors between jPOR (Grove & Jerram, 2011) and Point Counting. Data sourced from this study and Chayes and Fairbairn (1951); Griffiths and Rosenfeld (1954); Demirmen (1972).

Counting error can be estimated using the equations in Galehouse (1971) p396 (Fig. 3.1.). In this thesis all point counting errors are plotted at 1σ. Mineral and porosity % are all in this thesis are all area %.

The inter-operator error is rarely identified in geological studies using point counting and is often assumed to be negligible despite its magnitude exceeding the often used 'counting error', indeed any errors are often not quoted at all in published point counts, with common counting values between 200 and 400 (e.g. Purvis, 1992; Stokkendal et al., 2009; Khidir and Catuneanu, 2010). Operator errors in previous point count studies by Griffiths & Rosenfeld (1954), Chayes & Fairbairn (1951) and Demirmen (1972) are show in Table 3.2. One operator (me) counted all of the sections in this thesis, so interoperator error is not plotted on graphs.

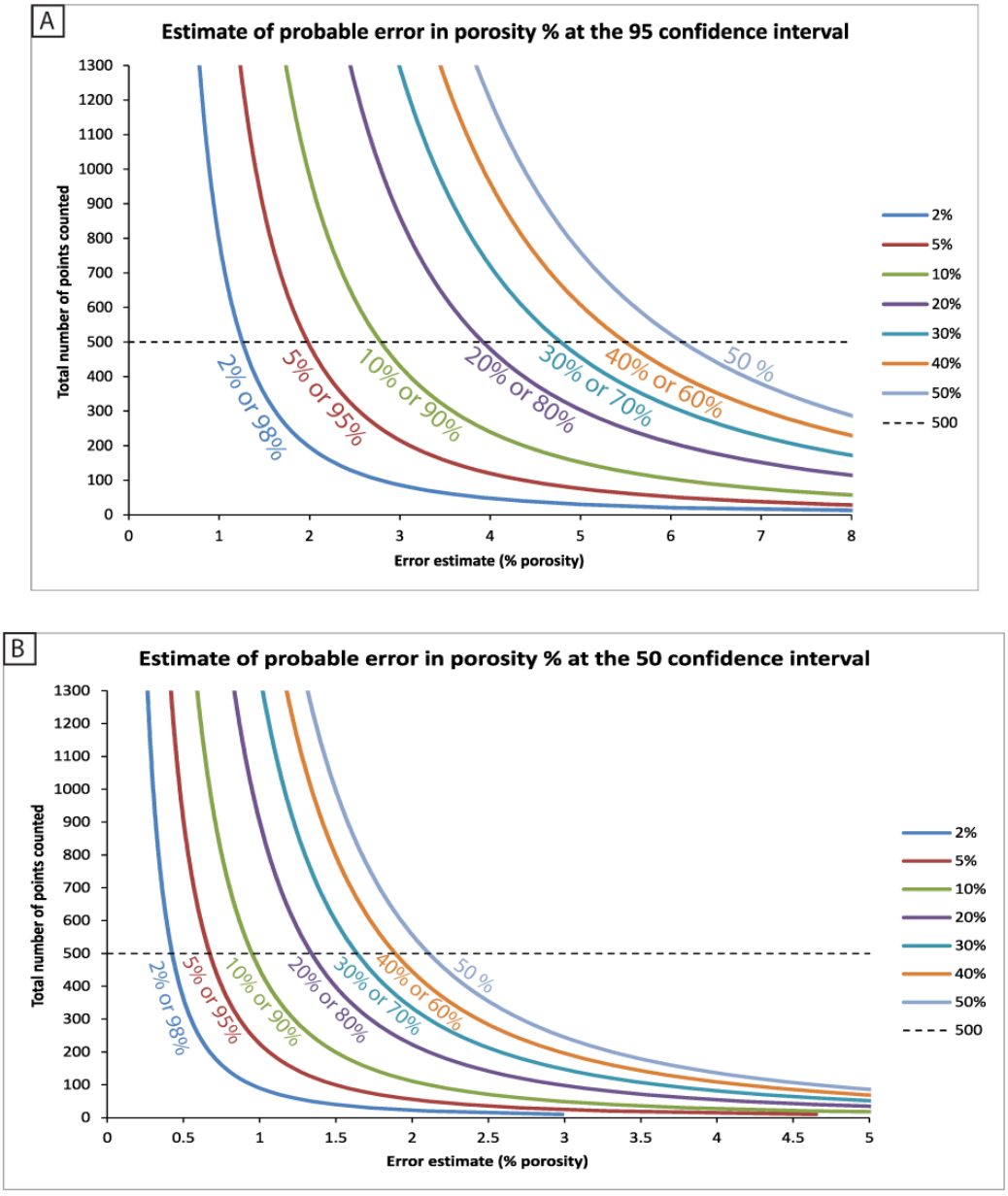

Fig. 3.1. Graphs showing estimating the point counting error at (A) the 50 confidence interval and (B) the 95.5 confidence interval. Note, the error is in actual porosity % not % of the observed porosity percentage.

Quantification of sandstone compaction

Point count data of detrital grains, mineral cements and porosity has been used to generate useful parameters to describe compaction during burial (or resulting from igneous processes). In this thesis extensive use has been made of the calculated Compactional Porosity Loss (COPL) and Cementational Porosity Loss (CEPL), which are both described by Lundegard (1992). The calculation of COPL rather than simply using the difference between a sandstones original porosity and its present minus-cement porosity overcomes the common error of underestimating the compaction due to unaccounted bulk volume changes (Lundegard, 1992).

$$COPL = P_i - (((100 - P_i) * P_{mc}) / (100 - P_{mc}))$$

$$CEPL = (P_i - COPL) * (C/P_{mc})$$

Where P_i is the depositional porosity, C is the proportion of pore-filling cement, P_{mc} is the minus-cement porosity which is calculated from the sum of C and the total optical porosity (TOP).

The introduction of an assumed depositional porosity introduces additional error because of natural variability of depositional porosity in sediments. Depositional porosities used in this thesis are from Pryor (1973) and are based on direct measurements of unburied natural sediments. The average depositional porosity and average standard deviation were used (Pryor investigated multiple localities) for each environment (fluvial sand bar and aeolian sand dune).

A depositional porosity of 49 % and a standard deviation of 2.6 % porosity was used for Aeolian sand. A depositional porosity of 45 % and standard deviation of

2 % porosity was used for fluvial sediments. Where the depositional porosity could be measured directly, that figure was used (see Chapter 5).

This uncertainty was propagated through the COPL calculation such that the uncertainty given graphically through this thesis factors in the uncertainty due to point counting and the uncertainty due to natural variability in depositional porosity. Note well that Lundegard (1992) states that the error is equal to the error in porosity determination; the error I report is therefore greater than the error Lundegard would report for the same data.

Control Sample

Sample **NG52** was deliberately collected in the 2011 field season in Namibia as a reference background sample with which to compare other samples. NG 52 has a porosity of 12.4 % (± 1.5 %). This sample is considered representative of the background red Twyfelfontein Formation sandstone away from igneous related diagenesis. This sample was carefully chosen with this in mind. Petrographical and geochemical parameters are referenced for comparison purposes to NG52 throughout the thesis.

3.2.2.2 Photography

All photomicroscopy was performed using a Nikon Optiphot T2-POL polarising microscope with a trinocular head. A Pentax K7 14 megapixel SLR camera attached to the trinocular was used for image acquisition. Images were acquired as RAW files and processed for white balance and exposure using Adobe Photoshop.

Field photographs were also taken with the Pentax K7 or a Pentax Optio WG-1 compact camera.

3.2.2.3 Scanning Electron Microscopy

A Hitachi TM-1000 tabletop SEM was used for all SEM analyses. Analyses were performed on polished thin-sections and on rock chips cleaved from samples with an accelerating voltage of 15 keV. The rock chips were cleaned under the tap, followed by acetone to remove dust and grease prior to examination. None of the samples were coated, all observations being made of un-coated samples.

3.3 Image Analysis

3.3.1 jPOR: Digital image analysis to quantify porosity

Due to the relatively poor accuracy of point counting as a tool for the estimation of porosity, an image analysis solution was developed. The method uses free to download software and requires no specialised scientific equipment. The intention was to use the method developed to perform rapid and accurate measurement of the samples. Despite the method being proved as at least, if not more accurate than point counting (Grove & Jerram, 2010). The method was not used extensively in the thesis due to variable thin-section blue resin impregnation. This made the requirement of operator decision making, aided by microscopic observation essential. Nevertheless, this forms an important part of the work undertaken and was published (Grove & Jerram, 2011).

The new developments in image analysis have the added advantage that they can potentially provide increased capacity to undertake standard measurements, with more speed and accuracy than traditional methods. For example, the quantification of rock porosity from thin sections impregnated with blue epoxy resin is routine in geosciences, and most commonly undertaken with point counting. Total porosity is defined as the ratio of void volume (pores) to the bulk volume of a rock and is commonly given as a percentage, hence: total porosity = Vp/Vb x 100. Where Vp is the pore volume and Vb is the bulk volume (Curtis, 1971). Porosity is important in determining the reservoir properties of a rock (for both aqueous and hydrocarbon fluids), and in studies of diagenesis, compaction and evolution of sediments (Curtis, 1971; Tucker, 2001). A number of techniques exist to quantify porosity including: 2D texture measurements (e.g., point counting), mercury injection and helium injection porosimetry. Measurements made from 2D sections, which form the basis of this study, record the porosity as resolvable from an optical image of the sample (total optical porosity).

Digital image analysis is potentially superior in speed and accuracy over point counting because millions of points can be analysed in the sample and this leads to far superior datasets. The key to be able to perform accurate digital porosity measurements is the ability to generate a porosity threshold image (one which separates the porosity-voids from the rest of the objects in the image). Poor quality data can arise from the introduction of noise and inadequate or overzealous pre-processing methods increasing user bias during thresholding. Additionally, existing techniques can require very specific software (e.g., costly proprietary software, microscope specific software, etc.).

The jPOR method described in this study overcomes these problems by streamlining and standardising colour pre-processing by applying our newly developed custom 8-bit palette which has been developed in conjunction with the jPOR macro for ImageJ (Rasband, 2009). The newly developed macro jPOR.txt has been designed to make quick and accurate porosity analysis available to any researcher in possession of a personal computer and high resolution colour digital images of blue stained thin sections (e.g., those captured from thin sections mounted on slide scanners).

The jPOR macro offers instructions at each stage so that inexperienced users with no prior image analysis experience will find it easy to use. The method uses technically non-specific hardware and software which should be familiar to most computer users. The jPOR methodology is discussed with advice about image preparation, the steps required for analysis and how the macro is installed. Results are presented for both point counting and jPOR calculated porosity for the same samples, and in the case of the four 'fell sandstone' samples He injection is also tested. Inter-operator variability is also tested on the same set of samples analysed by ten users, this is compared to point counting studies where multiple operators have been evaluated. jPOR is supplied with a user guide and the 8-bit paletted bitmap test files used in this study (see Appendix).

The jPOR macro for ImageJ requires an 8-bit paletted colour image file (a bitmap.bmp file works best in the platform independent version). For Petrographic Image Analysis (PIA) there must be a direct relationship between pixel colour and feature class (the phase of interest, in this case blue resin filling porosity); clearly the more straightforward this relationship, the more reliable the procedure becomes.

Here we are only interested in two feature classes (porosity and solids in the form of grains and pore-filling cements in the rock).

The classic method to measure TOP (total optical porosity) using PIA is to acquire a digital image of a thin section using an optical microscope combined with, for example, an analogue video camera output (Ehrlich et al., 1984) or as technology has advanced higher resolution digital cameras (Lamoureux and Bollmann, 2004). Previous workers have then separated the image into red, green and blue components and threshold a greyscale histogram of an individual channel (Ehrlich et al., 1984; Andriani and Walsh, 2002; Crawford and Mortensen, 2009; Dey et al., 2009). The image can then be thresholded to a 2 bit image where the class of interest is black and everything else is white. The drawback of greyscale thresholding is that the contrast between classes of interest can be low, which necessitates contrast enhancement and shading correction (Andriani and Walsh, 2002). Noise within grains can also pose problems. Noise from intra-granular texture difficult to threshold away from pore space using greyscale images; the best results came from the red band, but nevertheless were visually inferior to the jPOR method. When using greyscale thresholding methods it is difficult to produce a binary image where the pore space class is entirely thresholded without including some intragranular noise, thus inaccurately recording the porosity. To remove the noise component, the threshold value requires reduction, which also removes porosity, microporosity also becomes difficult to distinguish. A simpler and less subjective method using colour thresholding has been developed, that requires less pre-processing and removal of noise, thereby reducing inter-operator variability

In ImageJ (rasband, 1997-1999) free to download software, the normal way of thresholding a 24-bit colour image, using built in tools, is to open it as a 24-bit

image and use the built in 8-bit colour conversion tool (Image>Type>8-Bit Colour) set to 256 colours. This image can then be thresholded. The conversion creates an indexed 256 colour image which is not sorted according to hue; therefore the colours representing specific classes are separated by colours which represent other classes. Applying a threshold to separate two classes (e.g., all the blues in the image from the other colours) clearly will not work as there is no systematic order of colours belonging to individual feature classes, as thresholding only works with a block of colours that are numbered together in sequence. We have developed a custom 256 colour (8-bit) palette which forces the grouping of feature classes (e.g., blues) enabling ImageJ to threshold porosity based on colour (hue) which can be applied to any 24-bit image using common image editing software (Irfan View, Adobe Photoshop, Corel Photo Paint).

The custom 8-bit palette pre-processing method developed in this study addresses the drawbacks of greyscale thresholding porosity calculation methods, without the need for complicated filtering or adjustment. jPOR 60 is a custom 256 colour palette, sorted by hue, and designed to represent a typical blue resin impregnated thin section.

The palette was constructed using Corel Photo-Paint X3 from digital scans of blue resin impregnated thin sections. The thin sections chosen to produce the pallet were: 1) basaltic hyaloclastites from Iceland, and 2) aeolian sandstone examples from Namibia. The hyaloclastite was first chosen because it displayed a full range of colours from blue (resin) to dark brown (clays). The large range of naturally occurring colours in the hyaloclastite samples used here result from its diverse mineralogy. The nature of formation (hydroclastic fragmentation, and quenching of a lava flow entering seawater, in this case, Fischer and Schmincke, 1984), subsequent

rapid devitrification of glassy rims, and potentially varied burial diagenesis (clay transformation and hydrothermal mineralisation) of the basaltic hyaloclastites, provided a large number of characteristic minerals to build into the palette (volcanic glass, palagonite, illite, chlorite, zeolite, calcite, and unaltered phenocrysts within basalt clasts, such as plagioclase and olivine). The sandstone samples were chosen because they had a clear representation of porosity impregnating blue resin and are composed of quartz colours absent from the hyaloclastite samples. Corel Photo Paint was chosen for this operation over other graphics editing programs (Adobe Photoshop, Irfan View) because of its ability to generate an optimised palette which could be sorted by hue and then manually edited by dragging and colour editing. To further aid thresholding, a blank region was built into the palette of 9 colours which did not naturally occur in any of the thin sections. The finalised design comprises of 59 blues which represent blue resin impregnation of pore space, 9 separator colours and 188 rock colours. Most of these blues came directly from the hyaloclastite sample (40); additional colours (20) were added from other impregnated samples so that there was a more complete range to ensure an accurate capture of the porosity in the image. The 9 separator colours are all similar bright greens chosen because they did not occur in any test images. The 188 colours representing the rock include black and white which left 186 colours that were customisable. Initially there were 206 colours, 20 were taken up by the additional blues, and 2 were taken up by black and white. The Corel Photopaint optimised 8-bit palette automatically creates a 256 colour palette based on the highest percentage of colours in the image (Corel help); this was good as a starting point because the processed 8-bit image had the same visual appearance as the 24-bit image (Fig. 3.3.). However, it was biased towards similar brown colours; there were few light greys and creams which are common in

other sedimentary rocks. A proportion of the browns were therefore edited and changed into colours sampled from an aeolian sandstone thin section from the Twyfelfontein Formation, Namibia (Dickinson and Milliken, 1995; Jerram et al., 1999, 2000; Mountney et al., 1999). This supplies a palette of colours that best represent the types of colour variation we expect to see in a sedimentary thin section, when it is represented in an 8 bit colour image. The resulting custom palette (Fig. 3.3.) was then saved in a variety of formats so that any common graphics editing package can be used to apply it to other images, including Irfan View (freeware).

When the palette is applied to an image the graphics editor will assign pixels to the closest colour within the palette, blues will remain blue, but not necessarily an identical blue to the 24-bit image, likewise for other colours. While colour representation may not be entirely faithful (false colour) class representation is faithful, providing no dithering is set. Dithering introduces noise into the compressed representation to visually reproduce the image in the 24-bit image. Dithering therefore does not preserve areas and must be unselected when applying a custom 8-bit colour palette to the 24-bit image. By forcing the colours in a thin section image to our pallet, one can still see and assess the main sedimentary features, and now all the colours are grouped so that an accurate thresholding of the porosity can be realised.

3.3.2 Procedure

3.3.2.1 Procedure 1: Digital Image Acquisition

The aim is to produce a 24-bit colour .tiff image at high resolution of the whole sample without distortion. Typically a digital video camera attached to a microscope would be used to acquire a digital image directly from the thin section (Ehrlich et al., 1984; Tovey and Hounslow, 1995). The problem with this is the difficulty in acquiring a low magnification image of the entire thin section without distortion towards the edges of the frame. When measuring relative areas across a complete 2D sample variable distortion is detrimental to producing accurate results. Additionally, depending on the grain size of the sample, a larger region of interest may be required (e.g., whole thin section image), which can be difficult to achieve from a microscope. It is acknowledged that sophisticated systems exist that correct for image distortion and some examples of microscopes can capture large areas of thin sections but for the most part these are specialised systems that may not be available to many potential users.

In order for jPOR to conform to the ease of access and use principle, we chose to explore the capture of thin section images using scanning techniques. The method of De Keyser (1999) provides a rapid, cheap, and effective method of overcoming and circumventing the use of conventional light microscopy. The method used a Nikon LS-2000 digital film scanner capable of a 2700 dots per inch (dpi) resolution to directly capture an image of a standard size petrographic thin section. Our method is adapted from De Keyser's (1999) method to work with the Minolta Scan Elite II digital film scanner capable of 2820 dpi resolution. We have also experimented with the Epson Expression 1680 Pro flatbed scanner which is

designed to scan transparencies at 3200 dpi. The Epson flatbed scanner produced acceptable results, the drawback was the fixed dual-focus mechanism which made acquiring images as sharp as the Minolta 35 mm film scanner difficult. In order for a flatbed scanning system to work with a thin section the light source must be able to be transmitted through the sample (not reflected) which makes the slide scanners ideal for this type of capture, and limits the choice of multipurpose flatbed scanners to those with a top down light source.

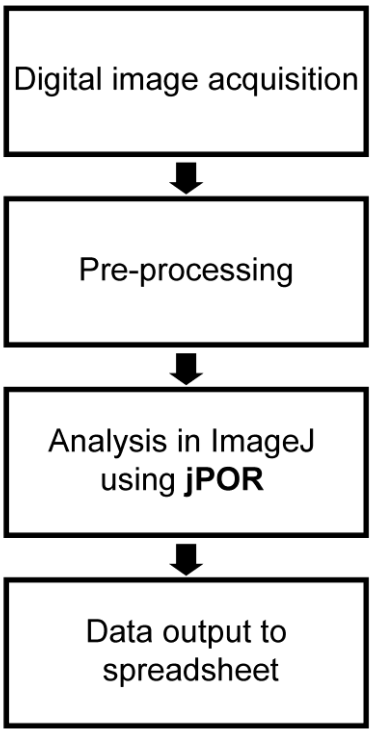

Fig. 3.2. Flowchart of total optical porosity (TOP) calculation using jPOR, from Grove & Jerram (2010).

3.3.2.2 Scanning

The most straightforward and most effective method of acquiring digital images for the jPOR porosity measurement method is to use a conventional 35 mm film scanner such as the Minolta Scan Elite II, which was used. Like the Nikon LS-2000 scanner used by De Keyser (1999), the Minolta Scan Elite II comes equipped with several adapters used for different sized slides. This method uses the adapter designed for 35 mm negative strips (of six exposures). The first stage is to open the adapter and place the thin section slide face up into one of the central slots (either '3' or '4') with the area to be digitised aligned with the window. The adapter is then closed and snapped shut. One slide may be scanned at a time because the elasticity of the plastic adapter is relied on to accommodate the glass slide. The adapter is then loaded into the scanner which will automatically grab the adapter after about 2.5 cm of insertion. The third stage is to acquire the image using the software bundled with the scanner. Images should be scanned at maximum resolution (2820 dpi) and saved as .tiff files. Prior to completing the final scan, a preview image should be reviewed. We have found that applying the auto focus function and increasing the colour saturation necessary to best reproduce the blue epoxy filling the pore spaces. The procedure is simply repeated for each sample, maintaining settings throughout the batch, typically taking around 2 minutes per sample. The functionality of the slide scanner and its software should be considered when using different systems; the ability of the scanner to be focused on the image is clearly a desirable to produce sharp images for porosity analysis.

3.3.2.3 Photomicroscopy

Low magnification photomicrograph images can be analysed by jPOR. The microscope should be used on the lowest magnification available and the recorded image resolution set to the highest setting. Photomicrographs on traditional colour transparency film or negative film can also be digitised for jPOR analysis. When acquiring images using conventional photomicroscopy researchers should be aware of the potential disadvantages compared to the method outlined in 3.1.1, and where possible use microscopy equipment designed to record high resolution colour images corrected for edge distortion.

3.3.3 Procedure 2: Pre-processing

Pre-processing prepares the digital image of the thin section for the jPOR macro in ImageJ. The image is trimmed and converted to an 8-bit paletted .bmp or .tiff, the development of the custom palette has already been discussed in 2.2. Alternatively each image can be converted to an 8-bit paletted file with its own custom optimised palette; this will require much more user biased thresholding within ImageJ. Successful pre-processing can be achieved in the freeware program IrfanView as well as common image editing programs such as Adobe Photoshop or Corel Photo-Paint, a method for all three is described:

1. Open image in chosen image processing software (Corel Photo Paint, Adobe Photoshop or IrfanView)

2. Crop image to make a rectangle only comprising of sample (i.e., no slide mounting or edges).

3. Convert to an 8-bit paletted file using the provided custom palette. Make sure that no dithering is set. The image may look slightly unnatural, but the area of porosity will be preserved, albeit with fewer colour values.

3a. In Corel photo paint: Image>Convert to Paletted 8-bit...>Palette set custom, open, navigate to the palette file-OK-set dithering to none-OK. Within the 'Convert to Paletted 8-bit' box there is the option to run this as a batch. All files within the batch must be open.

3b. In Adobe Photoshop: Image>Mode>Indexed Colour. Set 'Palette' to 'Custom' and you will be presented with a new window- click load and navigate to the custom JPOR palette (JPOR_60) and click load- OK this operation. Set dither to none under Indexed Colour options and click OK. The image will now be an 8-bit paletted file. This can be automated by recording the action then playing it via the Automate>Batch tool.

3c. In IrfanView: Image>Palette>Import Palette>navigate to palette-open.

4. ImageJ works best with .bmp images whereas the occasional .tif image will fail to be displayed. Therefore we recommend conversion to .bmp format. This can be done as a batch in Adobe Photoshop and Corel Photo-Paint. Images within a 'batch' must then be placed in a dedicated folder.

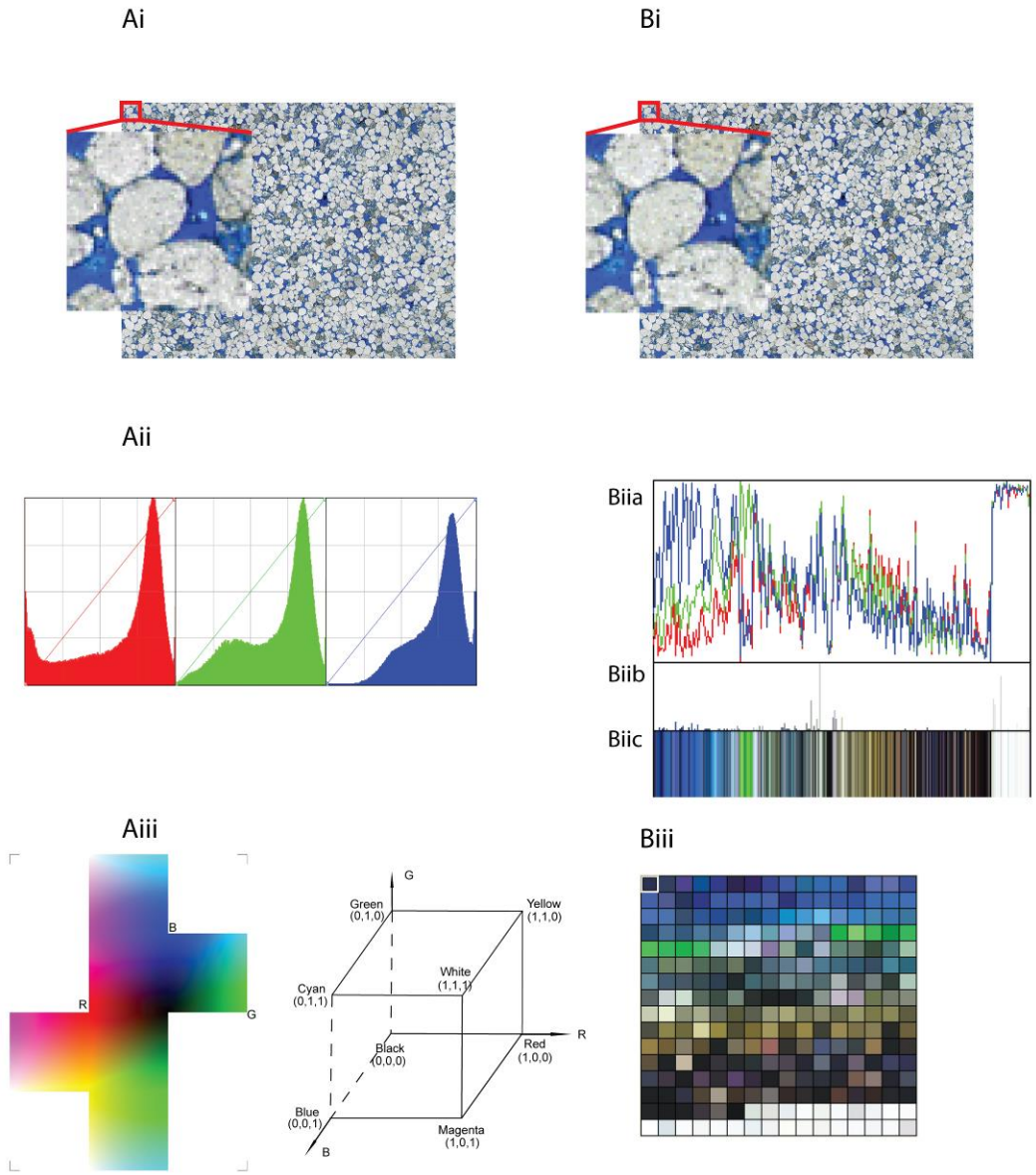

Fig. 3.3. Ai) 24-Bit cropped colour scan of PL12 each pixel is one of 14 million possible colours, described by RGB value. Aii) 24-bit PL12 RGB values plotted for each channel, traditional methods would threshold the red histogram. Aiii) Image of outside face of RGB cube showing R,G,B corners, courtesy of Steve Sangwine (2010) this wraps around cube labelled with RGB corners, white, black and CMY (after Kang 1997). Bi) 8-bit paletted image with jPOR60 palette applied. Note visual appearance very similar to 24-bit image. Biia) Image in Bi is composed of pixels with colours chosen from 256 colour palette, each colour has RGB value shown by red, green and blue lines. Biib) Histogram of number of pixels, for each jPOR 60 colour. Biic) Arrangement of porosity forming colours, enabling segmentation using ImageJ Threshold tool. Biii) 16x16 grid of jPOR60 palette, porosity separated from rock colours 9 green colours. From Grove & Jerram (2010).

3.3.4 Procedure 3: using jPOR to calculate porosity in ImageJ

ImageJ is a public domain image analysis software designed to be adapted for different roles. The 'freedom' of the ImageJ package is the cornerstone of jPOR. Once ImageJ has been installed, the jPOR macro requires installation. For jPOR to run on ImageJ startup replace the file StartupMacros.txt in the ImageJ macros folder with StartupMacros.txt distributed with jPOR. When jPOR is installed like this, a clickable jPOR icon will appear in the ImageJ menu bar. Alternatively jPOR can be installed after ImageJ startup by going to Plugins>Macros>Install… then navigating to jPOR.txt and clicking 'open'.

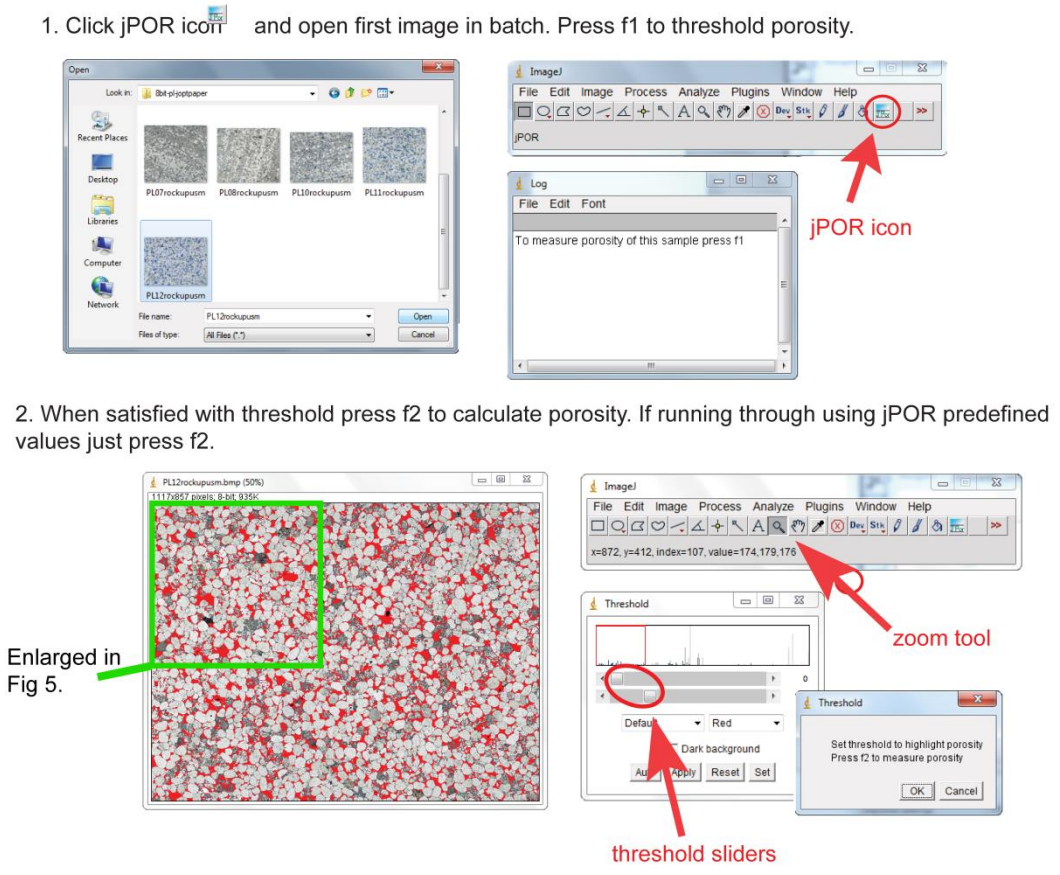

Fig. 3.4. Workflow using jPOR macro within ImageJ. Screenshots are shown for key operations. From Grove & Jerram (2010).

To run jPOR click the jPOR icon located in the top right corner of the ImageJ menu. This will open a window where the first file in a batch can be located, open the first file in the batch. jPOR will then prompt to press F1 to begin porosity measurement. Pressing F1 automatically thresholds the image using the default values, and displays the threshold command box where the threshold level can be manually adjusted to refine the porosity selection. The built in ImageJ zoom tool can be used at any stage. When the porosity selection is satisfactory press F2, which will perform the area calculation of the thresholded pixels and append it to the results table. The ImageJ threshold window has a button labelled 'Auto', this button is not for jPOR default. jPOR then prompts to press F3 to load the next image within the batch from where the process is restarted (F1, F2, F3, F1., etc.). When the processing of a batch is complete, F5 should be pressed which closes redundant windows and copies the results table to the clipboard for pasting into a spreadsheet. The jPOR workflow is illustrated in Figs. 3.4, 3.5 and 3.6. It should be noted that jPOR will work through the batch files in a loop and so will re-open the first file that you analysed once you have gone through all the files in the batch, you should press F5 at this point to avoid re-analysing the same sample.

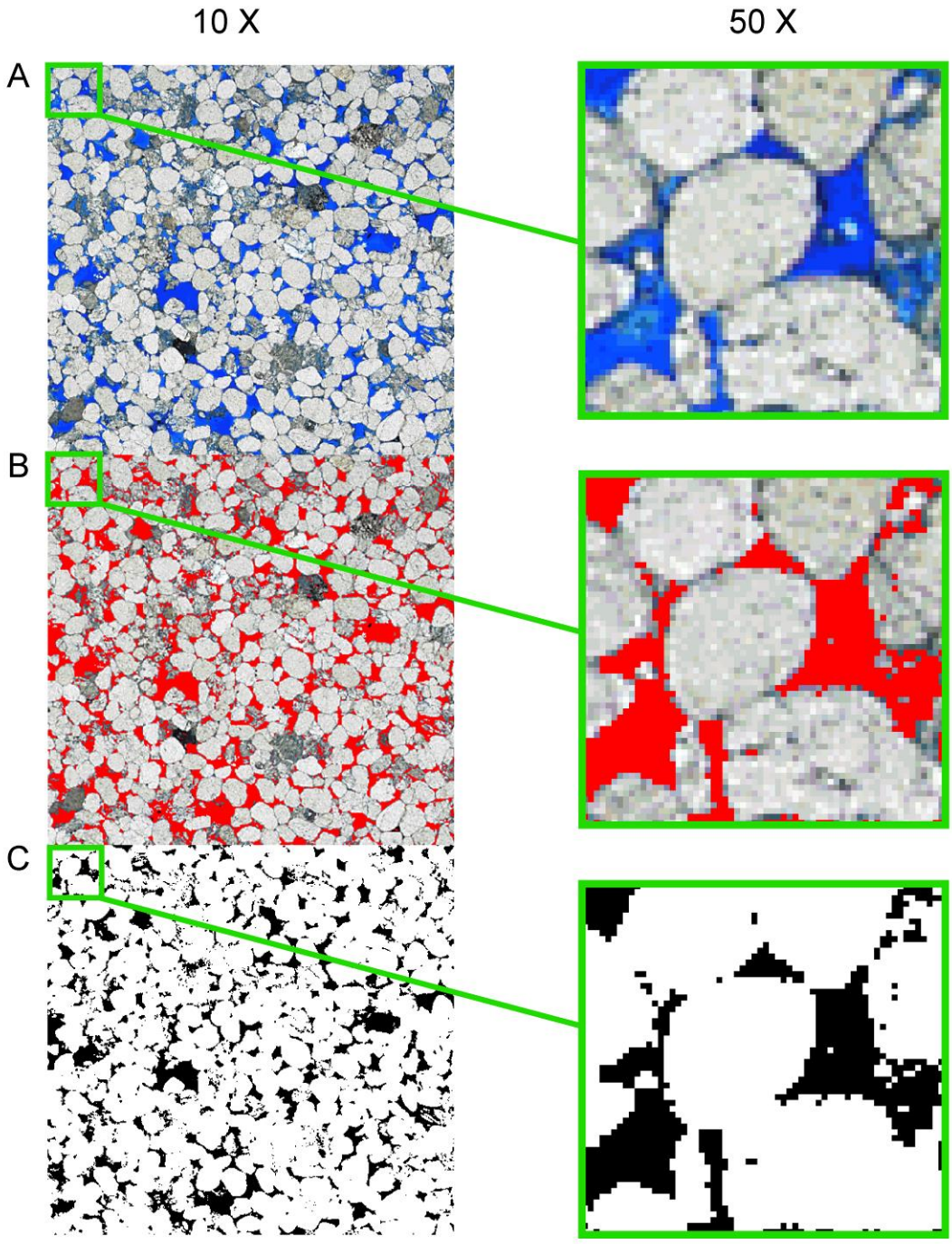

Fig. 3.5. Enlarged sections (10x and 50x) of sample in Fig.3.3 showing thresholding to binary image of pore space. A) 8-bit un-thresholded B) Red mask during thresholding operation covering thresholded pixels C) Binary image product of threshold operation. jPOR (default) values have been set. From Grove & Jerram (2010).

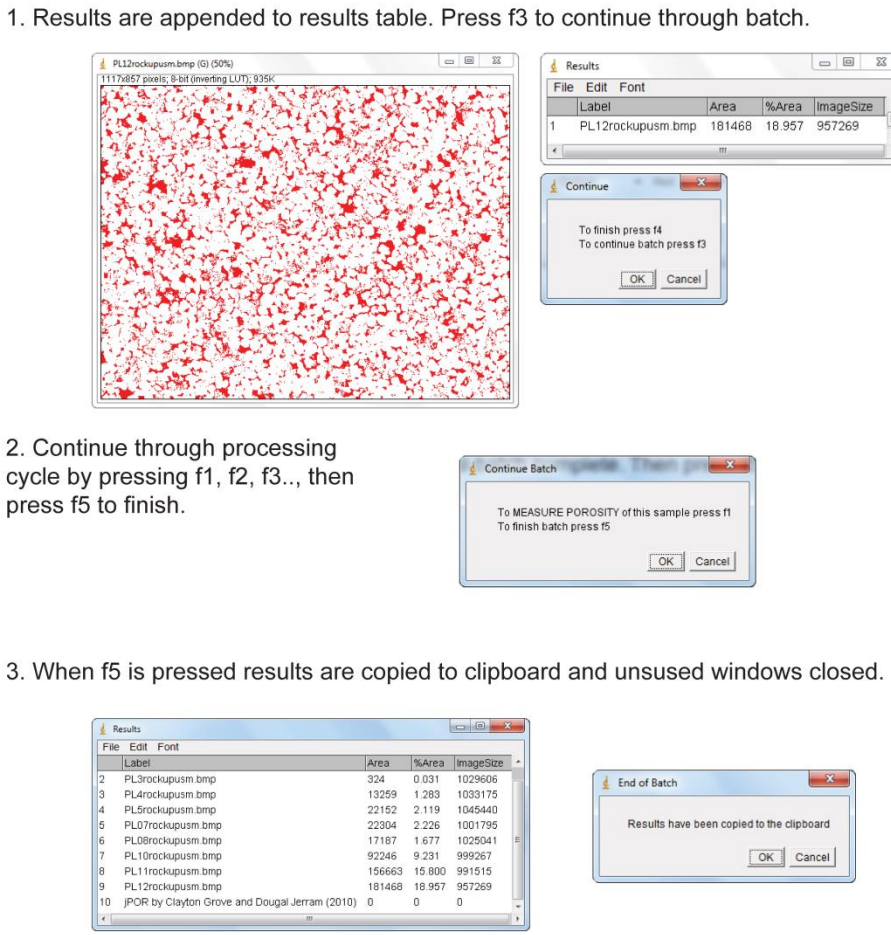

Fig. 3.6. jPOR workflow after thresholding. 1. Results window and option to finish or continue batch. 2. Porosity measurement of second sample. 3. Results output.

3.3.5 Testing jPOR

The performance of jPOR has been evaluated against point counting and He injection porosimetry. Additionally the series of test images have been evaluated by ten different users to measure the inter-operator variability of the technique. The object is to compare point counting with jPOR to show that the latter method is at least as precise and accurate. When point counting porosity can be considered as a mineral phase for the purpose of area fraction measurements (Ehrlich et al., 1984),

sources of error during point counting and PIA are the same as those encountered when counting mineral proportions. In this test, we counted 500 points for each slide, The number of 'points' counted by jPOR equals the number of pixels in the image, therefore dramatically reduces the analytical error as described above. The maximum image size encountered in our test samples was 3 983 252 pixels and the minimum was 957 269 pixels, which can be considered as the number of points analysed in comparison to the 500 used for point counting. The inter-operator variability for the jPOR method has been tested in the present study by ten different operators (termed Researcher 1, 2... 10). Results are presented in Table. 3.3 and Fig. 3.7.

Counting errors were calculated at the 95.4% confidence level (2σ) using the equations in Galehouse (1971) p396. 500 points were counted for each thin section which produced counting errors of between +/- 0 and +/- 3.8 %. Using the same equation errors calculated for jPOR were between +/- 0.002 and +/- 0.05 % (smaller than graph points so not plotted). For point counting the only variable (as 500 points were counted for each sample) was the percent porosity hence the counting error reflects that. Where zero porosity was counted the error is zero. jPOR has two variables as the number of 'points' counted depends on the image size(here between 3 983 252 and 957 269) and the percent porosity, the increase from 500 points to the large numbers of pixels within our prepared images is responsible for the decrease in counting error from a maximum of 3.8 % (point count) to 0.1 % (jPOR).

Tests between multiple operators showed a mean inter-operator variability of 3.5 %. The maximum inter-operator difference of 7.8 % which was on sample FellSstA. Nine out of fourteen samples had differences between researchers of less than 3.8 % (within the counting error of point counting). In this study the mean standard deviation between operators over the 14 sections was 1.2 %. For point

counting the inter-operator variability is generally considerably higher than between operators using jPOR. In the three studies we have used from the literature (Chayes and Fairbairn, 1951; Griffiths and Rosenfeld, 1954; Demirmen, 1972) the mean inter-operator variability was 6.4 % with a maximum of 12.2 %. The mean standard deviation between operators in the three studies was 2.3 % (Chayes and Fairbairn, 1951; Griffiths and Rosenfeld, 1954; Demirmen, 1972). The inter-operator error is rarely identified in geological studies that use point counting and is often assumed to be negligible despite its magnitude exceeding the often used 'counting error', indeed errors are often not quoted at all in published point counts, with common counting values between 200 and 400 (e.g. Purvis, 1992; Stokkendal et al., 2009; Khidir and Catuneanu, 2010).

The sample set used was the PL (Ponded Lava) thin-sections. The sections used in the jPOR test were unstained, un-coverslipped thin-sections. The thin-sections used in Chapter 4 are stained and coverslipped. The preparation difference accounts for the difference in point count values between Table 3.2 and the reported results in Chapter 4.

Sample	Point Counting (Porosity %)		He injection (Porosity %)	jPOR (Porosity %)	
	Point Count	2σ counting error		jPOR60 (default)	2σ counting error
PL1	0.00	0.00	-	0.01	0.00
PL3	0.10	0.28	-	0.03	0.00
PL4	2.60	1.42	-	1.28	0.02
PL5	3.00	1.53	-	2.12	0.03
PL07	2.90	1.50	-	2.23	0.03
PL08	2.30	1.34	-	1.68	0.03
PL10	9.10	2.57	-	9.23	0.06
PL11	13.60	3.07	-	15.80	0.07
PL12	15.00	3.19	-	18.96	0.08
FelISst13A-139	20.00	3.58	20.65	22.79	0.04
FelISst1A-3	16.00	3.28	15.57	14.09	0.05
FelISst286	21.10	3.65	17.39	21.76	0.05
FelISst9A-84	16.30	3.30	18.80	15.34	0.04
FelISstA	22.80	3.75	19.92	19.74	0.05

Sample	jPOR 10 tested with 10 researchers (Porosity %)											
	1	2	3	4	5	6	7	8	9	10	Mean	SD
PL1	0.012	0.012	0.012	0.000	0.012	0.012	0.012	0.012	0.001	0.000	0.009	0.006
PL3	1.755	0.031	0.031	0.001	0.003	0.031	0.031	0.031	0.031	0.031	0.180	0.547
PL4	7.902	1.065	1.283	6.324	1.044	1.283	1.283	1.025	1.283	1.430	2.270	2.519
PL5	1.323	2.119	2.119	2.119	1.648	2.119	2.119	1.648	2.464	2.119	1.950	0.334
PL07	1.585	2.226	2.226	0.535	1.438	2.226	2.145	1.439	1.711	2.226	1.745	0.553
PL08	1.677	1.789	1.677	1.413	1.677	1.677	1.677	1.258	1.677	1.677	1.625	0.158
PL10	9.231	8.282	9.231	6.275	9.231	9.231	9.231	7.681	7.137	9.231	8.545	1.092
PL11	13.830	15.800	15.800	15.800	14.467	15.800	15.800	14.313	16.178	15.800	15.278	0.821
PL12	16.291	18.957	18.957	18.957	19.658	16.783	17.531	16.783	16.783	18.957	18.120	1.247
FelISst13A-139	22.790	19.199	22.790	21.823	22.719	22.790	21.823	22.790	25.620	22.790	22.532	1.564
FelISst1A-3	18.099	14.092	14.092	10.338	14.015	14.092	15.506	14.092	14.092	14.092	14.230	1.883
FelISst286	20.769	17.695	21.764	21.764	21.763	21.764	21.764	21.764	20.769	21.763	21.213	1.285
FelISst9A-84	15.343	19.627	15.343	15.343	19.627	15.343	15.343	15.343	14.646	15.343	16.448	1.856
FelISstA	23.590	19.739	19.739	19.739	17.819	19.739	17.822	19.739	19.739	19.739	19.566	1.570

Table. 3.3. jPOR test results.

Most jPOR results fall within the 95.4 % counting error bars for those from point counting in the same samples. The mean jPOR value was always within the point count counting error and the jPOR 60 (default) value was within the point count counting error for 13/14 samples. The difference between jPOR 60 (default) and point counting was between 0.0 % and 4.0 % over the 14 sample thin sections with a mean difference of 1.4 % with a standard deviation of 1.2 %. The difference between the mean jPOR porosity value (10 researchers) and point counting ranged from 0.0 % to 3.3 % with a mean difference of 1.2 % and a standard deviation of 1.1 %. The comparison of jPOR 60 (default) with mean porosity values of the ten test researchers produced a good correlation (R2= 0.9923) with a mean difference of 0.6 %. The porosity measurements achieved by using jPOR can be considered as providing the most statistically robust compared to point counting, and considering

its speed and ease of use, a vast improvement to the way in which we routinely measure porosity from blue stained thin sections.

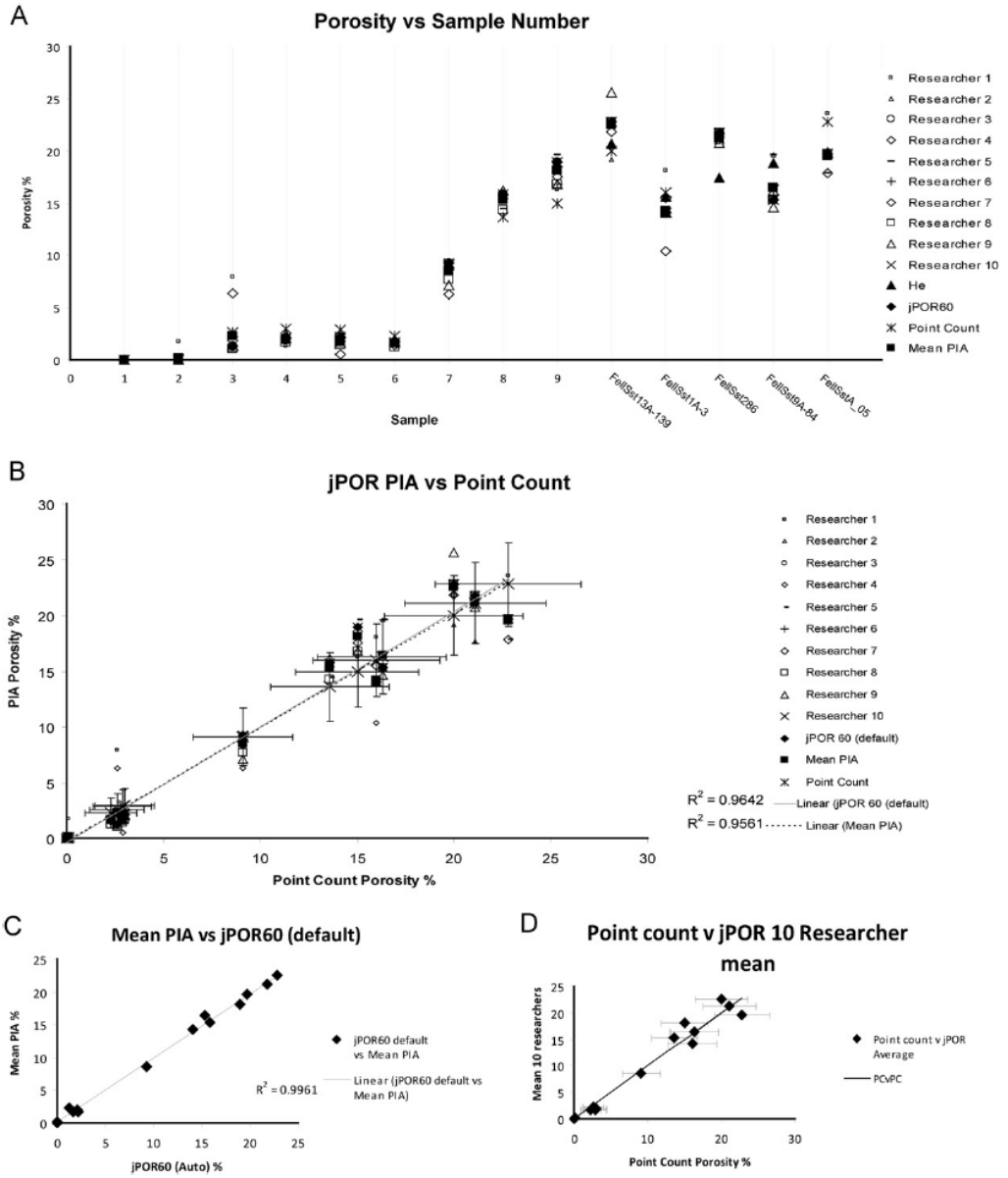

Fig. 3.7. Compilation of results graphs. (A) shows porosity vs. Sample for each of the 10 researchers (grey dashed lines with open markers), He injection porosity (solid triangle marker), jPOR60 (solid diamond marker). Point count (double cross marker) and mean PIA (solid square). (B) shows PIA vs. Point count with the same symbology as (A). Counting errors at the 2σ confidence level are for point count data. (C) Mean PIA vs. jPOR60 (D). Point count vs. jPOR 10 Researcher average.

3.3.6 jPOR test Conclusions

Porosity measurement using jPOR combined with the jPOR 60 custom palette makes an effective, accurate and easy method of measuring total optical porosity. The use of the custom 8-bit palette makes it possible to accurately threshold pore space from a rock based on hue rather than a single RGB greyscale channel. The calculated counting errors at the 95.4 % confidence level for point counting were higher than jPOR, as expected due to the vastly superior number of points counted with jPOR (whole image). Both methods (jPOR and point counting) have an inherent element of operator error defining porosity. The inter-operator variability using the jPOR method was less than point counting, probably due to the fact that the whole slide can be viewed in our process, making comparison within the slide possible before a threshold decision is made; this is impossible while point counting.

PIA calculated porosities generally agreed with point counting (within (2σ) point count counting errors), even with user variability between the ten researchers. The mean value of the ten researchers agreed well with the point counting values suggesting that the actual porosity of the rock was well defined by both methods. The fully default jPOR 60 values also produced good results compared with point counting. The similarity between jPOR 60 (default) and the mean value of the ten test researchers leads to the conclusion that running jPOR 60 without user action at the thresholding stage will produce results as good as point counting but with a smaller counting error and if run automatically with the default setting no operator variability (by definition) (Table 3.1.). Even if operator error is introduced by manual

adjustment during thresholding we have shown that to be less than the operator error routinely encountered while point counting.

3.3.7 Summary

The jPOR method is a significant step-forward and the paper has had 6 citations to-date, three of which directly use the method to estimate the porosity reported within the publication. The other three draw upon work relating to accuracy and statistics within the paper.

3.3.8 Other image analysis ideas

The basic jPOR custom palette and thresholding techniques have been developed into methods to extract additional petrographic parameters. For instance a complex workflow was developed to measure pore throat diameters, which is currently under testing in collaboration with Prof. Rodrigo Bagueira De V. Azeredo in Brazil.

Given the basic thresholded image, many parameters can be generated, including shape descriptors and orientation descriptors. These may be of use in future sedimentological analyses.

3.4 X-Ray Diffraction

3.4.1 Brief outline of theory

Physicists Sir W. H. Bragg and his son Sir W. L. Bragg developed a relationship in 1913 to explain why the cleavage faces of crystals appear to reflect X-ray beams at certain angles of incidence (2θ). The variable'd' is the distance between atomic layers in a crystal, and the variable λ is the wavelength of the incident X-ray beam; n is an integer. The Bragg's observation is an example of X-ray wave interference (http://web.pdx.edu/~pmoeck/phy381/Topic5a-XRD.pdf).

Bragg's Law:

$$n\lambda = 2d \sin\theta \qquad (1)$$

Understanding Bragg's law, with the use of an X-ray diffractometer, allows the detection of the 'd' spacings of planes within unidentified minerals. The comparison of measured d-spacings with known standards therefore allows identification of the mineral species, or species contained in a mixed sample.

For a full account of the development of the XRD technique and laboratory methods see Moore & Reynolds (1989).

The library of standard d-spacings used here is the one held by the Mineralogical Society of America, which includes the 3803 recognised minerals in their database (http://www.handbookofmineralogy.org/search.html?p=all).

3.4.2 Labs and equipment

All XRD analyses were carried out on the Bruker D8 diffractometer in the Department of Chemistry, Durham University. The D7 uses 1.5406 Å wavelength copper (Cu) K-Alpha 1 radiation.

Each sample was analysed using coupled detector and source shutter drive, starting at 2.0 ° 2θ and traversing to 90 ° 2θ with a step size of 0.02 ° 2θ. A knife blade was also used as recommended by regular users of the equipment. The output was then graphed in Microsoft Excel, where peaks were compared with the standards (http://www.handbookofmineralogy.org/search.html?p=all). No quantitative measurement was undertaken; XRD was purely used to identify minerals. Spectra were corrected to the quartz 100 peak (26.67 ° 2θ).

3.4.3 Sample preparation

As no quantitative measurement was required, samples were prepared using the oriented slide method, where minerals are allowed to settle, maximising the exposure of the basal reflections. Basal reflections of clay minerals are especially diagnostic of the mineral species (Gibbs, 1971). The exact method followed the advice and recommendations of Samantha Clark and Leo Newport (PhD students at Durham University).

Samples were lightly crushed by hand to a powder in an agate pestle and mortar, with care taken not to over-crush. Samples were then sieved (60 μm mesh) onto a special glass slide (designed to fit the diffractometer) which was pre-coated with a thin film of petroleum jelly. The petroleum jelly stops the powder blowing

off. Excess powder was removed from the slide by tapping on the bench. At this stage samples were directly loaded into the sample stage of the diffractometer and run according to the settings in 3.4.2. Only bulk rock samples were analysed, no clay separates were run.

3.5 X-Ray Fluorescence

3.5.1 Brief outline of theory

X-ray fluorescence spectrometry (XRF) is based on the excitation of a sample by X-rays. A primary beam excites secondary X-rays which have wavelengths characteristic of the elements present in the sample (Rollinson, 1993). The intensity of the secondary X-rays is used to determine the concentrations of the elements present by reference to calibration standards (Rollinson, 1993).

3.5.2 Labs and Technicians and procedure used

Powdered samples were sent to Dr Nicolas Odling, School of Geosciences, University of Edinburgh for analysis. The method followed was as follows (personal communication N. Odling, 2012):

"Major element concentrations were determined after fusion with a lithium borate flux containing La2O3 as a heavy absorber by a method similar to that of Norrish and Hutton (1969). Rock powder was first dried at 110°C for at least 2 hours, and a nominal but precisely weighed 1g aliquot ignited at 1100°C for 20

minutes to determine loss-on-ignition (LOI). The residue was then mixed with Johnston-Matthey Spectroflux 105 in a sample: flux ration of 1:5 based on the un-ignited sample mass and fused at 1100°C in Pt5%Au crucibles in a muffle furnace. After initial fusion the crucible and contents were re-weighed and any flux weight loss made up with extra flux. After a second fusion over a Meker burner, the mixture was thoroughly mixed by repeated swirling and cast onto a graphite mould and flattened into a thin disc using an aluminium plunger, both kept at 220°C on a hot plate.

Trace element concentrations were determined on pressed powder pellets. Eight grams of powder were mixed with 8 drops of a 2% solution of polyvinyl alcohol. The mixture was then backed and surrounded by a 0.5mm thick aluminium cup and formed into a 40mm diameter disc by pressing against an 40mm diameter polished tungsten carbide disc at a load of 0.6 tonnes/cm2.
The fused and pressed samples were analysed on a Phillips PW2404 automatic X-ray fluorescence spectrometer with a Rh-anode X-ray tube. Corrections for matrix effects on the intensities of major element line were made using theoretical alpha coefficients calculated on-line using Phillips software. The coefficients were calculated to allow for the amount of extra flux replacing volatile components in the sample so that analytical totals should be 100% less the measured LOI. Intensities of the longer wavelength lines (La, Ce, Nd, Cu, Ni, Co, Cr, V, Ba and Sc) were corrected for matrix effects using alpha coefficients based on major element concentrations measured at the same time on the powder samples. Matrix corrections were applied to the intensities of the other trace element lines by using the count rate from the Rh K alpha Compton scatter line as an internal standard. Line overlap corrections were applied using synthetic standards. The spectrometer

was calibrated with a range of USGS and CRPG standards using values given by Govindaraju (1994)"

Detection limits (ppm) reported were as follows:

Zn	Cu	Ni	Cr	V	Ba	Sc	La	Ce
0.7	0.8	1.0	1.4	2.5	3.6	0.9	1.7	2.2
Nd	**U**	**Th**	**Pb**	**Nb**	**Zr**	**Y**	**Sr**	**Rb**
1.4	0.4	0.4	0.5	0.1	0.4	0.3	0.3	0.3

Zn	Cu	Ni	Cr	V	Ba	Sc	La
0.7	0.8	1.0	1.4	2.5	3.6	0.9	1.7
Ce	**Nd**	**Sr**	**Rb**	**Th**	**Pb**	**Nb**	**Zr**
2.2	1.4	1.3	1.4	0.4	0.5	0.1	0.4
Sr	**Rb**	**U**	**Y**				
0.3	0.3	0.4	0.3				

Table. 3.4. XRF detection limits reported.

3.6 Stable Isotope Geochemistry

3.6.1 Brief outline of theory

Most naturally occurring elements exist of more than one stable isotope (Rollinson, 1993). The total number of naturally occurring stable isotopes for the elements varies from 10 for tin (Sn) to 0 for 21 elements that only consist of one kind of atom (i.e. a nucleide with no 'isotopes', Brownlow, 1996). In elements with an atomic mass less than 40, it is possible for the isotopes to be fractionated through physical processes as a consequence of the mass differences between isotopes (Rollinson, 1993). Of these elements, hydrogen, oxygen, sulphur, carbon and nitrogen have the necessary properties for extensive use in geological studies (Rollinson, 1993; Brownlow, 1996). Chemical, physical and biological processes can cause fractionation (change in relative abundance) of the isotopes of an element. This results in small isotopic differences in various compounds (Brownlow, 1996). Physical processes such as diffusion or evaporation are important, but more significantly, chemical and biological reactions are important (Rollinson, 1993; Brownlow, 1996).

The fractionation of an isotope between two substances A and B can be defined by the fractionation factor α:

$$\alpha_{A\text{-}B} = \text{ratio in A / ratio in B} \qquad (2)$$

For example, where ^{18}O and ^{16}O are exchanged between water and calcite, the fractionation of $^{18}O/^{16}O$ between water and calcite is expressed as

$$\alpha_{water\text{-}calcite} = (^{18}O/^{16}O) \text{ in calcite} / (^{18}O/^{16}O) \text{ in water} \qquad (3)$$

Normally exchange reactions are written so that only one atom is exchanges, in which case α= the equilibrium constant (K) (Rollinson, 1993).

When stable isotopic data for both oxygen ($\delta^{18}O$) and carbon ($\delta^{13}C$) are combined, they form a powerful means of distinguishing carbonates of different origins, different carbonates plotting as fields and showing characteristic trends (Rollinson, 1993).

This thesis makes use of both oxygen and carbon stable isotopes, both together and using the fractionation of oxygen between calcite and water to model precipitation temperatures and water compositions (e.g. Rollinson, 1993, p. 286; Brownlow, 1996, p 96) using the equation (Rollinson, 1993; Brownlow, 1996):

$$1000 \ln\alpha = A + B\,(10^6/T^2) \qquad (4)$$

Where A and B are the fractionation constants (from O'Neil, 1986, listed in Rollinson, 1993) and T is temperature. Lnα is calculated using equation 3.

3.6.2 Sample preparation and mass spectrometry

Forty-two samples were successfully analysed for oxygen ($\delta^{18}O$) and carbon ($\delta^{13}C$) stable isotopes of the calcite component. Samples were selected based on a point count calcite threshold of 3 %. Some of the chosen samples failed to yield sufficient CO_2 during analysis and were rejected.

About 10 g of each of the chosen samples were crushed with an agate mortar and pestle. Based on the point count, a quantity was then measured for a yield test (as advised by Joanne Peterkin, the lab manager). The yield test then determined the actual amount required for the analysis, these are reported in the Appendix.

Once the samples had been weighed, the stable isotope analysis was conducted at the University of Durham using a Thermo-Finnigan (Bremen, Germany, now Thermo Fisher Scientific) MAT 253 Isotope-Ratio Mass Spectrometer with Gasbench II, external precision of ca. 0.05–0.10‰. Samples were dissolved in up to 40 drops of orthophosphoric acid (H_3PO_4) under helium (grade 5) atmosphere. The solution was left to digest at 50 °C for 2 hours. The resultant gas mixture (CO_2 and He) was introduced to a gas chromatographic column and the CO_2 separated from the mixture. After passing through water traps the analyte was introduced to the mass spectrometer. Each batch of sample powders were run with 11 to 16 standard powders (depending on batch); NBS18 (Carbonatite), NBS19 (Limestone) and two internal standards DCSO1 and LS VEC. Normalisations and corrections were made to NBS19 and LS VEC. Isotope ratios are reported in standard delta notation relative to the Vienna Pee Dee Belemnite (‰VPDB) standard. The external analytical precision for both $\delta^{13}C$ and $\delta^{18}O$ is better than 0.1‰. Samples were run by Joanne Peterkin. 8 samples were run by Chris Harris at the University of Capetown, South Africa, these were included where a later repeat was not done at Durham (indicated in Appendix).

3.7 Fieldwork

3.7.1 Namibia

The main field area was the Huab Basin, Kunene Region, NW Namibia (see Chapter 2, Chapter 4, Chapter 6 and Chapter 7). Three field trips were conducted to Namibia one each in 2009, 2011 and 2012. The first trip (September 2009) consisted of 2 weeks in Namibia, undertkaing reconnaissance fieldwork on the main outcrops in the field area with Dougal Jerram (leader) and a group from Germany lead by Dr Bob Trumbull. Flights were SAA from London Heathrow to Windhoek via Johannesburg. Transport in Namibia was by 4x4, with all logistics arranged by Dougal Jerram. 2 vehicles were used.

The second trip was of 6 weeks duration and was led by myself in July and August 2011. Accompanying as field assistant was Tim Watton, Samantha Clark (1 week) and Victoria Gee (2 weeks). Richard Brown supervised for the first 2 weeks. Flights were with SAA on the same route as in 2009. Accommodation in Windhoek was at the property of the Karl Steiner, 72 Berg Strasse, Windhoek. Transport into the field was by 4x4 and camping was wild. The vehicle was rented from Avis car rentals. Resupply was made at Uis and Swakopmund. Accommodation in Uis was at the Brandberg Rest Camp and accommodation in Swakopmund was at the hotel Gruner Kranz (Swakop Lodge). This was the main sampling trip. Samples from this trip are prefixed by NG.

Recent rains had increased vegetation in the field area such that route finding was difficult, routes and tracks used are appended to the (1:50k) map in the Appendix. Entrance to the field area was made via Brandberg West mine and the

Rhino camp from the south and from the Doro Nawas Camp road and the Aba-Huab river or Fontein Farm from the north.

The guidance of Dr Gabi Schneider of the Geological Survey of Namibia was most encouraging and was valued.

The third trip was of 2 weeks duration and was led by Dougal Jerram in September 2012. The trip was in association with a group from Brazil led by Breno Waichel. Logistics were arranged by Dougal Jerram, 4x4 vehicles were rented from Advanced 4x4, Windhoek. Two vehicles were used. Accommodation was in the same as in 2011. Follow-up samples were taken to supplement the 2011 samples. These samples are prefixed by NG/12-.

Entry to Namibia was by way of a research visa, which was easily obtained from the Namibia High Commission, London with appropriate letters from Durham University. Sample export was by permission of the Ministry of Mines and Energy, Namibia in fulfilment of the Namibian Section 127 of the Minerals (Prospecting and Mining) Act, No. 33 of 1992 (form attached to Appendix). The rock export was a straightforward process with the support of Gabi Schneider once satisfied of the quantity and destiny of samples. Rocks from the 2011 field season were airfreighted to Newcastle Airport with Transworld Cargo. Rocks from the 2012 field trip were taken as hold luggage on SAA.

A list of contacts in Namibia is in the Appendix.

3.7.2 Iceland

The field trip to Iceland was for one month duration in June–July 2010. The trip was with Tim Watton (leader), who organised logistics. Flights were from

London Heathrow to Reykjavik. Transport was by car (4x4 Subaru). Accommodation was camping. Thor Thordarson took us to the area of the Langjokul in the interior and lent a Toyota 4x4 for the final part of the trip. Samples from this trip have the prefix IG. Rock export was by sea.

3.7.3 USA

The fieldtrip to the USA was organised by Tim Watton (leader) and was conducted in June–July 2011 for one month duration. The areas visited were the Columbia River Flood Basalts and the Snake River basalts. Flights were from Newcastle to Portland, Oregon, via Amsterdam on Delta Airlines.

Transport in USA was by 4x4 rented from Alamo and accommodation was camping, usually in State Park campgrounds, although sometimes wild as conditions dictated. Supplies were purchased in Walmart. Samples collected are prefixed USG. Rock export was via the US postal service as parcels from the Portland Airport office.

The first week of the trip was supervised by Richard Brown. Guidance in the USA was provided by Terry Tolan, Bill Bonnichsen, Martha Godchaux, and Dennis Geist.

4

Diagenesis at lava-sediment contacts in an arid palaeoenvironment, the Twyfelfontein Formation, Namibia.

4.1 Chapter summary

This chapter aims to fully characterise the nature and intensity of the direct diagenetic effects of basaltic lava flows on a dry, high depositional porosity, mature sand. Ideas investigated are the impact of increased heat, sudden loading and the effect of volcanic volatiles on the development of porosity and permeability in the sandstone.

The diagenesis in the sandstone that forms the substrate for the emplacement of lava flows is characterised by increased compaction porosity loss (COPL) compared to the background by ~10% in addition and a zone of calcite cementation restricted to high porosity grain flow horizons at contacts, but sometimes beyond the zone of maximum compaction, until background porosity is returned. Calcite is poikilitic in grain flow horizons at contacts, but is restricted to replacement and then partial replacement of plagioclase further below the lava. Increased compaction and cementation are no longer apparent at a distance below the lava flow dependent on the thickness of the flow.

Two case studies are presented for sandstone that has been drowned by the Tafelkop basalt lava flows. The Tafelkop lavas at the case study locations are a compound type lava. Three case studies are presented for sand that has been drowned by Tafelberg type lava. The Tafelberg flows are large tabular lava flows.

Petrography, X-Ray diffraction, whole rock major element and whole rock trace element (X-Ray fluorescence), stable isotope geochemistry ($\delta^{18}O$ and $\delta^{13}C$) and petrophysical measurements (probe permeability and Hasler sleeve (conventional permeability) are used.

4.2 Diagenesis of the Twyfelfontein Formation, Namibia at lava contacts

4.2.1 Dune Valley

Two case studies are presented from a valley to the SW of Awahab Mountain (1342 m) informally named 'Dune Valley' due to the large number of isolated barchans sand dunes within the Tafelkop-Interdune Member basalts (Jerram et al., 1999a). The case study aeolian sand dunes were both drowned by the low titanium, olivine-phyric Tafelkop-type compound pāhoehoe basalt lavas (see Chapter 2; Jerram et al., 1999a; Milner et al., 1994; Milner & Ewart 1989; Ewart 1998) which were compound pāhoehoe type lava flows (see 2.1.1.1).

The first case study is the uppermost of a sequence of three stacked isolated dunes encapsulated by Tafelkop type basalt (Fig. 4. And Fig. 4.2A.). The second is an individual isolated dune (Dune 16) located 1.7 km to the SE of the 'three dunes' outcrops. Both case studies are at 840 m altitude. Samples were taken at intervals below the upper lava contacts at each of these dunes and above the basal contact for the upper dune of the three dunes outcrops where it was exposed (Fig. 4.2; Table. 4.1.).

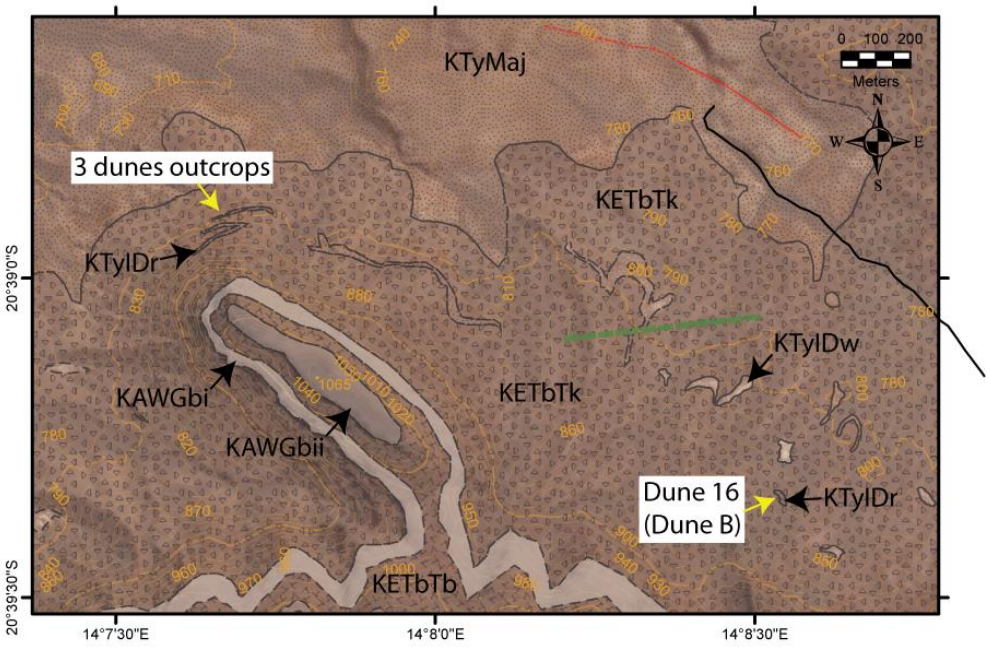

Fig. 4.1. Map of Dune Valley showing case studies presented for direct contact diagenesis. 3 Dunes outcrops and Dune 16 (Dune B) are indicated and are both 'red' dunes. Contour interval is 10 m.

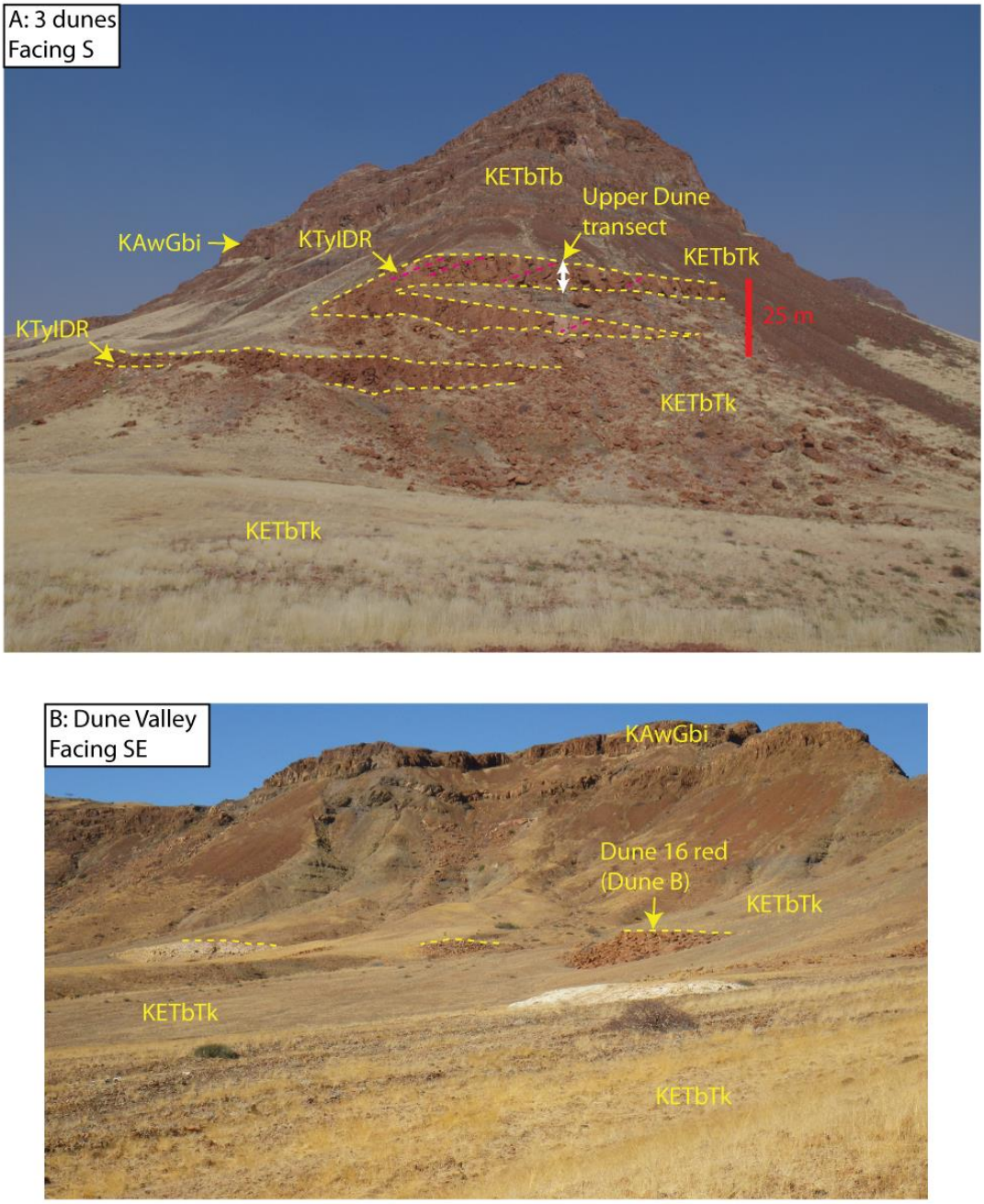

Fig. 4.2. Photographs of (A) 3 dunes case study and (B) isolated dunes (KTyID) with Dune 16 (Dune B) indicated. These two case studies can be seen to be red dunes; the alternative 'white' dunes discussed elsewhere are also visible in photograph B.

Upper Dune Sample 20° 38.949 S 14° 07.643E	Distance Below(m)	Porosity (%)	1 sigma error	Dune 16 sample 20° 39.350 S 14° 08.541 E	Distance Below(m)	Porosity (%)	1 sigma error
NG5	0.0	0.0	0	NG31	0.0	0.6	0.3
NG7	0.18	7.8	1.2	NG/12-12	0.5	4.6	0.9
NG6	0.3	12.0	1.1	NG32	1.0	7.6	1.2
NG8	1.0	16.6	1.7	NG/12-13	1.5	13.0	1.5
NG9	2.0	20.2	1.8	NG33	2.0	9.8	1.3
NG10	3.0	19.8	1.8	NG/12-14	2.5	12.2	1.5
NG11	5.0	16.6	1.7				
NG13	6.85	9.4	1.3				
NG14	6.9	12.2	1.5				
NG12	7.0	1.0	1.5				

Table. 4.1. Dune Valley samples, location, distance below lava and porosity (see Appendix for complete data table).

2.1.1.1 Evidence for dynamic sediment-lava interaction in Dune Valley.

Of importance when interpreting the nature of lava-sediment interactions and effects at the hot contact and downward into the sediment is the type of lava. The case studies in Dune Valley presented were exclusively drowned by the Tafelkop type lavas, although Tafelberg type lava crops out in the cliffs above beginning at about 900 m but only interact with small sand bodies not studied in Dune Valley. The lavas in dune valley are strongly weathered such that direct observations are difficult. Petrographical and geochemical studies are often fruitful, but additional information from field observations of the lava flows are important in constraining how the lava emplaced (e.g. Pāhoehoe tabular sheet, compound-braided (cf. Nelson et al., 2009) or as an Aa type flow (cf. Crisp & Baloga, 1994). It is clear from the best preserved outcrops that the basalt lavas are amygdaloidal and typically composed of compound-braided pāhoehoe lobes, but no well-preserved flows were observed directly.

Indirect preservation of the surface morphology and evidence for the lava emplacement mechanisms is however preserved by the Twyfelfontein Formation sandstone. The preserved features at contacts reveal detailed information relating to the lava emplacement. Most basal contacts are sharp, without clinker breccias (Jerram & Stollhofen, 2002), indicating that the sand was passively drowned by the lava without disturbance (Fig. 4.3A). Thin subjacent topset beds (~10 cm) complete with ripples are preserved along dune faces complete with ripples (Fig. 4.3A). Ripple preservation is commonly seen below lava flows where in contact with the Twyfelfontein Formation across the entire basin, in all Twyfelfontein Formation sub-units (KTyMaj, KTyMin, KTyID) and both basalt lava types (Tafelkop-type in Dune Valley and at the inflated flow locality (Appendix Map 2) and the Tafelberg-type at the Ponded Lava locality (4.2.5) and the hill south of Krone Farm (Appendix Map 2). Dune surfaces occasionally show imprints of a rough granular texture (Fig. 4.3B) interpreted to be clast imprints of glassy basaltic fragments impressed by the advancing lava into the sand surface. Where this texture exists, the basalt occasionally adheres to the sandstone, whereas usually the two lithologies cleave.

No breccias were found under the Tafelkop-type compound lava flows in Dune Valley, although elsewhere breccias have been found at sand contacts under

both the Tafelkop and Tafelberg lavas (at the PEP locality, Appendix Map 2 and Ponded Lava (4.2.5)). Evidence for dynamic interaction between lava and the substrate sand is however preserved in Dune Valley in the form of preservation of bulldozing (Jerram & Stollhofen, 2002). Preservation of bulldozing by the advancing pāhoehoe appears to occur either by proxy, where an object is scraped along in front of the lava (Fig. 4.4A) or directly where a pāhoehoe lobe confronts a steep pile of sand (e.g. the slip face of a sand dune). As the pāhoehoe lobe impacts steep sand, it naturally becomes apparently invasive as loose sand falls from the already unstable slip surface onto the surface of the pāhoehoe (Fig. 4.4C.). The example presented in Fig. 4.4C. Shows an invasive pāhoehoe lobe (surface texture preserved in the overlying sand) termination embayed in the sandstone. Further evidence for dynamic interaction is preserved by a fumerolic gas escape chimney above the invasive flow front. The chimney is an inverted cone of sandstone that lacks internal structure (bedding) and truncates pre-existing laminations and is cemented with calcite. This is evidence for degassing of the lava during and after emplacement of the lava flow.

The surface texture of a pāhoehoe lava flow is the basis for recognition in the field, as already explained, is not directly preserved in dune valley due to weathering. The basis for classification of the Tafelkop lavas in Dune Valley as pāhoehoe comes from the numerous inverse mould imprints in the overlying sand that are preserved (Fig. 4.4B.) (good localities are 20° 40.099’ S 14° 9.410’ E and 20° 39.937’S 14° 10.045’E). Where sand blows over solidified pāhoehoe layers, the surface texture is filled (sand finds its way into every connected volume). The sand layer, when covered by lava becomes indurated (see below) to a depth of ~50 cm. If the thin sand layer on top of the pāhoehoe is < ~50 cm thick it will be included within the induration and therefore preserved at an early stage. The sandstone is more resistant to the style of weathering in the Huab Outliers and so preserved a negative imprint of the pāhoehoe mould (Fig. 4.4B.). In summary, Recorded in the Twyfelfontein Formation sandstone at lava contacts is occasionally evidence dynamic interaction between the pāhoehoe lava and the substrate. The common interaction, however, is passive in nature, such that delicate sedimentary features are preserved (e.g. dune ripples on topset beds). The Tafelkop basalt in Dune Valley is dominantly compound braided type lava (cf. Walker, 1971; e.g. Jerram 2002) as recorded by the sediment substrate and limited basalt preservation. Compound braided lavas can vary from

0.05 m up to 10 m thick, though most are 0.05 m to 5 m thick (Walker, 1971). The Tafelberg type basalt comprises tabular sheet flows that both passively and dynamically interact with the substrate (Jerram & Stollhofen, 2002) (Fig. 4.36.).

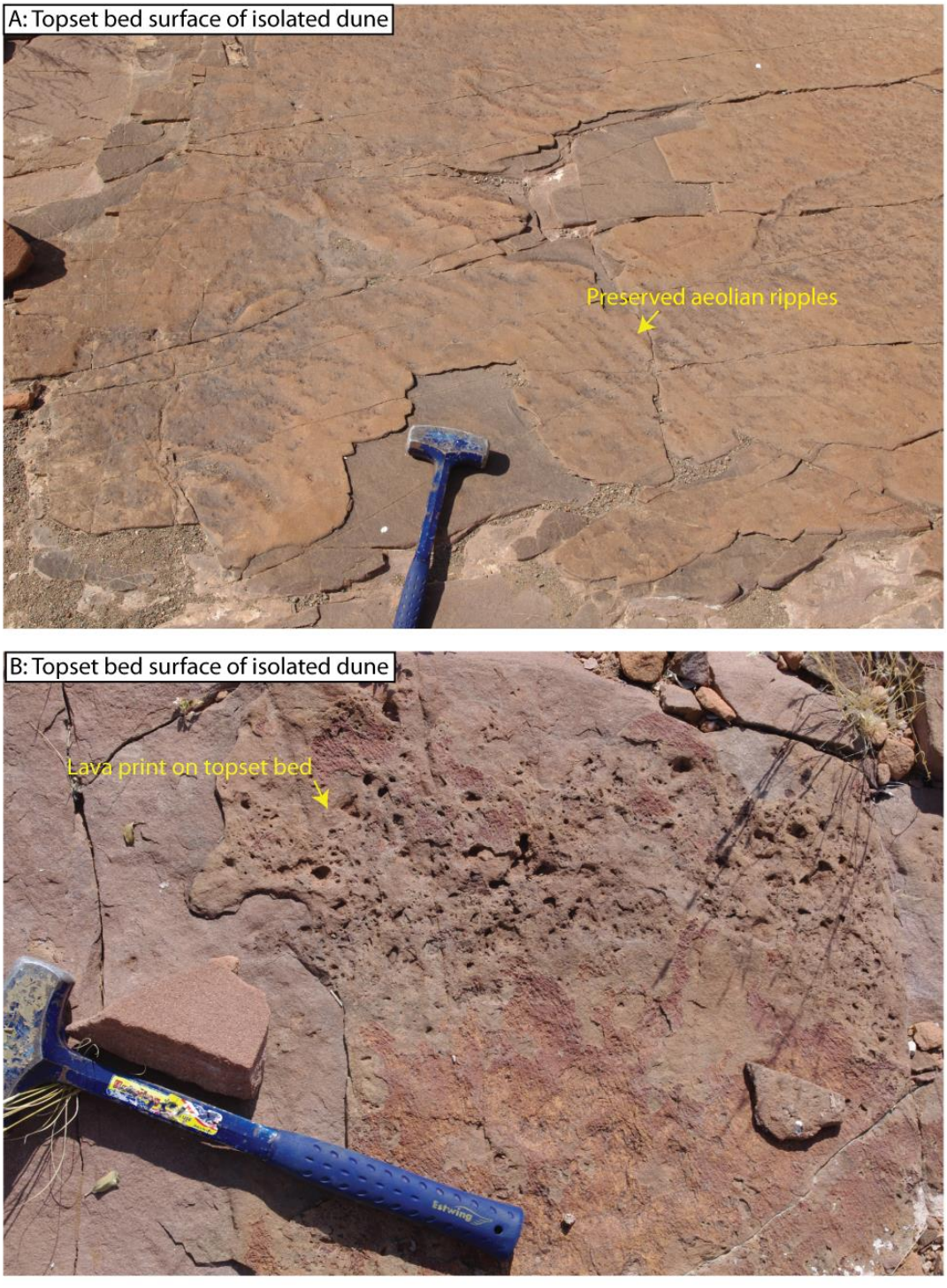

Fig. 4.3. Evidence of passive drowning of sand dunes by pāhoehoe. A) Preserved aeolian ripples on indurated topset bed of isolated dune. B) Imprint of rough lava base on topset bed of isolated dune, occasionally lava basal crust is still adhered to the sand.

Fig. 4.4. Evidence of lava emplacement preserved within sandstone. A) Disturbance in a topset bed caused by lava bulldozing a solid object no longer preserved. This locality is shown in Jerram et al., (2000a) B) Inverse pāhoehoe mould preserved in a calcite cemented interlayer (Image reproduced as cover of January 2013 *Geology*). C) Fumerolic gas escape structure, cemented with calcite above an invasive pāhoehoe lobe within what would have been unconsolidated sand at the time. This is the only invasive flow encountered in Dune Valley. Fig. 4.4B was published as the front cover of *Geology*, Jan 2013)

2.1.1.2 Direct effects of Tafelkop lava on isolated sand dunes in Dune Valley

3 Dunes Case Study

This locality is on the north-facing side of an un-named peak at 1065 m altitude (20° 38.949 S 14° 07.643 E). The exposure is best viewed from a knoll of basalt 300 m to the north, the location of the photographer in The outcrop comprises three cross sections of barchanoid sand dunes, each wholly or partially encased in Tafelkop lava (Fig. 4.2). The lowest dune overlies lava and is more laterally continuous than the upper two and could be classified as a 'Minor Erg' (KTyMin). The middle dune (KTyIDr) also overlies a lava and is isolated from the underlying dune. Flooding of this dune by lava was incomplete before deposition of the upper dune, such that the two sand bodies are continuous from the crest of the middle dune. At the point where the middle dune becomes the upper dune is an area displaying a small degree of dynamic lava-sediment interaction. Between the dunes, the lava ranges in thickness from ~10 cm in the east to ~10 m in the west due to the wedge shape of the dune. The upper dune (KTyIDr) is 7 m thick at the sample transect location (Fig. 4.2A). The topset bed is preserved at the top surface and the underlying forests dip to the NE, consistent with the regional aeolian depositional trend (Mountney et al., 1999).

To investigate the diagenesis in relation to distance below the lava a transect of ten samples was taken (Table. 4.1.).

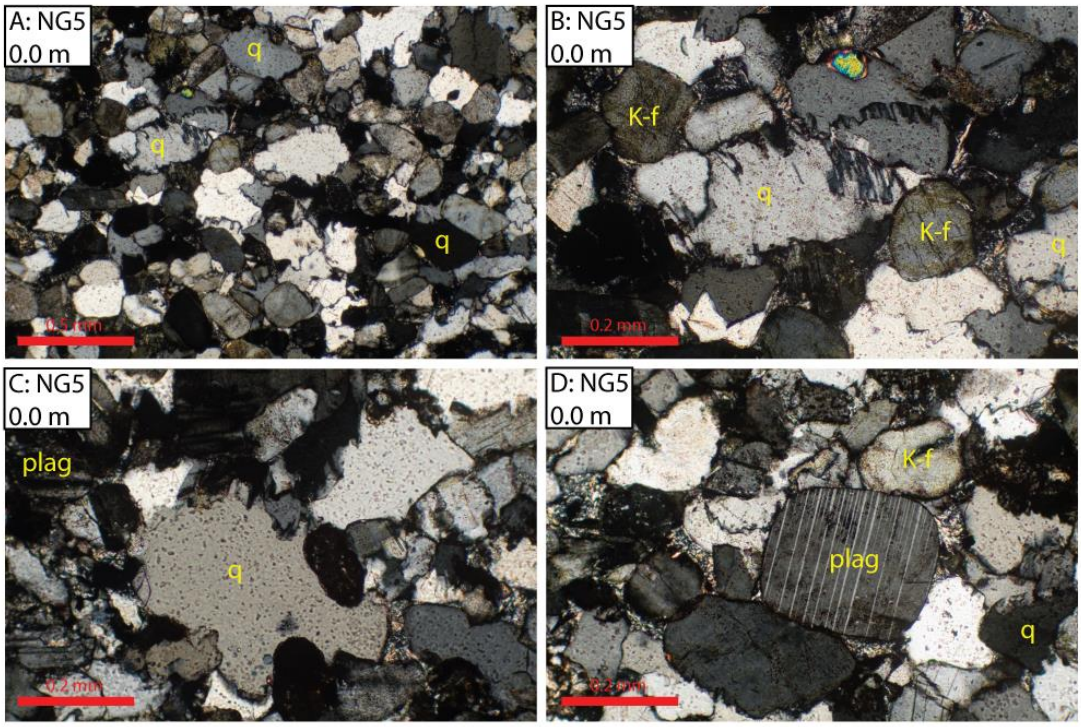

Fig. 4.5. XPL Photomicrographs of NG5 upper contact of upper dune with lava. A) High degree of compaction, detrital grains deformed so that all faces are in contact with adjacent grains. B) Grain contacts sometimes show stylolitic textures that are horizontal (i.e. perpendicular to lithostatic load). C) Close up of quartz grain showing degree of deformation due to compaction. D) Plagioclase grain is fresh compared to regions of lower compaction, suggesting compaction was early, protecting it from later fluids.

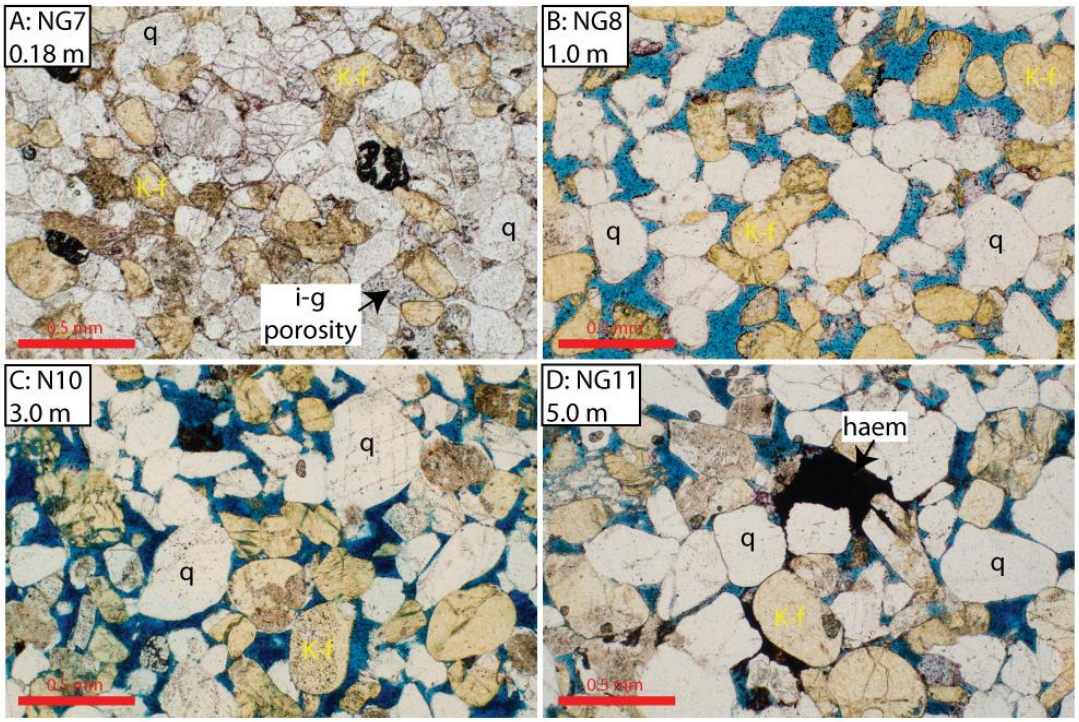

Fig. 4.6. A) PPL, NG7 0.18 m below lava, compaction still high. B) PPL, NG8 1.0 m below lava, porosity recovered haematite grain coatings rare. C) PPL, NG10 3.0 m below lava. D) PPL, NG11 5.0 m below lava, haematite redistributed into mottled patches.

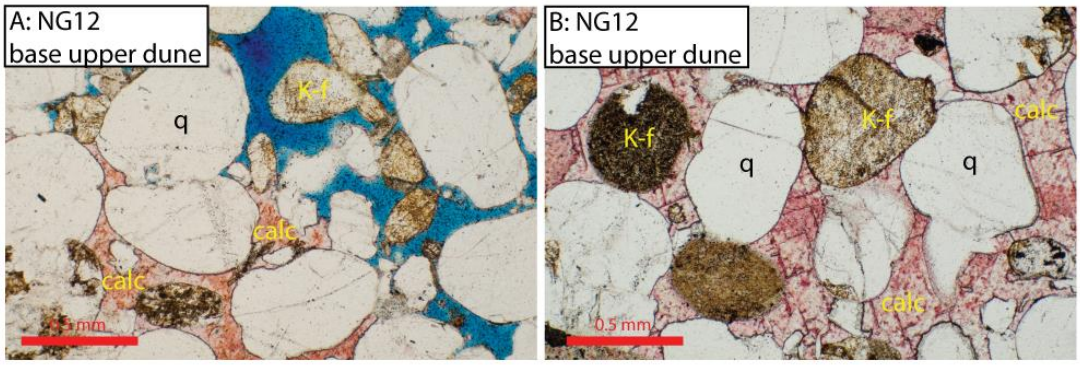

Fig. 4.7. PPL Photomicrographs of base of upper dune. Where dune rests on lava is a region cemented with calcite. A) calcite cemented region has sharp boundary with un-cemented sandstone suggesting caused by ponding of fluids above lava. B) Compaction appears less than un-cemented (e.g. Fig. 1.7C.) suggesting early precipitation protecting against burial compaction.

At the contact with the overlying lava (sample NG5, Fig. 4.5) the porosity of the sand has been reduced to a negligible value (TOP= 0 %). Permeability reduces with porosity following an exponential relationship. This porosity reduction occurs due to both increased compaction and increased cementation compared to the unaffected sandstone (e.g. NG52). Petrographic analysis shows that the major

porosity reducing mechanism is compactional porosity loss (COPL), which increases by about 10 % compared to the background (35 %, ±2.6) within ~ 1 m of the contact (Fig. 4.11) to 43 % of total porosity loss. Cementational porosity loss (CEPL) reaches ~ 6 % compared to a background of low values (2 or 3 %). Cementation increasing towards the contact is exclusively calcite. No correlations were found between clay and authigenic quartz overgrowths with distance below the lava (Fig. 4.9). The background porosity of NG52 is 12.4 % (± 1.5), so the additional effects at the contact can easily account for all of the porosity reduction. The compaction of the quartz grains appears to be greater than the feldspar grains (i.e. the quartz accommodates the compactional strain). Evidence for pressure solution (*senso* Rutter, 1983) between quartz grains (Fig. 4.5) is ubiquitous, as both interpenetrating grains and sutured grain contacts. Little evidence is preserved for plastic deformation of quartz such as undulose extinction, and although some quartz grains are undulose in XPL, they are very rare. Haematite grain coatings, common in unaffected sand, are absent in the sand at the contact.

The background intergranular primary porosity returns at depths of 0.18 m below the contact. Authigenic calcite is at a maxima at this distance (5.6 % ± 1.0), as is CEPL, although COPL still dominates. Figure 4.6A shows a PPL photomicrograph of sandstone at 0.18 m depth, and the lesser degree of quartz compaction is evident (as compared to Fig. 4.5) Haematite grain coatings are also absent at depths of >0.18 m.

At 1.0 m below the contact, the authigenic mineralisation in the sandstone is the same as the background, with calcite only existing as partial replacements of occasional plagioclase grains. Pore-filling authigenic phases are restricted to clays (probably kaolinite and smectite) which show no correlation with distance below the lava (Fig. 4.9, Fig. 4.10.). Haematite grain coatings are rare. Porosity loss is therefore dominantly COPL, with little enhancement over the background (~35 %, ±2.6). Based on petrographical observations, the direct effects of the lava are minimal at 1.0 m. Between 1.0 m and 5.0 m (samples NG8, NG9, NG, 10 and NG11) below the contact the sandstone is virtually indistinguishable from the background sandstone. Porosity reaches a maximum of 20.2 % (±1.8), which is the highest of all Twyfelfontein Formation sandstone samples. Haematite grain coatings remain rare,

but agglomerates of haematite, forming mottled patches filling pore space are frequent (Fig. 4.6D.).

The base of the upper dune is cemented by calcite (up to 19.2 %, ±1.8) (Fig. 4.7.), which reduces porosity to 1 % (±0.4). The calcite is non-ferroan poikilitic, and has a sharp horizontal boundary with the un-cemented background sandstone above (Fig. 4.7A). Analysis of the COPL and CEPL shows that the increased porosity loss here is due to this cementation as opposed to increased compaction (Fig. 4.11.). The interpretation is that this calcite is a later hydrothermal cement, precipitated in a perched aquifer at the base of the upper dune (see Chapter 7).

The overall interpretation of these petrographic data is that the emplacement of the lava flow caused early increased compaction due to its weight in the uppermost ~1 m of unconsolidated sand; this was accompanied by minor calcite precipitation in the remaining pore space during cooling of the lava. Calcite, at depths >0.18 m is restricted to replacement of plagioclase rather than pore filling cement. Compaction and calcite decrease away from the contact, allowing porosity to increase to background levels which are controlled by overburden compaction and minor quartz cementation (<1 %, ±0.4). The relevance and origin of the calcite will be discussed in 4.3 and Chapter 7. A discussion of the compaction below lava flows will be had in 4.6 and 5.4. The porosity against permeability relationship for this sandstone is shown in Fig. 4.8C. The porosity-permeability relationship shows nothing unusual.

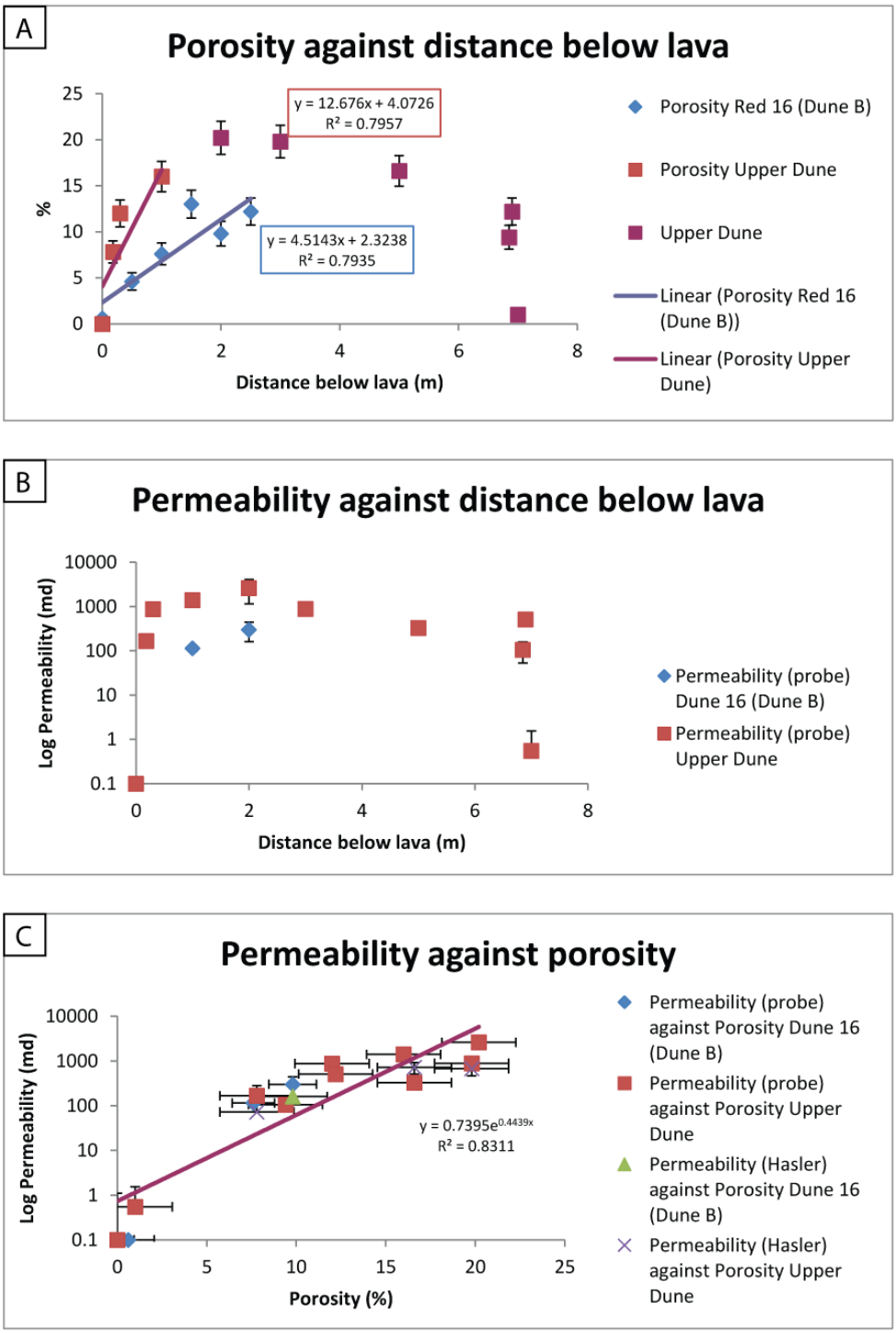

Fig. 4.8. Graphs against distance below lava. A) Porosity, for both case studies porosity increases away from contact to background levels of > 12.4 %. Upper dune porosity decreases at > 7 m due to calcite cementation shown in Fig. 1.8. B) Permeability, rapidly increases below lava. C) Permeability against porosity shows an exponential relationship.

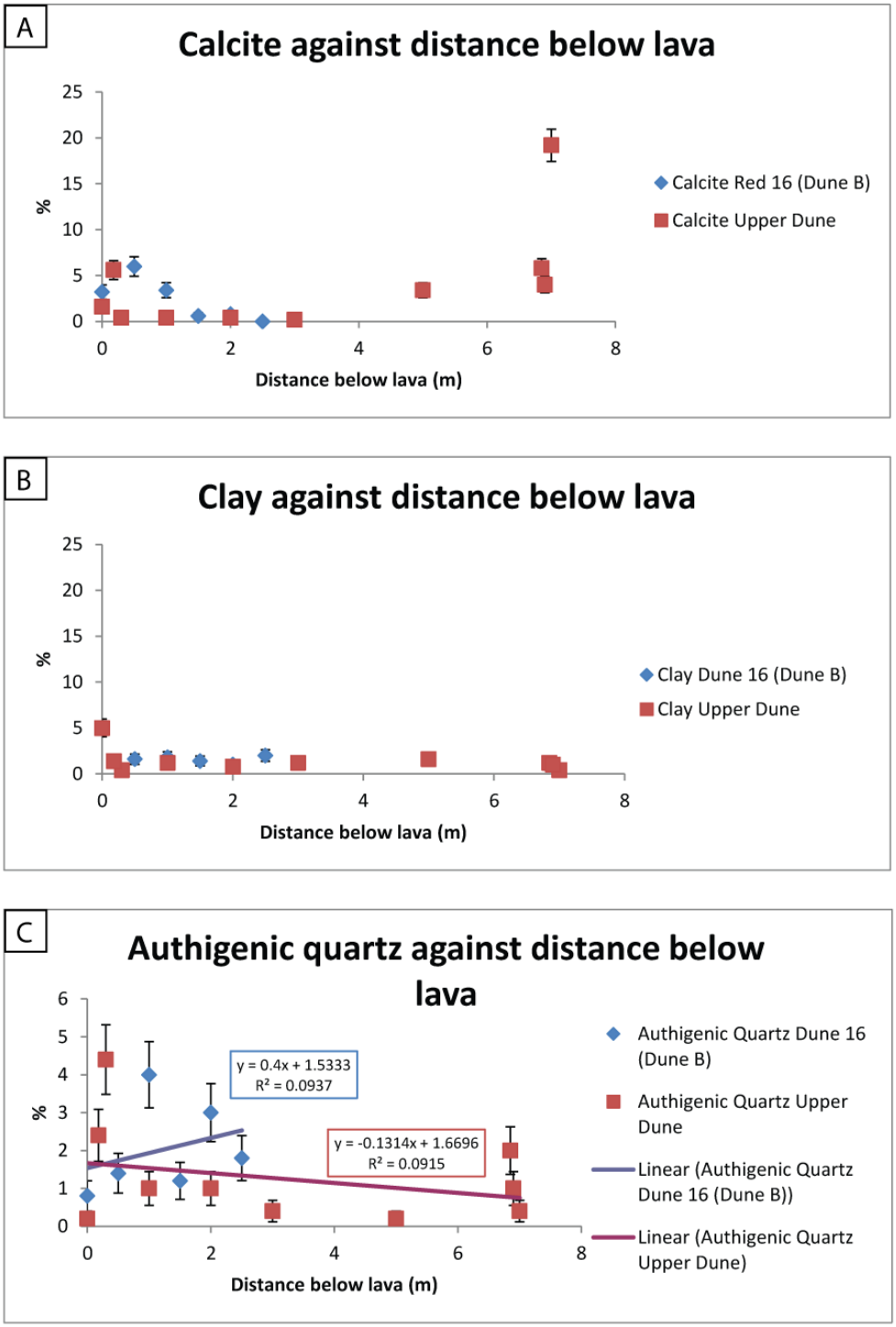

Fig. 4.9. Graphs against distance below lava. A) Calcite, Dune 16 shows a maxima at 0.5 m immediately below highly compacted zone which decreases to negligible by 1.5 m below. Upper Dune decreases away from upper contact and then increases at the calcite cemented zone at the base. B) Clay shows no variation with distance. C) Poor correlations between authigenic quartz and distance below lava suggest no relationship between lava and authigenic quartz.

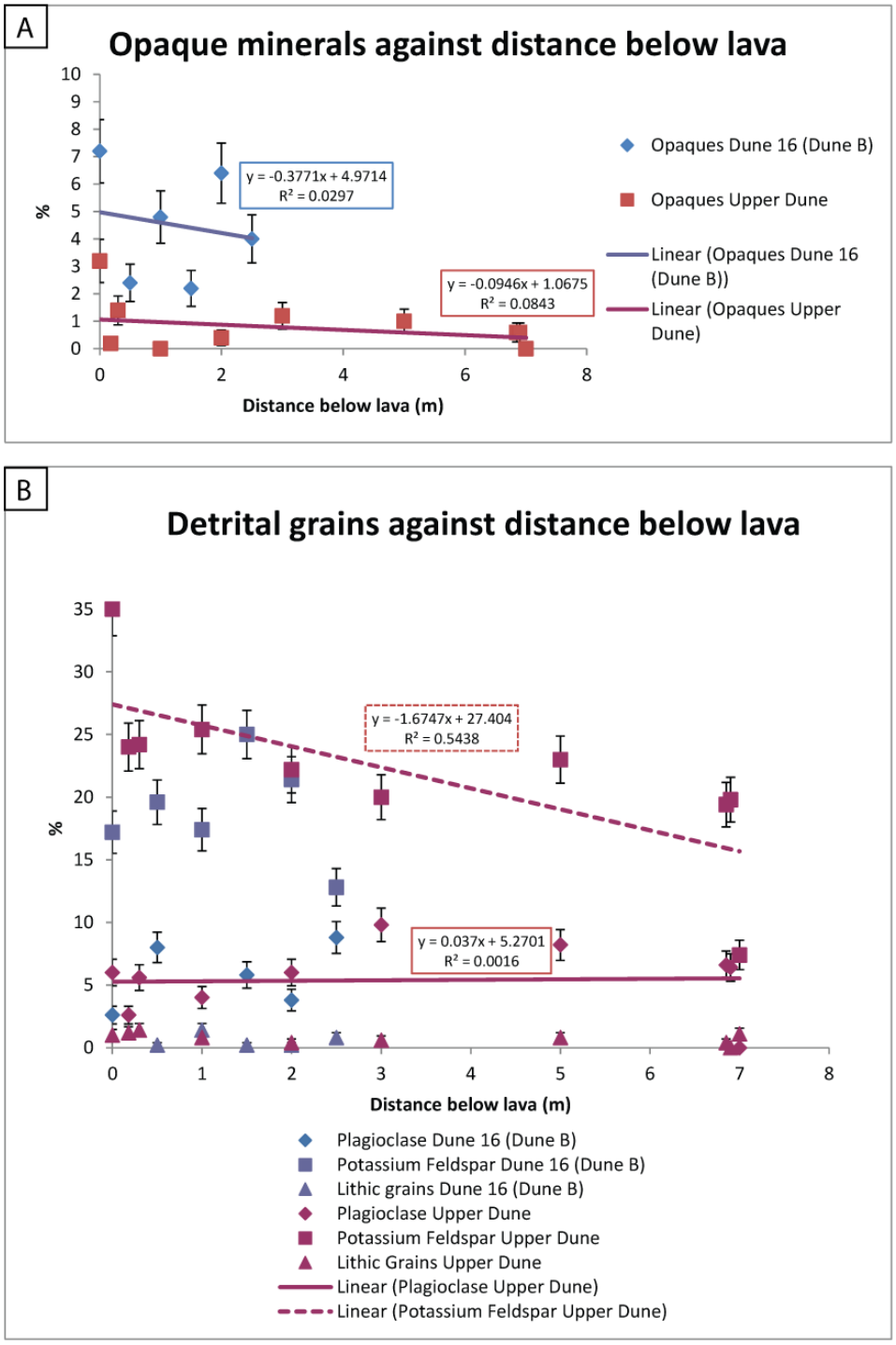

Fig. 4.10. Graphs against distance below lava. A) Like authigenic quartz, no relationship exists between opaque minerals and distance from lava, despite an observed textural change between grain coating haematite and pore filling haematite clusters suggesting redistribution. B) Upper dune shows a weak negative correlation between K-spar and distance below lava but no correlation between plagioclase and distance below lava.

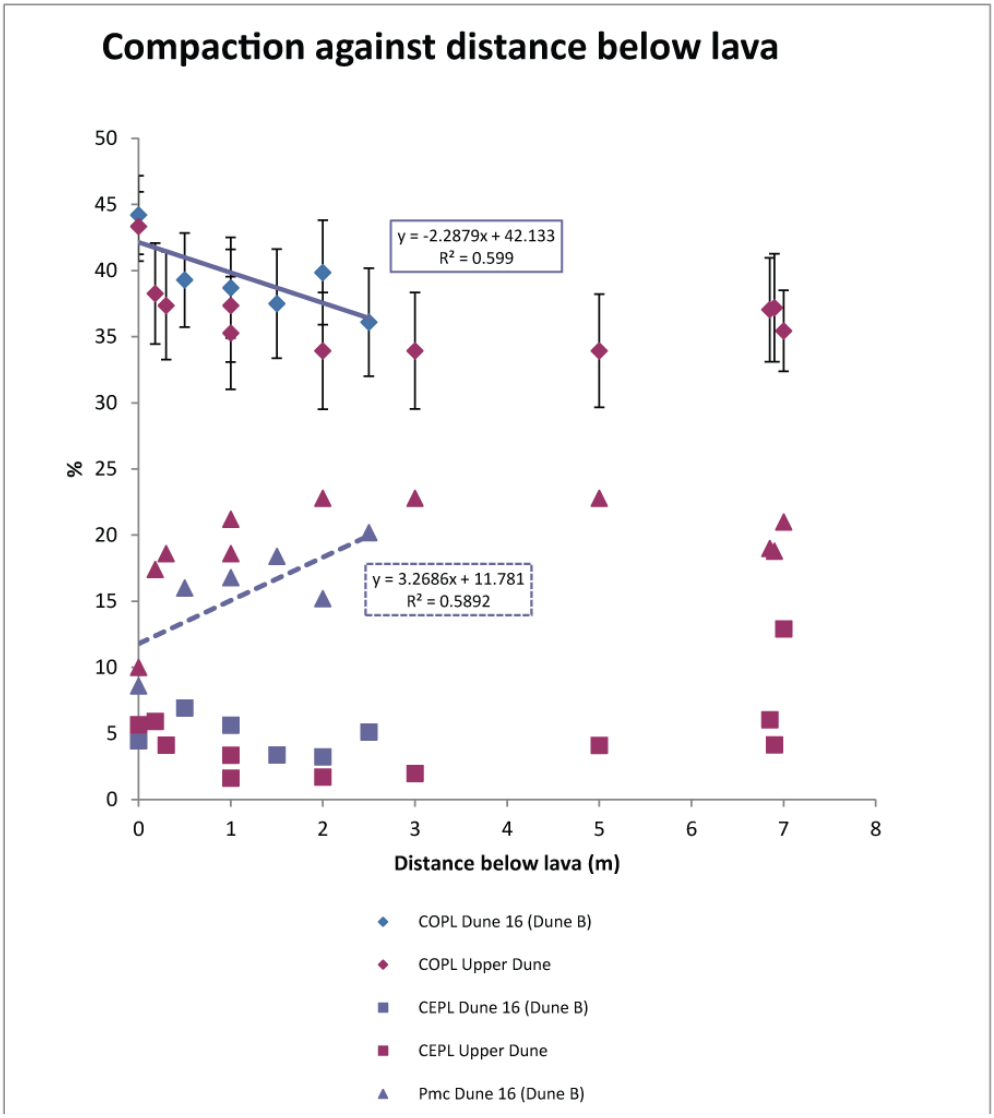

Fig. 4.11. Porosity reduction analysis of Dune Valley sandstone. Dune B COPL decreases away from upper contact and Pmc decreases towards contact suggesting compaction becomes more important closer to lava. This trend is mirrored by Upper Dune although complicated by the calcite zone at the base of the dune 'protecting' sand from later background compaction (> 6 m).

Dune 16 (Dune B) Case Study

Dune 16 is one of at least 19 isolated barchanoid dunes (KTyID) resting on the initial Tafelkop basalt (KETbTk) lava flows that are exposed in the valley floor of Dune Valley. Dune 16 is located on the south-western slope of the valley at 830 m altitude at 20° 39.350' S 14° 08.541' E. The outcrops includes the upper surface of the dune and onlapping lava (highly weathered) the sandstone outcrop is up to 3 m

thick. The basal contact with the lava is covered by scree. Dune 16 is a 'red' dune, unaffected by later hydrothermal fluid flow (see dune B in Grove at al., *in* review and Chapter 7). This dune was chosen for detailed analysis due to the ability to accurately define the upper lava contact and to 3.0 m of continuous exposure, which is lacking in the other dunes, despite their high surface exposure.

The drowning of Dune 16 by lava was by a passive process, no breccias were discovered and the contact is smooth. The lava is a compound pāhoehoe type so, the lava that drowned Dune 16, despite not exhibiting preserved structure was probably 0.05 m to 5 m thick (2.75 m +/- 2.25 m) based on evidence elsewhere in Dune Valley. The presence of dynamic lava-sediment interaction in other stratigraphic equivalent dunes (Fig. 4.3. and Fig. 4.4.) suggests the sand in this dune was also unconsolidated at the time of lava emplacement. The association of

Six samples were taken from Dune 16, at 0.5 m intervals below the lava contact with the topset bed (Table. 4.1). At the contact porosity has been reduced to a negligible value (0.6 %, ±0.3). Permeability at the contact is 0.1 md. For Dune 16, porosity and permeability values show an exponential relationship as in the 'upper dune'. Sample NG 31 sampled both grain flow and grain fall sand lamellae, which were found to exhibit related, but different styles of diagenesis. The finer-grained grain fall layers were similar to the upper dune and are typically composed of fine sand (~100 μm diameter) of the same modal proportions of detrital minerals found throughout the Twyfelfontein Formation (e.g. Fig. 4.10B). Quartz grains are highly interpenetrating, often with sutured contacts (Fig. 4.12B, C) and the feldspar grains always appear less susceptible to this compaction than quartz. This compaction is interpreted to be dominantly pressure solution as opposed to slip deformation (*senso* Bailey et al., 1958; Mainprice et al., 1986) due to the lack of abundant or frequent undulose extinction. Authigenic calcite is present, but is rare in the grain fall horizons and is restricted to the rims of plagioclase grains. Grain flow layers at the contact are apparently less compacted (Fig. 4.12A, B.) than the grain fall layers, and are cemented with poikilitic calcite that also replaces plagioclase. Chlorite pore-filling cements are also present (Fig. 4.12A), and may account for the slightly increased permeability value of 0.1 md. Haematite grain coatings are present at the contact of Dune 16, unlike at the contact of the 'upper dune', which is evident in Fig. 4.10A where Dune 16 opaque minerals are enriched by ~4% (±0.9)overall compared

to the upper dune. Like the upper dune, no correlation in abundance is seen with increasing distance below the lava. Porosity loss at Dune 16 lava contact is dominantly by compaction (CEPL), which is highest at the contact (44 %, ±3.0) and decreases away from the lava contact (Fig. 4.11) to the background value of ~35 % (±2.6). Note difference is well outside range of uncertainty.

Sample NG/12-12, taken from 0.5 m below the contact records the re-appearance of primary porosity (4.6 %, ±0.9) and the highest abundance of calcite (6 %, ±1.1). The calcite is non-ferroan, and both fills pores as poikilitic crystals and replaces plagioclase. The porosity is both primary and secondary resulting from potassium feldspar dissolution. Primary pores, occasionally have syntaxial quartz overgrowths growing from quartz grains that never completely fill the pore. Haematite coats most detrital grains. Compaction is less than at the contact, and lies on the linear trend of reduction in COPL away from the lava contact (Fig. 4.11). Cementational porosity loss is greatest in sample NG/12-12 due to the high calcite abundance, this is common with the upper dune example, where the most cemented region was immediately below the highly compacted contact (NG7).

Porosity and permeability values are 7.6 % (±1.2) and 115 md, respectively, at 1.0 m below the lava and calcite is the main cement phase. Clay and opaque minerals are at about the same abundances as in all the Dune 16 samples. Calcite both fills pores and replaces plagioclase, but the pore-filling variety less abundance than it is closer to the contact (Fig. 4.12F.). Haematite coats grains and quartz overgrowths are present. Porosity is dominantly primary in this sample, and secondary porosity is less important than at 0.5 m depth. Compaction (Fig. 4.11.) is less than closer to the contact (39 %, ±4.1) and cementational porosity loss is reduced compared to values at 0.5 m depth, but higher (5.6 %, ±1.0) than at the contact.

At depths of 1.5 m to 2.5 m below the lava contact the sandstone porosity increases to background levels by 1.5 m and calcite cementation is negligible (<1 %, ±0.4) and restricted to rare plagioclase partial replacement. Cements are mainly minor authigenic quartz overgrowths and redistributed haematite into mottled regions. Most haematite occurs as grain coatings formed during aeolian transport and deposition. Figure 4.13 shows sandstone samples at 1.5 m, 2.0 m and 2.5 m, and

illustrates that COPL is the dominant porosity reduction mechanism (mean 38 %, ±4.2) while CEPL accounts for < 5 %.

Petrographic analysis records porosity loss in the sandstone towards the basalt contact which is apparent at depths >2 m. The porosity reduction is largely due to compaction with only a minor contribution due to cementation. Cementation is always less important than compaction and reaches a maxima at 0.5 m below the lava. Compaction reaches a maxima at the contact. The increased compaction with proximity to the lava suggests that the weight of the emplacing and inflating lava flow caused the increased compaction and that it was an early effect. At the contact, compaction is about 10 % higher than the background.

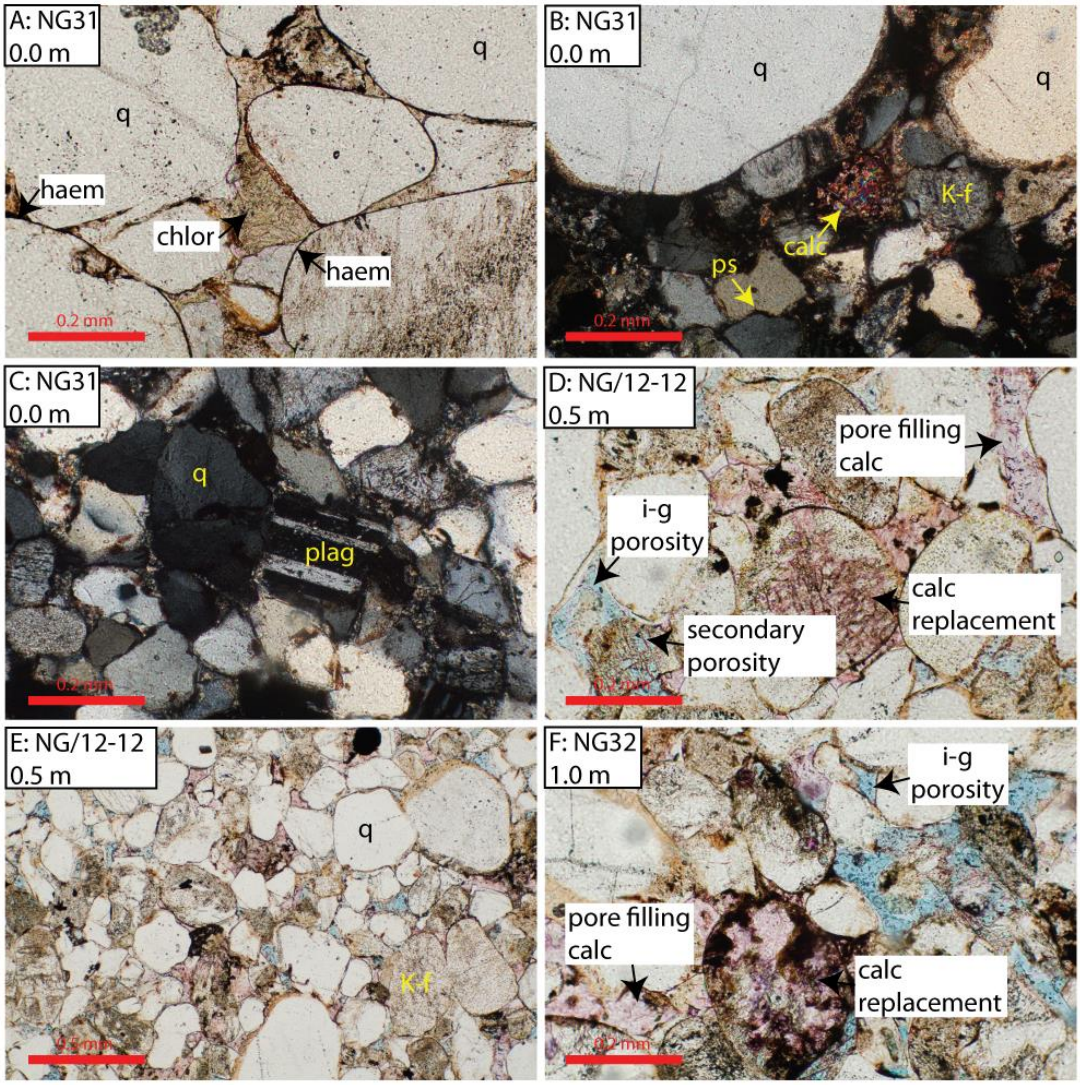

Fig. 4.12. Photomicrographs of sandstone below lava contact. A) PPL, Pore filling chlorite at contact with preserved haematite grain coatings. B) XPL Pore filling and feldspar replacing calcite at contact. C) XPL, Compaction at contact of similar degree to top of upper dune (Fig. 1.6.) with plagioclase freshly preserved. D, E) PPL, 0.5 m

below contact intergranular porosity reappears together with intensification of grain replacement by calcite and pore filling calcite, compaction porosity loss decreases in importance. F) PPL, 1.0 m below contact both calcite replacement of feldspar and pore filling calcite persists, but intergranular porosity increases.

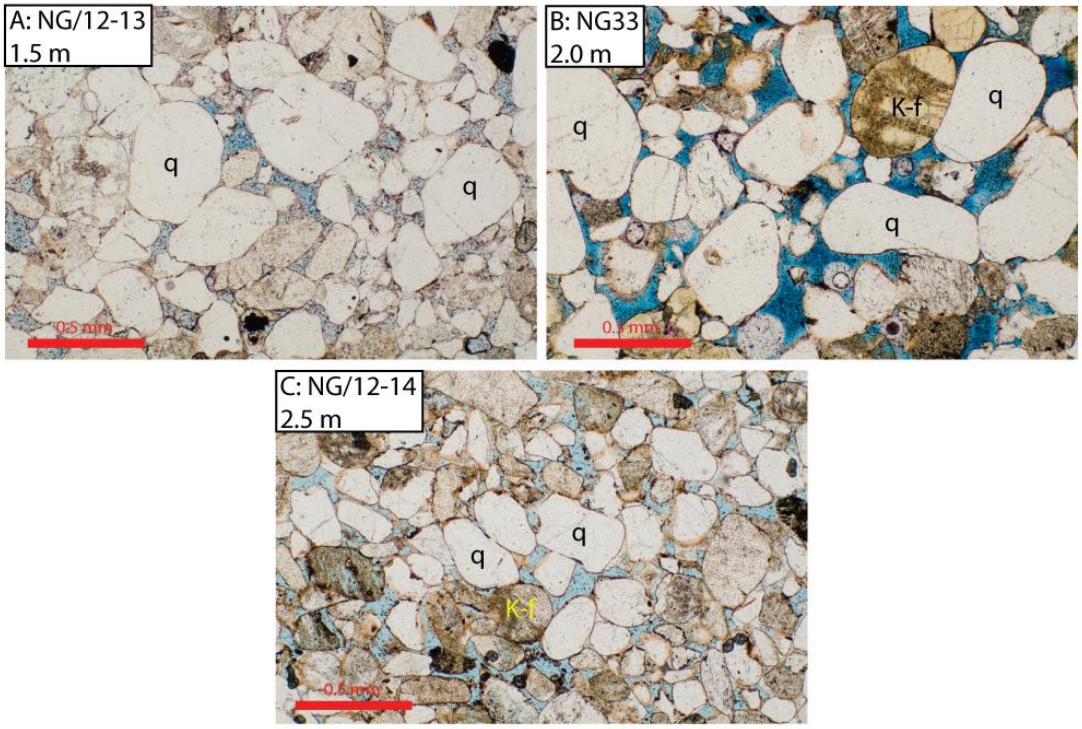

Fig. 4.13. A) PPL, 1.5 m below contact calcite is rare and feldspars not corroded. B, C) PPL, Return to background conditions by 2.0 m below lava, compaction is at background levels, haematite grain coatings and connected intergranular porosity present.

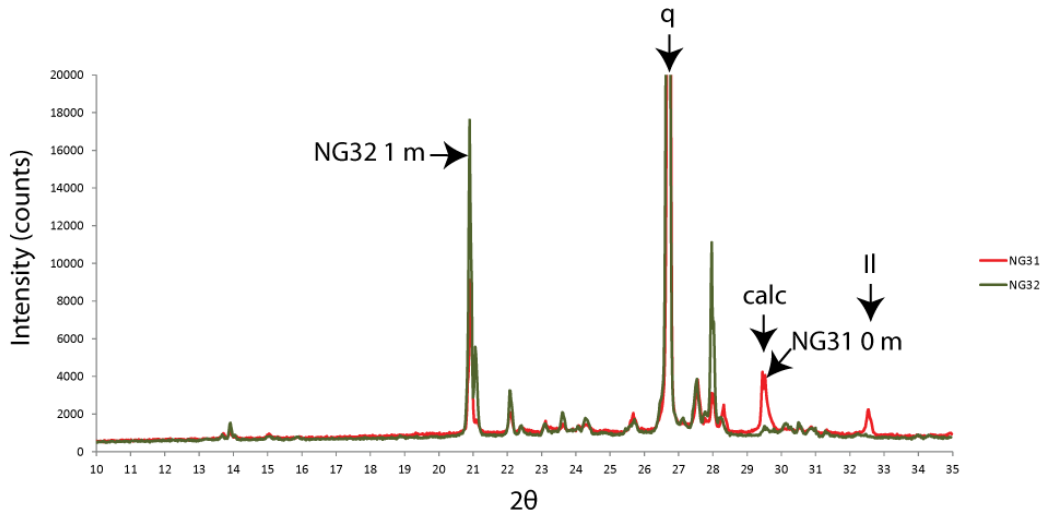

Fig. 4.14. X-Ray diffraction spectra for NG31 (0.0 m) and NG32 (1.0 m) whole rock fraction. Differences in the spectra show that NG31 has more abundant calcite,

ilmenite, and possibly fluorite compared to both NG32 and NG52. The petrographically identified chlorite was not resolved in XRD.

4.2.2 Red Yellow Dyke (RYD) lava pond

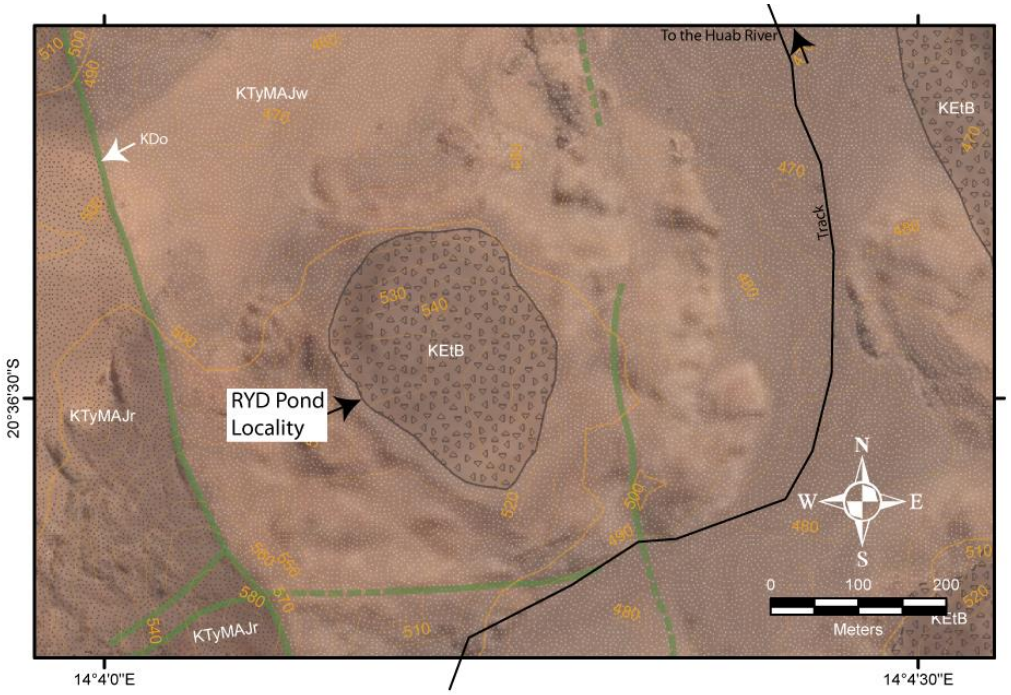

Fig. 4.15. Map of RYD lava pond (KETb). Contour interval is 10 m.

This case study (Fig. 4.15) is located at 20° 36.504' S 14° 4.151' E at 529 m altitude on the hill 440 m north of the RYD locality (Chapter 6). The petrographic analysis is based on a transect taken from the SW edge of the lava pond that has complete exposure from the lava to 5 m below, where the ground flattens.

The lava pond is preserved in an inter-dune depression (Fig. 4.16.) , which is sub-circular, 190 m in diameter and filled with at least 32.5 m of Tafelberg Type lava preserved at the deepest point (interpreted from photo and GoogleEarth). The summit of the pond does not display and lava surface features, or sediment bypass evidence (sand crack fills)/ interbeds, so this thickness is a minimum estimate. The underlying sandstone belongs to the Major Erg (KTyMAJ) unit of the Twyfelfontein Formation and is generally a 'white sand' (see Chapter 7 and Grove et al., *in review*), although the sand at the lava contact is preserved as red sand where affected by the lava, common to other white sand lava contacts.

The sandstone at the contact below the lava at the RYD lava pond locality has a porosity of 0.2 % (±0.2) and a negligible permeability of 0.1 md. The sample is

composed of grain fall sand of between 100–200 μm diameter (Fig. 4.17A, B, C). No coarser-grained material was found at the contact. The sediment detrital composition is similar to the background sandstone. Authigenic calcite is negligible, but there is potentially some authigenic fluorite. Fluorite in thin section is a low relief purple-blue mineral with defined cleavage that is isotropic in XPL (Fig. 4.17C.). A mineral fitting that description exists in this sample, *but* overzealous HCl etching during staining could thin the calcite, reducing its birefringence such that it appears in extinction on a complete stage rotation. Haematite grain coatings are absent.

Porosity loss appears petrographically to be due to compaction, the quartz grains are highly sutured and interpenetrate and occasional overgrowths (presumably early) exist at triple junctions; this is good evidence for pressure solution (*senso* Rutter, 1983). Feldspar grains retain detrital textures and do not appear so affected by pressure solution. Plastic deformation of quartz, as indicated by undulatory extinction is more common than for the Dune 16 or the Upper Dune case studies, but most grains show unit extinction. The compaction porosity loss (COPL) at the contact is 46 % (±3.2) compared to the background of ~35 % (±2.6) and cementational porosity loss (CEPL) is 2.5 %.

Detrital grains at 0.2 m depth below the contact are 200 μm in diameter on average and exhibit a similar assemblage to the background sandstone (Fig. 4.21B). Porosity is 2.6 % (±0.7), but permeability is still negligible (0.1 md) (Fig. 4.19A) . The authigenic mineral assemblage in the sample from 0.2 m below the contact is dominated by calcite, and exhibits quartz overgrowths and an increasing abundance of haematite grain coatings and mottled haematite aggregates (Fig. 4.17 D,E; Fig. 4.20). The calcite exclusively or partially replaces detrital plagioclase. Quartz grains are frequently sutured and interpenetrate, suggesting pressure solution is an important process. Porosity loss is dominated by compaction (45 %, ±3.1). CEPL is 2.5 % suggesting cementation is a minor contributor to porosity loss at this distance below the lava.

As distance increases below the lava contact, detrital grains remain ~ 200 μm in diameter and of similar composition to the background (Fig. 4.21B.). Porosity is negligible and permeability is 7 md. Authigenic minerals consist of calcite, quartz, redistributed haematite, and clay. Quartz, clay and opaques are not correlated with distance below the lava and are at background levels (Fig. 4.20C, Fig. 4.21.). The

calcite mostly replaces plagioclase grains, but occasionally fills pores. Compaction porosity loss is still major (46 %, ±3.2) presenting as sutured and embayed quartz crystals, plastic deformation is however possible due to the existence of undulatory extinction in occasional quartz grains.

By 2.0 m depth below the lava contact, the detrital mineralogy is dominated by quartz and potassium feldspar in background proportions, but plagioclase decreases as the calcite proportion increases (Fig. 4.18C, D; Fig. 4. 21B). Authigenic mineral cements are important at this depth: in sample NG81 calcite accounts for 16.6 % (±1.7) and is dominated by a pore-filling poikilitic phase with abundant replacement of plagioclase. Porosity (1.6 %, ±0.6) remains low due to the increased pore-filling calcite cement and permeability is 8.5 md. Cementational porosity loss has increased importance over compactional porosity loss as COPL (36.7 %, ±1.6) has been reduced to near background and CEPL has increased to 11.3 %. This change can be seen in the reduced amount of grain interpenetration and sutured contacts.

Porosity (12.6 %, ±1.5) and permeability (50 md) have increased to background levels at depths of 3.0 m below the lava contact. Detrital potassium feldspar and quartz abundances are background values; detrital plagioclase is reduced. Despite the high porosity, authigenic calcite remains high (10.6 %, ±1.4) and haematite grain coatings are present. The high porosity is due to background levels of COPL and the calcite replacing plagioclase rather than filling pores. This can be seen in Fig. 4.21B, where plagioclase shows a negative correlation with distance below the contact as it is consumed by calcite. Porosity loss is still dominated by compaction, but at levels no greater than the background burial compaction, and cementational porosity loss has almost reduced to background levels for the white sandstone.

Five meters below the lava contact, the sandstone is a background white sandstone, as its position, to the east of the RYD dyke (Chapter. 6 and 7) would suggest. Detrital grains are ~ 200 μm in diameter, potassium feldspar and quartz are at background levels, and plagioclase is reduced in abundance due to later hydrothermal reactions (Type 3 diagenesis, Grove et al., *in review*).

The trends away from the lava contact at the RYD pond locality record an increase in porosity from negligible values to 14 % (±1.6) over a distance of 5 m

(Fig. 4.19). This is mostly controlled by increased compaction at the base of the lava extending to at least 0.6 m (Fig. 4.22). Below the compacted zone is a region of increased calcite cementation which reduces away from the lava. No trends were seen in opaque minerals away from the contact as they are dominated by detrital ilmenite and magnetite that appear un-reactive. No trend was observed in clay mineral abundance, detrital quartz or detrital potassium feldspar abundance away from the contact.

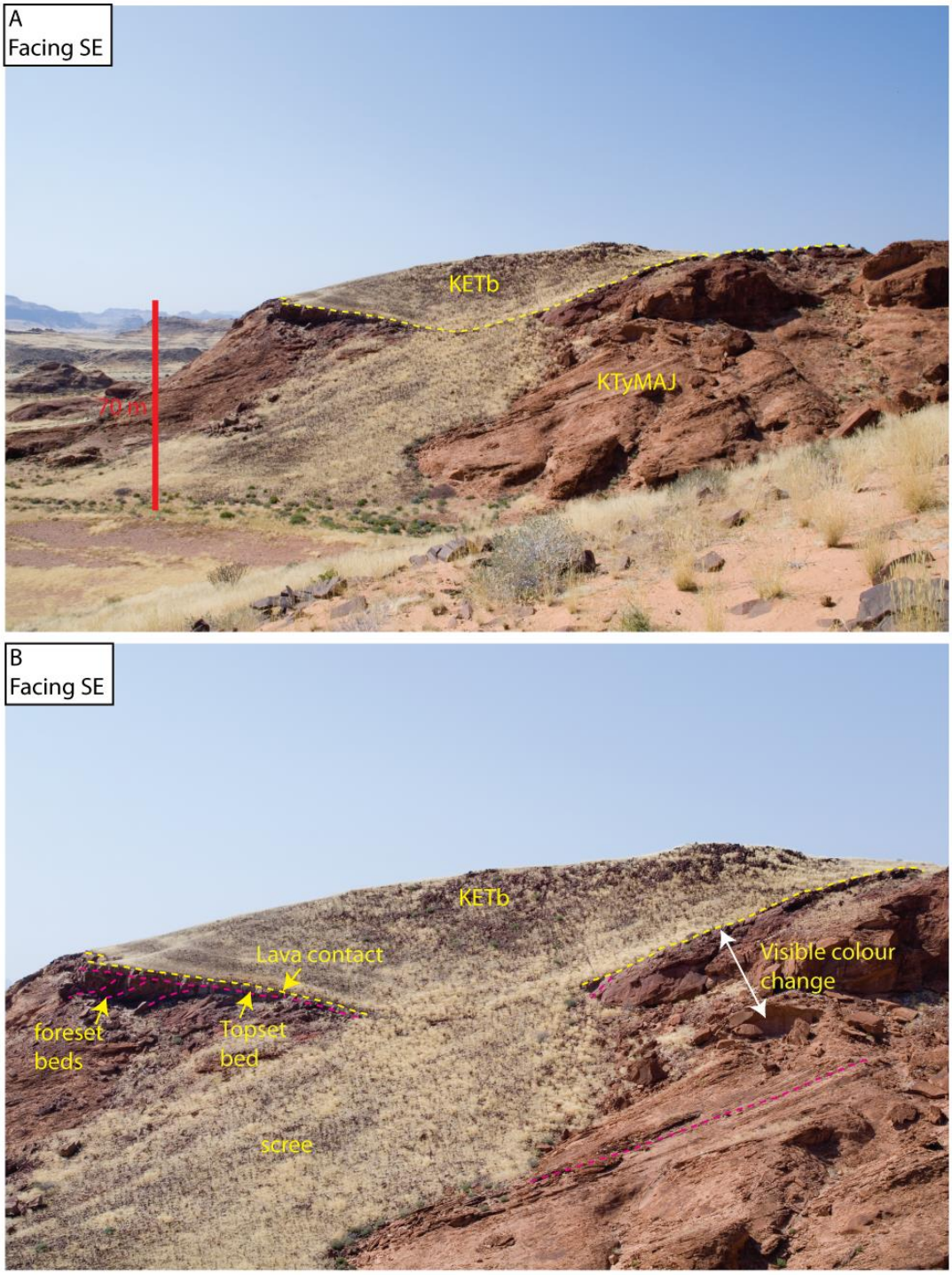

Fig. 4.16. A, B) RYD lava pond seen from the ridge to the northwest. The lava pond rests in an interdune depression of the Major Erg unit (KTyMAJw) which is a 'white sand' affected by later hydrothermal fluids (see Chapter XX). B) The Major Erg has preserved topset beds to the left of the pond (from this view) but not to the right, illustrating the migration of the erg from right to left (SSW-NNE).

RYD Lava Pond Sample Number 20° 36.504' S 14° 4.151' E	Distance Below Lava (m)	Porosity (%)	1 sigma error
NG78	0	0.2	0.2
NG79	0.2	2.6	0.7
NG80	0.6	0	0
NG81	2.0	1.6	0.6
NG82	3.0	12.6	1.5
NG83	5.0	14.0	1.6

Table. 4.2. RYD lava pond locality samples, location, distance below lava and porosity. (see Appendix for complete data table).

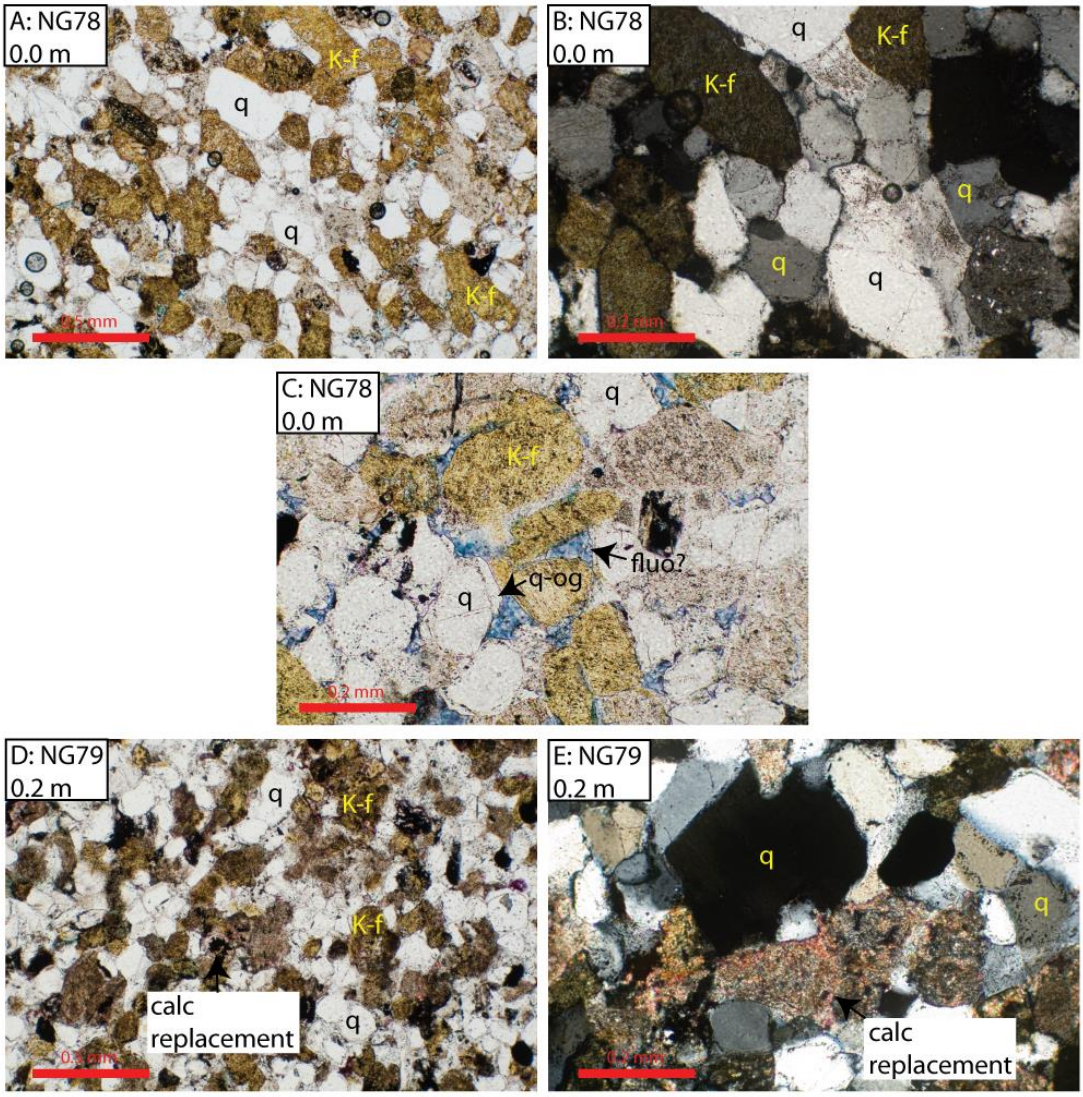

Fig. 4.17. Photomicrographs of sandstone below RYD lava pond contact. A, B) PPl and XPL of sand a contact showing high degree of compaction. C) PPL, sand at contact with possible fluorite cement based on low relief, colour and isotropic extinction; otherwise could be ferroan calcite, thinned by too long exposure to HCL or stain (see Chapter 3 Methods). D, E) PPL and XPL 0.2 m from contact. Increased compaction is still evident, but calcite replacement of plagioclase and pore-filling calcite is present.

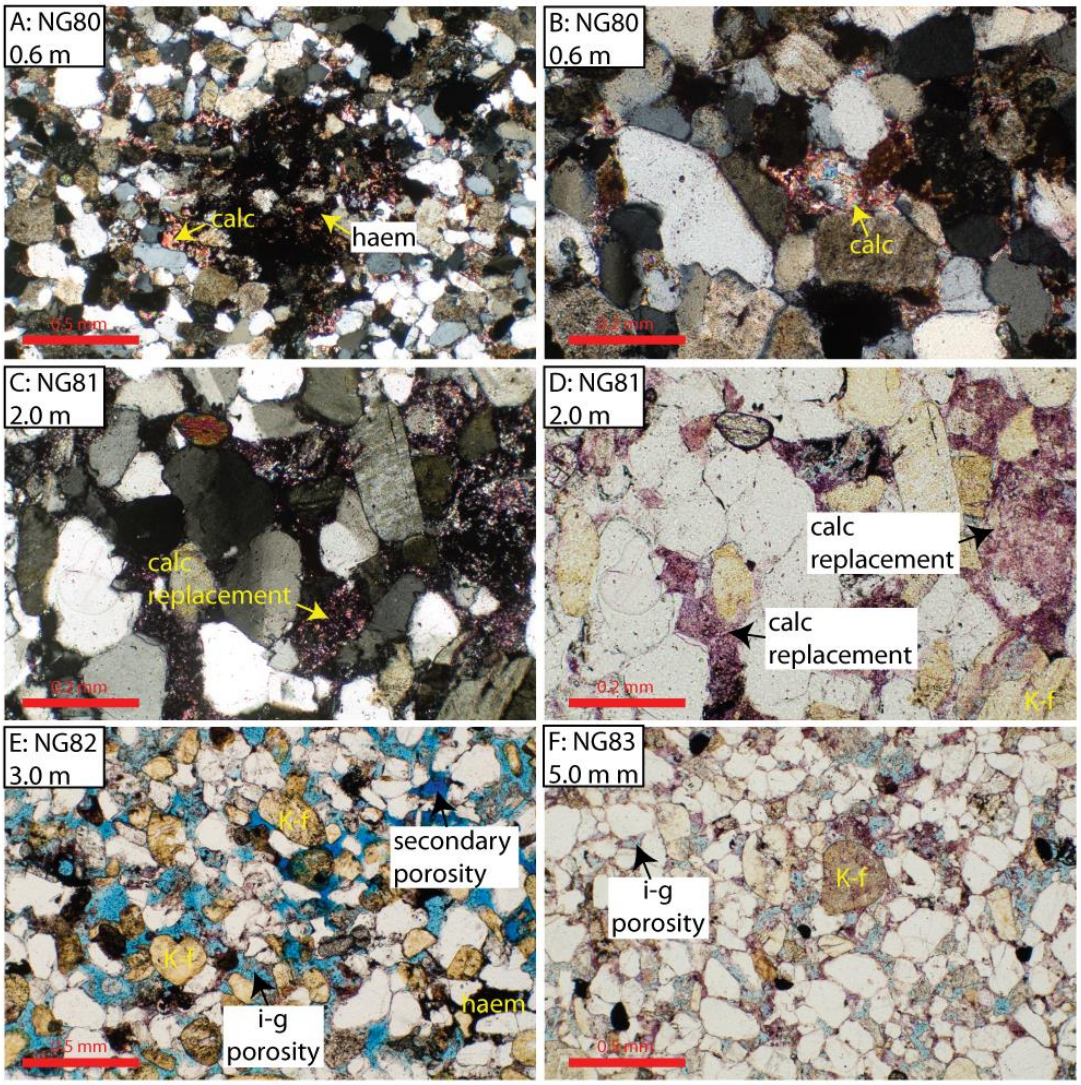

Fig. 4.18. Photomicrographs of sandstone below RYD lava pond contact. A, B) XPL 0.6 m below contact showing a now pervasive calcite cement that replaces plagioclase and fills pores. C, D) XPL and PPL 2.0 m below contact. Calcite cement now fills pore networks as compaction is less. E) PPL 3.0 m below contact, porosity is regained, compaction is at background levels and haematite grain coatings are redistributed as mottled patches filling pores. F) PPL 5.0 m below lava, porosity and mineralogy Is that of white sand (see Indirect Effects Chapter XX) ('Type 3' diagenesis Grove et al., *in review*).

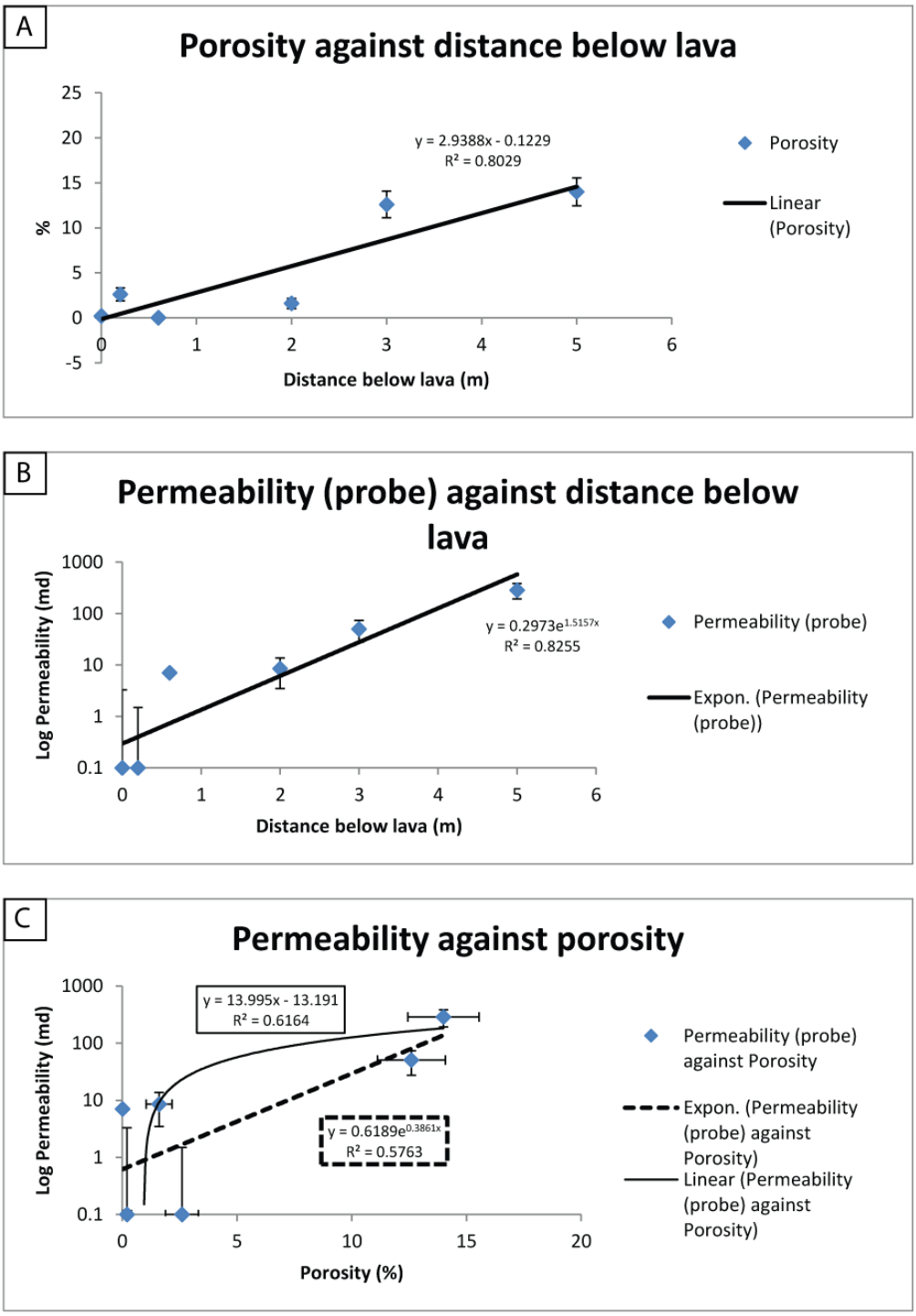

Fig. 4.19. Graphs against distance below lava for RYD lava pond. A) Porosity increases with distance from lava. B) Permeability increases exponentially with distance below lava. C) Permeability against porosity, linear relationship is weak, suggesting control of pore blocking is not simple compaction (i.e. pore throats blocked at even moderate (~5 %) porosities.

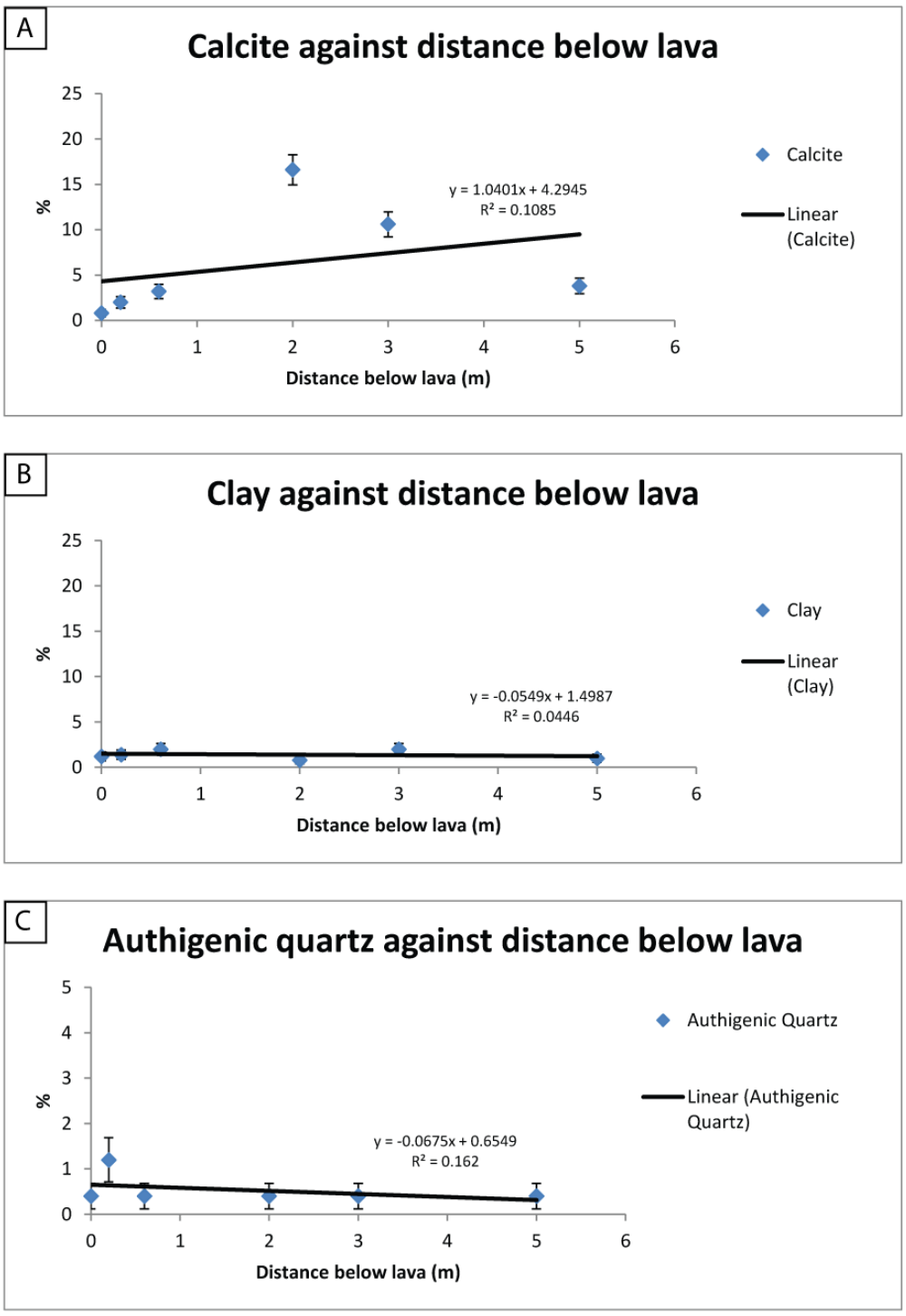

Fig. 4.20. Graphs against distance below lava. A) Calcite is low near lava due to early compaction removing porosity and fluid migration pathways, reaches a maxima at 2.0 m, then reduces to white dune background levels (5 m). B) Clay does not show correlation with distance. C) Authigenic quartz does not show correlation with distance.

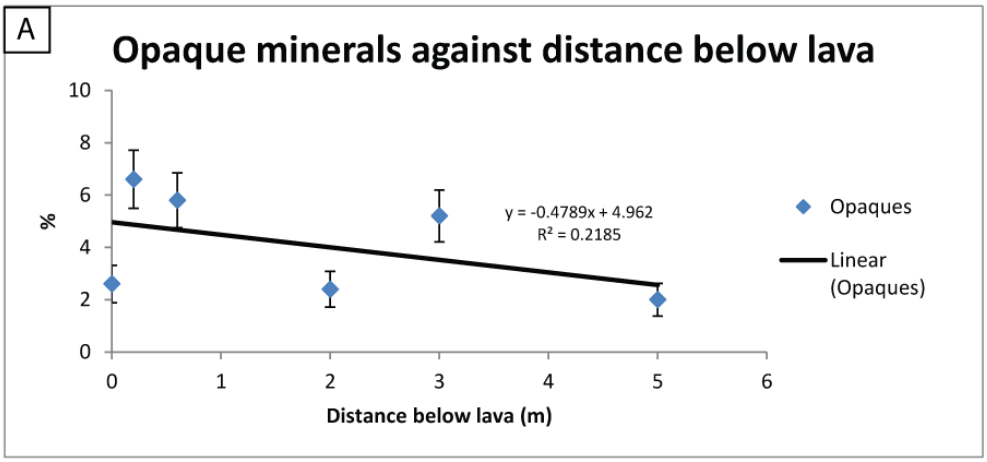

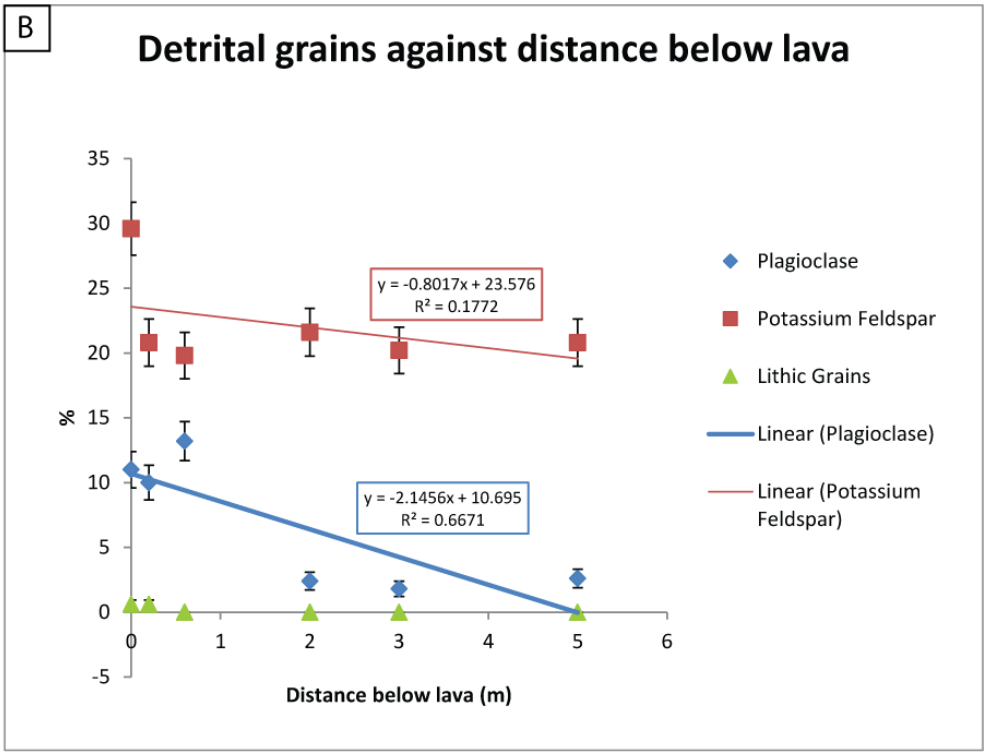

Fig. 4.21. Graphs against distance below lava. A) Opaque minerals show a weak negative correlation. B) Potassium feldspar shows no correlation, plagioclase shows a strong negative correlation due to 'white Type 3' diagenesis, lithic grains show no correlation.

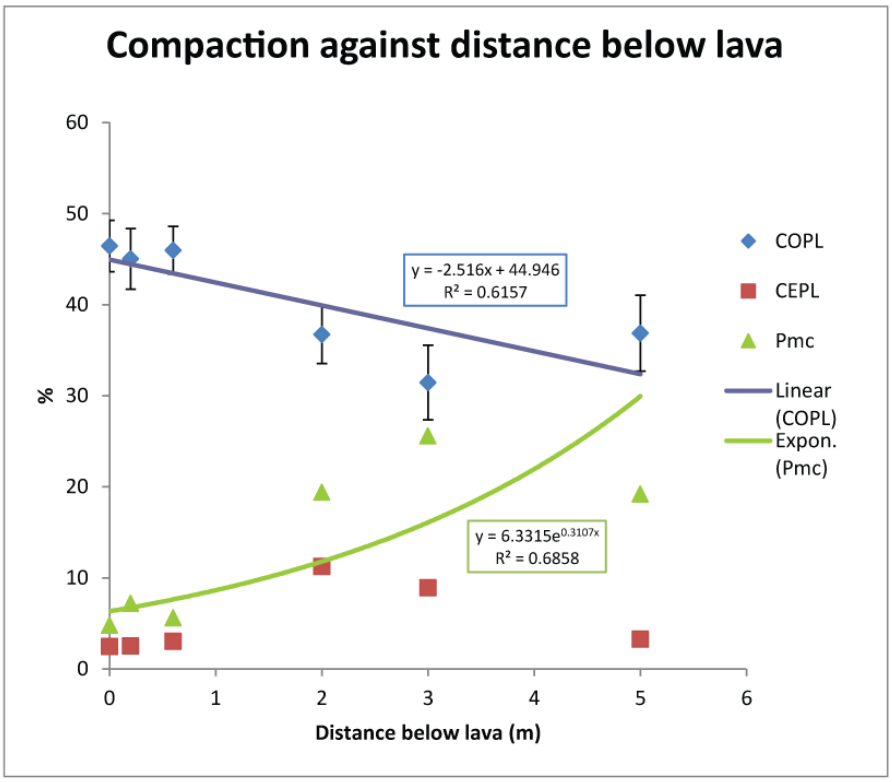

Fig. 4.22. Porosity reduction analysis of sandstone below RYD lava pond. Compaction porosity loss (COPL) is negatively correlated with distance below lava and Pmc shows an exponential correlation. This suggests compaction porosity loss is more important closer to the lava.

4.2.3 Big Dune (BD)

The Big Dune locality is at 20° 34.980' S 14° 0.850' E at 453 m altitude, 2.6 km south of the Huab River (Fig. 4.23.). The outcrop is on the north side of a hill that rises to 782 m altitude. The analysis at this locality is based on a suite of 6 samples collected by Dr Dougal Jerram and Mr Graham Thompson in a transect of the sandstone below the lava from 0.0 m to 4.0 m. The outcrop consists of a large transverse Twyfelfontein Formation (KTyMAJ) sand dune that has been drowned by Tafelberg Type lava (KETbTb) (Fig. 4.24.).

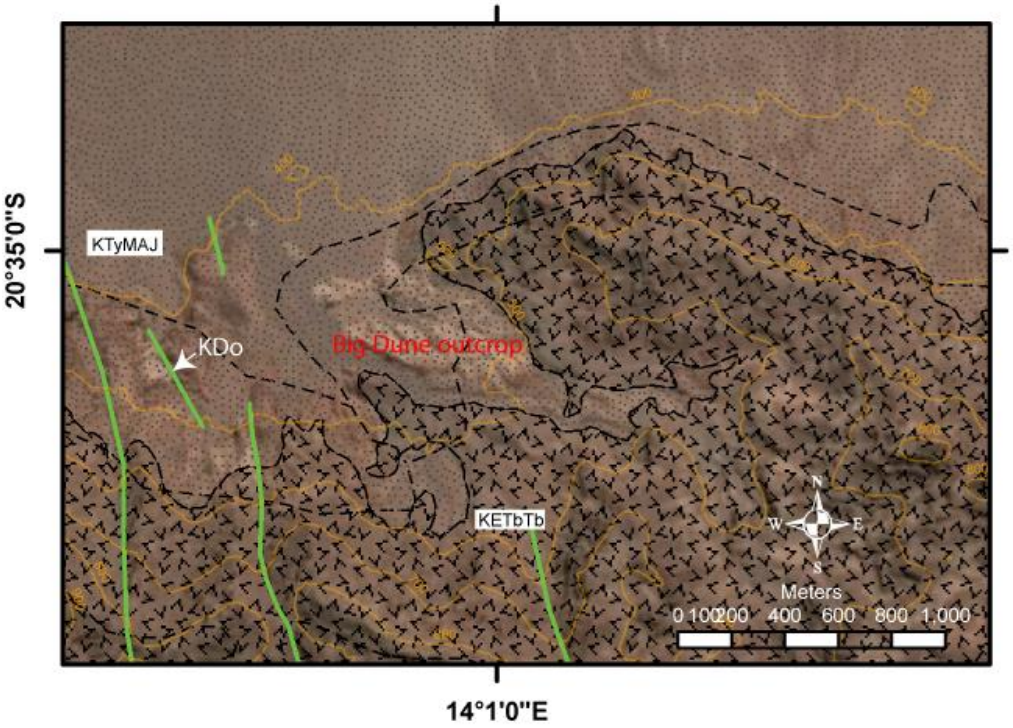

Fig. 4.23. Map of Big Dune locality. Contour spacing is 10 m.

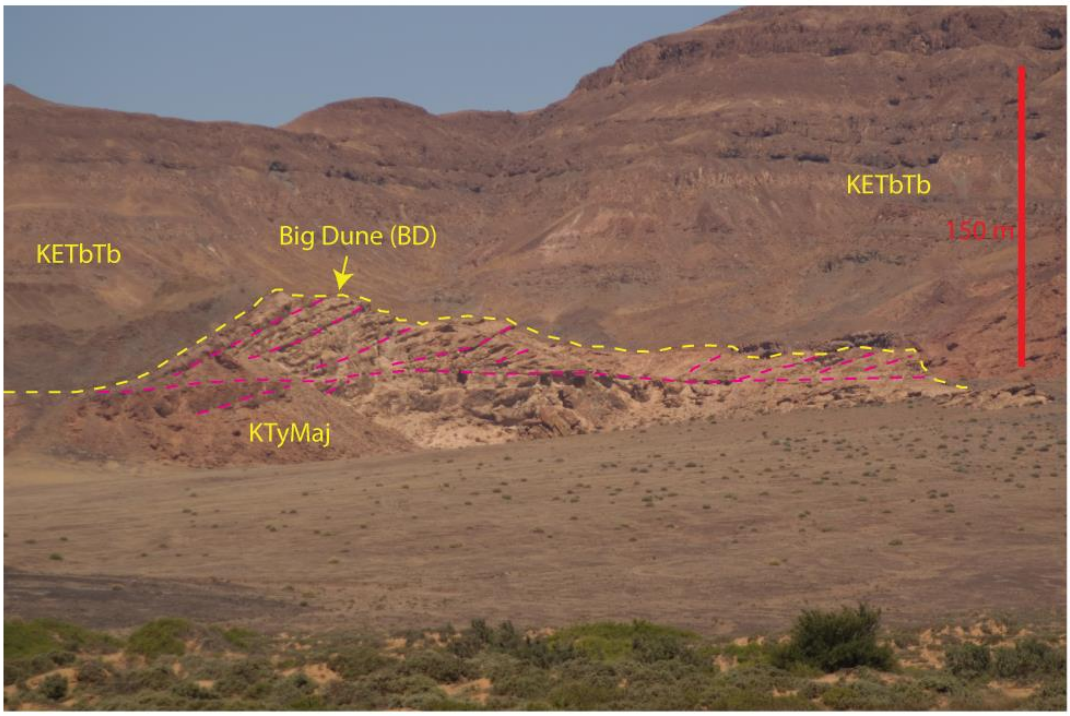

Fig. 4.24. Photograph of BD locality taken from the north. The transverse dune can be seen to be onlapped by lava flows and then completely drowned. Foreset beds are highlighted in pink.

Big Dune Sample Number 20° 34.980' S 14° 0.850' E	Distance below lava (m)	Porosity (%)	1 sigma error
BD6	0.0	0.0	0
BD1	0.0	0.0	0
BD2	0.12	2.0	0.6
BD3	0.24	1.2	0.5
BD4	2.0	5.8	1.0
BD5	4.0	13.6	1.5

Table. 4.3. BD samples, location, distance below lava and porosity. (see Appendix for complete data table).

Sample BD6 straddles the lava-sediment contact, and is preserved due to adhesion of the glassy lava crust to the sand. This is not common at Tafelkop Lava contacts, where weathering separates the lava from the more resistant sand. At this locality, the Tafelberg Type basalt is evidently not so weathered. At the contact sand grains range from 100 μm to 500 μm in diameter and are generally grain flow in depositional nature. The detrital composition is similar to the background Twyfelfontein Formation. Detrital grains frequently exhibit haematite coatings. The porosity and permeability are negligible . The contact with the sand is passive, and a single layer of sand grains is partially enveloped in the lava, which must have been a fluid at the time (Fig. 4.26A, B, C). Porosity loss determined from visual analysis appears to be mostly due to calcite cementation. The calcite is poikilitic and individual crystals are up to 1 mm in diameter and are continuous from the sedimentary pores into the basalt pore space (Fig. 4.26A.). The calcite cement has occasionally replaced quartz, (see corroded quartz grains in Fig. 4.26B and C). Feldspar grains are rare at the contact (within the upper most 2 mm) and I infer that they have been entirely replaced by calcite. Interestingly, one quartz grain at the contact has been sheared with a sinestral displacement of ~ 0.5 mm, suggesting

weakening of quartz and transfer of stress from a potentially moving lava, which is yet to be reconciled with the lava emplacement mechanism.

A second sample, BD1 also at 0 m below the contact does not include attached basalt. The detrital composition is similar to the background composition. Sand grains range from 200–500 μm in diameter. It is interpreted as a grain flow horizon. The sample has negligible porosity and permeability. Grains are coated with haematite. Porosity loss is dominated by compaction (41.8 %, ±2.9) and is ~ 7 % above the background. Cementational porosity loss is 7.2 %. Pressure solution compaction is evident in the thin sections as embayed grains (Fig. 4.27A, B, and C) and sutured contacts (Fig. 27B, C); quartz overgrowths exist as triple junctions between grains. Most grains show unit extinction, suggesting plastic deformation was minor.

The cements comprise quartz overgrowths and calcite, unlike below other lava contacts, these quartz cements, although volumetrically insignificant (0.8 %, ±0.4) reduce away from the contact, possibly related to pressure solution and compaction. The calcite (10.2 %, ±1.4) is poikilitic and identical in character to that in BD6. Figure 4.27D illustrates calcite replacing a quartz grain in extinction in the centre of the photomicrograph. X-ray diffraction confirms the petrographically determined mineralogy (Fig. 4.25.).

Sample BD2, at 0.12 m depth below the contact is characterised by a high degree of compaction and a low abundance of authigenic minerals. Porosity is 2 % (±0.6), no permeability data were obtainable (Fig. 4.30.). All pores found had quartz overgrowths protruding into the space. The detrital composition is similar to the background (Fig. 4.32B.). Authigenic mineralisation is minor, unusually for this close to the lava, authigenic quartz (2.8 %, ±0.7) is more abundant than calcite (0.6 %, ±0.3) which is restricted to grain replacement. The high quartz abundance may be due to the large degree of pressure solution (Fig. 4.28A, B.) indicated by highly embayed quartz grains (Fig. 4.28A.) and extensive suturing (Fig. 4.28B.). Most grains show unit extinction, with the occasional undulose quartz crystal. Rare polycrystalline quartz grains are highly plastically deformed. Compaction (COPL) is the major contributor to porosity loss (45.5 %, ±3.4), cementational porosity loss (CEPL) is minor (2.4 %). COPL is about 10 % above background levels.

Compaction remains high 0.24 m below the lava (BD3) and porosity remains low (1.2 %, ±0.5). Detrital minerals, clays and opaque grains, show little variation in abundance from the background. Authigenic calcite occurs as pore-filling poikilitic cement (Fig. 4.28C, D.) and as replacement of plagioclase. Calcite is the most important pore filling cement, but is volumetrically minor (2.0 %, ±0.6). Compaction is the largest contributor to porosity loss (COPL= 46.3 %, ±0.5), cementational porosity loss is minor (CEPL= 2.0 %).

At depths of 2.0 m below the lava, porosity is returning to background levels (5.8 %, ±1.0), and permeability is 7.2 md. Authigenic cements are rare, and limited to minor quartz overgrowths (1.0 %, ±0.4) (Fig. 4.29A, B.). Sand grains are between 200 μm and 500 μm with a modal composition similar to the background. Porosity loss is dominantly through compaction (COPL= 44.4 %, ±1.0), cementation porosity loss is minor (CEPL= 2.0 %).

At 4.0 m below the lava, porosity (13.6 %, ±1.5) is comparable to background levels and permeability is 201 md. Authigenic cements are limited to negligible quartz overgrowths (0.2 %, ±0.6). Detrital grains are within background levels, although plagioclase abundance is higher than it is closer to the contact. Porosity reduction is due to compaction (COPL=40.4 %, ±1.5), which is slightly higher than the background, suggesting that at 4.0 m, porosity may not have reached its peak below this lava. CEPL= 0.5 %. Compaction appears to be through pressure solution as many grains interpenetrate and are sutured, and through grain crushing, which affects feldspars to a greater degree than quartz (Fig. 4.29C.). Crush compaction of grains in the Twyfelfontein Formation has been studied by Dickinson & Milliken (1995), who noted under the optical microscope and at smaller scales under cathode luminescence imaging.

Overall, the porosity trend (Fig. 4.30.) is similar to those of the other three lava contact examples. Porosity increases with distance below the lava contact, until background porosity is reached. Compaction is the major contributor to porosity loss, although calcite cementation is important in grain flow layers <0.12 m below the contact. Calcite becomes less important further from the contact. Quartz cementation appears to accompany compaction through pressure solution, and is most intense closer to the contact where compaction is also the greatest. The abundance of authigenic quartz remains low, such that no statistical significance exists to the above

observation (see Chapter. 3. and Grove & Jerram, 2011, for discussion of point counting errors).

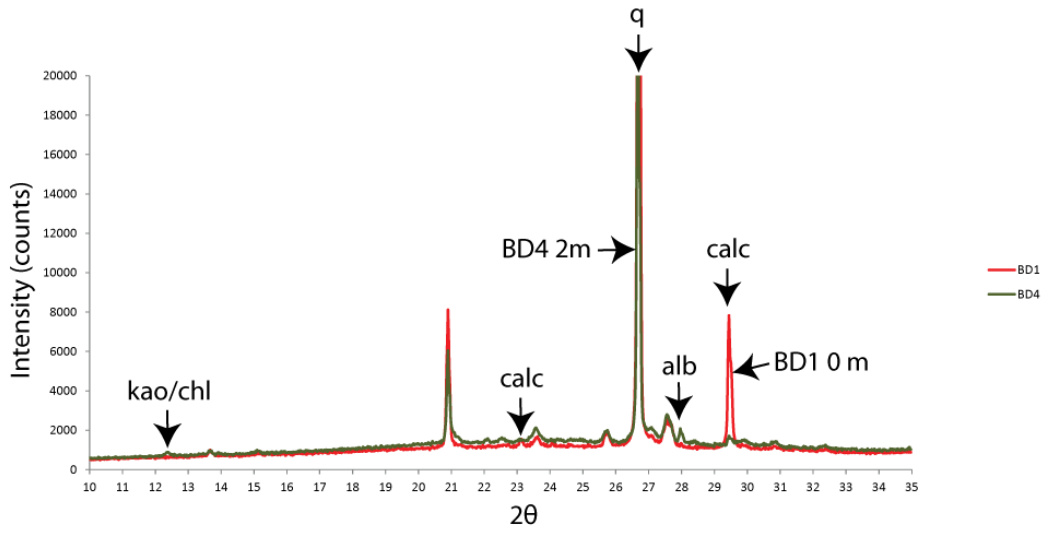

Fig. 4.25. X-Ray Diffraction spectra for BD1 (contact) and BD4 (2 m).

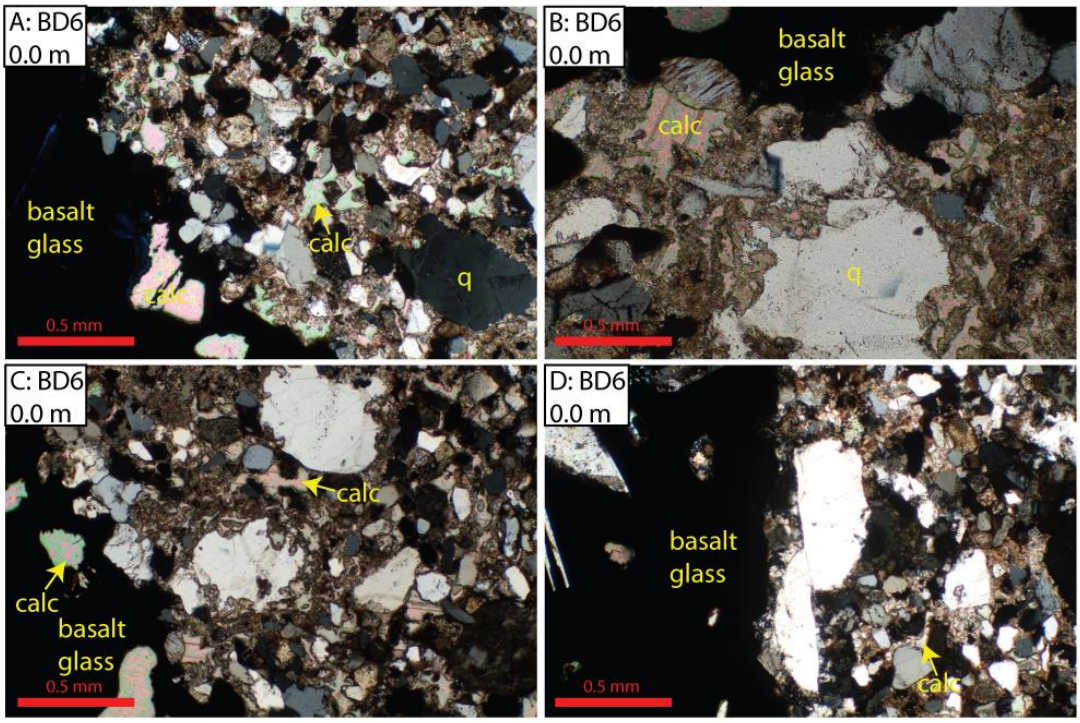

Fig. 4.26. XPL Photomicrographs of sample BD6 at lava contact. A) Glassy vesicular lava contact enveloping quartz grains that are thermally unaffected by cooling lava. Pokilitic calcite cement is pervasive and continuous into basalt pore space. B) Detrital quartz grain at contact is aggressively replaced by calcite. C) Calcite indurated sand at contact showing aggressive replacement of one quartz grain, but most keep detrital characteristics and are not replaced, feldspars are rare. D) Shearing of quartz grain at contact.

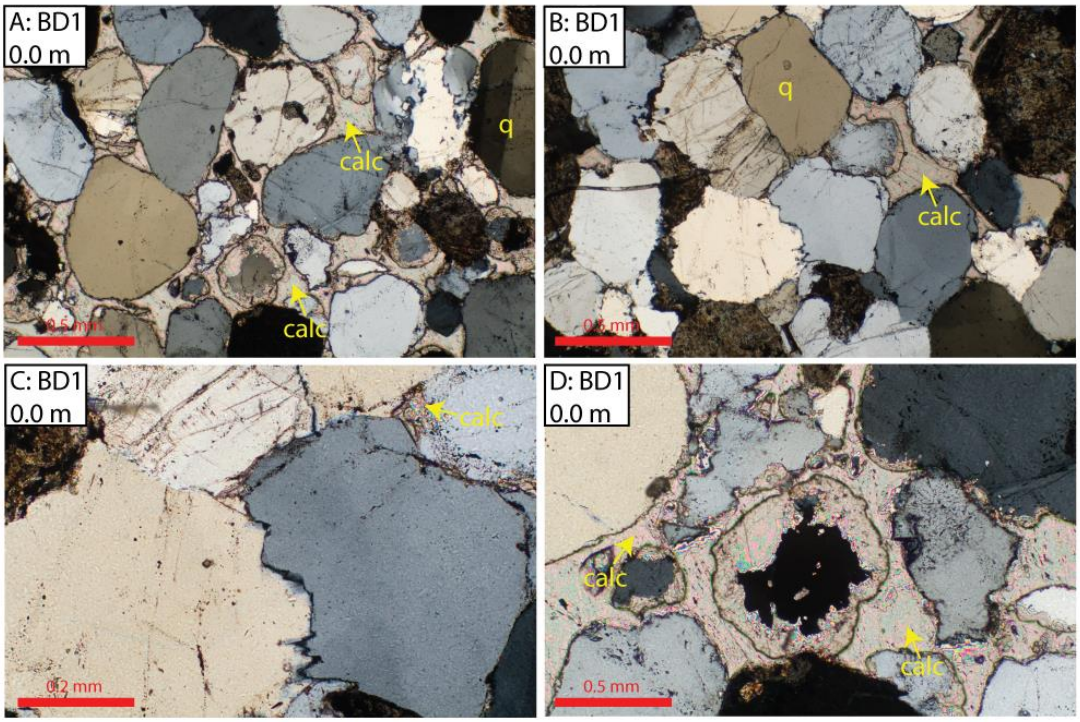

Fig. 4.27. XPL Photomicrograhs of grain flow lamination at contact showing aggressive calcite pokilitic cementation (D) and high compaction between detrital quartz grains (B, C).

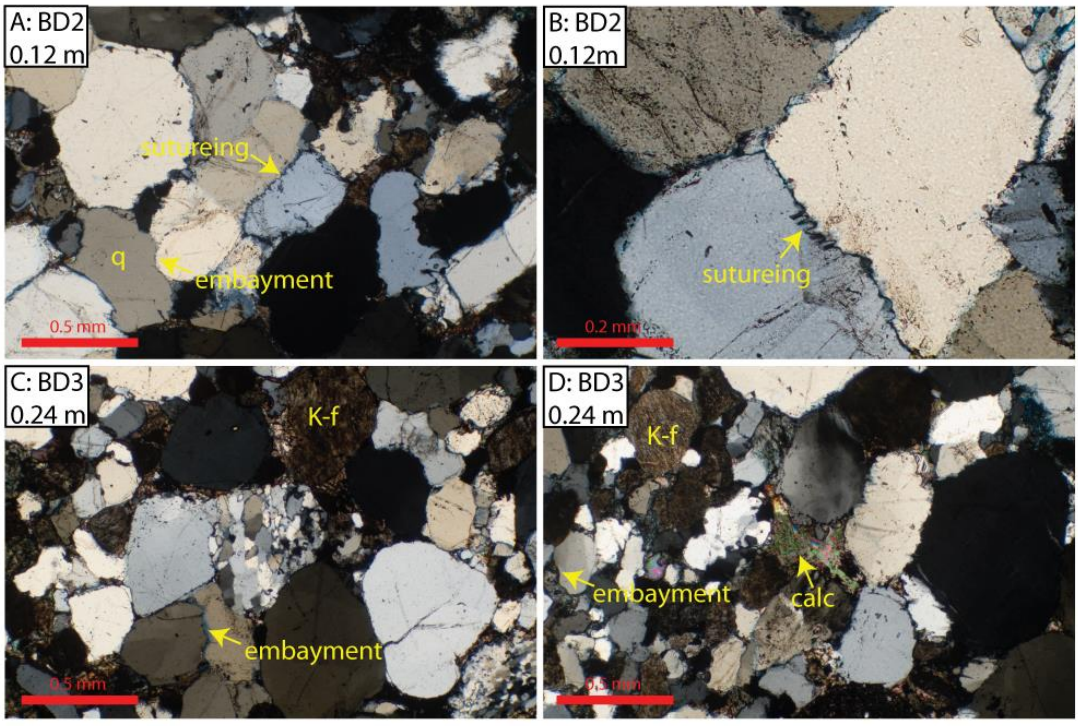

Fig. 4.28. XPL photomicrographs below BD contact. A, B) 0.12 m below lava contact, compaction is the dominant porosity reducing mechanism. The early calcite cement appears not to have developed. C, D) 0.24 m, compaction is still the major porosity

reducing mechanism. Grains show cuspate and sutured contacts and have deformed to fill pore space.

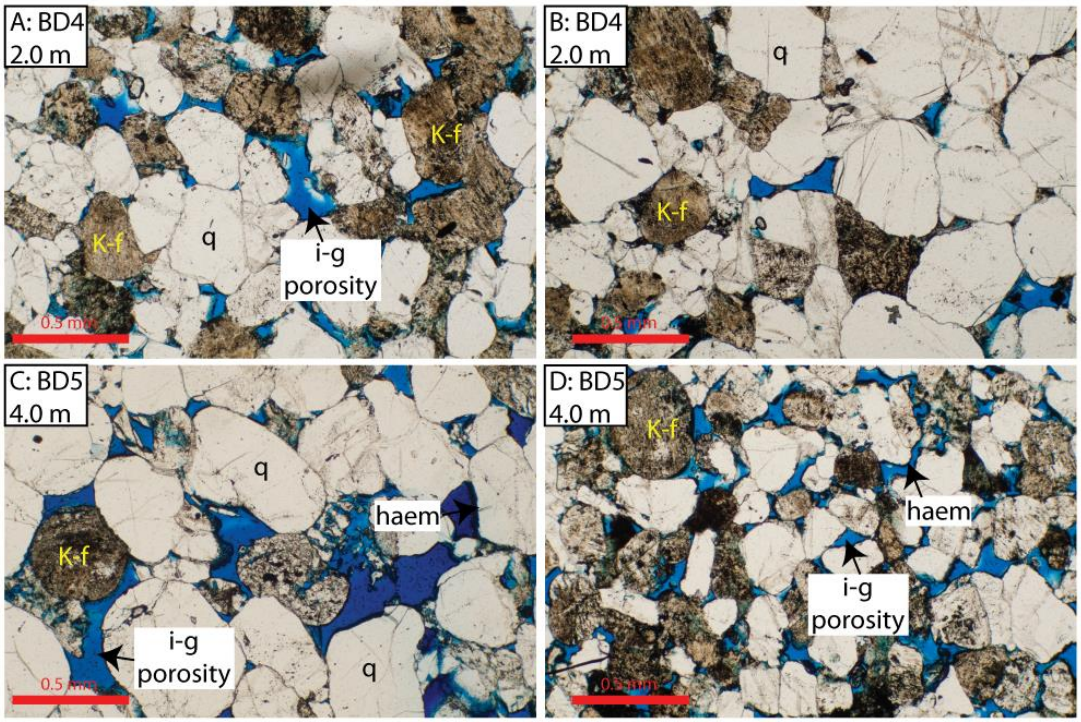

Fig. 4.29. PPL photomicrographs 2.0 m to 4.0 m below BD contact. A, B) By 2.0 m no calcite cement or increased compaction is evident. Diagenesis is dominated by quartz overgrowth, compaction to form sutured and interpenetrating cuspate grain contacts. C), D) 4.0 m below contact the rock is similar to 2.0 m but with less compaction porosity loss, diagenesis is the same as 2.0 m; crush compaction of feldspar grains becomes common.

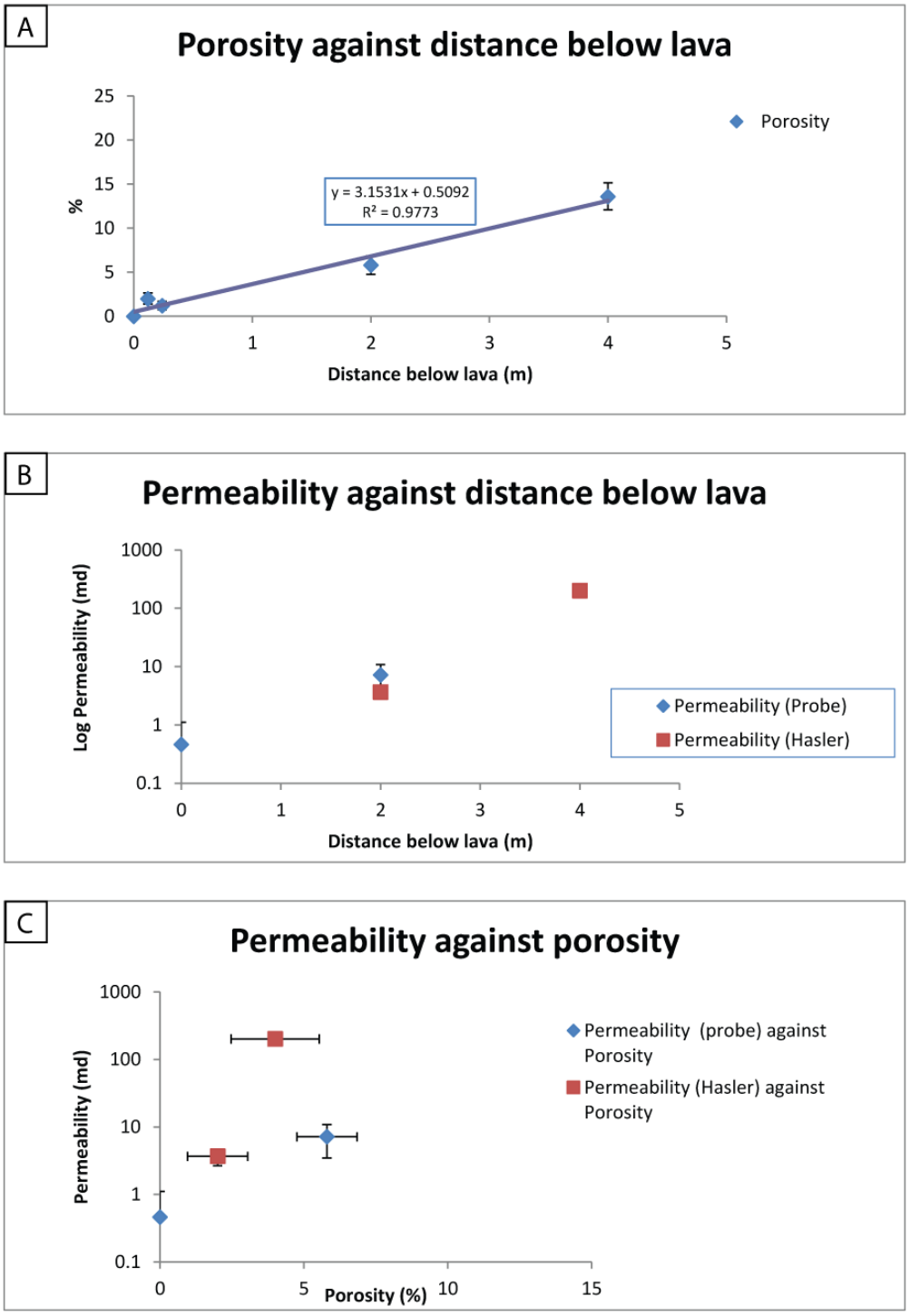

Fig. 4.30. Graphs against distance below lava. A) Porosity increases with distance below lava contact. B) Permeability increases below contact, albeit with very limited data. C) Permeability against porosity.

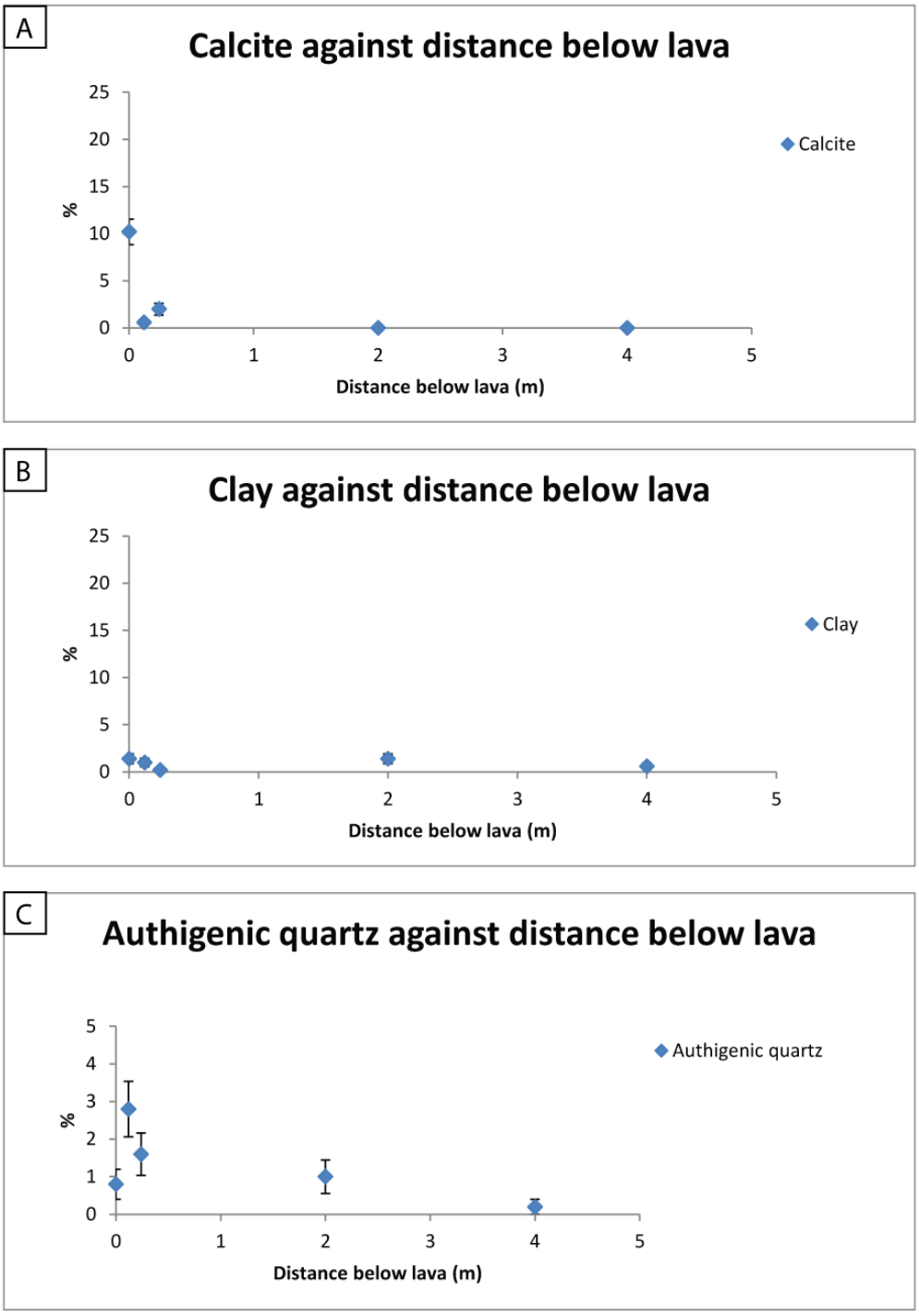

Fig. 4.31. Graphs against distance below lava. A) Calcite decreases immediately below contact, negligible > 0.24 m; although no valid correlation is shown. B) Clay shows no correlation with distance below lava. A) Authigenic quartz is higher near to contact, but only shows a very weak correlation with distance below lava.

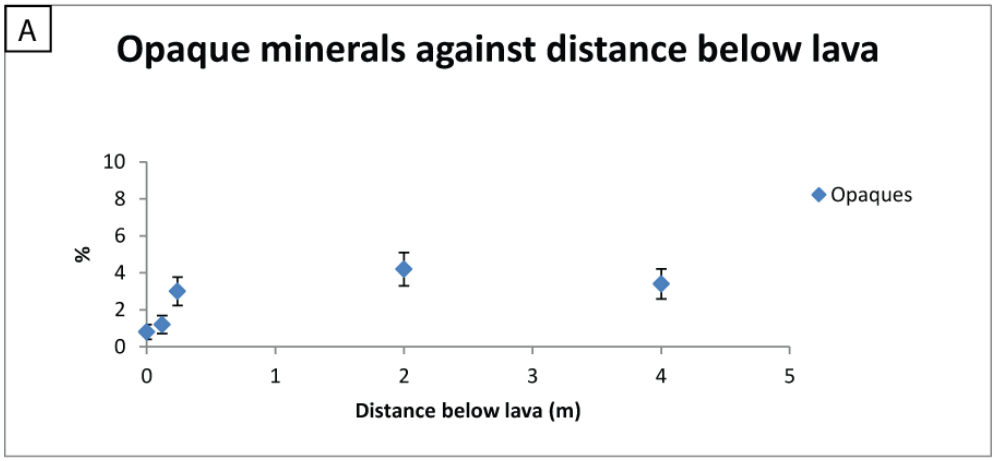

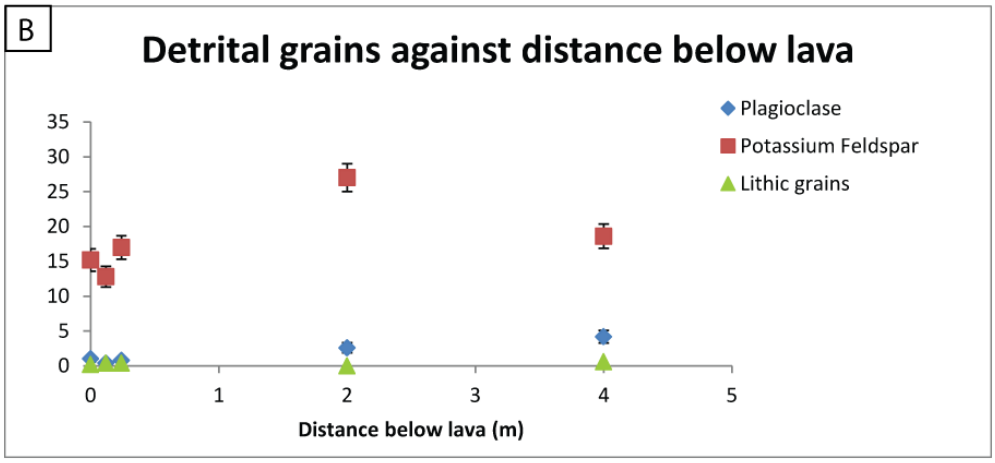

Fig. 4.32. Graphs against distance below LAVA. A) Opaque minerals show no correlation with distance below lava. B) All detrital mineral abundances show no correlation with distance below lava.

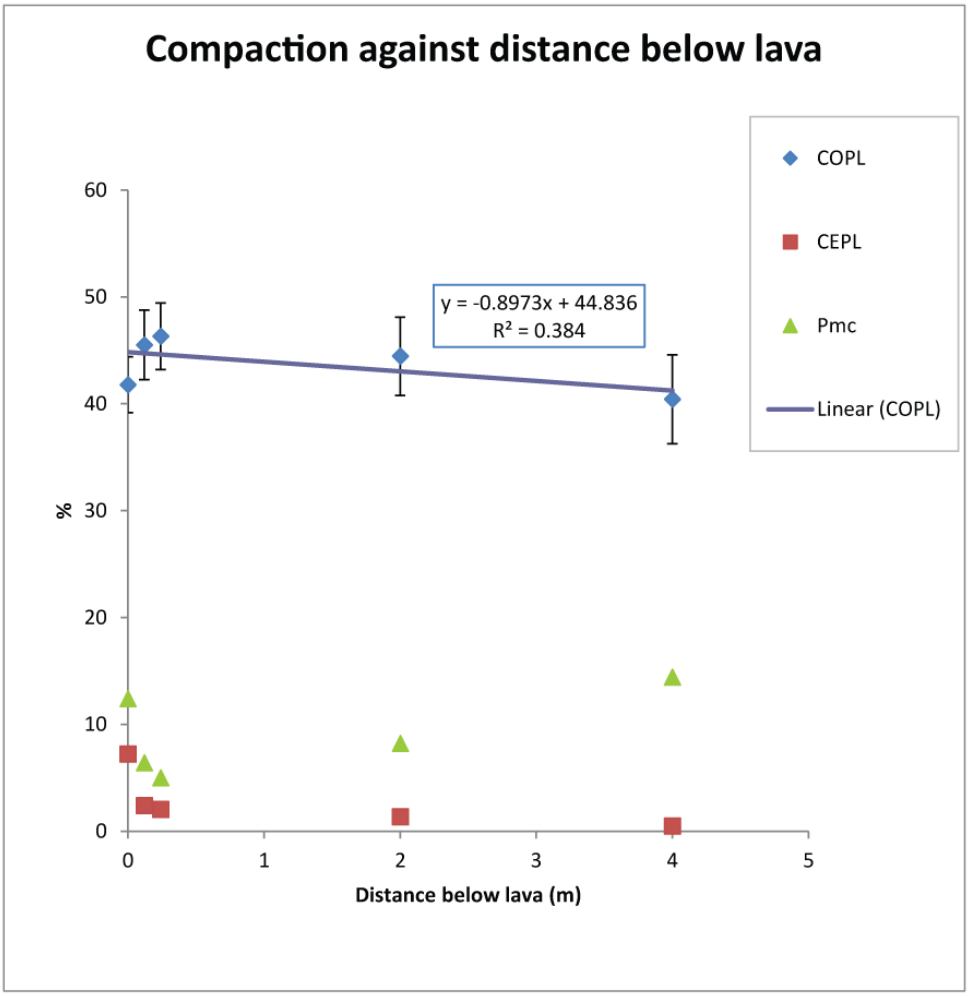

Fig. 4.33. Porosity reduction analysis of sandstone below BD lava. COPL shows a weak negative correlation, somewhat influenced by the highly cemented samples BD1 and BD6 at the contact. Pmc however strongly suggests increased compaction toward the contact (ignoring BD1 and BD6).

4.2.4 Bulk rock geochemistry of BD and Dune 16 samples.

X-ray diffraction analysis on four samples from below lava contacts were performed at the University of Edinburgh for major and trace elements (Fig. 4.34.). The values were normalised to sample NG52 that was analysed as a control as it is a good representative of the background red sandstone in the Twyfelfontein Formation. The aim was to test for variations in elemental abundances and to identify elements that have been enriched or depleted at contacts.

SiO_2, Al_2O_3, Fe_2O_3, K_2O, TiO_2 and P_2O_5 showed no significant difference to NG52 at either BD1 (0.0 m), BD4 (2.0 m), NG31 (0.0 m) or NG32 (1.0 m).

Significant differences between NG52 and the other samples were found in concentrations of MgO, CaO, MnO and in loss on ignition (LOI).

Samples BD1 and NG31, at the contacts, showed covariation in the major elemental plot (Fig. 4.34A.). NG31 CaO, is enriched 24 times over NG52 and BD1 is enriched 30 times compared to minor enrichment at NG32 and BD4. This is consistent with the petrographical and XRD occurrence and XRD (CaO) of calcite in NG31 and BD1. CaO in NG52 would be mostly hosted in anorthite ($CaAl_2Si_2O_8$). MgO is also enriched in samples NG31 and BD1, which is probably also related to increased calcite. If the calcite was simply due to the reaction of anorthite to release the required calcium, no enrichment would be noticed over NG52. The observed enrichment means an *external* source of calcium is required. It is proposed this is oxidising basaltic glass within the lowermost part of the basalt pile, which can liberate CaO and MgO as surface oxide phases (Cooper et al., 1996). This is supported by observations in sample BD6, where calcite poikilocrysts are continuous into the basalt porosity. The enrichment in CaO and MgO is also apparent in NG32 and BD4, which also covary. MnO is enriched in all except BD4 and is highest in NG31, which also is rich in opaque minerals compared to the other samples. MnO enrichment is either hosted in opaque minerals or in manganoan calcite. Opaque could be of detrital nature (heavy mineral placer deposits are common in aeolian settings. e.g. the Namib Desert south of Swakopmund) or diagenetic. Manganoan calcite is typically pink, the sandstone at lava contacts is sometimes pinker than the background (Fig. 4. 37). Loss on ignition (LOI) is also higher than NG52 for all four samples, and like CaO, LOI for NG31 and BD1 covary and NG32 and BD4 covary relative to NG52. The origin of the higher LOI values are probably related to the calcite abundance as CO_2 is driven off on ignition (Heiri et al., 2001).

Trace elements are plotted relative to NG52 in Fig. 4.34B. Covariation is apparent, but between sample transects (NG31 and NG32; BD1 and BD4) rather than distance below lava. This suggests the control on trace element distribution is detrital composition determined during deposition. Cu is enriched in NG31 and NG32 , less so at 1.0 m below the contact than at the contact. BD1 and BD4 show no enrichment over NG52. This is consistent with the Dune Valley samples being drowned by the Tafelkop basalt (KRTbTk) which is notable by its high Cu concentration (e.g. Ewart et al., 1998a).

In summary, bulk rock analyses suggest that divalent ions (Ca^{2+} and Mg^{2+}) are enriched relative to NG52 at contacts and become less enriched with distance below the lava. Such enrichment suggests that the source for these ions was external, as the detrital minerals cannot provide these quantities (e.g. 30 times the detrital background) alone. The proposed source is oxidation of basaltic glass in the overlying basalts (Cooper et al., 1996).

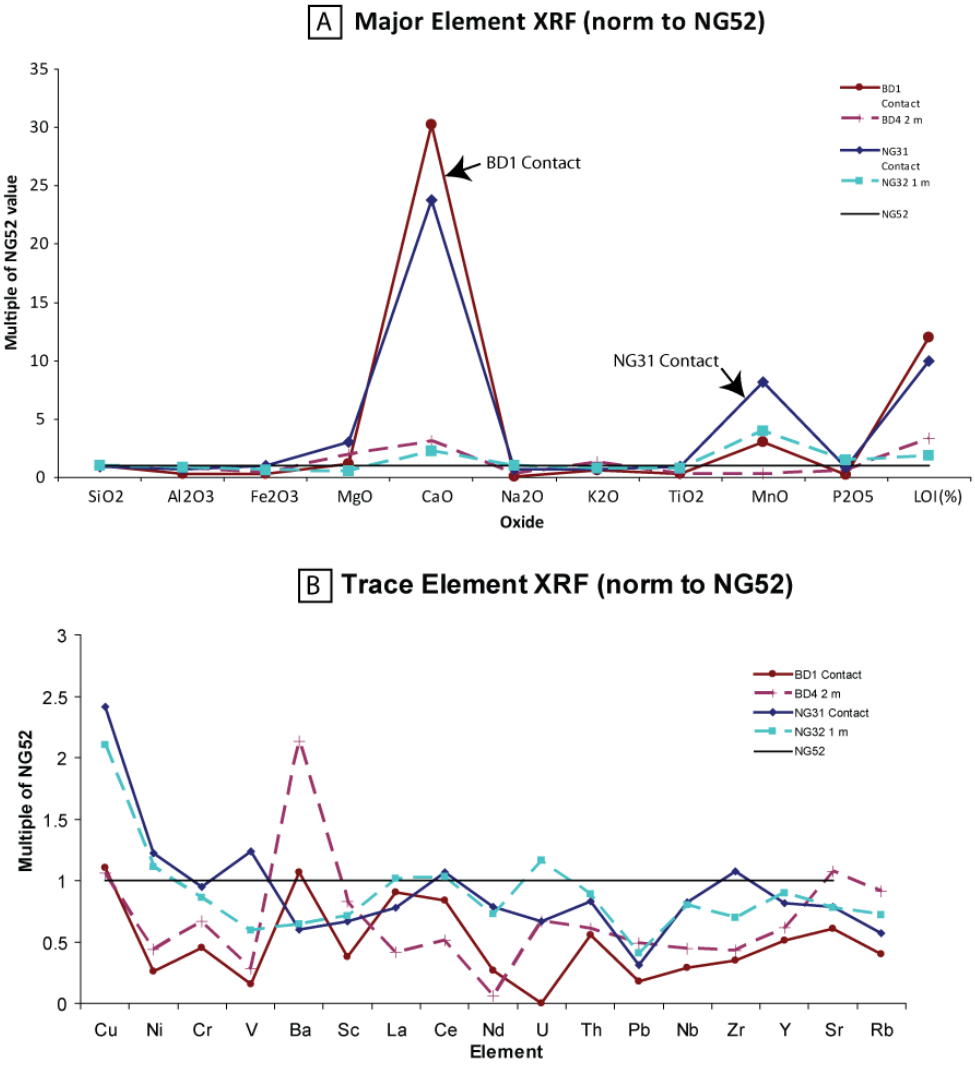

Fig. 4.34. Line graphs of major and trace element analysis of sandstone below lava at BD and Dune 16 localities. A) Major elements normalised to NG52. B) Trace elements normalised to NG52.

4.2.5 Ponded Lava

The Ponded Lava case study is the primary case study of this chapter and has been the most densely sampled with a total of 14 samples in a transect from the contact (0.0 m) to 15.0 m below the lava. The samples were collected by Dr Dougal Jerram (1996 to 2005) and myself (2012).

The Ponded Lava outcrop is north of the Huab River, and is approached by driving 3.2 km north off road across gravel-boulder debris flows and finally up a dry riverbed into the Etendeka mountains. The cliffs are remarkable for the exposure of the Tafelberg lava-sediment contact with the Major Erg of the Twyfelfontein Formation. The outcrop of interest is located at 20° 35.593' S 13°53.057' E, at 400 m in a SE facing cliff 50 m high, leading to a peak 0.5 km to the north of 515 m (Fig. 4.35.). The overlying ponded lava flow is ~45 m thick (Fig. 4.36.).

The Twyfelfontein Formation sandstone at the Ponded Lava outcrop is the SW face of a transverse dune of at least 20 m from interdune to crest amplitude and wavelength of ~850 m (measured in the ponded lava canyon from GoogleEarth). The forsets dip to the NNE and are covered by a topset bed that is sometimes preserved. At outcrop scale the lava pond appears columnar, with a break in jointing towards the base. The dune appears red far below the lava contact, but becomes purple/pink, then light tan coloured within 1 m of the contact as can be seen in Fig. 4.36.

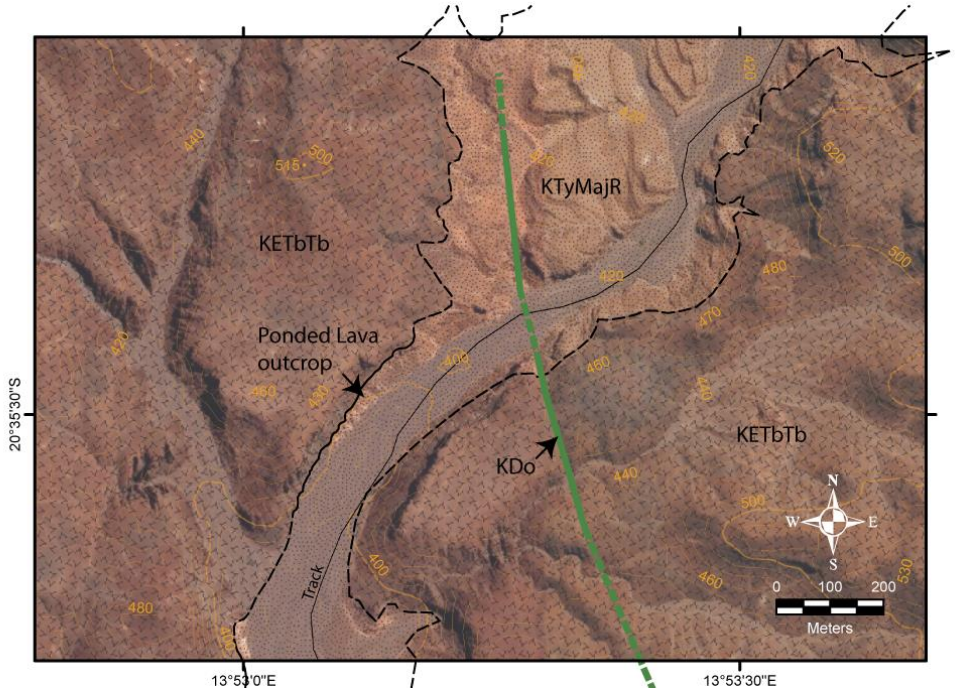

Fig. 4.35. Map of Ponded Lava locality. Contour spacing is 10 m.

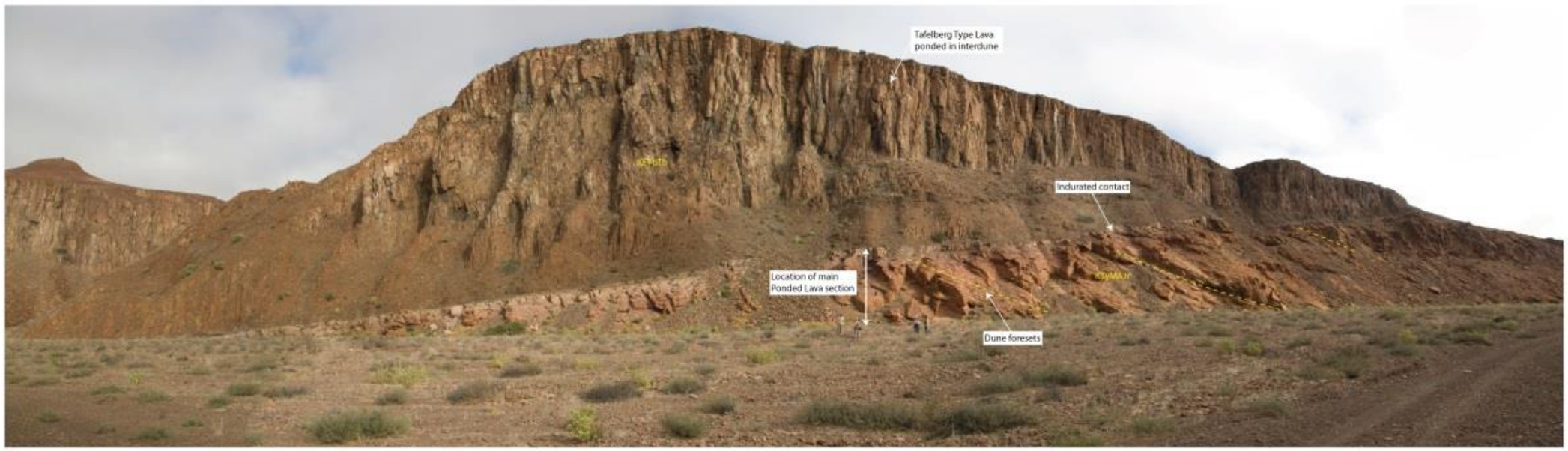

Fig. 4.36. Photo montage of PL locality facing NW towards the outcrop. Main Erg (KTyMajR) unit interdune is filled by one Tafelberg Type ponded lava flow. The sand dune is visibly altered below the lava contact from typical red colour of the red major erg to a lighter band to dark purple near the contact. Location of PL sample transect shown.

Ponded Lava Sample 20°35.593'S 13°53.057' E	Distance below lava (m)	Porosity (%)	1 sigma error
PL1	0.0	0.2	0.2
NG/12-31	0.05	0.6	0.3
PL3	0.1	0.4	0.3
PL4	0.2	1.4	0.5
PL5	0.4	3.2	0.8
PL7	1.3	5.8	1.0
PL8	1.6	7.2	1.2
PL9	2.0	13.2	1.5
PL10	2.7	9.2	1.3
PL11	3.6	16.2	1.6
PL12	4.4	13.0	1.5
NG/12-32	5.6	3.8	0.9
NG/12-33	10.0	10.0	1.3
NG/12-34	15.0	10.8	1.4

Table. 4.4. PL lava pond locality samples, location, distance below lava and porosity. (see Appendix for complete data table).

The contact between the lava and the sandstone at the ponded lava locality dune shows both passive and active interaction with the lava above. Active mixing is most dramatic 3 km to the NE, where at least 3 m thick of intense lava breccia in the sandstone has formed (see Jerram & Stollhofen, 2002). Near the sample site, which is more representative of the common conditions, lava breccia can extend up to ~ 10 cm into the sandstone or visa-versa (Fig. 4.37A, B.). Locations that exhibit this kind of dynamic mixing lack a well-defined topset bed, therefore grain flow and grain fall lamellae are exposed to the lava. Breccia clasts are either angular with clean contacts or subrounded with rough, vesicular contacts. Most of the contact is passive. At passive contacts (Fig. 4.37C, D) no evidence for dynamic mixing exists, the lava

simply envelopes the sand, preserving the topset bed with no erosion. The sample transect is in such a locality (Fig. 4.37C, D). Often, at passive contacts, there will be evidence of loading of the sand by the lava (Jerram & Stollhofen, 2002). Fig. 4.37B shows the location of the sample PL1, and 10 cm to the right is a flame structure (Fig. 4.37E.), where the lava has weighted the less dense, unconsolidated sand was then displaced as a result of the loading.

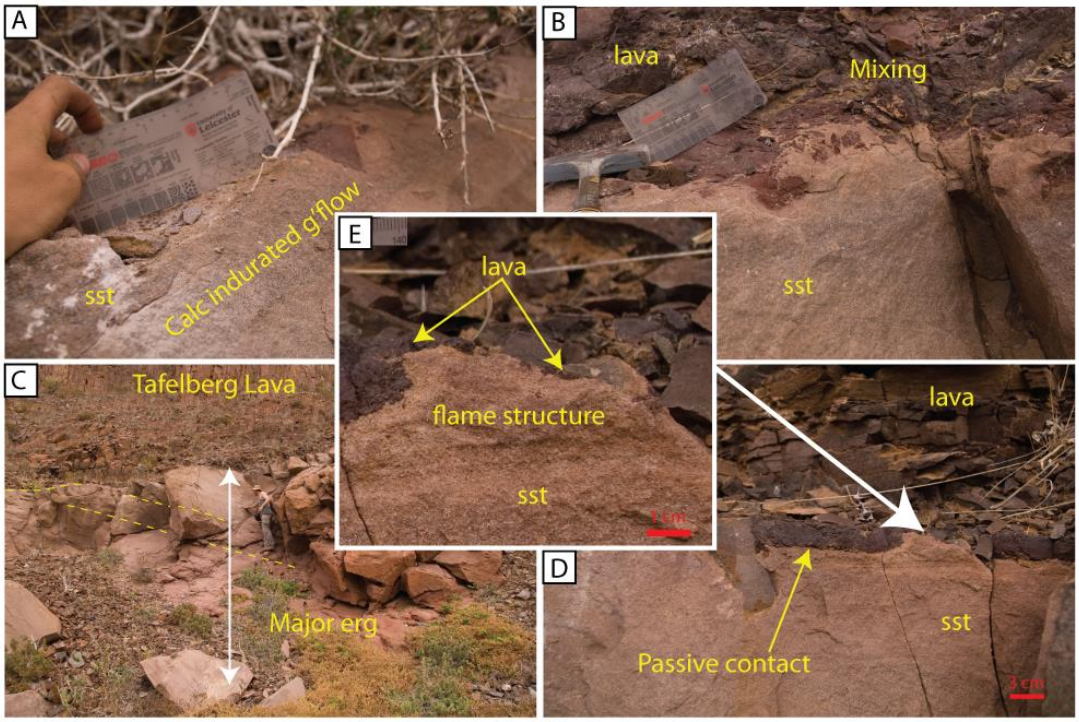

Fig. 4.37. Photographs showing the varied nature of lava-sediment interaction at PL locality. A) Grain flow and grain fall laminations dipping to the left of the image. Higher depositional porosity grain flow horizons tend to be most indurated by calcite compared to grain fall. Note angular lava breccia fragment. B) Dynamic mixing between lava and sand forming a 5 cm thick dry peperite layer. C, D) Section of PL samples showing (D) close up of passive lava-sediment contact where sample PL1 was taken.

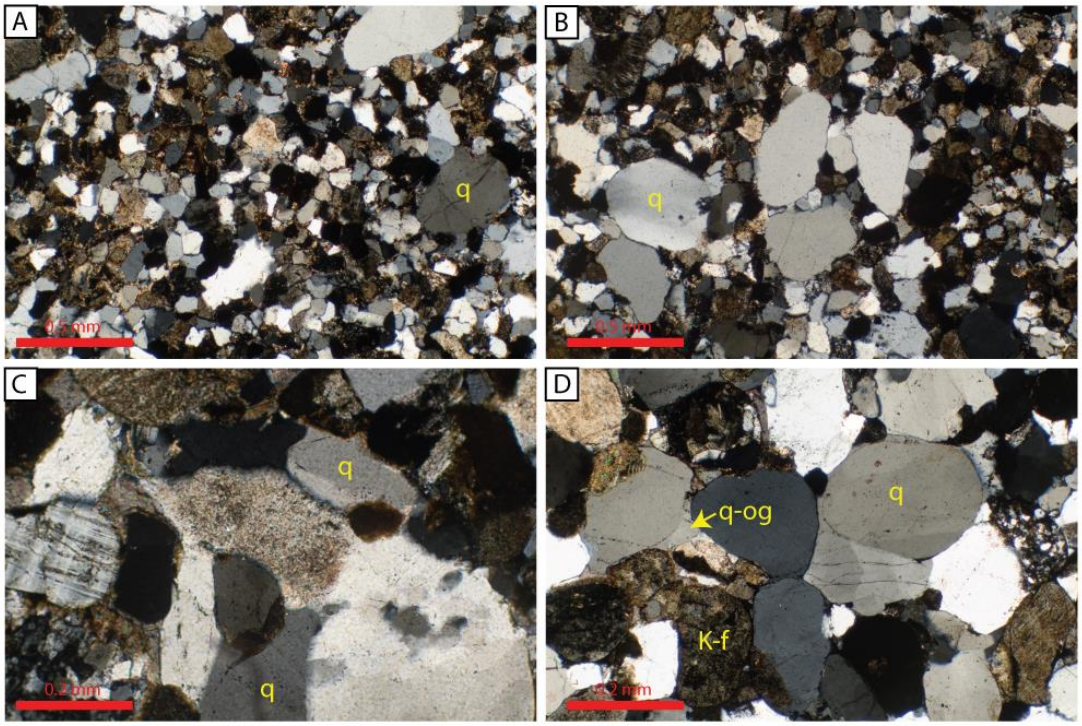

Fig. 4.38. XPL photomicrographs of PL1 at contact. Compaction is the dominant porosity reducing mechanism. Grains are deformed to porosity and are frequently cuspate at contacts.

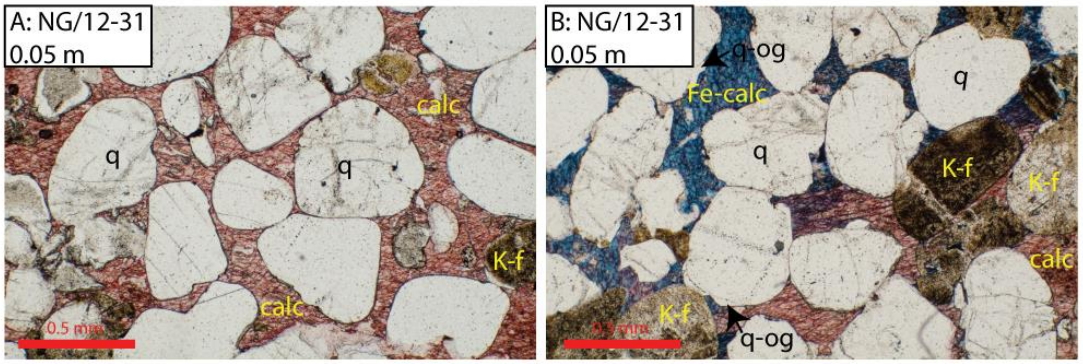

Fig. 4.39. PPL photomicrographs of grain flow layer 5 cm below contact (practically at contact). A) Non-ferroan calcite cement is poikilitic and protects against grain compaction. B) Ferroan calcite is also present, but is after quartz overgrowths, suggesting it is a later cement.

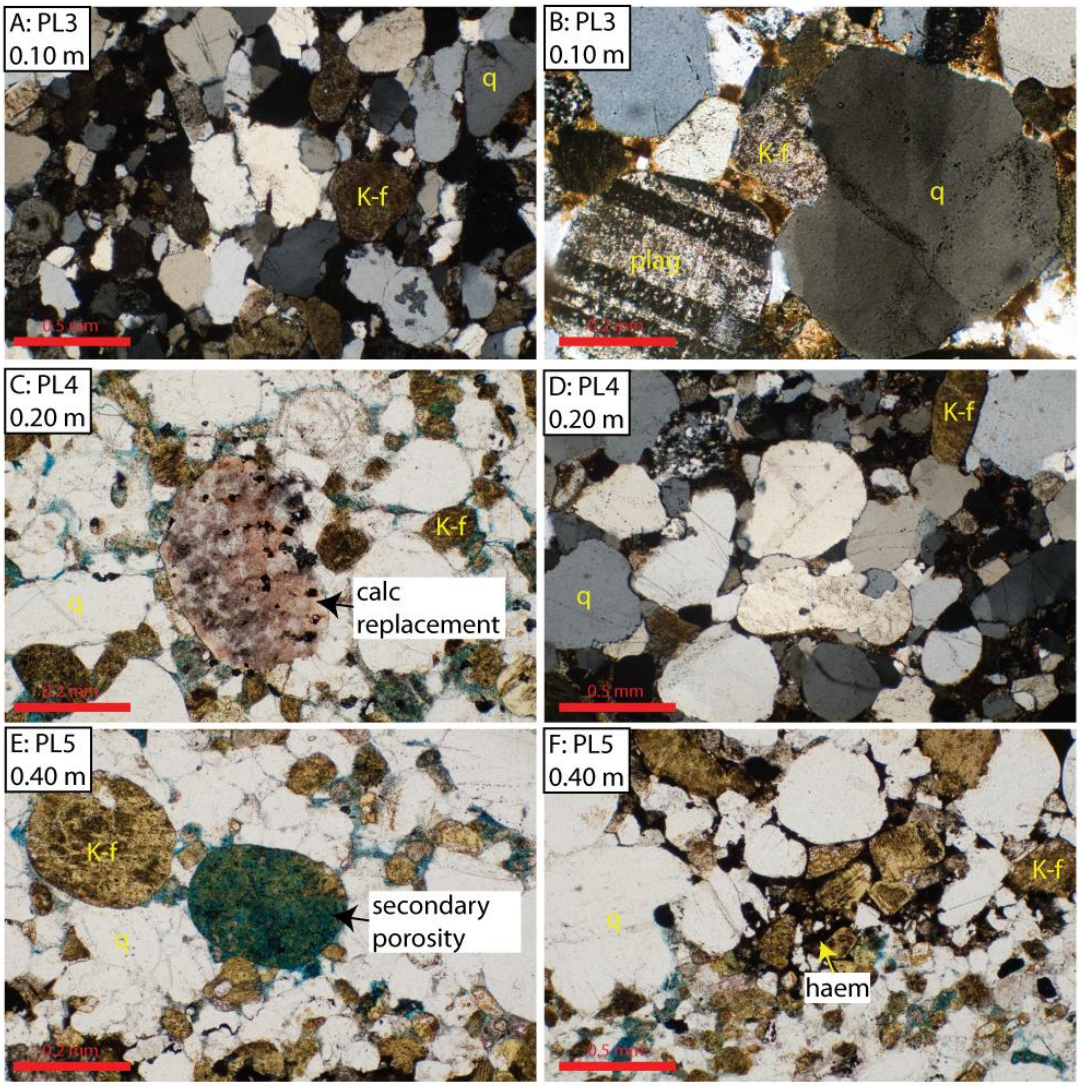

Fig. 4.40. Photomicrographs away from PL contact. A) XPL 0.1 m below contact showing dominance of compaction porosity loss, grains are highly deformed. B) XPL 0.1m below contact, grains are highly deformed, plagioclase is relatively un-weathered compared to below the compacted zone. C) PPL 0.2 m below contact, calcite replacement of feldspar grains is common, porosity appears as rare intergranular pores and secondary porosity within altered feldspar grains. D) XPL 0.2 m below contact shows grain compaction still is an important process compared to background compaction. E, F) PPL 0.4 m below contact calcite is rare, both primary and secondary porosity common, grain coating haematite is redistributed into mottled patches, giving outcrop an overall bleached appearance (Fig. 1.34.).

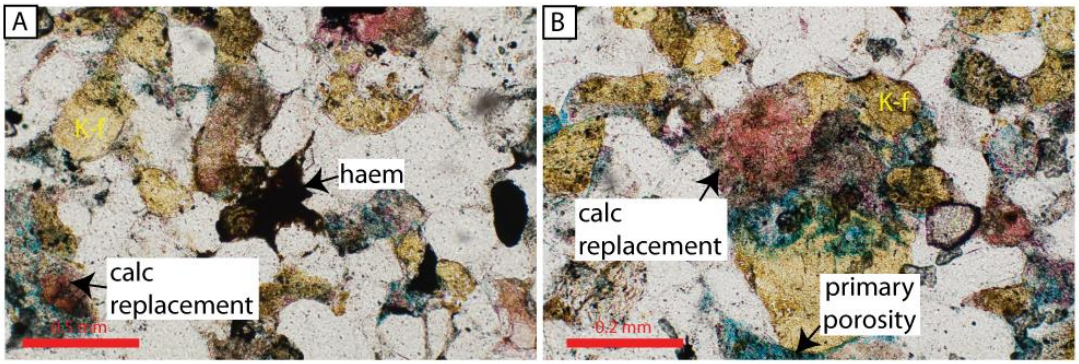

Fig. 4.41. PPL Photomicrographs 1.3 m below lava. A, B) Primary and secondary porosity is present, calcite only exists as grain replacement, haematite is redistributed as above.

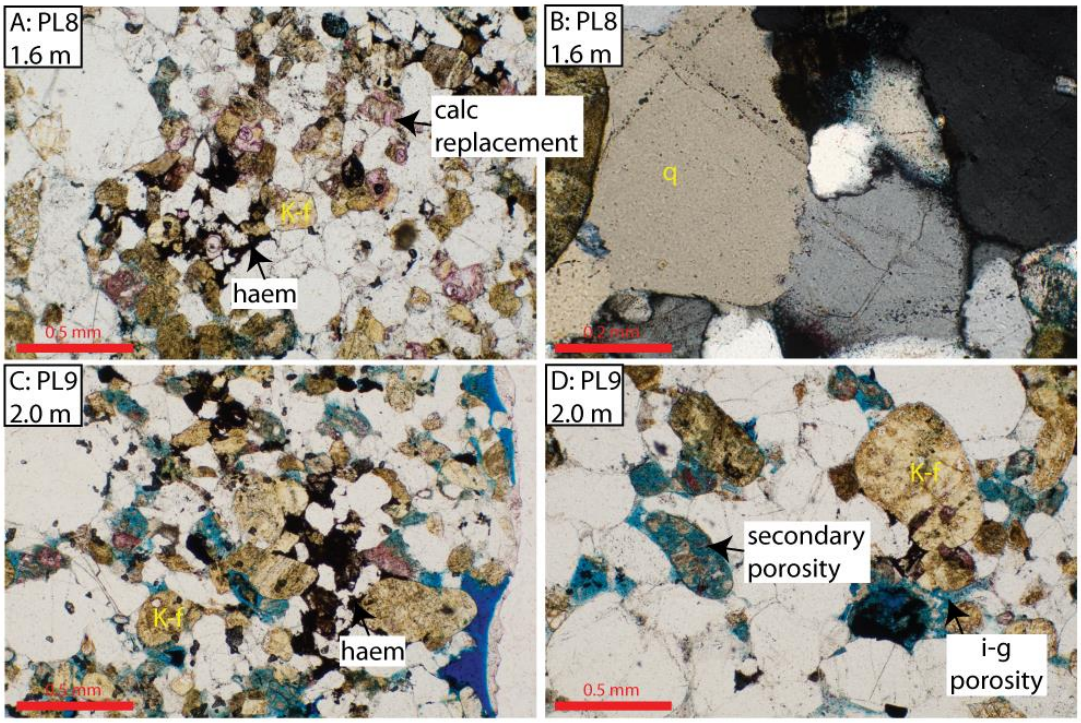

Fig. 4.42. Photomicrographs of sandstone 1.6 m and 2.0 m below lava. A) PPL 1.6 m below lava, porosity is dominantly primary, calcite is replacement only and haematite is redistributed. B) XPL 1.6 m below lava illustrating that grain compaction is still the dominant porosity reducing mechanism. C, D) PPL 2.0 m below lava, calcite is rare, compaction less than 1.6 m, porosity still primary and secondary.

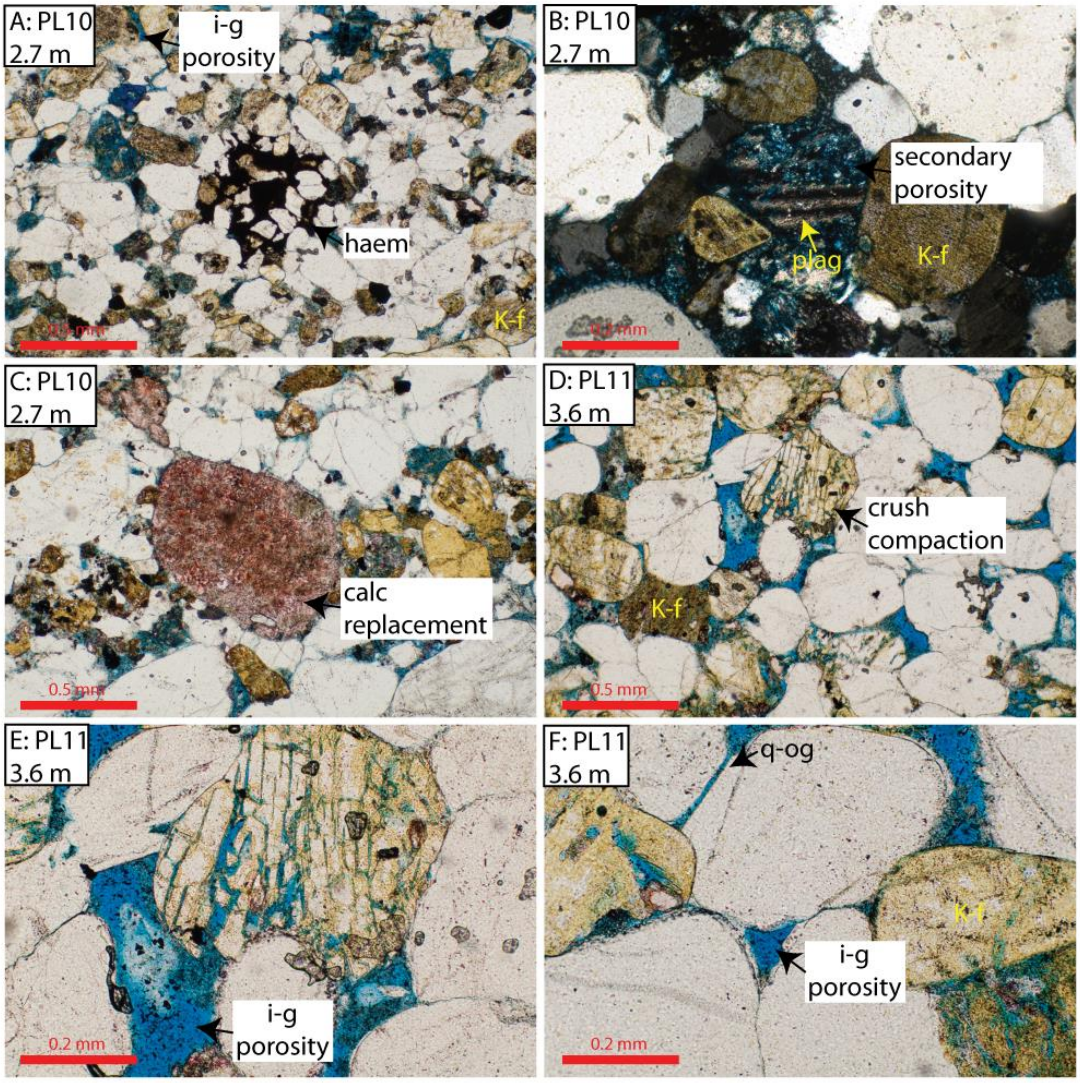

Fig. 4.43. Photomicrographs 2.7 m to 3.6 m below lava. A, B, C) PPL 2.7 m below lava, calcite very rare and restricted to grain replacements, haematite redistributed. D, E, F) PPL 3.6 m below lava, no calcite, haematite grain coatings present, occasional quartz overgrowths on detrital quartz. Diagenesis dominated by compaction which is less than close to contact, shown by cuspate and sutured grain contacts and common crush compaction of feldspar grains.

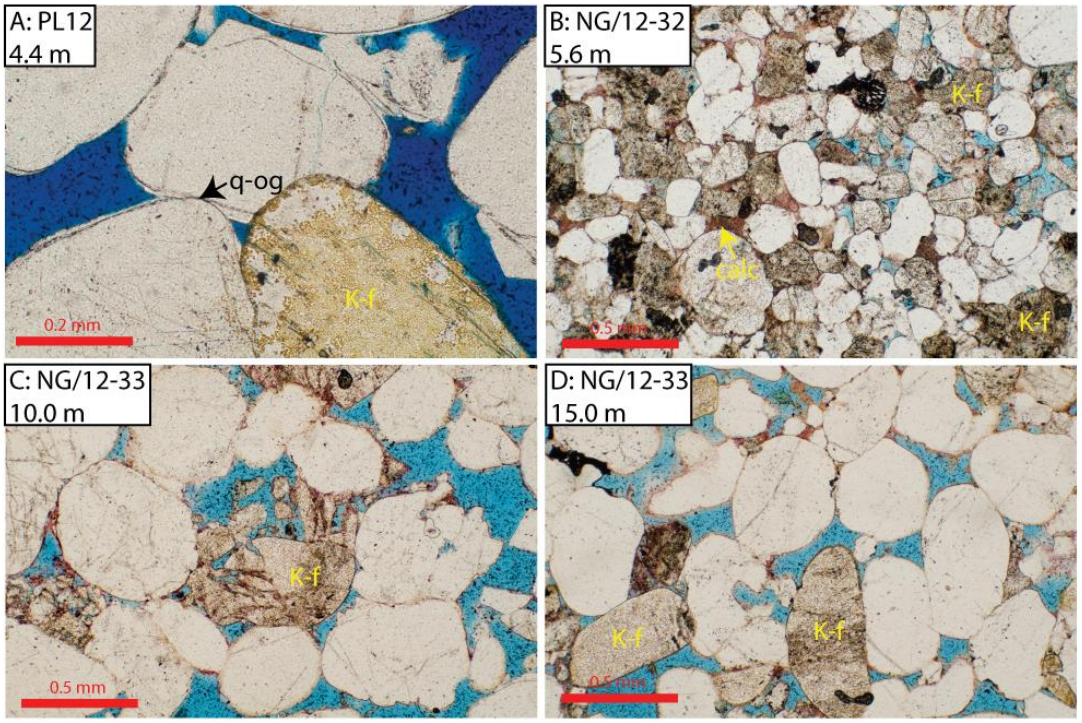

Fig. 4.44. Photomicrographs 4.4 m to 15. 0 m below lava contact. A) PPL 4.4 m porosity has reached background levels, compaction is evident in grain interpenetrations which occurred during and after quartz overgrowth development. B) PPL 5.6 m below lava, grain fall horizon primary porosity dominates, calcite present associated with plagioclase replacement. C, D) PPL 10.0 m and 15.0 m below lava, petrographically similar to 4.4 m, background porosity.

Petrographic analysis of the sand at the contact was performed on two samples: PL1 is very fine grained (100– 150 μm) topset bed < 5 cm below the contact and NG/12-31 is a medium sand (200– 500 μm) grain flow horizon, at 5 cm below the contact. Petrographically, these two samples are quite different.

Sample PL1 has negligible porosity (0.2 %, ±0.2) and negligible permeability (0.3 md). Detrital mineralogy is approximately the same as the background. Authigenic mineralisation is dominated by clay (4.4 %, ±0.9) (probably illite/chlorite), with minor abundances of calcite replacing plagioclase (1.6 %, ±0.6) and quartz (1.0 %, ±0.4) (Fig. 4.38D, C.). Porosity loss is dominated by compaction (COPL= 45 %, ±2.8), cementation is increased over the background (CEPL= 3.8 %). Compaction is evident in the thin section, dominated by pressure solution of quartz (Fig. 4.38.). Quartz grains interpenetrate, and are frequently sutured. Authigenic quartz, though rare always forms as overgrowths at grain triple junctions (i.e. the last remaining porosity during compaction). Undulose quartz grains are rare.

Sample NG/12-31 also has negligible porosity, permeability was not measured. Detrital potassium feldspar is near background, but plagioclase is absent. Authigenic mineralisation is dominated by calcite (23.8 %, ±1.9), which exists as poikilitic crystals of over 20 mm. Both ferroan and non-ferroan calcite are present. The non-ferroan calcite, common to all other lava contacts rarely grows over quartz overgrowths (Fig. 4. 39A.). The ferroan calcite has a diffuse boundary with the non-ferroan calcite (Fig. 4.39B.) and often grows over quartz overgrowths. Authigenic clay is not present as a pore filling phase. Quartz overgrowths are rare (0.6 %, ±0.3). Porosity loss is still dominated by compaction (COPL= 32 %, ±3.0), but is below background levels, suggesting this rock is under-compacted by ~3% or by 13 % compared to PL1. Cementational porosity loss is much higher than background (CEPL= 16.6 %). The calcite appears to have formed and protected the sandstone from subsequent compaction by (1) forming a framework and (2) partially isolating quartz grains, reducing grain contact area susceptible to pressure solution. The magnitude of the under-compaction being about the same as the difference between compacted sandstone (e.g. PL1) and the background is evidence for the calcite being early (eogenetic) cement, prior to burial.

Porosity is negligible 0.10 m below the contact (0.4 %, ±0.3). Detrital mineralogy is similar to the background. Authigenic minerals are dominated by clay (9.4 %, ±1.3), like PL1. Detrital plagioclase is usually intact (Fig. 4.40B.) The clay is probably chlorite and illite (Fig. 4.40A, B). Calcite (1.4 %, ±0.5) and quartz overgrowths (1.2 %, ±0.5) are minor. Porosity loss is dominated by compaction (COPL= 41.8 %, ±2.9), and cementational porosity loss is 7.0 %. The contribution of the clay cement to porosity loss is not insignificant.

By 20 cm below the lava, porosity has increased to 1.4 % (±0.5) and permeability is 3.3 md. Porosity is largely secondary within weathered feldspar grains, and less commonly as primary pores (Fig. 4.40C). Detrital mineralogy is similar to the background, but plagioclase abundance is reduced, possibly related to the secondary porosity and authigenic calcite. Authigenic mineralisation is dominated by clay (3.8 %, ±0.9), quartz overgrowths not being encountered while point counting and calcite forming 1.6 % (±0.6). Calcite almost exclusively replaces plagioclase and lithic grains (Fig 4.40C.). Porosity loss is largely through compaction (COPL= 45.2 %, ±3.2), cementational porosity loss is minor (CEPL= 3.1 %).

Compaction is ~ 10 % higher than the background. Fig. 4.40D shows the compaction of quartz grains, where grain interpenetration is common.

Sample PL5 (40 cm below lava), is characterised by haematite mineralisation as a pore filling cement. Porosity is 3.2 % (±0.8), which is still dominated by secondary dissolution of feldspar grains (Fig. 4.40E.). Detrital minerals are similar to the background; plagioclase is slightly less abundant, again probably related to the amount of secondary porosity. Authigenic minerals are common and dominated by precipitation of haematite in pore space (Fig. 4.40F.), which has probably been redistributed from closet to the contact, where detrital grains are not coated with haematite. Calcite (1.8 %, ±0.6) usually replaced plagioclase. Porosity loss is mostly due to compaction (COPL= 45.0 %, ±2.8).

Between 1.3 m and 2.0 m below the lava (sampled PL7, PL8 and PL9), porosity increases from 5.8 % (±1.0) to 13.2 % (±1.5) and permeability increases to 6.2 md from 3.4 md. Detrital mineral composition varies little between the samples and is approximately background. Grain size varies from 150 μm to 500 μm. Sample PL7 (1.3 m) has porosity dominated by secondary dissolution of feldspar grains (Fig. 4.41.), but by PL9 (2.0 m), porosity is dominantly primary (Fig. 4.42C, D.). Authigenic minerals are minor in all three samples and are dominated by calcite replacement of occasional plagioclase grains (Fig. 4.41B. Fig 4.42A.). Redistribution of haematite into nodules is important in all three samples, seen as a mottled brown in hand specimen and patches of pore-filling haematite in thin section. Porosity loss is dominated by compaction (COPL) and reduces from 44.7 % (± 3.7) to 40.6 % (±4.1) over the three samples; CEPL reduces from 1.1 % to 0.6 %. The compaction data suggests that the bulk of the porosity increase over the 0.7 m between PL7 and PL9 was due to a decrease in compaction. Compaction, like closer to the lava is not dominantly through pressure solution of quartz grains (Fig. 4.42B.), grains can be seen interpenetrating and to have sutured contacts, without interstitial opaque grain coatings, nor do the grains showing undulose extinction. The lack of haematite grain coatings suggests these were dissolved and mobilised synchronous or prior to major compaction.

PL10, 2.7 m below the contact has a porosity of 9.2 % (±1.3) and a permeability of 6.2 md. The sample is characterised by dominant primary porosity and poorly developed secondary porosity hosted in partially dissolved plagioclase

and the occasional potassium feldspar grains (Fig. 4.43B.). Detrital mineral grains show little variation form the background. Authigenic mineralisation is minor, and is dominated by occasional quartz overgrowths (1.2 %, ±0.5) and redistribution of haematite into nodules. Calcite was found to partially replace some feldspar grains, but these were not encountered during point counting (Fig. 4.43C.). Porosity loss is dominated by compaction (COPL= 43.1 %, ±3.9), which is visibly noticeably less in thin section than for samples closer to the contact. Cementational porosity loss is minor (1.5 %).

Sample PL11 (3.6 m below the contact) is marked by the apparent absence of significant secondary porosity resulting from feldspar dissolution. Porosity is 16.2 % (± 1.6) and permeability is 121.4 md. The detrital mineralogy is similar to the background. Detrital grains are coated with a thin layer of haematite, as can be seen in Fig. 4.43F. separating a quartz overgrowth from the detrital quartz grain. Authigenic mineralisation is negligible, quartz overgrowths making up the bulk (1.0 %, ±0.4). Calcite is confined to insignificant partial replacement of plagioclase along cleavage planes. Porosity loss is dominantly through compaction (Fig. 4.43D, E, and F.) (COPL= 43.1 %, ±3.9). Compaction appears to be through both pressure solution and crush compaction. Pressure solution is seen as interpenetrating grains, and was active after quartz cementation, due to overgrowths being compacted (Fig. 4.43F.). Crush compaction is seen as brittle deformation of framework grains (Dickinson & Milliken, 1995) and affects potassium feldspar to the greatest degree (Fig. 4.43E.). Healing of the fractures must have occurred to preserve the delicate structure observed, consistent with the comprehensive crush compaction study of Dickinson & Milliken (1995).

From 4.4 m to 15.0 m below the lava, porosity and permeability appear not to be reduced by the lava flow (e.g. PL12, 4.4 m porosity= 13 % (±1.5) and permeability= 328 md). The two grain flow samples (PL12 and NG/12-33) are characterised by detrital grains from 200–550 μm in diameter, with mineral abundances at background levels. Detrital grains have thin haematite rims (Fig. 4.44A, C, D.), which give the sandstone a red colouration. Authigenic mineralisation is dominated by quartz overgrowths, which pre-date much of the compaction (Fig. 4.44A.) at this distance below the lava. Quartz overgrowths are negligible in sample NG/12-34 (15.0 m below lava). Porosity loss is through compaction (CEPL= 39 % to

42 %). Cementational porosity loss is negligible. Sample NG/12-32 is slightly anomalous, in that the porosity is lower than its distance below the lava would suggest. Grain size is 100–500 μm in diameter. The reduced porosity appears to be due to cementation. Authigenic clay filling pores is in increased abundance (6.4 %, ±1.1) as is calcite (3.4 %, ±0.8) which tends to replace feldspars, rather than fill pores.

The trends away from the lava contact show increasing porosity with depth, from negligible at the contact, to 13 % (±1.5) at 4.4 m below. Further than 4.4 m porosity shows the normal background spread (~12.4 % ± 1.5) (Fig. 4.45A.). Permeability rapidly increases at 3.6 m below the contact, where primary porosity begins to dominate (Fig. 4.45B.). Permeability against porosity shows an exponential relationship. Detrital mineralogy (Fig. 4.47B.) appears not to vary much with distance below the lava, although plagioclase has a region between 2 m and 4.4 m where it is of negligible abundance, possibly due to increased plagioclase dissolution in this zone. Opaque minerals are both detrital and authigenic. Grain coatings on detrital grains are rare within 3.6 m of the contact, but common further than 4.4 m. Where haematite grain coatings are absent, the haematite is usually re-precipitated as pore filling nodules that give the outcrop a mottled appearance. Fig. 4.47A. shows abundance of opaque minerals, the highest values are closer to the contact, but no correlation exists with distance below lava. Authigenic mineralisation is minor in most of the samples, with calcite being important in grain flow horizons close to the lava. Pore filling clay is generally negligible, although close to the contact clay was found up to 9.4 % (±1.3) (PL3, 0.1m). Authigenic quartz abundance shows no correlation with distance below the lava.

Both the highest and the lowest magnitudes of compaction porosity loss were found within 0.2 m of the lava contact. Samples PL1 (0.0 m) and PL4 (0.2 m) have COPL of ~45 % (±2.8) whereas sample NG/12-31 (0.05 m) has a COPL of 32 % (±3.0), which is below the background for the high porosity sands away from lava contacts. Porosity minus cement (Pmc) values (Fig. 4.47.), although not as sophisticated as the COPL and CEPL indexes provide some insight here: Pmc reduces towards the contact from a distance of 3.6 m coinciding with the change of porosity type to dominant primary. The situation suggested, like the lava-sand contacts above is a compaction dominated early diagenetic regime, with early calcite

cement (prior to burial compaction) exploiting the highest permeability pathways near to the lava contact. As compaction decreases, porosity increases to background levels, with the increase between 2.0 m and 4.4 m.

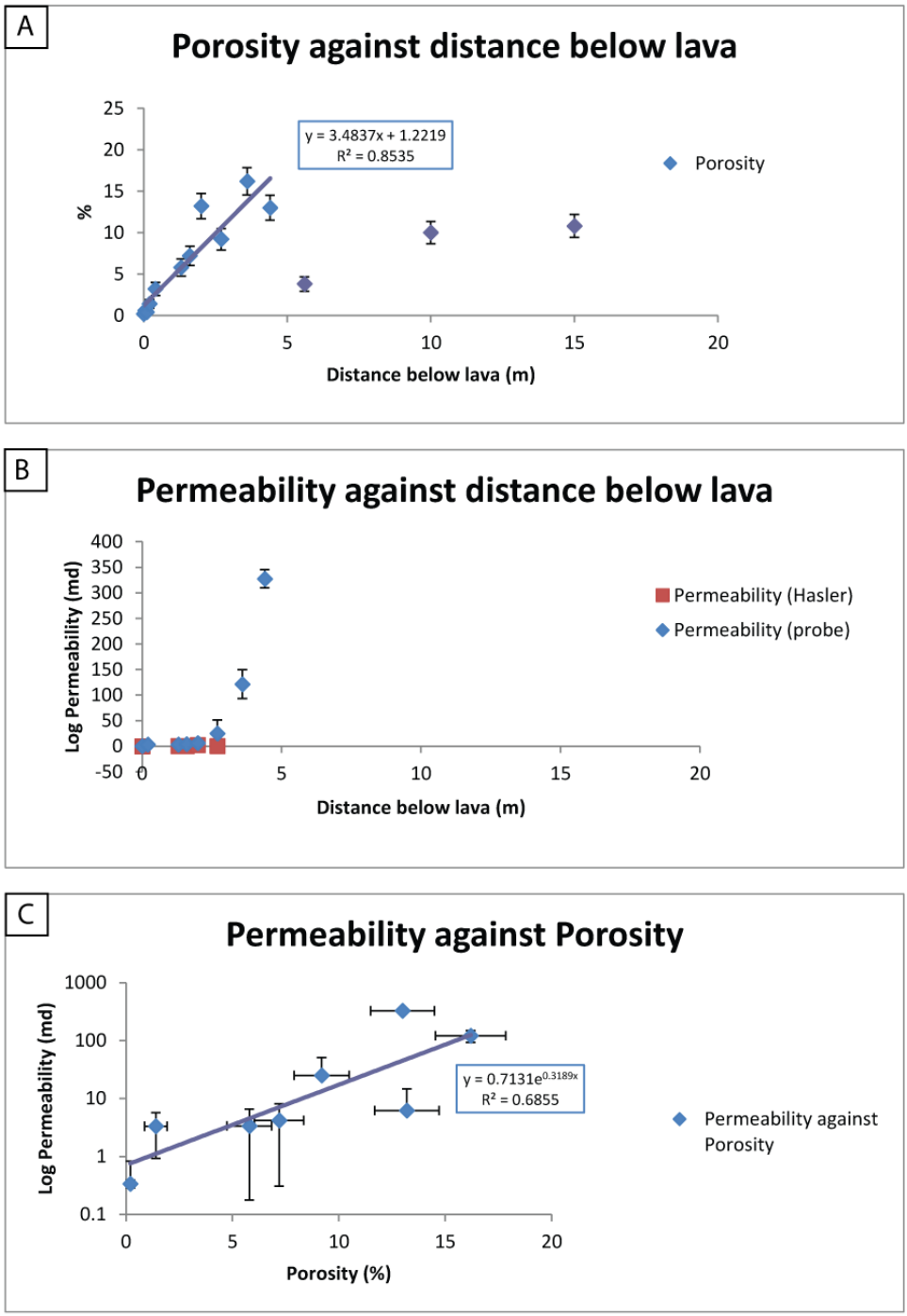

Fig. 4.45. Graphs against distance below lava contact. A) Porosity increases away from contact to background of ~ 12 %. Linear trend line calculated up to the point at which background porosity is reached. B) Permeability is low until 2.7 m where it rapidly

increases, this corresponds to opening of primary porosity. C) Permeability against porosity shown an exponential relationship.

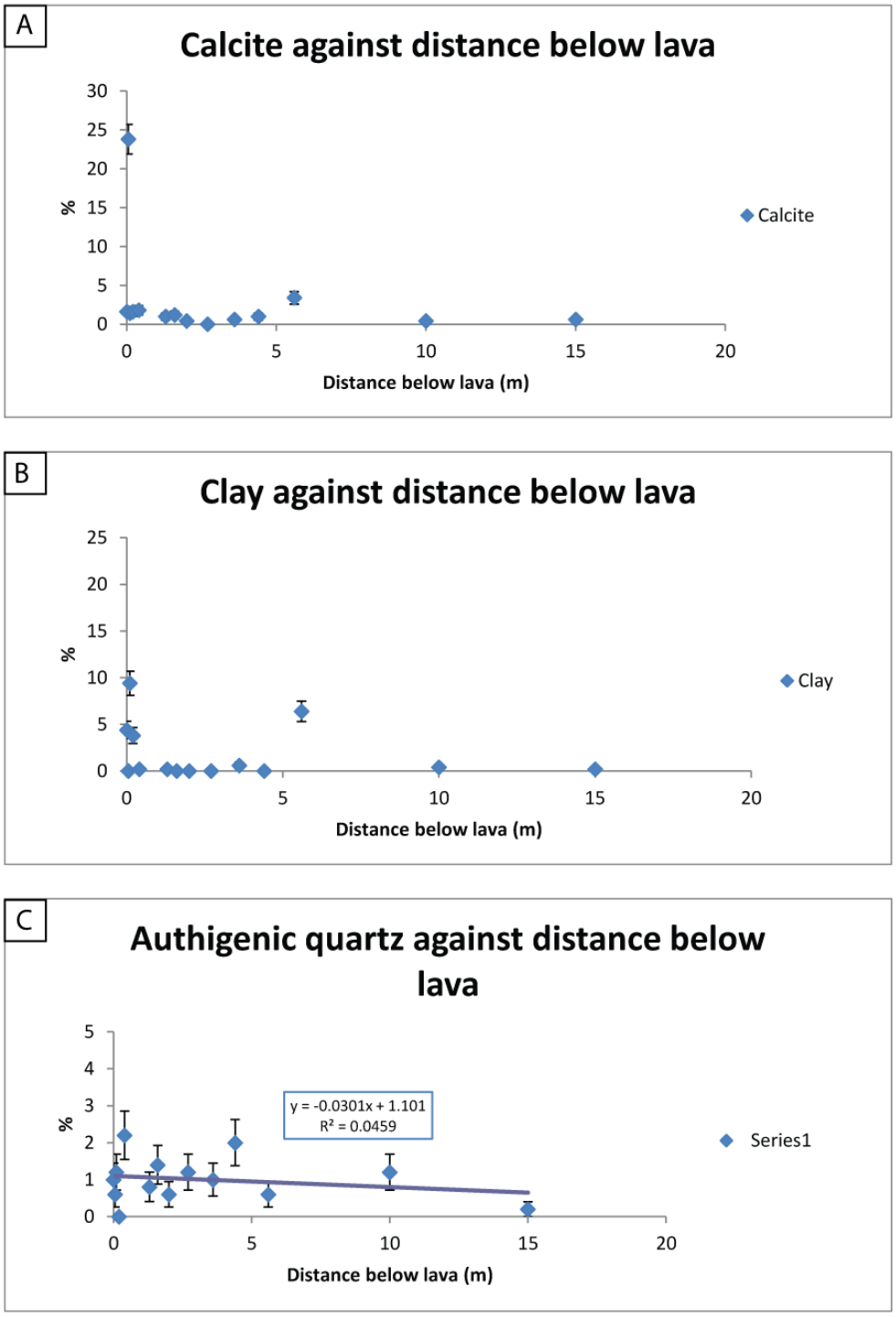

Fig. 4.46. Graphs against distance below lava contact. A) Calcite is generally low except in grain flow horizons at the contact. B) Clay bears no relationship with distance below lava. C) Authigenic quartz is not correlated with distance below lava.

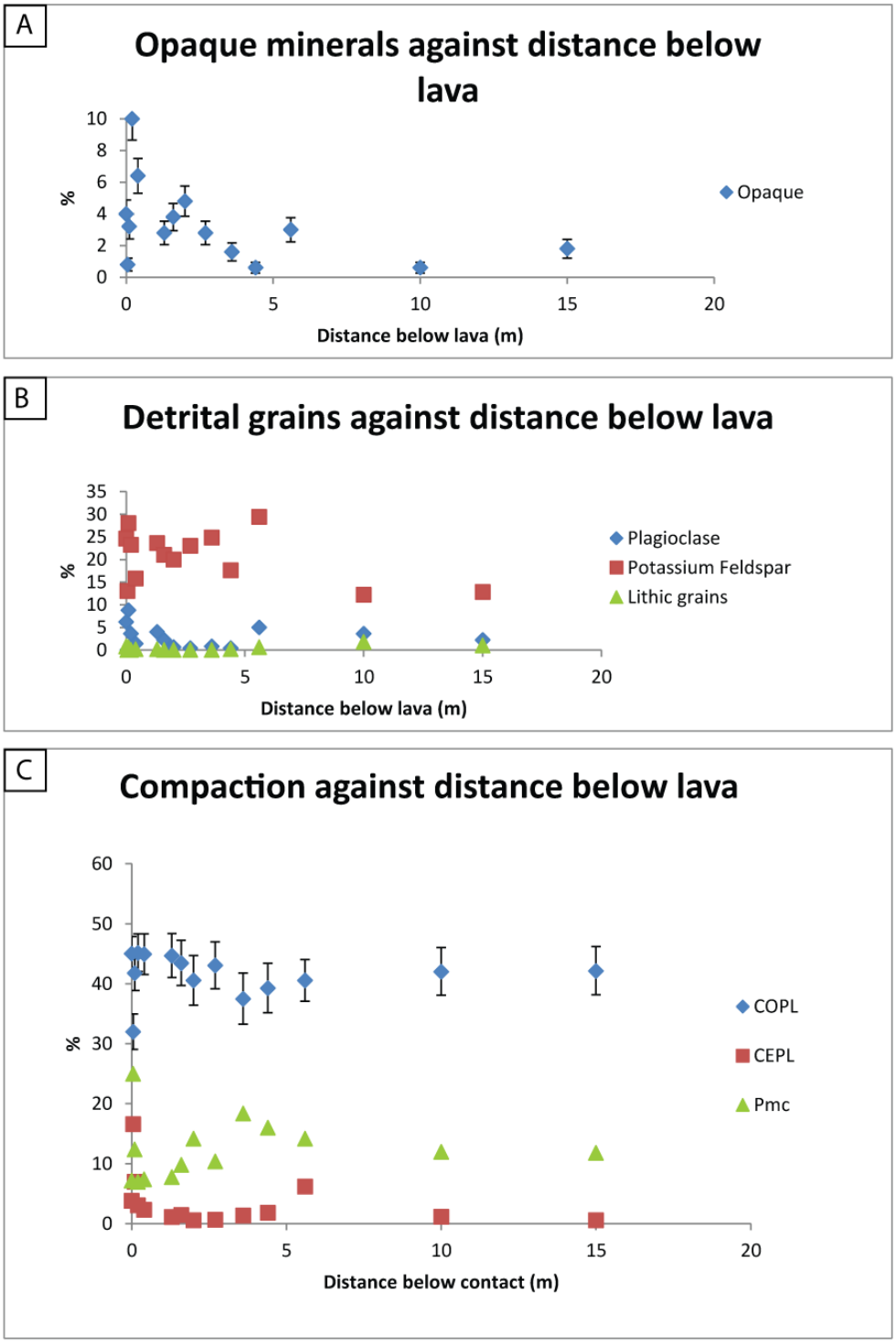

Fig. 4.47. Graphs against distance below lava. A) Opaque minerals are slightly more common near to the lava, but no strong correlation exists with distance. B) No correlations exist between detrital minerals and distance below lava. C) Porosity loss analysis for PL transect. COPL increases slightly approaching lava by ~ 5 % except for cemented samples. Pmc decreases strongly toward contact except for cemented samples suggesting increased compaction porosity loss near to contact.

4.3 On the compaction of the Twyfelfontein Formation

All of the case studies above have shown that compaction increases towards lava contacts, even considering the uncertainty plotted. It is important to identify the origin, magnitude and relationship of this compaction with the overlying lava. It is also important to identify whether the increased compaction (~10 % more than background) occurred in one episode (i.e. ~45 % compaction followed by no additional burial compaction) or as ~10 % compaction of unconsolidated sand followed by an additional ~35 % compaction during burial.

Compaction is evident during optical analyses of most of the contact rocks, even the highly calcite cemented samples (e.g. NG/12-31, BD6), albeit of a lower magnitude than the less cemented samples (e.g. PL1, BD2, NG78). The compaction is a result of increased pressure solution, indicated by abundant interpenetrating grains, sutured contacts and by the precipitation of quartz overgrowths in the local area (same grain). The these effects decrease away from lava contacts as grain contacts become less frequently sutured and concavo-convex, and instead tangential contacts become common. During pressure solution, grains dissolve at intergranular or intercrystalline contacts, where non-hydrostatic stress is highest (Tada & Siever, 1989; Rutter, 1983). During this process silica diffuses in an aqueous intergranular film and the diffusion is driven by local chemical potential gradients and gradients due to local chemical reactions (Rutter, 1983). The controls on pressure solution in nature (Tada & Siever, 1989) are:

Depth

Pressure solution becomes more intense with depth (increase in number of sutured grain contacts and concavo-convex contacts) (Tada & Siever, 1989). Pressure solution is common at depths of 1000 m but has been reported at depths of 900 m (Tada & Siever, 1989 and references therein)

Composition of rock

Pressure solution becomes more intense at higher total clay proportion (Tada & Siever, 1989), although the Green Pond Conglomerate (also Tada & Siever, 1989)

shows the opposite relationship. The increase is potentially due to the clay enhancing the rate of diffusion along contacts as a result of hydrated clay films providing increased diffusion paths (Tada & Siever, 1989). Clays may also promote pressure solution by impeding overgrowth precipitation. The destination of the quartz insolution, wen its nearby re-precipitation is blocked is a mystery. Polycrystalline grains are more susceptible to pressure solution than single crystals (Tada & Siever, 1989).

Grain Size

Grain size is a major control on pressure solution intensity. Grain size is inversely related to pressure solution. This has been shown in numerous field studies (Tada & Siever and references therein) and in a laboratory study (Renton et al., 1969).

Temperature

Temperatures of between 20 °C and 60 °C are required to initiate pressure solution in quartzose sandstone and lithostatic pressures of 18 MPa to 30 MPa, with minimum effective pressures of 9 MPa to 11 MPa (Tada & Siever, 1989), as calculated from burial depth data for natural sandstone. Tada & Siever (1989) also noted that 'It is also clear that intergranular pressure solution can proceed at relatively low pressures, and that very deep burial does not automatically result in extensive intergranular pressure solution compaction'.

Solution chemistry

Quartz dissolution is favoured in alkaline solutions due to increased solubility (Tada & Siever, 1989).

Time

The duration spent within the depth and temperature range.

An aqueous film is required to coat grains for pressure solution to proceed. This may appear problematic in a desert; however in this situation water can be sourced from the cooling lava as volcanic steam/ water vapour (e.g. Henley & Ellis,

1983; Rye, 2005; Delmelle & Stix, 2000). Furthermore, dune sand is commonly damp due to fog condensation (Eckardt et al., 2012) which would provide shallow subsurface water prior to lava emplacement. The origin of the water precipitating the calcite associated with the lava contacts is discussed in 4.4.

In the examples above, compaction in sandstone near to hot lava contacts is almost exclusively due to enhanced pressure solution as opposed to plastic deformation of quartz. Plastic deformation of potassium feldspar was however common, and was possibly enhanced by breakdown to clay minerals (evidence in the form of numerous 'bent' feldspar grains around stronger framework grains such as quartz). Most quartz grains showed unit extinction, with occasional to rare grains showing the undulose extinction characteristic of plastically deformed grains (cf. Bailey et al., 1958). The extinction characteristics of the quartz may have been inherited from the eroding source region, but originally un-deformed quartz would be expected to exhibit undulose extinction if subsequently plastically (*senso stricto*) deformed during lava emplacement. The conditions required for plastic deformation of quartz have generally been studied at high temperatures and pressures, characteristic of regional metamorphism (e.g. Blacic, 1975; Bailey et al., 1958; Carter et al., 1964) suggesting high pressures and temperatures are required. Kerrich et al (1977) used oxygen stable isotopes to study quartz in Dalradian metasediments from Scotland and found that for 100 μm quartz the transition from intercrystalline diffusion (pressure solution) to dislocation creep (plastic deformation) occurred at 450 °C, where temperatures were determined from inferred metamorphic temperature zones. Grain size was found to have the opposite effect on pressure solution; larger quartz grains (1000 μm) had a lower transition temperature of 300 °C. Kerrich et al (1977) also determined that the temperature transition between the two regimes was not dependent on stress in the pressure range studied (110 MPa (4 km) to 350 MPa (12 km)). Temperatures in excess of these are obtainable at the base of cooling pāhoehoe lava flows, at least for 8 minutes (Keszthelyi, 1995). A 13.4 m thick lava lake in Hawaii (Alae lava lake) cooled to below 100 °C in 5 years and another, the Makaopuhi 100 °C isotherm had only reached ~6 m deep after four years (Wright et al., 1976; Peck et al., 1977). Clearly in these examples, solidification from the base upwards was not measured.

Considering the above, pressure solution is certainly favoured under shallow sub-basalt conditions (up to 40 m deep burial, 1177 kPa). If the pressure independence noted by Kerrich et al (1977) is valid at low pressures, the substrate cannot have exceeded 450 °C for a duration sufficient to promote plastic quartz deformation, consistent with petrographic observations, even for coarse grains. Pressure solution requires much lower temperatures between 20 °C and 60 °C to initiate, so the duration it could last for under the cooling lava is much longer than potential plastic deformation. The effect of grain size on pressure solution is also consistent petrographic my observations. As noted above, for all of the case studies, grain fall and topset beds show the most intense compaction near contacts, whereas grain flow horizons are not so compacted, such that porosity may remain open for precipitation of authigenic pore-filling calcite. If plastic deformation was the case, the opposite might be expected.

Brittle compaction of the Twyfelfontein formation is petrographically significant outside of the highly compacted region near to lava contacts. Brittle compaction is however rare or absent within the highly compacted zone, suggesting the compaction occurred under conditions unfavourable for brittle processes. If the increased compaction near contacts was early, porosity would have been low during later burial, therefore preventing subsequent compaction by brittle mechanisms (e.g. Dickinson & Milliken, 1995; Makowitz & Milliken, 2003). This is evidence for an early compaction event near to the lava, separate from the later burial compaction of the sand not directly affected by the lava emplacement.

The effect of grain rotation and slip at low confining pressures may also contribute to the observed increase in compaction. The geologically sudden loading of the unconsolidated sand with up to 40 m of lava results in relatively low pressures (1177 kPa) compared to burial (Makowitz & Milliken, 2003), which can favour mechanical reorganisation of grains. Petrographic evidence for this was not found, nor expected in sandstone with rounded grains, nor with the overprint of such intense pressure solution. The early stage occurrence of this process cannot be ruled out however, especially considering the evidence for dynamic interaction between lava and sediment in some localities (e.g. flame structure in Fig. 4.37D, E.).

Since it has been established that sand below lava contacts shows increased compaction, dominated by pressure solution between quartz grains, but probably

contributed to by mechanical reorganisation of grains and potentially minor plastic deformation, it is necessary to attribute the correlation to a cause. The association of the increased compaction with lava is shown in Figure 4.48 and Fig. 4.49. Fig. 4.48. illustrates the relationship between COPL and CEPL for sandstones with porosities (A) > 8 % and (B) < 8 %. Since porosity is proportional to distance below lava, those with porosities < 8 % are near to lava contacts. 8 % was chosen as a threshold due to it being below the background porosity by ~ 1/3, no other basis exists for establishing this threshold. The two populations of interest for this chapter are KTyIDr and KTyMAJr, which are the isolated dunes (Dune 16 and Upper Dune) and the Major Erg (RYD pond, BD and PL) case studies respectively. It can be seen on the graph that COPL is inversely proportional to CEPL and that both isolated dunes and Major Erg have COPL ~ 40 % in this region. When compared to sandstone with porosity > 8 %, which exist away from the contacts, COPL and CEPL show no relationship and the mean COPL for the Major erg is higher than the stratigraphically higher isolated dunes by ~ 2 %. These analysis of the data show that out of the influence of the lava, compaction is controlled by burial, and within the influence of the lava compaction is inversely related to cementation and not related to stratigraphic position. The linear relationship between CEPL and COPL for the low porosity sands is striking compared to the lack of relationship for the high porosity sands. If the coarse-grained, grain flow (200 μm to 500μm) sample NG/12-31 (0.05 m) is used as an example due to its high cementation and low compaction a solution can be found. The question is: Does early compaction inhibit cementation or does cementation protect against compaction? Using the observations of Tada & Siever (1989) and petrographic observations in this chapter, it is apparent that pressure solution affects small grains more than larger grains. Early pressure solution would therefore have not affected this coarse-grained horizon as much as the finer less cemented horizons, and would have kept the pore network open for fluid flow, potentially during cooling of the lava (see 4.4). This fluid would then be able to precipitate the calcite in the pore space. However this mechanism does not account for why NG/12-31 is under-compacted (COPL= 32%, ±3.0) compared to the background Major Erg. The answer is that the calcite must have been formed prior to burial compaction but during or after lava emplacement compaction. The calcite would have separated quartz grains, preventing subsequent pressure solution and

compaction at grain contacts during regional burial. This is evidence for early compaction removing the majority of the porosity from the compacted sand at the contact prior to burial compaction. The emplacement of the lava caused up to 45 % porosity loss from the contact zone grain flow horizons immediately, rather than an initial 10 % loss followed by a later 35 % loss during burial. As distance from the contact increases the proportions of porosity loss from early compaction and burial compaction curves will converge.

When examined further (Fig. 4.49.) a clear distinction is found between the two populations of COPL (isolated dunes drowned by Tafelkop lava and Major Erg drowned by Tafelberg type lava) against distance below lava. Both populations follow the same trend away from the lava. On average the deeper buried Major Erg, (e.g., Fig. 4.48A is more compacted than the shallower, isolated dunes. However, when compared to Fig. 4.48B., where no difference is seen in COPL between low porosity sandstones from each population, it is concluded that the mean difference seen in Fig. 4.49 is due to burial compaction but the low porosity, near contact is due to early lava loading. CEPL does not appear to be related to depth below lava in either of the populations (Fig. 4.49.) and the trends shown are opposite, the isolated dune examples showing increased cementation with distance and the Major Erg showing decreased cement with distance.

In summary, the increased compaction observed below lava flows is due to the loading by the lava flow, combined with conductive heat transfer, and potentially volcanic steam providing aqueous films on quartz grains enabling pressure solution to occur. The pressure solution is restricted by the availability of water to form aqueous films and temperature, which according to Tada & Siever, (1989) must be at least between 20–60 ℃ at minimum effective pressures of 9–11 MPa (9 MPa corresponds to ~ 328 m burial depth). It is therefore, not inconceivable that the observed pressure solution compaction could occur at temperatures expected at the lava-sand contact (measured by Keszthelyi, 1995) of 850 ℃ to 900 ℃ for 8 minutes, followed by lava pond cooling to below 100 ℃ over a period of 4 to 5 years (Wright et al., 1976; Peck et al., 1977) would enable the observed pressure solution compaction. Temperatures probably did not exceed 450 ℃ for long, as little plastic deformation was observed near to lava contacts.

Beyond the limit where the effect of emplacement is observed in the sandstone beneath lava flows (4.3.1. and Fig. 4.50.) compaction is the dominant mechanism of porosity loss (as is common to most sandstones worldwide, Houseknecht, 1988; Gluyas & Cade, 1997). This compaction appears to have been dominated by pressure solution, with optically visible grain crushing of feldspars (usually along cleavage) and occasional quartz grains. Dickinson & Milliken (1995), in a study of the Twyfelfontein Formation (Etjo Formation at the time), with samples taken from the Huab area, noted that effects interpreted as pressure solution resulted predominantly through micro-scale brittle deformation. In the Twyfelfontein Formation, the brittle deformation was found by Dickinson & Milliken (1995) to dominate compaction by producing many intragranular microfractures only identifiable in cathode-luminescence, which reorganise to allow grain interpenetration. The microfractures then heal with authigenic quartz. Observations above of the Twyfelfontein Formation are broadly consistent with these observations, apart from the occurrence of sutured grain contacts in the formation, below the influence of the lavas.

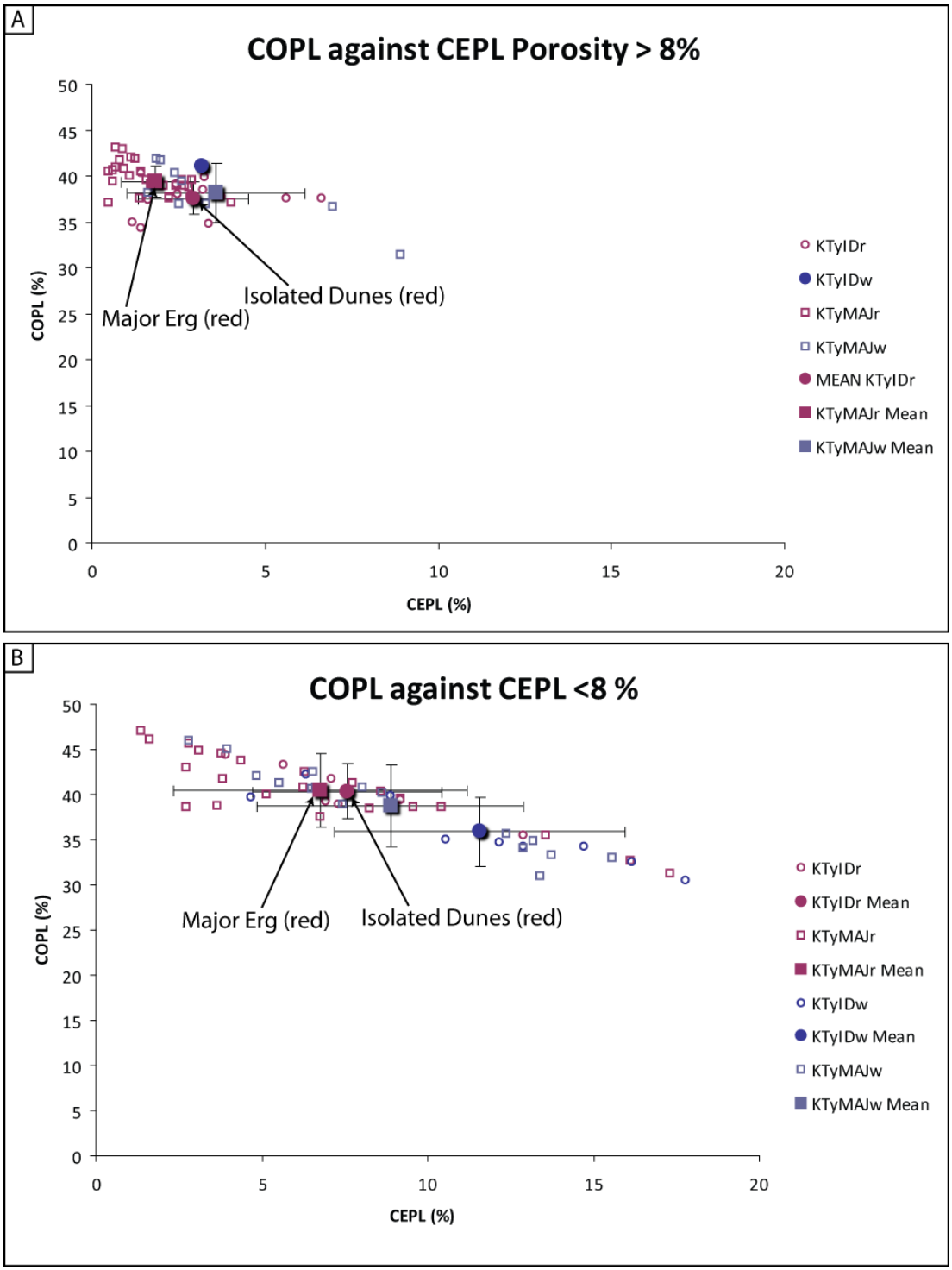

Fig. 4.48. A) Graph of COPL against CEPL for sandstones above with porosity > 8 %. These sandstones show no relationship between compaction and cementation. B) Graph of COPL against CEPL for sandstones above with porosity < 8 %. The negative correlation between COPL and CEPL suggests there is a relationship. Either early compaction inhibits cementation near contacts, or cementation inhibits compaction. Also shown are averages (with error bars of σ) for each Twyfelfontein unit. Where porosity > 8 %, the Major Erg (KTyMAJr and KTyMAJw) is more compacted than the shallower isolated dunes (KTyIDr and KTyIDw) which is a consequence of a higher stratigraphical position.

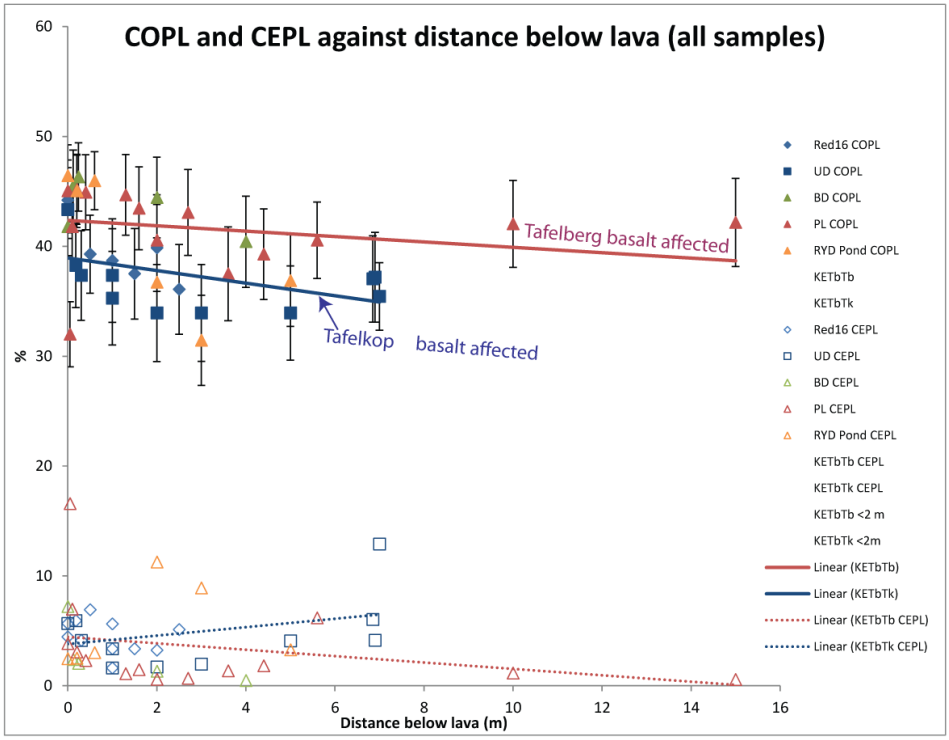

Fig. 4.49. Relationship of COPL and CEPL with distance below lava for each case study. Linear trend lines show that overall compaction increases towards the lava contact and that overall the sand below the thicker tabular Tafelberg lavas is more compacted than the sand below the thinner compound Tafelkop lavas. Trends for CEPL show that no difference exists (between the two lava units therefore cement (mainly calcite) is independent to the lava thickness or burial depth. The statistical difference was tested with the t-Test in MS Excel giving a P=0.001 suggesting the difference is HIGHLY STATISTICALLY SIGNIFICANT. It is important to appreciate the COPL uncertainty (Chapter 3), qualitative pretrographical observations strongly support the increase of compaction towards lava contacts.

4.3.1 Distance to background porosity in the Twyfelfontein Formation below the Tafelberg and Tafelkop lavas.

A more thorough discussion is given in Chapter 5, where comparisons will be made with lava flow-sediment contacts from Iceland, the Columbia River Basalt Province, WA, USA and from the Snake River, ID, USA. The intention here is to report on the range of porosity profiles below the lavas. Chapter 5 will show analysis of porosity and thickness of lava flows.

Each case study comprises a range of porosity measurements taken at increasing distances below the lava contact. For each example the linear best fit trend line was calculated in MS Excel up to the first porosity point to reach or exceed 12.5 % porosity (the background, see Chapter 3). The distance below the contact where the calculated gradient reached 12.5 % was then calculated. These trends are shown in Fig. 4.50B. The trends show that the two isolated dunes return to background levels most rapidly. The Upper Dune reaches 12.5 % porosity after 0.66 m and Dune 16 reaches 12.5 % porosity after 2.3 m. The Major Erg dunes were found to take a longer distance to return to 12.5 % porosity. The Ponded Lava case study reached 12.5 % porosity after 3.24 m, Big Dune after 3.8 m and RYD Pond after 4.29 m. These data are consistent with the compaction trends, i.e., the isolated dunes being less compacted than the Major Erg. Uncertainties in distance plotted (Chapter 5) are based on the 1σ error at 12.5 %. The uncertainty of this calculation has been propagated using the point count errors. These are plotted in the summary figures in Chapter 5.

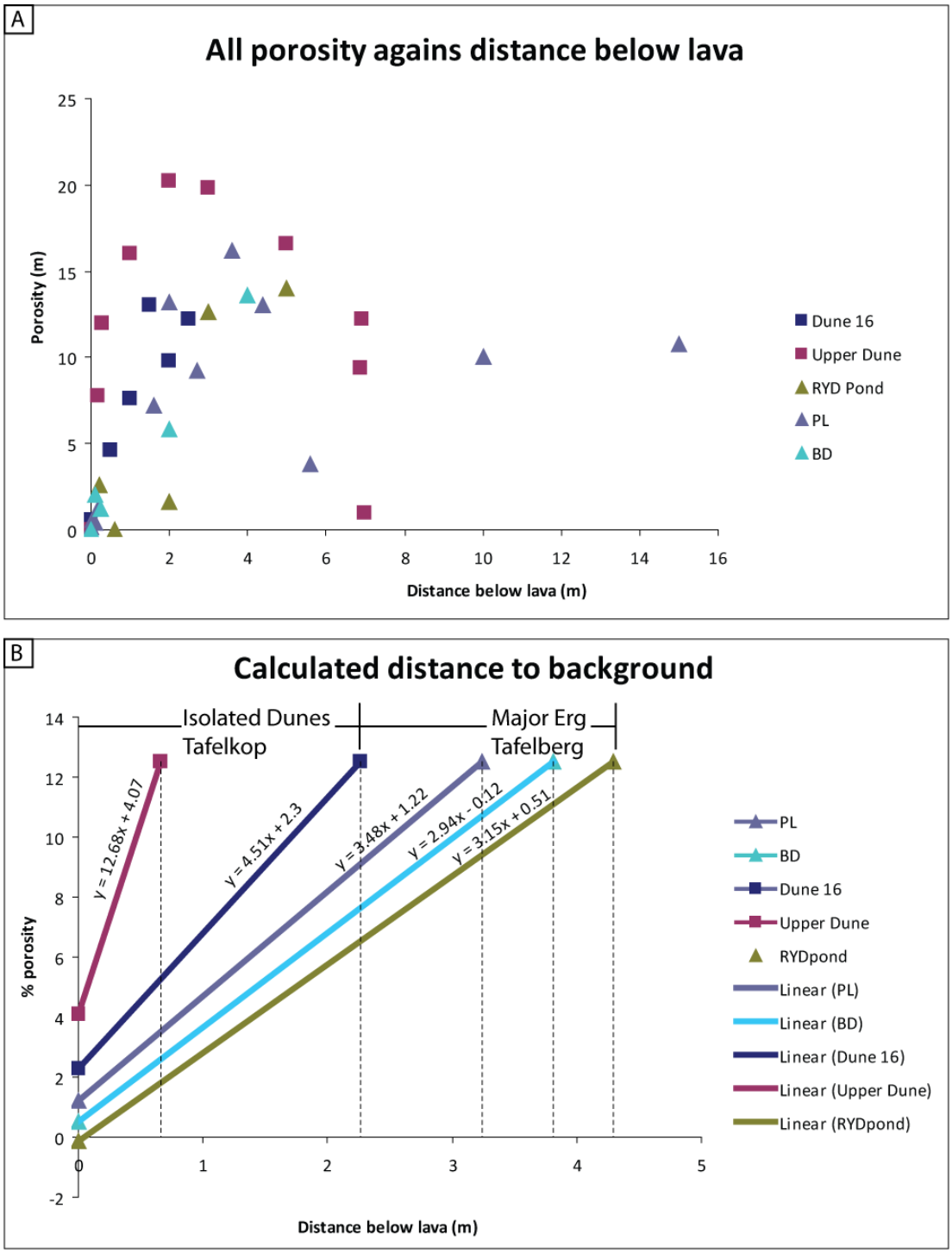

Fig. 4.50. A) All porosity data above plotted against distance below lava. B) Calculated gradients of porosity data plotted against distance terminating when background porosity (12.5 %) is reached. The trends come from data presented in this chapter in Figs 4.8A, 4.19A, 4.30A, 4.45A. These trends are plotted with uncertainties in Chapter 5.

4.4 On the origin and timing of the calcite

Calcite, near to lava contacts is a usually a minor contributor to porosity loss (CEPL), although it can be a major component in some samples (e.g. BD1, BG6 and NG/12-31). It is associated with lava contacts as a cement. It is important to examine the timing and origin of the calcite because this has the potential to elucidate, through simple modelling of stable isotope ratios, the temperature conditions under which the calcite precipitated. Measurement of carbon stable isotopes can identify the carbon source for the carbonate. Both of these isotopically determinable variables can be used as evidence for the paragenesis of the observed effects below lava flows, as petrographic links have already been established to compaction timing, porosity and detrital mineral replacement.

4.4.1 Stable isotopic evidence

Thirteen samples of red sandstone in transects below lava flows returned a CO_2 yield adequate for stable isotope analysis of calcite cements. Figure 4.51 shows the results of these analyses plotted as $\delta^{13}C$ (PDB) vs. $\delta^{18}O$ (PDB). Data for all analyses in this thesis are also plotted, which include calcite adjacent to sills and dykes, calcite from faults cutting the Twyfelfontein Formation (Chapter 6), calcite from an amygdale in the Tafelkop-type basalt from Dune Valley and calcite from hydrothermally altered white sandstone (Chapter 7). Data from geodes in the Parana published by Gilg et al., (2003) is also presented.

These data plot as two populations. The data collected from below lava flows plots with lower $\delta^{13}C$ and $\delta^{18}O$ compared with the calcite formed adjacent to dykes, sills and as hydrothermal mineralisation in faults and white sandstone. These two fields are labelled ‘hot lava contact field’ and ‘subsurface field’ in figure 5.51. The separation of these two fields suggests there is a difference in conditions. The $\delta^{13}C$ values of the lava contact calcites trend towards mantle values (Rollinson, 1993) and the $\delta^{18}O$ values, where there is sufficient data (e.g. PL locality) suggest a trend with distance, where $\delta^{18}O$ becomes heavier away from the lava (indicated on Fig. 4.51.).

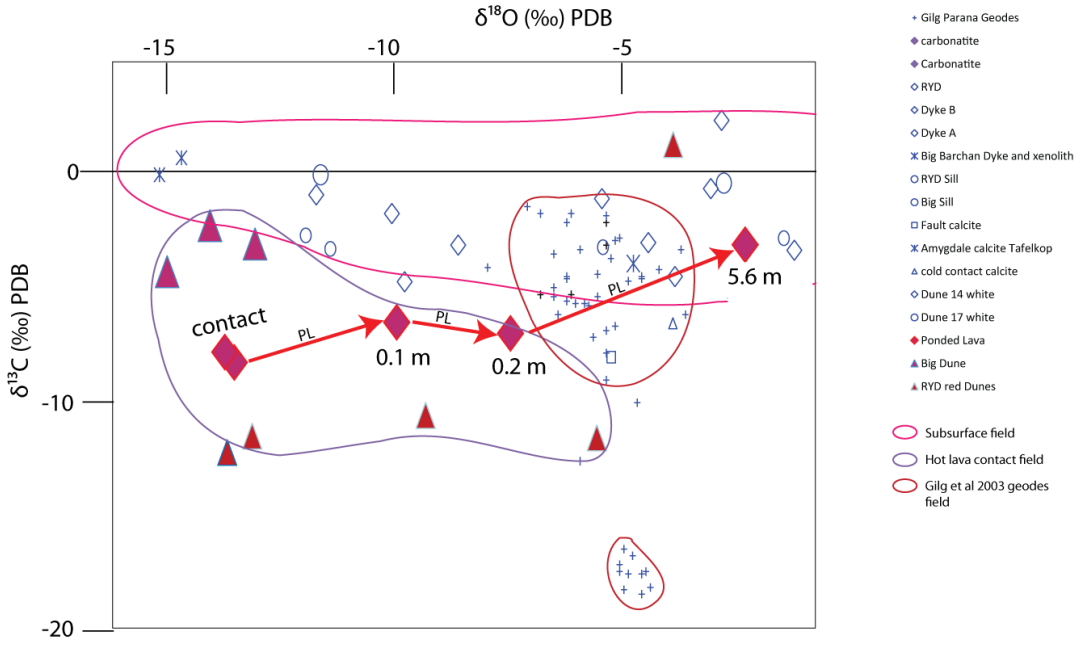

Fig. 4.51. $\delta^{13}C$ (PDB) against $\delta^{18}O$ (PDB) for all samples analysed, including calcite from intrusion contacts, hydrothermal calcite from 'white' sandstones (Chapter. 6.) and vein calcite from faults. Hydrothermal calcite, vein calcite and calcite near intrusions are plotted in blue. Each lava flow case study with data is plotted in a unique warm colour.

The identification of this trend prompted the modelling of possible oxygen isotopic and temperature variability in the water it would have precipitated from. Figure 4.52 shows results of the modelling.

The model was calculated using fractionation constants of A=-3.39 and B= 2.78, (O'Neil et al., 1969) and the equation:

$1000 \ln \alpha = A + B (10^6/T^2)$ from Rollinson (1993)

Where T is temperature and $\ln \alpha = \delta\ ^{18}O_{calcite} - \delta\ ^{18}O_{water}$. Using this, the expected $\delta\ ^{18}O_{calcite}$ can be calculated for any temperature and water.

The model shows for whichever water composition that is chosen, the calcite precipitated at a higher temperature closer to the lava contact than further away. For Cretaceous meteoric water in Namibia ($\delta^{18}O$ (SMOW) = 7 ‰, Bowen & Revenaugh,

2003) a temperature of 50 °C is calculated at the contact reducing to 15 °C at 20 cm depth. The lower magmatic water value (from Rollinson, 1993) calcite precipitation temperature at the contact is 190 °C, which reduces to 105 °C at 20 cm. The Upper magmatic water value suggests a maximum precipitation temperature of 360 °C at the contact. No independent temperature data exists for these samples, so true temperatures are not known. However, the range of temperatures calculated suggests that the calcite must have formed after initial cooling of the lava, which is consistent with the diagenetic sequence reported in this chapter. Given the arid palaeoenvironment, large quantities of meteoric water are hard to envisage, but occasional precipitation (annual) is expected. Considering the Ponded Lava lava pond would have taken several decades to cool, several precipitation episodes would have taken place over this time. It is therefore suggested that mixing of meteoric water and magmatic water is likely.

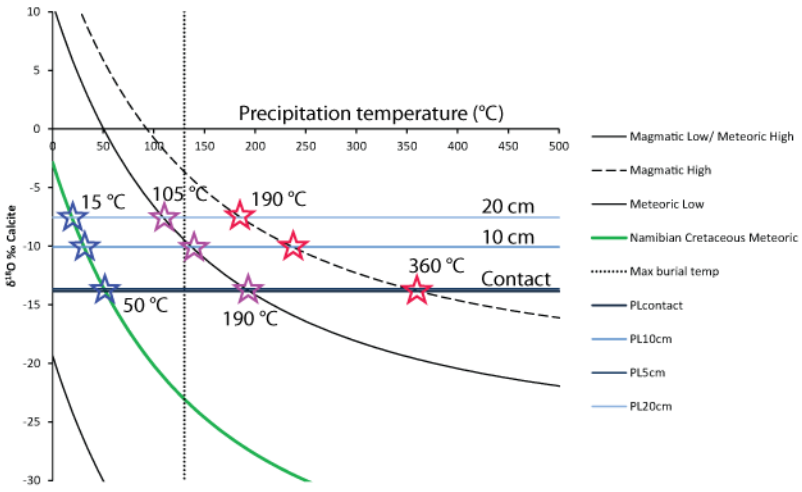

Fig. 4.52. (A) Modelled calcite δ ^{18}O values in equilibrium with waters of different origins. Calculated meteoric and magmatic fields are shown (using fractionation constants A=-3.39 and B= 2.78, O'Neil et al., 1969) as well as the expected meteoric water value for Namibia in the Cretaceous (green line). Max burial temp of 130 °C has been calculated based on geothermal gradients and burial data from Raab et al., (2005). It is clear that a temperature gradient exists in the measured calcite below PL lava, cooling away from the lava (whatever the water).

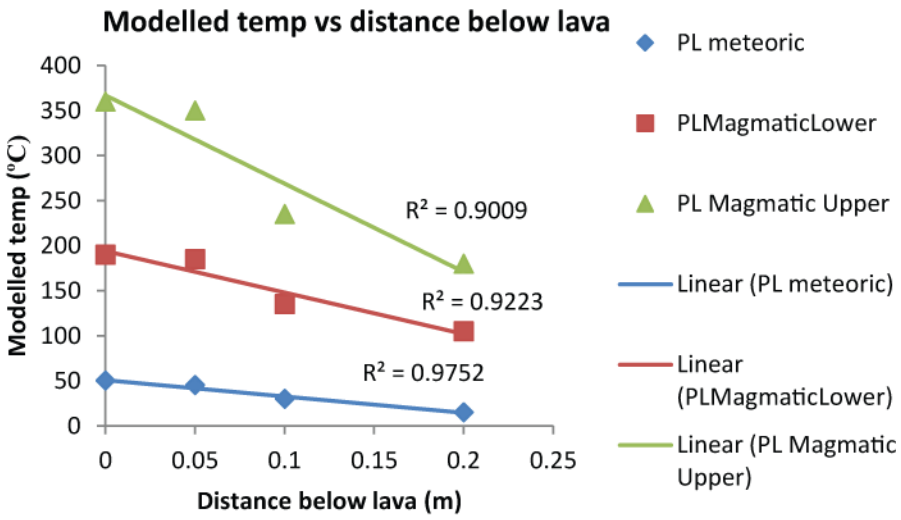

Fig. 4.53. Relationship between distance below the Ponded Lava contact and modelled carbonate precipitation temperature for Cretaceous meteoric water in Namibia, the lower magmatic water limit and the upper magmatic water limit, All show an increase in calcite precipitation temperature towards the lava, supporting an early diagenetic origin for the calcite.

Linear correlations between calculated calcite precipitation temperature and distance below lava have been calculated for the PL locality (Fig. 4.53.). It can be seen that temperature reduces away from the lava, suggesting the calcite formed during cooling and was an early cement.

4.5 Discussion

It has been demonstrated that the emplacement of basaltic lava onto unconsolidated sand causes a zone of increased compaction through pressure solution that reduces porosity. It has also been established that increased calcite cementation is associated with proximity to the lava contacts. Also noteworthy, is the common redistribution of haematite from the highly compacted zone to a zone further beneath the lava, where it is precipitated as small (< 5mm) nodules that give the sandstone a mottled appearance. The major diagenetic reactions above (pressure solution, calcite authigenesis and haematite redistribution) all require water. Large volumes of water in the setting are problematic, at an early diagenetic stage. Nevertheless, there is substantial evidence for the above being of an early diagenetic timing (i.e. immediately post lava emplacement) as noted by Jerram et al (2002) and Thompson & Jerram (2003) on the initial investigation of these types of contacts in the Huab Basin:

• Inverse correlation between compaction (COPL) and distance below lava for low porosity sandstone (before background characteristics are regained)

•Correlation of Pmc with distance below lava also suggesting compaction related to lava emplacement (albeit less sophisticated than COPL)

•Correlation between porosity and distance below lava in all cases

•Correlation between permeability and distance below lava in all cases

•Inverse relationship between calcite cementation and distance from lava in most cases, except for within highly compacted grain fall laminations.

•Linear relationship between COPL and CEPL near to contacts, combined with petrographic observations demonstrates calcite was precipitated during shallow compaction (lava induced) or shortly after but before burial compaction.

•Haematite redistribution requires dissolution, transportation and re-precipitation, and requires fluid movement or capillary movement (i.e. solvent required), which must be acidic (e.g. Ma et al., 2007; Surdam et al., 1993). It is often studied as the result of hydrogen sulphide in hydrocarbon systems (Kirkland et al., 1995; Beitler et al., 2003). It is proposed that degassing lava can provide both water and acidification, as the major phases degassed by basaltic lava are: water, carbon dioxide, chlorine, fluorine, sulphur dioxide, hydrogen sulphide and carbon monoxide (e.g. Delmelle & Stix, 2000; Lowenstern, 2001; Simmons and Christenson, 1994; Shevenell and Goff, 1993; White, 1957). Condensation of these volatiles within the sandstone, or indeed vapour presence during compaction would dissolve haematite (reduction of Fe^{3+} to soluble Fe^{2+}, equation 1), and if migration pathways existed downwards (i.e. not completely compacted) the iron-rich solution would dissipate until it either buffered by reacting with detrital grains (e.g. plagioclase, which is also reactive in acid environments e.g. Hangx & Spiers, 2009), or until the fluid dissipated due to its low volume in relation to rock volume.

$$4\,Fe_2O_3 + H_2S + 14\,H^+ \leftrightarrow 8\,Fe^{2+} + SO4^{2-} + 8\,H_2O \qquad (1)$$

Clearly if this is the mechanism for the origin of the haematite nodules in the sandstone, associated with lava contacts, volcanic fluids are necessary (organic influence can be ruled out because of the palaeoenvironment, large scale meteoric flux can be ruled out because of the palaeoenvironment). A low volume of water is

also suggested due to the location of the haematite nodules, if an aquifer existed, it is proposed that the iron would dissipate or precipitate as a front.

•Carbon stable isotopes $\delta^{13}C$ at the Ponded Lava locality have average values of –7.5 ‰ (n=4, SD= 0.8 ‰), which are within the range of mantle carbon (Rollinson, 1993) and magmatic carbon (Taylor, 1967). This suggests the CO_2 dissolved in the water precipitating these carbonates was potentially sourced from the degassing lava. This supports the existence of the magmatic fluids required for haematite redistribution and the petrographical interpretations of the calcite having an early diagenetic origin.

•When plotted in carbon and oxygen space, the values for the lava contacts plot as a different population to the hydrothermal calcites (white sand, and vein calcite) and distinct from calcite in hydrothermal calcite found in geodes in the equivalent lavas in the Parana Basin (Gilg et al., 2003). They also plot away from any field shown in Rollinson (1993). Where sufficient data exist (e.g. Ponded Lava), a temperature dependence is in $\delta^{18}O$ is evident, as lighter oxygen values are found closer to the contact, no trend is noticed in $\delta^{13}C$ suggesting the fluid is the same.

•When temperature dependence is modelled for various waters (sufficient data for Ponded Lava) precipitating calcite using a temperature gradient exists increasing towards the lava (for all water compositions). The lava must have been cooling during calcite precipitation, strongly supporting an early diagenetic origin. This gradient is the opposite of a normal geotherm, which cools upwards. Furthermore, when various water $\delta^{18}O$ compositions are modelled temperatures can be proposed. For an approximate Cretaceous Namibian meteoric water ($\delta^{18}O$ PDB= -36.8 ‰, SMOW= -7.9 ‰, Bowen & Revenaugh, 2003) the gradient ranges from 50 °C at the contact to 15 °C 0.2 m below. The gradient ranges from 190 °C at the contact to 105 °C 0.2 m below when modelled for the lower magmatic water value. The carbon origin suggests magmatic volatiles were present which supports a magmatic water, especially considering the carbonate must have formed during lava cooling. Meteoric water would not have been abundant in the region, due to its aridity, however some pre-existing moisture would have been present at depth. The model, combined with prior knowledge supports magmatic water with some meteoric input as the favoured diagenetic fluid.

There is however, also petrographic evidence for a later origin of the calcite cement. Occasionally the calcite cement near to contacts has grown over quartz overgrowths (e.g. BD1, Fig. 4.26B.). This would be regarded as evidence of the calcite being a late cement post-dating the quartz overgrowth. However it is known that quartz overgrowths are related to pressure solution (Rutter, 1983) and that here, the pressure solution facilitated compaction, which would have begun prior to lava cooling (i.e. as soon as loaded by hot lava), at temperatures of potentially 850 °C to 900 °C (Keszthelyi & Delinger, 1996). The duration of cooling to 100 °C taking in the order of five years (Wright et al., 1976; Peck et al., 1977). Modelling of $\delta\ ^{18}O$ shows that the likely maximum calcite precipitation temperature, taking the upper magmatic water value is 360 °C. So even with this assumption, cooling of the lava pond and the contact must have taken place before the initial precipitation of calcite, leaving time for early pressure solution, and quartz overgrowth precipitation prior to the initial calcite growth. The time for this increases, as the water becomes more meteoric, as this lowers the precipitation temperature for a given $\delta\ ^{18}O$ calcite value in the model (Fig. 4.52.). A detailed fluid inclusion study on both the quartz overgrowths and calcite would be of scientific merit for future work.

The magnitude of compaction, and hence porosity loss varies depending on case study. Correlations exist between both porosity and thickness of overlying lava: For instance the isolated dunes show less porosity reduction than the major erg and the Tafelkop lava flows that buried the sand are compound in nature (< 5 m for an individual flow). The more intense porosity reduction in the Major Erg is below the Tafelberg lavas– ponded Tafelberg lavas. The Major Erg case studies' more intense porosity loss, may therefore me due to the thicker lavas. However, the stratigraphic position of the two sand units is also separated by ~ 536 m vertically, with the isolated dunes, which show the lowest porosity loss the higher unit. This separation is apparent in the sandstone away from the influence of the lava (see Chapter 2.5.2.). However, the thickness of the indurated zone (influenced by lava) also varies. Is this due to burial or lava flow thickness? Based on the observations in this chapter, and the general interpretation that the increased porosity loss approaching lava contacts is the result of early diagenesis (lava compaction and minor calcite precipitation), it is likely that the variation observed is due to the lava style and thickness.

4.6 Chapter Conclusions

Lava emplacement onto the unconsolidated subarkosic arenite of the Twyfelfontein Formation has produced early diagenetic effects that have been preserved. The effects are likely to have formed during emplacement and cooling of the lavas and are related to the lava flow thickness. This relationship will be discussed in Chapter. 5.

The observed porosity loss below lava flows is due to compaction dominated by pressure solution, which is more intense in the finer grained grain fall horizons than the coarser grain flow horizons. Cementation is also apparent near to contacts, with calcite, probably originating from volcanic volatiles (e.g. CO_2 and H_2O) reacting with detrital plagioclase and volcanic glass in the lava to precipitate calcite. Calcite authigenesis occurred during lava flow cooling as evident from $\delta\ ^{18}O$ values in the calcite. Minor quartz overgrowths are related to pressure solution, which initiated during burial by hot lava. Where not indurated by early pore-filling calcite cement during lava cooling quartz cementation continued throughout burial. The volcanic volatiles released by the cooling lava were also responsible for the redistribution of the haematite from the region proximal to the lava flow to the mottled zone further below.

The Twyfelfontein Formation, where beyond the influence of the lava has a diagenetic history dominated by compaction, as both pressure solution and brittle deformation (Dickinson & Milliken, 1995), with minor quartz overgrowth authigenesis growing into pore space (< 1%, ±0.4). The overall difference in compactional porosity loss between the indurated contact zones below lavas and the background sandstone is ~ 10 %. This difference does not however reveal the timing: most of the compaction (~ 45 %) at contacts occurred at an early stage (during lava emplacement and cooling) and the background (COPL ~ 35 %, ±2.6) compaction (beyond influence of lava) occurred at a later stage.

5

Diagenesis at lava-sediment contacts in wet palaeoenvironments, case studies from Iceland, the Columbia River Flood Basalts and the Snake River Plain Volcanic Province.

5.1 Chapter summary

This work aims to characterise the direct effects of basaltic lava emplacement onto sediments that were initially saturated or partially saturated with water, with specific relevance to diagenesis. Numerous studies of sediment-lava interaction in settings where free water is present (moist, wet) have been undertaken to characterise the dynamics of the less 'normal' aspects of this kind of interaction, such as the formation of peperites (e.g. White et al., 2000; Passey et al., 2007; Brown & Bell, 2007). Much, if not most of the observations in this study are however, passive, with no dynamic mixing as in the above examples. Furthermore, few of the studies, even on the well-studied phenomenon of peperite formation have paid detailed attention to the petrography and diagenesis of the host sediment (e.g. Brown & Bell, 2007).

Here, the effects of lava emplacement onto a variety of wet sediments are investigated, in situations that, arguably, represent the normality (e.g. planar contact), rather than exception (e.g. peperite). The case studies presented are important in order to compare with the arid sediment-lava effects discussed in the preceding chapter. Are the effects noticed in arid settings universal or is there a palaeoenvironmental control?

The case studies in this chapter are a first attempt to broaden the study to a multitude of sedimentary settings, and are act as a control for the Huab Basin examples. The two outcrops in Iceland are both Quaternary in age and have not been significantly buried. Iceland is a wet country (Reykjavik mean annual rainfall between 1949 and 2012= 814 mm, Icelandic Met Office, 2013). By the nature of Icelandic geology, siliciclastic sediments do not exist, hence these examples are completely basaltic volcaniclastic. Secondly, outcrops of siliciclastic sandstone from below lava flows of the Miocene Columbia River Flood Basalts and the Snake River

Basalts (also Miocene) are described. These sediments are dominantly siliciclastic and are fluvial in the case of the CRB example and lacustrine in the case of the SRB examples. The water saturation of these sediments at the time of lava emplacement can be assumed as there is evidence for contemporaneous lava emplacement and sub-aqueous sedimentation (e.g. dynamic mixing strictures, re-establishment of drainage networks, pillow lavas forming in lakes).

The key variables introduced by the broadening of the study are: water saturation of the substrate and substrate composition. For all of the examples, burial depth is less than the Huab Basin examples, such that direct comparisons on a like for like basis are difficult. Certain parameters can however be reliably compared, such as distance to background porosity, increased compaction as a result of lava emplacement and the nature of early diagenesis.

5.1.1 Establishing influence of pre-existing sediment wetness

The direct diagenetic effects discussed in Chapter. 4 were a result of the cooling and degassing of lava combined with compaction loading. In the Huab Basin, all of the early diagenetic effects observed as a result of lava emplacement were inferred to have occurred during cooling of the lava, therefore at an elevated temperature. This is recorded by oxygen stable isotopes (Chapter 4) in the authigenic calcite as a temperature gradient increasing towards the lava and by the pressure solution enhanced compaction close to hot lava contacts that would have required elevated temperatures. This raised the question: What is the effect of pre-existing moisture within the substrate on the observed diagenetic effects on substrates where the lava-sediment contact is passive?

Firstly water may influence the cooling of the pahoehoe lava. It has been established by Wright et al., (1976) that rainfall on cooling lava *considerably hastened* post-solidification cooling of the Kilauea lava lakes, Hawaii (emplaced 1959 to 1965). It can therefore be expected that in wet palaeoenvironments, a given lava flow (equal thickness and composition) would cool more rapidly purely due to rainfall. Faster cooling should reduce the time that any underlying sediments are subjected to elevated temperatures favourable to early diagenesis as observed in the Huab Basin. Furthermore, pre-existing pore water saturating the substrate sediment would provide a cooling medium for the lava flow base, beyond that of air saturated sediment, increasing the initial cooling rate from the lava flow base. It can be expected that this water would boil, taking energy from the lava as the enthalpy of evaporation.

The presence of water within pore space of the substrate sediment would have the capability of modifying the sub-lava pressure regime. This has implications to the movement of volatiles in and out of the lava. If the pressure beneath the lava is increased by boiling water confined by the overlying lava flow, the pore space will be above atmospheric pressure, preventing potential downward degassing of magmatic volatiles. Increased pore pressure may also serve to limit compaction. The situation envisaged, where pore pressure can increase, would probably be rare due to areal extent of lava flows (gas could simply vent around the edges) and due to the total pore volume probably being large enough to allow the steam to expand without a large pressure increase. Where the pore pressure could potentially increase would be a shallow sediment layer, resting on a vertically impermeable rock with topographic confinement (e.g. a canyon through crystalline basement or shale, along which a later lava flows).

5.2 Diagenesis of volcanogenic sediments at lava contacts, Iceland

5.2.1 Rekjanes Peninsula (IGHC)

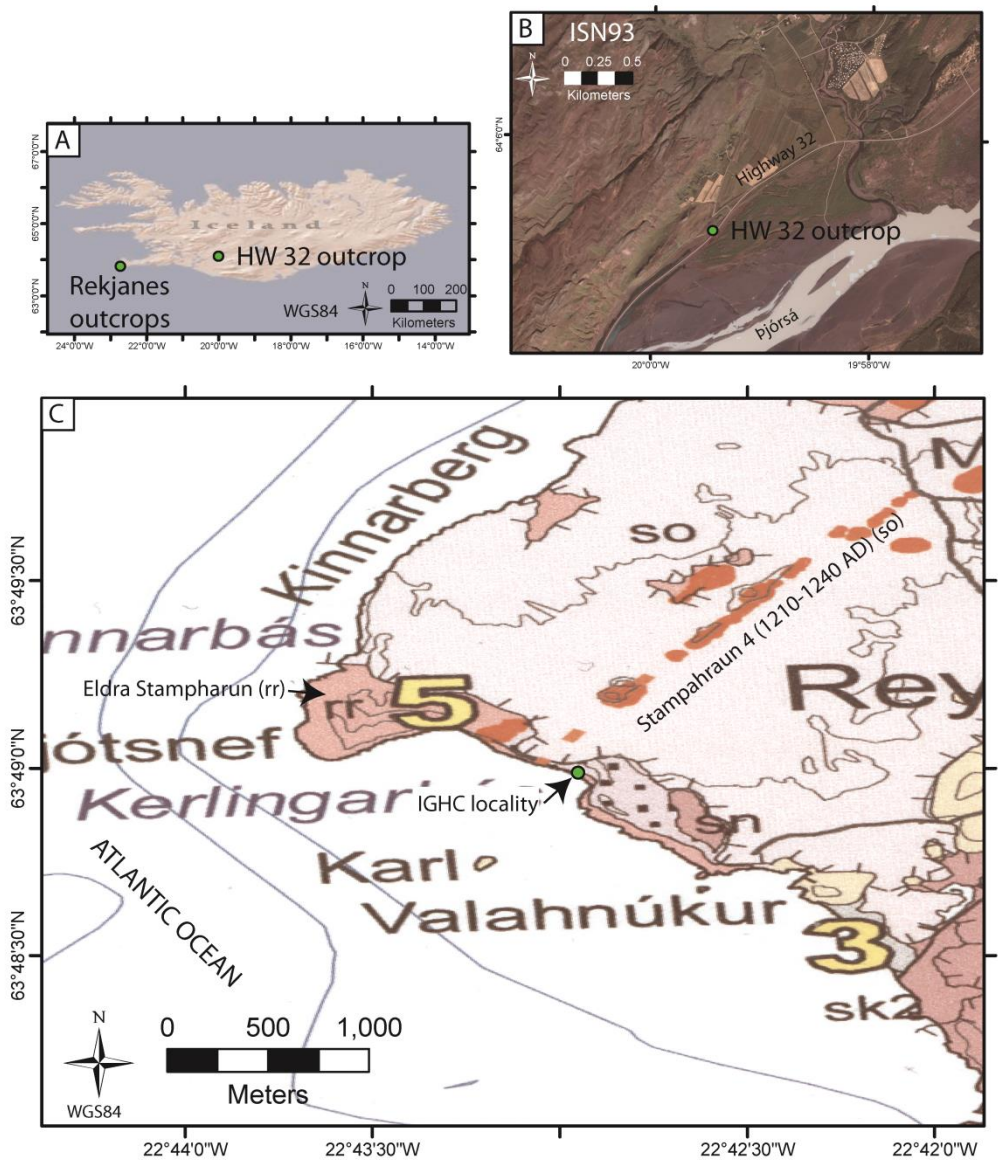

Fig. 5.1. Location maps. (A) Map showing location of Rekjanes Peninsular outcrops (1.2.1) and Highway 32 outcrop in Iceland. (B) Location of Highway 32 outcrop. (C) Location of Rekjanes Peninsular outcrops in Kerlingar Bay, 200 m east of the Stampahraun fissure dyke.

This locality is located at the SW tip of Iceland at the end of the Rekjanes Peninsular (Fig. 5.1.). The outcrop is at 63° 49.004’ N 22° 43.497’ W at 21m above sea level (GPS) located in a ~ 25 m high SSW facing sea cliff. The cliff is composed

of dominantly unconsolidated (or poorly consolidated) sediment capped by a 4 m thick basalt lava flow. The sediments are unlithified except in the lava contact zone and comprise angular basaltic scoria clasts with weakly developed clay cement. The scoria clasts are made up of volcanic glass, which is highly vesicular and contains occasional euhedral plagioclase phenocrysts. The glass shows a variable degree of hydration, generally less hydrated away from the lava contact, as shown by the brown colour (Watton, Personal communication). The sediments are parallel bedded and show no cross bedding.

Both the sediment and lava are of volcanic origin. Volcanism has been continuous in the Rekjanes peninsula since the Middle Pleistocene (Etienne & Paris, 2010) with twelve prehistoric eruptions and at least nine historic eruptions. The volcanism is related to the south-western rift zone in Iceland (Dietze et al., 2008), the active spreading initiated 6-7 Ma due to a major ridge jump (Saemundsson, 1979). The peninsula is characterised by numerous eruptive fissures, striking on average 040°, about 5 km apart (Fig. 5.1C.), one of which forms the Stampahraun fissure of 1210-1240 AD which is associated with four lava fields and underlying tuff cones (Sigurgeirsson, 1995).

The outcrop of interest occurs at the south end of the eruption fissure, where it extended into the sea. The eruption here was initially surtseyan due to phreatomagmatic activity. The Surtseyan activity produced two tuff cones made of scoria, the Karl and the Vatnsfell cones. The Karl cone pyroclastic sediments are exposed in the cliff section. After the cessation of Surtseyan activity, eruption became dominated by fire fountaining along a 4 km long NE trending fissure (Fig. 5.1C.). The capping lava was formed from the continuation of the same eruption that

formed the Karl tuff cone sediments that it rests on (Clifton, unpublished fieldtrip guide).

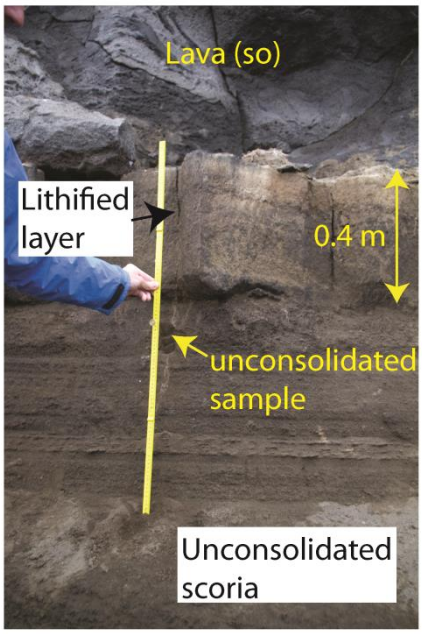

Fig. 5.2. Photograph of the Rekjanes Peninsula lava contact outcrop showing base of basalt lava flow resting on scoria deposited during the same eruption (1226 A.D). Under the lava is 40 cm of lithified sediment of the same composition as the unlithified scoria beneath.

The lava flow was emplaced onto unconsolidated sediments, which were unlithified. The sediments remain unlithified and unconsolidated at depths > than 40 cm below the lava flow base (Fig. 5.2.) The unconsolidated sediments were sampled by pouring superglue onto the unconsolidated surface, and exhuming the hardened block after the glue had hardened. This method was based on that of Dickinson & Ward (1994). Superglue does not undergo volume change during curing.

At the base of the lava, there is a 40 cm thick layer of lithified scoriaceous sediment. The strength is sufficient to require sledge hammer and chisel for sampling. In hand specimen the rock is grey, weathering to brown, coarse sediment with visible porosity. The morphology of individual scoria fragments can be

resolved. Examination of thin-sections at the contact reveals the sediment is composed of vesicular brown volcanic glass scoria clasts up to 1000 μm containing occasional plagioclase and clinopyroxene phenocrysts. The scoria is visibly compressed parallel to the contact (Fig. 5.3A, B.) where originally spheroidal vesicles have been compacted. Scoria clasts frequently have long contact intergranular contacts as opposed to point contacts. Undifferentiated clays (probably gel palagonite) (palagonite- the first stable product of volcanic glass alteration, see Stroncik & Schminke, 2002) occur at grain contacts and form a cement. Primary intergranular porosity exists up to the lava contact (Fig. 5.3C.). As depositional porosity could be directly measured from the unconsolidated sediment (62 cm depth below lava, primary intergranular porosity= 49.2 %, ±2.2) COPL was calculated. At the contact compaction porosity loss is 33.7 % (±3.7), and the porosity is 18. 4 % (±1.7).

At 20 cm depth below the lava (depth), the sediment is still lithified. Scoria clasts are similar to those at the contact and are visibly compacted. Scoria clasts are frequently surrounded by annuluses of broken glass (Fig. 5.3D.). The glass is brown sideromelane and is probably hydrated. Where the scoria clasts are small (e.g. broken clasts) brown clay is common. Long grain contacts are less common than at the contact. Primary intergranular porosity is 30.8 % (±2.1) and COPL is 24 % (±4.0).

The lower sample within the lithified layer is at 35 cm depth. Here the scoria clasts are brown. They only have point contacts with each other and no direct evidence for compaction is evident (i.e. no deformed scoria or broken annuluses present). Rare clay is present at grain contacts. Primary intergranular porosity is 40.6 % (±2.2) and COPL is 12.1 % (±3.5).

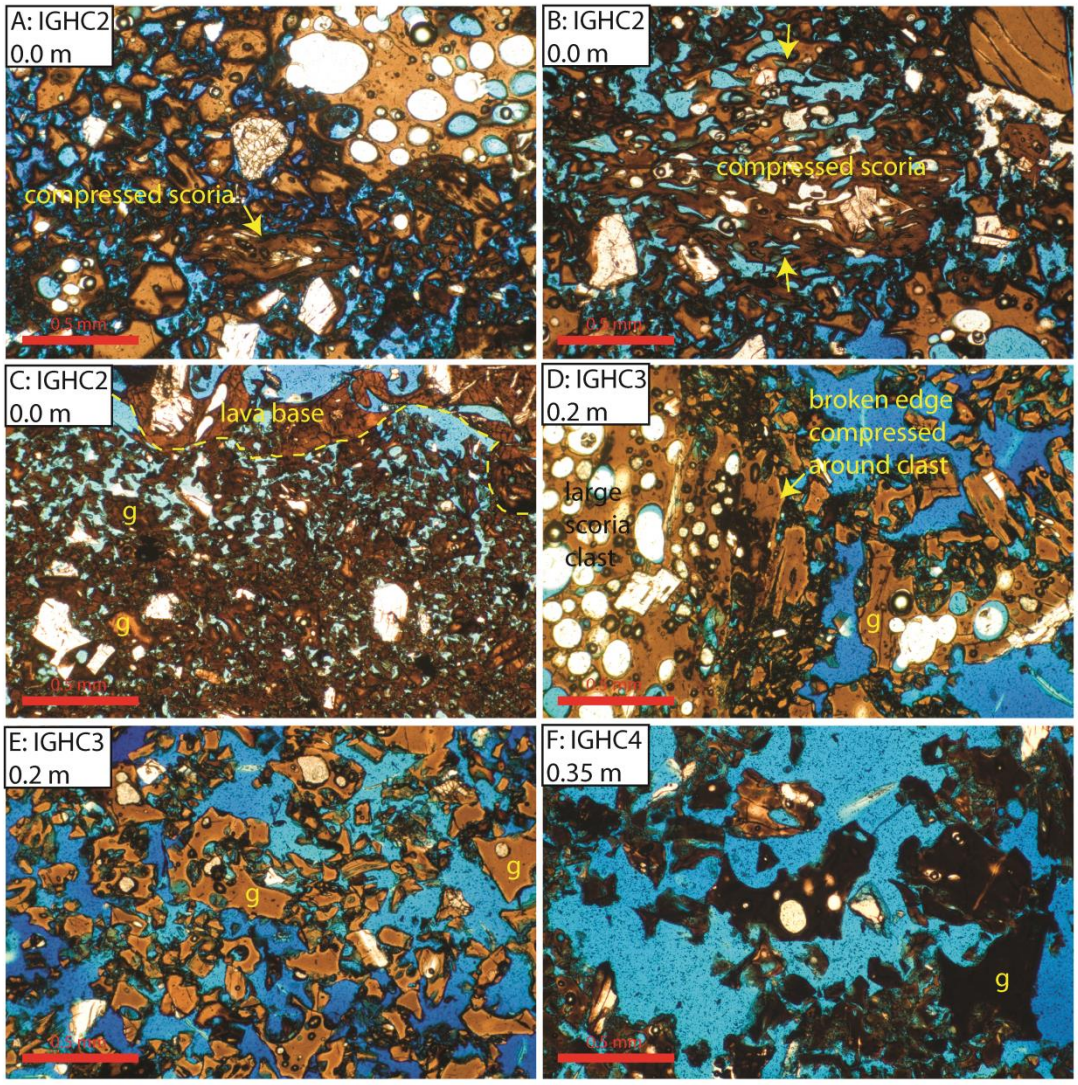

Fig. 5.3. PPL photomicrographs of scoria lithified sediment below lava in Fig. 5.2. (A) Scoria composed of vesicular basaltic glass fragments and clasts containing multiple vesicles, larger multi-vesicular clasts are compressed with direction indicated by arrow. (B) Larger scoria clast compressed so that originally round vesicles are flattened, arrows indicate direction of compression. (C) Lava contact with scoria, compaction of sediment is clear, although considerable primary porosity remains. (D) 0.2 m below lava contact compaction is evident, fragile edge of vesicular scoria has been compressed against clast, but remains *in situ*. (E) 0.2 m below lava, grains show less compaction than at 0.0 m (A, B, C). (F) 0.35 m below lava sediment is still lithified by compaction, but less than closer to lava.

The unconsolidated scoria is petrographically different to the lithified scoria. 55 cm depth, the scoria consists of both broken and whole clasts which are composed of volcanic glass and occasional phenocrysts (similar to the lithified rock above). However, the glass in the unconsolidated scoria is clear to very light brown (Fig.

5.4A, B vs. Fig 5.4D.). Grain contacts are point contacts and there are numerous floating grains (only touching in 3D). Deformed scoria clasts are not present. Clays are negligible (0.2 %), porosity is filled with superglue (white) and is 45.3 % (±2.2). Compactional porosity loss is 6.6 % (±4.2).

Porosity continues to increase until 1.2 cm depth, where the last sample was taken (superglue supply was exhausted). At 62 cm below the lava most scoria grains appear to be floating and are clear. Surprisingly delicate scoria textures are preserved such as the ~5 μm bubble walls in the scoria clast in Fig. 5.4C. Compaction is considered to be 0 % as it is the maximum intergranular porosity encountered of 49.2 % (±2.2).

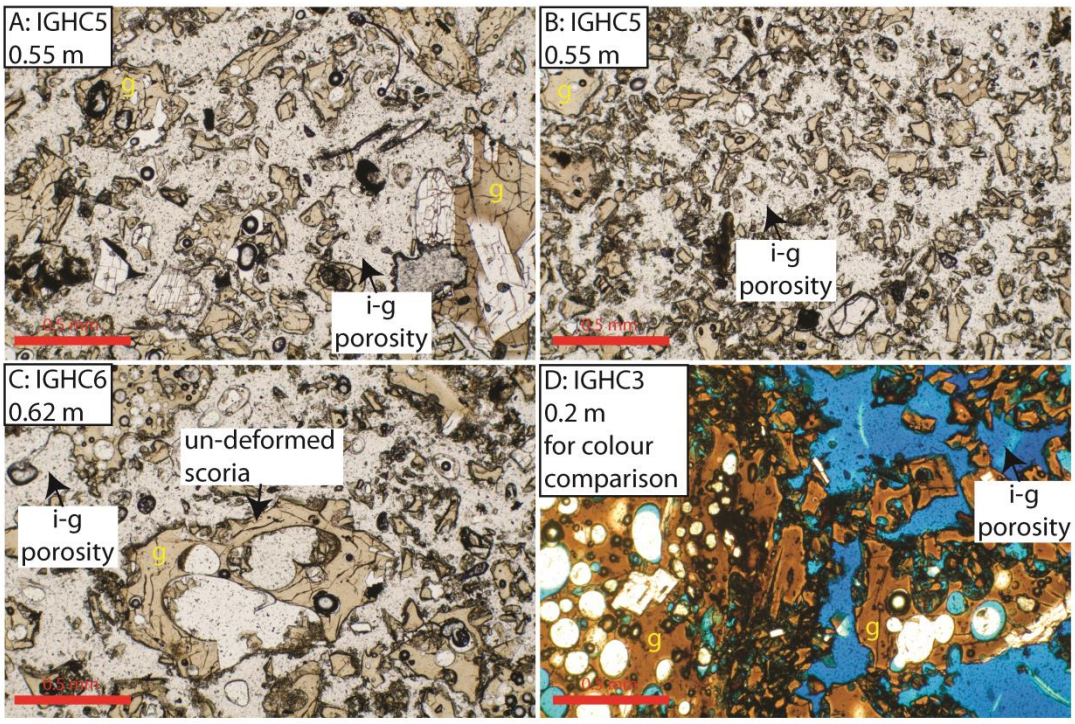

Fig. 5.4. PPL photomicrographs of the unlithified scoria below the 40 cm lithified layer. Loose sediment was impregnated with superglue in the field, porosity is white. (A, B) 0.55 m below lava contact the sediment is uncompacted, grains rarely touch. (C) 0.62 m below the lava, scoria clasts with multiple vesicles are not compressed or deformed by compaction. (D) Photomicrograph of lithified scoria for comparison. The glass where lithified is darker than the unlithified glass suggesting higher degree of hydration where lithified.

The trend developed below this 4 m thick lava flow is of porosity reduction towards the contact. The porosity reduction becomes apparent < 62 cm depth (Fig. 5.5A.) and reduces until the contact where porosity is 18.4 % (±1.7). Two permeability measurements also show reduction towards the contact from 4184 md 35 cm depth to 2036 md at the contact. Permeability measurements were not possible in the unconsolidated sediment. The porosity loss is dominated by compaction, and cementation is of negligible importance at depths greater than 20 cm below the contact. Compaction (COPL) increases from 0 % at 62 cm depth to 33.7 % (±3.7) at the contact (Fig. 5.5B.). Compaction follows a linear trend away from the lava contact (Fig. 5.5B).

Compaction alone cannot produce the lithification which here is due to the authigenic clay developed at grain contacts in the lithified zone (<40 cm). Intergranular clay increases towards the lava contact (Fig. 5.5C.). From Fig. 5.5C it can be seen that ~ 2 % of intergranular authigenic clay is required for lithification at 40 cm. The increase of clay corresponds to the colour change of the scoria clasts from light brown/clear to dark brown. It is proposed that at depths less than 40 cm below the lava, the scoria clasts were hydrated and compacted by the overlying lava flow. This hydration produced clay minerals at grain contacts that cemented grains together.

The lithified zone probably became hot enough to boil intergranular water within the scoria (it was deposited as a surtseyan eruption so the sea water table must be near or coincident). This boiling probably facilitated the rapid palagonitisation of the glass in a similar way to that observed on Surtsey (Jakobsson, 1978). On Surtsey, rapid palagonitisation is inferred to have proceeded at temperatures of 45–100 °C and pressure of 1 atm, the palagonitisation agent being vapourised sea water

(Jakobsson, 1978). The experimentally determined rate of palagonitisation was found to be three times greater at 90 °C than at 20 °C by Furnes (1975). If the volume of palagonite is taken to be 5 % at the contact (Fig. 5.5C.), one third of this is 1.7 %, which occurs at ~ 40 cm. I speculate, therefore, it falls that the temperatures reached in the lithified zone are probably ~ 100 °C at the lava contact (at which water boils at 1 atm) and ~ 20 °C 40 cm from the lava. It therefore follows that the lava base was cooled by boiling intergranular water within the scoria sediment. The boiling of this water is recorded by the lithified zone. Beyond the lithified zone, continuous cooling by sea water probably maintained a temperature closer to 20 ºC.

The increased compaction towards the lava contact is consistent with loading and the observed plastic grain deformation during hydration, brittle deformation (broken annuluses) and mechanical compaction. The weakening of clasts during palagonitisation probably facilitated increased compaction. Indeed, the brown glass may even be gel palagonite pseudomorph (cf. Stroncik & Schminke, 2002). Since the intergranular clay (palagonite) only appears to form where grains are in contact and does not fill pore throats, the major permeability reducing agent is porosity reduction by compaction loading.

Sample	Distance below Lava (m)	Porosity (%)	1σ error
IGHC2	0.00	18.40	1.7
IGHC3	0.20	30.80	2.0
IGHC4	0.35	40.60	2.2
IGHC5	0.55	45.30	2.2
IGHC6	0.62	49.20	2.3

Table. 5.1. Rekjanes peninsular locality samples (IGHC), distance below lava and porosity. See Appendix for full table including mineral phases.

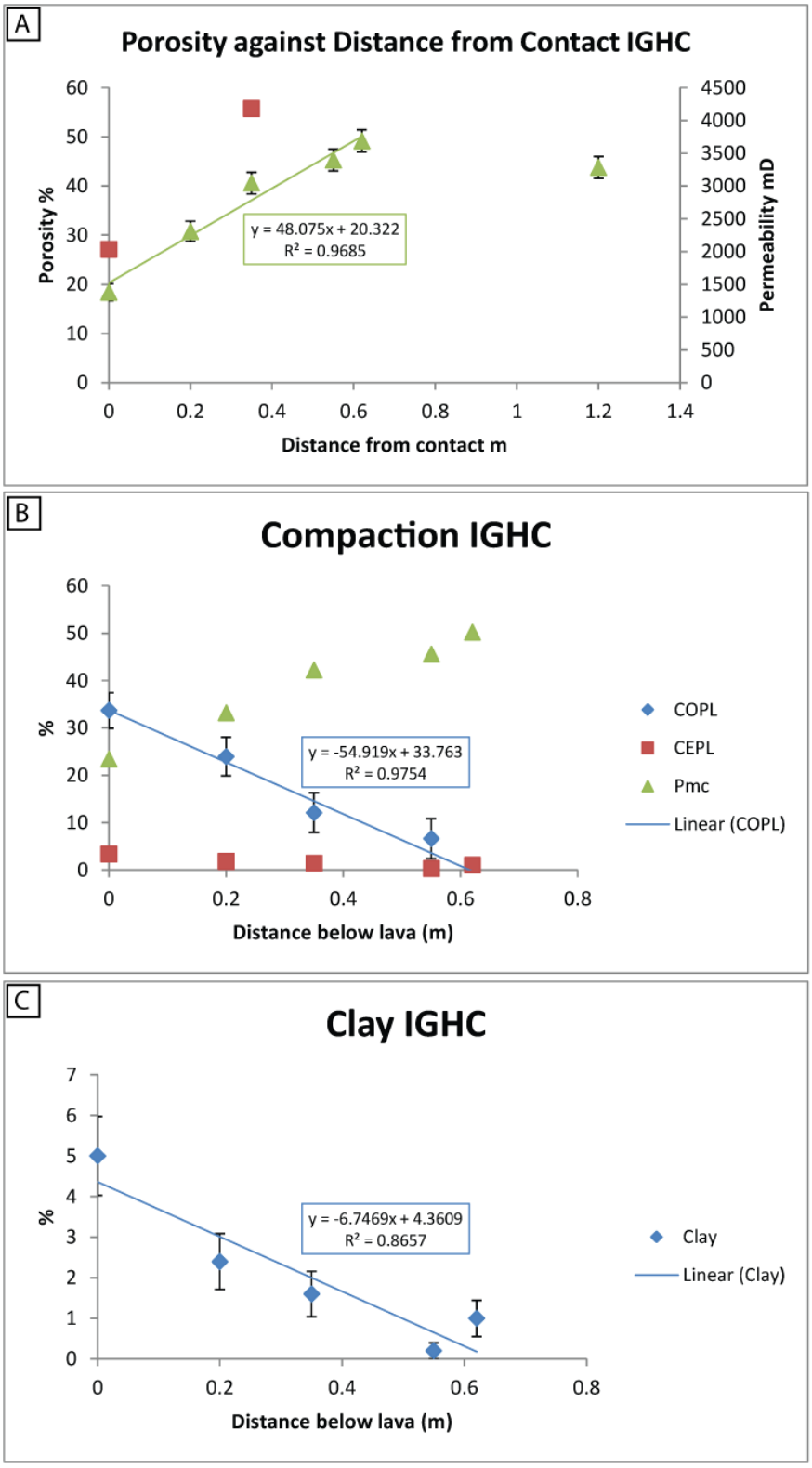

Fig. 5.5. Graphs against distance below lava. (A) Porosity decreases toward contact from 45-50 % background to 18 % at the contact. (B) Porosity loss is dominantly due to compaction (COPL) which increases in magnitude towards the contact. CEPL increases slightly towards the contact due to clay cementation increase. (C) Pore-filling clay increases towards the contact as glass alters to clay.

5.2.2 Outcrops beside Highway 32.

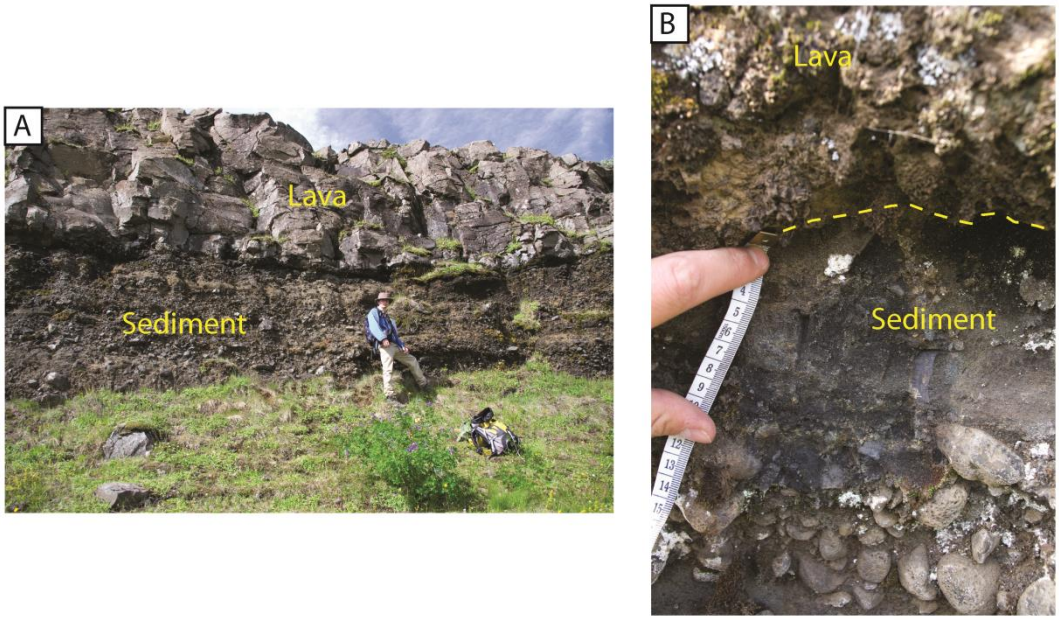

Fig. 5.6. Photographs of the outcrop north of Highway 32. (A) Photograph facing north, the fluvial volcaniclastic sediment consisting of sand to cobble sized clasts can be seen below the basalt lava flow. (B) Contact between lava and sediment, clearly the sediment is unlithified.

This is a roadside outcrop on the northwest side of Highway 32 near Asolfsstadhir (Fig. 5.1B.). The outcrop is a small cliff, about 10 m high which faces southeast. There is up to 5 m of consolidated fluvial conglomerate, with clasts ranging from <0.3 mm to 10 cm (Fig. 5.6A.). Most of the sedimentary rock is clast-supported, although some beds appear supported by a silt matrix (Fig. 5.6B.). Unlithified peaty palaeosols are intermittently present along the base of the lava.

Four samples were taken at increasing depths below the lava contact. All of the samples were lithified, but were too weak to transport without wrapping in soft paper.

At the contact the sediment consists of angular to sub-rounded dark brown basaltic glass fragments ranging from 50 μm to 1 mm in diameter. Some of the larger glass fragments contain plagioclase phenocrysts. The sample has a fine-grained

matrix at the lava contact. Primary porosity is 30.8 % (±2.1). Authigenic minerals are probably pore-filling clay, although a detrital origin for this cannot be ruled out. Compactional porosity loss was calculated using a depositional porosity typical of fluvial systems (44.75 % (±2.0), Lundegard, 1992, see Chapter 3) and was found to be 18 % (±4.0) and CEPL, 1.5 %. Visual evidence for compaction at thin-section scale is the abundance of long edge contacts between detrital grains (Fig. 5.7C.), although at the contact the grains show point contacts, where a matrix is present.

A second sample taken at the contact, which comprised coarser material with less matrix. This sample has a porosity of 13 % (±1.5) and COPL of 30 % (±3.5). Authigenic, intergranular clay (8 %, ±1.2) is more abundant than for the initially matrix-rich sample. The cementation component of porosity loss is 5.6 %.

At 10 cm below the contact the sediment is composed of larger volcanic glass fragments (~ 500 μm). Scoria clasts can be identified, albeit broken or rounded (Fig. 5.7D.). Intergranular clay minerals are present (6.2 %, ±1.1) and are usually associated with the finer-grained volcanic glass. An absolute authigenic origin cannot be attributed considering the depositional facies. Porosity is 15.6 % (±1.6), with most porosity reduction by compaction (COPL= 29 %, ±3.6). The cementation component of porosity loss, assuming an authigenic origin of the clays is 4.4 %. Compaction is evident in thin-section, through occasional long edge contacts between grains and rare interpenetrating grains are present where there is a hardness contrast (e.g. the two grains in the top right of Fig. 5.7D.).

At 30 cm below the lava, the outcrop is clast supported conglomerate composed of epiclastic rounded basalt clasts up to 3 cm diameter. The conglomerate was not sampled because of dissimilarity to previous samples and the potential difficulty in petrographic analysis due to large clast size. The material sampled at 30

cm depth was therefore selected to be similar to the appearance of the 10 cm sample. In thin-section, 30 cm below the lava, the sediment is coarser-grained, and is made up of highly vesicular scoria clasts and less vesicular dark brown glass clasts, both clast types are sub-rounded and up to 1 cm in diameter. Porosity is partially filled by a matrix composed of fine-grained volcanic glass fragments, which are inferred to be broken scoria. Intergranular porosity is 13.6 % (±1.5), with porosity reduction dominated by compaction (COPL= 33.4 % (±3.5), cementation is minor (CEPL= 2.3 %). Other than mechanical compaction through grain reorganisation, no other evidence for compaction is apparent such as grain deformation or crushing.

Sample	Distance below Lava (m)	Porosity (%)	1 sigma error
IG1	0.00	30.80	2.0
IG4	0.00	13.00	1.5
IG3	0.10	15.60	1.6
IG2	0.30	13.60	1.5

Table. 5.2. Highway 32 locality samples, distance below lava and porosity. See Appendix for full table including mineral phases.

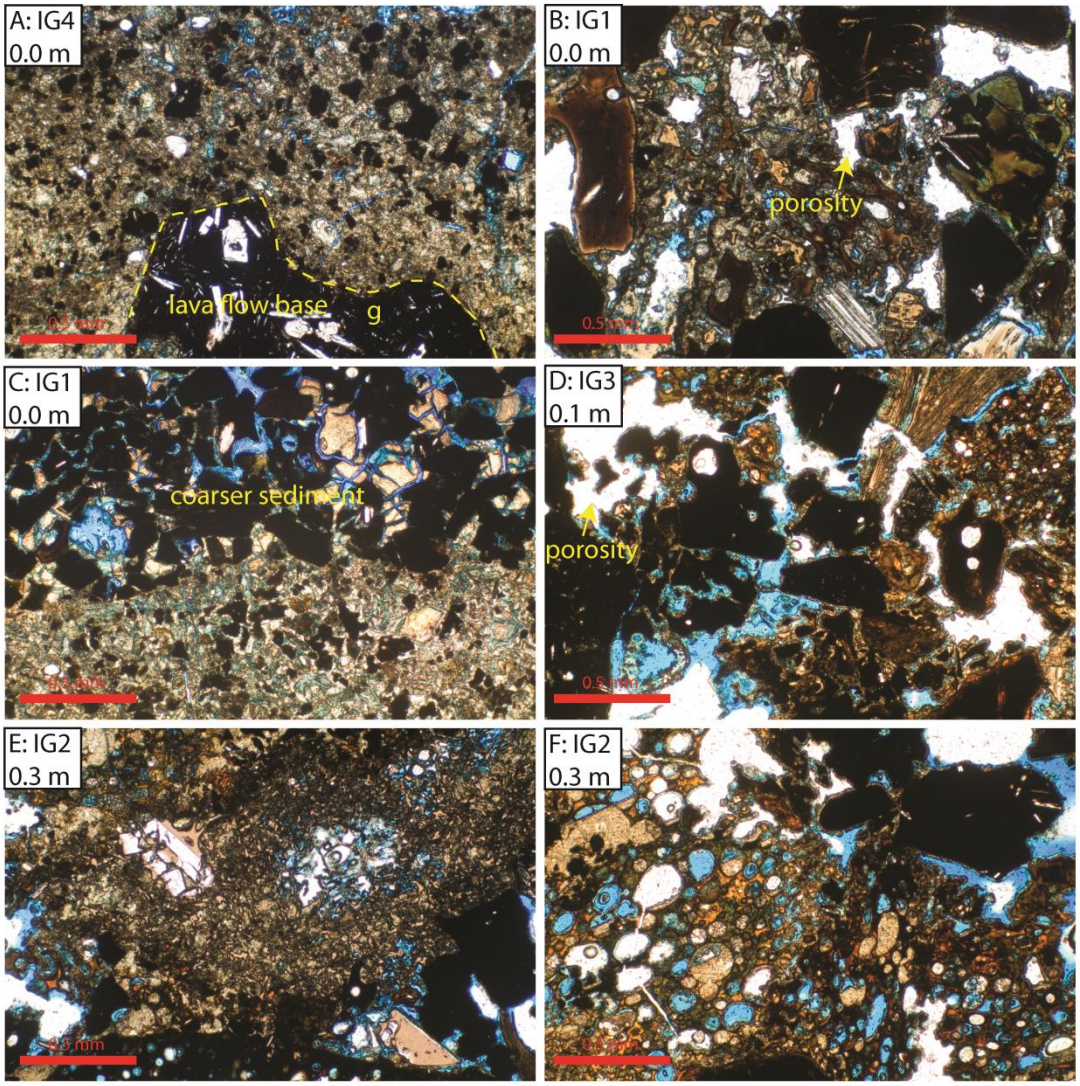

Fig. 5.7. PPL Photomicrographs of sediment below lava flow in Fig. 5.6. (A) At the contact sediment consists of fragments of basaltic glass and lithic clasts of basalt (epiclastic volcaniclastic sandstone). Porosity is present and clay minerals make up a large proportion of the matrix. (B) (some porosity is white-indicated) At the contact grain contacts are point contacts only, some grains show evidence of weathering to clays. (C) Where coarser sediment exists at the contact (upper), primary pores are larger and interconnected, angular grains contact along edges as well as points suggesting some compaction. (D) 0.1 m below the contact primary porosity increases and intragranular porosity (vesicles in volcanic glass) are rounded suggesting little compaction. (E) 0.3 m below the contact some of the detrital volcanic glass grains are light coloured (cf. Fig. 5.4.) and others are dark, the dark grains were probably in the fluvial system long before the lava emplaced, but the light glass is probably younger and not affected by lava emplacement. (F) 0.3 m below the lava primary and intragranular porosity is high, round vesicles appear undeformed.

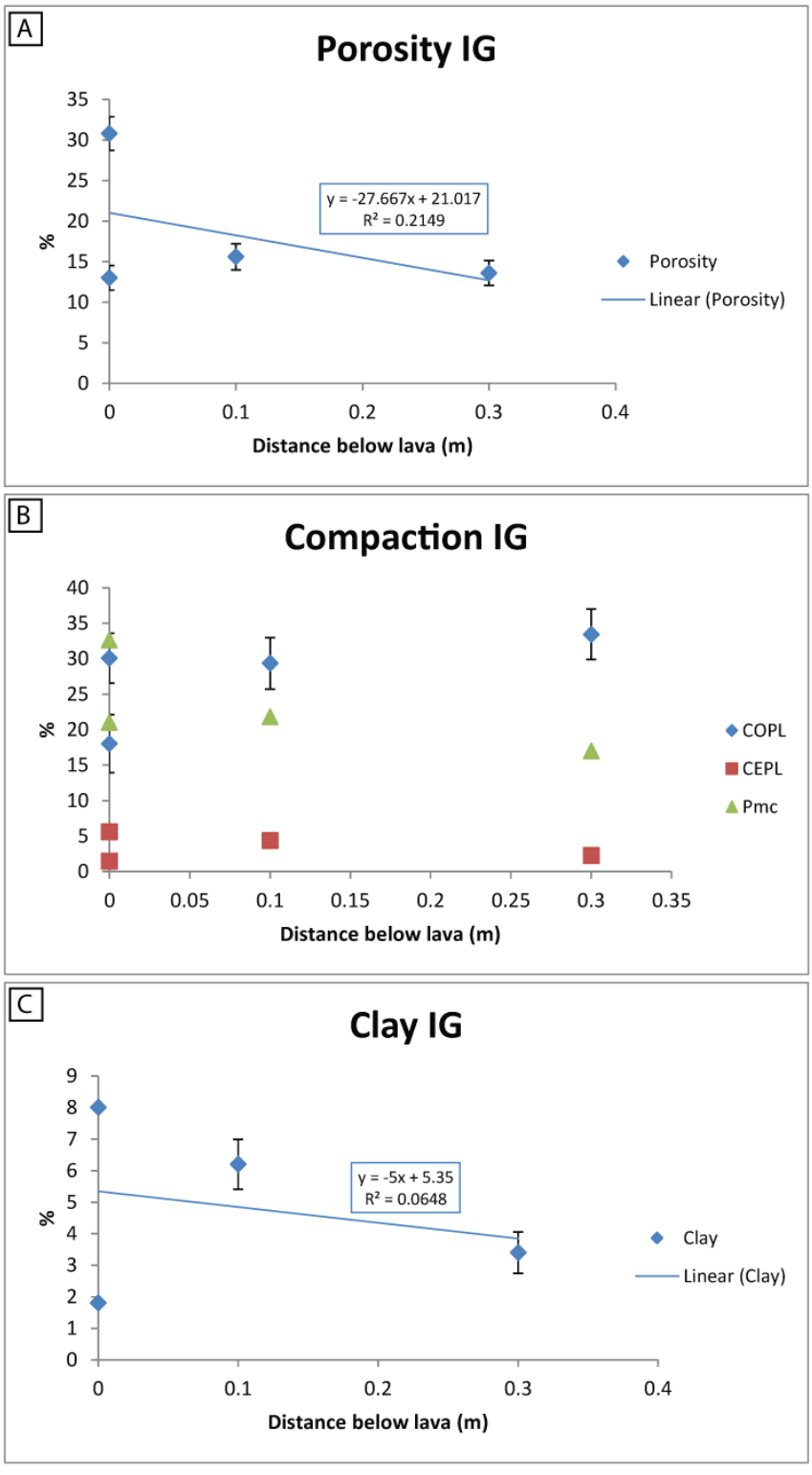

Fig. 5.8. **Graphs against distance below lava. (A) Porosity increases towards lava contact, unlike any other outcrop in this thesis. (B) No trends are apparent in the compaction data. (C) Pore filling clay decreases away from the contact, with a very weak correlation. The Highway 32 outcrop shows much variability, with no distinct trends developing.**

Significant variability was found to exist between all of the samples at the Highway 32 locality. This is probably inherited from the depositional facies; the sediment is temporally and texturally heterogeneous. The consequence is that no correlation between porosity and depth beneath the lava was observed (Fig. 5.8A. The weak negative correlation is the opposite of all other localities. The outcrop has been included because the overall COPL is high; indeed much higher than expected for sediment only buried by ~ 10 m of lava.

The average COPL for the highway 32 fluvial sedimentary rocks sampled is 27.7 % (±3.6). If the assumption is made that the fluvial sediments here behave like uncemented siliciclastic sediments (they are largely uncemented and composed of rounded to sub-rounded grains), then a comparison with the calculated COPL from the data in Gluyas & Cade (1998) would suggest burial depths of ~ 2.4 km (Fig. 5.9.). This is clearly much higher than the observed burial of ~ 10 m). Even considering the possible large uncertainty due to the sediment composition, the observed compaction is far in excess of the expected 'normal' compaction due to normal burial processes alone. It is therefore suggested that the emplacement of the lava flow facilitated enhanced compaction in the shallow subsurface. This compaction did not completely remove porosity, such that even at the lava contact porosity ranges from 13.0 % to 30.8 %.

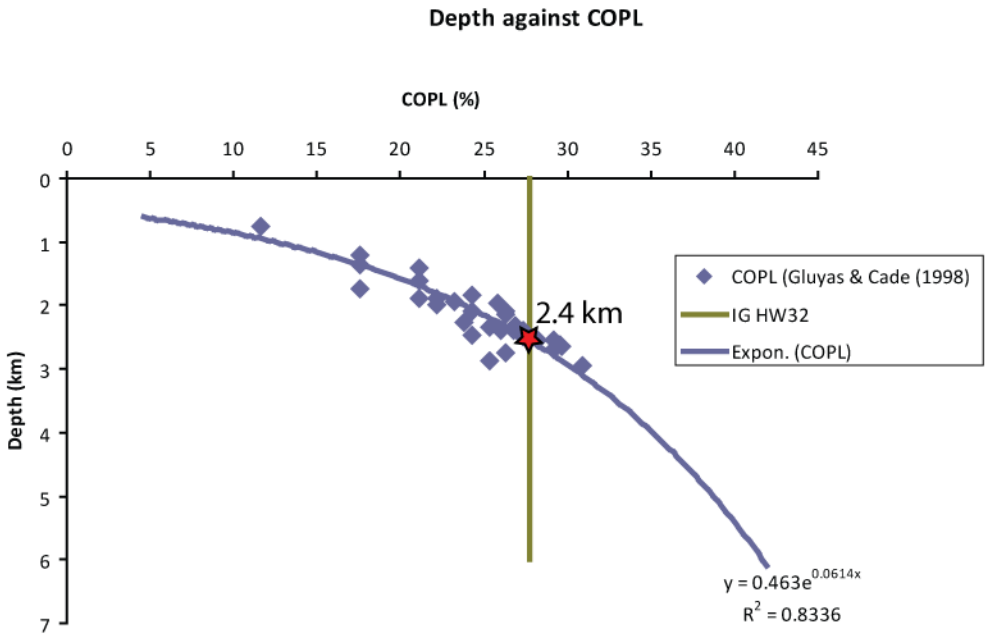

Fig. 5.9. Plot of burial depth against COPL calculated from data in Gluyas & Cade (1998). The vertical line is the measured average COPL at the Highway 32 outcrop, which corresponds to ~ 2.4 km burial depth. Clearly compaction is above what would be expected for ~ 10 m of burial.

5.3 Diagenesis of siliciclastic/volcaniclastic sediments, NW USA.

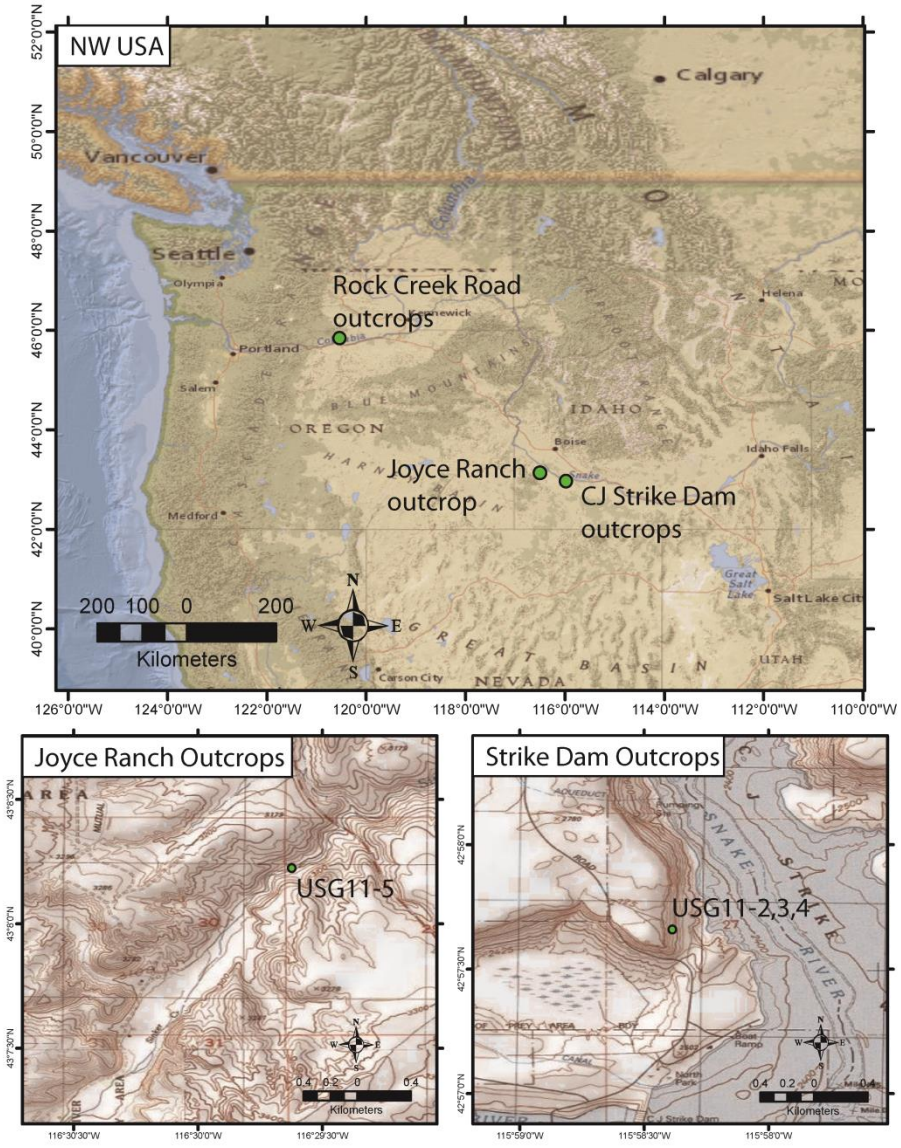

Fig. 5.10. Maps showing locations of case studies in NW USA. (A) Map centred on Idaho, Washington and Oregon. Rock Creek Road, Joyce Ranch and Strike Dam are indicated.

Three localities have been included from the Columbia River Basalt province (CRB) and Snake River Basalt province (SRB), NW USA.

5.3.1 Strike Dam, outcrops, Idaho, Snake River Basalts

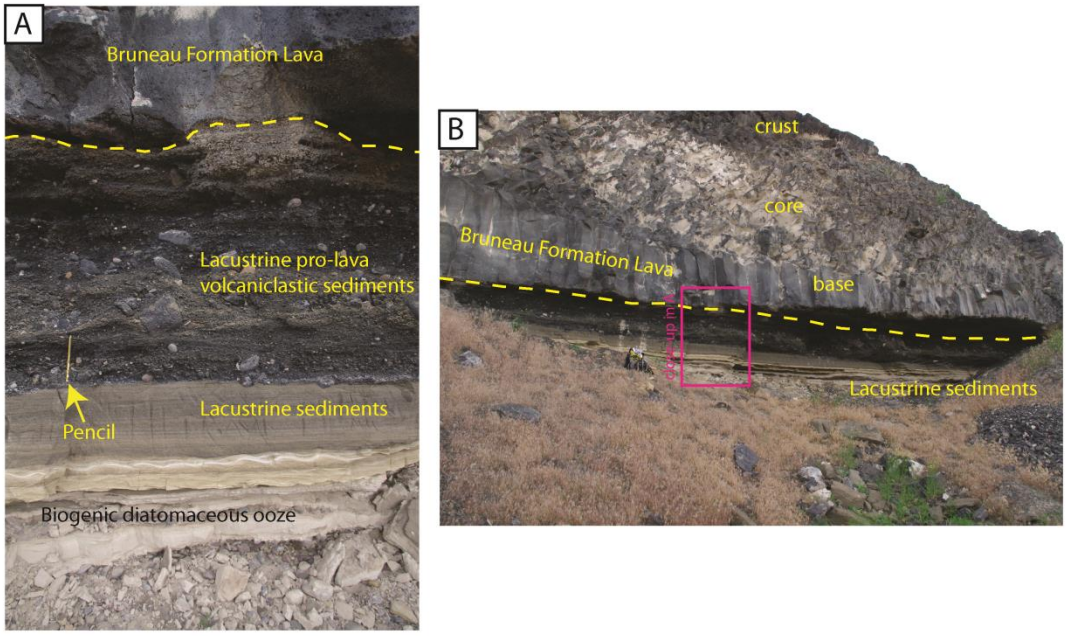

Fig. 5.11. Photographs of outcrops to the NW of Strike Dam. (A) Close up of the lacustrine sediments below the Bruneau Formation lava flow. The varied lithology of the sediments is labelled. (B) Overview of the outcrop in A (bag for scale). The lava flow is ~ 5 m thick and is a tabular sheet. Both facing NW.

The outcrops at Strike Dam are at 42° 57.677' N 115° 58.386' W at 809 m altitude in an east facing cliff (Fig. 5.11B.). At outcrop the sediments of interest are directly below a lava are lacustrine, and sediments have a significant volcaniclastic component (volcaniclastic= 22.4 % (±1.9), siliciclastic= 26.6 %(±2.0)). This sediment layer is composed of angular to rounded basalt clasts from large pebbles to coarse sand. This coarse layer is approximately 32 cm thick (Fig. 5.11A.). Below this layer is 38 cm of fine laminated sandstone composed of rounded to angular quartz grains and fragments of scoria or tuff (now broken angular glass). The sand is very fine to medium grained and overlies a diatomite ooze that reaches to the bottom of the exposure.

The palaeoenvironment in the region prior to lava emplacement is suggested to be a series of long lived lakes lying within NW-SE trending graben, which

probably initiated at 12 Ma (Godchaux & Bonnichsen, 2002). The initiation of volcanic activity (rhyolites erupting at 15 Ma and basaltic eruptions at 9 Ma) was initially in association with the lakes, producing sub-lacustrine vents and sub-aerial vents (Godchaux & Bonnichsen, 2002).

The sediments are overlain by a ~ 5 m thick basalt lava flow. The lava flow is basaltic and has a well-defined planar contact with the underlying sediments (Fig. 5.11.) It has a chilled base, which contains crude columnar jointing, the core of the lava flow is chaotically jointed (entablature) (cf. Long & Wood, 1986). The upper crust of the lava is vesicular. The lava is part of the Pleistocene Bruneau Formation (e.g. Bonnichsen & Godchaux, 2002; Malde, 1989).

At the lava-sediment contact, primary porosity is 30.6 % (±2.1), and intergranular clay is 8.2 % (±1.2). Cementation dominates porosity loss (CEPL= 10.9 %) and compaction is comparatively minor (COPL= 4.7 %, ±4.0). Evidence for compaction is rare; most grains are floating in thin-section.

At 30 cm below the contact (depth), both compaction and cementation are minor (COPL= 8.2 %(±4.2), CEPL= 0.4 %). porosity is 39.4 % (±2.2). In thin-section most grains are floating (Fig. 5.12B.).

At 50 cm depth, the sediment is finer grained and there is a component of biogenic silica (ooze) that fills pores. Porosity is 44.4 % (±2.2) and compaction is petrographically minor.

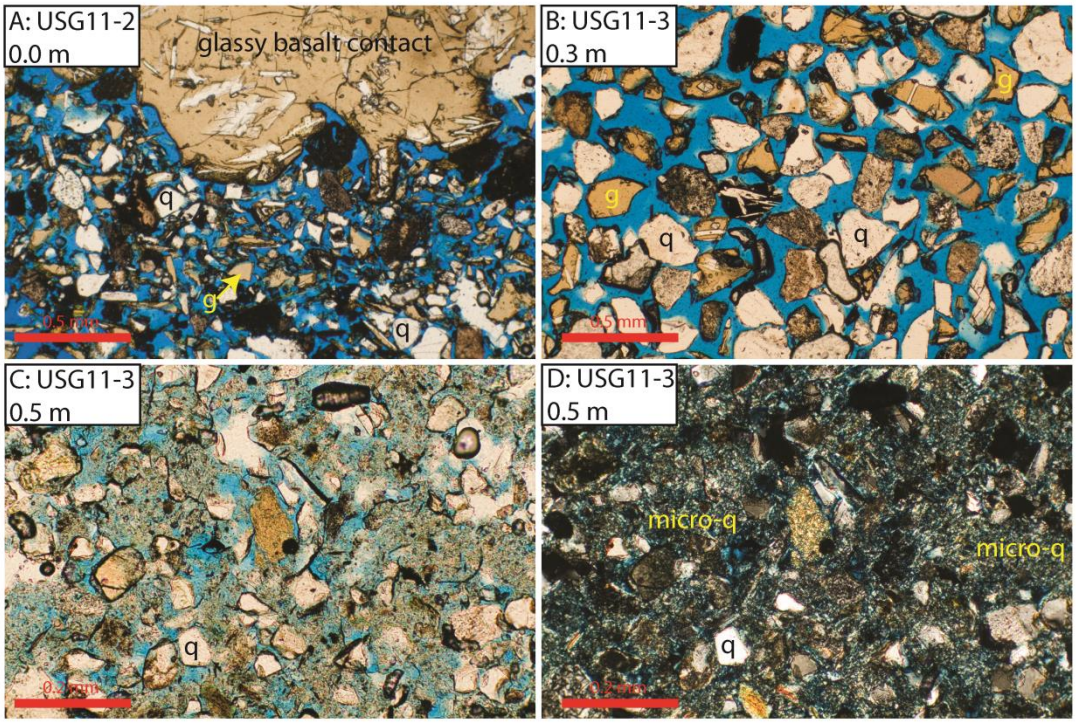

Fig. 5.12. Photomicrographs of sediment samples from below the lava at Strike Dam. (A PPL) Sediment at the contact, 30.6 % primary porosity is preserved. (B PPL) 0.3 m below contact sediment is same composition as at contact but less compacted. (C, D PPL) 0.5 m below the contact sediment has high proportion of microcrystalline quartz with high microporosity which is a biogenic siliceous ooze. Granular detrital clasts are not compacted.

The direct effects of the lava emplacement on these lacustrine sediments are minor. Porosity increases away from the contact due to decreasing compaction and cementation. Both of these measures, however show little real variation. Porosity only reduced to 30.6 % (±2.0) at the contact from a hypothesised depositional porosity of 44.75 % (Lundegard, 1992).

It is inferred that little heating occurred in these high porosity lacustrine sediments during lava emplacement. It has been shown that heating and mineral reactions facilitate enhanced compaction (above and Chapter 4.). Few such mineral reactions are in samples from this outcrop; the volcanic glass remains clear and un-palagonitised. One such mechanism that could cool the sediment is the heating and transport of an excess volume of water. If the lava emplaced onto the water saturated

porous sediment, with a hydraulic head generated by recharge at a higher level, water would flow through the sub-basalt sediment. If this head was sufficient to overcome the overpressure generated due to the heating of the water, continuous subsurface flow of water would be possible and cooling would be the effect. This is consistent with the palaeogeographical setting. It is in contrast with the Rekjanes peninsular outcrop, where due to the interstitial water being sea water, no hydraulic head would have existed. Any water would have only been mobile due to pressure gradients created by heating.

The implication is that somewhere, along the flanks of the lava flow a hot spring must have existed during lava cooling. The flow of groundwater through shallow sub-basalt sediments under a hydraulic head in fluvial-lacustrine depositional systems is not uncommon. For instance a lava flow that dammed a river at 64° 43.214’ N 19° 37.116’W in Iceland was found to have continued flow of the same river through the sub-basalt sediments (own work). The river reissues along the edge of the lava flow. This head would have also been present during flow cooling, at which time, these springs would have been at elevated temperatures.

Sample	Distance below Lava (m)	Porosity (%)	1 sigma error
USG11-2	0.00	30.60	2.0
USG11-3	0.30	39.40	2.2
USG11-4	0.50	44.40	2.2

Table. 5.3. Strike Dam, Snake River Basalt (SRB) locality samples, distance below lava and porosity. See Appendix for full table including mineral phases.

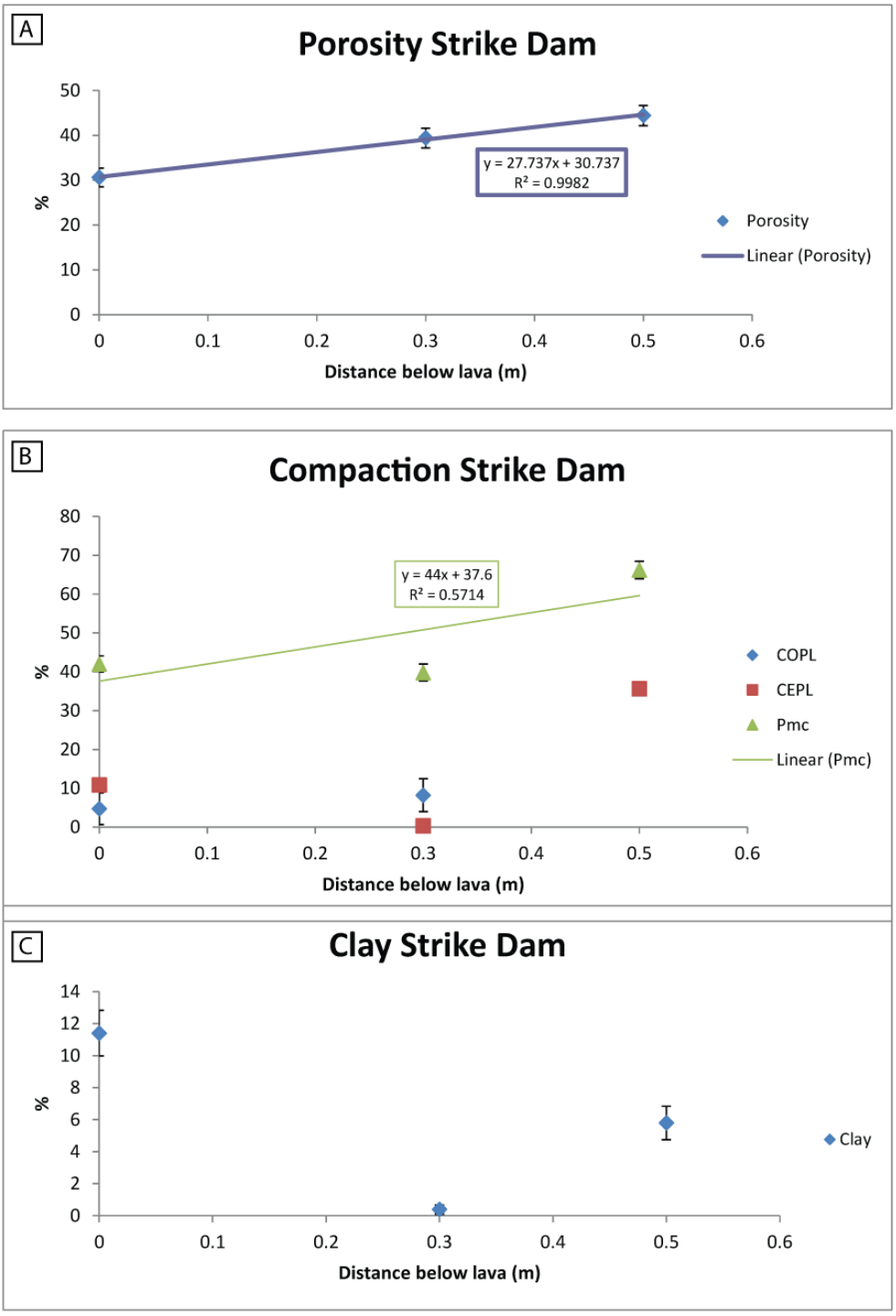

Fig. 5.13. Graphs against distance below lava. (A) Porosity decreases towards the lava flow from 44 % to 31 % at the contact. (B) Only 2 reliable points for compaction as the biogenic sediment appears not to compact the same way as the clastic sediment, no useable data. C) Clay increases towards the contact, although correlation is weak and same caveat as for the compaction applies.

5.3.2 Outcrop at Joyce Ranch, Idaho.

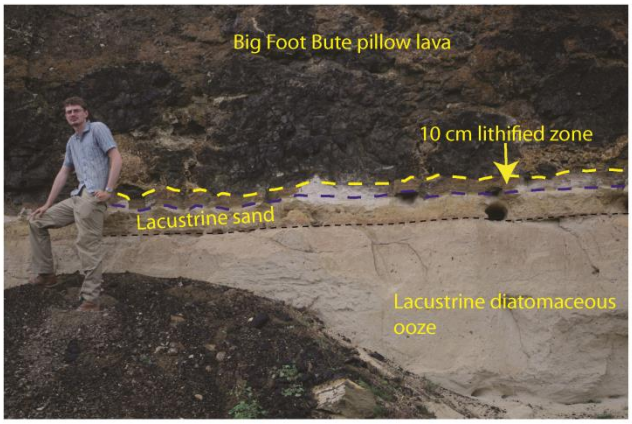

Fig. 5.14. Photograph of outcrop at Joyce Ranch facing east. Lacustrine sediments are directly below an un-invasive pillow lava layer from the Big Foot Bute pillow lava. 10 cm of the lacustrine sands are lithified with about 20 cm below that un-lithified. Below this layer is silicic ooze.

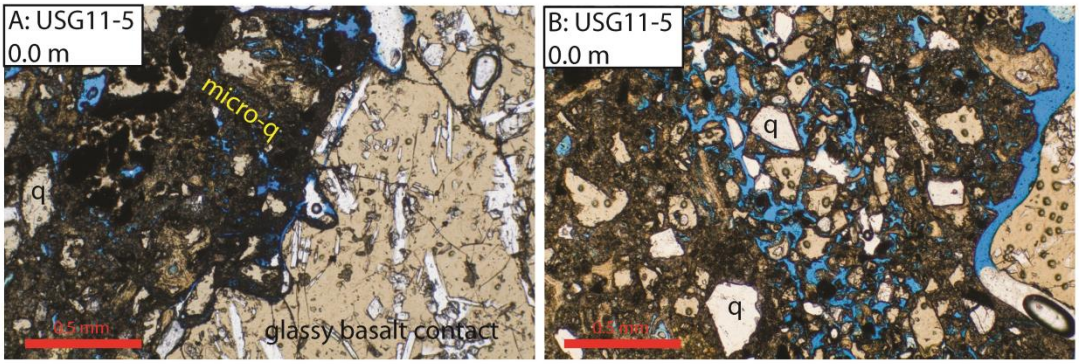

Fig. 5.15. PPL Photomicrographs of contact at Joyce Ranch. (A, B) Glass rich but compacted sediment dominated by angular fine to very fine sand quartz grains.

The Joyce Ranch outcrop is located on the small track that links Joyce Ranch with the Grand View to Murphy road. The outcrop is at 43° 07.839' N 116° 30.043' W and at 936 m altitude. The outcrop is a west facing road-cut about 8 m high. It is made up of ~ 3 m of lacustrine sediments that are overlain by 5 m of exposed pillow lavas. The sedimentary substrate is composed of an uppermost layer ~ 20 cm of mixed volcaniclastic-siliciclastic sand (volcaniclastic= 41.4 % (±2.2), siliciclastic= 10 %(±1.3)). The uppermost 10 cm nearest the pillow basalt is lithified. Below this is diatomaceous ooze which reaches to the base of the exposure. The pillow basalts are

of the Big Foot Bute formation and individual pillows are ~ 1 m in diameter, the skins/rinds of the lobes are palagonitised.

One sample was collected at the contact. In hand specimen the rock is lithified, with abundant visible porosity. Petrographic analysis reveals that the primary porosity is 18.2 % (±1.7), with most porosity reduction through cementation by intergranular clays (CEPL= 24.6 %, COPL= 2.4 %, ±3.7).

This high degree of cementation may be false at this locality, due to the difficulty in distinguishing authigenic clay from detrital clay. If the assumption is made that the clay is all authigenic, the production of such large quantities is problematic. The only suggestion is that the higher volcaniclastic component compared to the Strike Dam locality was more prone to clay authigenesis. It is also possible that the high degree of water-rock interaction in the cooling pillows (evident in the palagonitisation) enriched circulating water in H_2 (e.g. Sansone et al., 1991). This would have then provided the acid for enhanced chemical decomposition of the substrate to clay.

The porosity loss here is likely therefore, a consequence of hydrothermal fluids circulating through the sediment and the pillow lava during cooling. Such a circulation is less through lava flows than pillows due to pillows having a higher permeability due to potential open discontinuities between each pillow.

5.3.3 Rock Creek Road outcrops, Washington, Columbia River Basalts

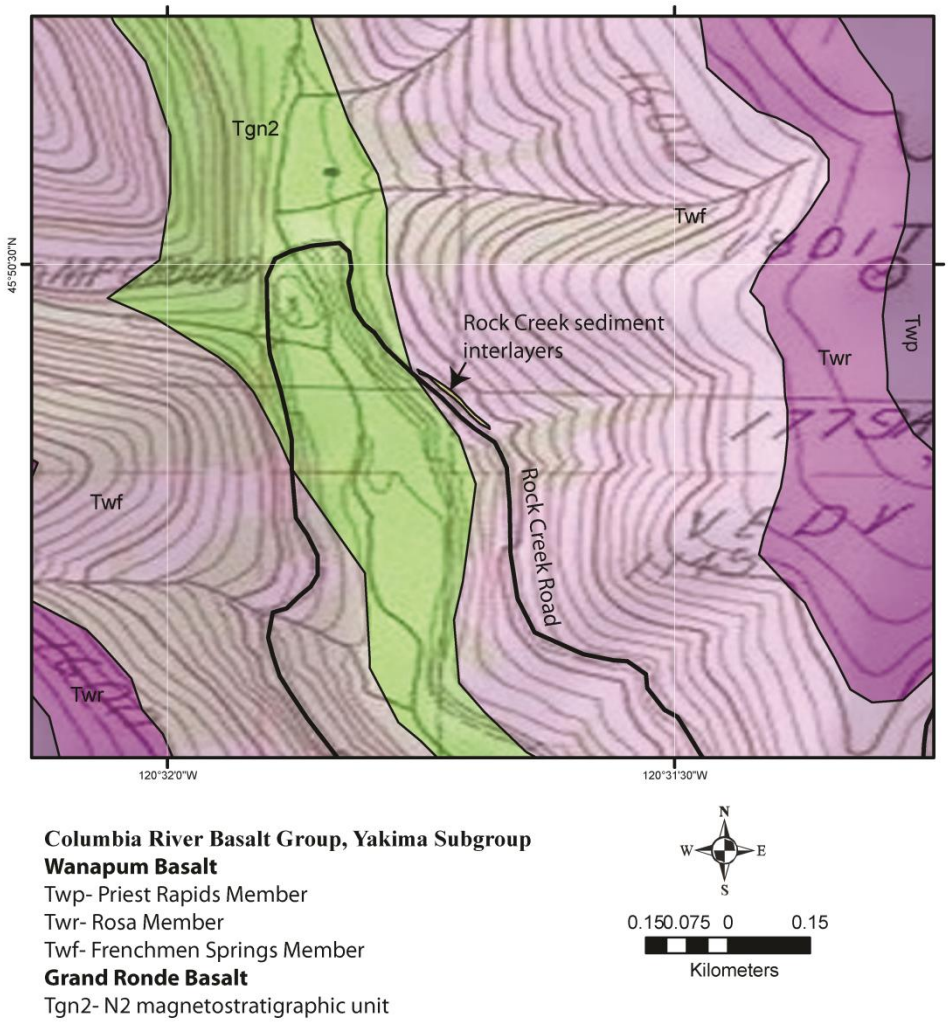

Fig. 5.16. Geological map of Rock Creek road at the location of the outcrop studied.

The Rock Creek Road outcrop is at 45° 50.206’ N 120° 31.660’ W at 350 m altitude (Fig. 5.17.). The outcrop comprises 1.8 m of siliciclastic sandstone (siliciclastic component average= 62.1 % (±2.1), volcaniclastic component average= 2.0 %, ±0.6) of the Vantage Member sediment interlayer. The sediments are resting on the Ginko flow of the Frenchmen Springs Member (Hooper, 1997), Wanapum Basalt, Columbia River Basalt Group. It is thought the sediment was invaded and rafted on the Ginko flow (Tolan et al. 2009), evidence for rafting suggested by Tolan et al., (2009) is the presence of several small dikelets extending upward from the

lower flow into the overlying sediment, quenching of the Ginko flow top to glass, fragments of the same sediment are found within the Ginko flow which are ‘baked’ (no description given of baking) and the sedimentary structure of the interbed is disturbed at the base. I was able to make these observations, with the exception of the baking. There is evidence for an invasive character of the Ginko flow, but this outcrop does not provide compelling evidence for rafting of the Vantage Member sediments based on my observations. The sediment interbed is overlain by the Sand Hollow flows (15.3 Ma) of the Frenchmen Springs Member (Hooper, 1997). No disturbance is noted at the base of the Sand Hollow lava flow (Tolan et al., 2009) and the contact is generally sharp.

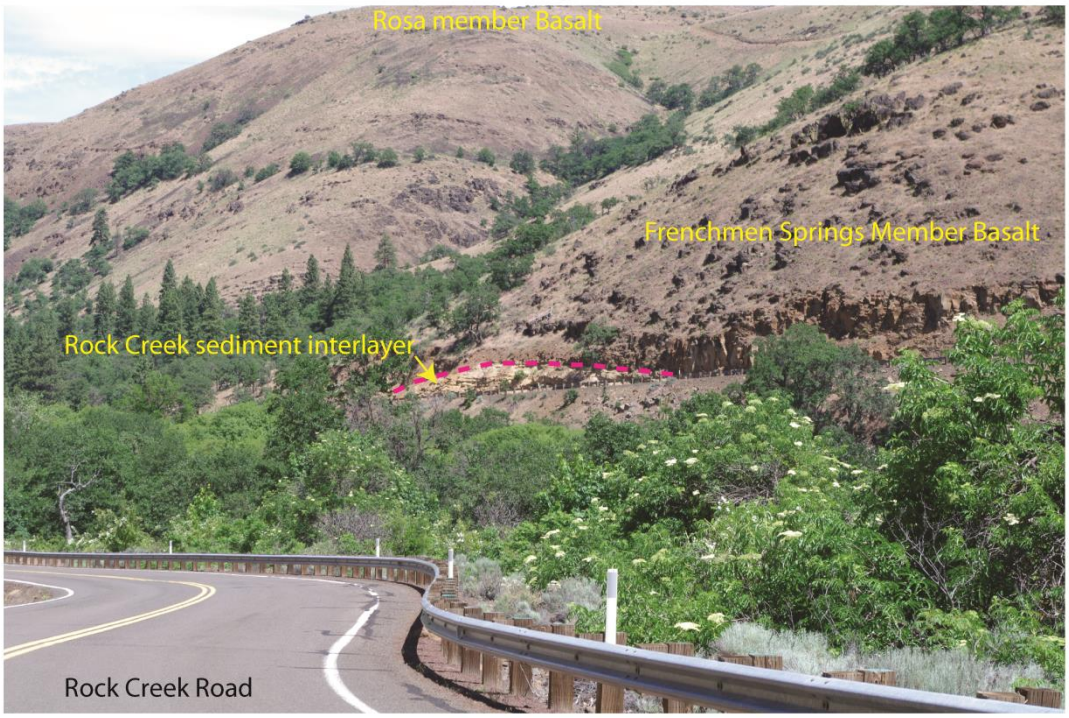

Fig. 5.17. Photograph of the outcrop studied, facing NE from the western part of Rock Creek road. The thin inter-basalt fluvial sediment body is outlined and indicated.

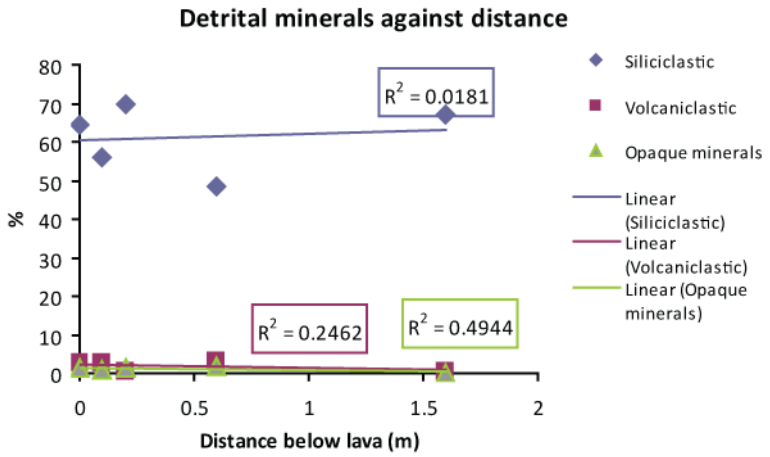

Fig. 5.18. Relationship between detrital sediment and distance below lava. No correlations exist with distance below the lava suggesting a relatively homogenous substrate.

Petrographically the sediment is a quartz arenite, with minor volcaniclastic (glass fragments) and bioclastic (wood, plant material) components. The siliciclastic sediment is sub angular to sub-rounded well sorted fine to medium-grained sand.

At the contact the sediment detrital composition is approximately the average. No correlations between detrital sediment composition and distance below the lava are apparent (Fig. 5.18). In hand specimen the sandstone at the contact is hard and clearly lithified, which is also apparent in the outcrop where it is harder than the underlying sediment and weathers slower than the underlying sediment. In thin-section the sediment porosity is 19 % (±1.8). Porosity reduction is primarily through compaction (COPL= 20.6 %, ±3.7). Compaction is evident in the thin-section: mechanical compaction through grain reorganisation is clear, point contacts are rare, most grains contact along long faces. Platy detrital fragments, such as the plant material in Fig. 5.19B are frequently bent around rigid detrital grains. No evidence for pressure solution was encountered. Porosity reduction is also through cementation. There is 11.4 % (±1.7) pore-filling clay (probably smectite?), which is the contributor to the cementational porosity loss (CEPL= 9 %).

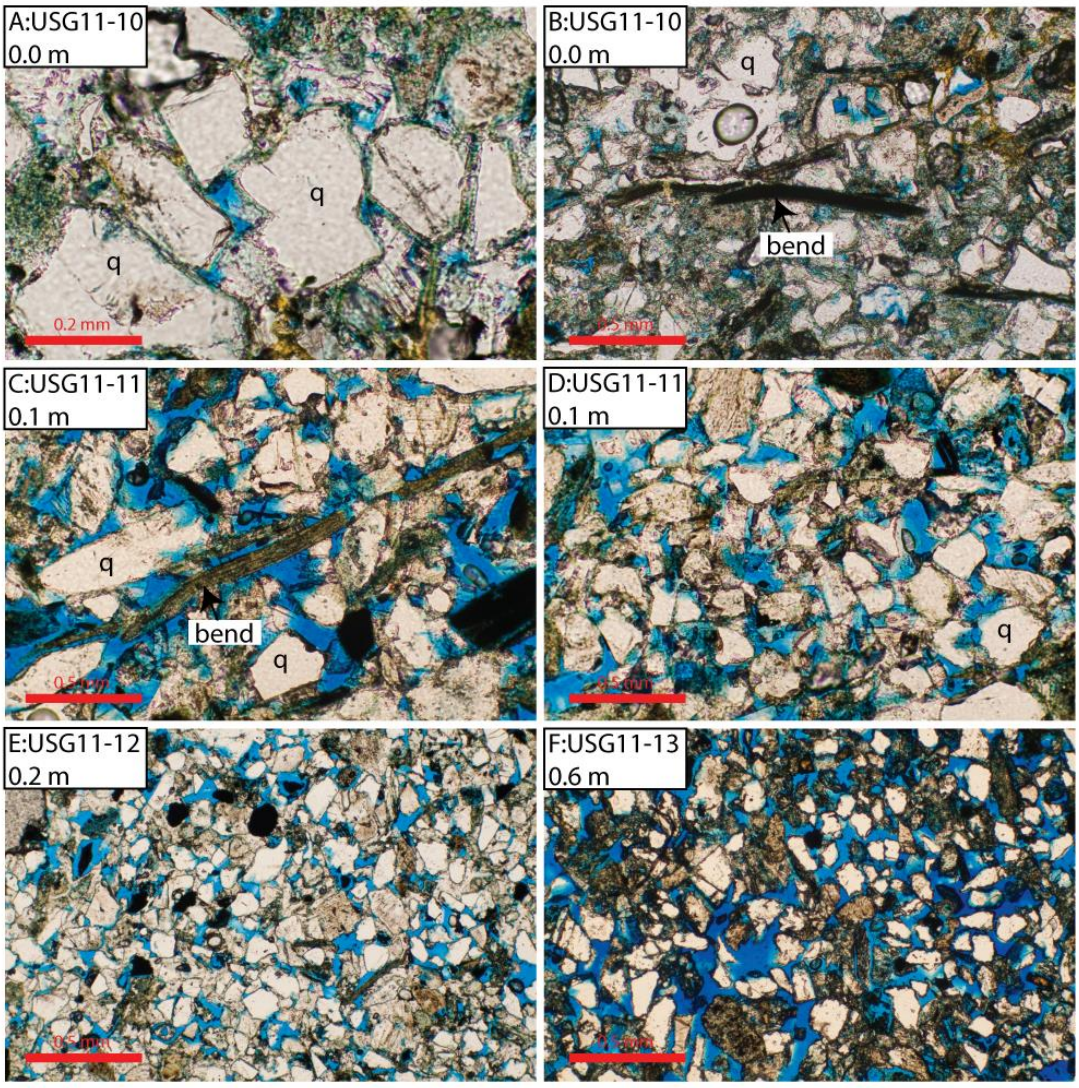

Fig. 5.19. Photomicrographs of the mixed, siliciclastic and volcaniclastic sediment at Rock Creek road. (A, B PPL) At the contact detrital grains frequently have edge to edge contacts clay fills some pores and high aspect ratio clasts (e.g. plant material) bend around detrital grains. (C, D PPL) 0.1 m below lava, compaction is less, plant material is still deformed around detrital grains, point contacts between grains are now dominant. (E PPL) 0.1 m below lava resembles 0.1 m below the lava. (F PPL) 0.6 m below lava, occasional grains are floating, point contacts are common and edge to edge contacts are rarer than closer to the lava, pore filling clay is rare.

At 10 cm depth below the lava, the sandstone is still lithified in hand specimen. In thin-section detrital mineral abundance is approximately average. Porosity is 28.8 % (±2.0). Porosity reduction, again is dominated by compaction (COPL= 12.9 %, ±4.0), which is evident in thin-section. Point contacts are rare, but more abundant that at the contact, the grain contacts are still dominated by long edge

to edge contacts. Platy detrital grains are bent around rigid grains (Fig. 5.19C, D). Clay proportion is 7.8 % (±1.2), giving a CEPL of 6.8 %.

At 20 cm depth below the lava, the sandstone is noticeably weaker than the lithified layer above. In thin-section detrital composition is near to average values. Porosity is 21.2 % (±1.8), porosity reduction is dominated by compaction (COPL= 25.9 %, ±3.7), which is evident in Fig. 5.19E. Grains are visibly mechanically compacted, with few point contacts, and many long edge to edge contacts. Cementation is minor, and clay is the authigenic phase (4.2 %, ±0.9) (CEPL= 3.1 %).

At 0.6 m depth, the sandstone is friable and uncemented. Porosity is 42.2 % (±2.2) (depositional porosity assumed to be 44.75 % (±2.0), Lundegard, 1992). Porosity reduction appears to have occurred completely through cementation by clay (2.8 %, ±0.7). The sandstone is under compacted (COPL= -0.5 %). The low compaction is evident in Fig. 5.19F, where most detrital grains are floating, or have point contacts.

The base of the sediment layer is cemented with analcite and a zeolite mineralisation, which is discussed in 5.3.4.

Sample	Distance below Lava (m)	Porosity (%)	1 sigma error
USG11-10	0.00	19.00	1.8
USG11-11	0.10	28.80	2.0
USG11-12	0.20	21.20	1.8
USG11-13	0.60	42.40	2.2
USG11-14	1.20	24.00	1.9

Table. 5.4. Rock Creek Road, Columbia River Basalt (CRB) locality samples, distance below lava and porosity. See Appendix for full table including mineral phases.

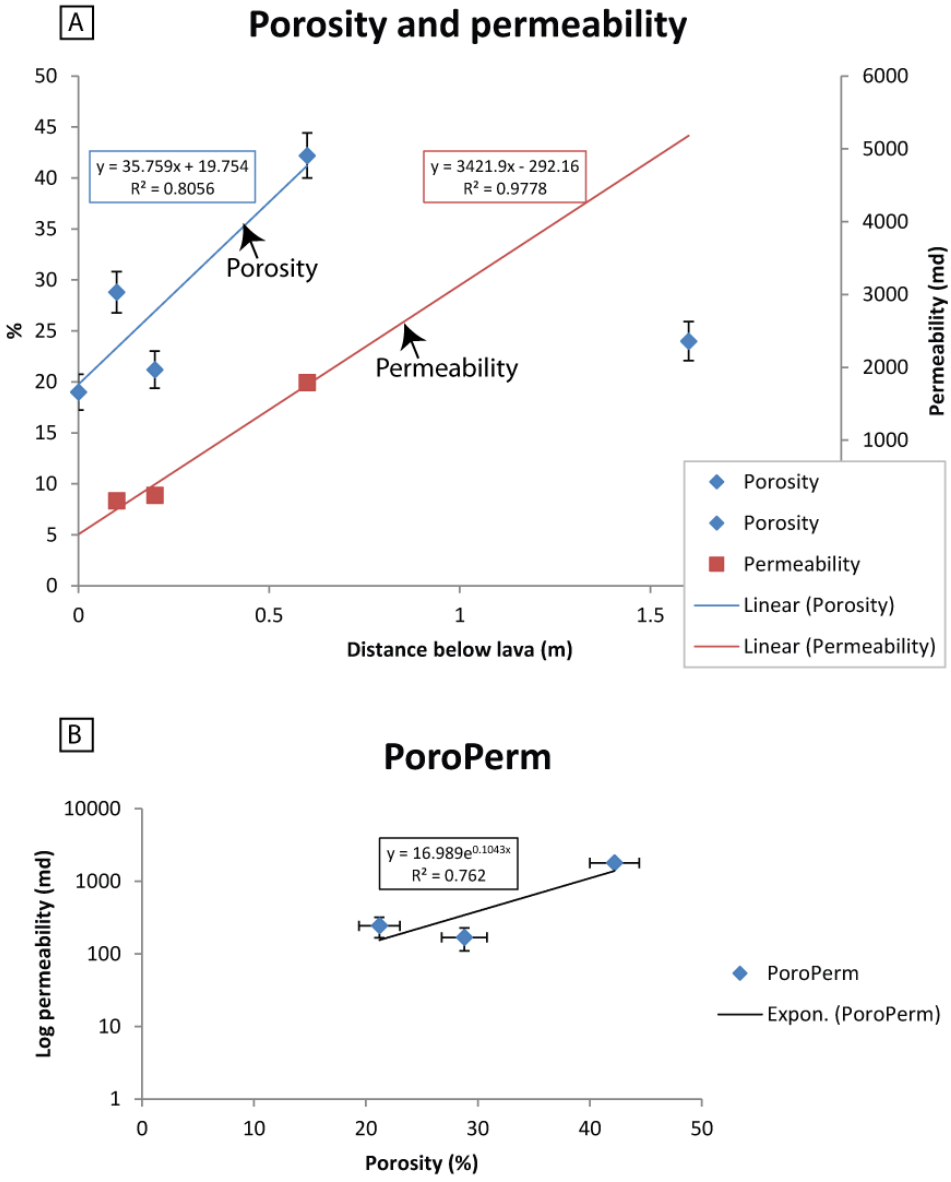

Fig. 5.20. **(A) Graphs of porosity and permeability against distance below contact. Both porosity and permeability increase below the lava. (B) Permeability has an exponential relationship with porosity, although it is weak with only 3 samples.**

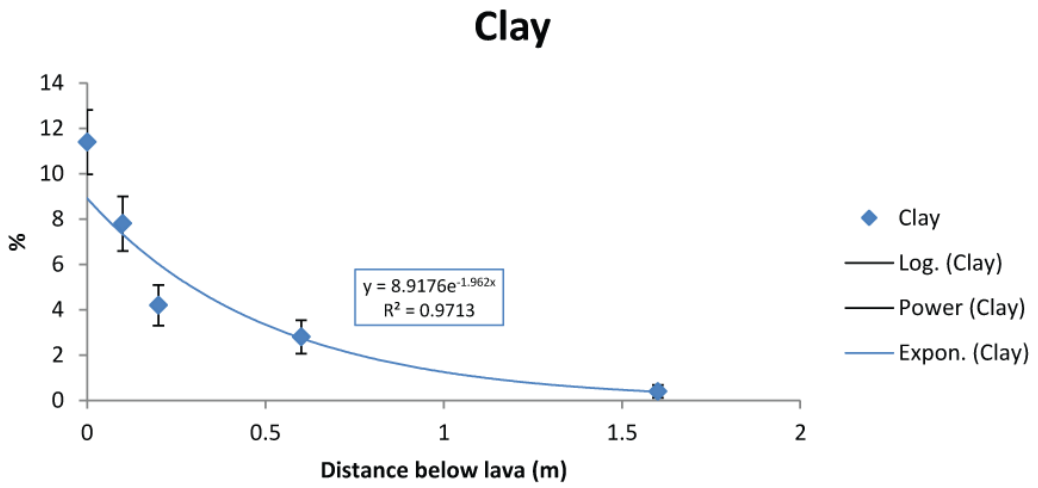

Fig. 5.21. Relationship of pore-filling clay against distance below lava is exponential and decreases below the contact.

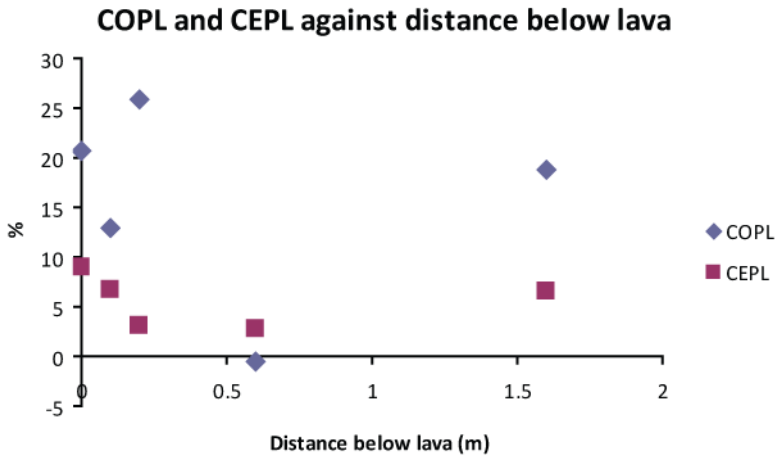

Fig. 5.22. Relationship between COPL & CEPL and distance below lava. Note the most distant point is strongly influenced by the zeolite cementation. The three samples nearest to the lava contact show an increase towards the lava.

Overall, the trend in the sediment layer is that of reducing porosity and permeability up towards the lava contact (Fig. 5.20A.). The porosity reduction is dominated by compaction near to the contact, with less compaction away from the contact (Fig. 5.22.). Cementation is also important, and decreases away from the contact. The lithification, like in the Rekjanes Peninsular example, is also due to the clay proportion, here ~ 4 % clay being required to cement the sandstone with ~ 26 %

COPL. The relationship between pore-filling clay abundance and the distance below the lava is shown in Fig. 5.21, and fits an exponential curve away from the lava.

The mechanism of porosity loss below the lava flow is therefore, like the other examples of lava resting on sediment, one where compaction dominates, with secondary importance of mineral authigenesis. The authigenesis of the clay is the important mechanism for lithification the rock. No evidence of 'baking' was found under this lava flow.

As the environment would have been fluvial at the time of lava emplacement, it is assumed that the sediments would have been saturated with water. A similar situation to the lacustrine examples (above) is inferred. The pore water would have been heated by the overlying lava, which would have facilitated the clay diagenesis via hydration of volcanic glass and reactive detrital grains. The weight of the lava provided the overburden for compaction. No calcite cement is present.

5.3.4 Zeolite cementation at Rock Creek

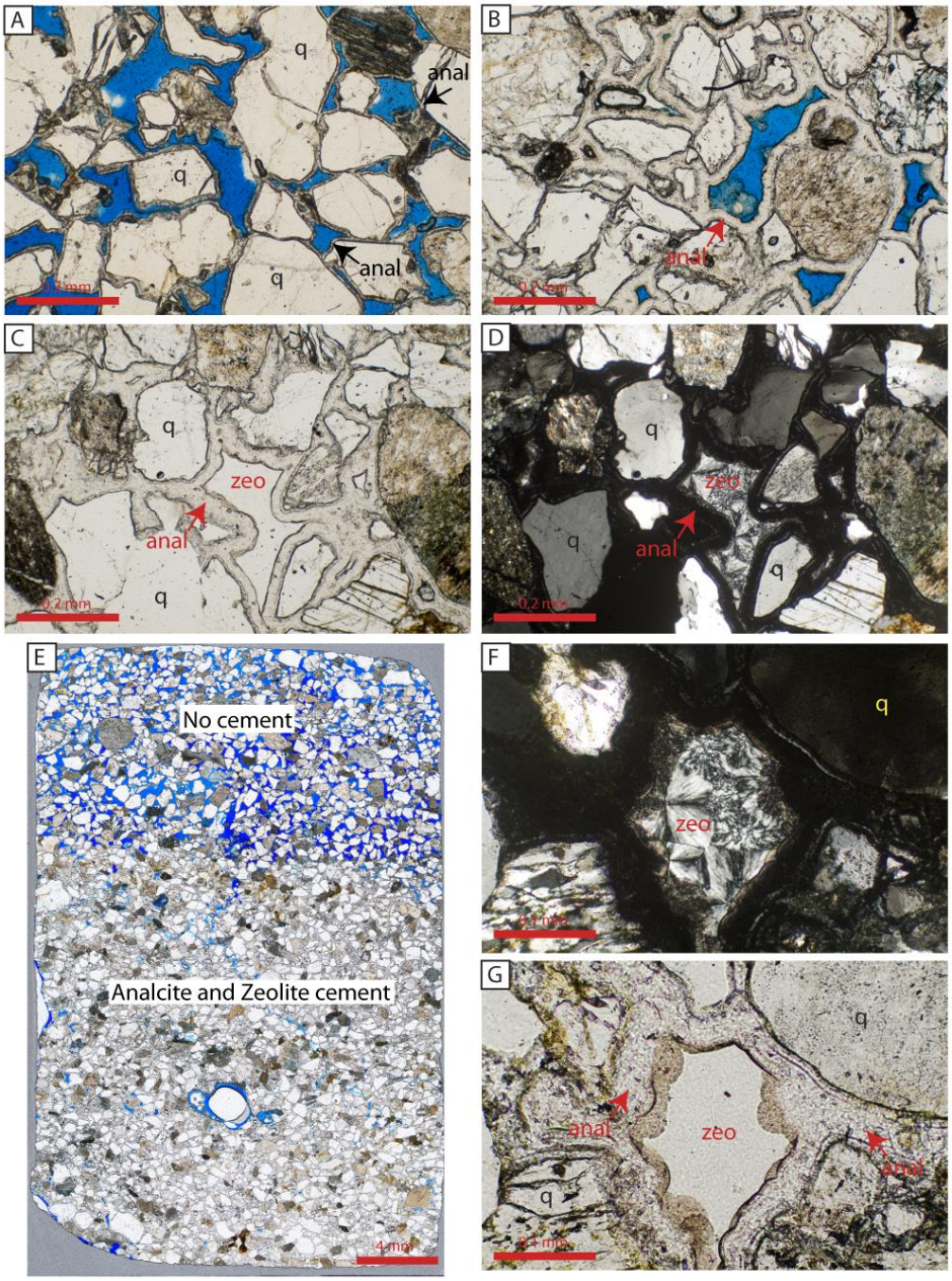

Fig. 5.23. Photomicrographs of the cemented sand at the base of the Rock Creek sediment interlayer. (A PPL) Relatively un-cemented sand at the interface between un-cemented sand and the cemented sand; the blue porous sand in E. The grain-coating mineral is analcite. (B PPL) At the boundary between un-cemented sand and cemented sand. The analcite begins to fill pores. This transition is over < 500 µm. (C PPL and D XPL) The sandstone within the cemented zone is first cemented with analcite (clear in PPL, nearly isotropic in XPL) and then with zeolite (possibly laumontite). (E) Full slide micrograph showing the upper un-cemented sandstone and the sharp transition to the analcite and zeolite cemented region. (F XPL and G PPL) Close up of zeolite cemented pore. The analcite precipitated first followed by the zeolite.

The basal 1.2 m of the sediment layer is cemented with analcite and zeolite (possibly laumontite). The hand specimen from the cemented sandstone is lithified and harder than the sandstone at the hot lava contact. Cross bedding is visible in the cemented sandstone. The cemented zone lays directly on the lava flow below, which has a glassy top. This glassy top of the underlying lava and the cemented sand (which was interpreted as 'baked') is used as evidence for an invasive flow and rafting of the sediment by Tolan et al., (2009). Tolan et al, (2009) also state that the sedimentary structures have been disturbed by the invasive flow. However, I made observations of cross bedding within the cemented zone at the base of the interlayer. The disturbance was localised and due to an invasion of the *overlying* Sand Hollow lava; this is restricted to a small area.

The nature of the sharp contact between the cemented and the un-cemented zone is of interest. The contact appears horizontal, despite the undulating surface of the lava below. It is very similar to the calcite cemented zone at the base of the upper of the three stacked dunes in Dune Valley, Namibia (Chapter 4.2.1.2). The interpretation is the same. It is suggested that a thin perched aquifer sat on the glassy flow top within the sediment interlayer. The aquifer water must have been hot for zeolite to form (Deer et al., 1992). The thin interface (Fig. 5.23A) where the analcite does not fill pores was probably due to capillary action above the phreatic zone lifting a meniscus of hydrothermal water along grain edges. Evidence of metamorphic re-equilibration of unstable silicic mineral phases was not observed.

5.4 Controls on reservoir quality at lava-sediment contacts

5.4.1 Lava flow thickness

The effect of lava flow thickness and how it related to the porosity reduction below the lava flow is of importance to this thesis. The effects have been investigated, firstly in a dry palaeoenvironment (siliciclastic Twyfelfontein Formation) and secondly in wet palaeoenvironments (CRB, SRB and Iceland). In the case of wet palaeoenvironments, both siliciclastic and volcaniclastic sediments have been studied.

To compare these case studies is fundamentally difficult because of the large differences in burial depth. The Namibian examples have been buried and exhumed ~ 5 km, the CRB and SRB have negligible burial and the Icelandic case studies have had only the capping lava burying the sediments. For all of the case studies, the sediment was unconsolidated at the time of lava emplacement.

Comparing the porosity and distance would therefore not be a useful analysis technique. Instead, the slope of the porosity-distance relationship has been calculated to the estimated background porosity for all of the case studies. The background porosity in the Twyfelfontein Formation is taken as 12.5 %, in Iceland the IGHC locality was directly measured as 49.2 %, the IG locality was taken as the fluvial depositional porosity in Lundegard (1992) 44.75 %, The CRB and SRB localities were taken to be the lacustrine depositional porosity in Lundegard (1992) 44.75 %. It is probably valid to take depositional porosities as the background for the CRB and SRB examples due to their very shallow burial. This measure therefore estimates the thickness of porosity reducing influence of the lava flow as opposed to the actual

porosity reduction. Fig. 5.24 shows these calculations in graphical form. Each line on the graph terminates at the background porosity, for which the distance can be found (see Table 1.5.).

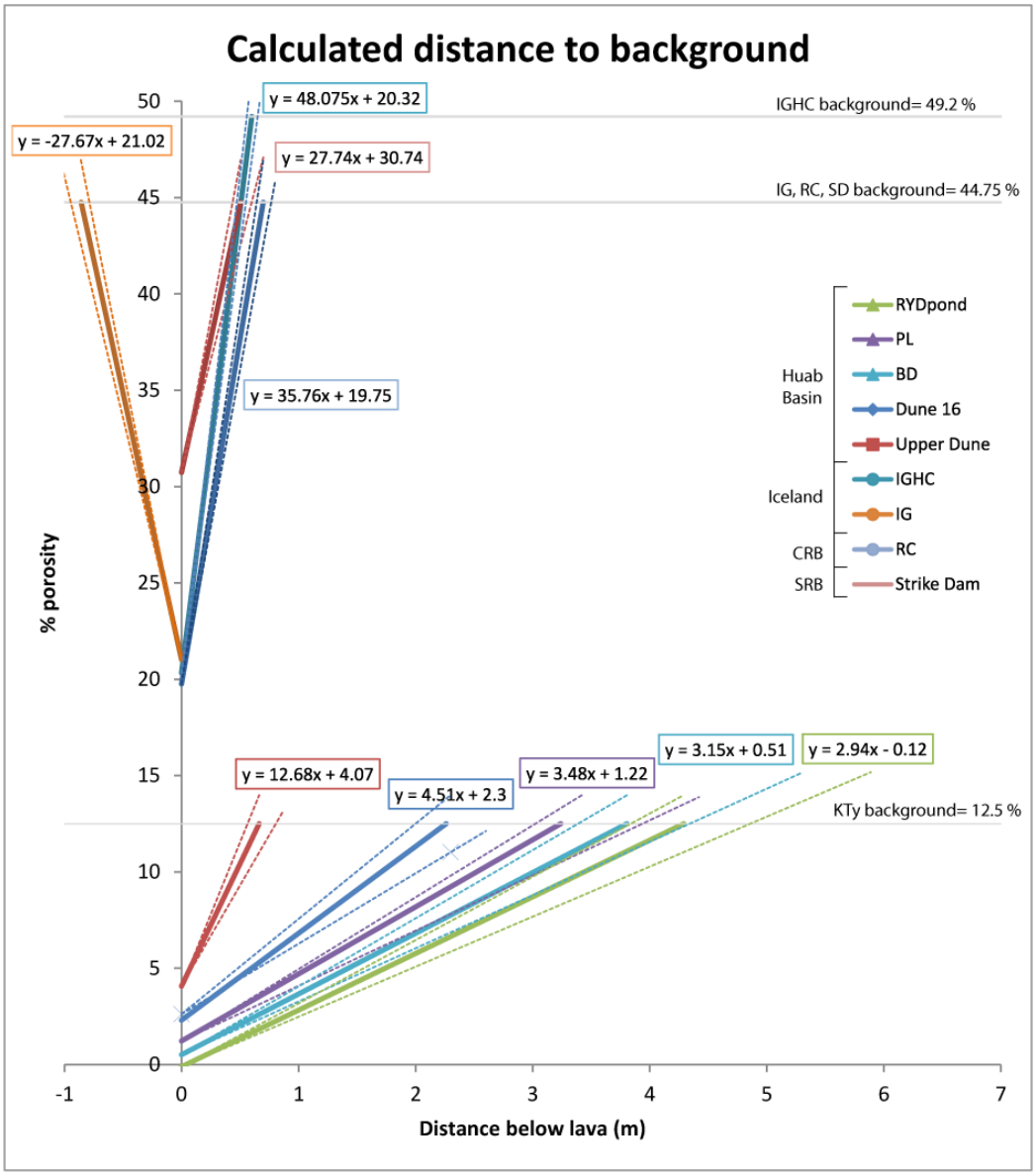

Fig. 5.24. Graphs calculating distance to background porosity. The linear trends calculated for the porosity depth relationships have been plotted to their respective background porosities. Huab basin= 12.5 %, IGHC= 49.2 %, IG= 44.75, RC= 44.75 %, Strike Dam= 44.75 %). Linear equations for each line are shown. To inspect each line relative to the constituent porosity points please refer to previous figures for each case study (this chapter and Chapter 4.). Dashed lines are 1σ uncertainties based on the error at 12.5 % porosity. These were used to calculate the uncertainty in distance to background porosity that is plotted in Fig. 5.25.

Uncertainties have been graphically propagated at the 1 σ level using the 1σ error in the point count porosity estimate. This therefore produces a range of distances to background which have been subsequently plotted in Fig. 5.25 (y axis error bars).

Case Study	Equation	R^2	Background porosity (%)	Distance to background (m)
PL	y=3.48x+1.22	0.85	12.50	3.24
BD	y=3.15x+0.51	0.98	12.50	3.81
Dune16	y=4.51x+2.3	0.79	12.50	2.26
Upper Dune	y=12.68x+4.07	0.80	12.50	0.66
RYDpond	y=2.94x-0.12	0.80	12.50	4.29
IGHC	y=48.075x+20.32	0.97	49.20	0.60
IG	y=-27.67x+21.02	0.22	44.75	N/A
RC	y=35.76x+19.75	0.81	44.75	0.70
StrikeDam	y=27.74x+3-.74	0.99	44.75	0.51

Table. 5.5. Equations in Fig. 5.24, R^2 values, background porosity and distance to background.

The distance calculated to background porosity is plotted against the thickness of lava flow (Fig. 5.25.) for all localities except IG (Highway 32), where no valid porosity trend was identified. The best fit trend line calculated in MS Excel for the Huab Basin case studies is a logarithmic relationship between distance to background porosity and lava flow thickness, which gave an R^2 value of 0.70. Thicker lava flows produced a greater thickness of porosity loss. When the same

trend is calculated for all the data (dry and wet together), the thickness drops due to the thickness of the lava influence generally reducing in the wet localities. This reduction can be attributed to the lack of calcite cementation. The R^2 value for the total dataset is 0.68. Errors in the distance to background have been propagated using the error in estimating the porosity of the background sandstone.

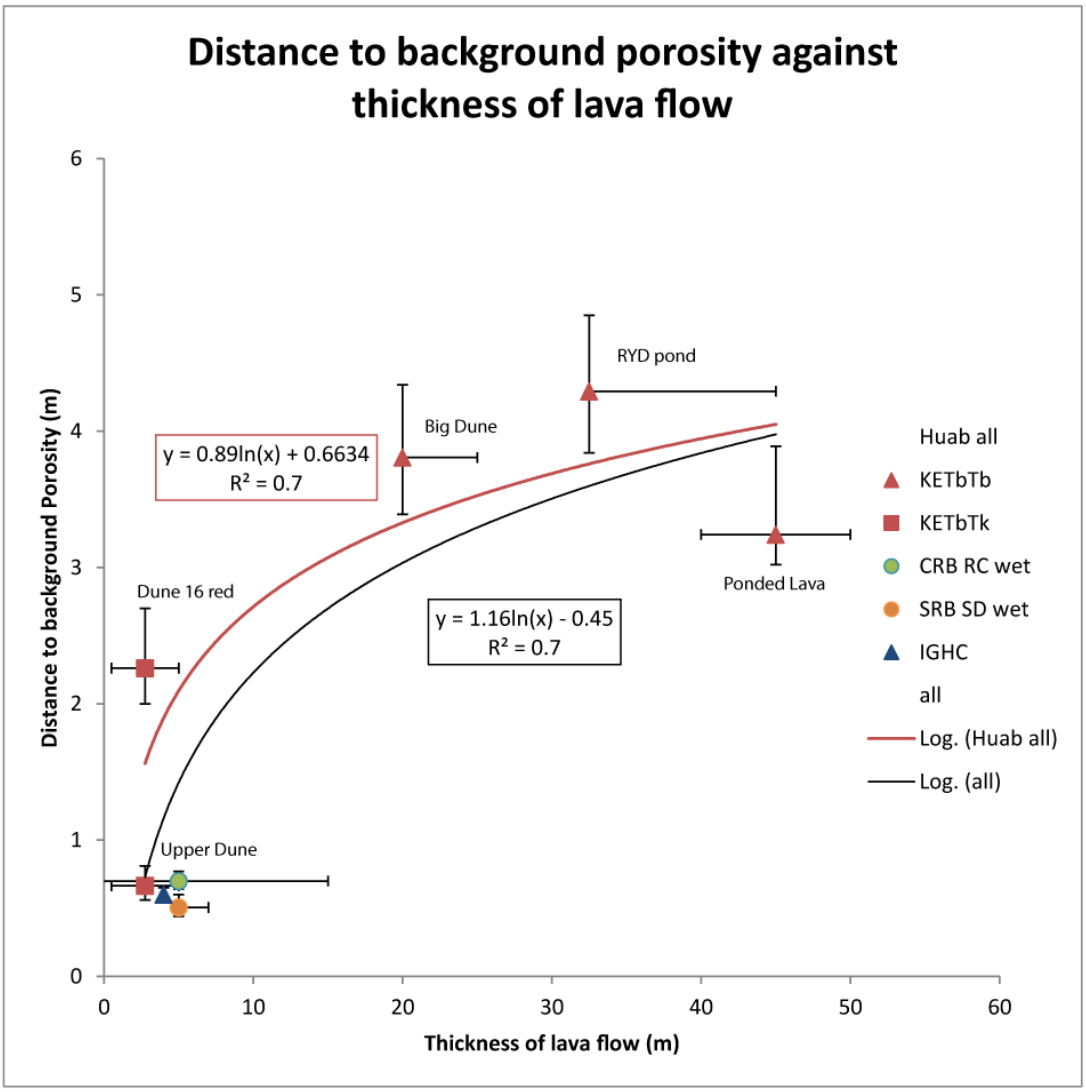

Fig. 5.25. Relationship between distance to background and lava flow thickness for all case studies (Huab Basin, Iceland, CRB, SRB). Errors plotted for lava flow thickness, due to not being able to measure whole flow thickness and reflect the maximum theorised thickness based on field relationships. Errors plotted for distance to background porosity are propagated from the 1σ error at the background porosity for each case study.

Case Study	Distance to background (m)	Thickness of lava flow (m)	Lava thickness error	
			pos	neg
PL	3.24	45.00	5.00	5.00
BD	3.81	20.00	5.00	0.00
Dune16	2.26	2.75	2.25	2.25
Upper Dune	0.66	2.75	2.25	2.25
RYDpond	4.29	32.50	12.50	0.00
IGHC	0.60	4.00	0.00	0.00
RC	0.70	5.00	10.00	0.00
StrikeDam	0.51	5.00	2.00	0.00

Table. 5.6. Data plotted in Fig. 5.25. Errors for lava flow thickness are positive (pos) and negative (neg). The neg error relates to the minimum thickness which most often was measured and the pos error relates to the maximum that was occasionally measured but sometimes eroded.

Lava flow thickness is therefore a major control on the distance over which porosity reduction is 'felt' by the underlying substrate sediment. This is consistent with compaction being the dominant porosity loss mechanism below lava flows when compared to background compaction. Compaction is probably related to the weight of the lava overburden.

5.4.2 Substrate composition and Palaeoenvironment

As compaction is the major contributor to lava emplacement-related porosity loss, the substrate composition is important. For instance, a weak, ductile substrate would be expected to deform more than a strong framework of interlocking grains.

This study has been restricted to sand substrate. The sand sized grains studied have largely been siliciclastic sub-arkoses (e.g. Twyfelfontein sandstone, Vantage interbed sandstone) or volcaniclastic sandstones comprising tuffaceous or scoriaceous material (e.g. Rekjanes Peninsular, IGHC).

It can be seen in Fig. 5.25 that the siliciclastic sands in the Huab Basin have the most extensive porosity loss for a given lava thickness. I infer that this results from the combined effects of the palaeoenvironmental conditions and the sediment composition affecting the rate of compaction and authigenic mineralisation. In the Huab Basin, the sediments would have been dry. The lava flow emplacing would have been degassing (likely components include: water, carbon dioxide, chlorine, fluorine, sulphur dioxide, hydrogen sulphide and carbon monoxide as major phases (e.g. Delmelle & Stix, 2000; Lowenstern, 2001; Simmons and Christenson, 1994; Shevenell and Goff, 1993; White, 1957). These gases will have been be emanating from the cooling lava flow, with the direction of movement determined by pressure gradients. This pressure gradient would be towards atmospheric pressure. Atmospheric pressure would have existed in the underlying pore space in the substrate sediment. A proportion of the volcanic gas would therefore have invaded the substrate porosity. It is proposed that these gases, when possibly condensing onto grains would have enhanced the pressure solution and dissolution of the quartz grains (e.g. H_2O, Cl_2, F_2), probably forming acidic concentrated conditions. This, combined with the added heat from the cooling lava (not water-cooled like in wet palaeoenvironments) is probably responsible for the increased pressure solution observed. The calcite cementation is also proposed as a result of the reaction of magmatic CO_2 and H_2O with detrital minerals and basaltic glass (see Chapter 4.).

This then raises the question, why do we not see calcite cemented zones related to the cooling of the lava in Iceland, the SRB and the CRB? The reason for this is suggested to be the existence of pre-existing water in the pore space of the substrate sediment. When lava is emplaced onto wet sediment, the pore water contained in the substrate below (either fully saturated or partially saturated) begins to boil. This boiling water, becoming water vapour would increase the sub-basalt pore pressure, such that no volatiles degassing from the lava would pass downwards into the sediment. Some volatiles may pass downwards through diffusion, but would be minor compared to a water-absent setting. If there are less volcanic volatiles invading the pore space it is expected that less diagenetic reactions will occur compared to where magmatic volatiles are abundant. Further, compaction will be limited to processes that do not require such a degree of grain dissolution, such as mechanical compaction. The water would probably serve to cool the base of the lava more rapidly, also acting against shallow pressure solution (cf. Houseknecht, 1984). If groundwater was able to pass through the substrate during cooling of the lava, the effects are anticipated to be even weaker than a static situation.

The exception to this theory is the observation of extensive pore-filling clay at the Joyce Ranch outcrop (unfortunately the sand was too thin for a sample transect). Here pillow lavas rested on the sand. It is proposed that the groundwater became acidified due to water-rock interaction (e.g. Sansone et al., 1991; Stevens & McKinley, 2000) between the permeable pillow lava field and the circulating water that would have been cooling the pillows. This acidified groundwater then reacted with the volcaniclastic fragments in the substrate. The other examples, where the igneous contribution was a lava flow did not have such fluid circulation and hence the water was not modified (acidified) by basalt-water interactions.

In wet settings, if the substrate was entirely siliciclastic, mineral authigenesis would be rare due to the effects of pre-existing water (substrate overpressure generation, cooling, dilution). In arid settings, where no water is present, the substrate overpressure is not developed, no water cooling or dilution is possible and the emplacement effects are at a maximum. In subaqueous conditions, where pillows form, clay forming mineral reactions are favoured in the substrate.

In conclusion, palaeoenvironment (wet or dry) and substrate sediment composition influence the porosity reducing effects below lava flows. The greatest influence is where compaction can be influenced by facilitating pressure solution at shallow depths (e.g. arid, siliciclastic palaeoenvironments). Mineral authigenesis at the time of lava emplacement is controlled by palaeoenvironment and sediment composition as volcanic volatiles are required to react with the more reactive detrital grains (glass or feldspars). Clearly the reactive detrital minerals need to be present for this to occur. The volatiles are less likely to make it into the substrate when it is overpressured due to interstitial water. The most important factor in controlling the distance, over which porosity reduction is apparent, remains, however, the thickness of the lava flow and the early compaction caused (Table 5.8.).

	Lava flows			Pillows
Palaeoenvironment	**Arid**	**Vadose e.g. beach**	**Water saturated**	
Substrate	**e.g. desert**	**sediments or lava damed fluvial**	**e.g. lacustrine**	
Sub-arkose (siliciclastic)	•High compaction due to increased pressure solution and mechanical compaction •Early calcite cement derived from chemical reactions beteween volcanic volatiles and substrate/ basalt	•Increased mechanical compaction, no early pressure solution due to cooling effect of abundant water •Limited early clay authigenesis increasing towards lava	• No data	•No data
Mixed siliciclastic-volcniclanstic (often characterised by abundant glass fragments)	• No data	•Hypothesised •Increased mechanical compaction •Minor clay authigenesis close to contact	•Minor increased mechanical compaction •Minor early clay authigenesis close to contact	•Increased mechanical compaction •Major enhanced early clay authigenesis due to water circulating through sediments *and* sediment substrate
Volcaniclastic (abundant glass, little or no siliciclastic material)	•No data	•Increased mechanical compaction •Early clay authigenesis close to contact (e.g. < 40 cm at the Rekjanes peninsular outcrop)	•Hypothesised •Minor increased mechanical compaction •Increased early clay authigenesis	•Hypothesised •Increased mechanical compaction •Major enhanced early clay authigenesis due to water circulating through sediments *and* volcaniclastic sediments
Summary	•Most intense compaction and cementation	•Compaction is the major porosity loss mechanism •Cementation volumetrically minor but important for lithification near lava contact	•Lowest compaction •Lowest cementation	•Compaction increased •Early clay authigenesis very important because of circulating water through permeable pillows

Table. 5.8. Matrix showing summary of observed effects of lave emplacement. Hypothesised effects are logical continuations of the effects into more reactive substrates (e.g. more volcaniclastic) where constraints exist through observation in this study. Extrapolations could not be made where 'no data' is indicated.

6

Direct effects on sandstone properties caused by the emplacement of dolerite sills and dykes, case studies from the Twyfelfontein Formation, Huab Outliers, Namibia.

6.1 Chapter summary

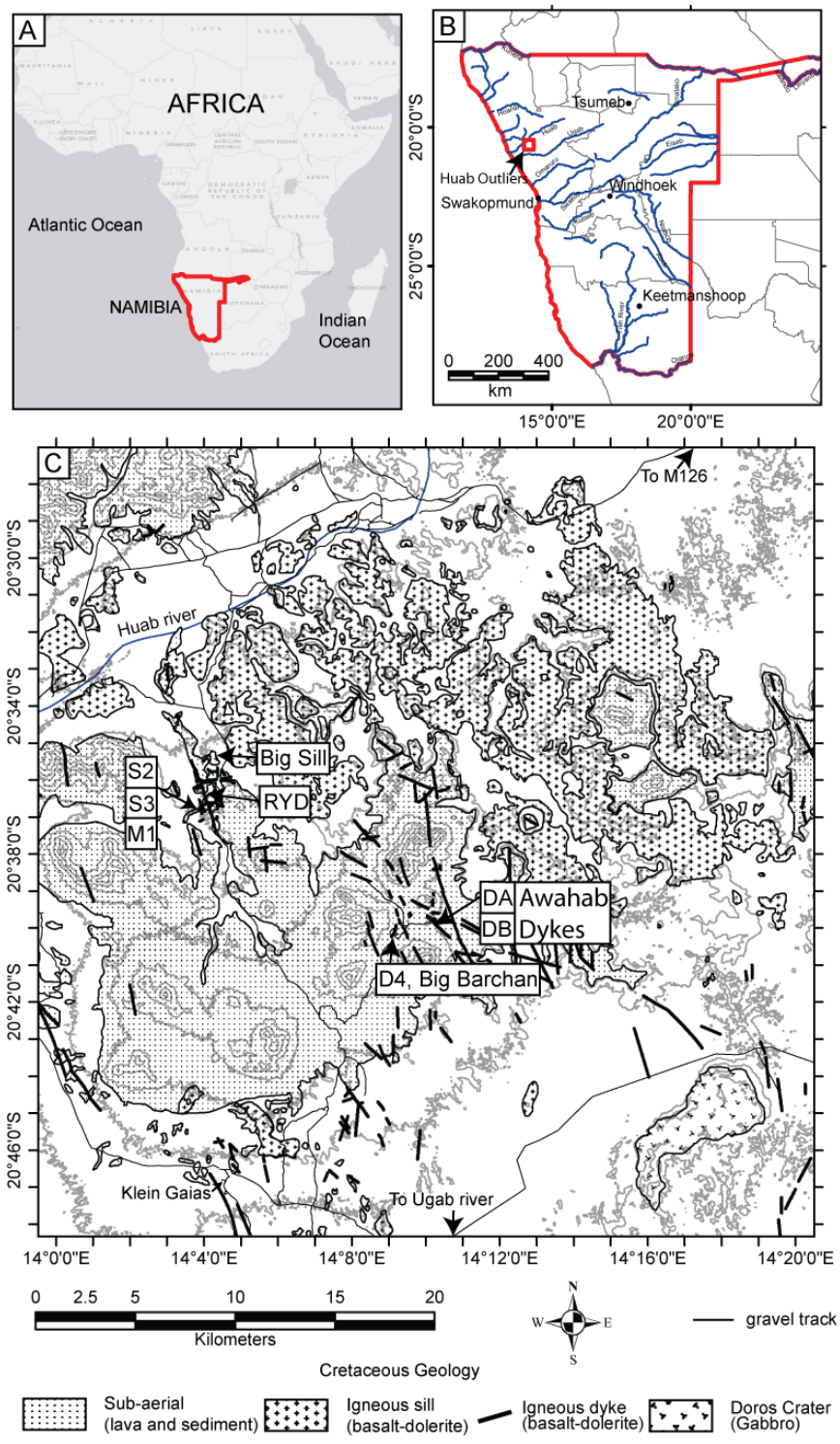

Fig. 6.1. A) Map of Africa showing Namibia. B) Map of Namibia with box showing the Huab Outliers enlarged in C. C) Map of the Huab Outliers showing location of case studies (in boxes). Cretaceous intrusive rocks (Dykes, Huab Sill Complex, Doros Crater) and Cretaceous sub-aerial rocks (Twyfelfontein Formation sandstones, Etendeka lava flows, Etendeka Quartz Latites) shown together.

The Huab Outliers study area, south of the Huab River, Kunene Region, Namibia (Fig. 6.1.) provides good outcrop (~70 %) in a currently arid area in which to study the interaction between the intrusive igneous rocks and the Twyfelfontein formation (Jerram et al., 1999a). The contacts between the Etendeka basaltic dykes and sills and the Twyfelfontein formation allow study of nature of hot contact effects (contact metamorphism, pyrometamorphism, pyrometasomatism and hydrothermal metamorphism) on clean petroleum reservoir quality sediment. The importance of understanding these effects has implications to the successful exploitation of sedimentary basins containing igneous intrusions around the globe (e.g. The Faroe-Shetland Basin (Bell & Butcher, 2002; Smallwood et al., 2004; Grove, 2013), Southern Atlantic passive volcanic margins (Jungslager, 1999; Stainistreet and Stollhofen, 1999; Davison, 1999), Australian passive volcanic margin basins (Holford et al., 2012)). Can non-fractured (cf. Bermúdez and Delpino, 2008) petroleum reservoirs potentially exist in sediments around igneous intrusions?

The effects of the emplacement and cooling of dykes and sills on host rocks have been the focus of some studies in the literature. Studies generally concern protolith material favouring diagnostic mineral reactions, such as fine grained aluminium rich (clay rich, mica rich) protoliths such as shale (e.g. Wang et al., 2012; Dutrow et al., 2001; Aarnes et al., 2011a; Brauckmann and Füchtbauer, 1983; Aarnes et al., 2011b; Barker et al., 1998; Hudson and Andrews, 1987). Studies of organic rich rocks such as coal or shale in proximity to intrusions have the benefit of the vitrinite-reflectance geothermometer (Barker et al., 1998; Cooper et al., 2007; Stewart et al., 2005). Other studies on organic rich rocks are concerned with the maturation and volatile (CO_2 and CH_4) release with relevance to petroleum sources

and global warming events (Summer and Verosub, 1992; Aarnes et al., 2011a; Aarnes et al., 2011b). Basaltic intrusions into metamorphic basement (comparatively mica rich and low porosity compared to clean reservoir sands) have also yielded successful studies, particularly in constraining mineral reaction texture and chemistry (e.g. Holness & Watt, 2002; Holness & Humphreys, 2003; Holness et al., 2005; Wartho et al., 2001; Nawaz, 1977).

Work on siliciclastic sandstones in contact with basaltic intrusions has had a variety of focusses, spanning a complete range of alteration. Many studies focus on the most intense (and rarest) effects leading to pyrometamorphism (Grapes, 2010; Butcher & Grapes 2011) where sufficient heat has been transferred to the intrusion wall rocks to cause partial melting and the formation of a buchite (e.g. Ackermann & Walker, 1960; Frankel, 1949; Spry & Solomon, 1964; Wyllie, 1961; Holness, 1999). Contacts that do not lead to melting are more common in the field, but not so well documented; effects are hydrothermal, leading to metasomatism and mineral authigenesis (e.g. Walker, 1959; Balance & Waiters, 2002; Summer & Ayalon, 1995; Brauckmann & Füchtbauer, 1983) , often recorded by clay mineralogy (e.g. McKinley et al., 2001; Ahmed, 2003, Balance & Waiters, 2002).

In the Huab Outliers (Fig. 6.1C.), a complete range of intensity is recorded in the sandstone wall rocks: from intense pyrometamorphism (Chapter 2, Grapes, 2010) and melt segregation where magma flow is intensified, minor pyrometamorphism above sills which gives way to hydrothermal mineralisation with distance from the intrusion, to hydrothermal mineral authigenesis with no pyrometamorphism flanking most dykes. The work presented in this chapter is not constrained to the most intense areas (e.g. buchites, Chapter 2.); rather, the aim is to give a realistic overview of the range of effects and their relative importance in the area. The tracing of the most

intense effects (pyrometamorphic) is used to infer localisation of magma flow in the sub-volcanic system.

The examples presented below show a range of types and magnitudes of direct contact effects. It has been found that the magnitude effects are not simply related to the thickness of the intrusion, for both sills and dykes. Instead it is suggested that the magma flow regime within the igneous body, combined with the country rocks' ability to dissipate heat (e.g. through an aquifer) controls the mineral authigenesis (and indeed melting) and hence porosity reduction. Compaction is also important adjacent to igneous intrusions, which is petrographically apparent; this is related to the emplacement as opposed to magma flow regime.

6.2 Direct effects of Dykes on the Twyfelfontein Formation

6.2.1 Awahab Dykes

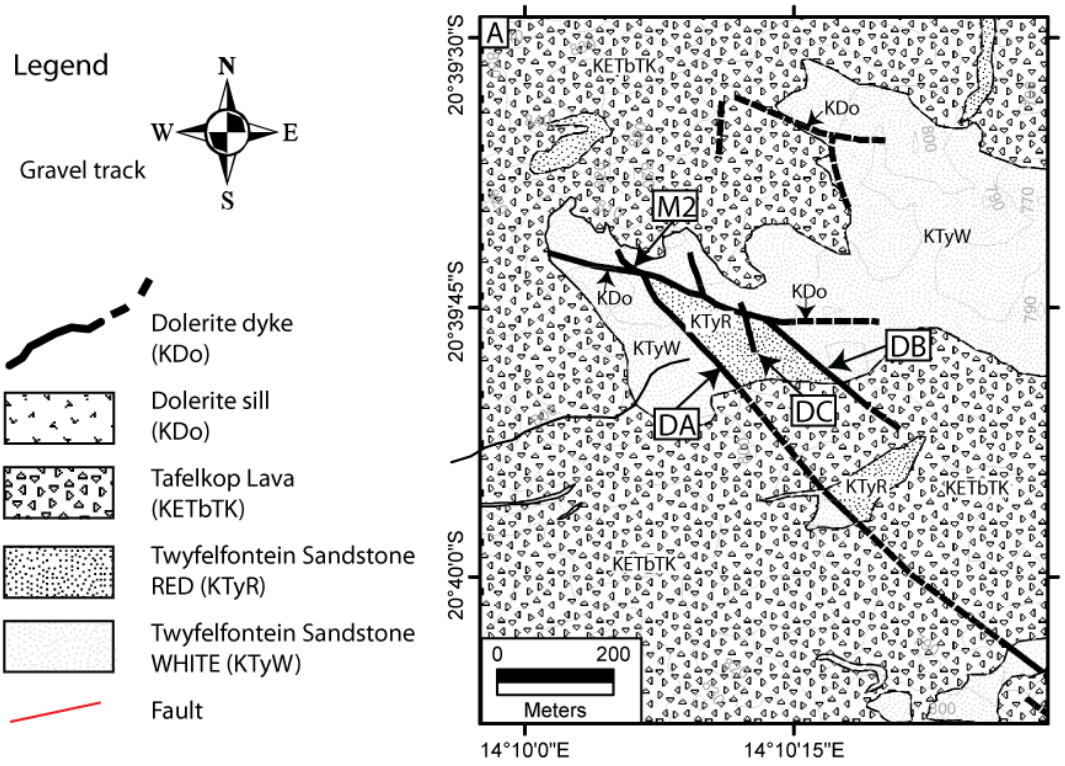

Fig. 6.2. Enlarged map of the Awahab dykes case study area. DA DB and DC refer to Dykes A, B and C. See also Fig. 6.7.

The Awahab Dykes locality is situated in the SE part of Dune Valley at approximately 20° 39.769' S 14° 10.188' E, at 792 m, 3.5 km SE of the Awahab campsite (see Appendix map). The outcrops consist of at least five dolerite dykes striking NW, WNW or N, varying from < 3 m thick up to 8 m thick. No cross cutting relationships were found, but definite evidence of co-existence exists in the form of linking sill-lets/ apophasis between Dyke A and the major WNW trending dyke (Fig. 6.2, Fig. 6.7.) A sample (NG/12-20) from Dyke B is an olivine phyric dolerite. The lowermost lavas of the Etendeka sequence are also olivine rich (Jerram et al., 1999a)

The sandstone intruded is the Minor Erg unit of the Twyfelfontein Formation (KTyMaj), and like the other two dyke localities presented, dykes separate red haematite coated sandstone from white bleached sandstone (detail in Chapter 7.). The bleaching is interpreted to be a syn-cooling hydrothermal effect (see 6.2.3. and Chapter 7.). Only red sandstone contacts are presented as 'directly' affected by the dyke.

Two transects were taken away from dykes, a transect to the east of Dyke A (Fig. 6.2.) and a transect to the west of Dyke B (Fig. 6.2.) were collected.

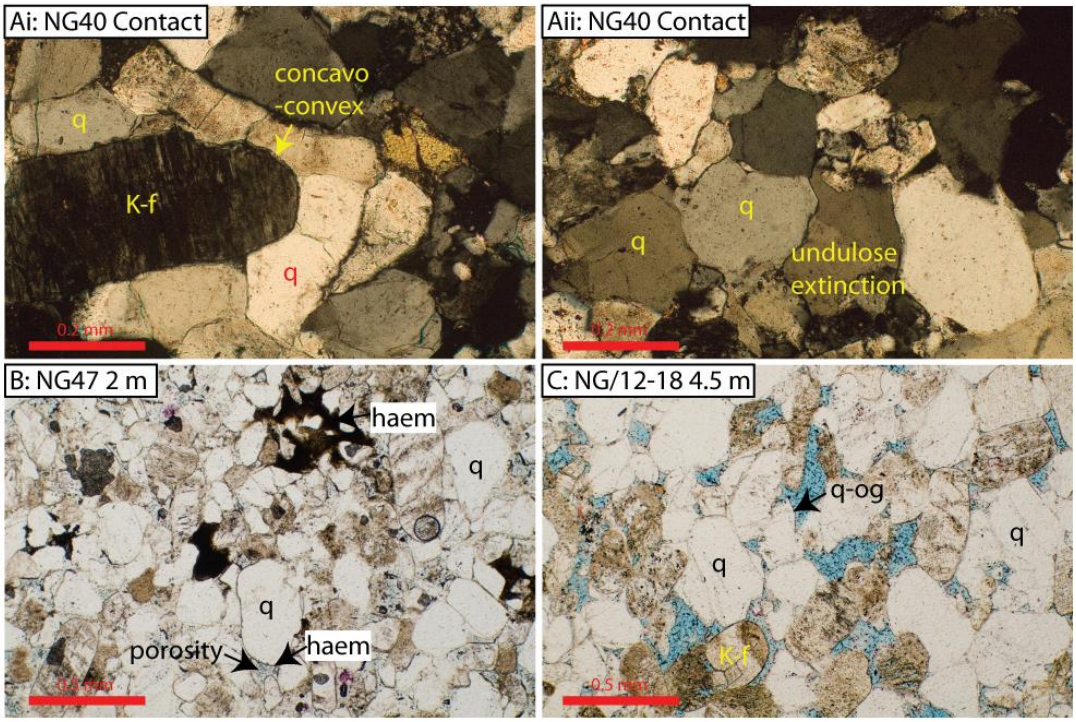

Fig. 6.3. Photomicrographs of red sandstone to the east of Dyke A (DA). (Ai, ii XPL) At contact sand is compacted, grains interpenetrate and frequently show undulose extinction. (B) 2 m from the dyke, compaction is still evident as abundant concavo-convex contacts, haematite is redistributed into nodules, porosity appears. (C) By 4.5 m compaction has reduced, haematite grain coatings are abundant. Authigenic minerals restricted to rare quartz overgrowths.

Dyke A is the westernmost of the dykes in Fig. 6.2. The dyke is at least 1.6 km long, with intermittent exposure. 0.1 m from the contact (NG40), the sandstone is visibly bleached and no porosity is visible. In thin section, (Fig. 6.3Ai, ii) detrital

mineralogy is approximately at the background proportions. Porosity is negligible. Porosity reduction is dominantly through compaction (COPL= 47 %) at the contact which is petrographically evident in Fig. 6.3. where quartz grains are commonly deformed by plastic deformation (*senso* Bailey et al., 1958; Mainprice et al., 1986) and by pressure solution (*senso* Rutter, 1983). Plastic deformation is betrayed by a dominant proportion of quartz grains showing undulose extinction, combined with clearly deformed outlines, and pressure solution is evident as sutured grain contacts and concavo-convex interpenetrating grains. Pressure solution leads to the formation of rare quartz overgrowths, which themselves are deformed, suggesting a degree of compaction (pressure solution) occurred prior to dyke intrusion. The remaining porosity 0.1 m from the contact is filled with calcite, which occasionally partially replaces detrital feldspars.

At ~ 2 m from the contact, are occasional primary pores, but porosity is still negligible. Compaction is the major porosity reduction mechanism, with grains showing dominantly undulose extinction, with sutured grain contacts and interpenetrating grains common. The compactional history is therefore much the same as at 0.1 m from the contact. Both deformed quartz overgrowths and quartz overgrowths into remaining primary pores suggest that pressure solution continued after igneous emplacement. Most remaining porosity is filled with haematite nodules and calcite. The haematite nodules are inferred to be redistributed haematite from former grain coatings. The calcite, is suggested to be hydrothermal in origin (6.3.).

By 4 m, porosity has increased to exceed 12.5 %, (sample NG48 porosity= 14.6 %, ±1.6). Porosity increase is largely due to less compaction (COPL= 37.5 %, ±4.3) and less due to less pore-filling authigenic phases (calcite and haematite) although total authigenic mineral proportions are higher than at the contact due to

increased clay replacement of feldspars. The sandstone is visibly red in outcrop and hand specimen due to haematite grain coatings.

Figure 6.3C shows sample NG/12-18, 4.5 m from the dyke contact, porosity is 12.2 % (±1.5). Authigenic minerals are quartz overgrowths (4.2 %, ±0.9) with negligible clay and calcite. Porosity loss is dominated by compaction (COPL= 38.6 %, ±4.0), 10 % less than at 0.1 m from the contact. Compaction is by pressure solution, as grains frequently interpenetrate, and suture; most quartz grains show unit extinction, undulose extinction is rare. Further than 4.5 m from the contact porosity and authigenic minerals fluctuate around the average. Two further samples, at 6 m and 15 m (NG/12-19) are similar to the background sandstone.

The transect into the red sandstone to the east of Dyke A depicts a situation where porosity and permeability increase away from the dyke (Fig. 6.5), largely influenced by increased compaction towards the dyke contact, and secondarily influenced by calcite mineralisation. Haematite has been mobilised away from the dyke contacts and re-precipitated in porosity outside of the zone of increased compaction (Fig. 6.5D.). The existence of quartz overgrowths, that have been deformed near to the contact and overgrown by calcite suggests Dyke A intruded into a sediment that was already at least partially lithified. Further quartz overgrowths growing into remaining porosity (e.g. NG47) shows that quartz authigenesis and probably pressure solution continued for some more time after dyke emplacement. This may be evidence for dyke emplacement prior to the maximum burial depth was achieved. Dyke A can be seen to cut all exposed stratigraphy (Fig. 6.7), which is up to 500 m above the Dyke A locality. Palaeodepth of intrusion is therefore confined to >0.5 km and <5 km. The existence of dominant undulose extinction within 2 m from the dyke, compared to the low frequency of undulose grains (displaying original

protolith inherited extinction) further than 2 m and in the background sandstone and below lava flows (Chapter 4.) suggests that conditions may be different. The plastic deformation that undulose extinction implies is normally associated with high pressures (in the order of >> 5 kbar, Carter et al., 1964). The lowest pressure that Carter et al., (1964) synthesised quartz with undulatory extinction from disaggregated natural sandstone was 5 kbar (18 km) at 925 °C for 523 minutes. 18 km of burial is not achievable for the Twyfelfontein Formation (Chapter. 2.), also, outlined below is a crude calculation of the depth of dyke emplacement (based on comparison of Dyke A and Dyke B) of ~760 m (an underestimate). If the depth is taken as 1 km, lithostatic pressure (ρ= 2800 kgm^{-3}) is 0.27 kbar, much less than the minimum required pressure from Carter et al (1964). The temperature required for plastic deformation increases as pressure decreases, so even if the lithostatic load permitted plastic deformation at 1 km, or indeed 5 km depth, the temperatures would need to be high enough to melt potassium feldspar under hydrous conditions (Holness, 1999; Holness et al., 2012). No feldspar melting is observed adjacent to dykes. Further, at 1 km, 925 °C is within the tridymite stability field (Grapes, 2010); no tridymite is present. The required conditions for plastic deformation of quartz under lithostatic pressure likely at the time of dyke intrusion are therefore unlikely, given the petrographic evidence. However, the dominance of undulose grains compared to elsewhere must have an explanation. I propose and hypothesis that the proximal pressure increase due to the intrusion of the dyke must raise the local pressure exerted on the wall rocks to a sufficient level, the required pressure (5 kbar – 0.27 kbar) is an internal pressure in the dyke during emplacement of 4.73 kbar. The mechanism for achieving such a pressure requires investigation beyond this thesis. An alternative explanation is that the presence of water, both pre-existing in the

aquifer, from degassing magma and from dehydration reactions could lower the pressure and temperature required for plastic deformation (e.g. Mainprice et al., 1986). The mechanism of plastic deformation remains unresolved for this case, however, it is sufficient to say conditions were appropriate adjacent to dykes, but not below lava flows, or in the background sandstone.

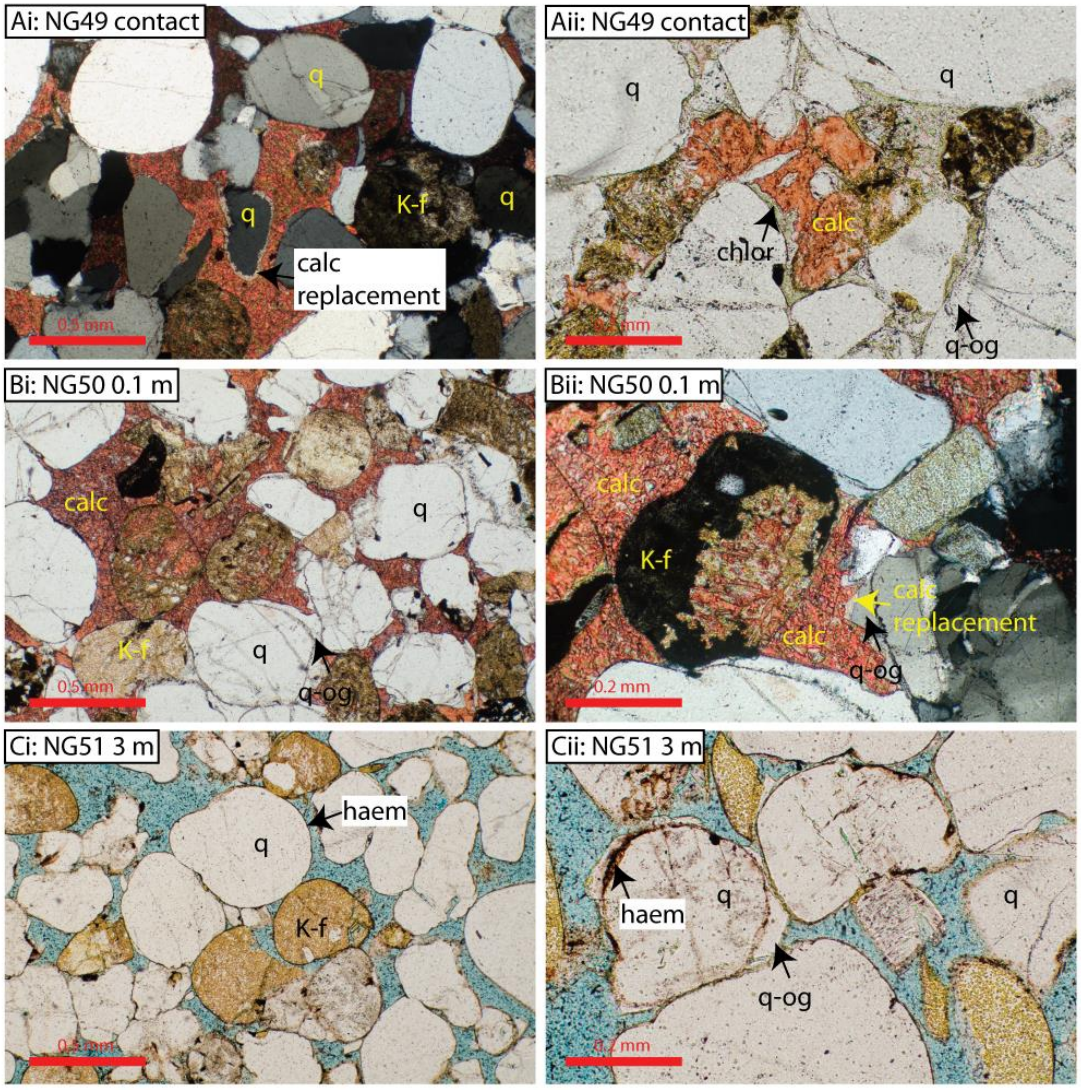

Fig. 6.4. Photomicrographs of contact to the west of Dyke B (DB). (Ai XPL) at the contact sand is cemented with aggressive calcite that begins to replace quartz, sample appears under compacted. (Aii PPL) At the contact, quartz overgrowths grew first, then rare chlorite, then calcite. (Bi PPL, Bii XPL)).1 m from the dyke, calcite partially replaces feldspars some quartz, note incipient replacement of quartz overgrowth. (Ci PPL) 3 m from the dyke, sandstone returned to background, occasional quartz overgrowths grow from detrital grains.

Dyke B is the eastern of the two dykes studied at this locality (Fig. 6.2.) and is parallel to Dyke A, the dyke is ~1.3 km long, although quality exposure is only 400 m. At the contact porosity is negligible (0 %) and permeability is low (3.7 md). Porosity reduction is dominated by compaction (COPL= 38.8 %, ±2.6), but cementational porosity loss is also important (CEPL= 10.1 %). Touching quartz grains commonly show sutured and interpenetrating contacts, which together with quartz overgrowths predate calcite cement. Quartz overgrowths also predate a minor chlorite cement, which partially coats grains (Fig. 6.4Aii). The calcite cement is in the form of pervasive poikilitic crystals of non-ferroan calcite, that postdates both the quartz and the chlorite. The calcite is aggressive, replacing the rims of detrital quartz grains (Fig. 6.4Ai) and partially replacing some feldspars.

At 0.1 m from the dyke, the sandstone is similar to at the contact, with calcite cement occurring after quartz cementation, as calcite overgrows is aggressive towards quartz overgrowths (Fig. 6.4Bii). Calcite partially replaces potassium feldspars (Fig. 6.4Bi, ii) and plagioclase. Compaction is through both plastic deformation and pressure solution at grain contacts and is the dominant mechanism of porosity loss (COPL= 36.6 % (±4.2), CEPL= 12.4 %).

At 3.0 m from the contact, porosity is up to 14.8 % (±1.6), COPL (39.4 %, ±2.6), interestingly is slightly higher (still within error, so not conclusive) than closer to the contact where the calcite cement is suggesting the calcite is ‘protecting’ the sand closer to the contact from further compaction. COPL is the dominant porosity reduction mechanism. The sand here is similar to the background; detrital grains are coated with haematite, which has occasional quartz overgrowths, postdating the haematite. All other cements are negligible. Compaction is evident, but restricted to

pressure solution as undulose extinction quartz grains are rare (probably inherited from protolith).

The contrasting nature of the porosity loss adjacent to these two dykes is useful. If we make two assumptions, a crude estimate of the intrusion depth can be calculated. The first assumption is that Dyke A intruded at the same time as Dyke B (supported by both separating the same red sand compartment) and the second is that the calcite cement adjacent to Dyke B protected the sand from subsequent compactional porosity loss (i.e. removed all remaining porosity) at the time of dyke emplacement. If these assumptions are true the compaction recorded by the cemented sample should be the pre-intrusion compaction and, the difference in COPL at the contact between Dyke A and Dyke B should be the COPL at the time of dyke emplacement. This difference is 8.1 %. When plotted on the COPL against depth plot in Chapter 2 (Fig. 2.12C.), this gives a depth of 756 m, which is consistent with the > 0.5 km and < 5 km palaeodepth for Dyke A. This depth is an underestimate, as some compaction would have continued after dyke emplacement. The main point is that the dyke was probably intruded at < 1 km depth. It is accepted that this calculation has a high uncertainty, probably in the order of 300 m.

Permeability and porosity in both examples was found to be exponentially related. Dyke A plots with all of the other dykes (Fig. 6.6.), whereas Dyke B plots separate, with permeability increasing at a faster rate. The reason for this is unknown, but it is proposed that the highly calcite cemented nature may be important, compared to the other dykes, where compaction is more important.

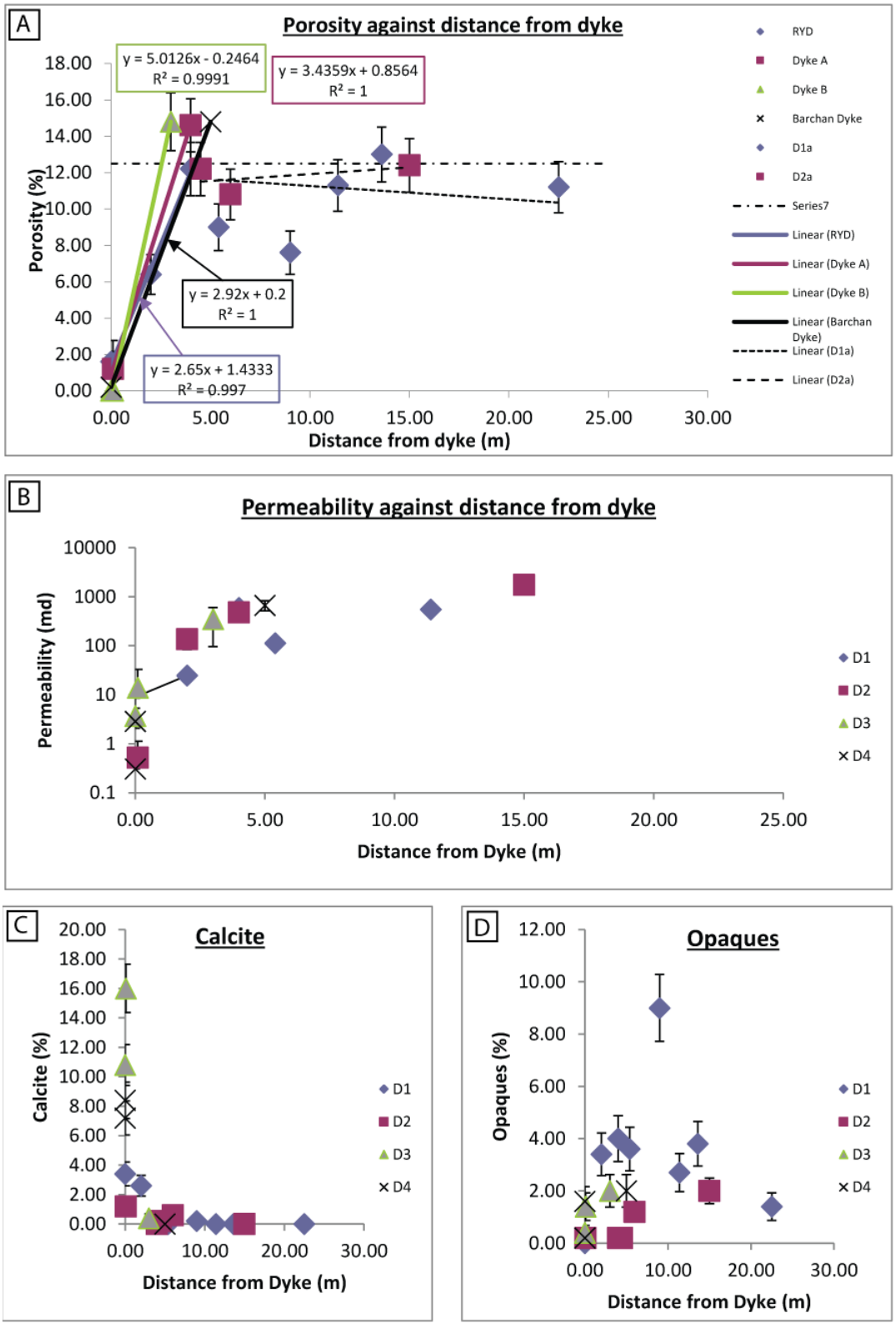

Fig. 6.5. **Graphs of point counted parameters against distance from dykes: Dyke A, Dyke B, Dyke 4 (barchan dyke) and RYD dyke. (A) Porosity increases away from all dykes. Linear trend line fitted to increase up to first point to exceed 12.5 % porosity. Note Dyke B only has 2 points. (B) Permeability increases with distance. (C) Calcite decreases with distance and is rare beyond 5 m. Opaque minerals are not correlated with distance.**

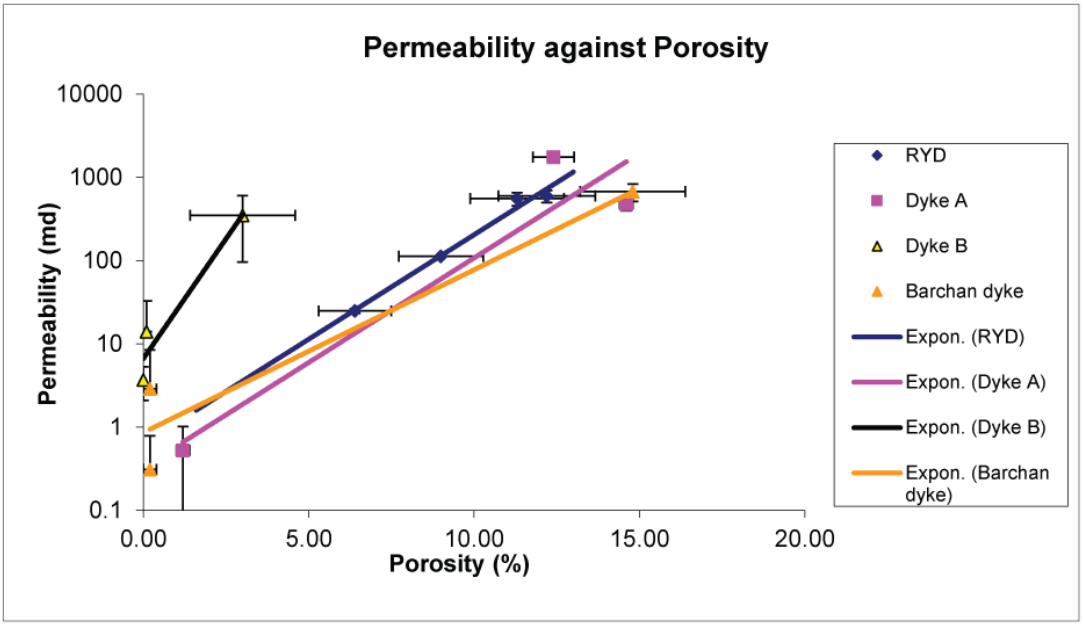

Fig. 6.6. Relationship between permeability and porosity for all red sand dykes. RYD, Dyke A and Barchan Dyke cluster, while Dyke B is distinct which reflects the petrographical differenced.

Sample	**Distance from intrusion (m)**	**Porosity (%)**
RYD Red sand		
NG88	0	1.6
NG89	2	6.4
NG90	4	12.2
RYD09	5.4	9
RYD08	9	7.6
RYD10	11.4	11.3
RYD12	13.6	13
RYD24	22.5	11.2
Dyke A		
NG40	0.1	1.2
NG47	2	
NG48	4	14.6
NG/12-8	4.5	12.2
NG/12-19	6	10.8
ng52	15	12.4
Dyke B		
NG49	0	0
NG50	0.1	0

NG51	3	14.8
Barchan dyke		
NG68	0	0.2
NG67	0	0.2
NG65	5	14.8

Table. 6.1 Porosity data for sandstone away from dyke-red sand contacts. See the Appendix for full data tables.

6.2.1.2 Intensified effects due to magma flow localisation

Where shallow dykes cut the Twyfelfontein Formation sandstone, there is usually a compacted contact zone, indurated with calcite inferred to be of hydrothermal origin, with little direct metamorphic influence (e.g. no pyrometamorphism) (e.g. Dyke A and Dyke B above). At 'normal' contacts magma was probably not turbulent and cooled rapidly (e.g. Delaney & Pollard 1982) (e.g. RYD, Dyke A, Dyke B, Barchan Dyke). However, the subject of this section is a 625 m^2 (25 m x 25 m) area of intensely thermally altered boulders and outcrop (outlined in orange, Fig. 6.7.). The dyke is < 10 m in width at this locality. Here, partial melt of the feldspar component has been extracted as melt. Surfaces formerly in contact with the dyke show textures indicative of thermal erosion (e.g. regmaglypts, cf. Lin et al. 1987) and the existence of a viscous-viscous contact between the magma and melted sandstone.

The locality shows high temperature contact metamorphism (e.g. pyrometamorphism, Grapes 2010); melt segregation and assimilation of this melt

into the mafic magma. The very small area of affected rock compared with the total amount of intruded sandstone, together with coincidence of several dykes at this location, suggests the increased heat required to produce the observations is due to magma flow localisation, possibly feeding a now eroded vent directly above. Such feeder dykes are found within this level of the stratigraphy, feeding the lowermost olivine rich Etendeka lavas (e.g. Jerram et al., 1999). Magma flow localisation into a 'tube' of ~10 m diameter is likely based on the < 10 m width of the dyke.

Thermal Alteration

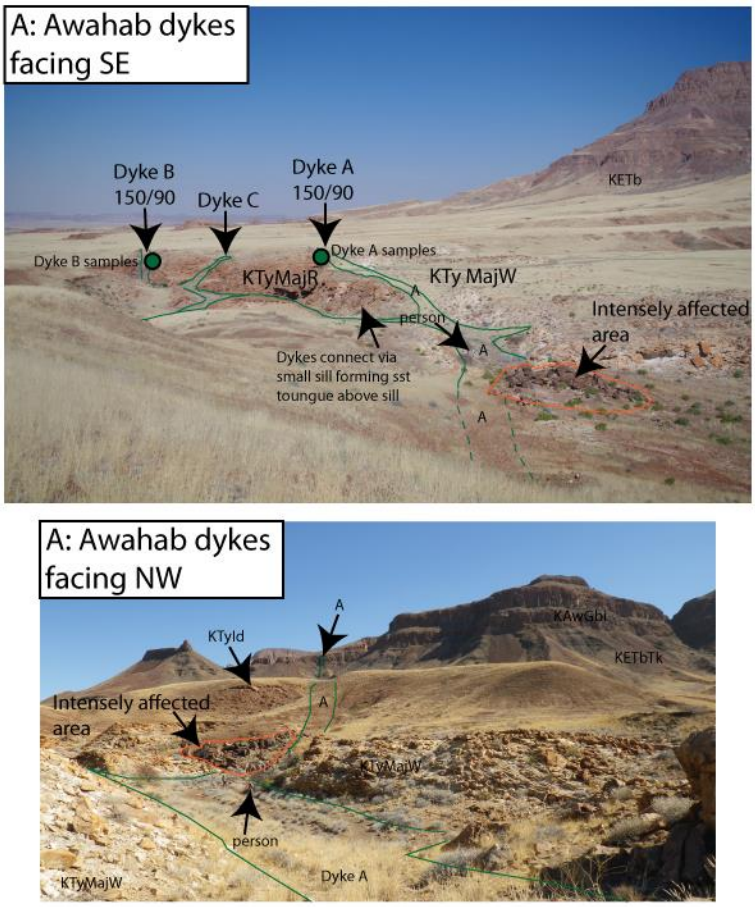

Fig. 6.7. Photograph of Awahab Dykes focussing on the area of intense thermal alteration

The bulk of the Twyfelfontein Formation (Fig. 2. B) is a very fine to coarse grained, grain fall and grain flow laminated sub-arkosic arenite (modal composition: quartz= 55 % (±2.2), K-spar= 21 % (±1.8), plag= 7 % (±1.7), porosity= 12 % (±1.5)) (cf. Chapter 2 and Mountney 2001), while the thermally affected sandstone is compositionally distinct from the sediment protolith. Partial melting of the sandstone under hydrous conditions (initially in an aquifer) has first melted the feldspar component (e.g. Eklund and Lindberg 1992; Holness 1999, Holness et al., 2012), of which none remains in the residue sandstone. Primary porosity, such as that normally preserved in the background sandstones (e.g. 6.4Ci, ii; Fig. 6.8C.)), is also absent.

Porosity present is secondary, in the form of microcrystalline quartz lined vugs, probably originally bubbles of gas (probably water vapour). These bubbles scale from thin section to the outcrop scale (up to 10 cm diameter), where they are often lined with quartz crystals up to 1 cm diameter. The loss of the porosity and detrital feldspars left the restic quartz to form a diagenetic quartzite. This process requires volume reduction, under lithostatic pressure. It is suggested, in the absence of finding segregated feldspar melt within the wall rocks, that the molten feldspars were forced into the magma under lithostatic loading, enriching it in potassium and silica (see darkness/colour gradient Fig.6.9D.). The remaining quartz grains show evidence of resorbtion, in that the rounded detrital character is often lost and solidified melt rims develop between grains (Sawyer 1999). At the boundary between sandstone and dolerite is a sheared brown glassy mineral which frequently contains plucked remnant detrital quartz grains (Fig.6.8A, C). Plucked grains are also present in the Si enriched boundary layer (Fig.6.8C, Fig. 6.9D).

As no tridymite paramorphs were identified petrographically, yet feldspar has melted, conditions can be constrained. If the calculated depth above holds (~1 km, certainly <<5 km), 0.27 kbar lithostatic pressure is appropriate. The melt producing reaction within the sandstone is likely Qtz+Ab+Or+H_2O→melt, if melting was H_2O absent pressure would need to be in excess of 0.5 kbar (1.8 km) (after Holness et al., 2012). The common vugs in the quartzite aureole suggest free fluid during cooling (i.e. water vapour). The temperature constraint of these wall rocks is therefore between 860 °C and 905 °C, with the onset of melting at 860 °C based on the P-T projection of the sanidine+quarz+liquid+gas and sanidine+tridimite+liquid+gas by Shaw (1963). Increasing the burial depth increases the range of temperatures that sanidine+quarz+liquid+gas is stable, and above 1.4 kbar (5 km) tridymite does not

crystallise (Grapes, 2010). It is likely therefore that the wall rocks reached a temperature of at least 860 °C if the depth estimate above holds. If intrusion was at the (unlikely) maximum burial depth of 5 km, the temperature is slightly lower, 780 °C. At 1 km, the temperature cannot have reached the tridymite isograd of 905 °C (Shaw, 1963; Grapes, 2010)

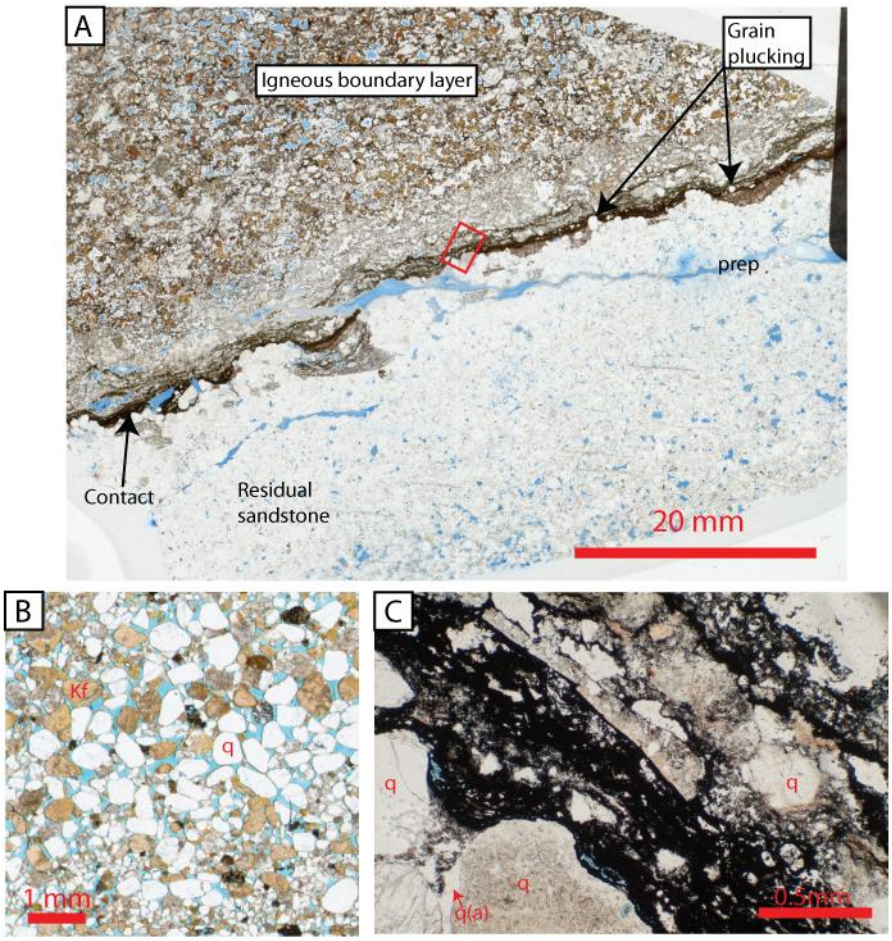

Fig. 6.8. A) Photomicrograph (PPL) of intrusion-sandstone contact. Residual sandstone has had feldspathic component (~30 %) melted and extracted (no feldspars or feldspar remains) into the igneous boundary layer which in outcrop grades to dark dolerite (Fig. 3. D). Residual sandstone shows evidence of partial melt and recrystallization along grain contacts, porosity exists as microcrystalline quartz lined vugs which are visible up to 10 cm scale in outcrop interpreted to be bubbles (H_2O rich vapour) within partially molten sandstone. B) Protolith sandstone, phi= 12.5%, 28 % feldspar. C) Magnified PPL micrograph of area in box (A). Contact is sheared is glass rich, evidence of grain plucking and assimilation is evident.

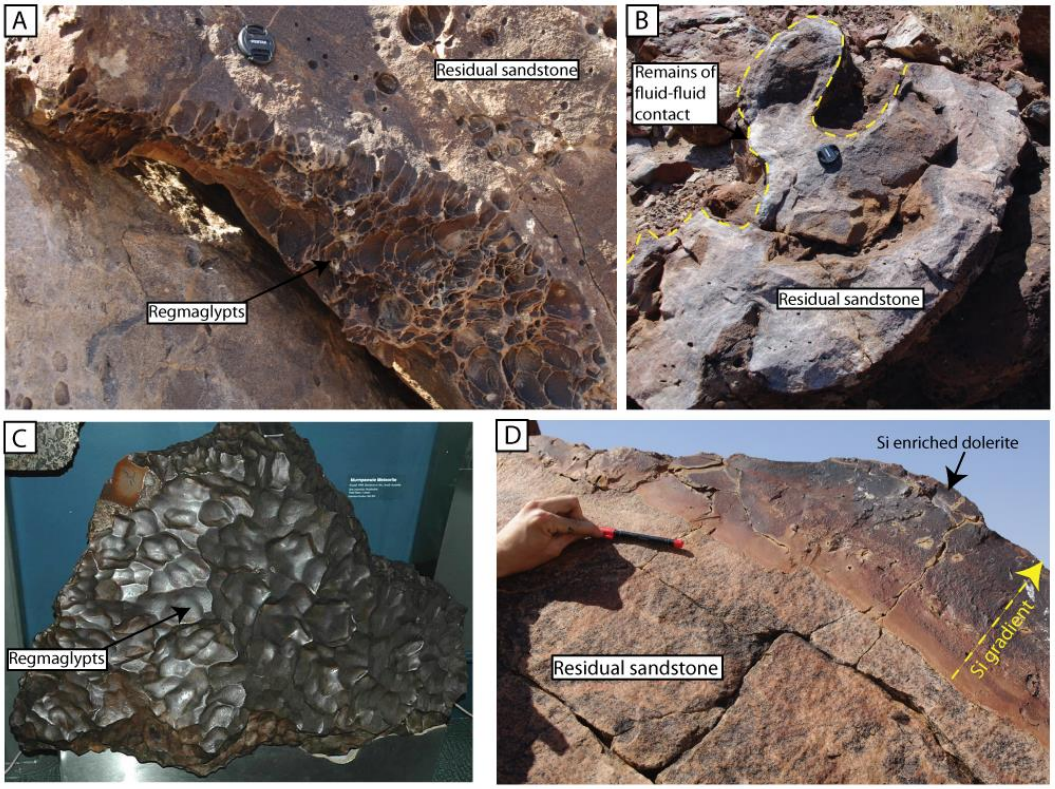

Fig. 6.9. A) Photograph of regmaglypts on surface of altered sandstone. B) bulbous/lobate sandstone contact (now broken) outlined in dash, inferred to be viscous contact between partially molten sandstone and magma. C) Iron meteorite with regmaglypts for comparison to textures in A (image courtesy of James StJohn). D) Contact between residual sandstone and dolerite. Dolerite becomes darker away from contact inferred to be due to silica enrichment from assimilation of feldspathic component and plucked quartz grains.

Thermal Erosion

Regmaglypts

A number of detached blocks of sandstone have surface ablation pits similar to regmaglypts found on the fusion surfaces of meteorites (Fig. 6.9A, C) (e.g. Lin & Qun 1986). The exposures of these surfaces is somewhat enhanced due to the resistant nature of the metamorphosed sandstone and the fact that the olivine rich volcanic rocks are weak and weather readily. In the case of meteorites a regmaglypt is a thumbprint like surface that forms due to interference between turbulent vortices developing on the ablation surface (during transit through the Earth's atmosphere). The nature of the ablation surface on a meteorite shows a sequential development

from smooth surface, narrow grooves, ablation pits, ablation grooves, ablation wedges, cross hatching and regmaglypt pattern as Reynolds number of the boundary layer on the ablation surface increases (Lin & Qun 1986). The transition to regmaglypt surface has been calculated to occur at Reynolds number of about 1.5 x 10^6 for the Jilin meteorite (Lin & Qun 1986). Essentially regmaglypts form during turbulent conditions on ablation surfaces where pre-existing irregularities on the ablation surface cause disturbances to the boundary layer setting up trailing vortices that interfere forming new disturbances (Lin & Qun 1986).

The existence of regmaglypts therefore infers turbulent conditions within the magma conduit at this location. Turbulent flow of magma causing sufficient heat transfer from magma to wall rock for melting and assimilation has been described before; in the field (e.g. Kille et al. 1986), geochemically (e.g. Rutter 1987; Kerr et al. 1995) and through simulations (Huppert & Sparks 1985). Normally it is difficult to achieve turbulent flow in magma (Galland et al. 2009), however in this case turbulent flow is feasible as concentration of magma flow into the < 10 m conduit from a dyke of length > 3 km would require a significant increase in velocity, eddies and physical stirring to maintain volume flux of magma (e.g. localisation of flow from fissure eruption above to point source).

Viscous-viscous contacts

Regmaglypts are not preserved on the entire contact area exposed. Figure 3 B shows one of many preserved apparently diapiric lobes. The lobes are composed of the same diagenetic quartzite material as in Fig. 6.8A, C.).

The interpretation of these lobes is as a fluid-fluid interface between the waning or stationary magma after cessation of flow, and the weakened (hot, ductile,

partially molten) wall rock. Either low density quartz rich wall rock has risen diapirically from the wall into the magma (like a drip) or the potentially overpressured magma has begun to invade the wall rocks. The process is clearly passive enough not to induce shearing textures on the lobes, or to affect the entirety of the wall rocks; hence regmaglypts are preserved.

Implications

Regmaglypt-like features preserve direct evidence of turbulent flow within a 10 m diameter region of concentrated basaltic magma flow, potentially underlying a now eroded vent. Evidence for increased heat transfer compared to 'normal' dyke contacts is preserved by partial melt of the feldspathic component of the wall rock and its subsequent extraction into the dolerite to form a silica enriched interface. Two mechanisms of shallow level crustal contamination were therefore in operation: Assimilation of partial melt extracted from wall rocks and assimilation of thermally ablated (process preserved as regmaglypt) bulk wall rock. As the magma flow rate waned, hot ductile wall rock interacted with the cooling magma conduit to produce apparent fluid-fluid features.

The locality is evidence for flow localisation within the dyke system and possibly evidence of a vent directly above. This is evidence for the volcanic system in the Etendeka being fed from a variety of eruptive locations, rather than a limited number of central complexes, probably along fissures that subsequently localise eruption to point sources (e.g. Thordarson & Self, 1993).

This case study also has implications for the velocity of the magma flowing through the conduit. Assuming a 10 m diameter pipe, a magma viscosity of 100 Pa s, and a density of 2700 kg m^{-3} (Galland et al., 2009), a velocity 8.2 ms^{-1} would be

required for the initiation of turbulent flow (Re= 2200, from Turcotte & Schubert 1982). It is likely for regmaglypt formation the Re would be higher than this, so 8.2 ms^{-1} is a minimum number. The volume flux of magma through this conduit would therefore (d=10 m, v= 8.2 ms^{-1}) be 2576 m^3s^{-1} or 7 x 10^6 kg s^{-1}, or crudely 7 x 10^5 kg s^{-1} per linear metre of vent (10 m section). Thordarson & Self (1993) estimated up to 5.6 x 10^3 kg s^{-1} per metre for the Laki eruptions of 1783–1785. The value calculated here is 2 orders of magnitude larger than for Laki, assuming the 10 m diameter holds to the surface. This magma flux suggests the eruption rate of the Etendeka basalts may have been very large compared to historic flood basalt eruptions. Calculations based on parameters for basaltic rock given in Galland et al. (2009), using the formula:

$$Re = \rho_{magma} \times h \times U / \eta$$

Where, ρ_{magma}= density of magma (2700 kgm^{-3}), h= 10 m, U= velocity and η= viscosity of magma= 100 Pa s.

6.2.2 Big Barchan Dyke

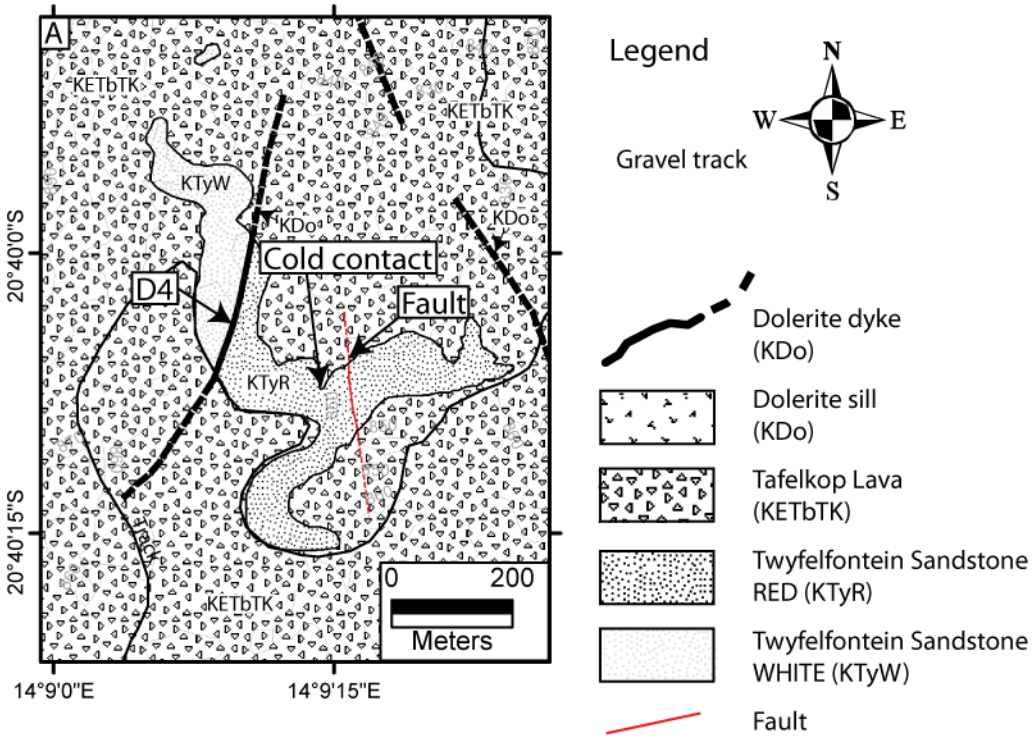

Fig. 6.10. Enlarged map of the Big Barchan dyke locality (see also Fig 6.1 for location).

The Big Barchan dyke case study (Fig. 6.10.) is located in the SW part of Dune Valley at 20° 40.049' S 14° 09.168' E, at 859 m, 2.8 km south of the Awahab campsite. The outcrop is that of an isolated dune (KTyId) cropping out within Tafelkop type lava, which weathers preferentially compared to the sandstone. The SE extent of the outcrop is the location of the pahoehoe prints described in Chapter 2 and Chapter 4. The sediment interlayer represents an isolated body of sand which was migrating over the lava landscape as a barchanoid dune, which was halted in its tracks by its encasement in lava from a new eruption. In the southern part of the outcrop a complete barchan dune form is preserved (Dune 2 of Jerram et al., 2000). The sand body is bisected by a dolerite dyke (sample NG69, see Chapter. 2), which is probably of the 'regional dolerite' affinity (Marsh et al., 2001). The dyke is

vertical and strikes 022 ° and is 3.8 m wide. To the west of the dyke, the sand is of the hydrothermally altered white variety and to the east it is red (see Chapter 7.).

Three samples were collected from the red sand side of the intrusion during the 2011 field work and three during the 2012 field work. Only the 2011 samples have been thin sectioned, but inspection of the 2012 hand specimens have been used as a guide for the diagenetic zone isograds. Sample NG49 is a xenothith of Twyfelfontein sandstone found within the dyke at the transect location, consequentially, it could have come from the stratigraphically lower Minor/Major Erg.

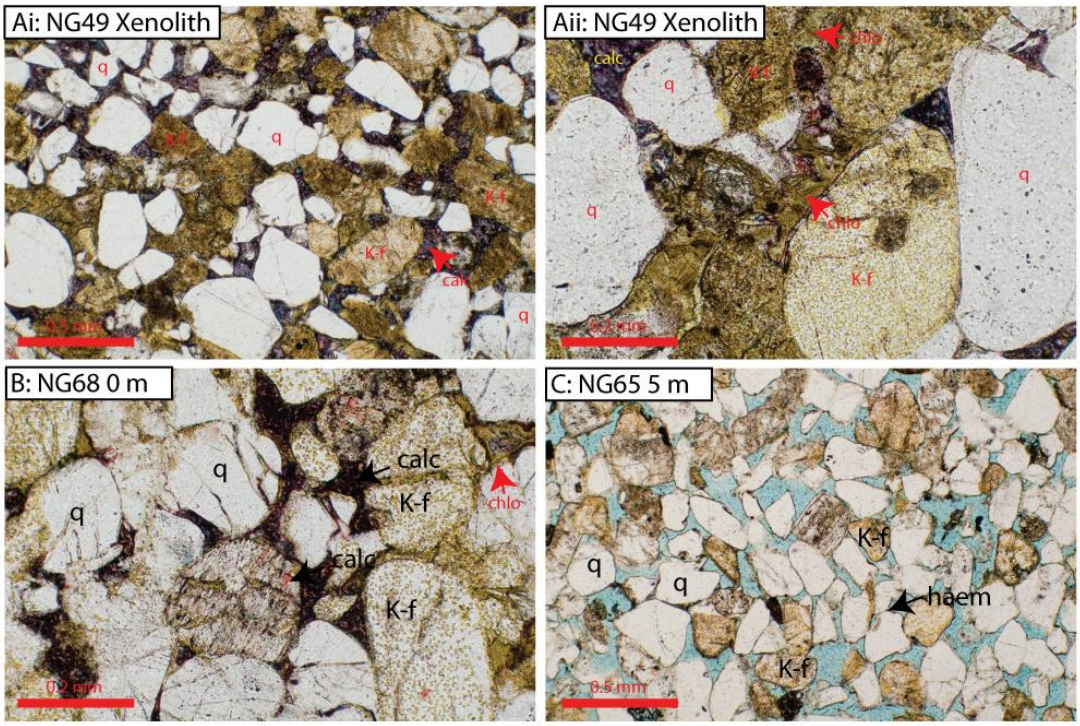

Fig. 6.11. Photomicrographs of red sandstone from the Big Barchan dyke locality. (Ai, ii PPL) A small xenolith within the dyke of Twyfelfontein Sandstone shows no pyrometamorphism. Sand is relatively under compacted compared to the wall rock contact and is cemented with chlorite, then ferroan calcite. (B) 0.1 m from the dyke, compaction is high, grains are frequently undulose, contacts are concavo-convex or sutured, remaining porosity is cemented with calcite usually non-ferroan. (C) 3 m from the contact compaction is normal, cement is limited to rare quartz overgrowths, haematite grain coatings are common.

The xenolith sample (Fig. 6.11Ai, ii) is a compacted (COPL= 39.4 %) arkosic sandstone, with quartz, chlorite and ferroan calcite authigenic mineralisation. Porosity is negligible. Quartz overgrowths are present but rare and grew first. The second cement was the chlorite, which is well developed, and can fill pores. Calcite, which is poikilitic, fills remaining porosity. Interestingly, this calcite is ferroan, whereas the majority of other calcites encountered have been non-ferroan. This sample is evidently rather rich in iron, as it is incorporated into the calcite and the chlorite.

At the contact, sample NG68 is similar to the xenolith, but compaction has been greater (COPL= 41.4 %, ±2.8). Detrital mineralogy is similar to background proportions. Authigenic cements comprise of: calcite, which is both ferroan and non-ferroan. The non-ferroan calcite replaced feldspar grains, whereas the ferroan fills pores. Both of these carbonate cements came after chlorite, which fills and lines pores. (Fig. 6.11B).

Five metres east of the dyke, sample NG65 shows that the sandstone has reached background sandstone petrographic parameters. Authigenic minerals are restricted to clays and quartz overgrowths, calcite is absent and porosity is 14.8 % (±1.6). Compaction is at a minima for the locality (COPL= 37.5 %, ±2.8).

These three samples provide limited statistical resolution, the un-sectioned samples provide some further clarification. 1 m from the contact, sample NG/12-7 is a hard, pale grey sandstone with no visible porosity. Permeability is low, but not negligible. Hammered faced are white, suggesting a calcite cement. 2 m from the contact, sample NG/12-2 is a red, friable sandstone, with considerable visible porosity and considerable permeability. Cements are present, which are probably rare calcite grain replacements. 3 m and 4 m from the contact the sandstone is friable,

red, with considerable visible porosity and considerable permeability. No cements are evident at hand specimen scale.

In summary, porosity increases away from the Big Barchan dyke, as compaction reduced and cementation reduces. By 2 m, porosity is considerable, and by 5 m porosity is 14.8 % (±1.6).

6.2.3 Red/Yellow Dyke area

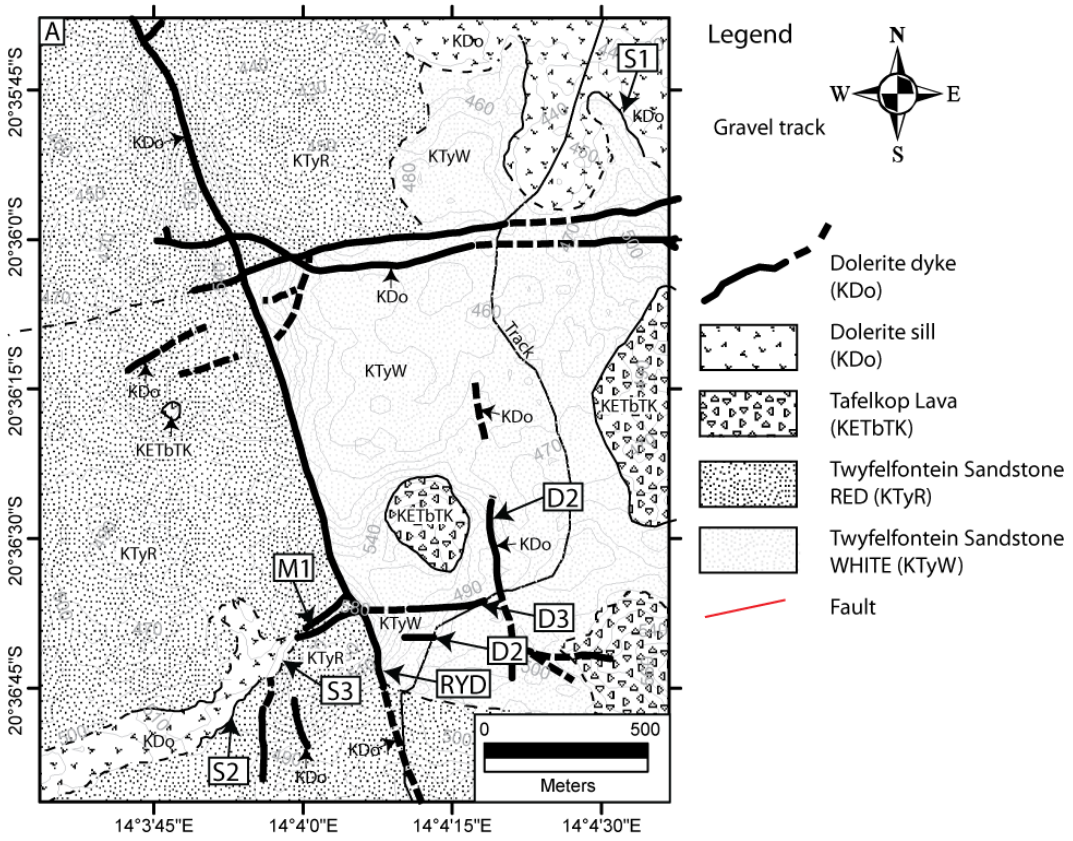

Fig. 6.12. Enlarged map of the Red/Yellow Dyke locality

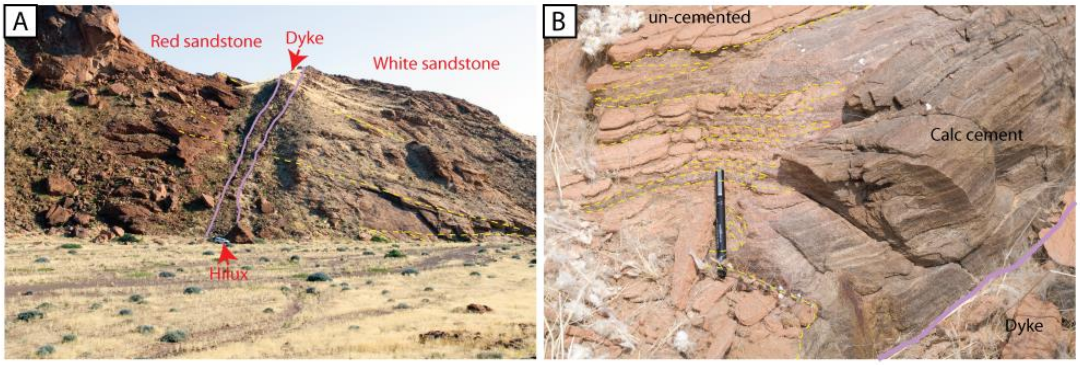

Fig. 6.13. A) Photograph of dyke (w= 5 m) facing north cross-cutting major erg unit of Twyfelfontein Fmn. Hilux 4x4 for scale, cliff is ~90 m high at dyke. West of dyke is red and has been unaffected by hydrothermal activity. East of dyke is bleached white due to hydrothermal activity. B) Photograph of dyke contact of dyke in A, pen for scale. Calcite cemented contact zone can be seen, this zone reaches into the un-cemented sandstone along originally high permeability grain flow horizons (outlined in yellow dash).

The Red/Yellow Dyke (RYD) locality is the primary case study for the direct and indirect effects of a dyke on the Twyfelfontein Formation. Here the data density is highest and exposure quality provides excellent 3D dissected outcrop, in excess of the Awahab dykes and the Big Barchan dyke localities. The RYD is so called due to the sandstone colour difference separated by the dyke. On the eastern side, the sand is bleached to a white colour and on the western side the sand is red. This thesis calls, what was originally termed yellow sand white sand, but the outcrop name of RYD stuck due to it being in common usage. Investigation into the indirect diagenetic effects leading to the white bleaching is discussed in Chapter 7.

The RYD dyke is 6.6 m thick at the foot of the 81 m high cliff in Fig. 6.13A and extends for probably at least 11 km striking 163 °. Of this 11 km, the central 3.3 km are of continuous exposure. The locality also has a number of additional dykes (Fig. 6. 12.) that differ in trend to the main RYD. To the west, two dykes < 3 m crop out 250 and 350 m from the main dyke, striking N-S. To the east, are at least three dykes in the main cliff. Dyke 2 (D2) strikes N-S, and dykes 2 and 3 (D2 and D3) strike E-W. Dyke 3 is probably the same dyke as crops out to the west of the main dyke. Dyke 3 is probably fed from the RYD sill (S2 and S3). Dyke 3 cross cuts the main RYD dyke, so is later. In this southern sector of the RYD exposure, only the main RYD dyke separates sandstones of white and red varieties. 1.2 km to the north, the RYD is intersected by numerous E-W trending dykes that do separate red from white sand, these will be discussed in detail in Chapter 7.

At the western contact with red sandstone (NG88), the sand has detrital composition similar to the background. Porosity is low (1.6 %, ±0.6), permeability is negligible (0 md recorded). Petrographically compaction is intense, grains are frequently undulose suggesting plastic deformation. Pressure solution is also evident

(Fig. 6.16Ai), particularly manifested as sutured grain contacts and re-precipitated quartz as overgrowths. Quartz overgrowths are frequently deformed themselves. Haematite grain coatings are absent. COPL is 43.7 % (±3.1), which is higher than the Major Erg red mean (>8 % porosity) of 39 % COPL. Remaining porosity is filled with poikilitic calcite that overgrows quartz overgrowths (Fig. 6.14Ai, ii., Fig. 6.16Aii.).

Sample NG89, 2 m from the contact shows the background detrital composition. Porosity is 6.4 % (±1.0), permeability is 24.8 md. Porosity loss is dominated by compaction (COPL= 42.3 %, ±3.2). Grains are frequently interpenetrating and sutured (Fig. 6.14Bi.), although undulose grains are less common. Cementation is important. Early quartz overgrowths are themselves compacted and sutured. Calcite cement, where present grows over the earlier quartz cement, but does not fill all remaining porosity (Fig. 6.14Bii.). Haematite appears disseminated as small nodules and pore linings around the sample.

The nature of the calcite cementation can be observed at the contact outcrop at the summit of the RYD dyke. Fig. 6.13B. shows the contact, facing NW. The calcite cemented rock appears brown, and the un-cemented rock is light red. The visibly cemented rock is 100 % near to the dyke contact, but only follows originally high permeability layers with increasing distance. These ‘tongues’ of calcite are highlighted in Fig 6.13B. Calcite is present in the red sandstone to a distance of 2 m, but it is not pervasive, as can be seen in the figure. The fact that the calcite cement is following permeability pathways suggests that a constituent, that follows permeability pathways has origins within the dyke. This could be calcium, CO_2, formation fluids driven by the heat of the dyke.

At 4 m from the dyke, porosity has increased to 12.2 % (±1.5) and permeability is 596.5 md. Detrital grains are approximately background. Compaction is the major contributor to porosity loss (COPL= 40.8 %, ±3.7), with cementation negligible (CEPL= 0.9 %). Authigenic minerals consist of rare quartz overgrowths (0.2 %, ±0.2) and redistributed haematite, that forms pore filling nodules (Fig. 6.14Ci.). Haematite coats most grains (Fig. 6.14Cii.). Comparison of the SEM images in Fig. 19. Shows the striking difference between the samples at the contact and at 4 m. 4 m away, detrital grains are rounded and clear, with connected porosity. At the contact grains are deformed and visible porosity is rare, and occluded by mineralisation.

Five additional samples to a distance of 22.5 m (RYD24) display a variation in background sandstone detrital composition typical for the Major Erg unit, with porosity ranging from 7.6 % (±1.6)for a grain fall dominated sample to 13.0 % (±1.5)for a grain flow dominated sample (RYD 12, Fig. 6.14Di, Dii). These red sandstone samples are characterised by red haematite grain coatings and occasional quartz overgrowths, but with compaction as the major porosity loss mechanism. Other cements are rare or absent. The petrography of these red samples unaffected by subsequent mineral authigenesis (other than compaction driven quartz cementation) are in stark contrast to the white sandstones. The white sandstones are similar at the contact, but are highly modified by later diagenesis away from the dyke.

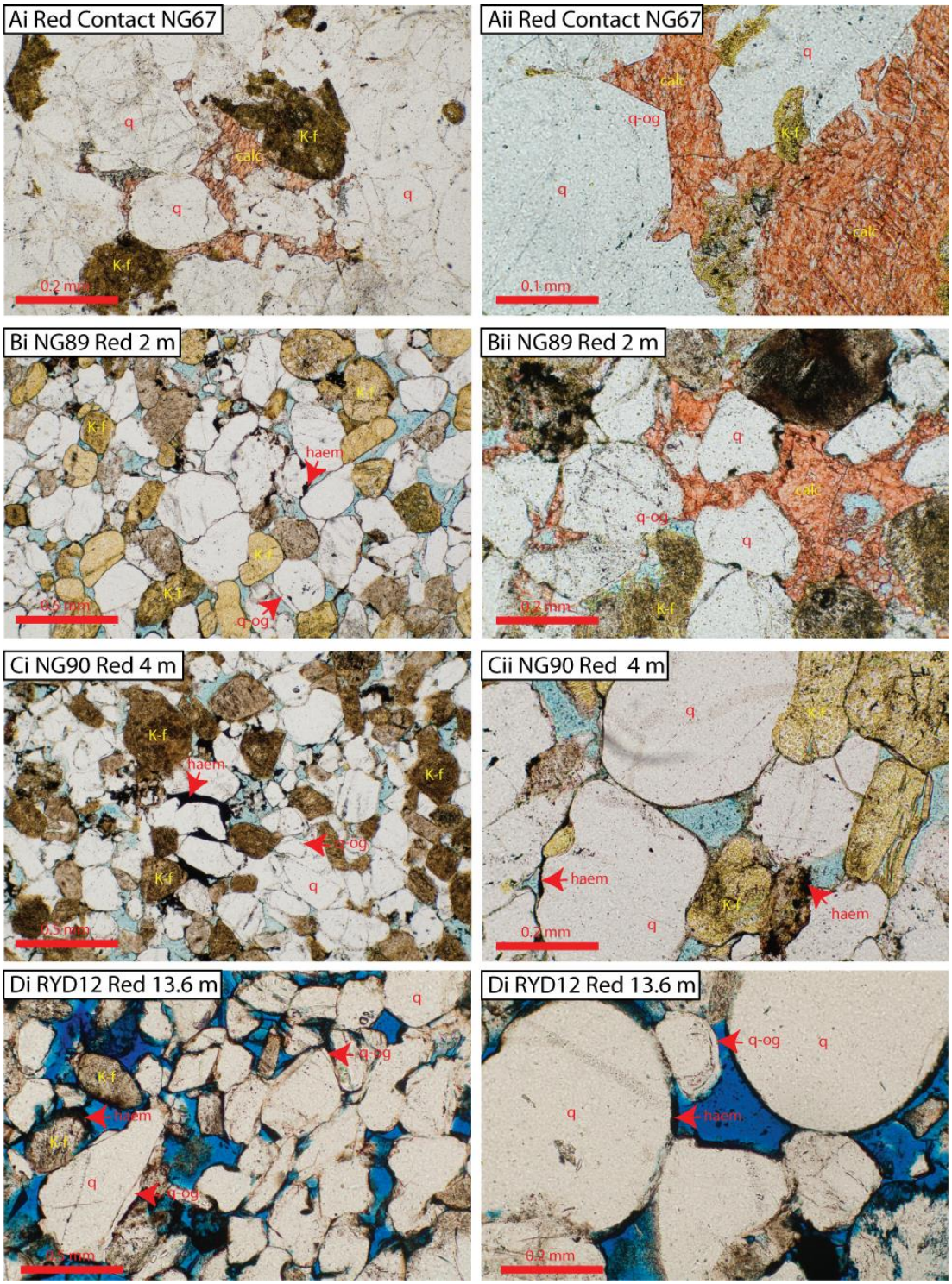

Fig. 6.14. PPL photomicrographs of sandstone from the western (red) contact of the RYD dyke. (Ai, ii) At the contact porosity is negligible. Authigenic minerals are calcite, developed over quartz overgrowths. Detrital grains are compacted and occasionally fractured. (Bi, ii) 2 m from the contact increased compaction is evident, grain contacts are sutured or concavo-convex. Haematite grain coatings are present and there is a poorly developed calcite cement over quartz overgrowths. (Ci, ii) 4 m from the contact the sandstone resembles background sandstone, but haematite is redistributed into nodules as well as coating grains. (Di, ii) 13. 6 m from the contact authigenic minerals are restricted to rare quartz overgrowths.

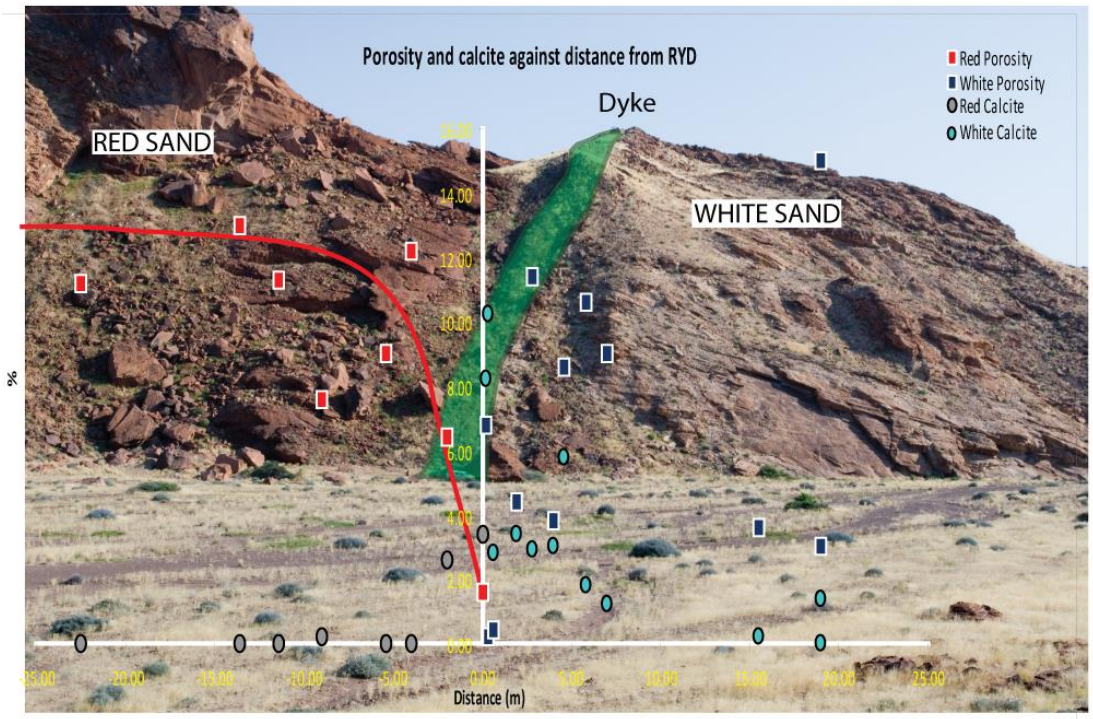

Fig. 6.15. Photograph of the RYD dyke with porosity and calcite graph overlay. Red (west) and white (east) sandstone is evident from image. Porosity increases away from contact for red sand, whereas, although there is a general increasing trend for the white sand, there is much more variation. Calcite decreases away from the contact in the red sand but remains variable in the white sand. The white sand has been affected by hydrothermal fluid circulation (Chapter 7.), whereas the red has not been affected to the same degree.

Figure 6.15 clearly illustrates the difference between the profiles away from the dyke contact on either side (red vs. white.). On the red side, porosity increases smoothly away from the contact until background values are reached at about 4 m, where the profile plateaus (Fig 6.5A., Fig. 6.15.). The porosity increase is accompanied by a decrease in calcite. Permeability also increases away from the contact (Fig. 6.5B.). The sandstone on the white side has low porosities at the contact, that increase away, but with large variability, calcite also has large variability and does not reach 0 %. More will be made of this in Chapter 7. Here, the direct contact rocks on the white side will be discussed, as the existence of calcite persisting with distance is important in constraining dyke and calcite cement timing.

Figure. 6.16Ci shows the sandstone 0.1 m from the contact. Compaction is high, and porosity is filled with calcite.

0.2 m from the contact sample RYD02, (Fig. 6.16Ai, ii) sand shows approximately detrital composition. Porosity loss is dominated by compaction (COPL=31.5 %, ±5.0), grains are dominantly undulose. Pressure solution is also evident, as grains are frequently sutured. Cementation is important (CEPL=12.9 %), and comprises of early and late quartz overgrowths, followed by chlorite and calcite (Fig. 6.16Ai, Aii). Chlorite appears to co-crystallise with the calcite. The calcite is aggressive towards quartz grains, as adjacent to Dyke B (above). The aggressive nature of the calcite can be seen clearly in Fig. 6.16Cii, where a quartz grain is getting dissolved at the rims and is being replaced with calcite. Porosity is secondary, relating to hydrothermal processes during later cooling. The hydrothermal mineral suite is also visible in Fig. 6.16Cii, typified by the pore filling kaolinite and unidentified barium containing mineral intergrowing with the kaolinite in the right hand side of the field of view.

Further from the dyke, at 0.6 m, sample RYD15 also shows marked porosity loss (porosity= 0.2 %, ±0.2), which is dominated by compaction (COPL=46.1 %, ±3.0). Compaction appears dominated by plastic deformation as nearly every quartz grain is undulose (Fig. 6.15Bii.) (cf. the background sandstone). Interpenetrating and sutured grains are present. Mineral authigenesis is apparent as early quartz overgrowths that are later grown over by calcite. Chlorite is rare.

Sample RYD17, 1.9 m from the contact has detrital compositions similar to the background, although plagioclase is less. Porosity reduction is dominated by compaction (COPL=39.1 %, ±4.7). Like at 0.6 m undulose grains are common suggesting plastic deformation occurred, sutured grains and concavo-convex grain

contacts are also common (Fig. 6.15Ci, Cii.). Grain fracturing is apparent, but usually healed with quartz.

Further than 2.8 m from the contact, plastically deformed quartz is rare (probably inherited) and compaction is exclusively through pressure solution, brittle compaction and grain reorganisation caused by later diagenesis (e.g. RYD04, 2.8 m).

Together, the contacts on either side of the dyke show that porosity loss occurs in proximity to the dyke, dominated by compaction, but aided by cementation that in the case of the red sandstone is absent further than 2 m from the dyke. In the case of the yellow sandstone, near-dyke effects are similar. Compaction, through pressure solution has clearly affected the sandstone prior to dyke emplacement as quartz cements pre-date increased compaction at the contact that is through plastic deformation *and* pressure solution (including of pre-existing quartz overgrowths). Quartz overgrowths grew before the calcite. The calcite is demonstrated using stable isotopes (below) to have formed during dyke cooling. A degree of lithification therefore existed prior to dyke emplacement. Walderhaug (1994) gives a range of temperatures for quartz overgrowths in Jurassic sandstones from the North Sea subsurface from 75 °C to 165 °C. Sandstones that have passed slowly through the temperature range (tens of millions of years) commonly have inclusions showing temperatures below 100 °C, but sandstones that have rapidly transited the temperature range usually have inclusions trapped above 100 °C (Walderhaug, 1994). If this holds for the Twyfelfontein Formation, any quartz overgrowths must have formed rapidly because initial burial by the lavas was rapid (< 2 Ma), suggesting an increased geothermal gradient compared with the current geothermal gradient of 22 °C km^{-1} (Raab et al., 2005). The palaeo-geothermal gradient could have reached up to 58 °C km^{-1} (Raab et al., 2005), suggesting 1.7 km of burial would

have been sufficient to provide enough heat for pressure solution, even assuming heat is just from the geothermal gradient, not regional or adjacent intrusions. This is clearly greater than the ~ 1 km estimated for the Awahab dykes, which also have pre-existing quartz overgrowths, but combined with a localised heating due to igneous activity, this depth could be reduced. It is therefore suggested that the aquifer that pre-existed dyke intrusion was probably above 100 °C at some point (possibly during regional intrusion episodes).

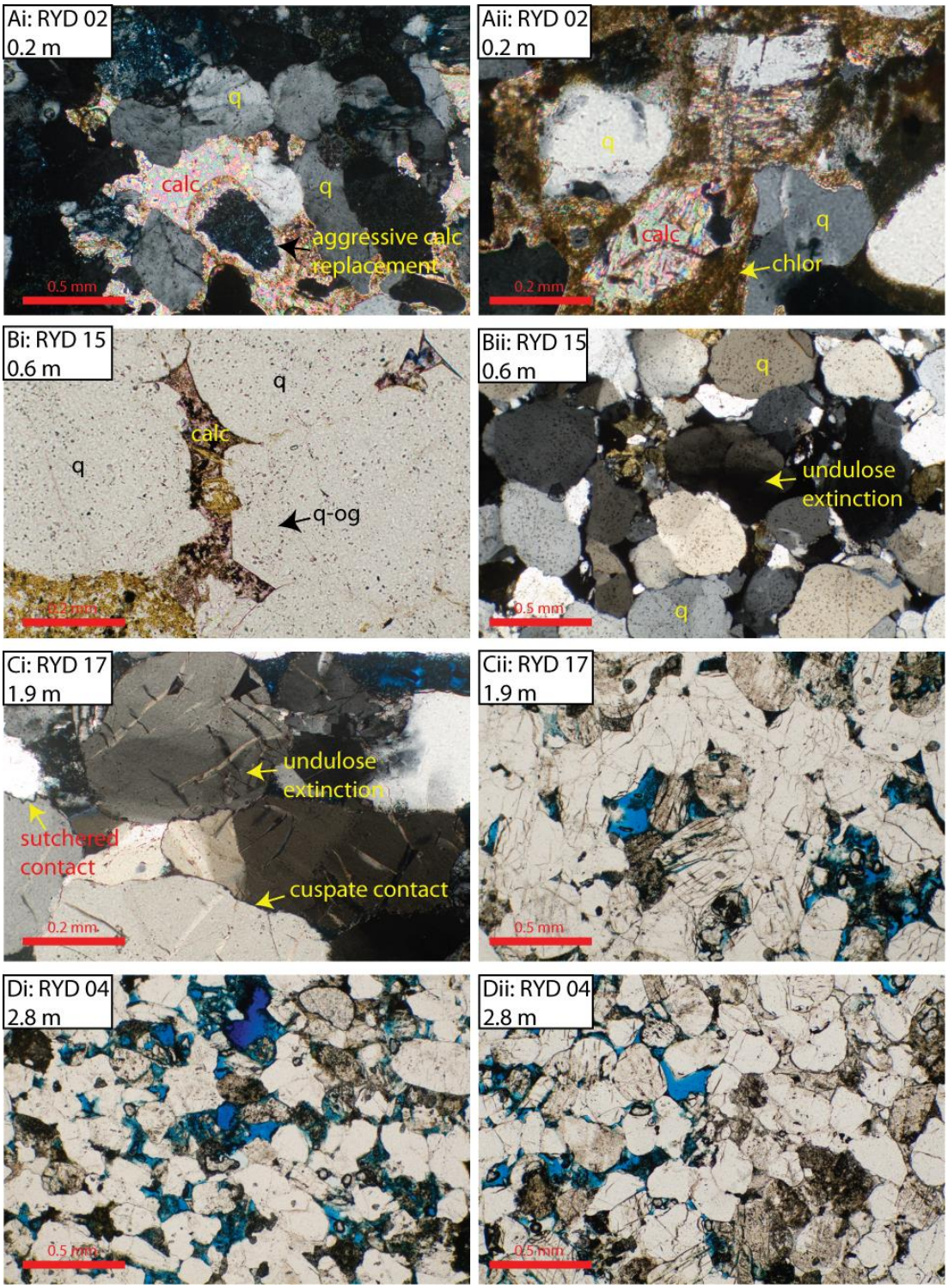

Fig. 6.16. Photomicrographs of sandstone away from the eastern (white) contact. (Ai, ii XPL) 0.2 m from the contact detrital grains are compacted and undulose. Calcite fills porosity and is often seen replacing quartz; chlorite is frequently intergrown with calcite. (Bi PPL) 0.6 m from the contact calcite and chlorite overgrow quartz overgrowths, although high compaction makes available pore space minimal. (Bii XPL) Image showing pervasive undulose extinction in detrital quartz grains 0.6 m from contact. (Ci XPL) 1.9 m from contact sand is still highly compacted, with evidence for both pressure solution and plastic deformation. (Cii PPL) Porosity is present as secondary grain dissolution and primary, quartz overgrowths are common and grains

are fractured. (Di, ii PPL) By 2.8 m from the contact, background white sand diagenesis is dominant, grain dissolution, calcite and clay authigenesis.

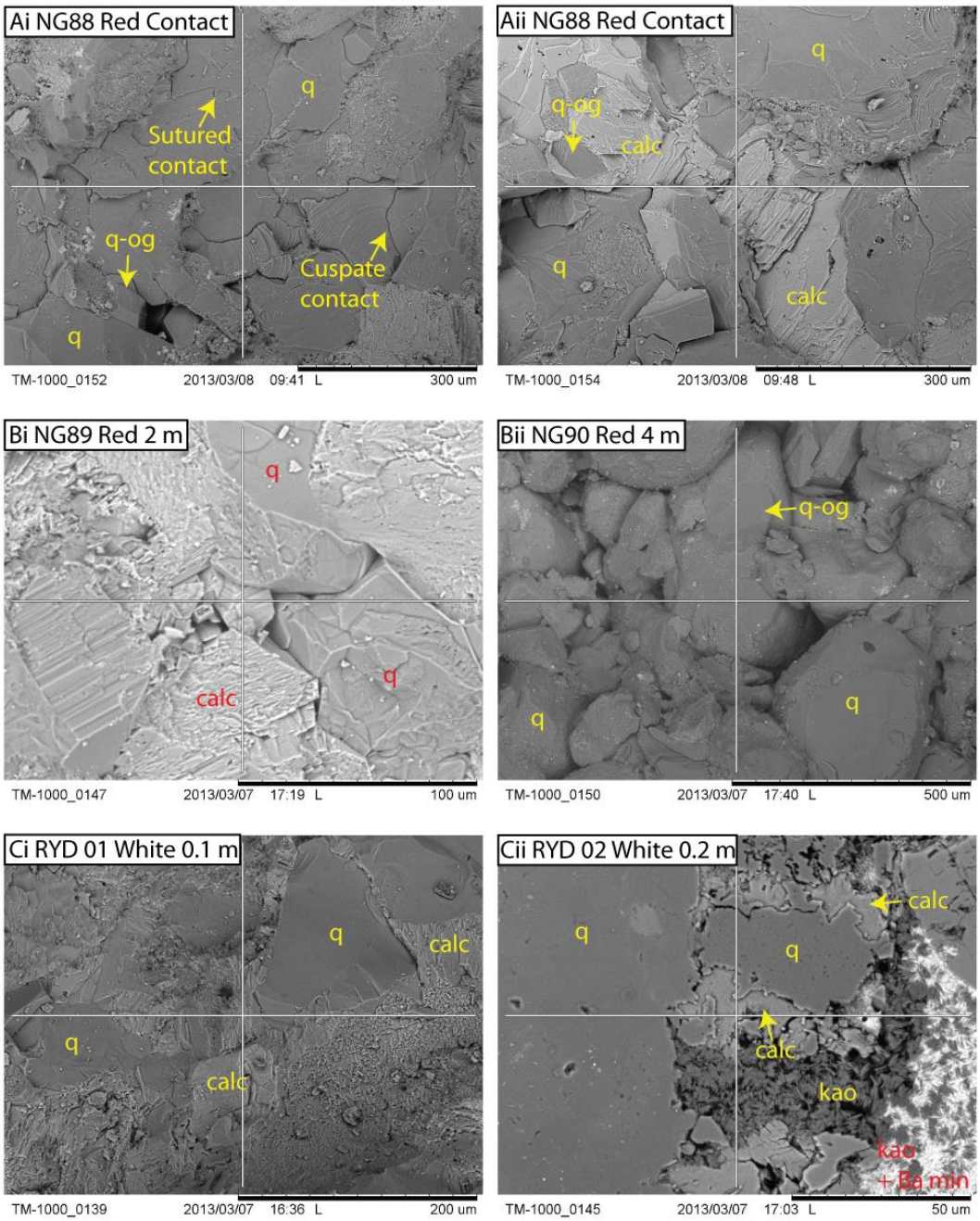

Fig. 6.17. SEM micrographs of sandstone away from the RYD dyke. (Ai, ii) At the red contact the high degree of compaction is evident as sutured grains, cuspate contacts and low porosity, calcite fills remaining porosity and is later than quartz overgrowths. (Bi) 2 m from the contact porosity is present and rare calcite grows over authigenic quartz. (Bii) 4 m from the contact, porosity is higher, detrital grains are clearly discerned and are dotted with very fine haematite (light specks). Authigenic minerals are restricted to rare quartz overgrowths. (Ci) 0.1 m from the contact, the white sandstone is similar to the red sandstone, high compaction with calcite cementation over quartz. (Cii) 0.2 m away from the contact, is evidence for the aggressive nature of the calcite cement, replacing a quartz grain.

6.3 Establishing the origin of the calcite

6.3.1 Stable isotopes

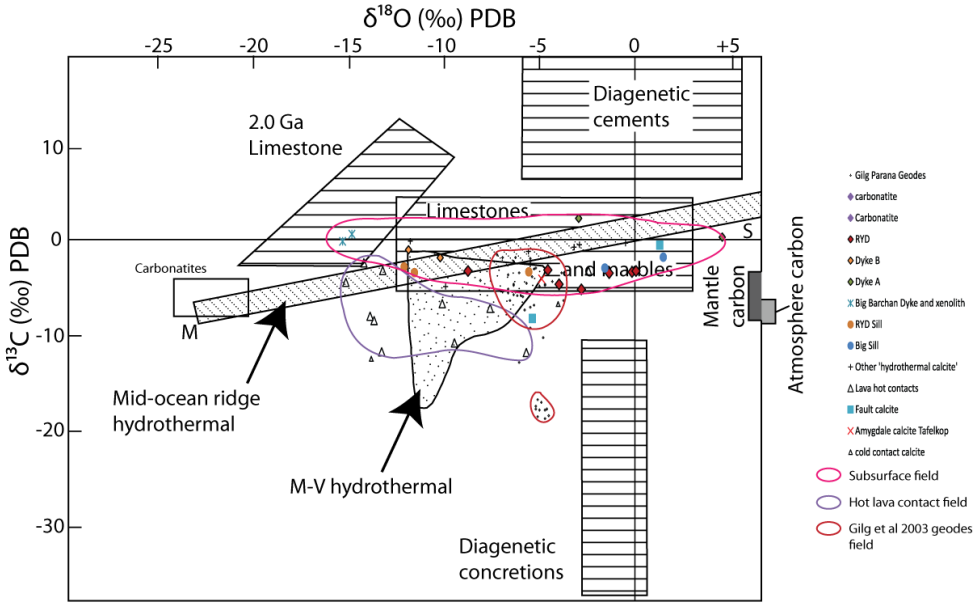

Fig. 6.18. δ ^{13}C (PDB) plotted against δ ^{18}O (PDB) all of the analysed samples Fields are from Rollinson (1993) and Barker (2007). Mid-ocean ridge hydrothermal lies along a trend with magmatic (M) and sea water (S) end members. Lava contact and hydrothermal diagenetic carbonates plot in two distinct populations, with sub-lava flow carbonate cements having more mantle-like δ ^{13}C values. Hydrothermal dyke contact samples have less mantle influence and suggest mixing with heavier carbon. Also plotted are the carbonate stable isotope values from geodes from Parana Flood Basalts (Gilg et al., (2003), which plot as two modes, the larger of which overlaps hydrothermal calcites from this study.

Fifteen samples from the Twyfelfontein Formation from transects away from intrusive rocks returned a CO_2 yield adequate for stable isotope analysis. Six samples produced data from the RYD case study on the eastern *white* side of the dune, which are the most useful. All intrusions produced some data, although those that produced only two data points are of limited statistical use, but nevertheless, combined with

other results are of qualitative interest. Also of interest are samples analysed below lava contacts (Chapter 6) which are also plotted for comparative purposes. Data from fault calcite, basalt amygdale fill and geode mineralisation are plotted. The geode isotope analyses are from Gilg et al. (2003).

Overall, when plotted over the fields of Rollinson (1993) and Barker (2007) the calcite samples that formed in the subsurface (pink outline, Fig. 6.18.) form a field with variable $\delta\ ^{18}O$ (PDB) values, from -15 ‰ to 4.7 ‰, $\delta\ ^{13}C$ (PDB) varies from -8.2 ‰ to 2.3 ‰. This field overlays Rollinson's (1993) limestones and marbles field, the mid-ocean ridge hydrothermal field and the Mississippi Valley type hydrothermal field. The field also overlays the field (red, Fig. 6.18.) of the calcite and amethyst-bearing geodes of the Rio Grande do Sul area, Brazil (Gilg et al., 2003). These geodes are found in Parana lava flows. They probably formed at < 100 °C, with calcium and carbon sourced from host rock basaltic glass (Raab et al., 2005). Similar smaller geodes are also found in some flows in the Etendeka and are mined by hand in the region of the Goboboseb mountains, east of Messum. Also plotted is the field of surface formed calcites, probably directly formed below hot lava flows. The surface field plots separately from the subsurface field, with lighter oxygen and carbon values. Overall the heavier oxygen and carbon stable isotope values of the subsurface field suggest cooler temperatures, less magmatic carbon influence and probably the influence of more meteoric water as opposed to a dominant magmatic water source. The subsurface field also encompasses calcite from faults in the field area, calcite that formed above cold lava contacts (i.e. buried lava and hydrothermal calcite forming in the subsurface) and calcite in Tafelkop type basalt amygdales.

Figure 6.19 shows the same data as in Fig. 6.18. but with the Rollinson (1993) fields removed for clarity. The aim here is to interrogate the subsurface calcite data in more detail. Within the subsurface field, each case study transect plots separately, and each case study shows low $\delta\ ^{13}C$ variability, but usually a fractionation trend in $\delta\ ^{18}O$. Three such trends are highlighted in Fig. 6.19. Two of the 'trends' (Dyke A and Sill S1 (Big Sill)) only have 2 data points, so should be treated with caution, but the third (RYD) has 6 samples (7 points due to double analysis of one sample) showing a strong trend. The trends are from light oxygen isotope ratios towards heavier ratios with small carbon isotope ratio variability. The samples closer to igneous bodies have lighter oxygen isotope signatures. The fact that each case study plots separately suggests that each calcite forming event responded to individual local conditions, but in the same manner (i.e. starting conditions were slightly different, but the regime was the same).

The identification of these trends prompted the modelling of possible oxygen isotopic and temperature variability in the water it would have precipitated from. The only sample transect with enough data to compare to the model, with a statistical authority is the RYD transect. Fig. 6.20. shows results of the modelling. Fig. 6.20C, D.) show plots of $\delta\ ^{13}C$ against distance from dyke and $\delta\ ^{13}C$ against δ^{18} O respectively, both of which show no correlation, which suggests isotopic equilibrium conditions (Alex Baker, *personal communication* 2013).

The model was calculated using fractionation constants of A=-3.39 and B= 2.78, (O'Neil et al., 1969) and the equation:

$1000 \ln \alpha = A + B (10^6/T^2)$ from Rollinson (1993)

Where T is temperature and $\ln \alpha = \delta^{18}O_{calcite} - \delta^{18}O_{water}$. Using this, the expected $\delta^{18}O_{calcite}$ can be calculated for any temperature and water.

The result of the modelling is that a cooling trend has been identified away from the RYD dyke. The trend exists for whatever water composition is modelled, but the actual temperature values vary. With a value of $\delta^{18}O$ (SMOW) = 7 ‰, which is a likely meteoric value for the latitude of Namibia in the Cretaceous (Bowen & Revenaugh, 2003), the temperatures ranges from 20 °C 0.5 m from the contact to 0 °C 1.9 m from the contact. No data was collected closer than 0.5 m due to low CO_2 yields (compaction dominating porosity loss). Using the lower limit of magmatic waters (Rollinson, 1993), the temperatures range from 115 °C at 0.5 m to 45 °C at 5.8 m distant. The upper limit of magmatic water, temperatures range from 205 °C 0.5 m from the contact to 90 °C 5.8 m away. These results from the model are plotted in Fig. 6.20B. Using the meteoric water value clearly produces unachievable results as freezing water is not likely in this system, nor could the calcite precipitate from frozen water. It is likely therefore that the water isotopic composition was heavier than meteoric composition. This could be caused by contamination with magmatic water or the action of organic fractionation in soils, which would affect both the oxygen and carbon isotopes. No soils are preserved in the Twyfelfontein formation, nor would any be expected. Water-basalt interaction could also produce the required water (Stevens & McKinley, 2000). The favoured explanation therefore is the contamination of a meteoric aquifer with magmatic water probably degassed from basaltic intrusions and hydrothermal interaction with the basalt pile (see Chapter 7). The likely temperatures of calcite precipitation therefore falling below the upper magmatic modelled values and likely meteoric values. If Gilg et al. (2003) are correct in their 100 °C temperature estimate, and this applies to areas

distal to igneous intrusion, our upper magmatic water values may hold. This is also consistent with the quartz overgrowths forming prior to dyke intrusion at 100 °C (Walderhaug, 1994).

The important point, whatever the actual temperatures of precipitation, is that the calcite was precipitated while a temperature gradient existed towards the RYD dyke. The calcite in the white sand therefore precipitated during dyke cooling. It holds therefore that the calcite is a cement formed as a result of dyke intrusion, probably supplying CO_2 required for the calcite forming reaction. Calcium was probably sourced from both the mafic igneous rocks (e.g. Matsui et al., 1974; Gilg et al., 2003) and the hydrothermal reaction of plagioclase (Hangx & Spiers, 2009). Plagioclase replacement is evident in the sandstone.

When δ^{18} O for all of the transects with data showing a lightening of measured oxygen isotope values within the calcite towards igneous contacts are plotted (Fig. 6.20E.), it is remarkable how the gradients of the lines are so similar (granted, amount of data makes it statistically weak). This suggests that the hydrothermal cooling regime of the intrusions, by the aquifer precipitating calcite was similar. This is not surprising, considering it is the same aquifer being intruded by all of the intrusions shown in Fig. 6.20E. This also provides evidence that the igneous bodies (both dykes and sills) were being cooled by the aquifer in addition to conductive cooling by the country rock as is typically assumed by current numerical models (Galland et al., 2009; Aarnes et al., 2010; Aarnes et al., 2011; Holness et al., 2012).

There are data collected in Fig. 6.19. that do not match the dominant trend of cooling away from intrusions. The two data points for Dyke B plot the opposite way around; these points were only 10 cm separate. The RYD sill samples also plot the

other way around, with lighter oxygen near to the contact. Both S2 and S3 samples were grouped here. The explanation for this could be *active* CO_2 degassing from the sill during calcite precipitation providing an influx of light water near to the sill. The 'Big Sill', S1, is probably the same intrusive body and does not show this reverse trend (see Fig 6.19, Fig 6.20.). The most negative $\delta\ ^{18}O$ values were both for the Barchan Dyke samples, either suggesting these were precipitated at elevated temperatures (up to 400 °C, if magmatic water). Complete isotopic data can be found in the Appendix, together with data for standards run with the Namibian samples.

ID	Description	Distance from Intrusion	13C12C v-pdb	18O/16O v-pdb	18O/16O v-smow
NG 109	Big sill 4 m	4	-2.90	-1.52	29.34
NG 110	Big sill 7 m	7	-1.75	1.55	32.51
NG/12-27	RYD sill S3 4 m	4	-2.77	-12.08	18.46
NG 73	RYD sill S2 1.2 m	1.2	-3.29	-5.52	25.22
NG 72	RYD sill S2 0.2 m	0.2	-3.37	-11.53	19.02
NG 42	Dyke A contact red	0	2.33	-2.90	27.92
NG 44	Dyke A 8 m white	8	0.35	4.65	35.71
NG 49	Dyke B contact	0	-1.81	-10.17	20.42
NG 50	Dyke B 10 cm	0.1	-0.98	-11.84	18.70
NG 68	big barchan red dyke contact	0	-0.09	-15.30	15.13
NG 67	dyke xenolith	0	0.66	-14.82	15.64
RYD01 CH	RYD 0.5 m	0.5	-3.20	-8.71	21.93
RYD 02	RYD 0.6 m	0.6	-3.10	-4.51	26.26
RYD17 CH	RYD 1.9 m	1.9	-4.61	-3.92	26.86
RYD 04	RYD y 2.8 m	2.8	-3.44	-1.29	29.58
RYD 05	RYD 4.6 m	4.6	-5.14	-2.75	28.07
RYD06 CH	RYD 5.8 m	5.8	-3.21	0.12	31.03

RYD 06	RYD 5.8 m	5.8	-3.31	-0.09	30.82
NG 59	Fault material Awahab Barchan	NA	-8.19	-5.33	25.42
NG 54	Awahab camp fault material	NA	-0.49	1.37	32.32
NG 62	Tafelkop lava amygdales	NA	-4.03	-4.84	25.92
NG 63	Cold Tafelkop contact big barchan	NA	-6.67	-3.97	26.82

Table 6.2. Stable isotope data for dyke and sill sandstone transect samples analysed.

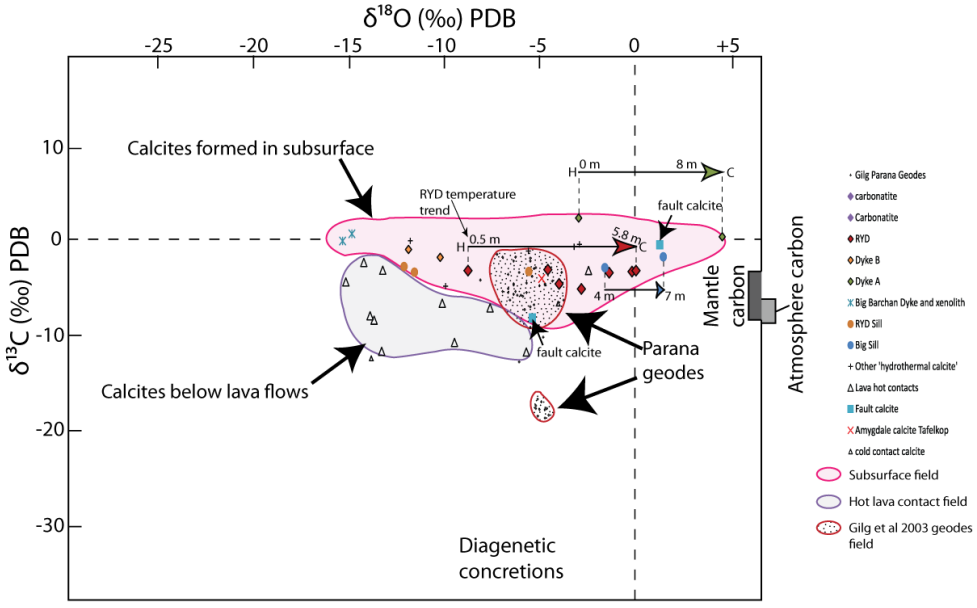

Fig. 6.19. δ ^{13}C (PDB) plotted against δ ^{18}O (PDB) all of the analysed samples with fields of Rollinson (1993) and Barker (2007) removed for clarity. Lava contact and hydrothermal diagenetic carbonates plot in two distinct populations, with sub-lava flow carbonate cements having more mantle-like δ ^{13}C values. Hydrothermal dyke contact samples have less mantle influence and suggest mixing with heavier carbon. Also plotted are the carbonate stable isotope values from geodes from Parana Flood Basalts (Gilg et al., (2003), which plot as two modes, the larger of which overlaps hydrothermal calcites from this study. Both populations, within each case study show temperature dependent δ ^{18}O fractionation trends, which are related to distance from dyke or sill in the case of the subsurface field (see Fig. 6.20.)

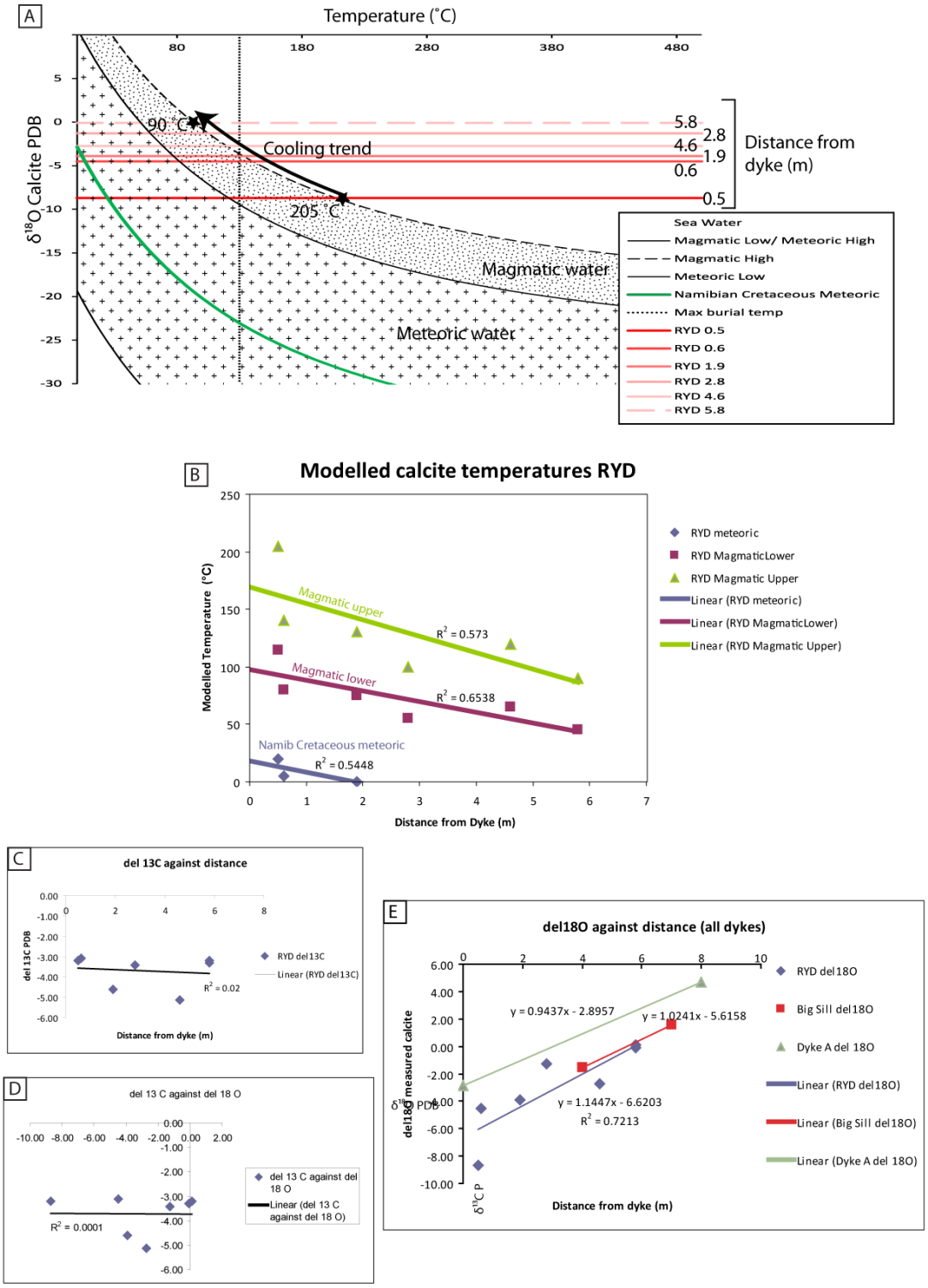

Fig. 6.20. (A) Modelled calcite δ ^{18}O values in equilibrium with waters of different origins. Calculated meteoric and magmatic fields are shown (using fractionation constants A=-3.39 and B= 2.78, O'Neil et al., 1969) as well as the expected meteoric water value for Namibia in the Cretaceous (green line). Max burial temp of 130 °C has been calculated based on geothermal gradients and burial data from Raab et al., (2005). δ ^{18}O values from our analyses are plotted. When measured δ ^{18}O calcite from the PL samples are plotted, the intersections with water compositions give a precipitation

temperature, that decreases away from the dyke. (B) Modelled temperatures for three water compositions, meteoric (-36.8 ‰ PDB), magmatic upper (-17.4 ‰ PDB) and magmatic lower (-23.2 ‰ PDB), all show temperature decreases away from the dyke. (C, D) No correlations exist between $\delta^{13}C$ and distance from dyke or $\delta^{18}O$ suggesting equilibrium conditions (personal communication, A Baker, 2013). (E) Relationship between $\delta^{18}O$ measured and distance from dyke for all intrusion samples successfully analysed shows that gradients are the same, suggesting similar cooling regimes (albeit only 2 points for Dyke A and Big Sill.

6.4 Direct effects of Sills on the Twyfelfontein Formation

Upper Huab sill contacts with the Twyfelfontein are well exposed leading into the Huab valley and have been studied to assess the sills effect on the sandstones. Sills are transgressive (i.e. step up stratigraphy as inclined sheets; sill at transects S2, S3) and propagate as magma fingers (cf. Schofield et al., 2010) (Fig. 6.21A.). Three contacts are presented, all from the same sill, but at different locations (transects S1, S2, S3, Fig. 6.12.). The direct effect varies depending on the location; at all locations a distinct pyrometamorphic zone exists involving partial melting of the sandstone, followed by distinct petrographic zones (marking palaeo-isograds). All three localities exhibit the same set of features, but the intensity varies.

The sill at transect S1 crops out in an east facing cliff (Fig. 6.21A.). The lowermost part of the outcrop is a Huab sill displaying a fingered morphology (cf. Schofield et al., 2010) with a shallow dip to the west. The fingers are up to 6 m high, although the total sill thickness is not exposed. Twyfelfontein Formation sandstone above the sill at transect S1 is up to 7 m thick.

The sill at transect S2 (Fig. 6.24.) crops out on a desert plain (vegetated in 2011) and is 35 m thick dipping 28° toward 098° and is continuous in outcrop to S3 (Fig.6.26.). The dolerite sill weathers more rapidly than the Twyfelfontein Formation

in contact. The upper contact sandstone was sampled for both S2 (up to 1.5 m above constrained by outcrop) and S3 (up to 5 m above).

6.4.1 Big Sill Locality

6.4.1.1 Sill S1

The sill that crops out at transect S1 is probably the same sill sampled at transects S2 and S3. Transect S1 is located at 20° 35.795' S 14° 04.367' E at 452 m in an east facing cliff. In outcrop the dolerite sill is up to 6 m high and is exposed as the upper surfaces of a number of solidified magma fingers similar to those of the Golden Valley Sill, South Africa (Schofield et al., 2010). The total sill thickness is probably at least twice that of the exposed outcrop. The sandstone above the sill is of the Twyfelfontein Formation, Major Erg unit. The outcrop is located 1.9 km NNE of the main RYD dyke outcrop along the track that runs north towards the Huab river (Fig. 6.12.). The outcrop at the contact (Fig. 6.21B.) consists of chilled dolerite below a 10 cm thick buchite (originally sandstone) contact zone, where original sedimentary structure is vague, this zone is discoloured to a darker green-brown. Above this the sedimentary structure is again visible, but the rock is still affected by pyrometamorphism, there is no visible porosity. Occasional vugs exist in the pyrometamorphic zone, that are lined with quartz crystals, suggesting free fluid during sediment aureole solidification (e.g. Holness et al., 2012).

At the contact (NG112) the dolerite originally had thin 250 μm glassy quenched contact, that has now altered to clay (Fig. 6.22A, B.). The material against this contact comprises of restic detrital quartz grains in a matrix of granophyre

composed of potassium feldspar intergrowth with quartz which contains smaller restic quartz grains, needles of quartz paramorphs after tridymite and orthopyroxene that has been largely pseudomorphed by chlorite. The quartz paramorphs after tridymite fringe restic quartz grains and grow within the granophyre. Chlorite also lines fractures within detrital quartz grains (Fig. 6.22B.). A detrital quartz grain that is in contact with the dolerite glass (Fig. 6.22B.) shows a thin film of quartz crystals that represent crystallised quartz melt (Sawyer, 1999). The granophyric matrix is also due to partial melt of the feldspathic component of the protolith, which is no longer present in detrital form. The melt reaction is $Qtz+Ab+Or+H_2O \rightarrow melt.$, if melting was H_2O absent pressure would need to be in excess of 0.5 kbar (1.8 km) (after Holness et al., 2012). Vugs in the contact zone suggest hydrous conditions. The melt crystallised, firstly as tridymite at high temperatures, then as cooling progressed as the granophyric intergrowth of quartz and potassium feldspar (possibly sanidine). The total melt proportion is in excess of 50 % (±2.2).

At 0.1 m from the contact the sample is much the same as at the contact, although chlorite alteration appears less intense (probably related to proximity to weathering dolerite). Restic quartz grains, rimmed with quartz paramorphs of tridymite exist in a granophyric intergrowth of potassium feldspar and quartz, with, now in tact porphyroblasts of orthopyroxene. Sample NG111, shows incipient melt segregation, with rare aggregations of restic quartz grains into larger grains (Fig. 6.22D.). The granophyric matrix contains well developed orthopyroxene crystals and rare Carlsbad twinned potassium feldspars, supporting the identification of sanidine as the potassium feldspar. Porosity is negligible (0 %) as is permeability (0 md recorded) (Fig. 6.23A.).Total melt is probably more than 50 % (±2.2).

Moving away, by 0.6 m the sandstone consists of restic quartz grains, and abundant restic potassium feldspar grains, with minimal granophyric matrix (probably ~ 5 %) which is confined to occasional quartz-feldspar grain boundaries (Fig. 6.22F.). Tridymite and orthopyroxene are absent. Detrital grains are deformed such that porosity is negligible and permeability is >1 md. Calcite is present, filling any remaining porosity (1.2 %, ±0.5).

Finally by 4m above the sill contact, no pyrometamorphic reactions are observed. The sediment is a highly compacted (COPL= 52 %, ±4.0) sandstone, with detrital composition similar to the background. Compaction appears dominated by pressure solution as sutured quartz grain contacts are abundant. Authigenic mineralisation comprised of calcite, which appears to fill remaining porosity and aggregates of haematite, probably remobilised from closer to the contact.

The furthest sample above the sill on transect S1 is at 7 m. This sample is characterised by the return of porosity. The detrital composition is approximately background. Porosity loss is dominated by intense compaction (COPL= 50.2 %, ±4.0), with minor quartz overgrowths and calcite partial pore fills (Fig. 6.22H.). Compaction is dominated by pressure solution, grains are rarely undulose and sutured contacts are common. Most grains interpenetrate, with feldspar-quartz contacts showing marked concavo-convexity.

Transect S1 defines two pyrometamorphic palaeo-isograds that can be assigned temperature ranges at given pressures: Firstly is the tridymite, orthopyroxene, granophyre assemblage, where tridymite is the diagnostic mineral. This is a typical pyrometamorphic assemblage created by the partial melting of an arkosic sediment protolith (e.g. Grapes, 2010; Wyllie, 1961; Spry & Solomon, 1964; Frankel, 1949; Ackermann & Walker, 1960; Balance & Waiters, 2002; Holness,

1999; Holness et al., 2012). In this zone, cooling was slow enough to allow crystallisation of the melt as opposed to vitrification. The pyrometamorphic assemblage depends on the composition of the protolith, and is similar for granitic metasediments (e.g. Holness & Watt, 2002). If the maximum pressure attained by the Twyfelfontein Formation during burial was 1.5 kbar, the likely pressure during sill emplacement is somewhere between 0.15 kbar (if emplaced at minimum depth of exposed outcrop) and 1.5 kbar (emplacement at maximum burial). Further constraint on pressure is that tridymite does not crystallise above 1.375 kbar (Grapes, 2010), so sill emplacement, must be shallower than 5 km (2800 kgm^{-3}). Using the tridymite stability field from Grapes (2010) the following constraints apply for the formation of tridymite in the Twyfelfontein Formation: At 1.375 kbar tridymite forms at 1170 °C, at 0.15 kbar tridymite is stable between 900 °C and 1420 °C. The lower temperature limit of this petrographic zone was therefore 900 °C and the upper was 1420 °C, with likely intrusion depth probably not significantly greater than a kilometre based on the dykes above (0.3 kbar). At 0.27 kbar tridymite is stable between 936 °C and 1268 °C. 1420 °C is higher than the likely temperature of the mafic magma (~1150 °C) which should be taken as an absolute maximum, therefore, the petrographically determined tridymite zone can be delimited as between ~ 936 °C and 1150 °C.

The second pyrometamorphic zone is where the melt reaction has occurred, but no tridymite has crystallised, instead the granophyre consists of intergrown quartz and potassium feldspar. This zone also frequently has spherulitic feldspar, suggesting quenching of the melt (or incipient vitrification). The absence of tridymite is an important temperature indicator. If the calculated depth above holds (~1 km, certainly <<5 km), 0.27 kbar lithostatic pressure is appropriate. The temperature

constraint this zone is therefore between 860 °C and 936 °C, with the onset of melting at 860 °C based on the P-T projection of the sanidine+quarz+liquid+gas and sanidine+tridimite+liquid+gas by Shaw (1963). Increasing the burial depth increases the range of temperatures that sanidine+quarz+liquid+gas is stable, and above 1.375 kbar (5 km) tridymite does not crystallise (Grapes, 2010). It is likely therefore that this petrographic zone reached a temperature of at least 860 °C if the depth estimate above holds. If intrusion was at the (unlikely) maximum burial depth of 5 km, the temperature is slightly lower, 780 °C. At 1 km, the temperature cannot have reached the tridymite isograd of 900 °C (Shaw, 1963; Grapes, 2010).

Where no melting of the sediment is observed, the sandstone shows increased compaction mainly through increased pressure solution, which is probably enhanced by the pressure exerted by the sill and the elevated aquifer temperatures (e.g. Houseknecht, 1984; Houseknecht, 1988) (evident in the $\delta^{18}O$ gradients, showing increased temperature approaching intrusions, including the S1 transect). Cementation with calcite also reduces porosity in this zone. The zone can be summarised as a hydrothermally dominated regime, where aquifer water is cooling the intrusion below. The water is probably part of a boiling hydrothermal system (if pressure allows) or superheated steam (Simmons & Christenson, 1994). The oxygen isotope model in Fig.6.20A. would suggest that the calcite here (NG109 $\delta^{18}O$= -1.52 ‰ and NG110 $\delta^{18}O$= 1.55 ‰) precipitated at between 60 °C at 7 m and 100 °C, at 4 m, assuming the discussed likely water composition of mixed magmatic-meteoric discussed above. Meteoric water only gives low temperatures not consistent with the observed gradient, paragenesis or burial depth. Background porosity or petrographic conditions were not observed at this transect due to exposure, but are calculated based on observed porosity increase to lie at ~22 m (see Fig. 6.33.).

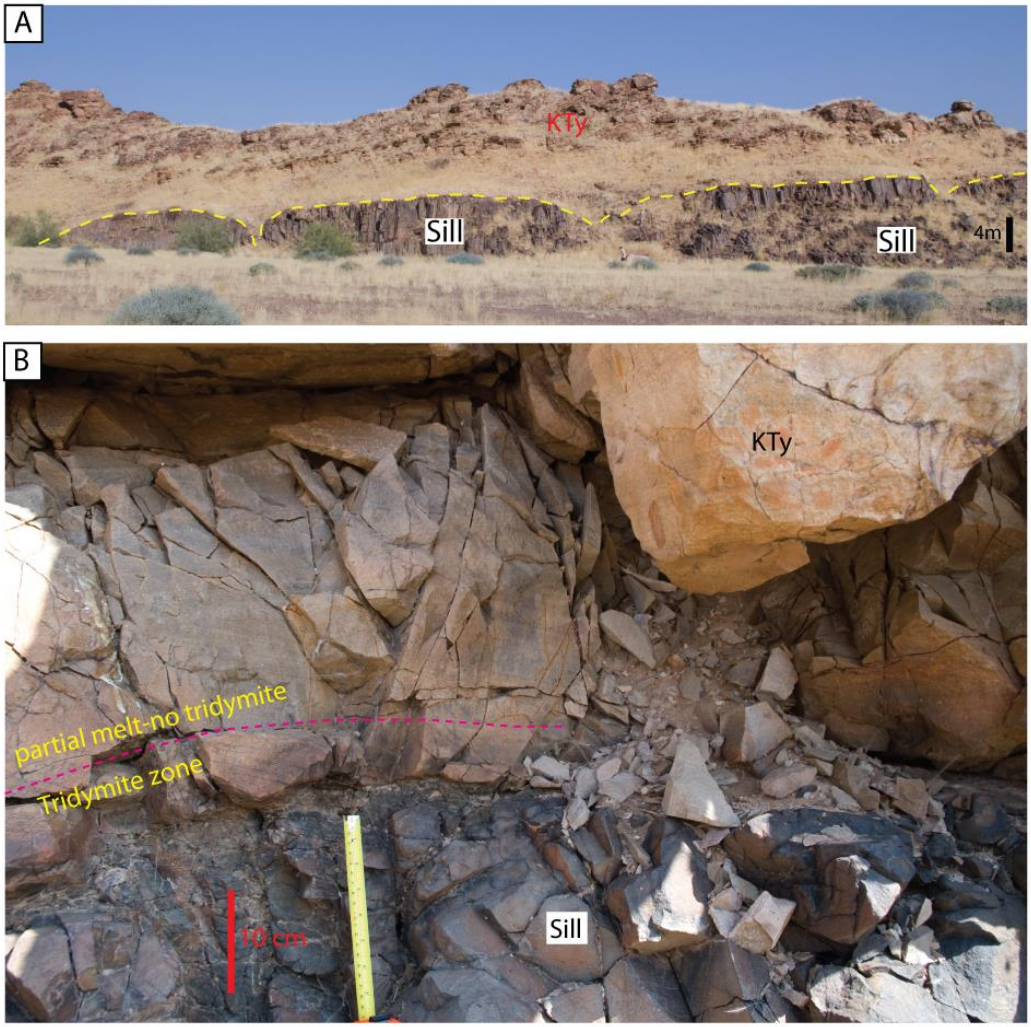

Fig. 6.21. Photographs of Big Sill (Sill S1) locality. (A) facing west towards the outcrop. Person for scale (Note lobe like morphology on top of sill highlighting location of early fingers of the sill during emplacement e.g. Schofield et al., 2010). (B) The sample locality at the contact facing west. Note that no sedimentary structure is visible within ~ 10 cm of the contact.

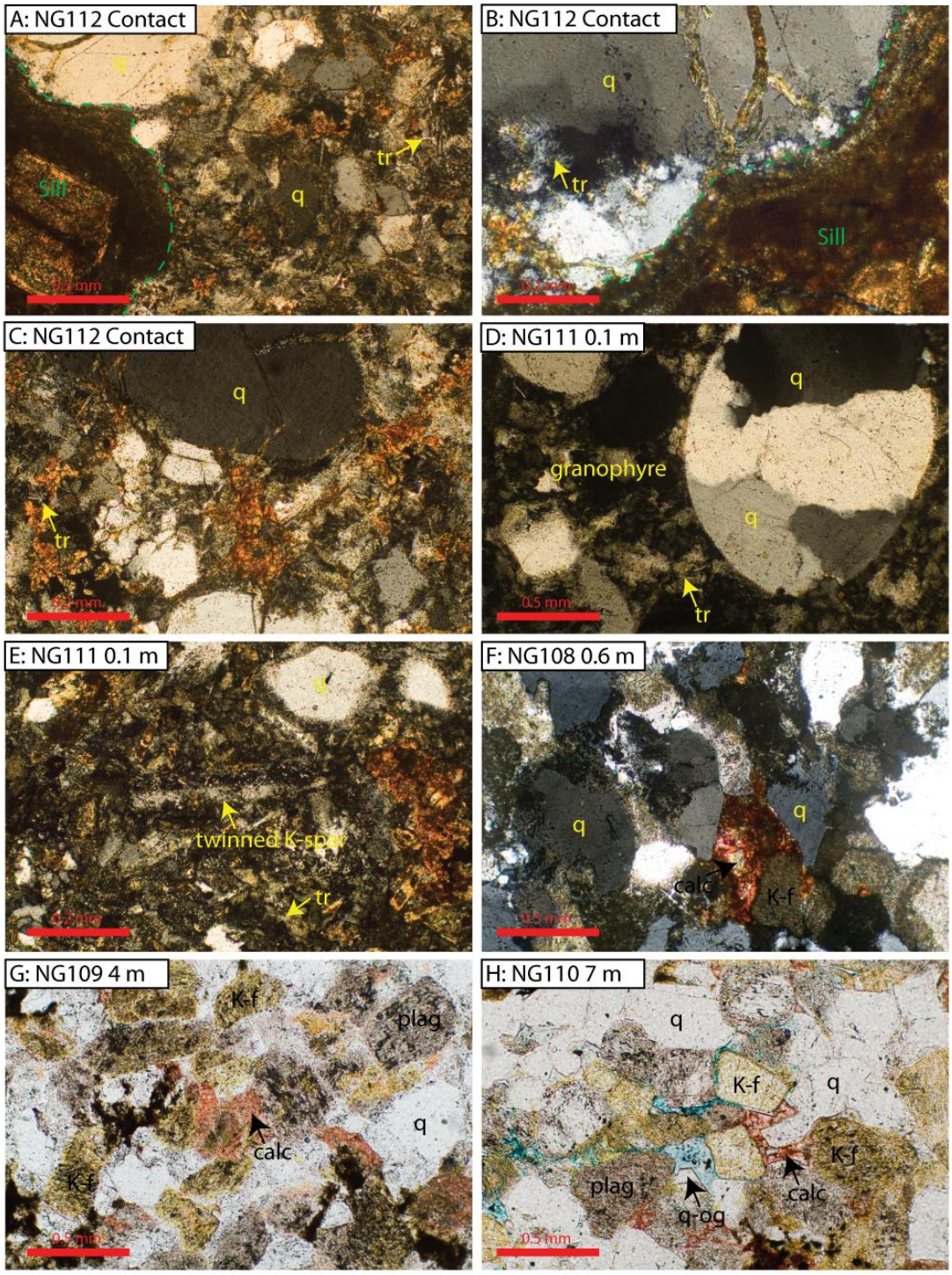

Fig. 6.22. Photomicrographs above sill S1. (A, B, C XPL) At the contact quartz is the only restic detrital mineral, and is rimes with quartz paramorphs after tridymite. The chilled sill contact is visible (now altered to clay). The matrix consists of granophyric intergrowth of potassium feldspar, quartz and tridymite with occasional opx now altered to chlorite. (D, E XPL) 0.1 m above the sill quartz is also the only restic mineral and is rimes with quartz paramorphs after tridymite. Detrital quartz occasionally is amalgamated to form quartzite 'conglomerate-like' clasts. The matrix is granophyric and contains occasional twinned potassium feldspars, probably sanidine. Vugs are filled with calcite. (F PPL)).6 m above the contact both quartz and potassium feldspar appear restic. Feldspars occasionally show evidence of melting at grain boundaries

where granophyre is poorly developed. (G PPL) 4 m above the sill no evidence of pyrometamorphism is apparent. Sandstone is highly compacted, haematite occurs in redistributed nodules and calcite fills remaining porosity. (H PPL) 7 m above the sill porosity returns. Compaction is high and authigenic minerals comprise quartz overgrowths and calcite.

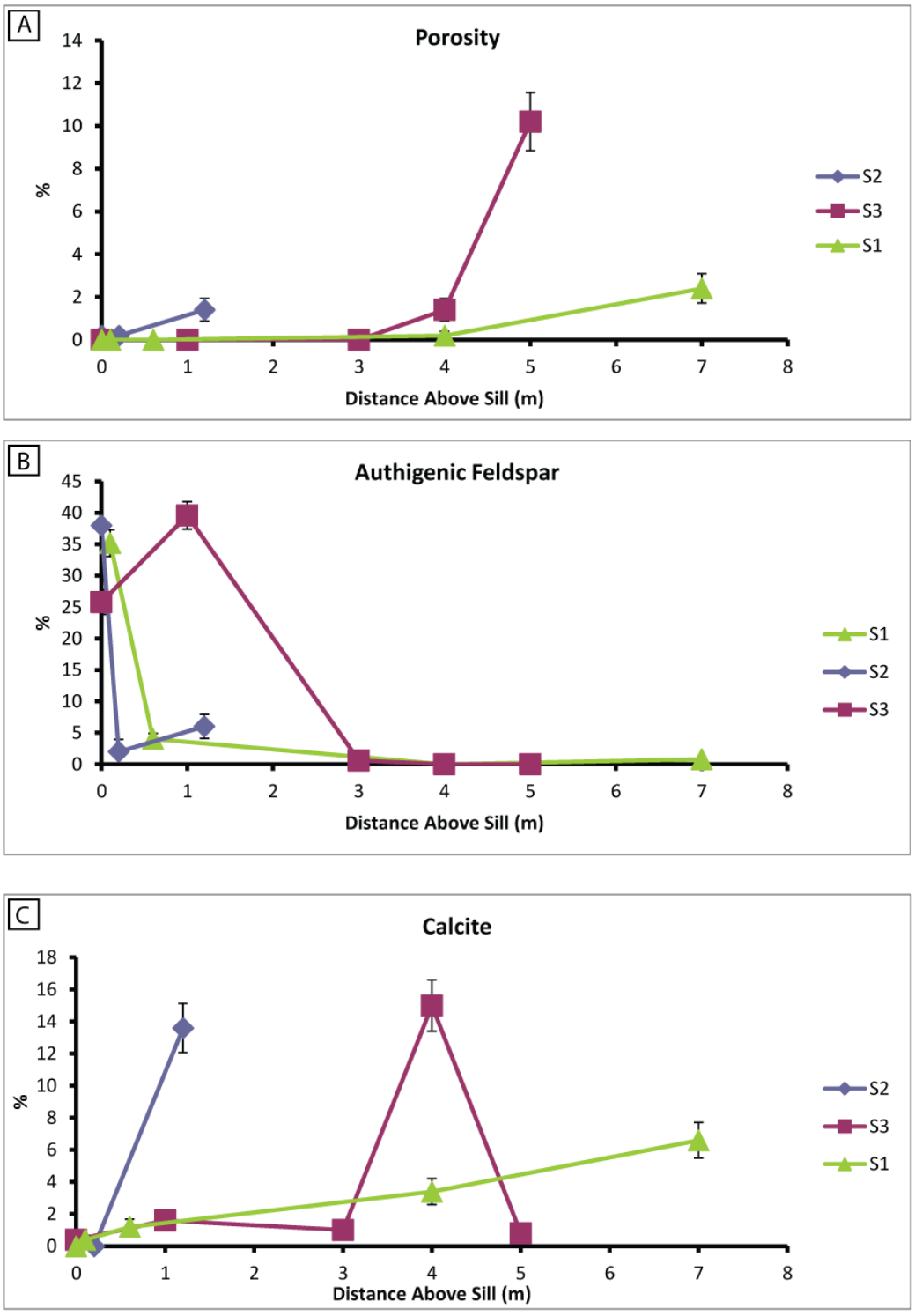

Fig. 6.23. Relationship between distance above sill and (A) sandstone porosity, (B) authigenic feldspar, (C) calcite.

6.4.2 Red Yellow Dyke sills

6.4.3.1 Sill S2

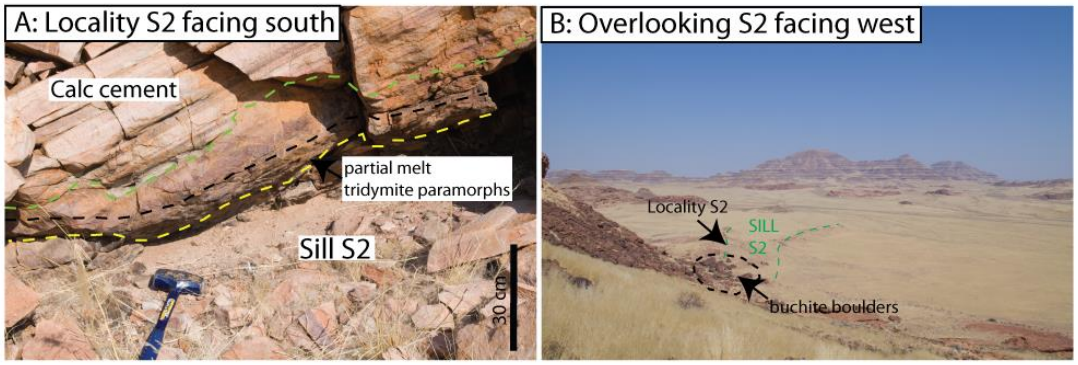

Fig. 6.24. Photos of RYD sill S2 showing location of transect. (A) Sandstone-Sill upper contact, the yellow dash is the boundary between sill and sandstone, the green dash is the upper limit of partial melt. (B) Looking down on the sill, the green dash shows the sill location.

Transect S2 lies on the sill exposed 500 m to the west of the main RYD dyke. The sill is 35 m thick dipping 28° toward 098° and is continuous in outcrop to S3 (Fig.6.26.). The exposure is at 20° 36.751' S 14°03.914' E and at 521 m, in a small cliff facing north. The sill can be traced for some distance to the west, where it disappears into a flat vegetated and regolith covered desert plane. To the east the sill is continuous to the main RYD sandstone cliff, via transect S3. The sill appears at the foot of the intensified effects described in section 6.5. but is no longer exposed shortly after, where it either veers to the north, disappearing into the desert plain or continues into the cliff.

Figure 6.24 shows the outcrop at the location of transect S2. The outcrop consists of a weathered dolerite sill (base of photo) which is overlain by a pyrometamorphic zone consisting of a buchite of ~20 cm thick, which is visible in

outcrop as the darker, more purple band. This zone is the tridymite zone described above. No sedimentary structure is visible in this zone. Above this is a transition from high temperature partial melt to the calcite zone, via a low volume partial melt, tridymite absent zone (green hash, Fig. 6.24A.).

Petrographic analysis of the rock at the contact (NG71) shows that porosity is absent, and permeability is negligible. Detrital potassium feldspars are absent, and plagioclase, which is more restic is rare (Fig. 6.25 Bi). Detrital quartz is rimmed with quartz paramorphs after tridymite (Fig. 6.25Ai, ii). Where detrital quartz crystals are in contact, there is evidence for compaction or possibly the incipient stages of melt segregation (Fig. 6.25C.) as noticed in Fig. 6.22D. The matrix consists of granophyric intergrowths of potassium feldspar and quartz with occasional quartz paramorph after tridymite needles. The granophyric matrix contains opaque grains, probably magnetite. The granophyre occasionally contains spherulitic potassium feldspar, which appears fibrous.

At 0.2 m above the contact, melting of potassium feldspars is apparent, but ghosts of the original grains can be made out. The matrix consists of granophyric intergrowth of quartz and potassium feldspar. Within the matrix are vugs, which are lined with quartz crystals. These suggest a free fluid phase within the molten matrix, probably water.

The furthest sample from the contact here is at 1.2 m, where feldspar melt is incipient. Melt rims crystallised as potassium feldspar rim detrital grains (Fig. 6.25F.). The authigenic feldspar is lighter yellow due to subsurface formation, whereas the detrital grains contain clays formed during transport and deposition. The fresher, authigenic feldspar picks up the potassium tricobaltinitrite stain more readily. Quartz is also present as pore linings, but with more of a melt character as

opposed to the classic quartz overgrowths noticed elsewhere in the Twyfelfontein Formation. Calcite is present at this distance, where it fills remaining porosity as poikilitic crystals.

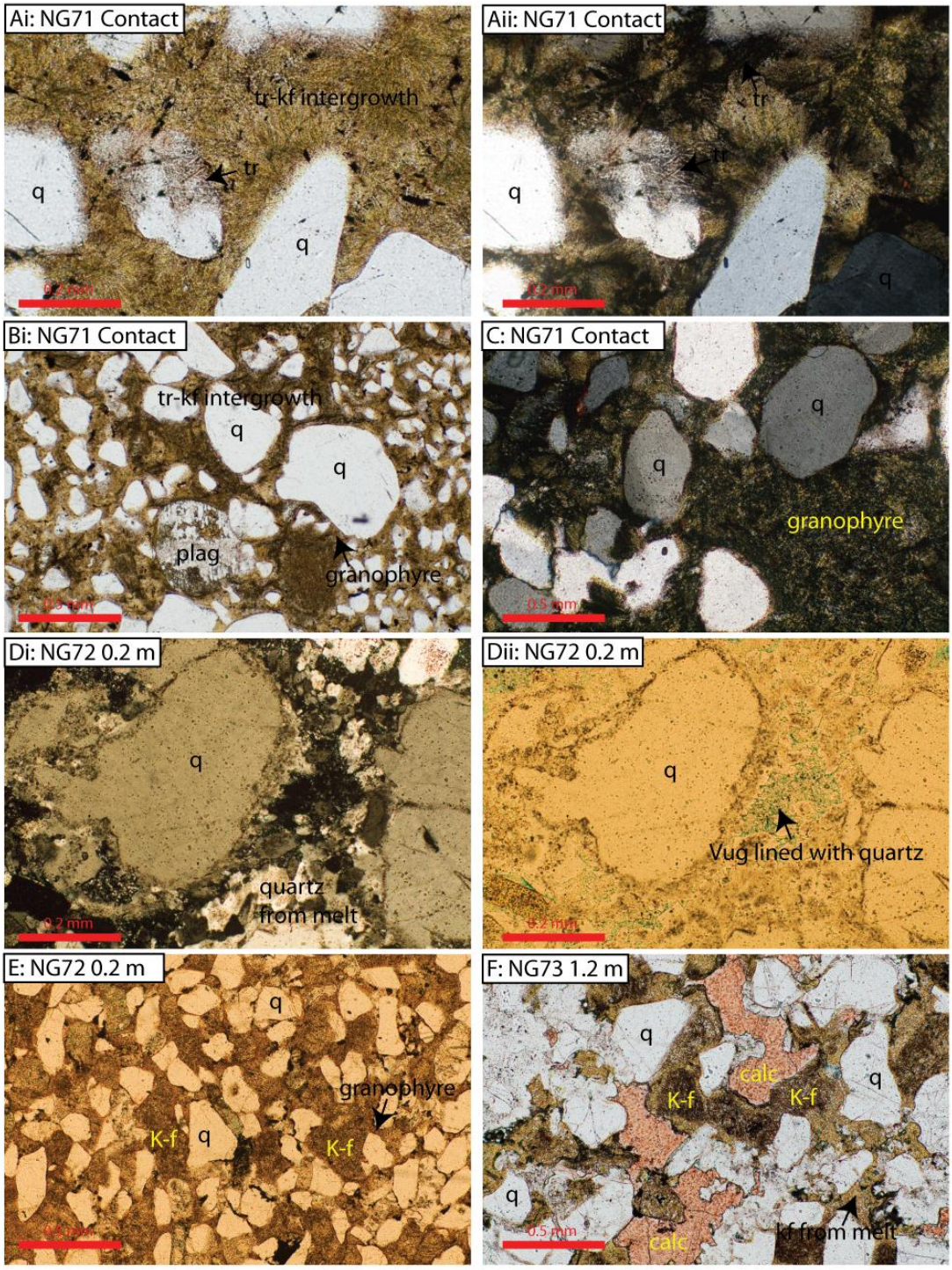

Fig. 6.25. Photomicrographs of samples above the sill at transect S2. (Ai PPL) Restic quartz rimmed with paramorphs after tridymite in a granophyric matrix. (Aii XPL)

Granophyric matrix, and quartz paramorphs of tridymite around the central quartz crystal. Fibrous nature of the feldspar in the matrix can be seen. (Bi) Low magnification view of the buchite at the contact, where a plagioclase grain can be seen as restic. (Bii) Image showing incipient melt segregation. (Di XPL) 0.2 m from the contact, matrix and incipient resorbtion of quartz. (Dii PPL) Version of Di in PPL showing the quartz lined vug. (E PPL) Low magnification view of the sand 0.2 m above the sill showing granophyric matrix from melt and ghosts from partially melted feldspars. (F) Incipient melting of feldspars and quartz, followed by retrograde hydrothermal calcite formed during cooling by aquifer.

The three samples above the sill at transect S2 show that the tridymite zone extends to ~ 0.2 m above the sill and the tridymite absent feldspar melt zone extends to ~ 1.2 m although, due to sampling difficulties this is approximate. The limit of the calcite zone is inferred to be ~ 9 m above the sill based on outcrop studies nearby, although high error is attached to this due to the complexity of the spatial distribution, and interaction of igneous intrusions closer to the RYD dyke.

6.4.3.2 Sill S3

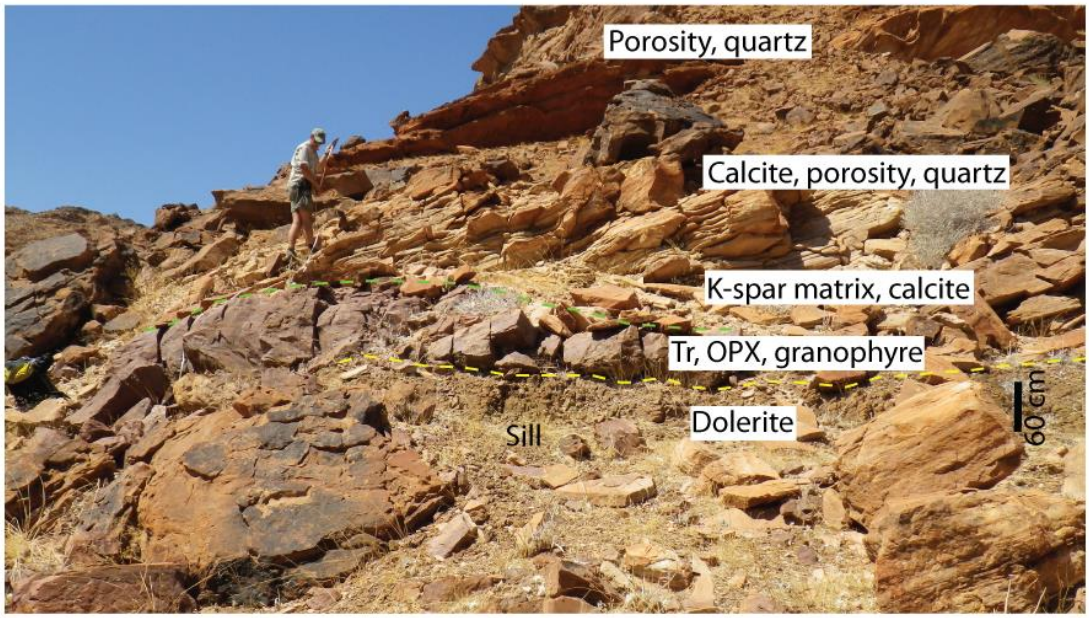

Fig. 6.26. Photograph of sill transect S3 contact

At the upper contact of the sill is a 60 cm zone of intense pyrometamorphism. In this zone, detrital potassium feldspar and plagioclase is absent, having been

completely resorbed. Detrital quartz grains are rounded and corroded, they have a reaction rim of needle and plate like quartz paramorphs after tridymite (Fig. 6.27A.). The matrix is granophyric and consists of quartz paramorphs after tridymite, potassium feldspar (often spherulitic, fibrous), orthopyroxene, usually rimmed with iron oxides, and quartz. The matrix also contains equant Carlsbad twinned potassium feldspars, probably sanidine. Porosity is absent. Interestingly, the tridymite is particularly well developed compared to other examples, the needled approach plate like dimensions rimming some quartz grains.

One meter above the sill is similar to at the contact. Detrital mineralology lacks potassium feldspar, quartz grains are restic and rimmed with quartz paramorphs after tridymite. Detrital quartz grains are also often rimmed with a mantle of disturbed quartz instead of tridymite. The matrix is a granophyric intergrowth of quartz and potassium feldspar again, with numerous needles of quartz after tridymite. The matrix contains rare vugs lined with quartz, then calcite. These suggest free vapour was present, followed by invasion of aquifer water during cooling, which precipitated the calcite.

At 3 m above the contact at S3 detrital minerals consist of rounded to sub-rounded quartz, rounded to sub-rounded plagioclase and occasionally remnants of potassium feldspar grains that are usually rounded. Porosity is absent and the pore filling mineralogy is dominated by anhedral fibrous and spherulitic potassium feldspar, rarely granophyric. Quartz grains are not corroded and reaction rims of quartz paramorphs after tridymite are absent. The interpretation is that at 3 m above the contact, temperatures were not reached sufficient for tridymite to form, but due to partial melt of potassium feldspars the K-spar solidus must have been exceeded. This interpretation therefor constrains the tridymite isograd to closer than 3 m above the

sill. The nature of the quartz rims on detrital quartz at 1 m, instead of a dominance of tridymite suggests the isograd may be nearer 1 m than 3 m.

Pyrometamorphism does not reach 4 m above the sill. At 4 m detrital minerals are sub-rounded and rounded quartz, potassium feldspar, plagioclase and opaques. Rims of haematite on detrital grains are absent and there is pervasive pokilitic non-ferroan calcite cement that also partially replaces calc plagioclase detrital grains. The poikilitic calcite grows over earlier quartz overgrowths as adjacent to dykes. Porosity is minimal, usually secondary moulds of detrital grains (possibly grains plucked during preparation). The existence of calcite suggests a hydrothermal system existed, probably representing convecting groundwater acting to cool the sill and hot wall rocks. When the measured $\delta^{18}O$ of -12 ‰ for calcite at 4 m is plotted on $\delta^{18}O$ model in Fig. 6.20A. a likely temperature, assuming mixing of meteoric and magmatic water as discussed above is ~ 200 °C.

Five metres above the sill contact detrital grains are sub-rounded and rounded quartz, potassium feldspar, plagioclase and opaques. Calcite cement is < 1% and occurs exclusively as replacement of calc plagioclase. Quartz overgrowths are present (8 %) in the highest modal proportion recorded in the Huab dataset. Zone 4 is interpreted to be the return to non-boiling hydrothermal conditions, not precipitating calcite. Compared to the NG52 control sample, the increased proportion of quartz overgrowths may suggest increased temperatures over time, possibly related to long term cooling of the sill below.

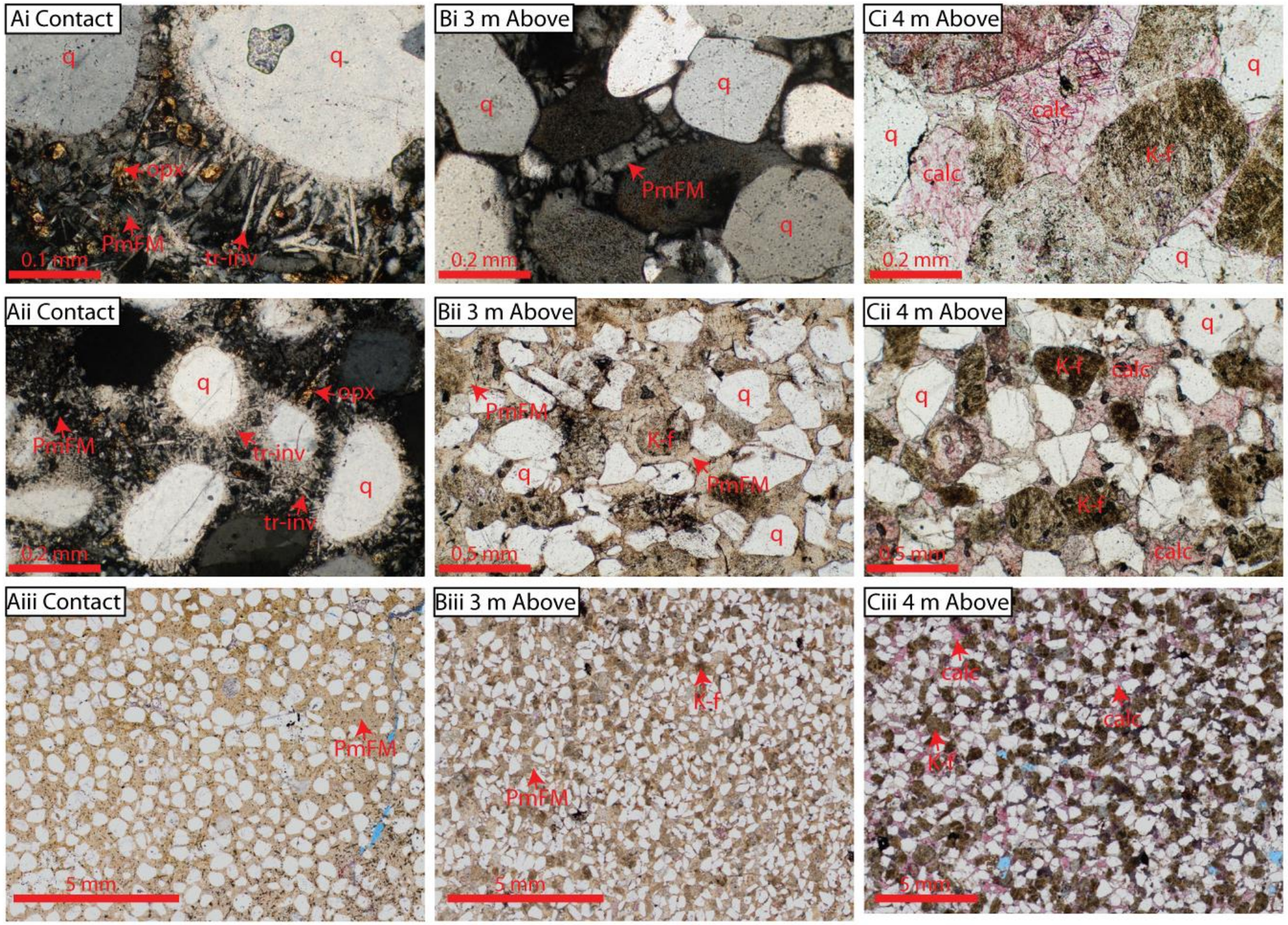

Fig. 6.27. Photomicrographs of Twyfelfontein sandstone affected directly by intrusion of dolerite sills, examples from sill S3 (Fig. 3). Ai, Aii, Aiii) At upper contact of sill. Detrital feldspars completely resorbed into melt which has crystallised into a matrix of tridymite (now inverted to quartz paramorphs), potassium feldspar, orthopyroxene and quartz, detrital quartz is restic. Bi, Bii, Biii) 3 m above sill, detrital feldspars resorbed and crystallised into a matrix of fibrous potassium feldspar, note absence of tridymite paramorphs and opx. Ci, Cii, Ciii) 4 m above sill. Feldspars are all detrital in character, authigenic calcite fills most pores and replaces calcic plagioclase grains (similar to Fig. 6.14 and Fig. 6.25.).

6.5 Intensification of effects at sill-dyke divergence

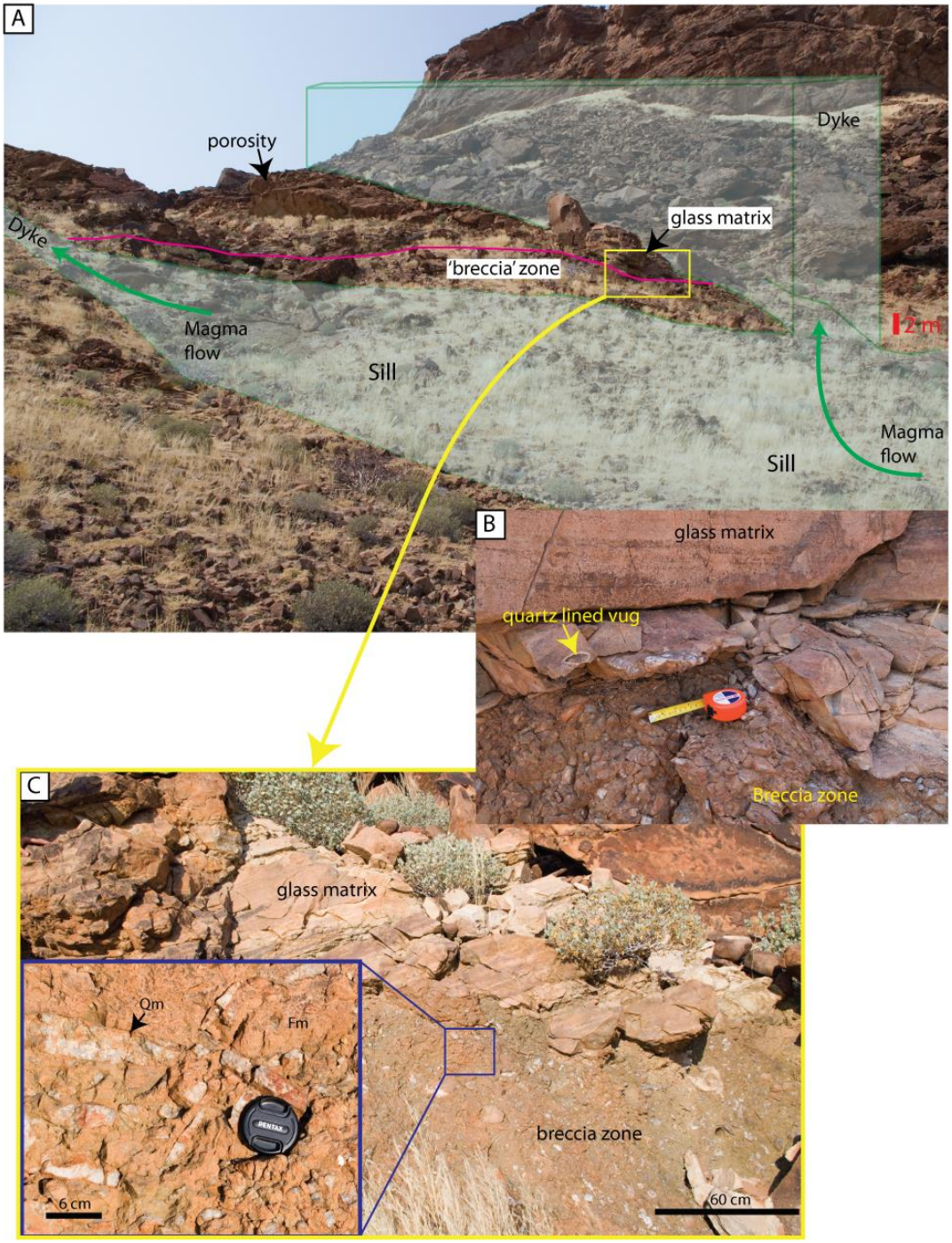

Fig. 6.28. Photographs of locality where pyrometamorphic effects are intensified. (A) Facing east towards the intensified outcrop. Igneous intrusions highlighted in green, scale bar is 2 m. (B) Close up of contact between segregated breccia-like melt and glass matrix zone. (C) Overview of the breccia-like melt segregation with a super close up on the melt segregation 'breccia'.

The divergence of two NE-SW trending dykes from the sill in Fig. 6.28A. (transect M1) has concentrated the magmatic flux. The junction may have promoted turbulent magma flow to further intensify the heat transfer (e.g. Kille et al., 1986). Above the sill, at the junction, pyrometamorphism progressed to a stage where enough partial melt had formed to begin the process of melt segregation (Fig. 6.28B, C, Fig. 6.29.). At this locality the outer two petrographic zones are the same as petrographic above normal sill contacts (hydrothermal calcite zone and normal sand), but the lower zones exhibit different characteristics:

The lowermost petrographic zone consists of what at outcrop appears to resemble a matrix supported conglomerate of sub-rounded quartzite clasts within a light brown matrix (Fig. 6.28B, C).). This 'conglomerate' zone is 5 m thick and rests on dolerite sill. Petrographic analysis of the material (Fig. 6.29Ci, Cii) reveals that the matrix is composed of euhedral, often Carlsbad twinned potassium feldspar (possibly sanidine),subhedral plagioclase, clinopyroxene, orthopyroxene and opaque minerals within a granophyric groundmass of potassium feldspar and quartz. Quartz paramorphs after tridymite are present, but are rare. Alteration of both pyroxenes to chlorite is common. The quartzite clasts are composed of formerly detrital quartz grains that have combined. Occasionally, the outline of a grain can be discerned (Fig. 6.29Ci.). Detrital grains have completely lost their original shapes and are intergrown as either highly sutured contacts, intergrowth along thin films of microcrystalline quartz as 'brain' boundaries (Sawyer, 1999). Often at the boundaries between quartzite clasts and the matrix the form of original detrital grains are truncated (corroded). Within quartzite clasts are numerous dykelets filled with a granophyric groundmass connected to the matrix (Fig. 6.29Cii).

This petrographic zone is interpreted to be segregation of a high degree of partial melt (restic quartz also beginning to melt). The melted feldspars and oxides are clearly separating from the quartz component, with the process preserved as the granophyric dykelets.

At the top of the breccia zone, 5 m above the sill, there is a thin transition (~10 cm) to un-segregated material (Fig. 6.28B, C). Over this interval incipient melt segregation is observed (Fig. 6.29B.). Fig. 6.29Bi shows this segregation, two distinct regions are developing: the first is similar to the tridymite zone above normal dyke contacts. Restic detrital quartz is rimmed with needles (e.g. Holness, 1999; Holness et al., 2012) of quartz paramorphs after tridymite which are set in a matrix of granophyric potassium feldspar, quartz paramorphs after tridymite and quartz. The second is in the centre of the photomicrograph (Fig. 6.29 Bi), where the quartz components are in the process of amalgamating and the feldspathic components (including oxides) are forming a darker matrix. The amalgamated quartz clasts have the appearance of the quartz clasts in the segregated material above. The darker matrix has crystallised into an assemblage comprising occasional detrital quartz grains rimmed with tridymite, some are visibly corroded, quartz paramorphs after tridymite, potassium feldspar, orthopyroxene and clinopyroxene and quartz. The dark matrix is similar in composition to the matrix in the conglomerate, but crystals are not so large (faster cooling?). The interpretation is that the darker matrix material has been depleted in silica and enriched in the more iron, magnesium, potassium and aluminium rich material that has crystallised from a more mafic segregate.

Moving from this transition layer (5 m above sill), up to > 9.2 m is a zone composed of restic detrital quartz grains rimmed with needle-like quartz paramorphs after tridymite (Fig. 6.29A.), detrital plagioclase is rare at 5 m, but by 9.2 m detrital

plagioclase is in similar abundance to the background range (2.4 %) (e.g. NG52). Opaque detrital grains are preserved as groups of circular droplets, pseudomorphing the original grain shape with interstitial clear glass. The matrix is composed of clear glass, with occasional clusters of free floating tridymite needles (now quartz) (cf. Ackermann & Walker, 1960, plate XVII). The restic detrital quartz grains are notably fractured (Fig. 6.29Aii), with perlitic fractures sometimes extending into the glass across quartz-glass boundary.

This zone shows that partial melt of the arkosic component persisted to > 9.2 m above the sill, although melt segregation ceased at 5 m above the sill. The distribution of plagioclase, which is less refractory than quartz, shows a temperature gradient away from the sill, although still within the tridymite stability field. The interstitial melt has clearly completely vitrified, whereas at other sample locations, it has crystallised. Together with the perlitic fracturing (interpreted to be the result of rapid cooling); the glass suggests the melt in this zone cooled more rapidly than elsewhere. This is consistent with being further from the sill than the crystallised melt examples; potentially groundwater ingress could have cause the rapid cooling. Further than 10 m above the sill, there has been no melting, and porosity appears, the detrital assemblage is similar to NG52.

Transect M1 records intense pyrometamorphism reaching to at least 9.2 m above the sill. Melt segregation is evident in the lowermost 5 m of the sample transect. Increased heat flow into these rocks must have existed at the time of metamorphism compared to transects S2 and S3, less than 100 m to the SW. It is suggested that the increase in heat flow is due to magma flow localisation and concentration at the divergence of dykes from the underlying sill. Indeed, other parts

of the sill may have solidified while magma was still flowing through the flow localisation over time and prolonged heating of the country rocks.

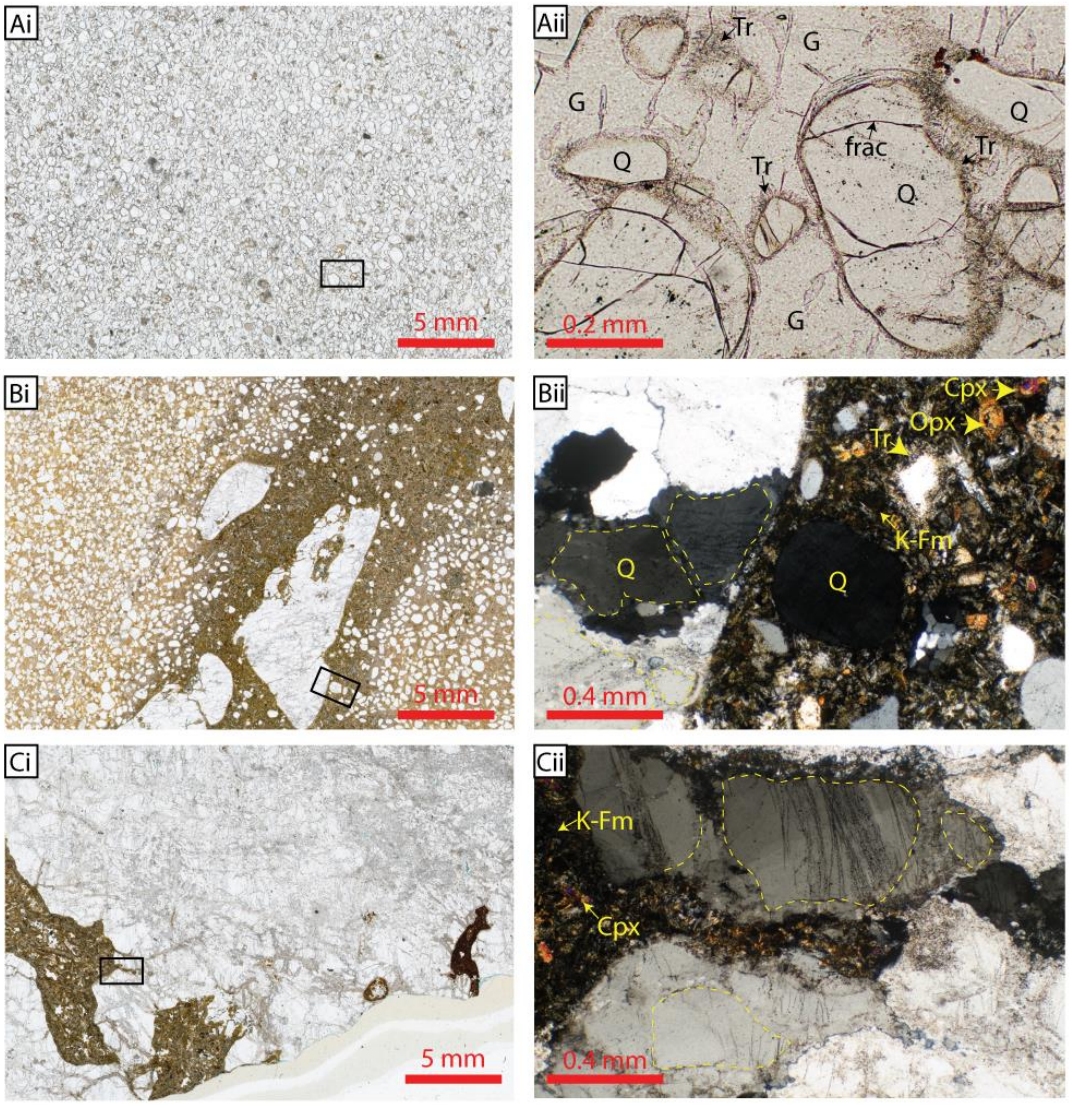

Fig. 6.29. Photomicrographs of intense pyrometamorphism at sill-dyke divergence where magma flow was intensified (M1, Fig. 6.1. Fig. 6.12). (Ai, Aii) Detrital feldspars have been resorbed into melt which has crystallised quartz paramorphs after tridymite fringing restic detrital quartz, subsequently melt quenched to form clear glass matrix (rapid cooling by groundwater?). (Bi, Bii) Closer to sill melt has begun to segregate into quartz rich enclaves and more mafic matrix, matrix crystallises to fibrous potassium feldspar and tridymite where not segregated (same as Fig. 6.25A.) and as tridymite, orthopyroxene, clinopyroxene , quartz and potassium feldspar where segregated. Ci, Cii) Fully segregated melt, detrital quartz grains becoming resorbed, feldspar melt crystallising as orthopyroxene, clinopyroxene, potassium feldspar, plagioclase and quartz, granophyric veins occur within quartz enclaves.

6.6 Chapter Conclusions

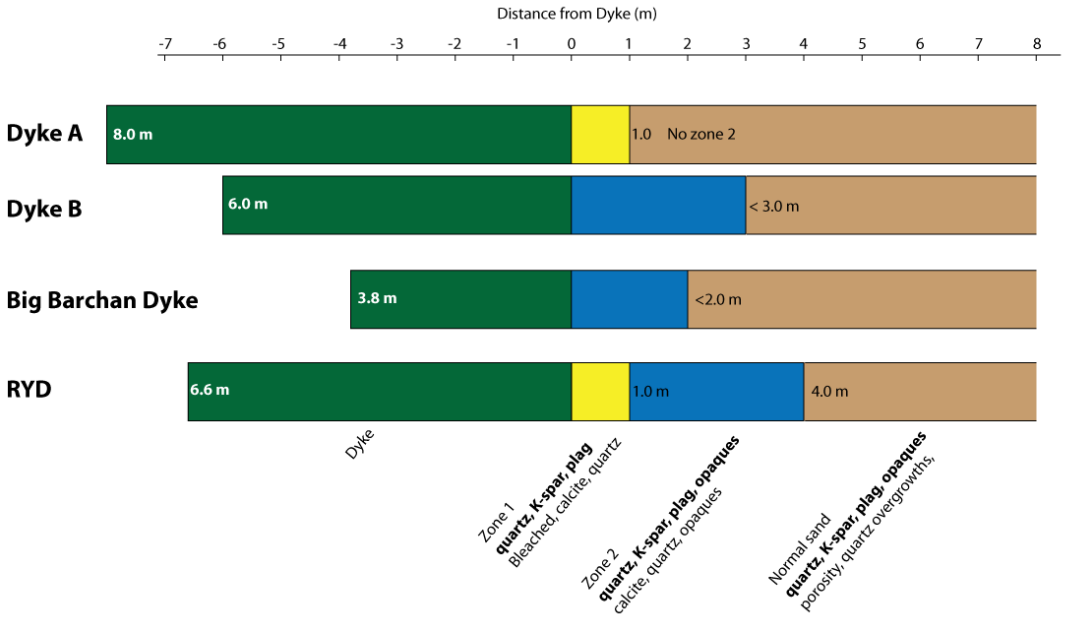

Fig. 6.30. Summary of dyke-sediment contacts showing detrital (bold) and authigenic (regular) mineral assemblages. Dyke thickness is indicated in green.

The diagenetic, metamorphic and pyrometamorphic record in the Tywfelfontein Formation sandstones adjacent to sills and dykes in the Huab Outliers area of NW Namibia has recorded a complete range of effects driven by the heat from cooling igneous intrusions. Adjacent to dykes, the direct effects are hydrothermal and due to increased compaction. The intrusion of the dyke is recorded by grain compaction and the cooling hydrothermal groundwater is evident, preserved by the authigenic calcite.

Compaction adjacent to dykes has been found to be by two mechanisms: (1) plastic deformation of quartz grains and (2) increased pressure solution between quartz grains. Plastic deformation suggests very high pressures and, the lowest recorded pressures (5 kbar, 925 °C, Carter et al., 1964) are not achievable through

burial in the Huab Basin. It is therefore suggested that increased heat (must be < 860 °C due to no melt) supplied by the intrusion combined with pressure differential of 4.75 kbar over the lithostatic confinement. Whether or not these conditions satisfy the conditions for the degree of plastic deformation observed is not resolved. It is suggested by Rutter (1983) that for quartz sand, plastic deformation begins at 450 °C, but no pressure estimates are supplied, comparison with Carter et al. (1964) suggests such low temperatures would need in excess of 20 kbar pressure. The increased pressure solution is understandable and supported by literature. It is proposed that increased temperature and pressure increased the rate of pressure solution (after Rutter, 1983; Houseknecht, 1984; Houseknecht, 1988; Tada & Siever, 1989). As the conditions for initiation of pressure solution were met prior to dyke intrusion, we cannot use this as a geothermometer.

A scale summary of the four dyke/red sandstone transects studied is presented in Fig. 6.30. From the figure it is clear that more variation exists in dyke width than width of the cemented zones. Not all dykes exhibit all of the three recorded zones. For instance, RYD shows all of the three zones. Firstly a 1 m thick zone where opaque grain coatings are removed and the cement is calcite (Zone 1) followed by a calcite cemented zone, with grain coating opaque minerals (Zone 2) out to 4 m. Further than 4 m, sand is normal. The barchan dyke does not have zone 1, instead zone 2 extends from the contact to < 2 m. Dyke B is the same, both opaque grain coatings and calcite are present from the dyke contact. Dyke A does not have zone 2. At Dyke A, the calcite zone, with no haematite grain coatings persists until no calcite remains at 1 m from the dyke.

As cementation is the minor contribution to porosity loss, and compaction is the major contributor, Fig. 6.30. is not as useful as Fig. 6.31. at describing the effects

of dykes on reservoir quality. Calculated porosity increase up the background of 12.5 % is remarkably similar for all of the dykes (Fig. 6.30A.) even considering the error, although Dyke B behaves slightly differently (outside of error), as it does with other parameters). The distance to 12.5 % is plotted against dyke width in Fig. 30B. where, based on these four examples it can be seen that no relationship exists between width and distance to background porosity. Based on these data, background porosity is however always regained after ~ 4 m. Uncertainties were propagated from the 1σ at 12.5 % porosity.

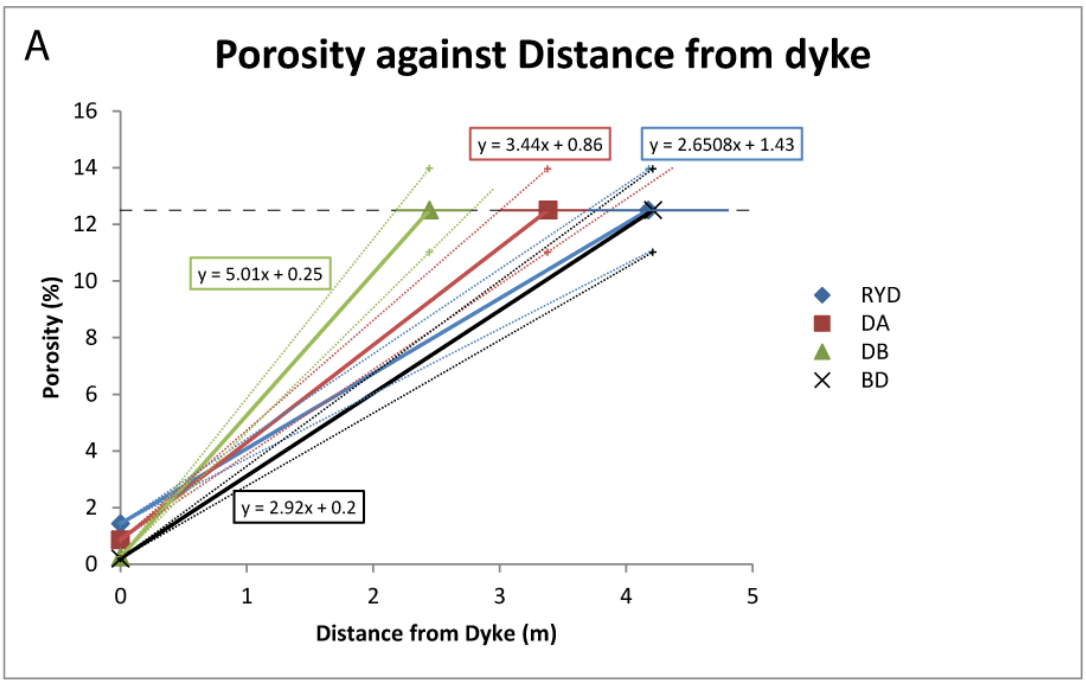

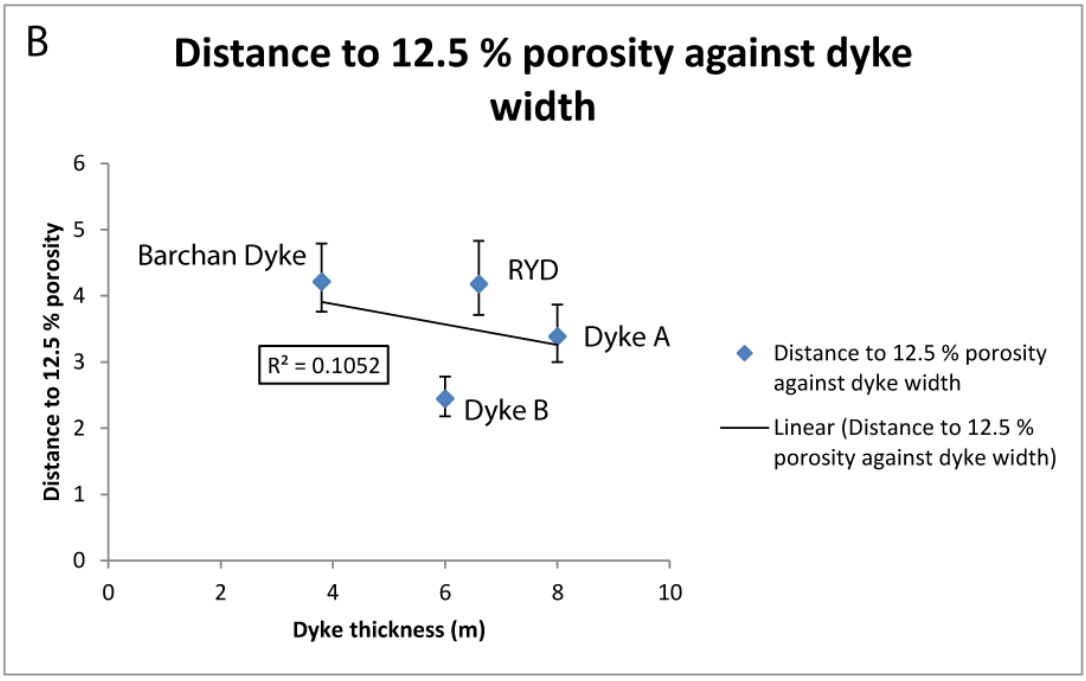

Fig. 6.31. (A) Graphical summary of dyke porosity loss. Porosity equations generated in Fig. 6.5. extrapolated and plotted to 12.5 % porosity to find distance to background. Dashed lines are 1σ errors at 12.5 % porosity. (B) Distance to background plotted against dyke thickness with error bars calculated in A.

Above sills, direct effect intensity varies depending on the magma flow regime. For parts of the sill that have intruded and cooled, without significant throughput of magma (e.g. S2), the high temperature petrographic the tridymite

stability field is <0.2 m. Near the edge of the sill, where fingers are preserved (indicating near to the propagating sill tip, Schofield et al., 2010), the tridymite zone is at a minima, (although carbonate cementation is high). Where magma flow has been concentrated by divergence of dykes from the sill, the magnitude of pyrometamorphism increases towards the divergence; this is recorded by transect S3 having a thicker tridymite zone than the nearby transect S2. At the divergence of the dykes pyrometamorphism was found to be at a maximum, with a ~9.2 m tridymite zone above sill, compared to 0.1 m to 0.2 m above the sill where no evidence of sustained flow exists (S2).

Hydrothermal mineralisation (calcite) above sills was found to be variable (2 to 3 m thick) and independent to the thickness of the pyrometamorphic aureole. The relative magnitudes for each of the petrographic zones (melt+ tridymite, melt only, calcite) varies between each of the three transects taken (S1, S2, S3). Fig. 6.23. illustrates the variability plotted as porosity, authigenic feldspar (from melt) and calcite against distance above sill. Porosity variations between each transect reveal that overall the magnitude of porosity loss is S3<S2<S1. The porosity loss is primarily influenced by: (1a) compaction by loss of grain framework as feldspars melt and subsequently recrystallize. (1b) increased compaction of un melted overburden sandstone by increased pressure solution. (2) Hydrothermal calcite precipitation in pore space above the pyrometamorphic zone. The thickness of the pyrometamorphic zone (tridymite+ melt and melt only) and the hydrothermal zone do not appear to be directly related. For instance, the order of pyrometamorphic zone thickness (tridymite zone as proxy) is S3<S2<S1 and for hydrothermal calcite it is S1<S3<S3. S1 has the smallest tridymite zone, but the greatest extent of calcite (S2 calcite limit not known). Whereas S3 has the thickest tridymite zone, but the

thinnest hydrothermal calcite zone. No correlation exists between sill thickness and distance to background porosity (Fig. 6.33B.).

Pyrometamorphism (tridymite zone as proxy) is most intense above the sill between the dyke divergences. Here the tridymite zone is 9 times as thick as the maximum recorded elsewhere (S2). It is proposed that the internal magma dynamics within the sill are responsible for the observed differences in pyrometamorphic zone thickness. At this point, more heat has been transferred to the country rock. It is probably that this heat transfer is due to magma flow localisation. Where magma flow has been localised, flow duration would have been longer, and possibly turbulent at the junction. It is possible that the rest of the sill could have solidified, while this location remained molten and a conduit for ascending magma. The dykes could have fed sills higher in the stratigraphy or now eroded extrusive geology. It is common in 3D seismic data to see such inter-related feeder relationships (own unpublished work, Thompson & Schofield, 2008).

Transect S3 is nearer a sill-dyke divergence (Fig. 6.28; Fig. 6.12.) than S2. It is proposed that intensification and localisation of magma flux approaching the dyke began to have an effect on the wall rocks by S3, thereby transferring heat over a longer period of time, while the magma at S2 had ceased to flow (i.e. flow localisation within the sill with a bias to feed branching dykes). Magma flow localisation has previously been shown using pyrometamorphic aureoles by Holness & Humphreys (2003) and Holness et al. (2012) around Palaeocene dykes, sills and plugs, intruding metasediments and schists in Scotland.

Overall, sandstones proximal to sills (top sill contacts) show greater thermal alteration than near dykes. Porosity loss by pyrometamorphism is controlled by magma flow regime (e.g. M1, Awahab and M2, near RYD). Other porosity loss

appears controlled by compaction enhanced by the dyke. Near to the dyke, pressure perturbation by the intruding magma is probably felt, but further away, elevated pore water temperatures (evident as δ18O calcite) facilitate enhanced quartz pressure solution. This situation is the same for sills outside of the pyrometamorphic zone. Calcite cementation is important in revealing the subsurface conditions at the time of igneous intrusion, but less so in reducing porosity, although it certainly contributes. The independence of porosity loss on dyke thickness is striking, but understandable considering enhanced pressure solution is the key mechanism of porosity loss over distance, under lithostatic pressure; the intrusion pressure only being felt << 1 m as evident in the undulose extinction.

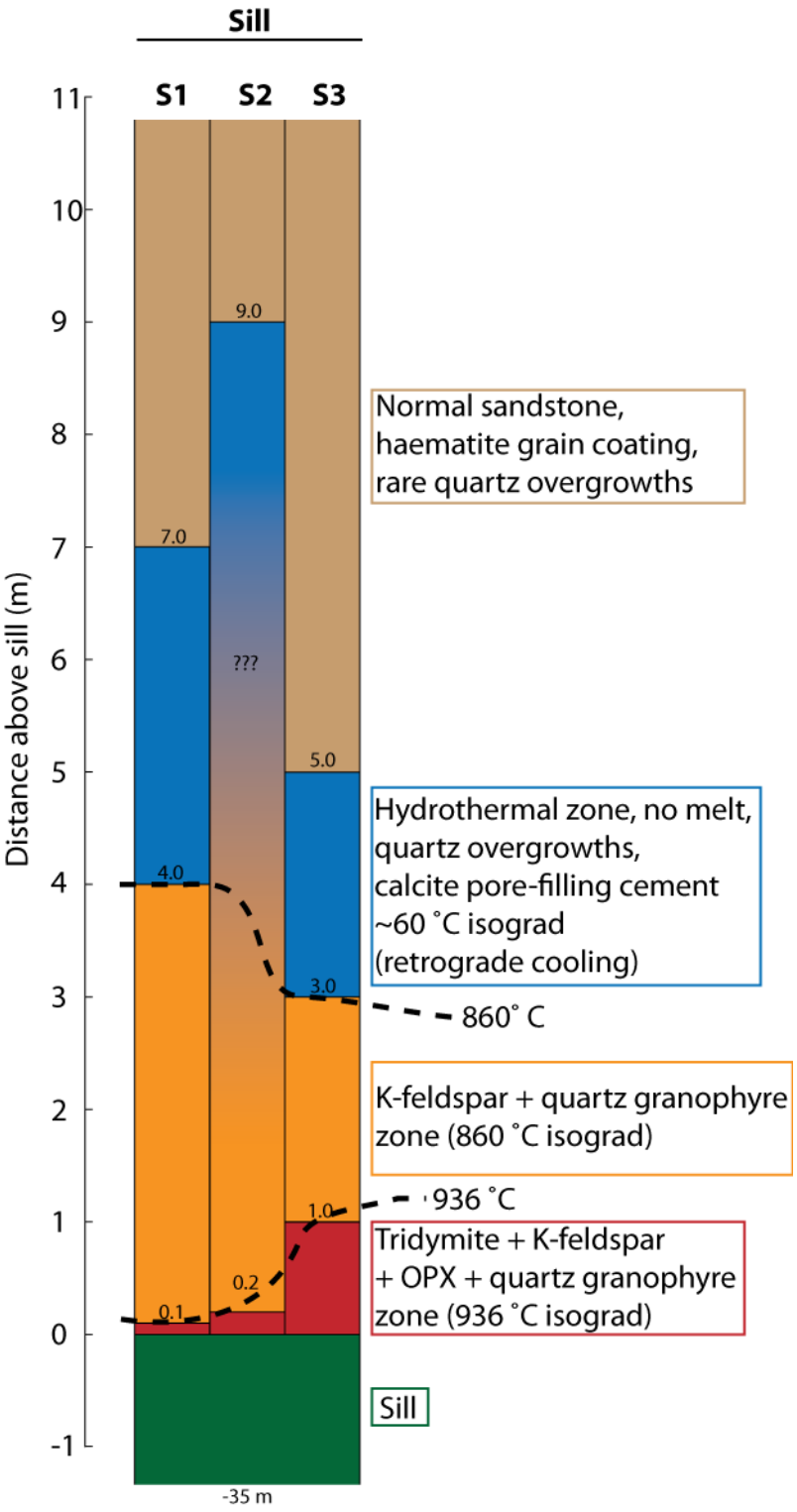

Fig. 6.32. Summary of sill-sediment (S1, S2, S3), intense melt segregation (M1) showing major mineral assemblages and relevant distances from igneous intrusion for each zone. Detrital minerals are in bold type, authigenic minerals are in regular type.

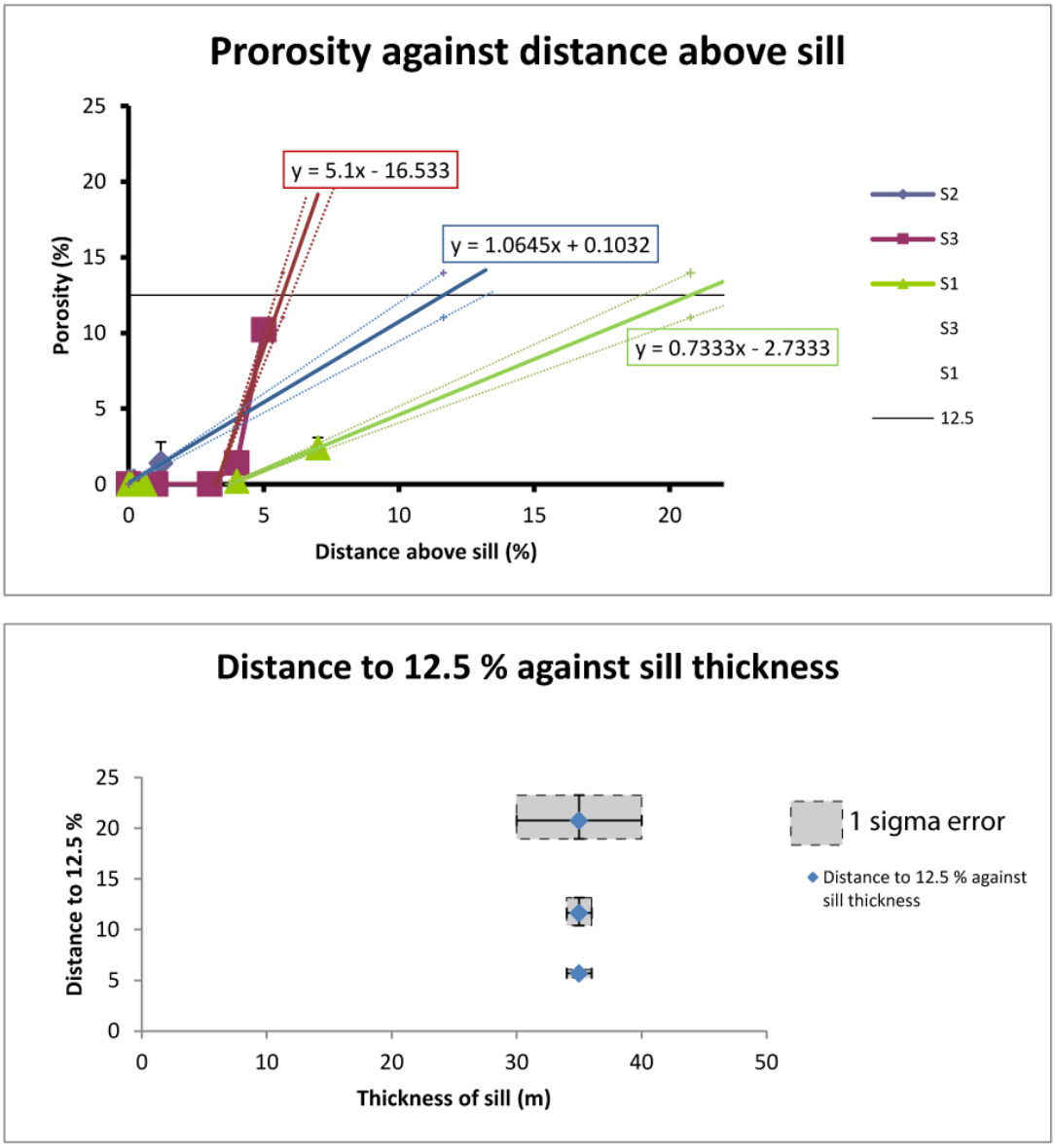

Fig. 6.33. (A) Graphical summary of sill porosity loss. Trend lines for porosity significantly extrapolated. Dashed lines are the 1σ error at 12.5 % porosity. (B) Distance to background (12.5 %) plotted against sill thickness, note large error bars on sill S1 due to exposure, sill S2 and S2 transects entire sill measured. Error in distance to background calculated in A.

7

Indirect effects of flood basalt provinces on the diagenesis of sub-basalt and inter-basalt sandstone: compartmentalisation of hydrothermal fluids. Case studies from the Twyfelfontein Formation, Huab Outliers, Namibia.

7.1 Chapter Summary

After the initial lava flows drowned the Cretaceous desert that was to become the Twyfelfontein Formation causing the direct effects described in Chapter 4, further diagenetic effects related to the igneous activity occurred. The 'indirect' diagenetic effects were probably synchronous with the emplacement of igneous intrusions, for which there is stable isotopic evidence (this chapter and Chapter 6.).

The most common manifestation of indirect diagenetic effects is the common bleaching of the Major Erg (KTyMAJ) and of the Isolated Dunes (KTyID) which is visible at outcrop. This chapter investigates the causes of the bleaching using petrography, X-ray diffraction, X-ray fluorescence (major and trace elements) and stable isotope geochemistry ($\delta^{18}O$ and $\delta^{13}C$).

The white, bleached sandstone was found to have had the red iron oxide grain coatings reduced and either removed or re-precipitated in nodules. The fluid that was unique to the white sandstone also caused a hydrothermal mineral assemblage of kaolinite, calcite and böhmite to form at the expense of plagioclase feldspars. This assemblage has been produced in the laboratory under hydrothermal conditions, from plagioclase feldspars by Hangx & Spiers (2009). The diagenetic conditions required for the observed mineral assemblage involve a CO_2 and H_2S rich hydrothermal fluid, which is inferred to be of magmatic origin (isotope supported), as hydrocarbon generation and migration can be ruled out. Another possibility is the reaction of haematite with hydrogen sourced from hot hydrothermal water interacting with basalt (Stevens & McKinley, 2000). The bleached sandstone is less porous and less permeable than red dunes.

Outcrops of the red and white sandstone reveal that the spatial distribution of the different sandstones is complex. If the white sandstone is a result of hydrothermal fluid flow, this suggests there is a high degree of heterogeneity and compartmentalisation of the sandstone. Both within the lava pile, where the isolated dunes occur and in the Major Erg below, igneous dolerite dykes have been found to be the major control. The dykes separate compartments of red and white sandstone. The dykes are also of fundamental importance in driving the hydrothermal system. Within the lava pile, where the Isolated Dunes have been studied in Dune Valley, the Tafelkop basalts are vesicular and would have allowed some horizontal fluid flow, although 3D basalt relationships may also isolate sand bodies. This suggests even within the basalt pile, dykes are the major fluid barrier.

Conclusions are: firstly these highly reactive hydrothermal fluids have been used to trace heterogeneous fluid migration through a mixed volcanic–sedimentary stratigraphy and secondly on the potential reservoir quality-reducing ability of the fluids. The fluids have also sequestered natural magmatic CO_2 that has been degassed by the igneous intrusions as calcite.

Also raised in this chapter are three other observations made in the Huab Outliers, where diagenesis is different to that of the normal red sandstone. The most striking is a band of quartz cemented sandstone that has no association with any obvious permeability pathway, nor the direct emplacement of any igneous rock. The second is an unidentified green mineral that occurs where white sandstone meets altered basalt. The third, the most common, is at some cold sand-lava contacts where a calcite cemented zone is often developed, with stable isotopic signatures in the field of Type 2 (subsurface formed) calcite rather than the Type 3 hot contact calcite.

These are interpreted to be remnants of perched aquifers resting on the lava flow crusts of the basalt below.

7.2 Indirect effects within the lava pile- Isolated Dunes: red and white

7.2.1 Differential Diagenesis

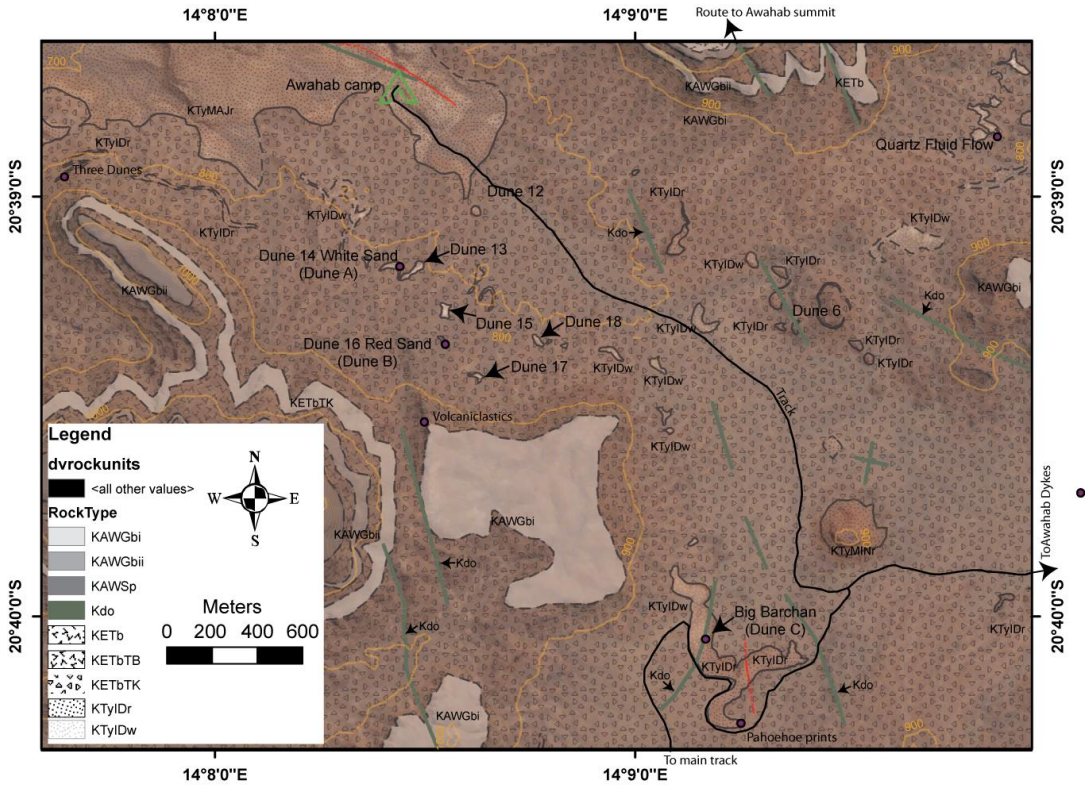

Fig. 7.1. Geological map of Dune Valley showing the three case studies: Dune 14 White Sand (Dune A), Dune 16 Red Sand (Dune B) and Big Barchan (Dune C).

Three types of diagenesis have been petrographically and mineralogically identified and described in detail below. Both red and white isolated dunes display '**Type 3**' diagenesis near to hot lava contacts, with no appreciable difference between red or white isolated dune contact zones. **Type 3** hot contact diagenesis is the same as described detail within Chapter 4. '**Type 1**' diagenesis is only found in red

isolated dunes and red Major Erg sandstone, it is the 'background' (e.g. NG52.).'**Type 2**' diagenesis is only found in white isolated dunes and is the major subject of this chapter. Type 2 diagenesis is recognised in the field by conspicuous bleaching of the ordinarily red sandstone to white. In the major and minor erg unit, stratigraphically below the lava interbedded isolated dunes (Jerram et al., 1999a), gradations can be seen between Type 1 and Type 2 diagenesis; however in the isolated dunes, the styles appear mutually exclusive.

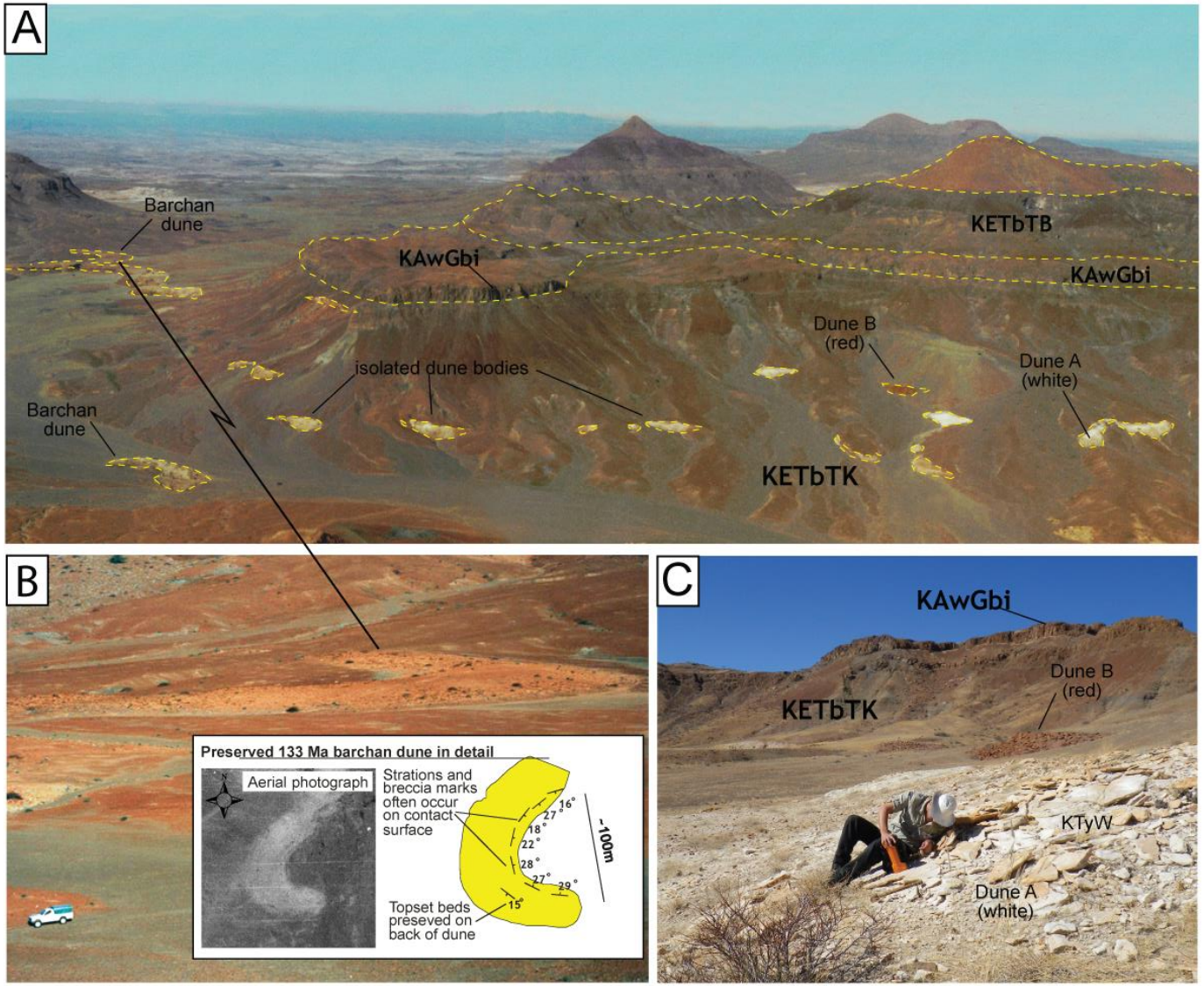

Fig. 7.2. (A) Photograph of Dune Valley taken from the top of Awahab/Mikberg mountain (facing ~SSW), numerous isolated dunes/sand bodies visible, completely preserved barchans dunes, Dune A (Type 2 white) and Dune B (Type 1 red) labelled. (B) Close up of completely preserved barchans dune with inset showing detailed measurements around the dune (adapted from Jerram et al., 2000a). (C) Photograph of Dune B (facing S) the contrasting sand colour apparent together with equivalent stratigraphic level and proximity to each other.

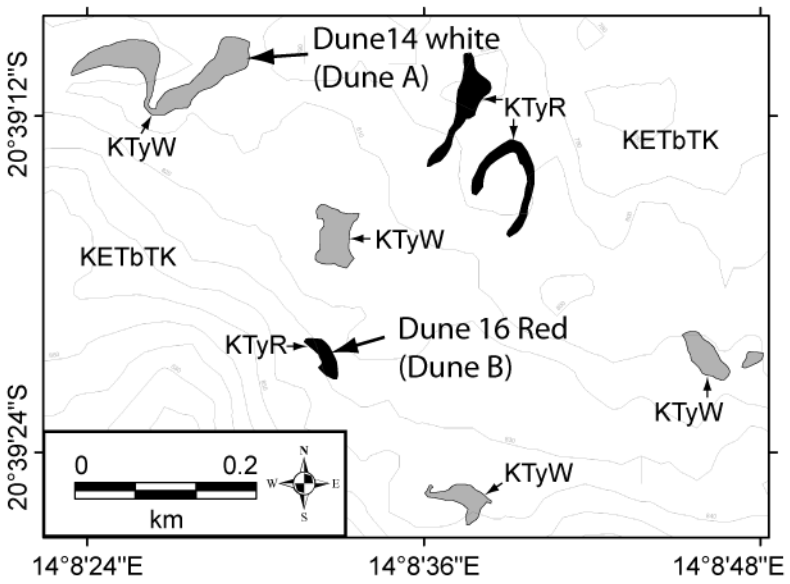

Fig. 7.3. Geological map of Dune Valley showing a higher resolution of Dune A white and Dune B red sampled in this study. Contour spacing is 10 m, rock unit abbreviations are as in Fig.2.

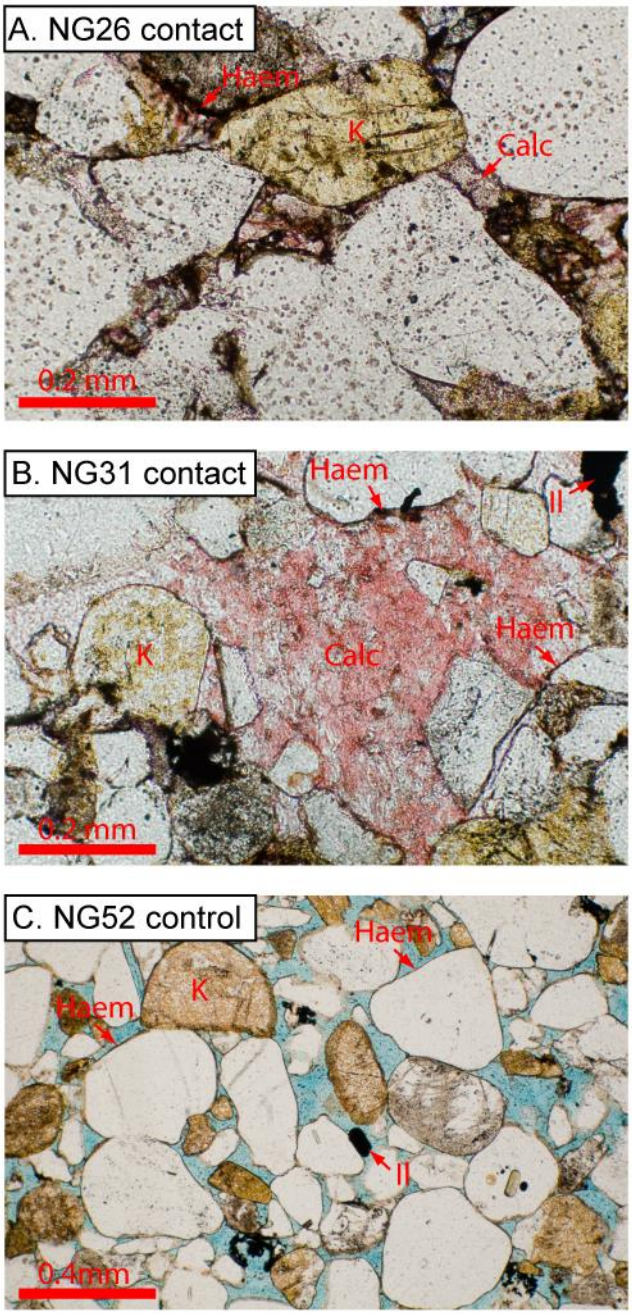

Fig. 7.4. Petrological and mineralogical comparison of lava contact sediments at Dune A white and Dune B red. (A) White dune 14 contact. (B) Red dune 16 contact. Note no appreciable microscopic difference exists between the two contacts.

Type 3 Digenesis- Hot lava contacts (Same as Chapter 4)

The upper surfaces of fossil dunes in the study area often display features such as topset beds and aeolian ripples as well as preserved lava emplacement features such as striations and lava imprints (see Jerram et al., 2000a; Jerram & Stollhofen, 2002; Chapter 4 for description). These features indicate that the upper dune surface was contemporaneous with and covered by flowing lava. Type 3 diagenesis is only found in these upper dune surfaces. Basal surfaces (i.e. sands that were deposited on top of the solid cooled upper surface of lava) usually display Type 1 or Type 2 depending on overall dune diagenetic type. Generally there is no evidence of significant early weathering of the cold lava top surfaces, indicating that little time passed between the emplacement of the lava and migration of sand dunes.

Sandstones in the Twyfelfontein Formation can be classified as subarkosic arenite based on modal mineralogy (Chapter 2, 4). For both Dune A white (NG26) and Dune B red (NG31) contacts porosity is always found to decrease towards the hot contact (Fig. 7.4; Fig. 7.6A.). Reductions in porosity in the sandstones start to become apparent at depths of <2 m from the contact with the base of lavas. At these depths porosity values are ~20% and they decrease to <1% at the contacts with the lava (see Chapter 4). To summarise, at contacts there is increased compaction due to increased pressure solution of the quartz, which combined with calcite cementation provides an early mechanism for porosity loss and lithification prior to significant burial (Fig. 1.6 A, B.).

The results of the X-Ray diffraction are presented in Fig. 7.5. These data generally confirm the petrographic observations (Fig. 7.4). Both, red and white dune contacts produce strong calcite peaks at 3.035 Å (~29.46° 2θ). NG 31 produced a peak at 3.15 Å (28.3 ° 2θ) that corresponds to fluorite, this supports a tentative

petrographic identification of this mineral. Fluorite pore fills are also occasionally found in the Twyfelfontein Formation elsewhere under other hot other contacts. NG26 produced clay peaks at 7.17 Å (12.35 ° 2θ) and 3.58 Å (24.83 ° 2θ), the strength of the 3.58 Å peak supports the interpretation clinochlore as the clay phase, but kaolinite is possible. Haematite was not detected with XRD, possibly due to its presence in very low abundances (petrographic observations overestimating its abundance). The key point is that mineralogically and petrographically both red and white dunes behave in an identical fashion at hot lava contacts. This suggests that the early diagenesis due to lava emplacement affected the same sediment and any differential diagenesis after this time must be due to a different process. This also provides a 'locked in' snapshot of the white sediment unaffected by later processes near to the contact. It is for this reason that white sandstone compartments are frequently reddened near to to lava contacts (e.g. RYD pond and the Dune Valley white dunes).

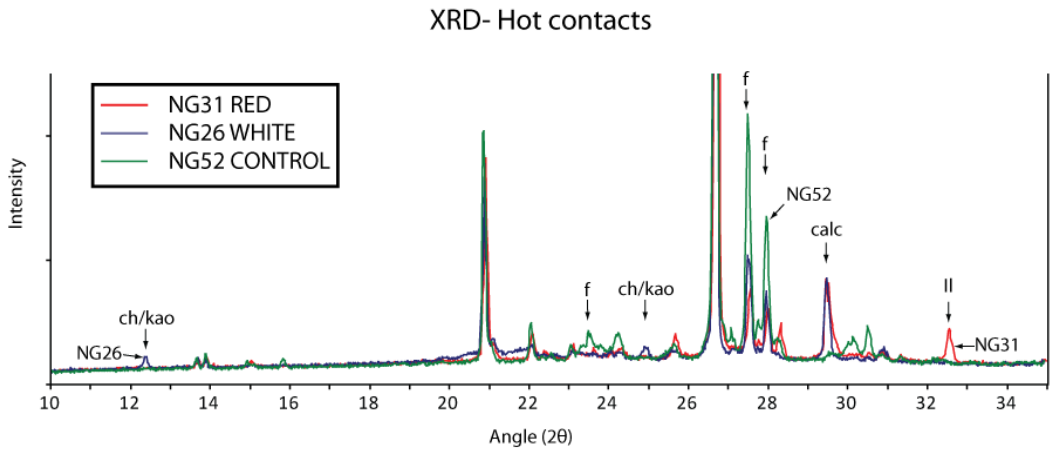

Fig. 7.5. X-Ray diffraction spectra for three samples: NG52 control, NG31 Dune B red contact and NG26 white contact. Note appearance of calcite peak for both contacts and weakening of all feldspar peaks. Important minerals labelled. ch= chlorite, kao= kaolinite, f= feldspar, calc= calcite, Il= ilmenite.

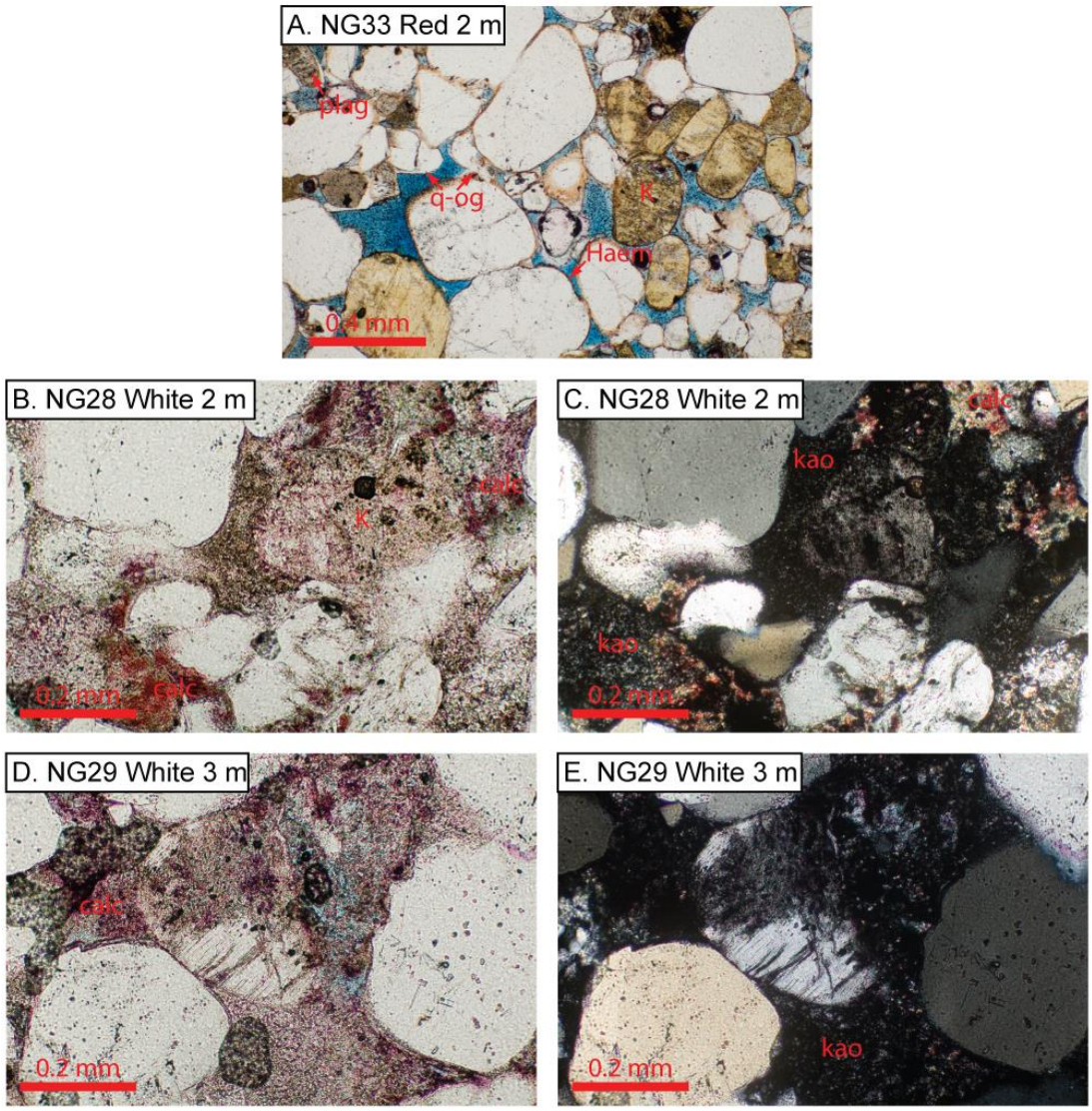

Fig. 7.6. Photomicrographs of white sandstone from Dune 14 white (Dune A). (A PPL) NG33 Dune 16 red, 2 m below the lava for comparison with the white samples. (B PPL, C XPL) NG 28, 2 m below the lava in dune 14 white. Porosity is secondary of micro. Authigenic minerals visible are kaolinite, calcite.

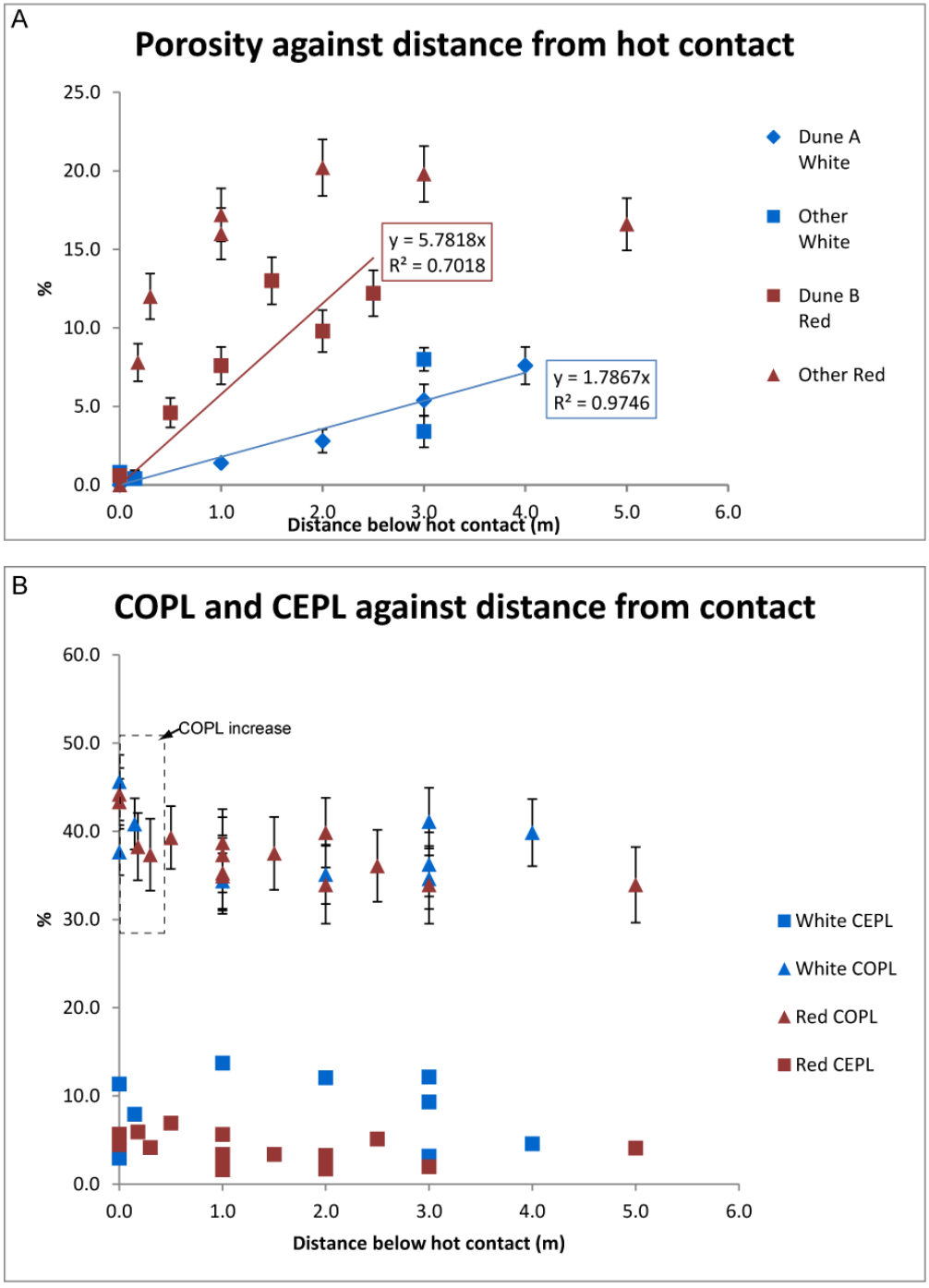

Fig. 7.7. (A) Porosity against distance below lava for Dune 14 white and Dune 16 red. Porosity higher for a given distance for red dunes. (B) Compaction and cementation plotted for Dune 14 white and Dune 16 reed against distance below lava. Both dunes have sharp increase in compaction immediately below lava common to Type 3 diagenesis. Cementation is greater for a given distance for white sandstone.

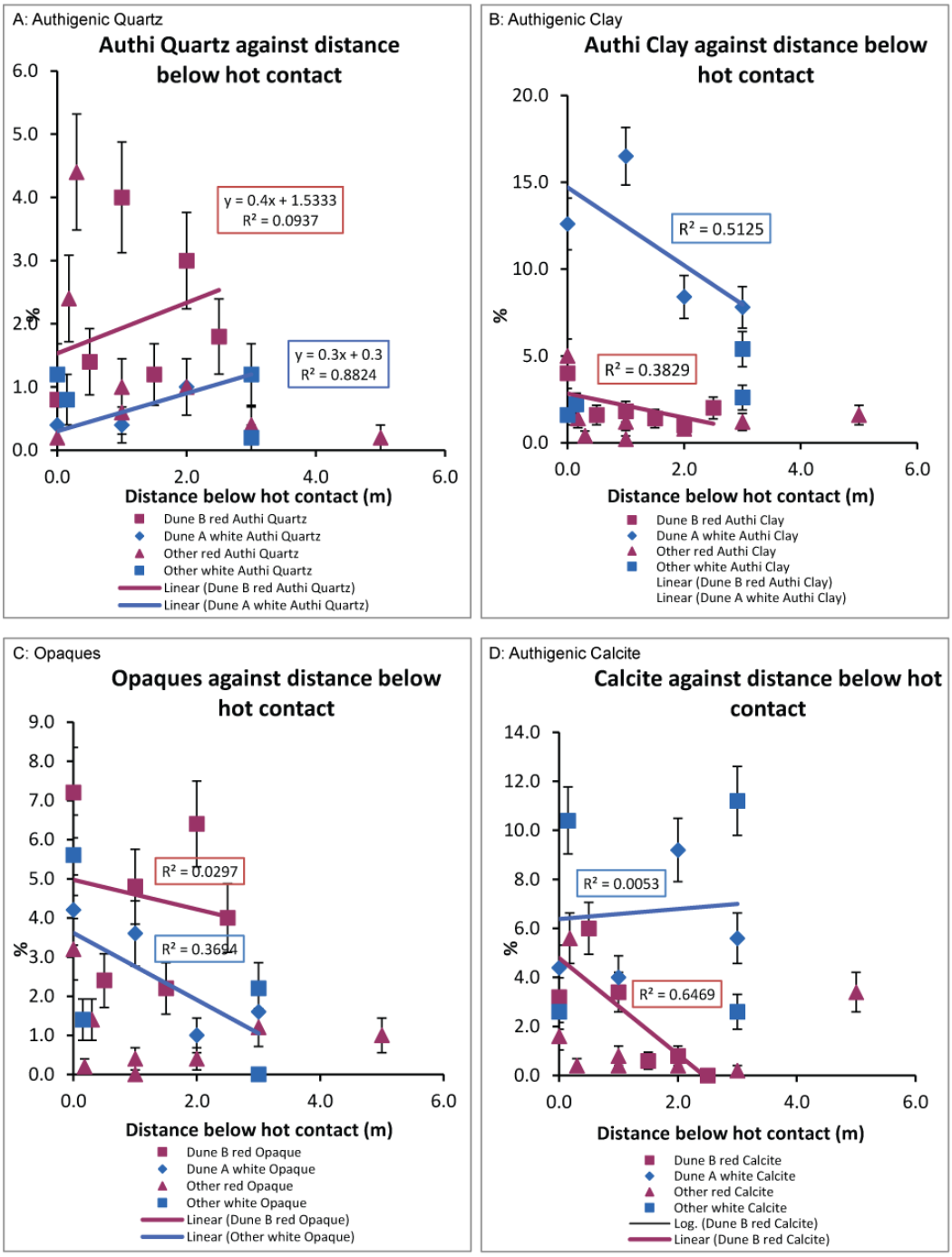

Fig. 7.8. **Graphs against distance below hot contact for Dune 14 white (Dune A) and Dune 16 red (Dune B). (A) Red dunes appear to have more authigenic quartz for a given distance. (B) The red dune has significantly less authigenic clay for a given distance. (C) The red dunes have a greater abundance of opaque minerals. (D) White dunes have greater abundance of calcite with distance, persisting well below the influence of Type 3 diagenesis.**

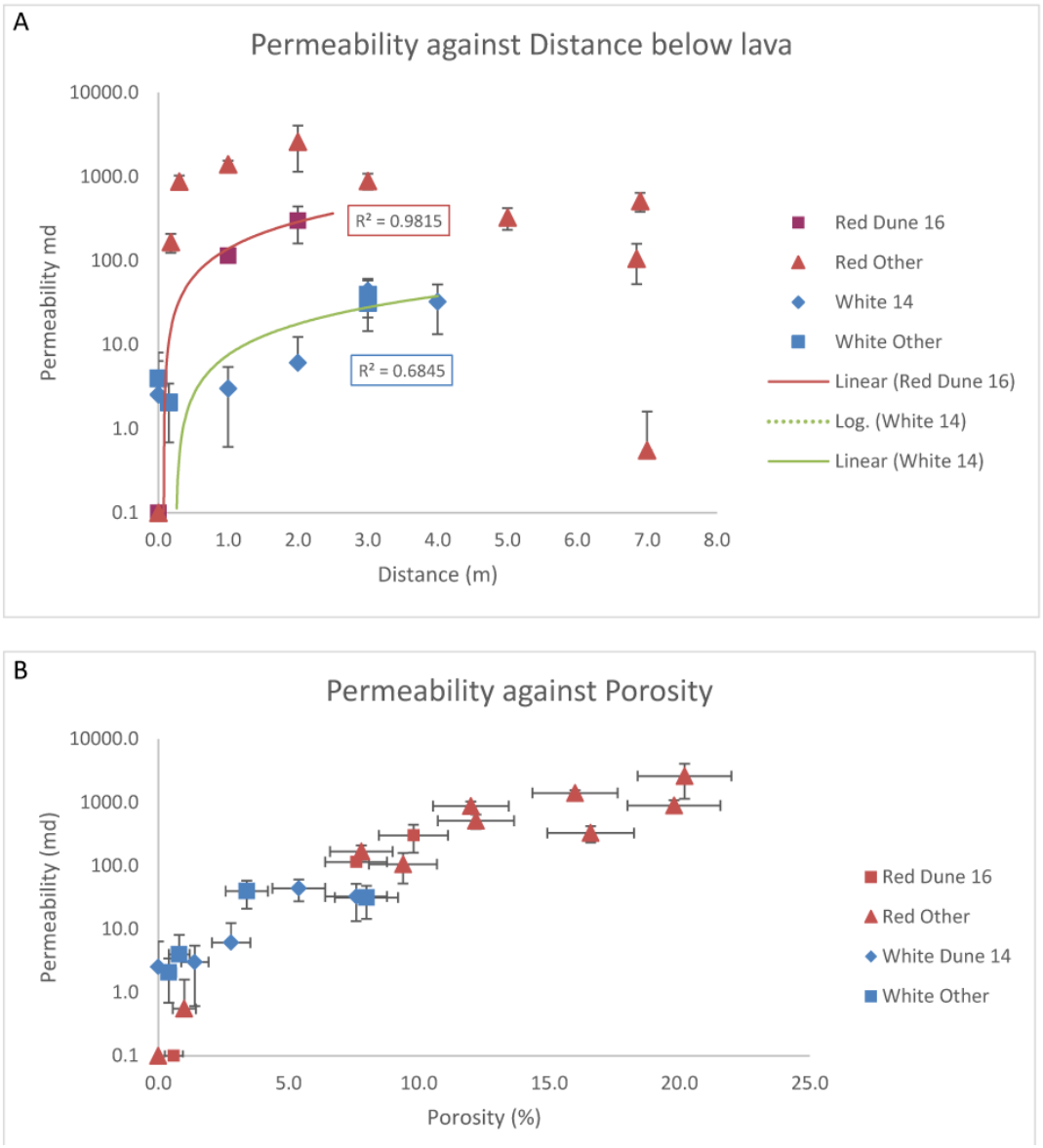

Fig. 7.9. (A) Permeability against distance below lava for Dune 14 white (Dune A) and Dune 16 red (Dune B). Permeability for a given distance is always higher for the red dune. (B) Relationship between permeability and porosity. Apart from samples affected by Type 1 diagenesis, each diagenetic type plots as a clearly separate field.

Type 1 diagenesis-Burial diagenesis- Normal red sand

Type 1 sandstone is present beyond the influence of igneous rocks. The nature of the sandstones unaffected by igneous activity is presented in Chapter 2. This is a summary. Isolated red dunes are compacted subarkosic arenites. They are composed of rounded aeolian grains in well sorted grain flow (fine to coarse sand)

less well sorted rounded to subrounded grain fall (very fine to fine sand) lamellae (Howell & Mountney, 2001). The detrital grains comprise of quartz, potassium feldspar, plagioclase, lithic grains and opaque minerals (ilmenite). Ilmenite is not widely disseminated and appears to form small placer deposits controlled by grain density. Detrital grains are coated with haematite, which gives the red colouration (Fig. 7.2A). Compaction and pressure solution appears to be the major diagenetic control (e.g. Fig 7.4C sutured grains). Cements are rare, although occasional quartz overgrowths are present on some grains. Where present, quartz overgrowths do not exceed 1 % (±0.4) modal area. Compaction diagenesis of the formation is described by Dickinson & Miliken (1995).

Dune B has been chosen as a type example of Type 1 diagenesis because its superior vertical exposure (2.5 m) and it is only 120 m south of Dune A (white dune). In the field, Type 1 dunes are clearly identified compared to Type 2 dunes based on colour (Fig. 7.2C B). Red sand is dominant in the minor and major erg units, stratigraphically below (Fig. 7.1), separated by lava (e.g. Jerram et al., 1999b). We propose that Type 1 diagenesis represents sandstone that has not been subject to hot contact diagenesis, or to a flux of fluid that was responsible for Type 2 diagenesis.

Type 2 diagenesis- isolated white dunes

White coloured sandstones are distributed throughout the Twyfelfontein Formation, and where interbedded by lava as isolated dunes, there appears to be no intrinsic pattern to their distribution (Fig. 7.1; Fig. 7.2A.). At outcrop scale, the only difference appears to be colour, with sedimentary structure showing no difference in morphology. It can be shown that the white dunes were deposited in the same way as

the red dunes (e.g. Mountney et al., 1998; Jerram et al., 2000b, a). The question then arises about the diagenesis of these white sandstones, and how it differs from the red aeolian units.

Thin-sections of the white sandstone indicate that it is also a subarkosic arenite. Rounded to subrounded quartz grains occur in grain fall and grain flow lamellae, which is usually well sorted. Detrital grains are similar to those in the red dunes. Feldspar grains are visibly corroded or are completely replaced by clay (Fig. 7.6.). Plagioclase feldspar grains show the most intense alteration, with no petrographically identifiable grains being encountered under optical microscopy that could be identified based on albite twinning. Any plagioclase encountered was identified based on lack of yellow staining from sodium cobalinitrite and not being quartz (crossed polar examination), therefore plagioclase has probably been petrographically overestimated; most counted plagioclase grains are probably in fact completely kaolinitised pseudomorphs (SEM analysis confirms this). Potassium feldspars in white sandstone (Fig. 7.6.) samples are also frequently corroded or partially transformed into clay minerals. Haematite grain coatings are absent in the white sandstone, but opaque detrital minerals are still present as are occasional nodular aggregates of haematite in pore spaces.

Porosity reduction due to compaction appears more intense in thin-sections of the white sandstone than in the red sandstone (Fig 7.7 A; Fig. 7.6.). Increased compaction may have resulted from the weakening of feldspar grains during dissolution. These grains were then deformed to fill adjacent pores, or dissolved, thus reducing their volume. Compaction porosity loss (COPL) is generally slightly greater in the white dunes than in the red dunes (Fig. 7.7B.) and porosity, as a result of this and increased cementation porosity loss (CEPL), is lower than for red. Unlike the red

dunes, the white dunes contain an authigenic mineral assemblage that is identifiable using petrographic techniques. This assemblage is composed of, kaolinite, calcite, and occasional quartz overgrowths. Calcite and kaolinite are usually associated and both replace feldspars and fill pore space.

Modal analysis of thin-sections indicates that with distance from hot contacts white dunes have up to 4 times the amount of clay and 5 times the amount of calcite (Fig. 7.8) as the red dunes. Authigenic quartz occurs in approximately the same proportions in both red and white dunes, but showing significant variability in the white sandstone. Clays may inhibit the formation of quartz overgrowths over geological time. Opaque minerals are significantly less abundant in white sandstone (the haematite grain coating being absent).

SEM examination of the samples confirms the identified assemblage from light microscopy and enabled the identification of pore lining böhmite (as pisolithic aggregates (Fig. 7.10A, B, D, E.), cf. Wu et al., 2012; Cai et al., 2009, Fig. 7.11 A, B). Böhmite proved to be a common lining of pores in the white sandstone, with all white samples having the mineral in abundance. Kaolinite can be seen in SEM to form books that fill pore space and aggregates that replace feldspars (e.g. Fig. 7.11C, D). Calcite in SEM is always found to be associated with kaolinite and frequently filled pores. Under SEM observation, comparison between Type 1 red sandstone (NG33, Fig. 7.10F) and the Type 2 white sandstone reveals two very different diagenetic lithologies.

The point count data presented in Fig. 7.7 and Fig. 7.8 were tested using the T-Test to show the statistical significance of the differences between the red sandstone and the white sandstone petrography. Table 7.1 summarises these results. The T-Test supports the petrographic observations showing the differences between

the sandstones. Permeability, authigenic quartz and calcite were found to be statistically significantly different between the red and white isolated dunes. Porosity and clay were found to be highly statistically significant. Opaque mineral abundance was not found to be statistically different between the sandstone types supporting the re-distribution hypothesis.

Study	T Tests	Probability	Statistically Significant (95 %)
Awahab Dyke A	Porosity	0.002	Yes*
	Permeability	0.096	No
	Authigenic Quartz	0.084	No
	Authigenic Calcite	0.006	Yes*
	Clay	0.000	Yes*
	Opaques	0.095	No
	COPL	0.021	Yes
RYD	Porosity	0.098	No
	Permeability	0.048	Yes
	Authigenic Quartz	0.026	Yes
	Authigenic Calcite	0.020	Yes
	Clay	0.004	Yes*
	Opaques	0.011	Yes
	COPL	0.108	No
Isolated Dunes	Porosity	0.001	Yes*
	Permeability	0.013	Yes
	Authigenic Quartz	0.046	Yes
	Authigenic Calcite	0.048	Yes
	Clay	0.000	Yes*
	Opaques	0.411	No
	COPL	0.237	No

Parameter	Count Yes	Count No
Porosity	2.00	1.00
Permeability	2.00	1.00
Authi Quartz	2.00	1.00
Authi Calcite	3.00	0.00
Clay*	3.00	0.00
Opaques	1.00	2.00
COPL	1.00	2.00
Total	14.00	7.00

One tailed T-Test results from MS Excel. 95 % significance level= statistically significant. 99 % level= highly statistically significant, which are indicated with *.

Table. 7.1. Summary of T-test results for red and white sandstone. Most parameters are statistically different such that the means are different at the 95 % confidence level. Calcite and clay were found to be statistically significant for all case studies and clay was found to be highly statistically different for all case studies. These parameters' statistically differences are not surprising considering they represent the main petrographic differences between the red and white sandstones.

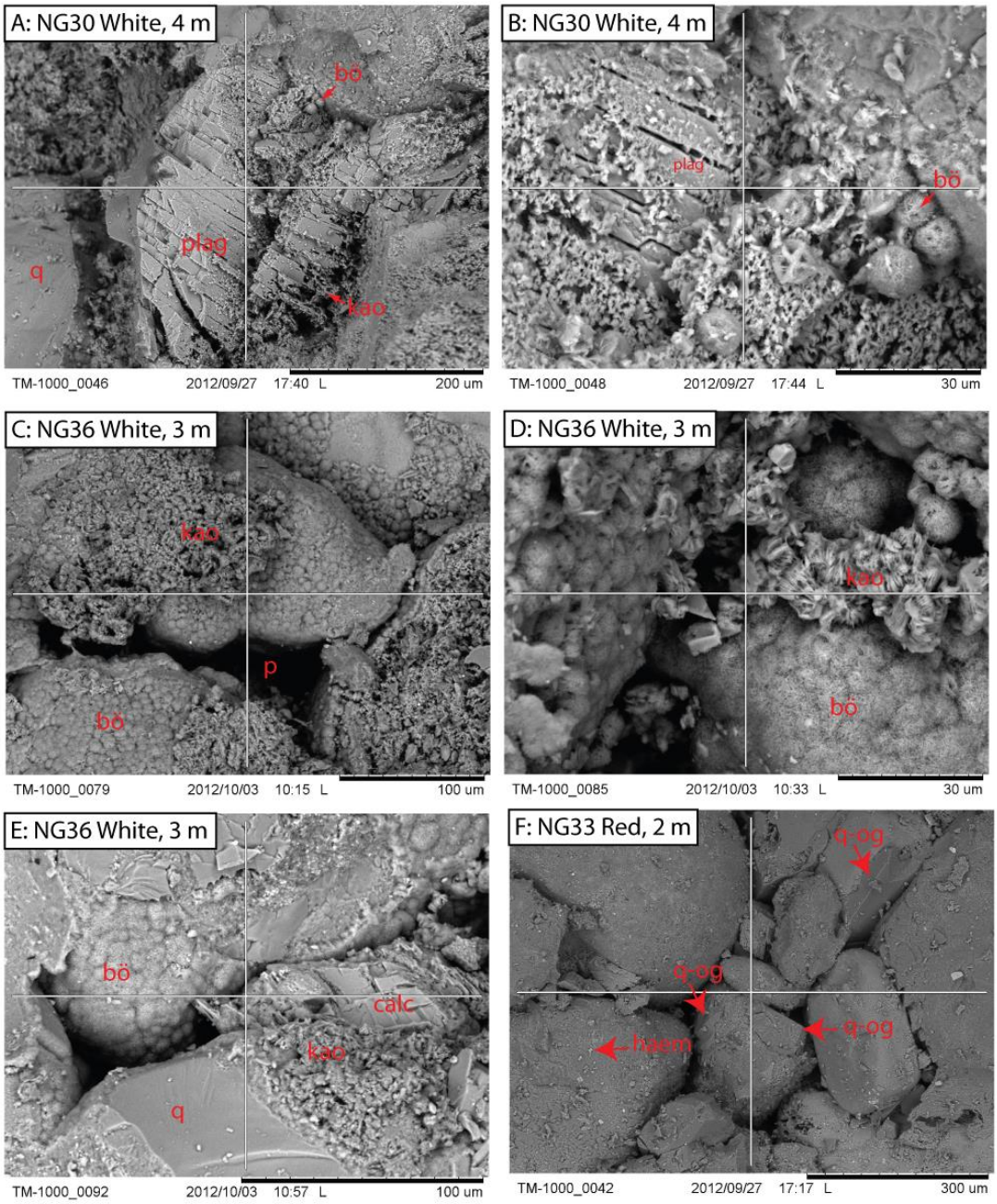

Fig. 7.10. SEM images for Dune 14 white (Dune A) showing characteristic authigenic minerals and diagenesis. (A, B (enlargement of A)). Detrital plagioclase grain being replaced by kaolinite and böhmite. (C, D) Böhmite lining pores with kaolinite both lining and filling pores. Note feldspar framework in bottom right of C with a veneer of böhmite, (E) Complete authigenic assemblage of böhmite, kaolinite and calcite filling pore. (F) NG33 red from Dune 16 (Dune B), note how detrital grains are not corroded or replaced and are coated with small haematite crystals.

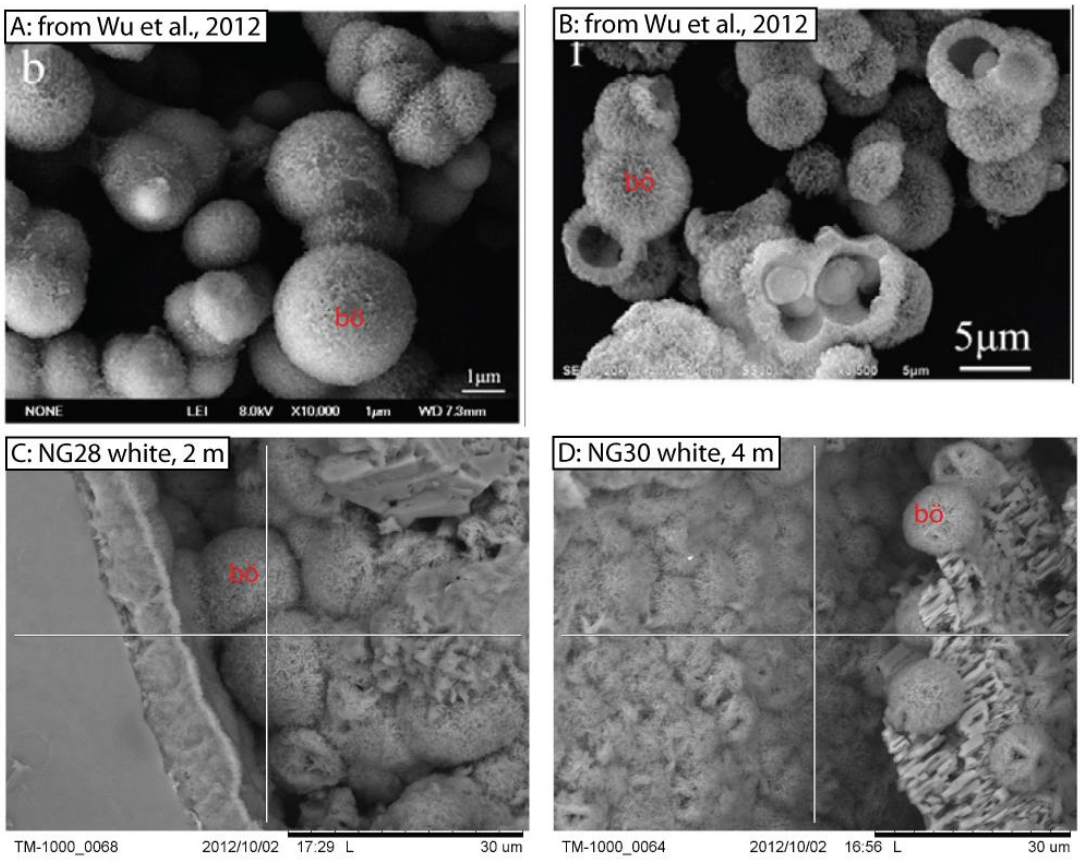

Fig. 7.11. Figure to compare böhmite identification with the hydrothermal synthetic böhmite of Wu et al., 2012. (A, B) Synthetic böhmite (C, D) natural böhmite found in Dune 14 white.

X-Ray diffraction analysis was performed on sample NG29, which comes from 3 m below the hot contact in isolated white Dune A (Fig. 7.30). This distance is significantly below the ~ 30 cm contact zone where Type 3 diagenesis occurs. The spectrum for NG 29 was compared with NG32 isolated red Dune B 2 m below the contact (limited by outcrop exposure). The white sandstone did not display any plagioclase peaks (e.g. Anorthite 100 peak, 3.19 Å (27.96° 2θ)) and orthoclase peaks were weakened. Kaolinite (7.17 Å (12.35 ° 2θ) and 3.58 Å (24.83 ° 2θ) peaks are present in the white sand (not found in the red sand). Böhmite was not detected in XRD, despite it being an obvious phase in SEM. This is probably due to its low

abundance. Calcite did not show a clear spike, despite being seen in optical microscopy and SEM. Illite does not appear in XRD.

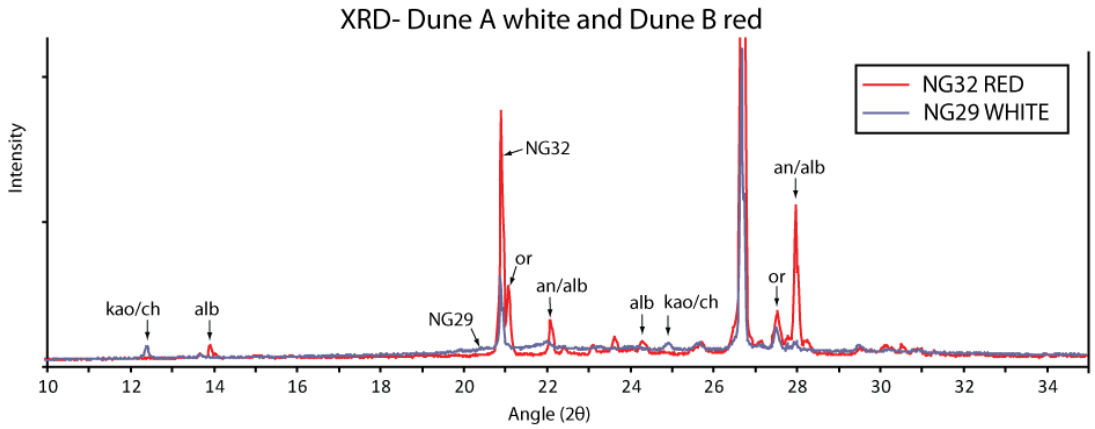

Fig. 7.12. X-Ray diffraction spectra for samples NG32 (red line, red sand, Type 1) and NG29 (blue line, white sand, Type 2), important peaks labelled. Plagioclase (Albite and Anorthite) peaks present in red sand are absent in white sand consistent with petrographical observations. White sand has peaks for kaolinite/chlorite whereas red sand does not. Orthoclase peaks are also weakened in white sand. Interestingly no peak for böhmite was produced despite its identification under SEM. kao= kaolinite, ch= chlorite, alb= albite, an= anorthite, or= orthoclase.

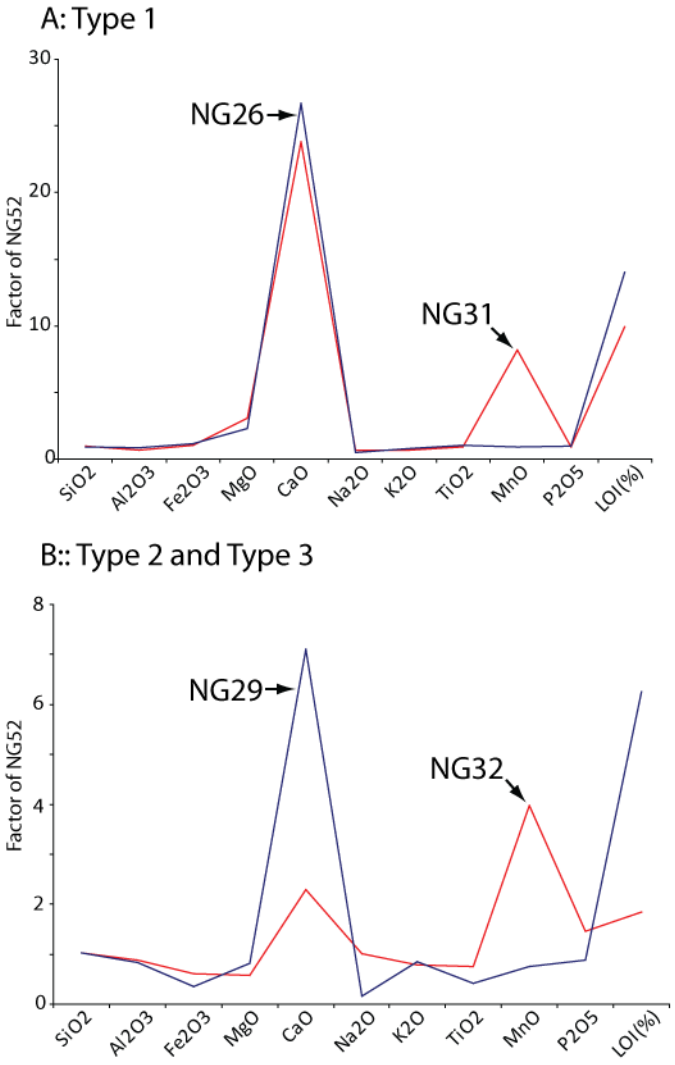

Fig. 7.13. Graph of major element data in Appendix normalised to NG52 values. (A) NG26 white contact (blue line) and NG31 red contact (red line). CaO is enriched in both contact samples, other elements except MnO show little variation. (B) NG32 red dune (red line) and NG29 white dune (blue line). Note difference between NG52 is order of magnitude less. NG29 white has enriched CaO, and LOI and is leached of Fe2O3 and Na2O.

These observations together depict a system in the isolated white dunes where haematite is being dissolved from grain rims, and böhmite, kaolinite and calcite were being formed at the expense of feldspar. The haematite re-precipitating as nodules close by. These mineral transformations resulted in bleached and compacted sandstone, with reduced primary porosity.

Given that all dunes were deposited at the same stratigraphic level and subsequently either bleached white or not, it is instructive to determine how the two main types of diagenesis in the dunes evolved, red and white, and whether there has been any net flux of elements in or out of each system. X-Ray fluorescence analyses were performed on 5 samples with the aim of testing enrichment or depletion in elements as a result of dune bleaching. Specifically the hypothesis was that iron should have been lost in white dune sandstones. For analysis the data were normalised to NG52 which is considered to be a normal background red sandstone.

In samples from hot contacts (Fig. 7.13A.) both samples (red and white dunes) were geochemically similar with the exception of manganese, which may relate to the presence of Ilmenite in NG31. Both contacts were enriched in magnesium and calcium, and showed minor enrichment in iron. LOI was also higher than NG52, which is an indication of the presence of trapped H_2O, probably within the clay minerals or release of CO_2 from the calcite during fusion. It is inferred that enriched magnesium and calcium are hosted in the calcite cement and iron and magnesium are in the chlorite. If the elements were simply redistributed from feldspars during the Type 3 diagenesis, there should be no enrichment in these elements. It is therefore proposed that calcium, magnesium and iron are at least partially sourced from the overlying lava, probably during initial cooling and hydrothermal decomposition of volcanic glass. Note that the enrichment in calcium is ~27 times that of NG52 (also see Chapter 4.).

The geochemical differences between the red and white dunes (Fig. 7.13B.) match the petrographic observations. Iron and sodium are depleted compared with NG52 and NG32. Calcium is enriched in the white sample and LOI is ~ 7 times that of NG52 . The interpretation is that a flux of fluid must have been necessary to show

enrichment and depletions in minerals. If feldspars were simply transformed into the authigenic minerals, with no loss or gain from the system, the bulk rock would be similar to NG52. Importantly the loss of sodium in the white dune shows that only the calcium from plagioclase was being completely sequestered into authigenic minerals as no sodium containing authigenic minerals were found in quantity, sodium being mobile in groundwater. Aluminium is conserved, presumably being rapidly incorporated into böhmite and kaolinite. The calcium enrichment suggests that calcium was being transported from elsewhere in the system and being precipitated in white Dune A. A possible source for this calcium is other sand bodies being depleted or volcanic glass and/or plagioclase in lavas part of the pile. High LOI confirms that NG29 was rich in hydrated minerals (clays) compared to NG52.

In both cases (red and white dunes), in once, hot lava contact areas where subject to Type 3 diagenesis have permeability approaching negligible values (Fig. 7.9A.). Permeability in red dunes increases rapidly away from the contact, reaching background permeability of between 100 md and 1000 md at depths of ~30 cm below the once hot lava contact. Permeability in white dunes does not return to these normal background values outside of the contact zone. Permeability in the white sandstone increases from negligible values in the contact zone, but do not exceed 44 md. Permeability reduction in the white sandstone is a result of Type 2 diagenesis (hydrothermal dissolution, compaction and precipitation of authigenetic minerals).

7.3 Indirect effects below the lavas- Major Erg: red and white.

7.3.1 Awahab Dykes

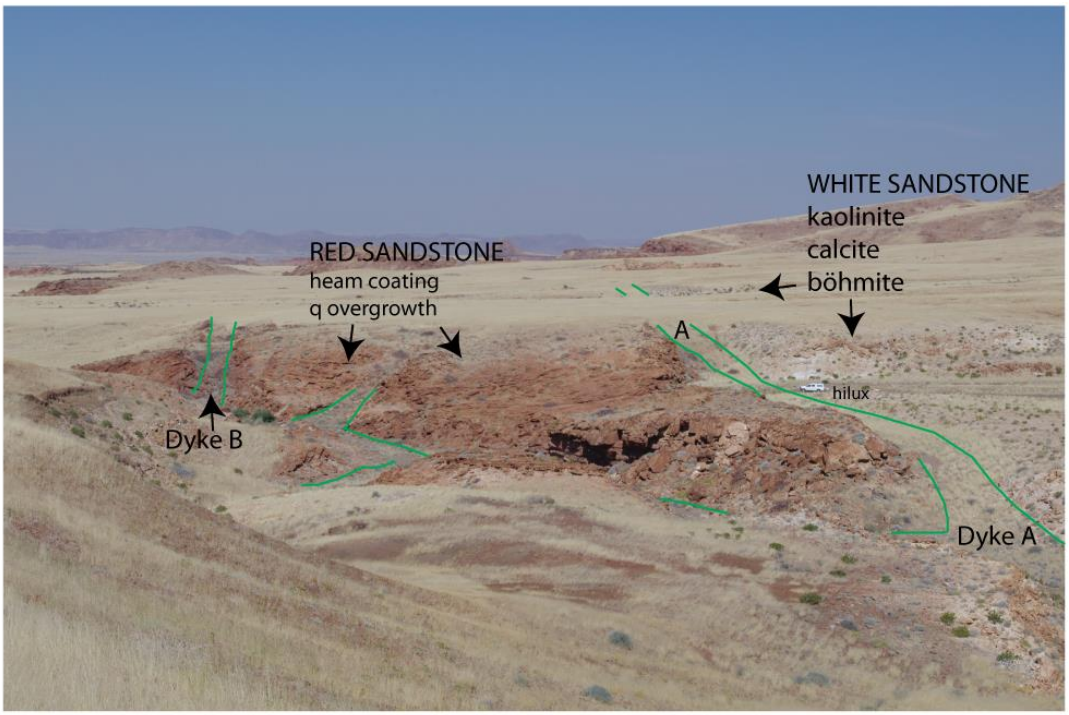

Fig. 7.14. Photograph facing south from 20° 39.640' S 14° 10.075' E towards the Awahab dykes locality. Note Dyke A separates red sand to the left from white sand to the right. The other visible dykes do not appear to separate diagenetic sand types.

The direct effects of the Awahab dykes on the Twyfelfontein Formation have been discussed in Chapter 6. Here the indirect effects are approached. The Awahab Dykes locality is situated in the SE part of Dune Valley at approximately 20° 39.769' S 14° 10.188' E, at 792 m, 3.5 km SE of the Awahab campsite. The outcrops consist of at least five dolerite dykes striking NW, WNW or N, varying from < 3 m thick up to 8 m thick. Of interest here is the difference in sandstone diagenetic style between the red sandstone to the east of Dyke A and the white sandstone to the west of Dyke A (Fig. 7.14.). At outcrop scale the two styles of sandstone diagenesis (Red= Type 1 and White = Type 2) are immediately visible as the red sandstone is friable and

visibly reddened and the white is bleached to a brilliant white. Occasionally at the surface the white sandstone will appear slightly red due to detrital opaque minerals leaching under surface conditions, but examination with a geological hammer will reveal the white sandstone less than a mm below the surface.

Samples were collected in a westwards transect away from the dyke in the white sandstone to the south of the parked vehicle in Fig. 7.14. which was directly opposite the red sandstone transect discussed with relevance to direct effects in Chapter 6. The form of this discussion will not take the style of describing changing mineralogy away from a contact, but rather an integrated approach as these diagenetic effects are not specifically related to the dyke-sediment contact, but rather the whole compartment.

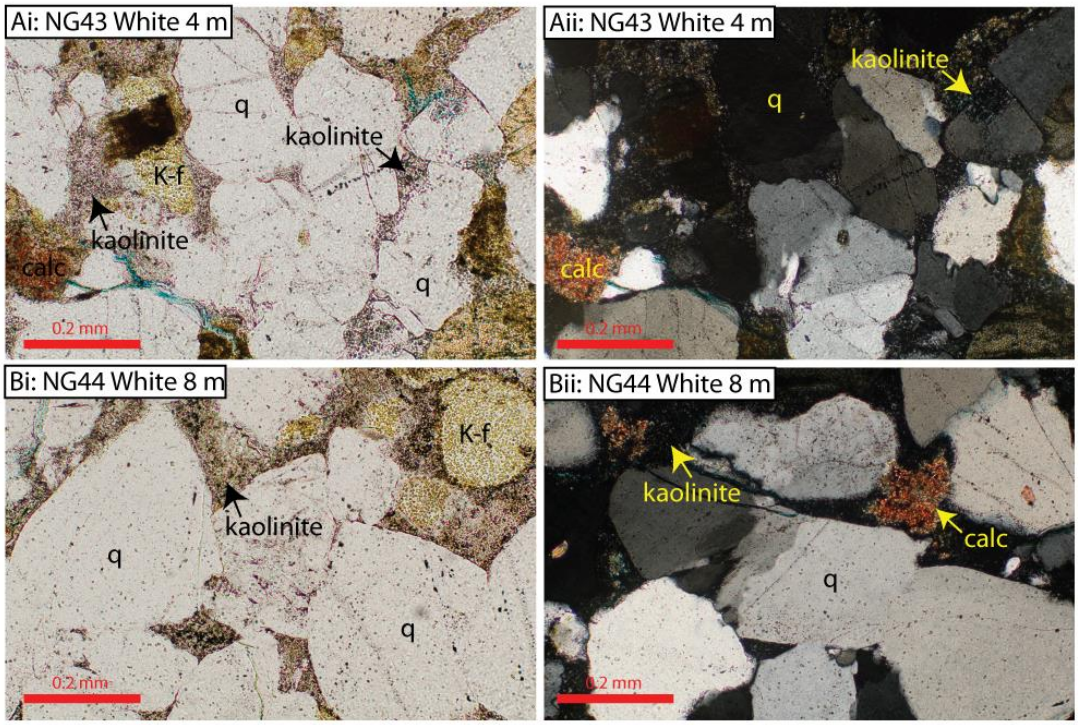

Fig. 7.15. Photomicrographs of the white (Type 2) sand to the west of Dyke A. (Ai PPL, Aii XPL) 4 m from the contact, beyond major direct effects the sandstone is compacted and has an authigenic assemblage comprising kaolinite, calcite and minor other clays, probably chlorite. (Bi PPL, Bii XPL) 8 m from the contact, the sand is little changed compared to that 4 m from the contact. Authigenic phases are kaolinite and calcite.

The direct effects of the emplacement of Dyke A are still partially apparent at 4 m into the white sandstone (NG43, Fig. 7.15.) as increased compaction, but are minor compared to closer to the contact, where the indirect effects are difficult to discern from the direct effects. NG43 has detrital quartz and potassium feldspar at approximately background levels, but plagioclase is only 0.2 %. Porosity is 1.6 %. The authigenic assemblage consists of kaolinite (Fig. 7.15A, B; Fig 7.17Ai, ii.) which replaces plagioclase, lines pores and fills pores and calcite which replaces plagioclase feldspars. Böhmite is present in small quantities, where it lines pores (Fig 7.17Aii.) Porosity loss is still dominated by compaction (COPL= 35.9 %, ±4.3) but cementation is considerable (CEPL= 12.0 %).

There is little variation with distance away from the dyke. Sample NG44, 8 m to the west of the dyke contact is virtually the same as NG43 (Fig. 7.15Bi, ii.). The white sandstone outcrop is continuous to 100 m from the dyke, where sample NG42 white was collected. This sample is the whitest of all the sandstone samples collected. NG42 white, shows a particularly well developed mineral assemblage typical of Type 2 diagenesis. Porosity is reduced by both compaction and cementation. Detrital mineralogy lacks plagioclase but has background abundances of quartz and potassium feldspar. The authigenic assemblage comprises of böhmite, which lines nearly all pores (Fig. 7.16A, B, C). In cross polarised light (Fig. 7.16B.) böhmite is clear, it has first order birefringence, which rules out being a pisolithic illite polymorph on an optical basis. The böhmite can be seen in SEM (Fig. 7.17B, C, D, E) to be comprised of pisolithic aggregates of needle-like crystals, with interstitial böhmite growing from detrital grain surfaces. Kaolinite generally fills pores and replaces plagioclase (Fig. 7.16C, D.) and exists as books that grow over and with böhmite. Fig. 7.17D. shows calcite growing as small rhombs growing within pore

space with kaolinite. In thin section, calcite appears to replace plagioclase, with minor staining attached to kaolinite, which must be the disseminated calcite rhombs.

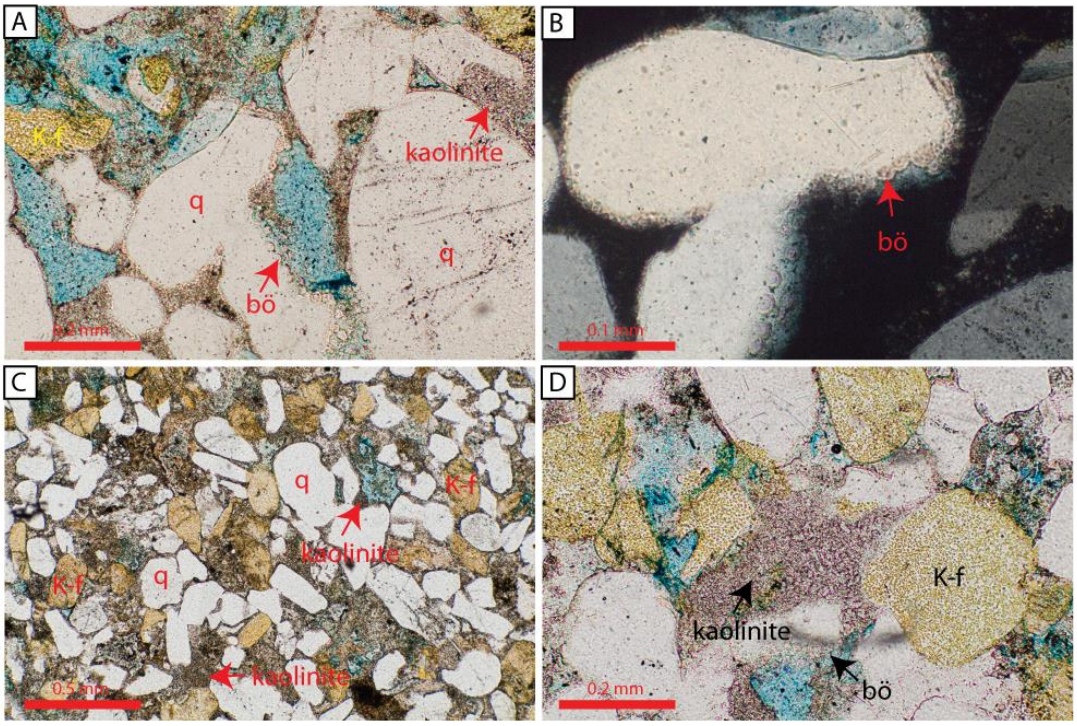

Fig. 7.16. In the same sand compartment ~100 m away from Dyke A, sample NG42 white that compaction is less but the mineral assemblage is typical of the white sandstone. This sample was the whitest of a ll the white sandstone collected. (A PPL) Detrital minerals lack plagioclase and authigenic minerals comprise pore lining böhmite, pore filling kaolinite and minor calcite. (B XPL) Close up of böhmite pore lining in XPL to illustrate it cannot be illite due to low birefringence. (C PPL) Low power image of NG42 white showing abundance of pore filling kaolinite and the preservation of very few primary pores. (D PPL) Close up of pore being filled by kaolinite with some böhmite visible. Note potassium feldspars appear intact and no plagioclase is present.

These cements must have come after deposition and burial as where grains have been separated by sample preparation (Fig. 7.17E.) no cements exist within pits left as a result of compaction and pressure solution. This rules out a detrital origin of the observed differences between the red and white dunes (as does the equal hot contact diagenesis).

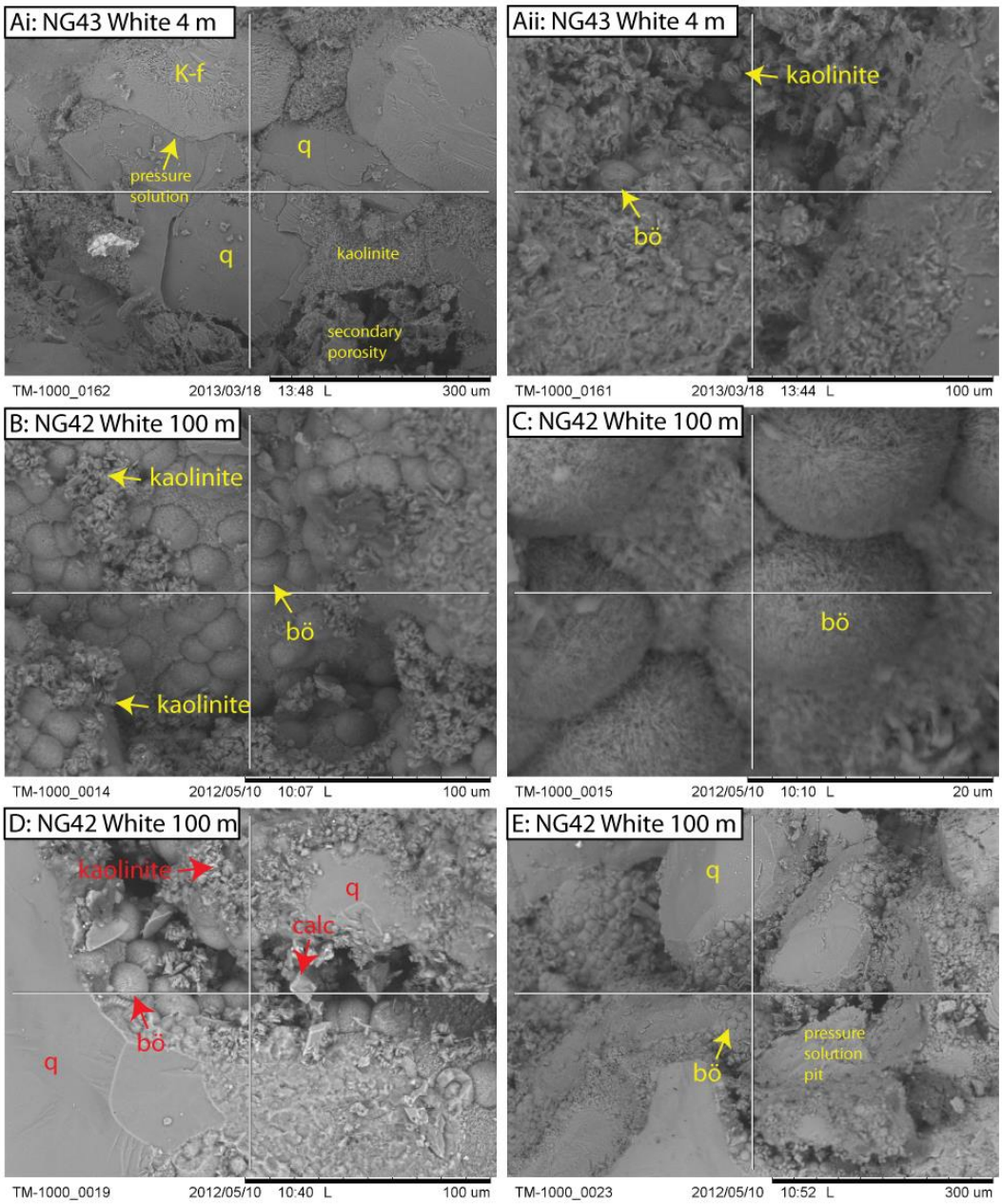

Fig. 7.17. SEM images of white sandstone from the Awahab Dykes locality. (Ai, ii.) Four meters from the contact, compaction is still increased, but the pore filling cement is clearly kaolinite which is in the form of booklets. Böhmite is present as a small percentage. (B) Image showing pisolithic böhmite aggregates lining pores with associated kaolinite. (C) Close up of B showing the clear pisolithic aggregates of böhmite. (D) Image showing the complete authigenic assemblage of böhmite, kaolinite and calcite. (E) Image chosen to show that the cements came after at least some burial evident as the indicated pressure solution pit, where grains were previously in contact prior to sample preparation having no authigenic phases embedded.

Trends and separation between fields of point counted parameters clearly display a difference between red Type 1 sandstone and white Type 2 sandstone. Red

sandstone has 1–3 % (±0.3) more authigenic quartz on average (based on linear trend line) at a given distance compared to the white sandstone (Fig. 7.18A.). This difference is probably due to the inhibition of quartz overgrowths by the clay cements (cf. Bloch et al., 2002). Authigenic clay is significantly more abundant in the white sandstone than the red sandstone (Fig. 7.18B.), but is not related to distance from the dyke (i.e. it is pervasive). In the red sandstone it is negligible. This suggests the clay is not related to the direct effects of dyke emplacement. Opaque minerals, as expected are more abundant in the red sandstone, due to the haematite coating grains. Opaque minerals are however still present in the white sandstone as detrital heavy mineral grains of magnetite, ilmenite etc., which increase away from the dyke contact as direct effects reduce in intensity (like the red sandstone) (Fig. 7.18C.). Calcite abundance is higher within the white sandstone and is highly variable with distance (Fig. 7.18D.).

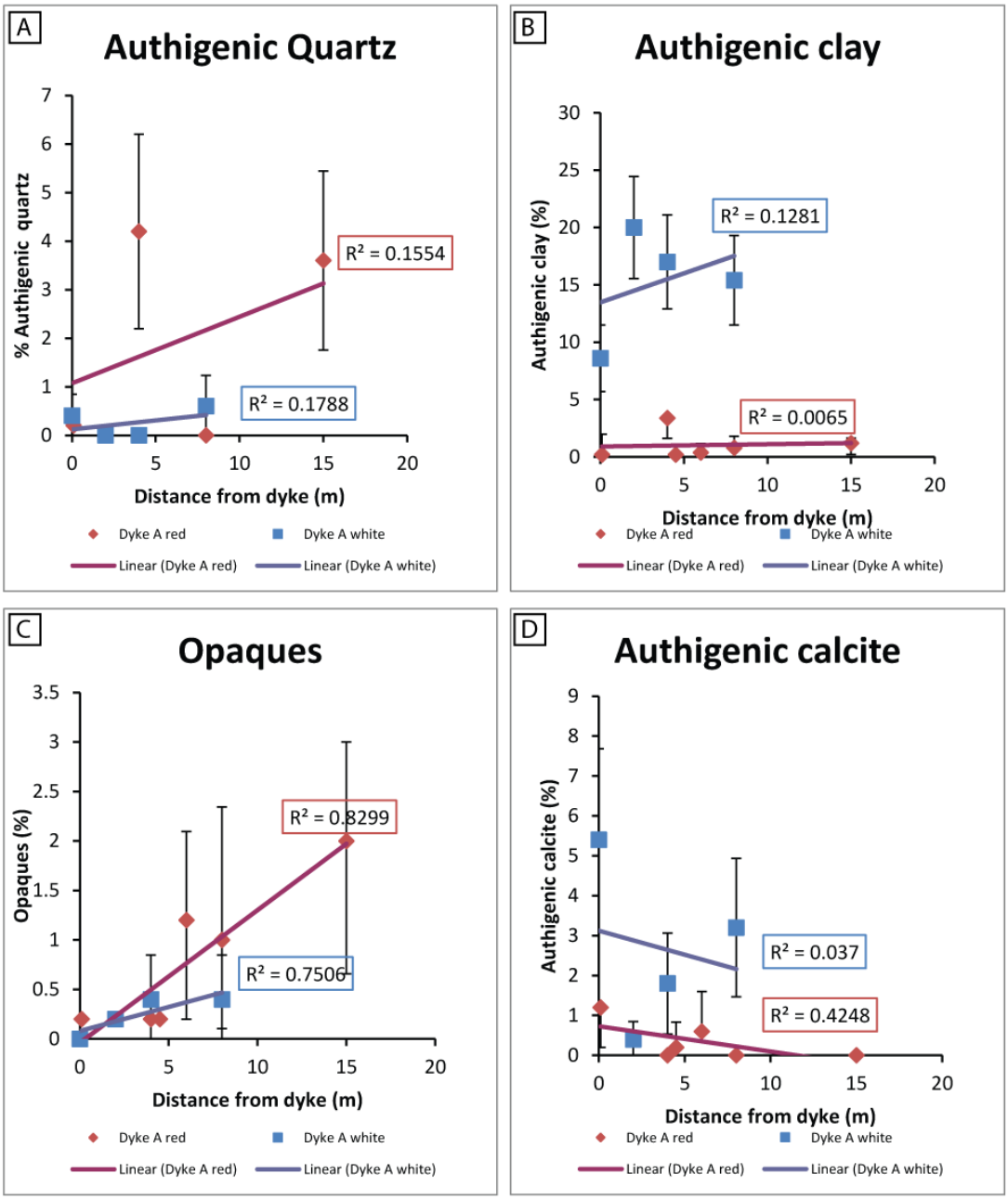

Fig. 7.18. Graphs of point counted phases against distance from Dyke A for both the white (Type 2) sandstone and the red (Type 1) sandstone. (A) Authigenic quartz is more abundant in the red sand, probably due to clays inhibiting quartz overgrowth development (e.g. Bloch et al., 2002). (B) Authigenic clay (mainly kaolinite in the white sandstone) is greater in abundance in the white sandstone by ~ 15 % and is usually negligible in the red sandstone. (C) Opaque minerals increase away from the bleached contact zone for both red and white (bleached contact zone identified in Chapter 5) but the increase is more significant in the red sandstone and at higher levels in the red sandstone. Opaques in the white sandstone are mainly detrital.

The red sandstone and the white sandstone have separate porosity–Distance trends (Fig. 7.19A.). In the red sandstone porosity increases away from the dyke

contact, until the background value of ~ 12.5 % is reached, from where it stabilises. The white sandstone porosity increases a little away from the contact, but the porosity remains low to 8 m, where the final sample was collected. Fig. 7.19B shows analysis of the porosity loss. Compaction is the major contributor in both cases (red and white); with red sandstone always being slightly more compacted than the white. The white sandstone is more cemented at a given distance than the red sandstone by ~ 10 %.

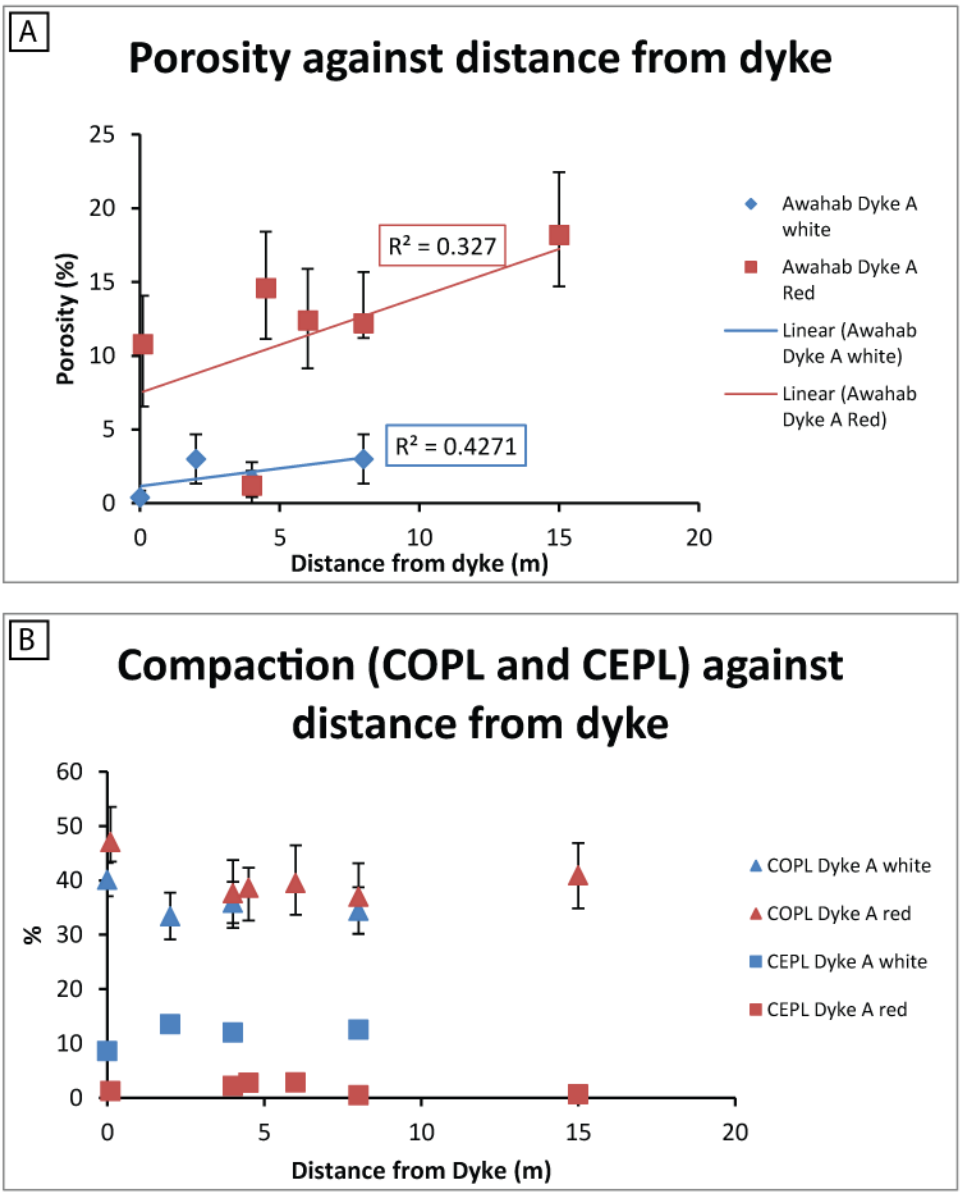

Fig. 7.19. (A) Porosity increases away from Dyke A for both red and white sand due to the direct effects of the dyke. Porosity increases more rapidly for the red sandstone and to higher levels. The white sandstone porosity remains low, not exceeding 3 %. (B) Porosity loss in both samples is dominated by compaction, which largely occurred after dyke emplacement and during subsequent burial (Chapter 5.). Note however that COPL is slightly lower for white sandstone and that CEPL is always higher due to the increased authigenesis.

Permeability, like porosity, plots as separate fields for both red and white sandstone. Permeability is always higher for the red sandstone (Fig. 7.20A.). When

permeability is plotted against porosity, as is the case for the isolated dunes, two populations develop, separating the white sandstone from the red sandstone.

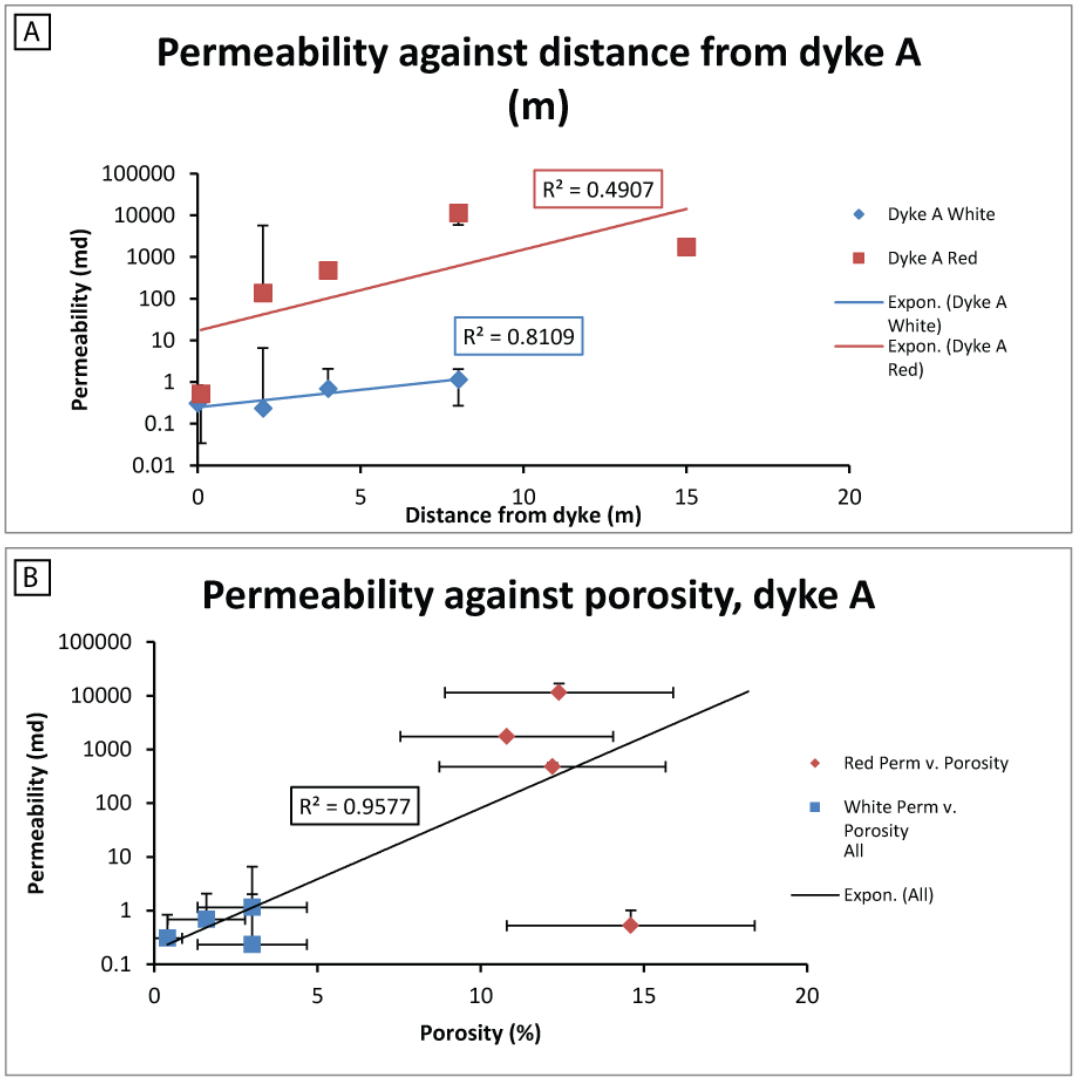

Fig. 7.20. (A) Like porosity, two clear trends exist between permeability and distance for each red and white sandstone. The red sandstone has increased permeability and a faster rate of gain in permeability with distance. (B) Two populations plot in permeability-porosity space as in the isolated dunes (Fig. 7.9B.) with the red sandstone showing as the high permeability and porosity population.

For this case study T-Test results show that porosity, calcite, and clay are highly statistically different between red and white sandstone. COPL is statistically

significantly different. These analyses support the hypothesis that different diagenetic pathways where followed by the sand either side of the dyke. The statistically insignificant differences for the other parameters support the proposed mechanism in that authigenic quartz was probably formed prior to the dyke emplacement and that opaques are *redistributed* on either side of the dyke into nodules.

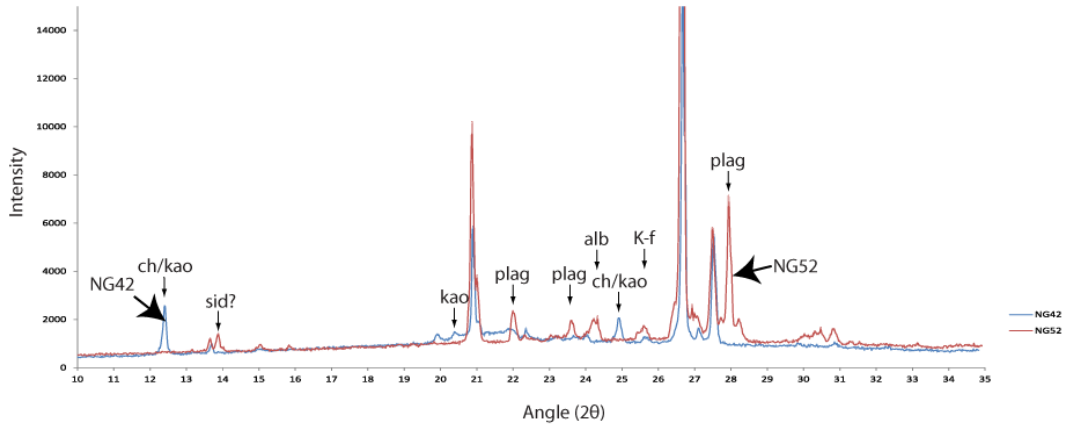

Fig. 7.21. X-Ray diffraction spectra for sample NG52 (red) and sample NG42 (white). Important peaks labelled. Peaks absent in the white sandstone are for plagioclase feldspars. Peaks present in the white sandstone but not in the red sandstone are chlorite or kaolinite, substantiated as kaolinite based on SEM analysis. kao= kaolinite, ch= chlorite, alb= albite, an= anorthite, or= orthoclase, plag= plagioclase, K-f= potassium feldspar, sid= siderite.

The petrographical analyses are confirmed by the X-ray diffraction analyses of two representative samples from the red (NG52) and white sand (NG 42 white). Fig. 7.21. shows that the white sand completely lacks any plagioclase peak but has gained strong kaolinite peaks. Potassium feldspar peaks have also been weakened in NG42 white. Böhmite was not identified in XRD, probably due to the oriented slide method used favouring the clay minerals and abundant minerals. The XRD spectra are very similar to the white sands in the isolated dunes, but more pronounced; this is not surprising considering how NG42 white is the whitest of the sandstones encountered.

Major and trace element data are presented in Fig. 7.22. normalised to NG52. Major elements within the white sandstone (NG42, dotted line is NG29 3 m Dune 14 white) show enrichment in calcium and increased LOI. NG42 is depleted in iron, sodium, titanium and manganese. This profile is mirrored (except manganese) by the isolated dune example. The enrichment in calcium can be explained by the increased abundance of calcite, which, like for the isolated dunes must have come from an external source. This source is inferred to be basic glass within the basalt pile or areas of sandstone depleted in calcium through plagioclase dissolution without calcite precipitation. Depletions in sodium can be explained by plagioclase dissolution, but the removal of sodium in solution as it is highly mobile in water. The depleted metal ions are entirely consistent with the outcrop and petrographic observations of bleaching and reduced abundance of opaque minerals. Potassium and Aluminium are conserved; the aluminium from the observed feldspar dissolution is probably rapidly consumed by kaolinite and böhmite precipitation, which can be rapid under hydrothermal conditions, on the order of hours for the observed 5–10 μm pisoliths of Wu et al. (2012). The increased LOI is consistent with the kaolinite and calcite releasing volatiles when fused during the XRF process. Conservation of potassium suggests that the dissolution of potassium feldspars is probably a minor process, or the potassium is being sequestered into other clay minerals such as illite, despite no 10 Å peak being observed in XRD.

The observations are interpreted as two separate compartments either side of Dyke A, undergoing separate diagenetic histories. Chapter 6 showed that in the RYD white sandstone, the calcite growth was coterminous with the cooling dyke. If this also holds for this dyke, showing similar effects it is likely that the divergence of diagenetic histories diverged shortly after the intrusion of the dyke and probably

during its cooling. This is supported by the contacts of both sandstones being similar. The origin of the bleaching and differential diagenesis is discussed in 7.4.

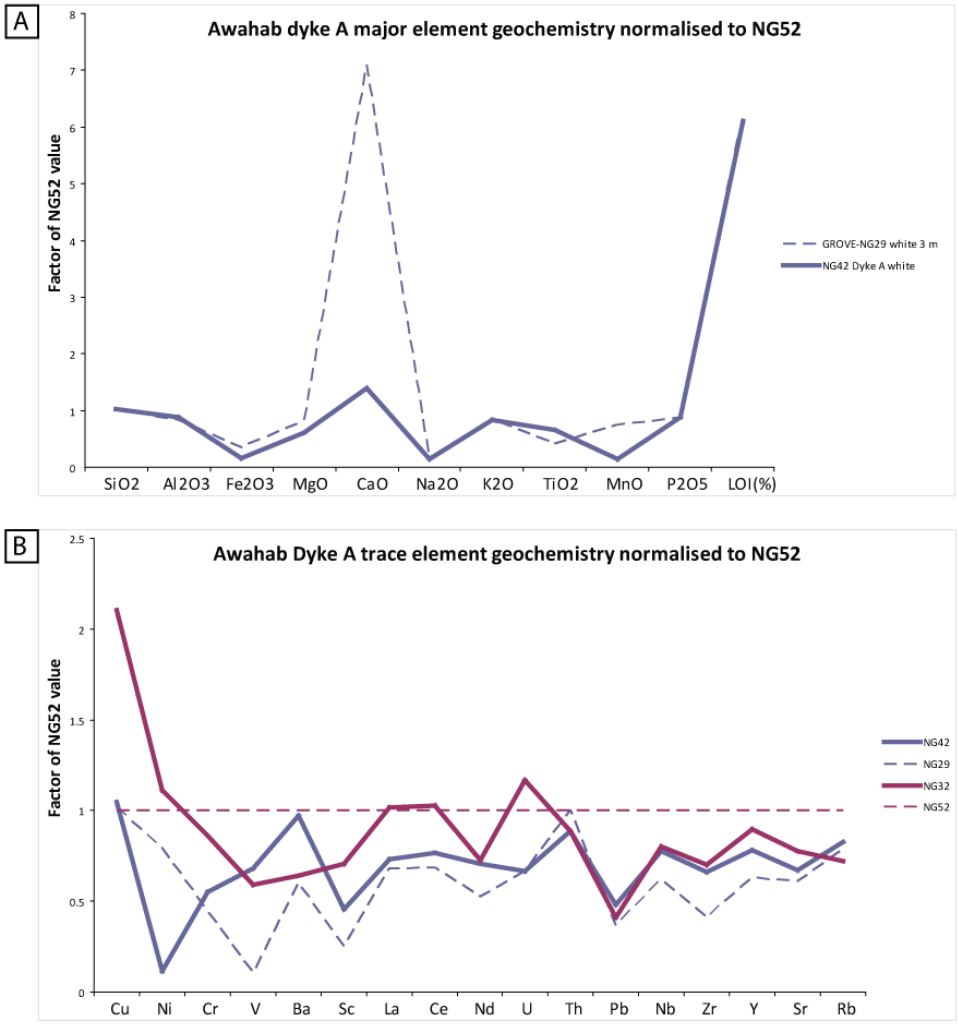

Fig. 7.22. (A) Major element geochemistry for NG42 white (solid line) and NG29 white 3 m normalised to NG52. Both samples show enrichment in calcium and depletion in iron and manganese. LOI is increased in both samples. (B) Trace element data plotted for NG42 white (solid blue), NG29 (white Dune 14, dashed blue), NG32 (red Dune 16, red) and NG52 (red). White sand can generally be seen to be depleted in most trace elements compared to the red sand.

7.4 Red Yellow Dyke area

The Red Yellow Dyke locality is so named because of the separation of compartments of red (Type 1) sandstone from white (Type 2) sandstone by a prominent dyke (see Chapter 6.). Here, the sandstones outside of the direct effects of the intrusion are studied, as well as the larger scale compartmentalisation evident to the north where the white compartment is bounded by another E-W trending dyke (Fig. 7.23A, B).

7.4.1 The main RYD dyke white compartment

The foot of the RYD dyke that separates the sandstone compartments is located at 20° 36.743’ S 14° 4.136’ E below a prominent south facing cliff (Fig. 7.23.). At outcrop scale the red sandstone to the west is clear from distance, as is the white sandstone to the east. The white compartment is bounded to the west by the main RYD dyke, to the north by the E-W trending dyke (Fig. 7.23.), to the east it appears unconfined, as the outcrop thins due to erosion and to the south outcrop disappears under basalt, but confinement is considered limited due to white sand re-appearing from the other side of the basalt cover 2.5 km south of the main cliff outcrop. From Fig. 7.23. it is evident that the demarcation between the red and white sandstones is by dykes.

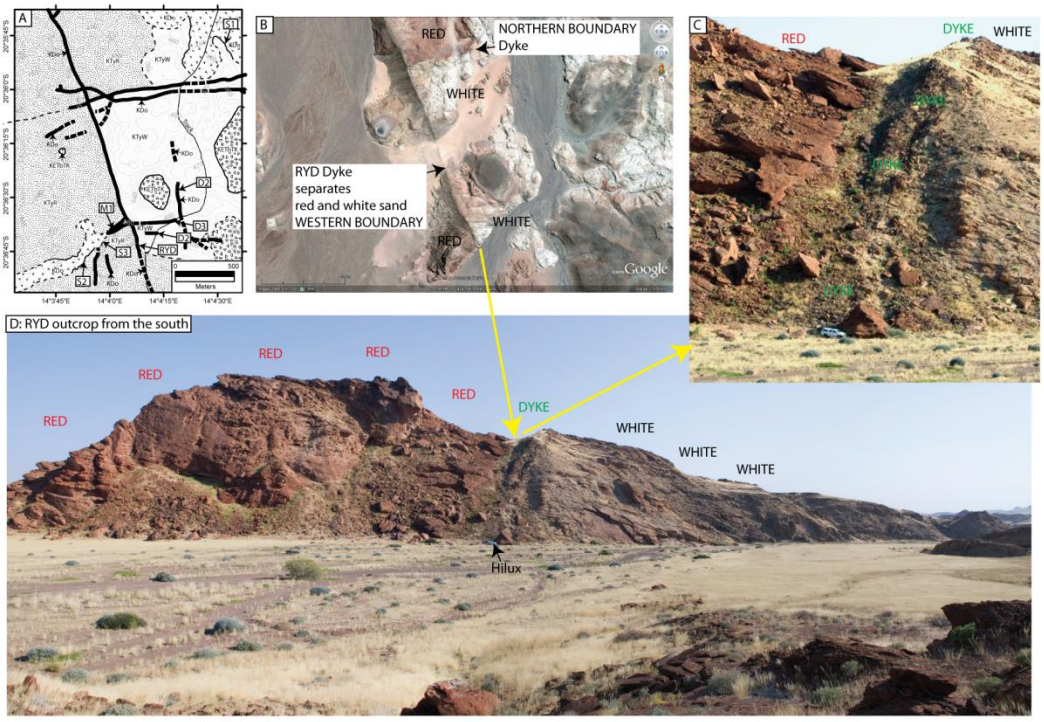

Fig. 7.23. (A) Map of the RYD locality, see Fig. 6.12. for key). (B) GoogleEarth image of RYD locality showing striking appearance and contrast of the red and white sandstone compartments. (C)Facing north. Close up of the RYD dolerite dyke showing how it separates red sand to the left (west) from white sand to the right (east). (D) Panorama of the entire southern cliff of the RYD outcrop with Toyota Hilux for scale.

The main diagenetic case study is based on a transect away from the main RYD dyke at the foot of the major cliff. Samples were also collected from the northern compartments for comparison.

The white sandstone in hand specimen ranges from a hard white sub-arkose with no visible porosity near to the dyke, to a yellow/brown mottled (mottles of haematite nodules 1/10's of mm up to 3 mm), slightly friable white sandstone with visible porosity from about 4 m to 6 m. Further than this the sandstone is less mottled and visible pores are filled with fine grained white material. Overall, despite the sandstone being visibly bleached compared to the red sandstone; it is not as brilliant white as the Awahab examples.

It has been established in Chapter 6 that the calcite formed in the white sandstone was coterminous with the cooling of the RYD dyke based on an oxygen stable isotope trend suggesting higher temperatures closer to the dyke. Petrographically the white sandstone here can be grouped into three categories: (A) Near to the dyke contact where compaction is increased (<2 m), (B) the more friable mottled zone with low clay abundance (< 10 m) and (C) the zone with minor mottling and high clay abundance (> 10 m). The mottled zone (B) is visibly weakened at outcrop scale. All zones have occasional to abundant calcite.

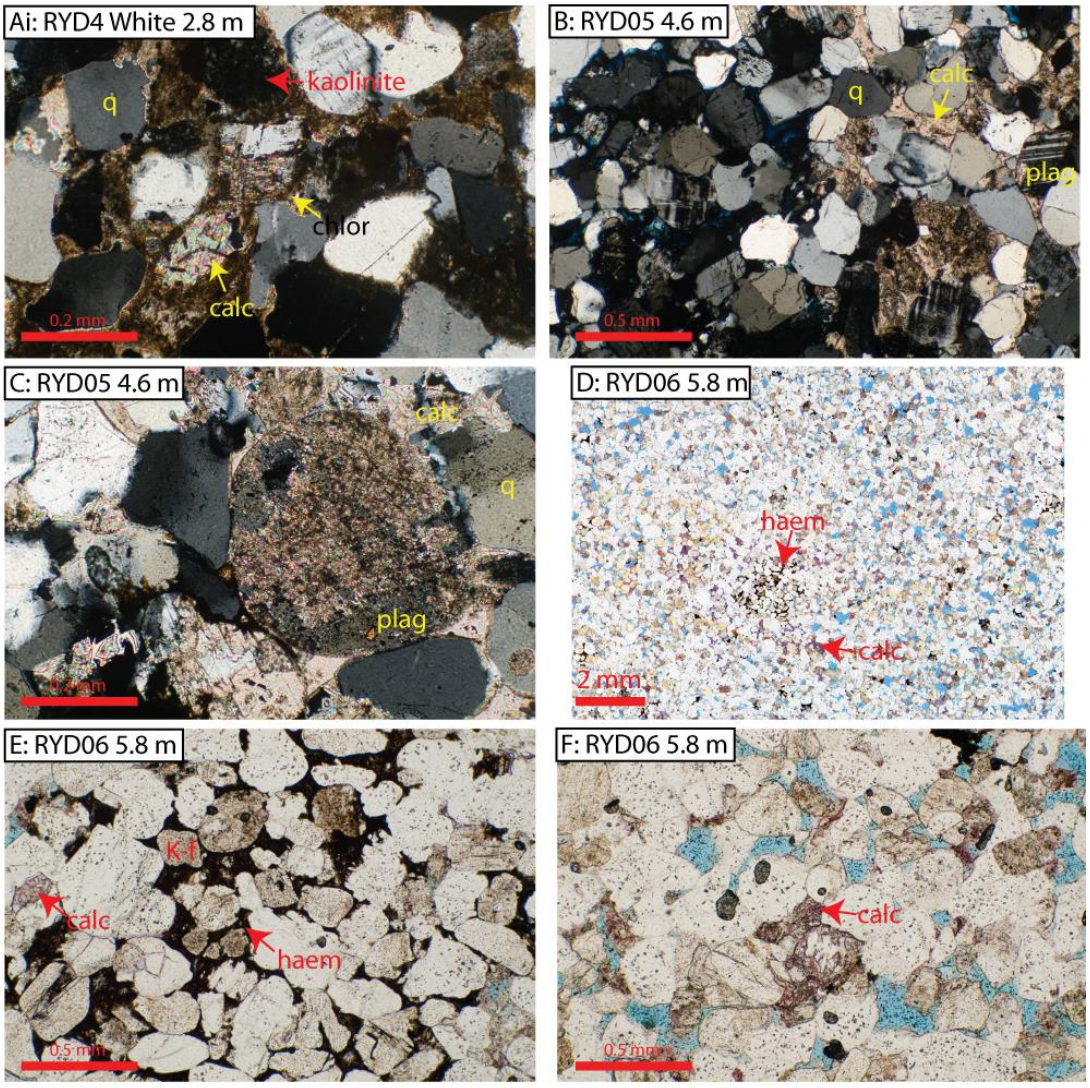

Fig. 7.24. Photomicrographs of white sandstone to the east of the RYD dyke. (Ai XPL) 2.8 m from the dyke, direct effects are still apparent as increased compaction, chlorite and calcite. (B, C XPL) Calcite and kaolinite replaces feldspars. (D PPL) wide view image of RYD06 slide showing lack of haematite grain coatings, calcite cement, and haematite nodule. Note oversized secondary pores resulting from plagioclase dissolution. (E PPL) Close up of haematite nodule in D. (F) Pore filling calcite also exists in poikilitic patches.

2.8 m from the dyke, the contact zone of direct diagenetic effects is in transition to the indirect effects dominated sandstone. Grains become apparently less compacted in thin-section (COPL= 39.6 % (±4.3), compared with up to 46 % (±3.5) closer to the contact). Detrital mineralogy appears approximately equal to the background. Authigenic minerals are dominated by calcite and clay. The calcite fills pores and is often aggressive towards both feldspars and quartz (Fig. 7.24Ai.). The

calcite is normally associated with clays, identified as kaolinite under SEM (Fi. 7.25Bi, Bii.), although the brown colour within the calcite suggests chlorite (Mg, Mn rich) is also present (Fig. 7.24Ai.). RYD06 (5.8 m and RYD05 (4.6 m) are typical of the white sand in the white mottled zone. Porosity is present in thin-section as both primary pores and secondary porosity comprising oversized pores; probably dissolved feldspar (Fig. 7.24D, F.). The detrital assemblage appears approximately background in phase abundances. Authigenic minerals are usually grouped into nodular masses rather than disseminated. The nodules primarily comprise of: haematite (and goethite) (Fig. 7.24D, E; Fig. 7.25Cii.) which form the outcrop and hand specimen visible mottled nodules: Calcite forms within and around the iron oxide nodules (Fig. 7.24D.), as well as in nodules of just calcite consisting of 250 μm poikilitic crystals (Fig. 7.24F.) and as replacements of plagioclase feldspar grains (Fig. 7.24C.): Kaolinite is present throughout as pore throat fills (Fig. 7.25Bi.) and attached to skeletal remains of partially dissolved feldspar grains (Fig. 7.25Ci, D.).

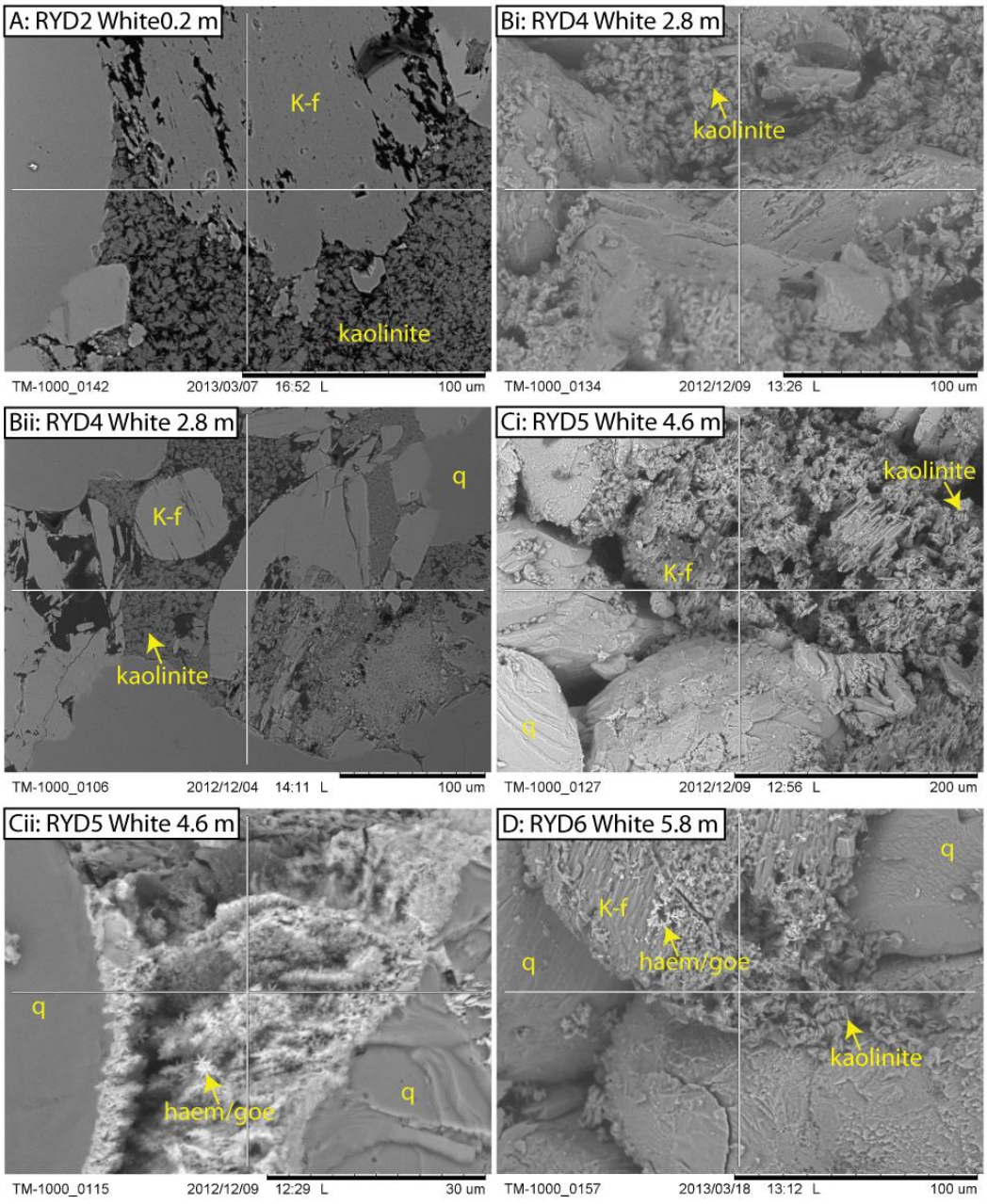

Fig. 7.25. SEM images of white sandstone to the east of the RYD. (A) 0.2 m from the contact kaolinite fills pores. (Bi, ii) 2.8 m kaolinite is still the major authigenic phase where it also replaces feldspars (ii). (Ci) Skeletal remains of a potassium feldspar partially dissolved and partially replaced with kaolinite. (Cii) Mineralisation within a haematite nodule pore fill is small radiating disc and rod shaped haematite and probably some goethite. EDS confirmed. (D) 5.8 m from the contact, only feldspars are partial framework grains with associated kaolinite.

The zone to the east of the mottled zone is characterised by sample NG20 and NG21 (both 19 m). In these samples porosity is variable (3 % (±0.8) or 15 % (±1.6)). Compaction is about the same as the mottled zone (COPL=38 % (±4.3) and 42 %

(±4.0)). Detrital mineralogy is also apparently the same as in the mottled zone. Authigenic minerals are dominated by kaolinite with minor calcite associated as disseminated grains within the clay. Mottled patches of pore-filling iron oxides are absent, but detrital opaque minerals exist.

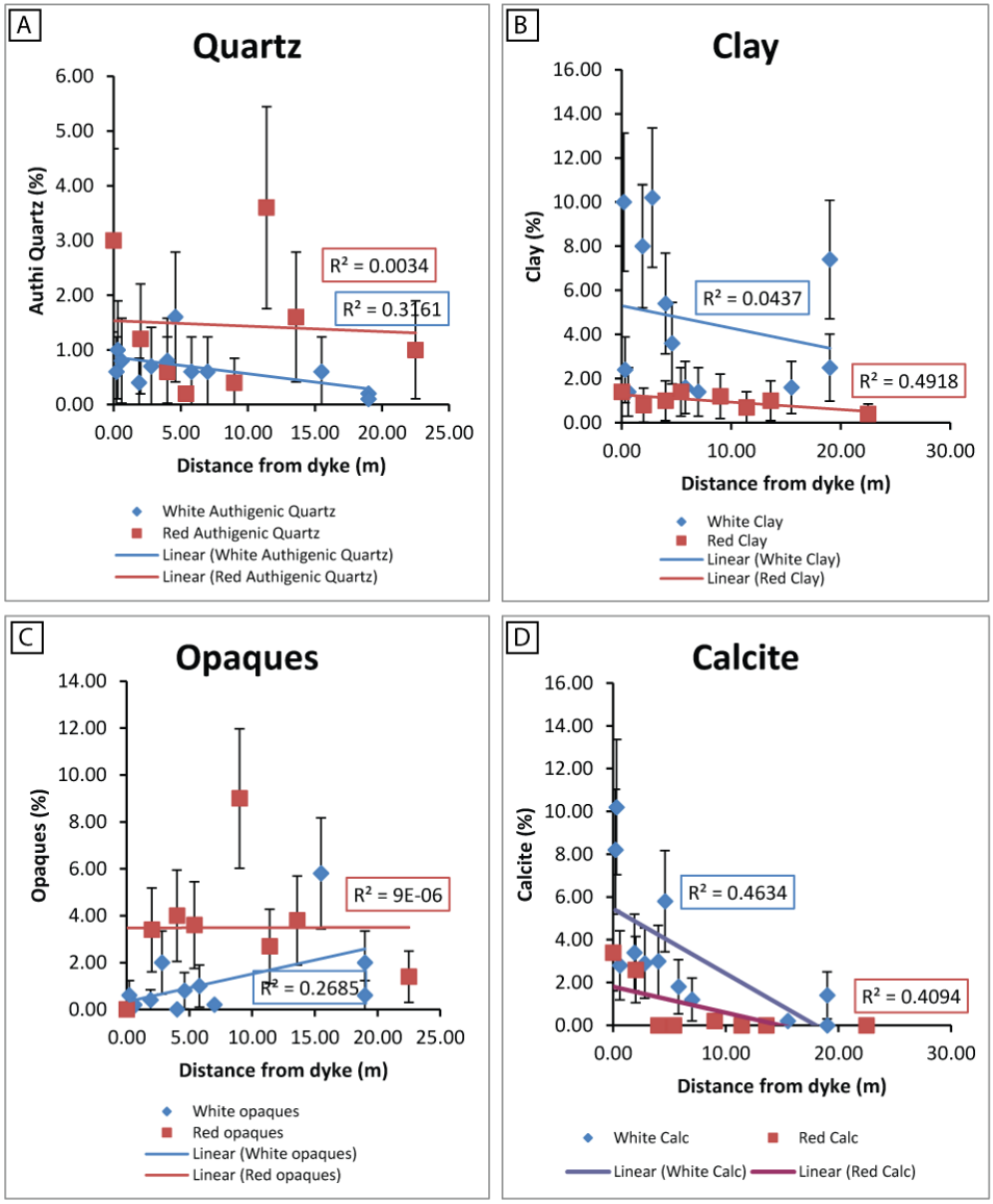

Fig. 7.26. Point counted phases away from the RYD dyke for both white sand and red sand. (A) Like other examples quartz overgrowths are more abundant in the red sandstone. (B) Authigenic clay is greater and more variable within the white sandstone. (C) Opaque minerals are more abundant in the red sandstone. Calcite is more abundant in the white sandstone.

Like the other examples of sandstone bleaching and indirect diagenesis as a result of igneous geology, there is a clear separation between the red sandstone and the white sandstone based on point counted petrographic trends (also see T-Test results).

Authigenic quartz overgrowths (Fig. 7.26A.) are consistently more abundant within the red sandstone. The abundance is not significantly related to distance from the dyke, suggesting formation was not related to the intrusion event or cooling. This is common with the other case studies. Like other case studies, this is probably due to quartz precipitation being inhibited by clay minerals developed during bleaching. The evidence suggests the bleaching being a relatively early process, probably prior to all the authigenic quartz forming (e.g. prior to the rapid Late Cretaceous exhumation, Raab et al., 2005).

Authigenic clay abundance is higher in the white sandstone than the red in nearly every sample for a given distance. Both sandstone types show little clay variation with distance overall, although the white sandstone does show a 'trough' in the trend between ~ 5 m and 15 m coincident with the mottled zone and high secondary porosity. This trough probably represents a zone where during clay precipitation; pore water transported mobile clays away, and destroyed weakened feldspars. The existence of remaining clays in pore throats supports this.

Opaque minerals, comprising both detrital opaques and authigenic opaques are higher in the red sandstone than the white sandstone, as expected.

Authigenic calcite is higher abundance in the white sandstone than the red sandstone. In the red sandstone calcite is very rare beyond 4 m, whereas in the white sandstone it persists until at least 19 m.

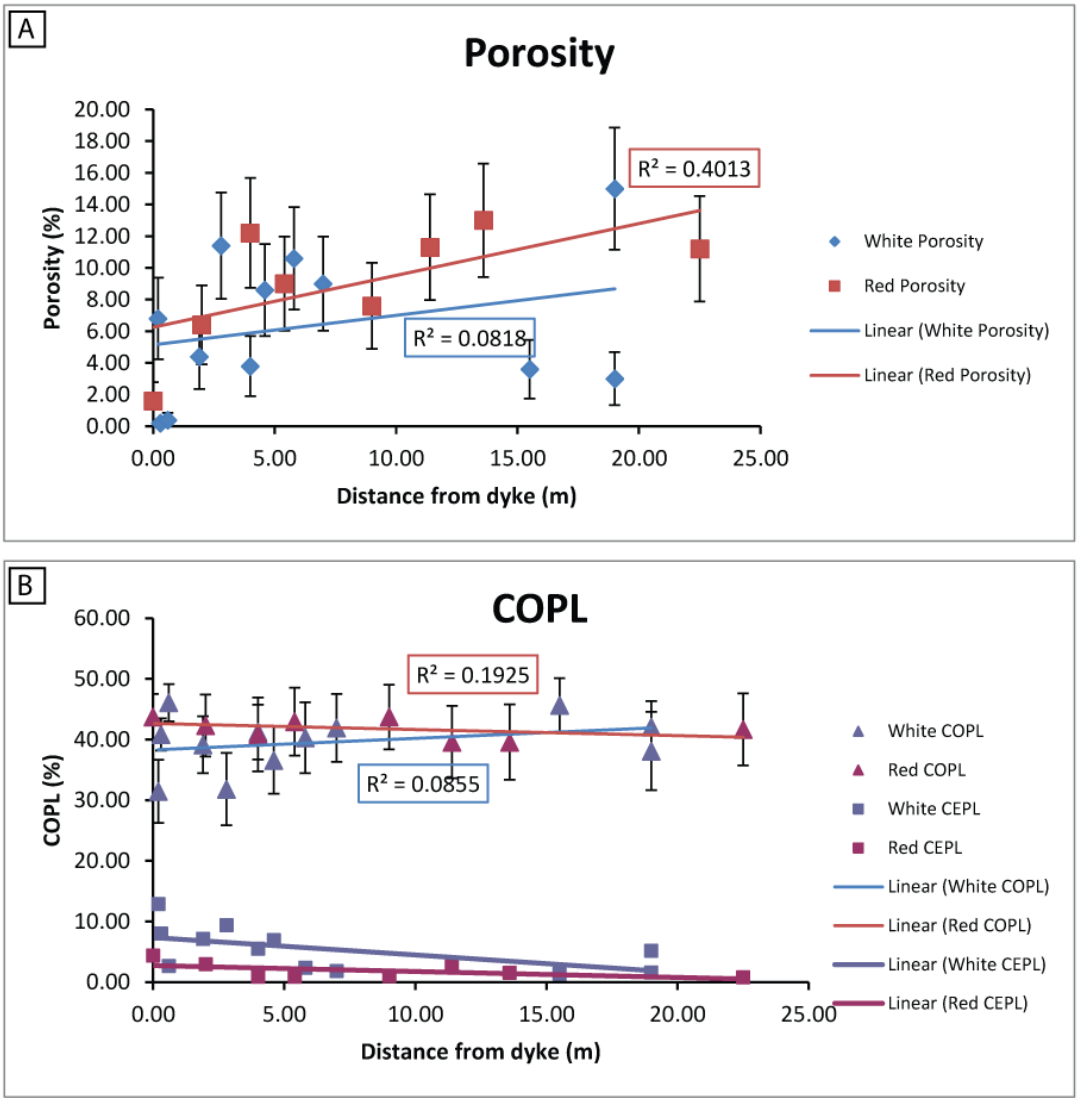

Fig. 7.27. (A) Porosity increases away from the dyke for both red and white sand. Porosity increases to greater levels in the red sandstone and is less variable than in the white sandstone. (B) White sandstone compaction is dominated by COPL, but is more variable than the red sandstone. CEPL is higher for white sandstone than red sandstone.

Porosity increases away from the dyke contact for both sandstone types. Fig. 7.27A. show the relationship between porosity and distance from the dyke. The trend lines have been applied to the whole data set rather than just the porosity increase to background levels. The trends show that porosity for a given distance is always higher in the red sandstone than the white sandstone and that the white sandstone

shows more variation. The porosity loss (Fig. 7.27B.) in both sandstones is dominated by compaction (COPL). The compaction was underway prior to dyke emplacement (Chapter 6.) but most occurred during continued burial. There is not much to separate the degree of compaction in the red and white sandstone for a given distance. The cementation component of porosity loss is however, significantly higher for a given distance within the white sandstone and is controlled mostly by clay and calcite authigenesis, which is absent in the red sandstone outside of the directly affected zone.

Limited permeability data exists for the RYD area. The small amount of data suggest that permeability increases away from the dyke in both cases and is approximately the same (Fig.7.28A.). In permeability-porosity space, no separation is observed between the two sandstone types, as it is in the other two case studies.

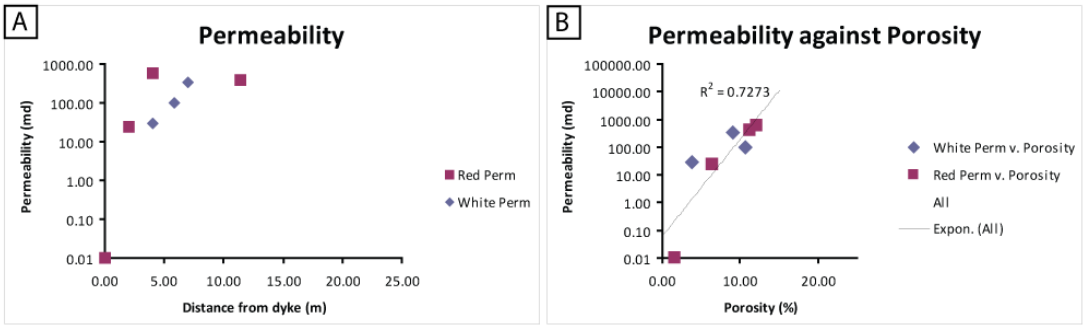

Fig. 7.28. (A) White sandstone permeability appears to lie on trend with the red sandstone. Data limited. (B) No separation was observed for this locality between red and white sandstone in permeability-porosity space.

Anyalsis using the T-Test (Table 7.1) for the RYD case study shows that the permeability, authigenic quartz, calcite, clay and opaques are statistically different between the red sandstone and the white sandstone. This supports the assertions above. Notably, compared to the other case studies (Isolated Dunes

and Awahab RYD) there is a statistical difference between the abundance of opaque minerals in the red and white sandstone; this may suggest that the fluid flux here actually transported the iron away to be precipitated elsewhere. A possible location for this is the identified 'mottled zone'.

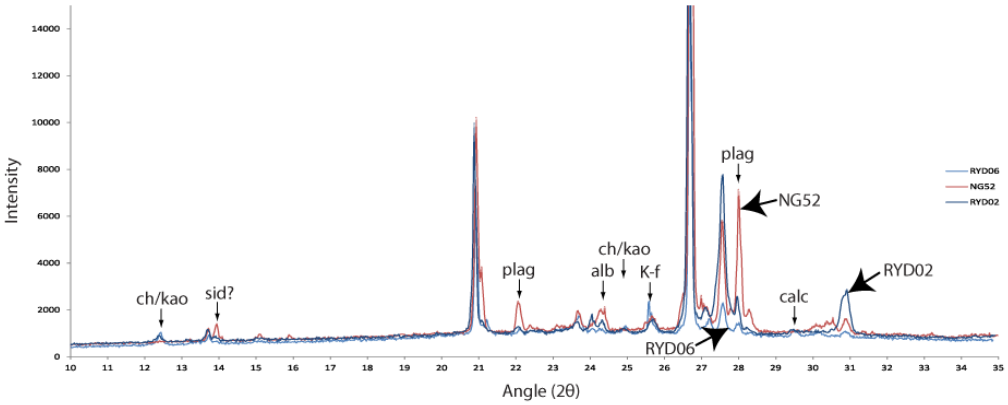

Fig. 7.29. Two RYD white samples, RYD 02 and RYO06 are shown with NG52 red. Plagioclase peaks are weakened or absent in the white sandstone and weak kaolinite/chlorite peaks appear (confirmed as chlorite by SEM). The calcite peak is very weak in the white sandstone, but present at 29.56 ° 2θ.

Investigation of the mineralogy of the white sandstone with X-ray diffraction results in similar overall mineral transformations to those observed in the other two case studies; although the effects are weaker, no böhmite has been found in the RYD case study. Both RYD06 and RYD02 show reductions in the peak height of plagioclase feldspars compared with NG52. Unlike the Awahab case study and Dune 14 white, the plagioclase peaks do not completely disappear. A weak kaolinite (possibly chlorite) peak appears in both examples at 7.17 Å (12.35 ° 2θ) and a very weak peak for kaolinite appears at 3.58 Å (24.83 ° 2θ), confirming the SEM observations. A weak calcite peak is also present at 3.035 Å (~29.46° 2θ) which is detecting calcite.

Samples RYD02 and RYD06 from the white sandstone show that the white sandstone is enriched compared to NG52 in magnesium, calcium and manganese.

LOI is significantly higher than NG52 (Fig. 7.30A.). The enrichment is magnesium and calcium is consistent with the other white sandstones and suggests these divalent metal ions were sourced at least partially from elsewhere. Manganese enrichment in RYD06, may be related to the mottled texture and the opaque minerals containing manganese as well as iron, it would also be consistent with brown Mn chlorite (pennantite). Aluminium, iron, sodium, potassium, titanium and phosphorous appear conserved. Trace elements (Fig. 7.30B.) are scattered around the NG52 levels. Notable enrichment exists in vanadium and uranium in RYD06, which, again is probably related to the mottled character of the sample.

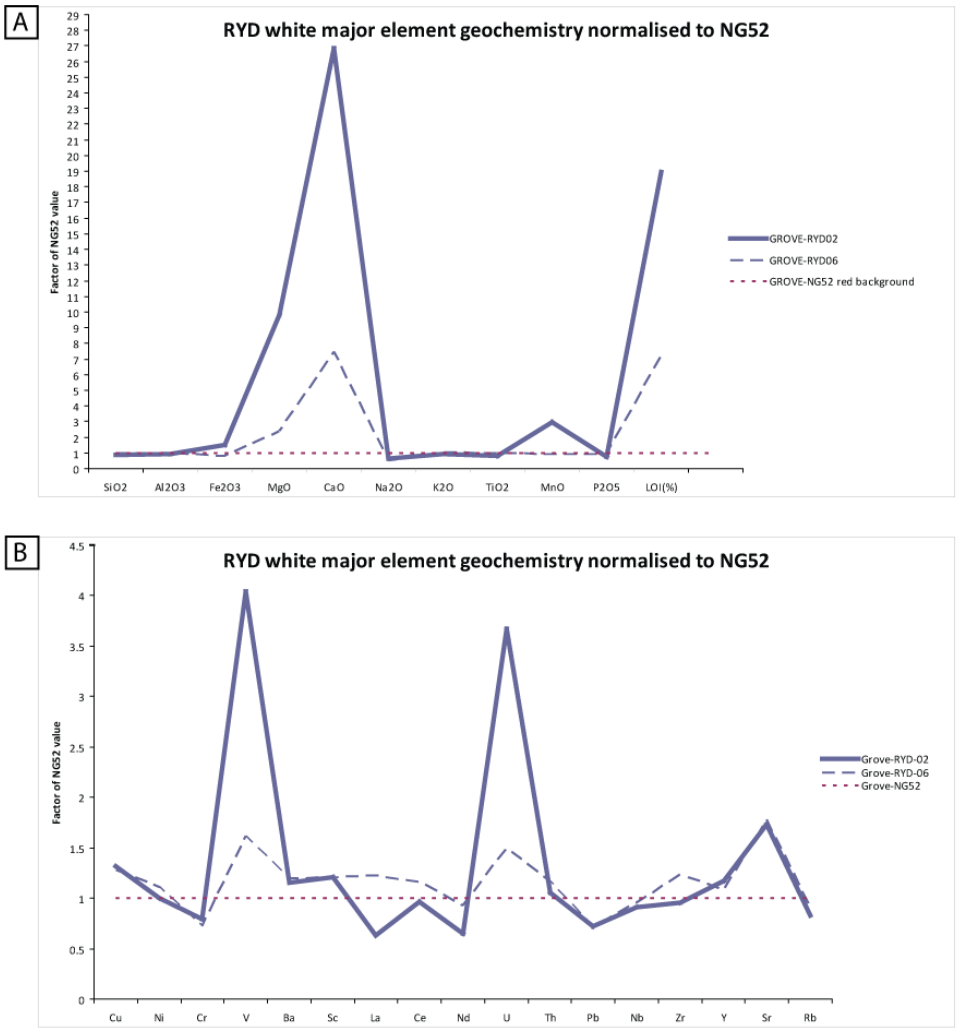

Fig. 7.30. X-ray fluorescence data plotted for RYD02 and RYD06 plotted normalised to NG52. (A) Major elements plotted for white samples show enrichment in calcium, magnesium and manganese compared to NG52. LOI is also higher. (B) Trace elements are generally clustered around NG52 values but enrichment is noticed in elements compatible with calcite. Interestingly vanadium and uranium are enriched, no explanation can be offered for this other than the presence of a minor detrital phase skewing the data.

7.4.2 Compartments to the north

1.3 km to the north of the main RYD cliff, the western white compartment is truncated by a major E-W trending dyke of ~ 5 m thickness. The dyke runs across the main RYD dyke and is at least 3 km long. No cross cutting relationship could be observed.

Sample NG87 was taken from the white compartment 40 m south of the E-W dyke and 20 m east of the RYD dyke. The sample has porosity of 9.2 % and mineralogy similar to RYD21 (19 m) confirming diagenetic style is the same as the white sand in the RYD cliff. This is clearly supported by continuous outcrop between the two localities.

Sample NG84 is from 25 m north of the E-W dyke within the red compartment. The sandstone is red, slightly friable with visible porosity in hand specimen. Detrital minerals are approximately background. Porosity is 13.4 % (±1.5), and opaque mineral abundance is 4.2 % (±0.9) which positively confirms that it is of red sandstone affinity. To the west of the main RYD, the sandstone is also still red. Samples NG86 (1 m from dyke) and NG85 (20 m from dyke) confirm this. They also confirm that the direct effects (Chapter 6) are also still in operation here.

7.5 Origin of Type 2 Diagenesis- Sand Bleaching in the Huab Area

Study of the three case studies above has shown that all three share diagenetic styles, with the higher level Awahab and Isolated Dunes examples possessing the most intense bleaching and authigenesis, followed by the larger compartment of the RYD white sand showing broadly similar but less intense bleaching.

The observed mineralogy and trends can be used to make an interpretation of the origin of this distinct bleached diagenetic style. The data collected can also be used to reveal the role that the dykes have played in the compartmentalisation of the sandstones. This compartmentalisation is particularly enigmatic as the dyke cooling

was coterminous with the diagenesis (evident in the calcite), so why are both sides of dykes frequently not displaying the same type of sandstone?

7.5.1 Stable isotopes

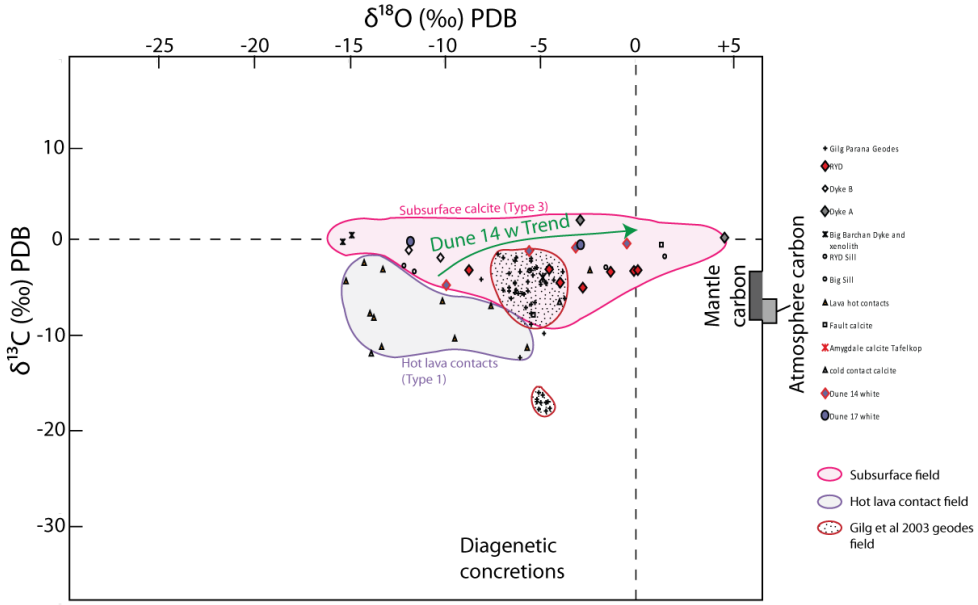

Fig. 7.31. δ ^{13}C (PDB) plotted against δ ^{18}O (PDB) all of the analysed samples with fields of Rollinson (1993) and Barker (2007) removed for clarity. Lava contact and hydrothermal diagenetic carbonates plot in two distinct populations, with sub-lava flow carbonate cements having more mantle-like δ ^{13}C values. Hydrothermal samples have less mantle influence and suggest mixing with heavier carbon. Also plotted are the carbonate stable isotope values from geodes from Parana Flood Basalts (Gilg et al., (2003), which plot as two modes, the larger of which overlaps hydrothermal calcites from this study. Both populations, within each case study show temperature dependent δ ^{18}O fractionation trends, which are related to distance from dyke or sill in the case of the subsurface field (see Fig. 6.20.). The RYD trend is presented in Chapter 6. The Dune 14 trend follows the same temperature dependent path, but is not related to distance from igneous any igneous body nearby.

Stable isotopic analysis of calcite within samples from Dune 14 white, the white sandstone from west of Dyke A and the white sandstone east of the RYD dyke are used to speculate upon the origin of the diagenetic fluids. The samples from the

RYD white sandstone have already been discussed in Chapter 6. The conclusion was that the calcite must have been precipitated during the cooling of the dyke based on $\delta^{18}O$ values and at temperatures (depending on water oxygen isotope composition) of ~ 115 °C near to the contact and 45 °C 5.8 m away.

Four samples from Dune B returned an adequate CO_2 yield for stable isotopic analysis. It is clear from Fig. 7.31. that when δ^{13} C is plotted against δ^{18} O the Type 2 (white) sandstone samples (subsurface calcite field) form a separate field from Type 3 diagenesis calcite which formed under cooling lava flows. δ^{18} O and δ^{13} C are heavier for Type 2 calcite than for Type 3 calcite. This could be due to influence of meteoric groundwater mixing with magmatic volatiles (consistent with magmatic volatiles from igneous intrusions at depth contaminating an aquifer) or due to fluid-basalt interaction (e.g. Xiong & Zhai, 1992; Stevens & McKinley, 2000). No relationship is seen between δ^{13} C and distance from dykes or below lava (Dune 14), this suggests equilibrium conditions and that the carbon source was the same for all the calcite in each case study. Heavier δ^{18} O could also be consistent with a cooler system than for Type 3 diagenesis for a given water composition A dominant meteoric sourced groundwater mixing with magmatic water is possible based on modelling fractionation of various waters into calcite (Fig. 7.33.). There is a trend developed for Dune 14 white in Fig. 7.31 between δ^{13} C and δ^{18} O, indicated by the green annotation. Such a trend could suggest that H_2CO_3 is the dominant carbon species in solution (Zheng & Hoefs, 1993). Further analysis of this trend (and a similar trend below Dune 17 white) shows that there is no correlation of the δ^{18} O value of the calcite in Dune 14 with distance below the lava. This shows that the calcite is not a result of direct diagenesis (Type 3), as the calcites below the Ponded Lava (Chapter 4.), they must be due to a later process (Fig. 7.32A.). Where calcite

occurs in Type 2 white sand near to dykes (RYD, Awahab), the δ^{18} O always shows a trend towards the dyke, which represents increasing temperature towards the igneous body (Fig. 7.32A.). As no such trends exist in white sandstone, not in proximity to a dyke (e.g. Dune 14), the white sand must have become white after burial, and during dyke intrusion into the sandstone aquifer. Dyke intrusion is stimulating the hydrothermal system.

Modelling the isotopic concentration of calcite in equilibrium with Cretaceous meteoric water (using fractionation constants A=-3.39 and B= 2.78, O'Neil et al., 1969) for Namibia (δ 18O ≈ -37 ‰ VPDB) (Bowen & Revebaugh, 2003) would precipitate calcite with the observed values at temperatures between 10 °C and below 0 °C, which is clearly not achievable considering: A) the observed hydrothermal mineral assemblage, and B) water is solid at temperatures < 0 °C. When magmatic values for water and calcite are modelled temperatures required are between 50 °C and 150 °C, however a 100 % magmatic water aquifer is not likely so the actual temperatures are probably somewhat less than 150 °C, unless the water was a product of interaction with the basalt. If the water was isotopically enriched with O^{18} by basalt-water interaction, the high temperatures (recorded in the calcite) could be achieved without significant magmatic input; a 100 % meteoric aquifer is also not likely given the geological situation. Our favoured model is therefore that of a magmatic volatile enriched aquifer circulating through both the now white sandstone and the basalt as the water precipitating the calcite.

The stable isotope data illustrate a hydrothermal system (~100 °C) where magmatic volatiles (CO_2 and H_2O) are probably mixing with the pre-existing water in the sandstone-basalt aquifer. The heat and volatiles are sourced from basic igneous intrusions into the aquifer at the time of hydrothermal activity (Chapter 6

observations). The intrusions are probably supplying the magmatic volatiles (H_2O and CO_2) during ascent and cooling. The intrusions are also supplying heat to the aquifer, which is evident in the isotopic signature in the calcites away from intrusions (e.g. RYD, Chapter 6.).

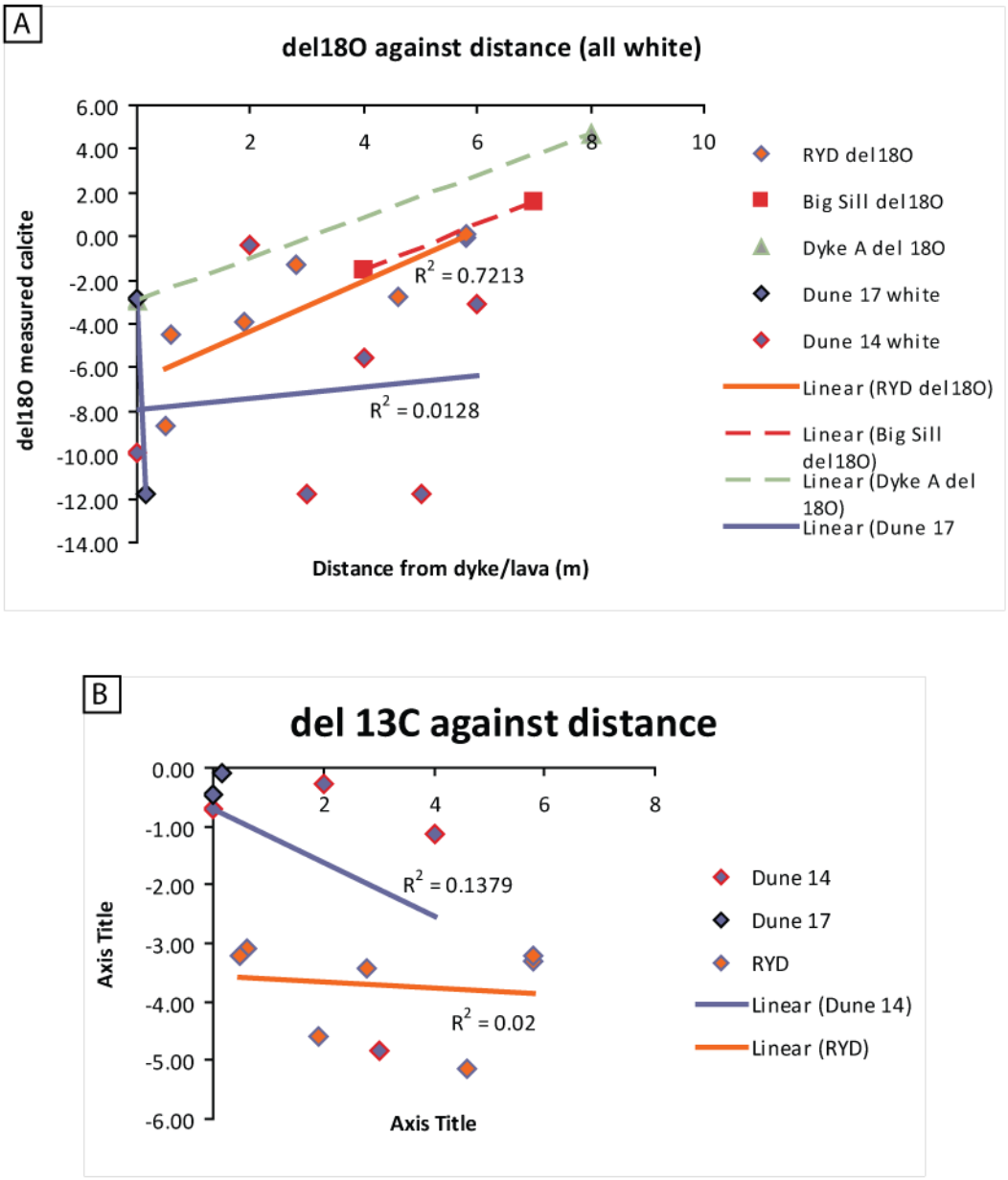

Fig. 7.32. (A) Graphs showing dependence of $\delta^{18}O$ of calcite formed in the subsurface on distance from dyke but *no* dependence on distance from lava flow. All calcite formed proximal to dykes shows correlation with distance suggesting it formed while the dyke was cooling. Calcite formed in isolated Dune 14 shows no such correlation with the lava suggesting it was formed after lava cooling (or isotopes were reset). (B) No correlations exist with $\delta^{13}C$ suggesting isotopic equilibrium.

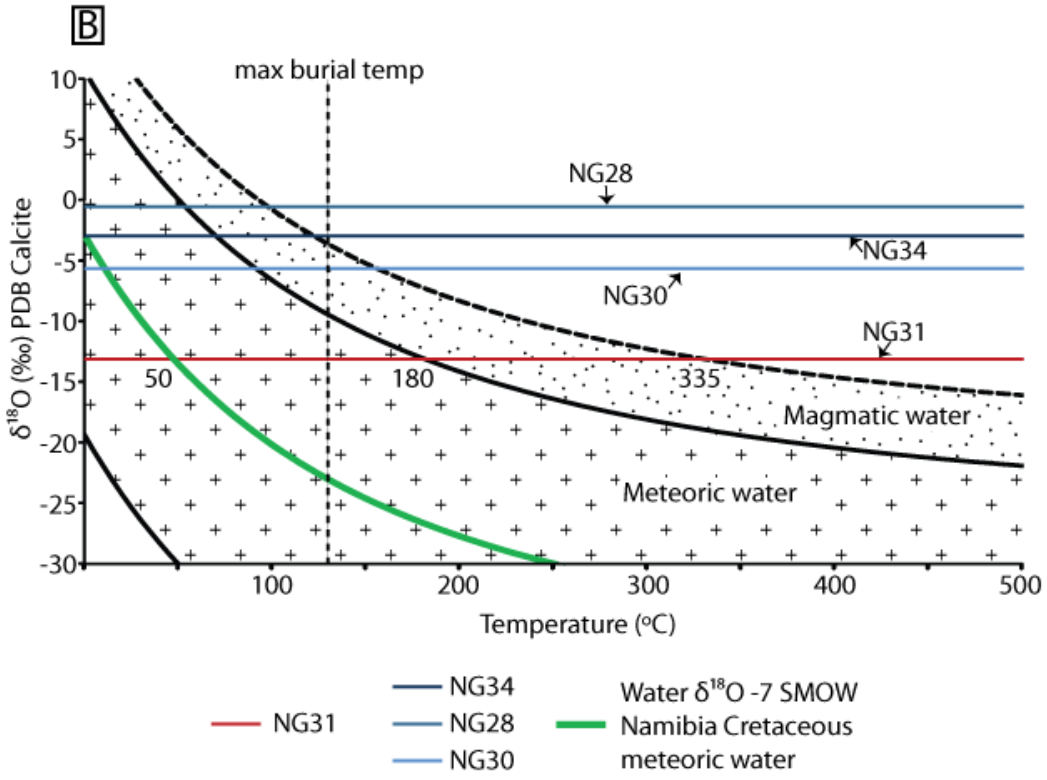

Fig. 7.33. (For RYD see Chapter 6.) (A) Modelled calcite δ ^{18}O values in equilibrium with waters of different origins. Calculated meteoric and magmatic fields are shown (using fractionation constants A=-3.39 and B= 2.78, O'Neil et al., 1969) as well as the expected meteoric water value for Namibia in the Cretaceous (green line). Max burial temp of 130 °C has been calculated based on geothermal gradients and burial data from Raab et al., (2005). Although no trend with distance exists in these samples (Fig. 7.32A.) the trend in Fig. 7.31. suggests calcite was precipitating over a range of temperatures. The model, assuming meteoric-magmatic mixing suggests precipitation temperatures in the order of 80–100 °C.

7.5.2 Petrology and geochemistry

The petrographical, mineralogical and geochemical differences between isolated red dunes (Type 1 diagenesis) and isolated white dunes (Type 2 diagenesis) and between Major Erg compartments separated by dykes have been established. Table 7.1 shows the statistical significance of the petrographic observations. Clay and calcite are always statistically different between the red and white sandstone,

strongly supporting the hydrothermal origin and compartmentalising hypothesis. Porosity, permeability and authigenic quartz were found to be statistically significantly different in 2/3 cases reflecting the possible further or earlier development of these after hydrothermal activity or before hydrothermal activity. Opaque minerals and COPL were only significantly different 1/3 cases, reflecting the continued compaction and generally local redistribution of iron oxides.

All of the case studies show that the white sand is distinct from the red sand that is separated by vertical or sub-vertical dykes. Petrographic distinctions are:

•Red sandstone always has a higher abundance of quartz overgrowths for a given distance from the dyke or lava flow.

Quartz overgrowth formation clearly took place before dyke intrusion (Chapter 6) and continued after in the red sandstone case, but where the sand experienced Type 2 diagenesis the kaolinite prevented subsequent quartz overgrowth formation.

•White sandstone always has more clay (kaolinite) for a given distance compared to red sandstone, and does not appear related to distance from the nearest igneous body.

•The red sandstone always has increased abundance of opaque minerals and the white sandstone has had haematite grain coatings removed, which are often re-precipitated as opaque pore-filling nodules.

•The white sandstone always has increased abundance of calcite compared to the red sandstone.

•Böhmite is present in the white isolated dunes and in the Awahab white sand.

•The white sandstone authigenic assemblage appears to have formed at the expense of detrital plagioclase (XRD, SEM and polarising microscope).

•There is evidence of geochemical enrichment in calcium and magnesium in all case studies and evidence for depletion in sodium in all case studies.

•Iron usually shows depletion in the white sand, although this is not major as a proportion.

Iron, despite controlling the colour is a minor component by weight % in the red sandstone (0.91 wt %) and reduces to 0.14 wt % in NG42 and 0.75 wt % in RYD06. So to achieve bleaching, only 0.77 wt % needs to be lost or redistributed into nodules (RYD06).

The petrographic observations suggest that a fluid has either been present in the white sandstone and absent in the red sandstone that has had the capability of producing the observed reactions, noticeably bleaching.

Chemical bleaching of sandstones is not rare; it has been documented elsewhere as a result of hydrocarbon migration through sandstone (Moulton, 1926; Surdam et al., 1993; Kirkland et al., 1995; Schöner & Gaupp, 2005; Ma et al., 2007). Bleached zones have been used to indicate migration pathways of hydrocarbons and

to infer the existence of emptied reservoirs (Kirkland et al., 1995; Beitler et al., 2003).

Where hydrocarbons have migrated through red coloured sandstones, the bleaching has been attributed to acidic, reducing conditions (e.g. Ma et al., 2007; Surdam et al., 1993). These conditions can be achieved by biologically mediated oxidation of CH_4 to produce CO_2 and simultaneous reduction of SO_4^{2-} to H_2S (Kirkland et al., 1995). In such a reaction the CO_2 and H_2S are achieved in conditions where dissolved H_2S (present as HS-) reacts with ferric iron oxide (haematite) to form soluble ferrous iron. The HCO_3^- reacts with Ca^{2+} and Mg^{2+} to form carbonate (Surdam et al., 1993; Kirkland et al., 1995). Dissolved ferrous iron and H_2S would not necessarily react immediately to precipitate as iron minerals (e.g. pyrite) and can migrate in pore waters (Kirkland et al., 1995). These conditions could also be achieved without contemporary biological mediation, as many hydrocarbons are associated with H_2S and CO_2. Petrographic study of bleached sandstones has documented alteration of feldspars to clay (kaolinite) in these settings (Ma et al., 2007).

The migration of hydrocarbons is an unlikely mechanism for the bleaching of the sandstones in the study area because (A) there is no significant source rock in the thin underlying Karoo sequence this far south in the Huab Basin, and (B) hydrocarbon residues have not been observed in the field or during subsequent petrographic studies (with UV light). However, the same chemical species required (H_2S and CO_2) can be generated by magmatic degassing (e.g. Henley & Ellis, 1983; Rye, 2005; Delmelle & Stix, 2000) and are common in hydrothermal systems (e.g. White, 1957; Henley & Ellis, 1983). We infer that the fluids that passed through the isolated dunes of the Twyfelfontein Formation were hydrothermal in origin and were

enriched in magmatic gases originating from degassing mafic intrusions at depth. The association of white sandstone with cooling dykes has been shown in Chapter 6 and this chapter.

Our observations test this hypothesis. Firstly, both red and white isolated dunes were deposited at similar or the same stratigraphic levels, and have identical detrital compositions; this is illustrated by the fact that the Type 3 diagenesis affects both the red and white dunes. The eogenic Type 3 diagenesis effectively 'locked in' the reduced porosity contact zone at an early stage, isolating the detrital red sediments from later large fluid fluxes. The oxidation/coating of the sand grains with haematite prior to deposition is supported by our observations of present-day migrating red dunes in the Namib desert and by numerous other examples cited (e.g. Folk 1976 and references therein). This is can also be applied to dyke contacts, where both the red and white sides appear affected equally. Evidence for the Major Erg being deposited as a red sandstone also comes from the RYD area, where the RYD lava pond (Chapter 4.) has 'locked in' the red sand above the white, this can be seen in Fig. 7.23B. around the base of lava flows over the white sandstone.

Secondly, considering that both the red and white isolated dunes were deposited as red haematite coated aeolian sands, the white isolated dunes must result from chemical bleaching. It is proposed that this bleaching may have resulted from reaction of grain-coating haematite with H_2S in hydrothermal groundwater, which has circulated through white dunes only. Haematite is reduced to form soluble ferrous iron that is transported away in solution (Fe_2O_3 depletion, Fig. 7.13. and Fig. 7.22A.):

$$4\ Fe_2O_3 + H_2S + 14\ H^+ \leftrightarrow 8\ Fe^{2+} + SO_4^{2-} + 8\ H_2O \qquad (1)$$

This reaction should produce pyrite as noted by Kirkland et al (1995), which has not been identified in the isolated white dunes. Pyrite is however present in the basalt and occasional haematite nodules are present in the white sandstone. These haematite nodules may be the oxidation product of diagenetic pyrite. If no pyrite was present in the white sandstone it could suggest either: (A) The Fe2+ and SO42- were able to migrate into the basalt prior to precipitating or (B) that any H2S within the aquifer rapidly reacted with the iron rich basalt prior to reducing iron in the red dunes. If the latter is true, the above reaction was doubtfully in operation in the white dunes. An alternative explanation that requires less acid and no sulphur is that of a hydrothermal system with abundant dissolved hydrogen. Hydrogen could be sourced from hot hydrothermal water interacting with basalt (Stevens & McKinley, 2000) or from magma degassing at depth (Arnórsson, 1986). Hydrogen and carbon dioxide could then bleach the sandstone:

$$Fe_2O_3 + H_2 \overset{+2}{} CO_2 \leftrightarrow 2\ FeCO_3 + H_2O \qquad (2)$$

The ferrous iron carbonate would have then been transported away in solution (e.g. King, 1998). Based on the lack of pyrite (or other diagenetic sulphides) in the white sandstone, the latter reaction (2) is probably most likely.

Thirdly, the feldspar dissolution and mineral authigenesis observed in the sandstones in the study area is inferred to result from CO_2 rich hydrothermal fluids. White dunes are almost completely devoid of plagioclase feldspar (XRD analysis) and show reduced modal abundances (petrographical analysis, probably overestimated due to kaolinite replacement pseudomorphs) and show reduced

strength orthoclase XRD peaks compared to red sandstone. Authigenic kaolinite, böhmite and calcite, found in the white sandstone (Type 2), are not found in the red sandstone (Type 1) and are suggested to have formed at the expense of the feldspars during reaction with CO_2. Hangx & Spiers (2009) proposed and tested reactions between plagioclase feldspars and CO_2-H_2O under laboratory conditions simulating hydrothermal conditions. Both albite and anorthite were reacted under a variety of pressure and temperature conditions (200– 300 °C and 6– 18 MPa) with the aim to test the ideal reactions:

$$\text{Anorthite} + CO_2 + 2\,H_2O \leftrightarrow \text{Calcite} + \text{Kaolinite} \qquad (2)$$

And

$$\text{Albite} + CO_2 + H_2O \leftrightarrow \text{Dawsonite} + 3\,\text{Silica} \qquad (3)$$

Hangx & Spiers' (2009) results failed to fully replicate the above reactions and instead produced clays (kaolinite and smectite or illite), böhmite and a nickel, iron-hydrotalcite phase derived from their reaction vessel. Dawsonite and calcite were not produced in Hanx & Spiers' (2009) experiments, possibly due to sub-critical solution state for crystal nucleation and conditions not being alkaline enough for dawsonite precipitation. Given sufficient time for further dissolution of plagioclase, carbonate phases would be anticipated (Hangx & Spiers, 2009). It is proposed that in the white sandstone, the Type 2 diagenesis is a natural analogue for the reactions actually observed by Hangx & Spiers (2009) based on the identical mineral reaction being observed. Calcite in the natural Type 2 white dunes is inferred

to be the result of trace amounts of carbonate dust (common in aeolian environments – pers comm Maurice Tucker). This dust provides the nuclei for calcite precipitation absent in Hanx & Spiers' (2009) experiments. Longer duration of plagioclase-CO_2 reaction in our natural geological system produced enough Ca^{2+} ions, combined with calcium from basic volcanic rocks in the pile interacting with the fluid. This supports the proposed origin of the diagenetic fluids and supports timing coincident with emplacement and cooling of the igneous intrusions in the area. Reaction of feldspar to form böhmite and kaolinite was also performed by Fu et al., (2009) on perthitic alkali-feldspars under acidic hydrothermal conditions, who noted the albite (Na-feldspar) component reacted preferentially, which conforms to the observation in Fig 7.30 and supports the Na depletion observed (Fig. 15). Sodium, once released from plagioclase would have gone into solution, but no authigenic minerals found contain significant sodium. The sodium must have therefore been transported away in the hydrothermal water.

The system depicted is a flux of heated groundwater (by intrusions) enriched in magmatic volatiles (e.g. CO_2, H_2S) moving through the sandstone. This water has the pre-requisite chemistry to produce all of the mineral reactions identified.

7.5.3 Controls on Fluid Flow

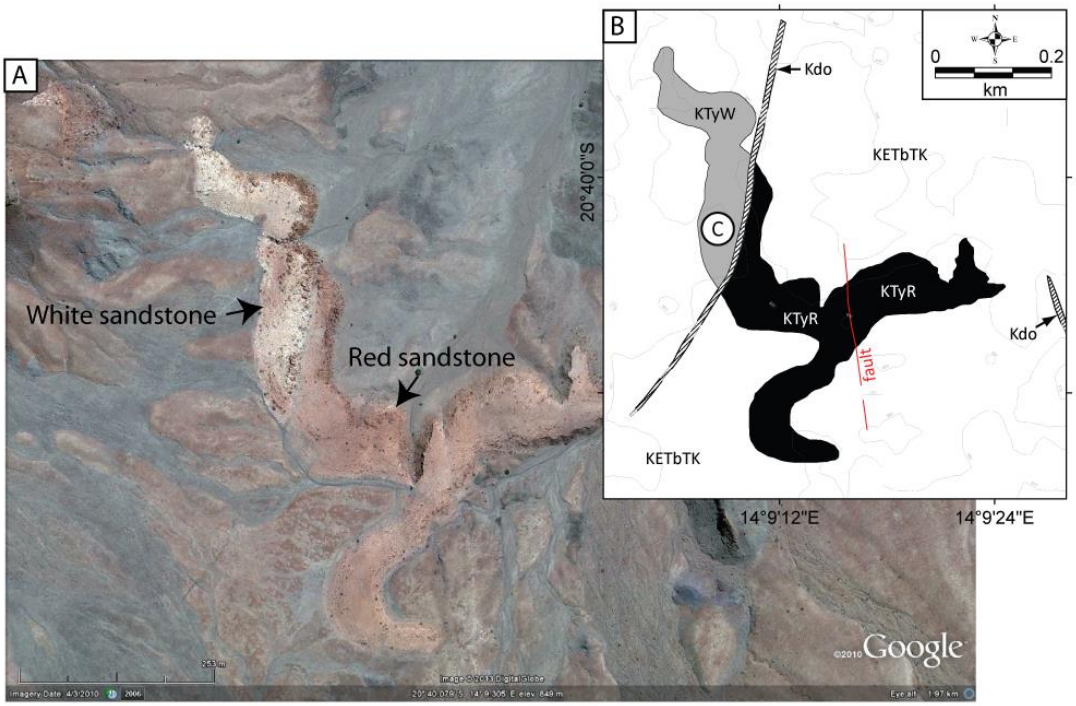

Fig. 7.34. (A) GoogleEarth photo of the Big Barchan, in which the white sandstone to the north is clearly separated from the red sandstone to the south by a dyke. (B) Geological map of the image in A.

In the Major Erg, lateral and horizontal permeability would have been high (certainly with the 756 m of burial and 8.1 % COPL predicted at the time of dyke emplacement in Chapter 6.). Where sandstone is bleached white, it tends to be in compartments separated from the red sandstone by dykes. It, very clear from the RYD dyke white compartment and the Awahab Dyke A compartmentalisation that the dykes are responsible for separating red from white sandstone. This observation is problematic as it is likely that the bleaching occurred during dyke cooling. Why then is only one side affected? In fact some dykes show that both sides are affected (e.g. Dyke A) for a limited distance. If the bleaching came after dyke cooling (unlikely with the isotope evidence) the fluids must have come from below; then why do the dykes form compartments?

In the isolated dunes, if Type 2 diagenesis is a result of fluid flux and Type 1 diagenesis is a result of absence of this flux, it is logical to conclude that the enveloping lithology (lava) is responsible for compartmentalising either individual dunes or volumes of rock encompassing dunes. If we consider that the lava is completely impermeable (which is unrealistic), it would also be logical to infer that fracture connectivity (i.e. faults and joints) controls fluid flow and some dunes are simply part of this fracture network and others have not been intersected. However, lava piles are not impermeable (e.g. Saar & Manga, 1999), indeed, they can be major conductors of subsurface fluids such as in the Columbia River Basalts, where the major aquifers are basalt (Newcomb, 1961; see also Saar & Manga, 1999). Permeability in pāhoehoe lava flows is generally highest within the highly vesicular upper and lower crusts, the massive central lava cores are typically impermeable (Newcomb, 1961; Smith, 2004) and through cooling fractures (Petford, 2003).

The lowermost Tafelkop type lava flows exhibit a compound-braided facies nature and do not form thick tabular sheets (Jerram, 2002). Such lava flows have markedly higher crust to core ratios (e.g. Nelson et al., 2009) and, contain abundant vesicles and fractures. The compound nature of these Tafelkop type lavas in Dune Valley, combined with the visible occurrence of vesicle rich zones suggests that the lava was, at least, partially permeable in the horizontal direction. The stacking of many compound pāhoehoe lava flows with relatively permeable crusts and relatively impermeable cores would have resulted in a complex permeability distribution. However, we consider that this alone could not completely isolate sand bodies from groundwater flux. This hypothesis is supported by field relationships in the 'Big Barchan' Dune C (Fig. 7.34) where the isolated dune is cross–cut by a ~4 m thick dolerite dyke (Described in Chapter 6.). An impermeable contact zone is developed

where the dyke intersects the sandstone. The dyke separates red Type 1 sand from white Type 2 sand. The dyke follows the same ~N-S trend as most dykes in the Huab Outliers. Some dykes pass into the lower Tafelkop lava (e.g. Jerram et al., 1999a) while others fed lavas that were younger than the youngest exposed lavas in the region. Although it is possible that dyke pathways are weaknesses that can be re-used by later phases of dyke intrusion, the information from the dykes and outcrops in the Huab Outliers suggests that the timing and depth of compartment formation (igneous intrusion) could be from as little as 300 m of burial up to the complete volcanic pile thickness. The calculations in Chapter 6 suggest the Awahab dykes may have intruded as shallow as 756 m.

Fractures are not well preserved in the Tafelkop basalt lavas due to the intense desert weathering, but fractures would have formed during cooling and possibly subsequent tectonic activity. N-S trending low displacement faults (cm s) frequently cross cut sandstone horizons in Dune Valley (Fig. 7.34), but have not been found separating Type 1 sand from Type 2 sand. Faults are frequently mineralised with calcite, and, depending on timing, may have been pathways for the flow of diagenetic fluids. It is therefore proposed that within the Tafelkop lavas, vertical to sub-vertical igneous intrusions are largely responsible for isolating red dunes from diagenetic fluids, with some control exerted by heterogeneous lava lithology and fractures. This is therefore the same control as in the lower Major Erg that is not interbedded with lava.

The conclusion is therefore that in all cases the compartmentalisation leading to differential diagenesis (red and white) is by basic igneous dykes cutting the sandstone unit (Major Erg or isolated dune). The origin of the bleaching and diagenesis is hydrothermal and related to Cretaceous igneous activity. The timing is

therefore before the sediments reached their maximum burial and further diagenesis occurred after igneous activity ceased (e.g. quartz overgrowths in the red sand and compaction in both). Unresolved at this stage is why the dykes should act as compartments and why the diagenetic fluid could not rise and circulate on both sides of the dyke.

There are three possible explanations:

1. The compartment forming dyke intrudes, followed by more dykes on one side only; the hydrothermal system is then only active on one side of the dyke

   This is unlikely because dykes are noticed throughout the field area; some are not associated with bleaching.

2. The aquifer prior to dyke intrusion was flowing due to a hydraulic head (as most unconfined aquifers e.g. Hiscock, 2005). The intrusion of the dyke dammed this. One side was upstream and the other downstream: this leaves two options that could result in our observations:

   a) The downstream side emptied such that little or no water remained for hydrothermal cooling of the dyke and hydrothermal activity. This would be the red side.
   b) The upstream side had a trapped body of water, isolated from the regional groundwater flow which concentrated magmatic volatiles and dissolution products in hydrothermal water (white side); while the downstream side

remained connected to the regional aquifer which easily cooled and diluted any magmatic products (red side).

3. None of the above

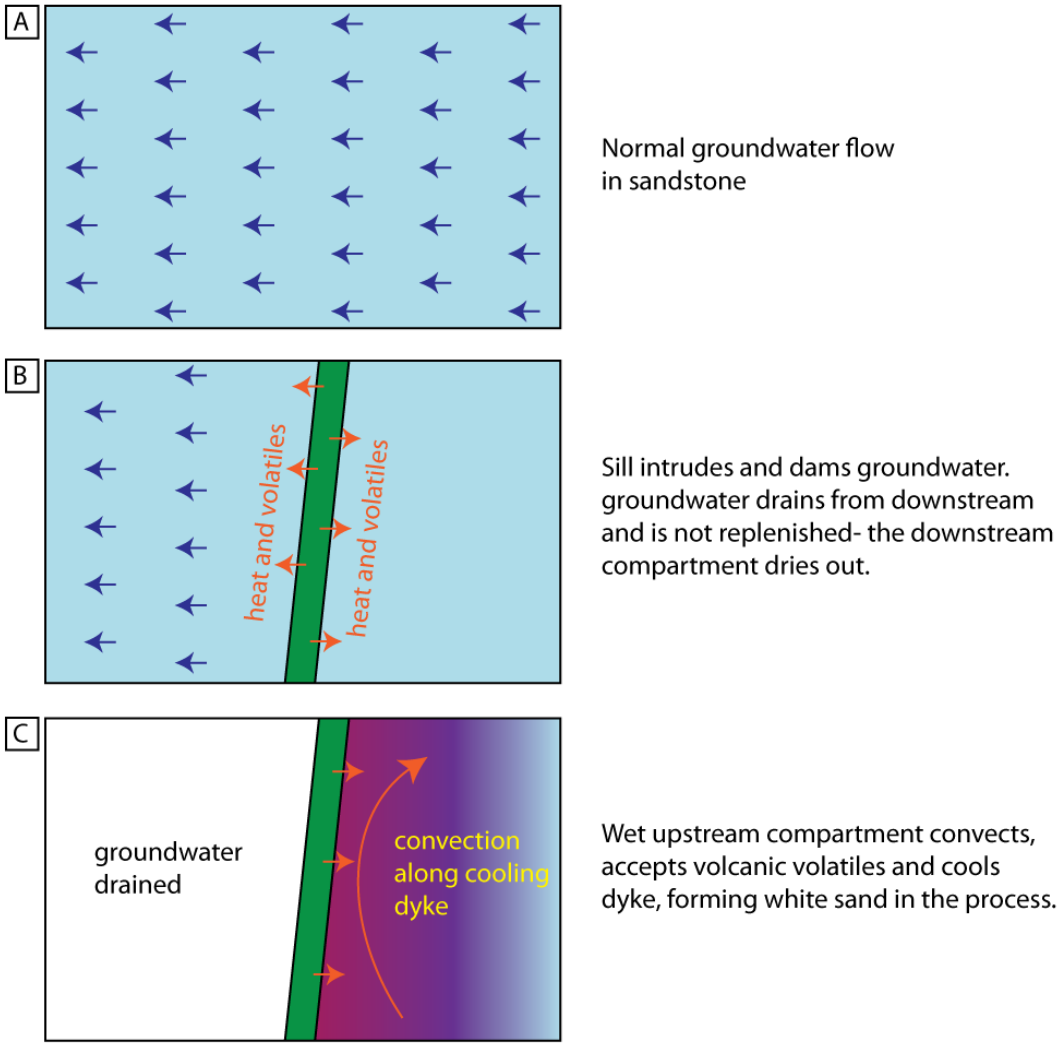

Fig. 7.35. Illustration of option a. (A) Groundwater flow normal before dyke intrusion. (B) Sill intrusion dams groundwater. (C) Resulting cooling and diagenesis regime.

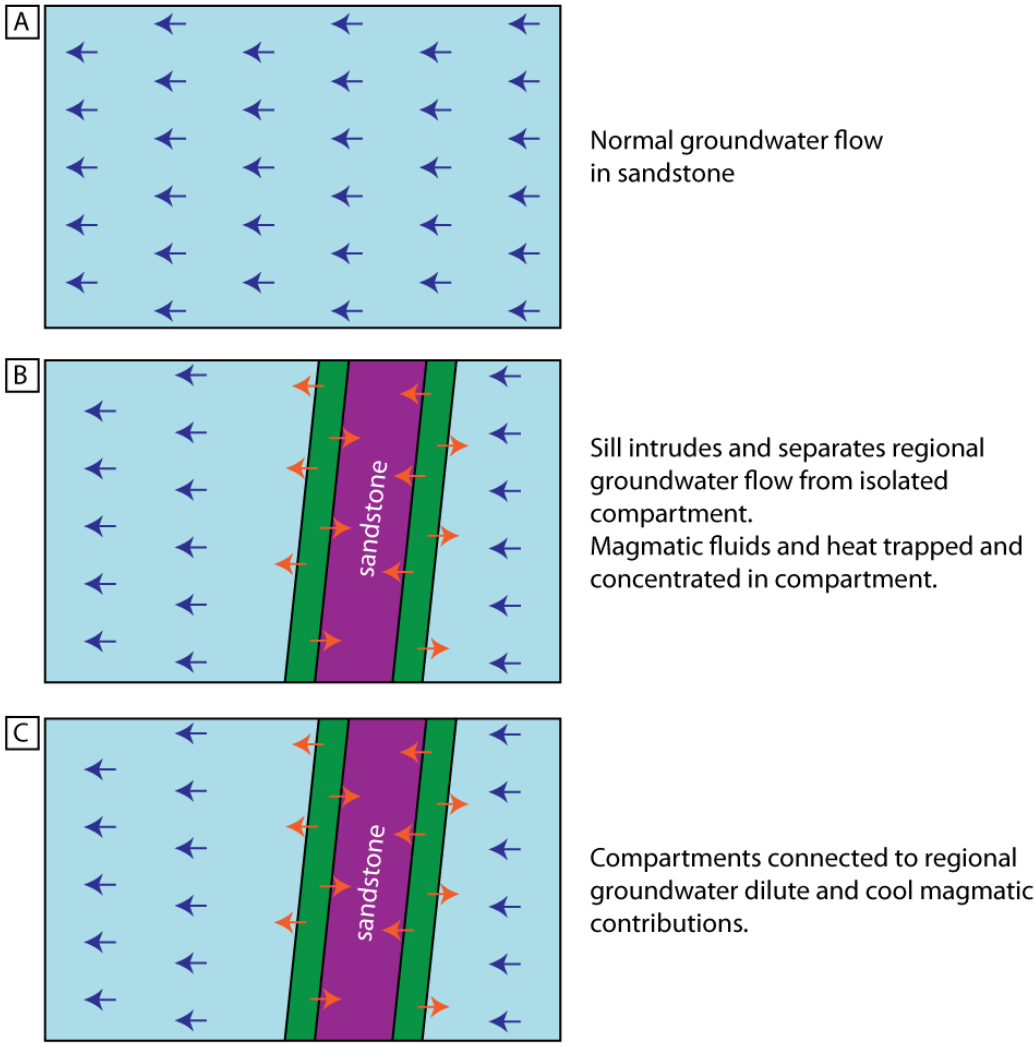

Fig. 7.36. Illustration of option b. Two dykes are intruded (green) (A) Groundwater flow normal before dyke intrusion. (B) Dyke intrusion traps groundwater in compartment, which concentrates heat and magmatic volatiles. (C) Compartments connected to regional groundwater flow are kept cool and do not concentrate magmatic volatiles.

7.6 Other diagenetic observations

In the course of the fieldwork, other localities were visited that showed interesting diagenetic effects that have not been fully investigated, but warrant mention, if just to stimulate further examination. Firstly, a group of outcrops exists south of Mikberg at 20° 38.853'S 14° 09.862'E at 834 m in a white isolated dune

where unusual quartz cementation is found (7.5.1). Secondly 295 m northeast of the quartz cementation, via a plateau showing the same cementation is another white isolated dune that rests on basalt, bleached white (probably talc). The white basalt has a high abundance of an unidentified green mineral (7.5.2).

Both of these case studies are interesting features that deserve reporting, even though no meaningful analysis has been conducted.

7.6.1 Intense quartz cementation

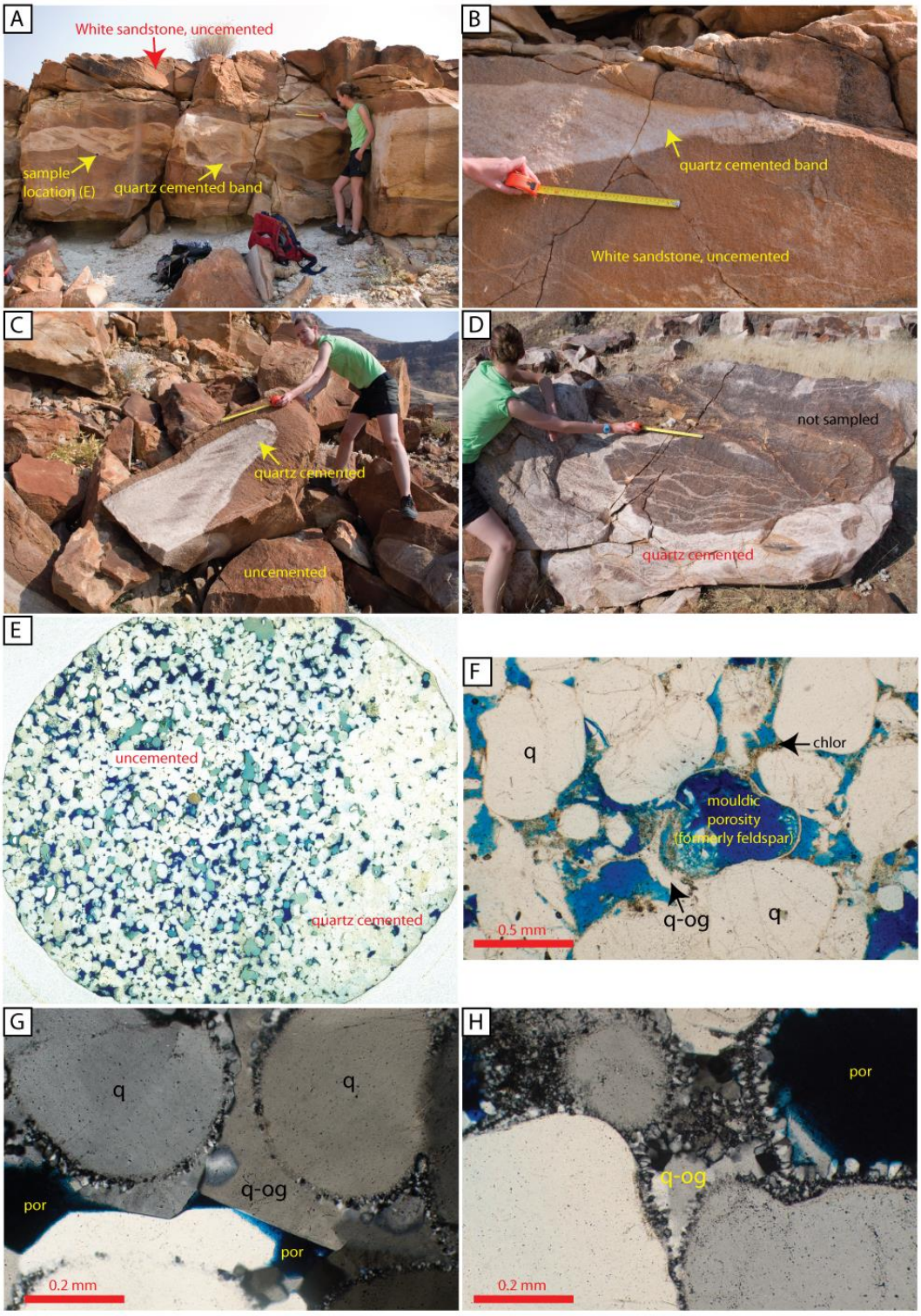

Fig. 7.37. Photographs of the 'fluid flow' locality. (A) The quartz cemented band does not follow any sedimentary feature and is ~ 1 m above the top basalt which has transformed to a white friable mineral (probably talc). (B) The eastern tip of the band, note sharp contact between cemented and un-cemented sandstone. (C) A detached block of the same. (D) Boulder below outcrop showing chaotic veining associated with this part of the cementation. (E PPL) Photomicrograph of sample in A. Un-cemented sand to left and quartz cemented to right, note sharp boundary. (F PPL) Un-cemented sandstone showing mouldic porosity at the expense of feldspar. Quartz overgrowths came before feldspar dissolution. Chlorite coats grains. (G XPL) Quartz cementation in the cemented band consists of syntaxial overgrowths and microcrystalline overgrowths. (H XPL) Overgrowths vary in size and came after (or during) feldspar dissolution.

The main outcrop of interest (Fig. 7.37A.) is a 3 m thick white isolated dune resting on intensely altered basalt. 3.5 m below the sandstone, the basalt is grey, fissile and resembles the normal Tafelkop compound type basalt flows of the area. This grades upwards into the white, altered basalt, by 2 m below the sandstone the originally grey basalt is brilliant white, soft and powdery. Sand-filled cracks penetrate into the whitened basalt up to 30 cm deep. Resting on the basalt is a high porosity white sandstone (appears red compared to the quartz fluid flow due to surface weathering in Fig 7.37A.). One metre above the basalt contact is the base of the white, quartz cemented band. The band has been identified as a 'fluid flow' in the past (Jerram, *personal communication*), although this term may not in fact be correct. The band is characterised at outcrop be increased strength (sampling is difficult), and the complete removal of detrital grains other than quartz giving the brilliant white colour. Little visible porosity is present. The band does not follow any observed sedimentary structure (Fig. 7.37A, B, C.), it cuts cross-beds in the outcrop. The upper and lower surfaces of the band are frequently wavy. To the east of the outcrop the band terminates abruptly (Fig. 7.37B.), another abrupt termination is apparent in a detached block 5 m to the south of the outcrop (Fig. 7.37C.). The contact between the quartz cemented sand and the un-cemented sand is abrupt, transitioning over ~ 500 μm. Detached blocks in the environs of the outcrop are also frequently quartz

cemented and resemble the example in Fig. 7.37D, where the quartz cementation is equally as abrupt as in the outcrop, but veins of the same material are present.

In thin-section the un-cemented white sand is a diagenetic quartz arenite. Both primary and secondary porosity is present. All detrital feldspars have completely dissolved and have left a mouldic porosity, often with relic diagenetic rims of quartz or chlorite around the now removed feldspar grains (Fig. 7.37F.) Compaction appears to be the major porosity reduction mechanism. No haematite grain coatings are present.

Within the quartz cemented band, the detrital mineralogy is entirely quartz, like outside of the band. Mouldic porosity exists where feldspars have been removed, but this mouldic porosity is frequently occluded by authigenic quartz overgrowths from the edges of the oversized pore. Primary and secondary pores are filled with both microcrystalline quartz crystals growing inwards of ~ 10-30 μm (Fig. 7.37G, H.) or with macro crystalline quartz overgrowths that appear to only affect primary pores (Fig. 7.37G.). The larger quartz overgrowths frequently grow over the microcrystalline quartz overgrowths (Fig. 7.37G.).

The likely order of events was: Deposition> burial> some fluid removes haematite and feldspars (probably common to white isolated dunes)> selective quartz cementation occurs to form the band.

The quartz cementation does not petrographically resemble the quartzite in Chapter 6 that formed as a result of partial melt. No partial melt is evident at this locality and the quartz cementation is entirely due to precipitation from a fluid (presumes aqueous).

The problematic part of offering an interpretation of the observations is the isolated nature of the quartz band and how it is not related to any sedimentary

structure. If it was the result of fluid migration through the sandstone, it would follow natural permeability pathways, possibly ponding on top of the basalt, like the calcite at the base of the upper of the three isolated dunes (Chapter 4.2.1.2.) or the zeolite at the base of the Rock Creek Road sediment interlayer (Chapter 5.3.3.). It simply does not appear to be controlled by gravity! Fluids were clearly migrating through the sandstone and basalt to achieve (a) the bleaching and (b) the feldspar dissolution and (c) the basalt alteration, prior to or during the quartz cementation. It is suggested that the normal white sand forming diagenetic fluid first came through which caused the bleaching, followed by another fluid that removed the alteration products of the feldspars (clay, calcite and böhmite) to leave the mouldic porosity. The quartz band could have formed at a fluid miscibility boundary between a fluid rich in dissolved silica and another fluid of a different composition, or density. This is the only mechanism that I can envisage for a band with such abrupt boundaries occurring with no relationship with the permeability structure of the host rock.

Further understanding of this outcrop would require fluid inclusion thermometry and stable isotope geochemistry of the sandstone (overgrowth separates, and detrital grains) to establish conditions during quartz authigenesis. The diagenesis of the basalt to form the white substance recorded is also of interest; the association of the quartz cementation and the white basalt is unique in the field area.

7.6.2 Green mineralisation

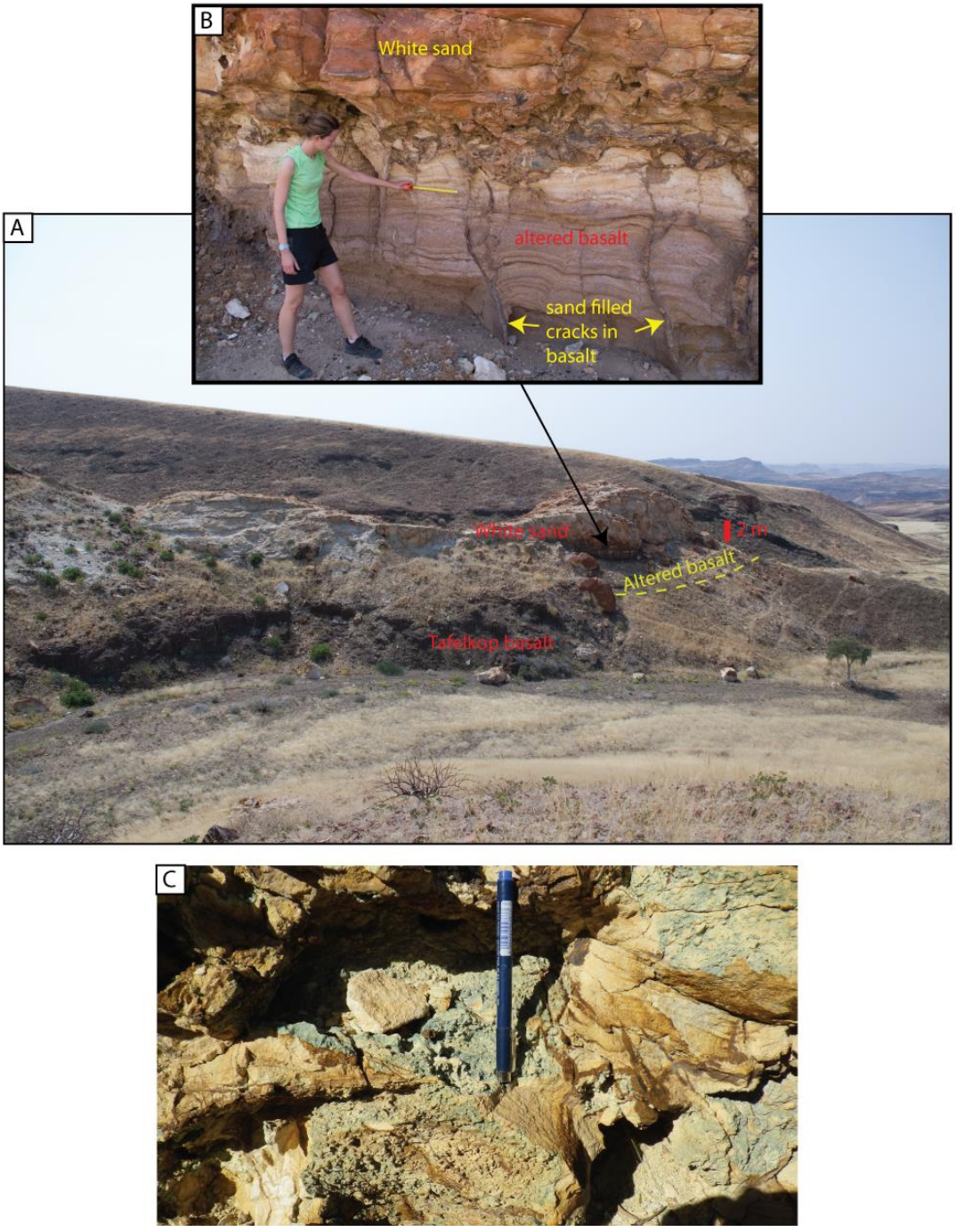

Fig. 7.38. Photographs of the locality with the green mineralisation. (A) Facing east towards outcrops from the 'fluid flow' locality. Note a white isolated dune sitting on highly altered basalt. (B) Close up of base of dune contact showing basalt which is brown, friable and altered to clays (identified as formerly basalt by sand filled cracks). (C) Close-up of the unidentified green mineral that is present in the altered basalt and within the basal part of the white dune.

The green mineralisation 295 m northeast of the quartz cemented band is at the same stratigraphic level and also occurs in a white isolated dune. The outcrop consists of ~ 2 m of highly altered basalt. The altered basalt is white within 50 cm of the sand contact above, and becomes brown further below, by 5 m the basalt is normal grey Tafelkop basalt. At outcrop the white and brown basalt is not recognisably igneous; identification as basalt (or formerly basalt) is based on sand filled cracks (common to basalt cold contacts) penetrating into the igneous material. Within the altered basalt are preserved many concentric bands of a rust brown mineral (probably an iron oxide) (Fig. 7.38A.). Both the sand and the altered basalt at the contact are mineralised with a green-blue mineral, which is always associated with fine grained light brown material. The fine grained material is probably diagenetic clay. This green mineral remains unidentified, SEM and EDS analysis were not conclusive but confirmed it contains iron and does not contain sulphur. The mineral is finely disseminated among various potassium-aluminium-calcium silicates, probably clays.

A similar green mineralisation exists at the base of Dune 18 white (20° 39.340’ S 14° 08.793’ E), which also has sand-filled cracks extending into the underlying basalt. The basalt here is the normal grey typical of the Tafelkop basalts in the area.

7.6.3 Pore-filling cements resting on cold basalt contacts

In the Huab basin Pore-filling calcite cements resting on cold sand-basalt contacts have been found in three localities:

1. Base of the upper of the three isolated dunes (see above and Chapter 4.2.1.2.)

Here the calcite fills primary porosity and has a sharp upper contact with the un-cemented red sandstone. The calcite cemented sandstone remains friable, whereas the calcite cemented sandstone at hot contacts is always hardened. The calcite cementation appears to fill the lava topography below and is suggested to be a small perched aquifer containing a fluid rich in the calcium and carbonate required to precipitate calcite.

2. Base of the big barchan, sampled as sample NG63.

This calcite is similar in petrographic character to at the base of the upper dune. Stable isotopic analysis places it within the field of Type 2 (subsurface formed) calcites, plotting separately to calcites formed at hot lava-sand contacts. The suggestion is that it is also a perched aquifer resting on the basalt formed during burial.

3. The base of the ‘cold contact’ locality.

Twyfelfontein sandstone fills a network of cracks in underlying lava, the sandstone is partially cemented with calcite. It is suggested this is a later calcite cement, the same as the examples above.

At the Rock Creek Road locality, Washington, USA as similar cementation phenomena is observed. At outcrop, a cemented basal contact of the fluvial sandstone and the underlying lava can be observed. The cemented sandstone has a sharp upper contact with the un-cemented sandstone, which is level, not following sedimentary structure. The cemented sandstone fills lava topography, such that some of the lava topography extends above the limit of the cementation into the un-cemented sandstone. Petrographic analysis (Chapter 5.) shows that this is a zeolite cement. It is suggested therefore that this cement is formed by a perched aquifer within the sandstone, resting on the basalt surface. The aquifer must have been sufficiently saturated and hot enough to precipitate zeolite.

7.7 IMPLICATIONS AND CONCLUSIONS

7.7.1 Major Erg and Isolated Dunes

- The Major Erg is highly compartmentalised by igneous dykes. These dykes separate sand that has had *indirect effects* relating to igneous geology that are hydrothermal in origin.
- The indirect diagenesis significantly reduces the reservoir quality of the sediment (porosity and permeability) by introducing pore-filling and pore throat filling authigenic minerals derived from the reaction of detrital

minerals with the hydrothermal waters. These directly affected volumes can be large, in the case of the RYD white compartment which is at least 5 km x 3 km x 0.1 m.

In the case of the isolated dunes, these poorer reservoir rocks a connected to the fluid migration pathways, whereas the better reservoir quality red sandstones are not. This dichotomy should be appreciated if similar rocks are encountered during exploration.

The porosity and permeability characteristics of the Twyfelfontein Formation are controlled by diagenetic processes which are both caused by igneous intrusions and spatially controlled by igneous intrusions.

- The identification of the indirectly affected sandstone allows tracing and proof of compartmentalisation of the Major Erg sandstone unit by dykes.

- Hydrothermal fluid flow traced through inter-basalt sediments (isolated dunes) has also been found to be heterogeneous and controlled by igneous dykes. Some isolated sediment bodies being connected to the flow regime, and some apparently isolated. The implication is that any fluid could be controlled in this manner, including petroleum.

- The Dune Valley and Awahab Dyke white sandstone outcrops have been identified as natural analogues to the proposed carbon sequestration method of Hangx and Spiers (2009); in our case magmatic CO_2 is being sequestered.

- Apart from the tracing of heterogeneous hydrothermal fluid flow through the basalt pile, the results of Type 2 diagenesis left reduced porosity and permeability compartments (the white sandstone) which, do not relate to depositional environment or geological structure.

Volume estimates of sediment/lava interbed and sub-basalt reservoirs should take into account that not all sediment bodies predicted in similar situations will be charged with hydrocarbons, despite sharing stratigraphical location, depositional environment and geological structure.

The existence of highly cemented sandstone, not apparently related to any geological structure, igneous processes (lava flow emplacement, intrusion emplacement, or intrusion distribution) has implications for E&P as it is not predictable. Encountering a cemented zone such as this during drilling would give a false impression of the gross porosity as this study shows that they are rare and volumetrically minor. Nevertheless cemented bands would provide significant baffles within the reservoir, which the understanding of would be advantageous during development and production.

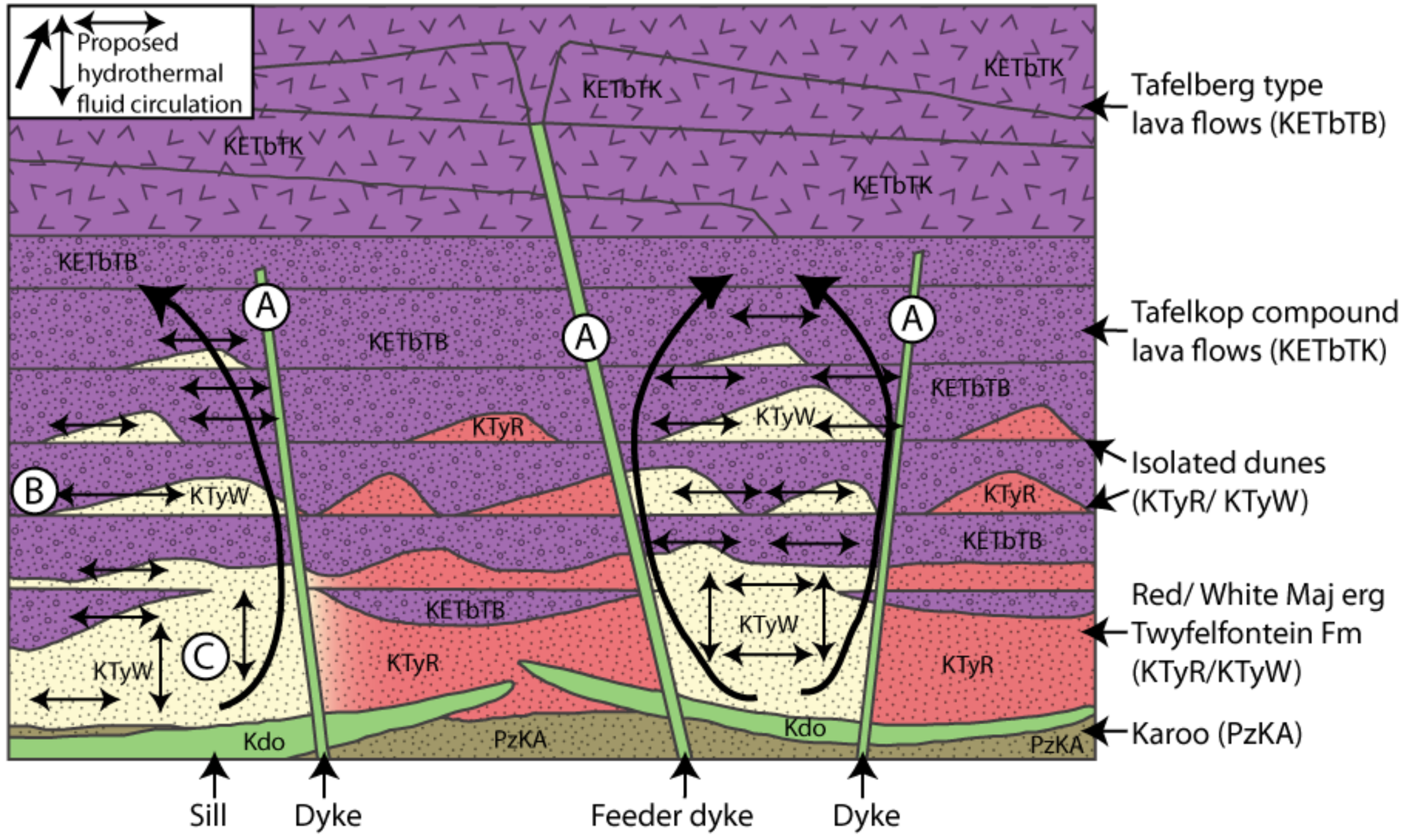

Fig. 7.39. Conceptual model of the fluid flow responsible for the bleaching of parts of the Twyfelfontein Formation. Model as described in Fig. 7.36. (A) Dolerite dykes acting as barriers to horizontal fluid flow. (B) Lateral fluid flow permitted through sandstone and basalt. (C) Multidirectional flow permitted through sandstone. Diagram is not to scale.

8

Conclusions

8.1 Direct effects at lava flow–substrate contacts

The early diagenetic effect on substrates common to both dry and wet environments is compaction, which is through mechanical grain reorganisation resulting from the weight of the lava and through chemical processes affecting detrital grains. In dry environments where the substrate is quartz dominated (e.g. Twyfelfontein Formation) early pressure solution dominates, which is enabled by the temperature increase and is probably enhanced by condensing acidic volcanic gas (e.g. water, carbon dioxide, chlorine, fluorine). In wet siliciclastic settings (e.g. CRB) compaction is through mechanical processes and pressure solution is not evident. This is probably due to the existence of pre-existing water, which when heated created positive pressure below the lava, preventing such quantity of volcanic volatiles passing into the substrate; the water would also cool the substrate reducing the chance of pressure solution taking place. Where volcaniclastic substrate is present (Rekjanes, SRB) both mechanical and chemical compaction processes occur. Volcanic glass is unstable and, where substrate pore water has elevated temperatures (boiling or near boiling) reacts to form clays, with compaction associated. Where there is enhanced basalt-water interaction, such as in pillow lavas, the volcaniclastic substrate shows the greatest chemical change due to acidification of the hydrothermal waters through interaction with the overlying pillow complex. Where the lava is largely impermeable (tabular flow) low degrees of basalt-water interaction occur and chemical effects are less during cooling.

Cementation has been found to be controlled by palaeoenvironment and substrate composition. In dry settings, where volcanic volatiles infiltrate the

substrate, calcite is the major early diagenetic phase. It can be shown in the Huab Basin using stable isotopes that the calcite precipitated when the lava was still hot (cooling) as a temperature gradient is recorded towards the contact. The calcite likely formed due to the reaction of magmatic carbon dioxide with basaltic glass and detrital plagioclase. Minor phases are fluorite and clay authigenesis is also apparent. The clays are usually non-pore-filling feldspar partial replacements although pore-filling chlorite was encountered. In wet settings early authigenic mineralisation is less pervasive and is limited to the formation of clays from reactive detrital grains such as feldspar or volcanic glass.

The most important porosity reduction mechanism below lava flows is early compaction, with authigenesis secondary. In Chapter 5 a logarithmic relationship between the thickness of the lava flow and the distance until background porosity is regained was found (Fig. 5.25.). For a given flow thickness the distance to the background porosity is slightly greater for dry palaeoenvironments than for wet, although the confidence in this suffers from the lack of thick ponded lavas studied in wet settings.

The implications of this work are that porosity can be preserved under lava flows in wet settings and that the total porosity reduction is related to the thickness of the lava flow. In dry settings, porosity reduction at the lava-sediment contact is intense due to compaction and mineral authigenesis, but the distance to which porosity reduction persists is controlled by the lava thickness (compaction). This has clear implications to exploration and the prediction of hydrocarbons in place in such settings.

8.2 Direct effects at igneous intrusion–sediment contacts

Direct effects of igneous intrusions on porous, clean sandstone studied in the Twyfelfontein Formation are good analogues for similar geological situations in other locations as surface palaeoenvironment (assuming an aquifer exists) is of little importance (Chapter 6.). It has been shown that the effects encountered are usually minor, never with more than 9 m of authigenesis directly related to normal sills (Fig. 6.30.) and never more than 4 m of authigenesis directly related to dykes (Fig. 6.32.). Background porosity has been calculated to return after a maximum of 20.8 m above the most intense 'normal' sill and 4 m from dykes (Fig. 6.33. and Fig. 6.31.). The discrepancy due to porosity loss also being influenced by increased compaction (even if no additional authigenic minerals are present). Rarely, for both dykes (6.2.1.2.) and sills (6.5.) intensification of the effects occurs due to concentration of magma flow (over time and possibly with magma velocity increase) in the subsurface magma plumbing. The impact of this on the host sandstone is intense pyrometamorphism, causing partial melt of the feldspar component and an increased zone of porosity reduction.

Interestingly, the thickness of sills and dykes studied does not appear to control the distance to background porosity (Fig. 6.33. and Fig. 6.31.). Dyke case studies studied all cluster around 2m–4 m until background porosity is reached, showing no or little correlation with dyke thickness. This is probably because outside of the compacted zone (e.g. Fig. 6.14A.) porosity reduction is controlled by mineral authigenesis which is a hydrothermal process with heat and reactive volatiles supplied from the cooling dyke. Stable isotope data supports the authigenic calcite

formed during dyke cooling (Fig. 6.20.). The dyke cooling is controlled by the magma flow duration, which may not be related to the dyke thickness. The same applies for the sills (Fig. 6. 33.), where no relationship was found between sill thickness and distance to background porosity (Fig. 6.33.), instead it is proposed that the magma flow regime within the sill controls the magnitude of the porosity reduction due to combined pyrometamorphism and hydrothermal processes.

The applicability to petroleum E & P activities of this research is in that sill geometries can be detected in 3 D seismic reflection data and their internal magma flow characteristics can be inferred (e.g. Thompson & Schofield, 2008; Schofield et al., 2010). Localisation of flow can therefore be mapped in the subsurface and these areas marked as where maximum reservoir degradation can be expected. Areas where long-lived magma flow is less likely can be mapped as areas where less reservoir degradation can be expected. Importantly, this research has shown that porous sandstone can exist relatively near to dyke and sill intrusions: in the case of dykes, reservoir quality sand occurs less than the width of the dyke from the contact and for sills reservoir quality sand can exist less than the thickness of the sill above the intrusion top contact.

8.3 Indirect effects of flood basalt provinces on sedimentary rocks

- Later fluid flow traced through inter-basalt sediments has been found to be heterogeneous and controlled by igneous geology (Fig. 7.39.). Some sediment bodies being connected to the flow regime, and some apparently isolated. The

implication is that any fluid could be controlled in this manner, including hydrocarbons.

- The white (Type 2) sandstone outcrops have been identified as a natural analogue to the proposed carbon sequestration method of Hangx and Spiers (2009); in our case magmatic CO_2 is being sequestered. Our findings have implications to the total amount of CO_2 thought to have been emitted from large igneous provinces (e.g. The Paraná-Etendeka or the Deccan Traps). Such estimates should account for CO_2 that is sequestrated within sediments in hydraulic connection with the igneous province (e.g. Caldeira & Ramoino, 1990; Wignall, 2001; McHone, 2003) as well as within the igneous rock themselves.
- Apart from the tracing of heterogeneous hydrothermal fluid flow through the basalt pile, the results of Type 2 (bleaching) diagenesis left reduced porosity and permeability compartments (the white sandstone) which, do not relate to depositional environment or tectonic structure. These poorer reservoir rocks are connected to the fluid migration pathways, whereas the better reservoir quality red sandstones are not. This dichotomy should be appreciated if similar rocks are encountered during exploration in volcanic provinces. For instance, development of mixed basalt-siliciclastic reservoirs (such as Rosebank) should not expect all stratigraphically trapped sandstone units in the paly to show identical diagenesis, and hence reservoir properties. Similarly, if exploration drilling encounters poor quality sandstone, with evidence of Type 2 diagenesis, it should be considered that *good quality sandstone may exist in close proximity*.

- Volume estimates of sediment/lava interbed reservoirs should take into account that not all sediment bodies predicted in similar situations will be charged with hydrocarbons, despite sharing stratigraphical location, depositional environment and geological structure.
- Reduced permeability and porosity in hydrothermally affected sandstones, combined with compartmentalisation from higher permeability and porosity (but hydraulically isolated) sandstone within such settings is likely. It is suggested that, because this hydrothermal activity is a subsurface process, any siliciclastic sandstone containing plagioclase feldspar with subsequent exposure to igneous processed (dyke intrusion) has the potential to be affected in a similar manner.

8.4 Recommendations for future work

This thesis is a first look at the effects of lava emplacement on the porosity and permeability of porous sediments and is the first study of the entire range of contact effects of igneous intrusions on porous sandstone. As a consequence it is very broad; it places ballpark figures on a range of processes and suggests likely mechanisms that could cause the observations. As such, it is a beginning rather than the end of research in this field.

Future research should focus on specific aspects highlighted in the thesis, elaborating on scientific methods used and collecting higher resolution datasets. I recommend that the effects of lava flows are tackled separately from intrusions as this thesis has become very large as a result of attempting to characterise both. All of

the techniques employed have yielded useful data and should be used in future work, additionally fluid inclusion thermometry should be attempted on authigenic minerals (quartz and calcite). It was the intention to make use of fluid inclusions in calcite in collaboration with Norman Oxtoby, but my time ran out. Preliminary inspection by Norman Oxtoby confirmed the presence of multiphase fluid inclusions within calcite samples from the Huab Basin.

Research on the effects of igneous intrusions on porous sandstone in the Huab Basin should also be explored in more detail. The effect of magma flow localisation of host sediments could potentially be used to map the *internal* magma routing within an intrusive complex given high enough resolution sampling. The Huab Sill complex also provides an ideal natural laboratory to study anatectic melting of country rocks and melt segregation (Chapter 6), for which, greater sampling and high precision geochemistry on melt components and detrital minerals would yield useful results. Given the exact nature of the country rock (protolith) being known, useful experimental petrology could also be performed by melting *actual* Twyfelfontein Sandstone in the laboratory and comparing with the natural melts. The architecture of the sill-dyke system is also ideal to study in the Huab Basin, specifically how dykes interact with sills. Is there a sweet spot where dykes bud from sills that we can map in outcrop and take to 3D seismic?

The final aspect of the thesis is compartmentalisation and hydrothermal fluid flow in the sandstone related to volcanism. This aspect opens up research avenues related to many fields: petroleum exploration in volcanic margins, carbon sequestration and hydrothermal geology. The study of the white Type 2 sandstone in the Twyfelfontein formation has much to give to these fields. For instance, it would

be instructive to take the red (Type 1) sandstone and react it in laboratory conditions with the hypothesised reagents (and basalt) to attempt to synthesise the observed bleaching and calcite precipitation. Quantification of this process with reference to CO_2 flux could have important implication to understanding carbon flux into the atmosphere in igneous provinces where the CO_2 must travel through sedimentary strata to reach the atmosphere. Experiments should also be conducted with a range of reservoir lithologies (e.g. different sandstones from the Faroe-Shetland basin) to determine how they behave during a flux of likely hydrothermal fluids. This would be instructive in identifying how each reservoir is affected, thereby delimiting prospective regions where sill intrusions are numerous and stratigraphy that is likely to be adversely affected. A stable isotope study into the Tafelkop type basalts in the Awahab Formation to determine the degree of water-rock interaction would also be highly informative in deciphering the hydrothermal system.

9

Supporting Publications

Geology

Submarine hydrothermal vent complexes in the Paleocene of the Faroe-Shetland Basin: Insights from three-dimensional seismic and petrographical data

Clayton Grove

Geology published online 19 October 2012;
doi: 10.1130/G33559.1

Geology, published online on 19 October 2012 as doi:10.1130/G33559.1

Submarine hydrothermal vent complexes in the Paleocene of the Faroe-Shetland Basin: Insights from three-dimensional seismic and petrographical data

Clayton Grove
Earth Sciences, Durham University, Durham DH1 3LE, UK

ABSTRACT

This work presents a new method of coarse-grained sediment input into a deep sedimentary basin and presents a new example of igneous processes controlling sedimentary facies. The Mesozoic–Cenozoic Faroe-Shetland Basin sediments are intruded by Late Paleocene igneous sills and dikes. Sill intrusions are frequently expressed on the paleosurface as hydrothermal mounds and vents occurring directly above sill tips. Three-dimensional seismic data are used to image a Paleocene submarine mounded structure that has been penetrated by an exploration well drilled in A.D. 1984. Seismic morphology is combined with petrographic data to show that the mound was erupted from a central vent as a series of sediment pulses consisting of sediments disaggregated and recycled from depth—a submarine sediment volcano.

INTRODUCTION

The exploration well 214/28-1 was drilled in A.D. 1984 in the Faroe-Shetland Basin (Andersen, 1988; Smallwood et al., 2004); one of the targets was the mound structure that forms the basis of this contribution. The predrill interpretation was a Paleocene turbidite lobe, either mounded or subject to differential compaction, based on A.D. 1981 vintage two-dimensional seismic data.

The new interpretation in this paper uses recent three-dimensional seismic data and state-of-the-art seismic attribute computations to map the structure drilled in 1984. Interpretation of these three-dimensional seismic data reveals multiple subcircular mounds, along a north-south trend, dominated by a major conical mound ~380 m high and 3000 m diameter (Fig. 1), which dips 0° to 3° away from the center. The mound is linked by a chimney structure to seismically resolvable and exploration-well–penetrated transgressive dolerite sill intrusions at 0.7–3 km paleodepth below the seabed (now 2.5–4.7 km subsea) (Fig. 2, A–A′).

When combined with petrological interpretation of samples taken from a cored section within the mound, it is suggested that the mounds are subsea sediment volcanoes resulting from intrusion-driven disaggregation of lithified sediment, which was subsequently transported to the surface where it erupted to form the conical mounds imaged.

The hydrothermal vents recognized in three dimensions in the Faroe-Shetland Basin are similar in morphology and petrography to vent complexes found in the Karoo Basin, South Africa (Jamtveit et al., 2004; Svensen et al., 2006), suggesting that the "chimney" structures are probably sediment pipes and dikes. Seismic morphologies of hydrothermal vents studied here are identical to those reported in the Vøring and Møre Basins (Norway) by Planke et al. (2005) and regionally by Hansen (2006). The only other offshore example that has been drilled is reported by Svensen et al. (2003) in the Vøring Basin, which is seep carbonate–rich and finer-grained than the 214/28-1 example. Previously, hydrothermal mounds have been linked to global climate change (Svensen et al., 2004), but due to lack of offshore data their importance in linking igneous intrusions to offshore sedimentology has not been appreciated.

It is believed this is the first time the lithological nature of a sand-dominated submarine hydrothermal vent complex has been reported and combined with three-dimensional seismic methods to link gross three-dimensional morphology, seismic facies, and petrography. This new understanding has implications for fluid movements around the basin, and identifies a new mechanism to rapidly deposit high-porosity clastic sediments in deep marine settings.

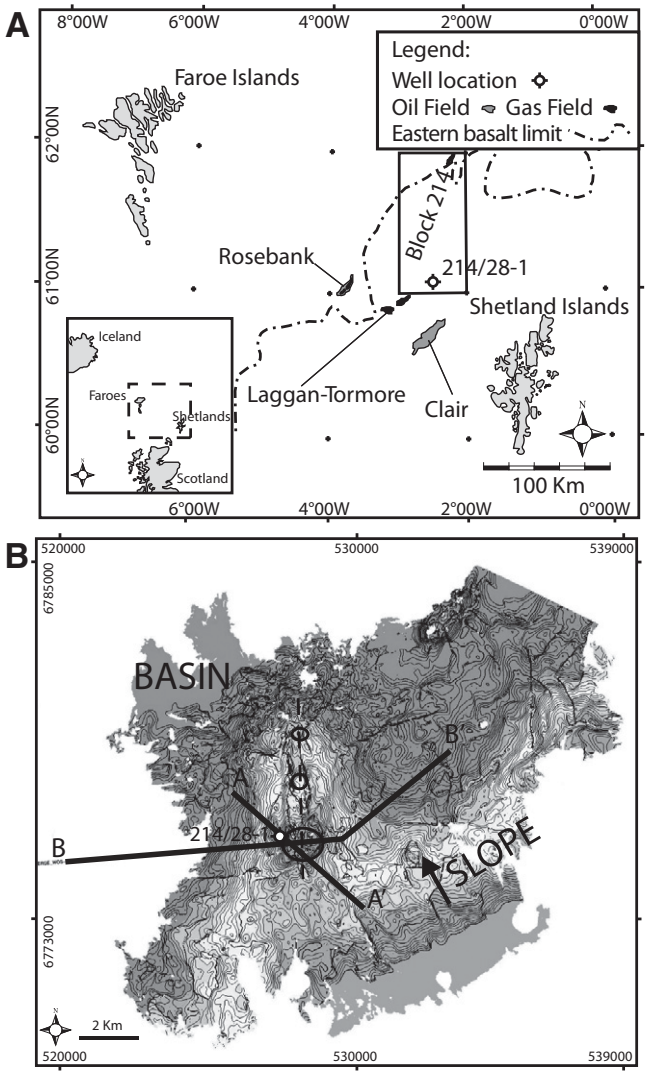

Figure 1. A: Location map showing Block 214, major hydrocarbon fields, and location of well 214/28-1 in the Faroe-Shetland Basin. B: Contoured isochron (TWT) map of Horizon M (see Fig. 2), showing topography of three mounded features (black circles). Well 214/28-1 is shown as white circle. Sections A–A′ and B–B′ are seismic lines shown in Figure 2 (grid is UTM zone 30N). Note that the southern mound is largest, and northern mounds show evidence of vent collapse along north-south axis.

PALEOGENE INTRUSIVE IGNEOUS ACTIVITY IN THE FAROE-SHETLAND BASIN

The conical mound is directly above, and linked to, transgressive saucer-shaped sill intrusions of the Faroe-Shetland sill complex (Gibb and

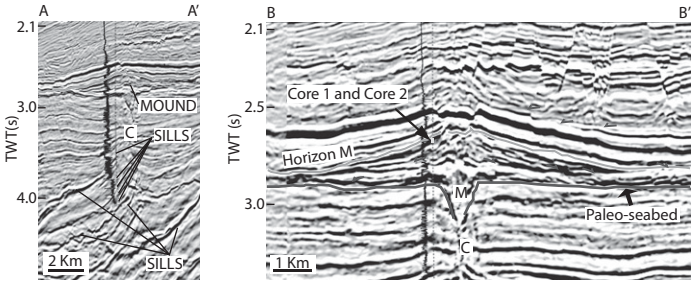

Figure 2. Left: A–A′ seismic line showing relationship between mound and underlying sill intrusions. C—hydrothermal chimney feature. Gamma ray trace is in black. Well 214/28-1 is thin dotted line. Right: B–B′ seismic line through largest mound, showing downlap of mound reflectors onto paleoseafloor and onlap of later reflectors. Onlap shows that topography must have existed prior to compaction and burial. M—maar-like crater; C—hydrothermal chimney structure. Location of drill cores are shown.

Kanaris-Sotiriou, 1988; Thompson and Schofield, 2008). Faroe-Shetland Basin sills are generally accepted to be of Late Paleocene age (Ritchie and Hitchen, 1996; Jolley et al., 2002; Trude et al., 2003), which correlates to the age of sediment the mound rests on (T40; Ebdon et al., 1995). The sills are dominantly dolerite of transitional mid-oceanic-ridge basalt (T-MORB) composition (Gibb and Kanaris-Sotiriou, 1988) resulting from ridge-plume interaction (Smallwood and Gill, 2002). Sills appear on three-dimensional seismic data as high-amplitude reflectors, usually assuming a saucer-shaped morphology (Thompson and Schofield, 2008) and can be seen to transgress from the Lower Cretaceous into the Paleocene sediments, although they probably exist in deeper basin fill. Sills intrude by a combination of brittle failure and host rock fluidization (Kokelaar, 1982; Schofield et al., 2010, 2012). Importantly, the model of Schofield et al. (2010) invokes disaggregation of host rock accompanied by tensile failure of the overburden and fluid boiling. Based upon interpretation of the three-dimensional seismic data, the sills in the study area do not reach the Late Paleocene paleosurface, nor can they be linked with extrusive activity in the form of the lava flows seen to the west, which are fed from different sills of similar age (T40, T45).

SEISMIC INTERPRETATION

Three-dimensional seismic interpretation reveals that the cored mound is in fact the largest of a cluster of three mounds that lie along a north-south structure, which mirrors the extent of the sill intrusions below (Figs. 1B and 2 [A–A′]). The mound is connected to the intrusion tips by a prominent "chimney" structure that can be recognized as a vertical region of disturbed seismic reflections with apparent disruption of sedimentary bed reflectors. Such chimneys have been recognized farther north in the Faroe-Shetland Basin (Davies et al., 2002) and interpreted as vertical fluid-migration pathways linking sill tips with extrusive igneous mounds (e.g., hyaloclastite). Davies et al. (2002) did not have lithological data in the form of core. In the Vøring and Møre Basins, 734 hydrothermal vent complexes have been identified, linked to transgressive sill tips at paleodepths of 3–9 km, with vent complexes frequently exhibiting a mounded morphology (Planke et al., 2005). Where the 214/28-1 chimney structure reaches the base of the mound, there is an inverted conical structure, reminiscent of a maar crater (White and Ross, 2011). Above this is a tepee-shaped mound structure, which is broadly conical (although where the three mounds merge, forms a ridge-like structure trending north-south) and consists of reflectors that dip away from a central point (at 0°–3°) and downlap onto the proposed paleoseabed reflector (Fig. 2, B–B′). The mound is then covered by the T45 sequence sediments (Ebdon et al., 1995), which consist of approximately parallel bedded reflectors that initially onlap, then drape the tepee structure. The end of the T45 sequence and onset of T50 is recognized by a high-amplitude trough followed by a peak.

To the east of the mound is a prograding delta system feeding deep marine turbidity currents; the relationship between these and the mounds is apparent in the east where the distal mound flanks meet the southeast-northwest slope (Fig. 1B). The sediments sourced from the east subsequently prograded onto the mound flanks, filling the remaining topography between the mound and the slope.

The mound consists of a number of lobate reflectors that are not continuous around the whole circumference, suggesting pulsed sediment supply and channel avulsion. The first circumferentially constant reflector was picked (Horizon M, Fig. 2) and is inferred to be the last sediments deposited during hydrothermal activity or a condensed horizon (in the west). This reflector drapes the structure and provides the best way of mapping the three-dimensional configuration of the mounds.

Horizon M also provided a "Top Horizon" for spectral decomposition. Spectral decomposition transforms the seismic data into the frequency domain using the discrete Fourier transform. Appropriate frequency modules (in this case, 8 Hz, 39 Hz, and 47 Hz) displayed as an RBG blend reveal subtle frequency response characteristics (Fig. 3). Spectral decomposition reveals a number of radial high-frequency (47 Hz) dominant lobate branching features trending downslope, away from the center of the vent. These are interpreted as submarine density current deposits, flowing down flank, much like turbidity currents.

The seismic morphology and spectra suggest that sediment was sourced at the center and the top of the mound, which prograded in all directions, radially forming the downlapping reflectors onto the seafloor. This is not consistent with the mound as a turbidite lobe sourced from the east, as originally proposed.

WELL 214/28-1 INTERPRETATION

Log Responses

My hypothesis, developed from the seismic interpretation, was tested with well data. Exploration well 214/28-1 penetrated the northwest flank of the mound, as imaged in three dimensions. Two cores were

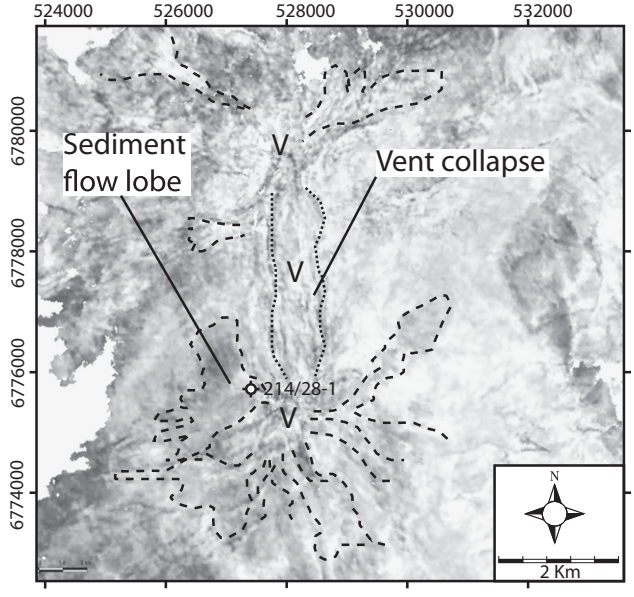

Figure 3. Spectral decomposition layer of Horizon M. Blue—8 Hz; green—39 Hz; red—47 Hz (now as greyscale). Radial lobate features are indicated, and north-south–trending vent collapse of upper vents is outlined. Area to east is affected by other mounds (grid is UTM zone 30N).

taken, and a suite of wireline logs was acquired. Based on log responses, the mound lithology is distinct from the surrounding sediments, having a higher porosity, lower density, lower sonic velocity, and lower gamma ray (GR) response. All logs show marked cyclicity through the mound. GR variability and curve shape suggests multiple fining-up cycles, typical of many turbidite interpretations (Shanmugam, 2000). Sills at depth, below the mound, show low GR and high P-wave velocities, with sonic velocity distributions consistent with the ideal Nelson et al. (2009) P-wave velocity histograms.

Core Interpretation

Two cores were cut from the mound (Core 1 and Core 2; see Appendix DR1 in the GSA Data Repository[1]), which form a continuous length from 2550.26 to 2587.14 m. The core comprises sequences of granule to sand beds, characterized by erosive bases with rip-up clasts, fining up into horizontally bedded sands with minor cross beds and ripple lamination. The fining-upward sequences are dominantly separated by interludes of pelagic sedimentation characterized by silt-to-clay deposition and incorporation of minor carbonaceous debris. These sequences are interpreted as high-density Newtonian flows (Shanmugam, 2000).

Core 1 consists of 34 fining-up sequences that usually start with an erosive basal contact containing gravel or granules with frequent rip-up clasts from the subjacent layer. Coarse-grained base lithologies are poorly sorted and consist of subrounded quartz and abundant sedimentary and crystalline lithic clasts, often with visible original bedding preserved. In this basal lithology, dewatering structures injected from the subjacent bed are occasional. The fining-up sequence usually grades into very fine or fine sand before the onset of condensed pelagic sedimentation of dark gray silt or clay with occasional woody fragments.

The uppermost part of Core 2 consists of six fining-up packages, of the same style as in Core 1. At 2567 m, there is a prominent erosive base, cutting the core at a steeper angle than other erosive sequence bases. This is interpreted to be closer to a channel axis, whereas other sequences may have been more peripheral.

My interpretation is a series of downslope gravity-driven deposits originating at the hydrothermal vent, composed of disaggregated sediments from depth, which could have been sourced from anywhere in the hydrothermal column identified in the three-dimensional seismic data. On submarine eruption, these flows would have moved under gravity as a Newtonian flow, much like a classical turbidity current (Shanmugam, 2000). Between eruptive episodes, or on lobe switching, the core records interludes of hemipelagic sedimentation and bottom current reworking. Notable at hand-specimen scale is the abundance of lithic grains in the clastic fining-up sequences and the frequent coarse-grained nature of the sequence bases.

Petrography

Two samples were thin sectioned, SSK 7236 (2549.3 m) and SSK 7238 (2568 m), with preparation for petrographic analysis (blue resin impregnation and staining for carbonates and K-feldspar).

Both samples contain abundant sedimentary and crystalline lithic clasts of varying compositions and shapes. Sedimentary clasts range from aggregates of detrital quartz to laminated siltstone up to granule size (Fig. 4B). Crystalline clasts consist of basic-composition crystalline fragments such as plagioclase and clinopyroxene. The basic crystalline fragments are composed of coarse subhedral plagioclase and clinopyroxene components exhibiting a holocrystalline texture, typical of an intrusive dolerite sill (Fig. 4A). Crystalline fragments show remarkably little weathering, such as is expected for a detrital grain that has undergone subaerial erosion and transport. A subaerial basalt provenance for the igneous component is unlikely, based on this texture and low degree of weathering. Cements were not encountered in the sections, and authigenic mineralization was restricted to occasional kaolinite and minor clays (probably smectite) unidentifiable with light microscopy. Porosity was 12.6% and 15% in the sections examined, which were both from the coarse-grained sequence bases; porosity is likely to decrease as sediments fine upward and the detrital clay component increases. In the areas sampled, compaction was minor, and the main reason for porosity degradation was authigenic clay and moderate to poor sorting.

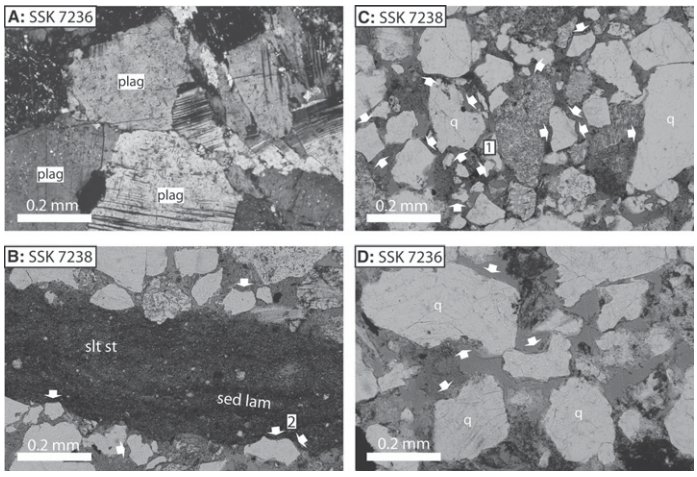

Figure 4. Photomicrographs from Core 1 and Core 2. A: Plagioclase-dominated crystalline lithic clast (dolerite). B: Siltstone lithic clast with preserved sedimentary laminations surrounded by embayed quartz grains. C and D: Quartz grains with embayments indicated by arrows. "1" and "2" show evidence for embayments being of recycled origin. plag—plagioclase; q—quartz; slt st—siltstone; sed lam—preserved sedimentary laminations.

The detrital composition suggests that the sediment was sourced from multiple locations, including dolerite intrusions, recycled sandstone, and recycled siltstone. The immature nature and remarkable preservation of mafic-composition lithic grains suggests that the sediment has not been part of a long transport system.

Texture

Grains are generally subangular and do not show evidence of significant compaction. The most important textural observation is the frequent embayments (Figs. 4B–4D) on isolated quartz grains, suggesting they have been recycled from a lithified sedimentary rock. The embayments were probably formed where the source sedimentary rock was compacted at grain contacts. Disaggregation of this rock has re-granulized grains, which were probably not highly cemented (no evidence of recycled overgrowths or calcite cements). It is not uncommon for sedimentary grains to be recycled in the Faroe-Shetland Basin (Jolley and Morton, 2007); however, the grains here preserve such angularity (Fig. 4C) that it would be impossible if they were ever part of a sediment transport system of any length, such as from the Hebrides or West Shetland Platform, which are thought to supply the majority of sediment into the region (Ebdon et al., 1995; Jolley and Morton, 2007). The embayments record a previously lithified rock, as opposed to recording dissolution of a formerly present granular component, because embayments frequently occur abutting solid grains (Figs. 4C [1] and 4B [2]). I propose that the grain texture in these two samples is a result of fluidization and disaggregation of rock at depth, as a consequence of intrusive igneous activity (Kokelaar, 1982) and subsequent transport in hydrothermal fluids to the surface.

[1]GSA Data Repository item 2013015, uninterpreted seismic lines A–A′ and B–B′ through hydrothermal sediment volcano (see Figure 1 for locations, and Figure 2 for interpretation), is available online at www.geosociety.org/pubs/ft2013.htm, or on request from editing@geosociety.org or Documents Secretary, GSA, P.O. Box 9140, Boulder, CO 80301, USA.

CONCLUSIONS

Petrological analysis suggests that the mound sediments were mainly sourced from disaggregation of sedimentary rock, and incorporate both sedimentary lithic grains and coarse crystalline lithic grains of a probable dolerite intrusive origin. Sedimentologically, the core could suggest a classical turbidite-type deposit; however, when combined with the three-dimensional seismic and petrological data, the likely origin of the mound is a hydrothermal sediment volcano. I propose that the mounds studied here are submarine equivalents to the exposed hydrothermal mounds in the Karoo Basin (South Africa; Jamtveit et al., 2004; Svensen et al., 2006), and are direct equivalents to the examples in the Vøring and Møre Basins (Norway; Svensen et al., 2003; Planke et al., 2005; Hansen, 2006). Furthermore, identification of this type of mound in the Faroe-Shetland Basin supports the host-rock fluidization emplacement mechanism of Schofield et al. (2010) by linking sill tips with the eruptive products of host rock disaggregation (see also Jamtveit et al., 2004). This interpretation contrasts with the interpretation of Davies et al. (2002), who used three-dimensional seismic data to suggest that mounds of this nature were composed of volcanic material and directly fed from dikes. I conclude that the mounds consist of multiple radial, stacked, normally graded sediment deposits, erupted from a hydrothermal vent at the cone center. Importantly, the sediment-rich nature of the mound may be a future hydrocarbon play type in volcanic basins globally.

ACKNOWLEDGMENTS

This work was carried out during an internship with TOTAL E&P UK, who are acknowledged for their permission to publish. Seismic data are courtesy of Petroleum Geo-Services. I thank the British Geological Survey for the loan of specimens and for access to the drill core. Vincent Curinier, Martin Specht, Samuel Beaumont, Jennifer Shepherd, Tim Watton, and Jon Gluyas are acknowledged for helpful discussions. The reviewers are thanked for their constructive comments.

REFERENCES CITED

Andersen, M.S., 1988, Late Cretaceous and early Tertiary extension and volcanism around the Faroe Islands, *in* Morton, A.C., and Parson, L.M., eds., Early Tertiary volcanism and the opening of the NE Atlantic: The Geological Society of London Special Publication 39, p. 241–252.

Davies, R., Bell, B.R., Cartwright, J.A., and Shoulders, S., 2002, Three-dimensional seismic imaging of Paleogene dike-fed submarine volcanoes from the northeast Atlantic margin: Geology, v. 30, p. 223–226, doi:10.1130/0091-7613(2002)030<0223:TDSIOP>2.0.CO;2.

Ebdon, C.C., Granger, P.J., Johnson, H.D., and Evans, A.M., 1995, Early Tertiary evolution and sequence stratigraphy of the Faeroe-Shetland Basin: Implications for hydrocarbon prospectivity, *in* Scrutton, R.A., et al., eds., The tectonics, sedimentation and palaeoceanography of the North Atlantic region: The Geological Society of London Special Publication 90, p. 51–69.

Gibb, F.G.F., and Kanaris-Sotiriou, R., 1988, The geochemistry and origin of the Faeroe-Shetland sill complex, *in* Morton, A.C., and Parson, L.M., eds., Early Tertiary volcanism and the opening of the NE Atlantic: The Geological Society of London Special Publication 39, p. 241–252.

Hansen, D.M., 2006, The morphology of intrusion-related vent structures and their implications for constraining the timing of intrusive events along the NE Atlantic margin: The Geological Society of London Journal, v. 163, p. 789–800, doi:10.1144/0016-76492004-167.

Jamtveit, B., Svensen, H., Podladadchikov, Y.Y., and Planke, S., 2004, Hydrothermal vent complexes associated with sill intrusions in sedimentary basins, *in* Breitkreuz, C., and Petford, N., eds., Physical geology of high-level magmatic systems: The Geological Society of London Special Publication 234, p. 215–227.

Jolley, D.W., and Morton, A.C., 2007, Understanding basin sedimentary provenance: Evidence from allied phytogeographic and heavy mineral analysis of the Palaeocene of the NE Atlantic: The Geological Society of London Journal, v. 164, p. 553–563, doi:10.1144/0016-76492005-187.

Jolley, D.W., Clarke, B., and Kelley, S., 2002, Paleogene time scale miscalibration: Evidence from the dating of the North Atlantic igneous province: Geology, v. 30, p. 7–10, doi:10.1130/0091-7613(2002)030<0007:PTSMEF>2.0.CO;2.

Kokelaar, B.P., 1982, Fluidization of wet sediments during the emplacement and cooling of various igneous bodies: The Geological Society of London Journal, v. 139, p. 21–33, doi:10.1144/gsjgs.139.1.0021.

Nelson, C.E., Jerram, D.A., and Hobbs, R.W., 2009, Flood basalt facies from borehole data: Implications for prospectivity and volcanology in volcanic rifted margins: Petroleum Geoscience, v. 15, p. 313–324, doi:10.1144/1354-079309-842.

Planke, S., Rasmussen, T., Rey, S.S., and Myklebust, R., 2005, Seismic characteristics and distribution of volcanic intrusions and hydrothermal vent complexes in the Vøring and Møre basins, *in* Dore, A.G., and Vining, B., eds., Petroleum geology: North-west Europe and global perspectives: Proceedings of the 6th Petroleum Geology Conference: London, The Geological Society of London, p. 833–844.

Ritchie, J.D., and Hitchen, K., 1996, Early Paleogene offshore igneous activity to the northwest of the UK and its relationship to the North Atlantic Igneous Province, *in* Knox, R.W.O'B., et al., eds., Correlation of the early Paleogene in northwest Europe: The Geological Society of London Special Publication 101, p. 63–78.

Schofield, N., Stevenson, C.T., and Reston, T., 2010, Magma fingers and host rock fluidization in the emplacement of sills: Geology, v. 38, p. 63–66, doi:10.1130/G30142.1.

Schofield, N., Brown, D.J., Magee, C., and Stevenson, C.T., 2012, Sill morphology and comparison of brittle and non-brittle emplacement mechanisms: The Geological Society of London Journal, v. 169, p. 127–141, doi:10.1144/0016-76492011-078.

Shanmugam, G., 2000, 50 years of the turbidite paradigm (1950s–1990s): Deep-water processes and facies models—A critical perspective: Marine and Petroleum Geology, v. 17, p. 285–342, doi:10.1016/S0264-8172(99)00011-2.

Smallwood, J.R., and Gill, C.E., 2002, The rise and fall of the Faroe-Shetland Basin: Evidence from seismic mapping of the Balder Formation: The Geological Society of London Journal, v. 159, p. 627–630, doi:10.1144/0016-764902-064.

Smallwood, J.R., Prescott, D., and Kirk, W., 2004, Alternatives in Paleocene exploration West of Shetland: A case study: Scottish Journal of Geology, v. 40**,** p. 131–143.

Svensen, H., Planke, S., Jamtveit, B., and Pedersen, T., 2003, Seep carbonate formation controlled by hydrothermal vent complexes: A case study from the Vøring volcanic basin, the Norwegian Sea: Geo-Marine Letters, v. 23, p. 351–358, doi:10.1007/s00367-003-0141-2.

Svensen, H., Planke, S., Malthe-Sørenssen, A., Jamtveit, B., Myklebust, R., Eidem, T., and Rey, S.S., 2004, Release of methane from a volcanic basin as a mechanism for initial Eocene global warming: Nature, v. 429, p. 542–545, doi:10.1038/nature02566.

Svensen, H., Jamtveit, B., Planke, S., and Chevallier, L., 2006, Structure and evolution of hydrothermal vent complexes in the Karoo Basin, South Africa: The Geological Society of London Journal, v. 163, p. 671–682, doi:10.1144/1144-764905-037.

Thompson, K., and Schofield, N., 2008, Lithological and structural controls on the emplacement and morphology of sills in sedimentary basins, *in* Thompson, K., and Petford, N., eds., Structure and emplacement of high-level magmatic systems: The Geological Society of London Special Publication 302, p. 31–44.

Trude, J., Cartwright, J., Davies, R.J., and Smallwood, J., 2003, New technique for dating igneous sills: Geology, v. 31, p. 813–816, doi:10.1130/G19559.1.

White, J.D.L., and Ross, P.-S., 2011, Maar-diatreme volcanoes: A review: Journal of Volcanology and Geothermal Research, v. 201, p. 1–29, doi:10.1016/j.jvolgeores.2011.01.010.

Manuscript received 25 April 2012
Revised manuscript received 16 July 2012
Manuscript accepted 20 July 2012

Printed in USA

Computers & Geosciences 37 (2011) 1850–1859

Contents lists available at ScienceDirect

Computers & Geosciences

journal homepage: www.elsevier.com/locate/cageo

jPOR: An ImageJ macro to quantify total optical porosity from blue-stained thin sections

Clayton Grove*, Dougal A. Jerram

Department of Earth Sciences, Science Labs, Durham University, Durham, UK

ARTICLE INFO

Article history:
Received 2 December 2010
Received in revised form
28 February 2011
Accepted 2 March 2011
Available online 21 March 2011

Keywords:
Image analysis
Porosity
Image processing
Point count
Petrology
Operator error

ABSTRACT

A fast and effective method has been developed to measure total optical porosity (TOP) of blue resin-impregnated thin sections. This utilises a macro file (jPOR.txt) for ImageJ, which can be used on digital photomicrographs of thin sections. The method requires no specialised scientific equipment and can be run entirely using free to download software. Digital images are acquired from blue resin-impregnated thin sections using a conventional film scanner in the present study, though the technique can be applied to any high resolution colour digital acquired by different means (e.g., flat bed scanning, digital capture). Images are preprocessed using a newly developed custom 8-bit palette and analysed for porosity in ImageJ using the simple to use jPOR macro. Our method rapidly calculates TOP for batches of images with or without the option of user adjustment. Results are compared with conventional methods (e.g., to point counting), and tested with several users to estimate any user variability. jPOR provided comparable results to more time-consuming point counting, but with significantly less "counting error" and less interoperator variability than published point counting studies. The jPOR macro has been integrated into a macro tool set that can be configured to be run on ImageJ start up.

1. Introduction

The development of digital images and of computer software that can perform a variety of image analysis techniques has revitalised the way that we do modern petrography (e.g., Higgins, 2006; Beggan and Hamilton, 2010). Textures can be digitised and measurements of, for example, size, shape, and sorting of constituent grains or crystals quickly acquired (e.g., Higgins and Roberge, 2007; Jerram et al., 2009). Computer models can be used to generate virtual textures with known 3D properties to be used as reference textures for image analysis of natural samples (e.g., Jerram, 2001; Jerram and Cheadle, 2000; Hersum and Marsh, 2007), and even true 3D rock textures can be imaged and analysed directly with the application of serial sectioning and X-ray CT analysis (e.g., Jerram and Higgins 2007; Jerram et al., 2009). All of these techniques have advanced, and in some way been developed in order to push forward our range and types of analysis that we can perform on geological samples, but what of the simple standard measurements that we need to routinely undertake on our rocks?

The new developments in image analysis have the added advantage in that they can potentially provide increased capacity to undertake standard measurements, with more speed and accuracy than traditional methods. For example, the quantification of rock porosity from thin sections impregnated with blue epoxy resin is routine in geosciences, and most commonly undertaken with point counting. Total porosity is defined as the ratio of void volume (pores) to the bulk volume of a rock and is commonly given as a percentage; hence, total porosity $= V_p/V_b \times 100$, where V_p is the pore volume and V_b is the bulk volume (Curtis, 1971). Porosity is important in determining the reservoir properties of a rock (for both aqueous and hydrocarbon fluids), and in studies of diagenesis, compaction, and evolution of sediments (Curtis, 1971; Tucker, 2001). A number of techniques exist to quantify porosity, including 2D texture measurements (e.g., point counting), mercury injection, and helium injection porosimetry. Measurements made from 2D sections, which form the basis of this study, record the porosity as resolvable from an optical image of the sample (total optical porosity). Point counting of thin sections is slow, laborious, and requires specialised equipment whereas digital image analysis is potentially superior in speed and accuracy over point counting as millions of points can be analysed in the sample, which leads to far superior datasets. The key to be able to perform accurate digital porosity measurements is the ability to generate a porosity threshold image (one which separates the porosity voids from the rest of the objects in the image). Poor quality data can arise from the introduction of noise and inadequate or over-zealous preprocessing methods, increasing user bias during thresholding. Additionally, existing techniques can require very specific software (e.g., costly proprietary software, microscope specific software).

The jPOR method described in this study overcomes these problems by streamlining and standardising colour preprocessing by applying our newly developed custom 8-bit palette, which has

* Corresponding author.
E-mail address: clayton.grove@durham.ac.uk (C. Grove).

0098-3004/$ - see front matter © 2011 Elsevier Ltd. All rights reserved.
doi:10.1016/j.cageo.2011.03.002

been developed in conjunction with the jPOR macro for ImageJ (Rasband, 2009). The newly developed macro jPOR.txt has been designed to make quick and accurate porosity analysis available to any researcher in possession of a personal computer and high resolution colour digital images of blue-stained thin sections (e.g., those captured from thin sections mounted on slide scanners).

The jPOR macro offers instructions at each stage so that inexperienced users with no prior image analysis experience will find it easy to use. The method uses technically nonspecific hardware and software which should be familiar to most computer users. In this contribution we introduce the jPOR macro and how it can be used to validate the porosity of digital photomicrographs of thin sections produced using desktop scanning equipment. The methodology is discussed with advice about image preparation, the steps required for analysis, and how the macro is installed. Results are presented for both point counting and jPOR calculated porosity for the same samples, and in the case of the four "fell sandstone" samples He injection is also tested. Inter-operator variability is also tested on the same set of samples analysed by 10 users; this is compared to point counting studies where multiple operators have been evaluated. jPOR is supplied with a user guide and the 8-bit paletted bitmap test files used in this study (see Appendix) (Fig. 1).

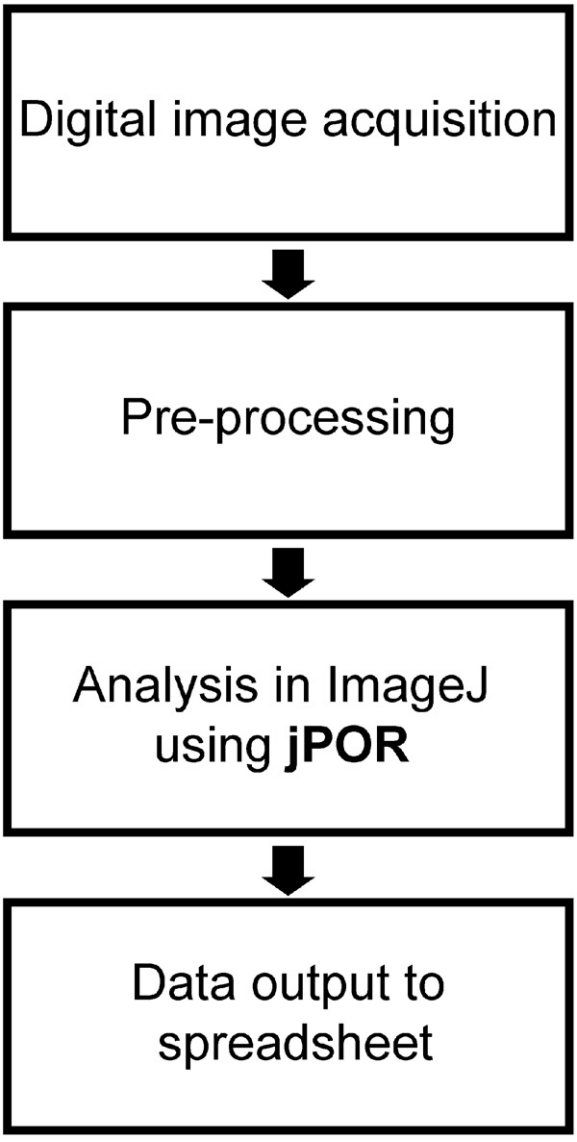

Fig. 1. Flowchart of total optical porosity (TOP) calculation using jPOR.

2. Development

2.1. Principles and background

The principle behind the development of the jPOR method was to provide a macro where a wide range of researchers would be able to use digital image analysis to measure total optical porosity (TOP) from blue resin-impregnated thin sections with great accuracy and speed. To fulfil this goal the following criteria had to be met: (1) no specialised equipment beyond standard IT (Information Technology) facilities would be needed, (2) novice users should generate meaningful data without specialist skills, (3) preprocessing should be minimal and standard, (4) the method must be more rapid and at least accurate as existing methods of optical porosity measurement, and (5) users should have the ability to improve and modify the method.

Nonspecialised equipment use (both software and hardware) is of fundamental importance in making this method accessible. Software and hardware choice has reflected this in that the entire method can be completed using free to download software and standard computer hardware. The use of a flat bed scanner, such as the conventional film scanner used in this study, can be superior to most photomicrographs captured from cameras attached to microscopes (discussed in detail in Section 3.1). The equipment used in the present study is listed in Table 1.

2.2. Developing the custom palette

The jPOR macro for ImageJ requires an 8-bit paletted colour image file (a bitmap.bmp file works best in the platform-independent version). For Petrographic Image Analysis (PIA) there must be a direct relationship between pixel colour and feature class (the phase of interest, in this case blue resin filling porosity); clearly the more straightforward this relationship, the more reliable the procedure becomes. Here we are only interested in two feature classes (porosity and solids in the form of grains and pore filling cements in the rock).

The classic method to measure TOP using PIA is to acquire a digital image of a thin section using an optical microscope combined with, for example, an analogue video camera output (Ehrlich et al., 1984) or as technology has advanced higher resolution digital cameras (Lamoureux and Bollmann, 2004). Previous workers have then separated the image into red, green, and blue components and threshold a greyscale histogram of an individual channel (Ehrlich et al., 1984; Andriani and Walsh, 2002; Crawford and Mortensen, 2009; Dey et al., 2009). The image can then be thresholded to a 2-bit image where the class of interest is black and everything else is white. The drawback of greyscale thresholding is that contrast between classes of interest can be low, which necessitates contrast enhancement

Table 1
Equipment required to use calculate total optical porosity using jPOR method.

Hardware	Software
Scanner—either slide scanner (recommended) or flatbed scanner capable of handling transparencies	ImageJ- free from http://rsb.info.nih.gov/ij/
PC or Mac	Image processing software—Adobe Photoshop/Corel Photo Paint or Irfan View (free from www.irfanview.com)
	Spreadsheet to receive exported data

and shading correction (Andriani and Walsh, 2002). Noise within grains can also pose problems. We have found noise from intragranular texture difficult to threshold away from pore space using greyscale images; the best results came from the red band but nevertheless were visually inferior to the jPOR method. When using the greyscale thresholding methods it is difficult to produce a binary image where the pore space class is entirely thresholded without including some intragranular noise, thus inaccurately recording the porosity. To remove the noise component the threshold value requires reduction, which also removes porosity; microporosity also becomes difficult to distinguish. We have developed a simpler and less subjective method using colour thresholding that requires less preprocessing and removal of noise, thereby reducing interoperator variability.

In ImageJ the normal way of thresholding a 24-bit colour image, using built in tools, is to open it as a 24-bit image and use the built in 8-bit colour conversion tool (Image > Type > 8-Bit Colour) set to 256 colours. This image can then be thresholded. The conversion creates an indexed 256 colour image which is not sorted according to hue; therefore, the colours representing specific classes are separated by colours which represent other classes. Applying a threshold to separate two classes (e.g., all the blues in the image from the other colours) clearly will not work as there is no systematic order of colours belonging to individual feature classes, as thresholding only works with a block of colours that are numbered together in sequence. We have developed a custom 256 colour (8-bit) palette which forces the grouping of feature classes (e.g., blues), enabling ImageJ to threshold porosity based on colour (hue), which can be applied to any 24-bit image using common image editing software (Irfan View, Adobe Photoshop, Corel Photo Paint).

The custom 8-bit palette preprocessing method developed in this study addresses the drawbacks of greyscale thresholding porosity calculation methods, without the need for complicated filtering or adjustment. jPOR 60 is a custom 256 colour palette, sorted by hue, and designed to represent a typical blue resin-impregnated thin section. The palette was constructed using Corel Photo Paint X3 from digital scans of blue resin-impregnated thin sections. The thin sections chosen to produce the pallet were: (1) basaltic hyaloclastites from Iceland and (2) aeolian sandstone examples from Namibia. The hyaloclastite was first chosen because it displayed a full range of colours from blue (resin) to dark brown (clays). The large range of naturally occurring colours in the hyaloclastite samples used here results from a diverse mineralogy. The nature of formation (hydroclastic fragmentation and quenching of a lava flow entering seawater, in this case) (Fischer and Schmincke, 1984), subsequent rapid devitrification of glassy rims, and potentially varied burial diagenesis (clay transformation and hydrothermal mineralisation) of our basaltic hyaloclastites provided a large number of characteristic minerals to build into the palette (volcanic glass, palagonite, illite, chlorite, zeolite, calcite, and unaltered phenocrysts within basalt clasts, such as plagioclase and olivine). The sandstone samples were chosen because they had a clear representation of porosity impregnating blue resin and comprised quartz colours absent from the hyaloclastite samples. Corel Photo Paint was chosen for this operation over other graphics editing programs (Adobe Photoshop, Irfan View) because of its ability to generate an optimised palette, which could be sorted by hue and then manually edited by dragging and colour editing. To further aid thresholding a blank region was built into the palette of 9 colours, which did not naturally occur in any of the thin sections. The finalised design comprises 59 blues, which represent blue resin impregnation of pore space, 9 separator colours, and 188 rock colours. Most of these blues came directly from the hyaloclastite sample (40); additional colours (20) were added from other impregnated samples so that there was a more complete range to ensure an accurate capture of the porosity in the image. The 9 separator colours are all similar bright greens chosen because they did not occur in any test images. The 188 colours representing the rock include black and white, which left 186 colours that were customisable. Initially there were 206 colours, 20 were taken up by the additional blues, and 2 were taken up by black and white. The Corel Photo Paint optimised 8-bit palette automatically creates a 256 colour palette based on the highest percentage of colours in the image (Corel Help, 2005); this was good as a starting point because the processed 8-bit image had the same visual appearance as the 24-bit image (Fig. 2). However, it was biased toward similar brown colours; there were few light greys and creams that are common in other sedimentary rocks. A proportion of the browns were therefore edited and changed into colours sampled from an aeolian sandstone thin section from the Twyfelfontein Formation, Namibia (Dickinson and Milliken, 1995; Jerram et al., 1999, 2000; Mountney et al., 1999). This supplies a palette of colours that best represent the types of colour variation we expect to see in a sedimentary thin section, when it is represented in an 8-bit colour image. The resulting custom palette (Fig. 2) was then saved in a variety of formats so that any common graphics editing package can be used to apply it to other images, including Irfan View (freeware). When the palette is applied to an image the graphics editor will assign pixels to the closest colour within the palette; blues will remain blue, but not necessarily an identical blue to the 24-bit image, likewise for other colours. While colour representation may not be entirely faithful (false colour) class representation is faithful, providing no dithering is set. Dithering introduces noise into the compressed representation to visually reproduce the image in the 24-bit image. Dithering therefore does not preserve areas and must be unselected when applying a custom 8-bit colour palette to the 24-bit image. By forcing the colours in a thin section image to our pallet, one can still see and assess the main sedimentary features, and now all the colours are grouped so that an accurate thresholding of the porosity can be realised.

3. Procedure

3.1. Procedure 1: Digital image acquisition

The aim is to produce a 24-bit colour.tiff image at high resolution of the whole sample without distortion. Typically a digital video camera attached to a microscope would be used to acquire a digital image directly from the thin section (Ehrlich et al., 1984; Tovey and Hounslow, 1995). The problem with this is the difficulty in acquiring a low magnification image of the entire thin section without distortion toward the edges of the frame. When measuring relative areas across a complete 2D sample variable distortion is detrimental to producing accurate results. Additionally, depending on the grain size of the sample, a larger region of interest may be required (e.g., whole thin section image), which can be difficult to achieve from a microscope. We acknowledge that sophisticated systems exist that correct for image distortion and some examples of microscopes can capture large areas of thin sections but for the most part these are specialised systems that may not be available to many potential users.

In order for jPOR to conform to the ease of access and use principle, we chose to explore the capture of thin section images using scanning techniques. The method of DeKeyser (1999) provides a rapid, cheap, and effective method of overcoming and circumventing the use of conventional light microscopy. The method used a Nikon LS-2000 digital film scanner capable of a 2700 dots per inch (dpi) resolution to directly capture an image of

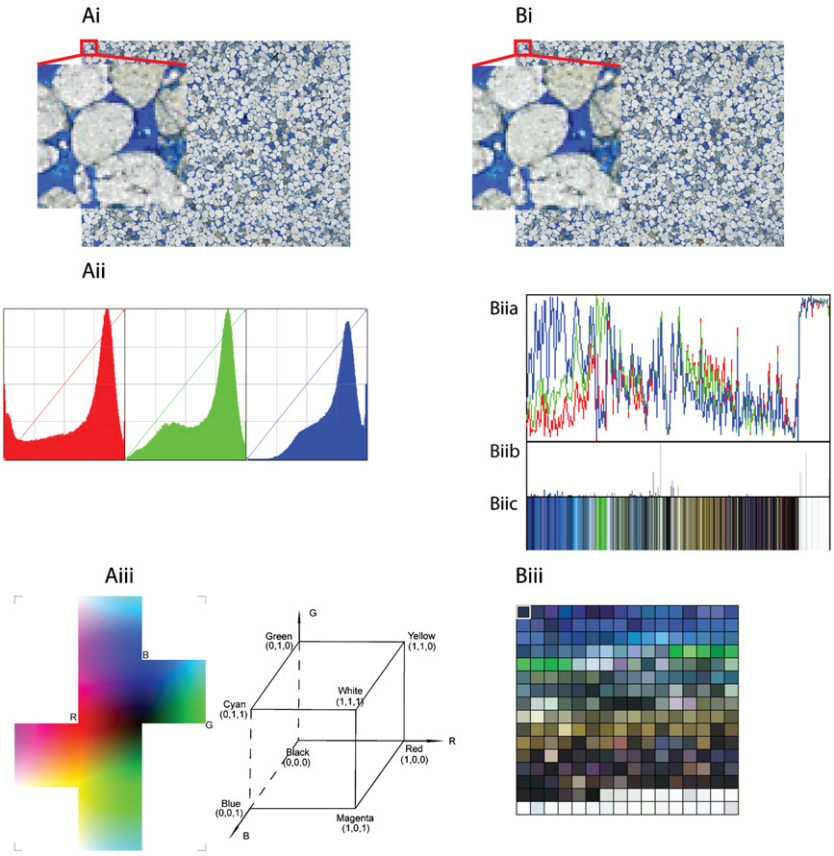

Fig. 2. (Ai) A 24-bit cropped colour scan of PL12. Each pixel is one of 14 million possible colours, described by RGB value. (Aii) The 24-bit PL12 RGB values plotted for each channel; traditional methods would threshold the red histogram. (Aiii) Image of outside face of RGB cube showing R, G, B corners (courtesy of Steve Sangwine, 2010). This wraps around cube labelled with RGB corners, white, black, and CMY (after Kang, 1997). (Bi) An 8-bit paletted image with jPOR60 palette applied. Note visual appearance very similar to 24-bit image. (Biia) Image in Bi is composed of pixels with colours chosen from 256 colour palette; each colour has RGB value shown by red, green, and blue lines. (Biib) Histogram of number of pixels, for each jPOR 60 colour. (Biic) Arrangement of porosity forming colours, enabling segmentation using ImageJ Threshold tool. (Biii) A 16 × 16 grid of jPOR60 palette, porosity separated from rock colours, 9 green colours. (For interpretation of the references to colour in this figure legend, the reader is referred to the web version of this article.)

a standard size petrographic thin section. Our method is adapted from DeKeyser (1999) method to work with the Minolta Scan Elite II digital film scanner capable of 2820 dpi resolution. We have also experimented with the Epson Expression 1680 Pro flatbed scanner which is designed to scan transparencies at 3200 dpi. The Epson flatbed scanner produced acceptable results; the drawback was the fixed dual-focus mechanism which made acquiring images as sharp as the Minolta 35-mm film scanner difficult. In order for a flat bed scanning system to work with a thin section the light source must be able to be transmitted through the sample (not reflected), which makes the slide scanners ideal for this type of capture and limits the choice of multipurpose flat bed scanners to those with a top down light source.

3.1.1. Scanning

The most straightforward and most effective method of acquiring digital images for the jPOR porosity measurement method is to use a conventional 35-mm film scanner such as the Minolta Scan Elite II, which was used. Like the Nikon LS-2000 scanner used by DeKeyser (1999), the Minolta Scan Elite II comes equipped with several adapters used for different sized slides. This method uses the adapter designed for 35-mm negative strips (of six exposures). The first stage is to open the adapter and place the thin section slide face up into one of the central slots (either '3' or '4') with the area to be digitised aligned with the window. The adapter is then closed and snapped shut. One slide may be scanned at a time because the elasticity of the plastic adapter is relied on to accommodate the glass slide. The adapter is then loaded into the scanner which will automatically grab the adapter after about 2.5 cm of insertion. The third stage is to acquire the image using the software bundled with the scanner. Images should be scanned at maximum resolution (2820 dpi) and saved as .tiff files. Prior to completing the final scan, a preview image should be reviewed. We have found that applying the auto focus function and increasing the colour saturation necessary are best for reproducing the blue epoxy filling the pore spaces. The procedure is simply repeated for each sample, maintaining settings throughout the batch, typically taking around 2 min per sample. The functionality of the slide scanner and its software should be considered when using different systems; the ability of the scanner to be focused on the image is clearly a desirable to produce sharp images for porosity analysis.

3.1.2. Photomicroscopy

Low magnification photomicrograph images can be analysed by jPOR. The microscope should be used on the lowest magnification available and the recorded image resolution set to the highest setting. Photomicrographs on traditional colour transparency film or negative film can also be digitised for jPOR analysis. When acquiring images using conventional photomicroscopy researchers should be aware of the potential disadvantages compared to the method outlined in Section 3.1.1), and where possible use microscopy equipment designed to record high resolution colour images corrected for edge distortion.

3.2. Procedure 2: Preprocessing

Preprocessing prepares the digital image of the thin section for the jPOR macro in ImageJ. The image is trimmed and converted to an 8-bit paletted .bmp or .tiff; the development of the custom palette has already been discussed in Section 2.2). Alternatively each image can be converted to an 8-bit paletted file with its own custom optimised palette; this will require much more user biased thresholding within ImageJ. Successful preprocessing can be achieved in the freeware program IrfanView as well as common image editing programs such as Adobe Photoshop or Corel Photo Paint, a method for all three is described:

1. Open image in your chosen image processing software (Corel Photo Paint, Adobe Photoshop or IrfanView).
2. Crop image to make a rectangle only comprising sample (i.e., no slide mounting or edges).
3. Convert to an 8-bit paletted file using the provided custom palette. Make sure that no dithering is set. The image may look slightly unnatural, but the area of porosity will be preserved, albeit with fewer colour values.
   (a) In Corel Photo Paint: Image > Convert to Paletted 8-bit… > Palette set custom, open, navigate to the palette file-OK-set dithering to none-OK. Within the "Convert to Paletted 8-bit" box there is the option to run this as a batch. All files within the batch must be open.
   (b) In Adobe Photoshop: Image > Mode > Indexed Colour. Set "Palette" to "Custom" and you will be presented with a new window—click load and navigate to the custom JPOR palette (JPOR_60) and click load—OK this operation. Set dither to none under Indexed Colour options and click OK. The image will now be an 8-bit paletted file. This can be automated by recording the action then playing it via the Automate > Batch tool.
   (c) In IrfanView: Image > Palette > Import Palette > navigate to palette-open.
4. ImageJ works best with .bmp images whereas the occasional .tif image will fail to be displayed. Therefore we recommend conversion to .bmp format. This can be done as a batch in Adobe Photoshop and Corel Photo Paint. Images within a "batch" must then be placed in a dedicated folder.

3.3. Procedure 3: Using jPOR to calculate porosity in ImageJ

ImageJ is a public domain image analysis software designed to be adapted for different roles. The "freedom" of the ImageJ package is the cornerstone of jPOR. Once ImageJ has been installed, the jPOR macro requires installation. For jPOR to run on ImageJ startup replace the file StartupMacros.txt in the ImageJ macros folder with StartupMacros.txt distributed with jPOR. When jPOR is installed like this, a clickable jPOR icon will appear in the ImageJ menu bar. Alternatively jPOR can be installed after ImageJ startup by going to Plugins > Macros > Install… then navigating to jPOR.txt and clicking "open."

To run jPOR click the jPOR icon located in the top right corner of the ImageJ menu. This will open a window where the first file in a batch can be located; open the first file in the batch. jPOR will then prompt to press F1 to begin porosity measurement. Pressing F1 automatically thresholds the image using the default values, and displays the threshold command box where the threshold level can be manually adjusted to refine the porosity selection. The built in ImageJ zoom tool can be used at any stage. When the porosity selection is satisfactory press F2, which will perform the area calculation of the thresholded pixels and append it to the results table. The ImageJ threshold window has a button labelled "Auto," this button is not for jPOR default. jPOR then prompts to press F3 to load the next image within the batch from where the process is restarted (F1, F2, F3, F1., etc.). When the processing of a batch is complete, F5 should be pressed which closes redundant windows and copies the results table to the clipboard for pasting into a spreadsheet. The jPOR workflow is illustrated in Figs. 3–5. It should be noted that jPOR will work through the batch files in a loop and so will reopen the first file that you analysed once you have gone through all the files in the batch; you should press F5 at this point to avoid reanalysing the same sample.

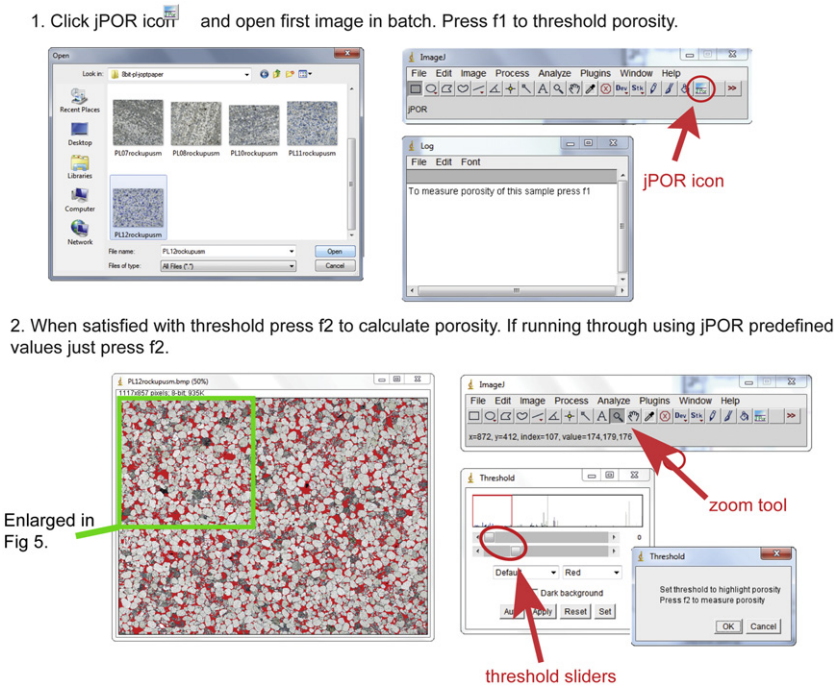

Fig. 3. Workflow using jPOR macro within ImageJ. Screenshots are shown for key operations.

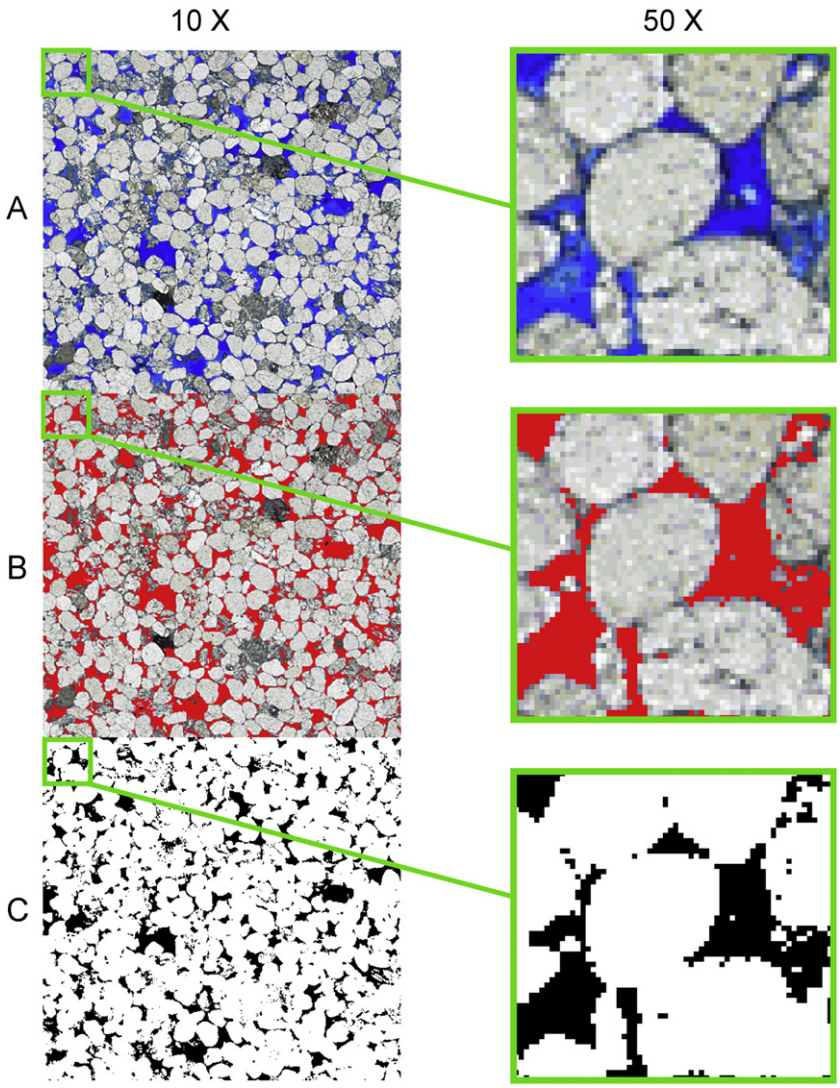

Fig. 4. Enlarged sections (10 × and 50 ×) of sample in Fig. 3 showing thresholding to binary image of pore space. (A) An 8-bit unthresholded. (B) Red mask during thresholding operation covering thresholded pixels. (C) Binary image product of threshold operation. jPOR (default) values have been set.

4. Testing jPOR

The performance of jPOR has been evaluated against point counting and He injection porosimetry. Additionally the series of test images have been evaluated by 10 different users to measure the interoperator variability of the technique. The object is to compare point counting with jPOR to show that the latter method is at least as precise and accurate. When point counting porosity it can be considered as a mineral phase for the purpose of area fraction measurements (Ehrlich et al., 1984); sources of error during point counting and PIA are the same as those encountered when counting mineral proportions. The sources of error are: (1) Errors as a result of taking systematic observations of a thin section and using for areal analysis (Chayes, 1949; Demirmen, 1971; Galehouse, 1971); this is termed "counting error" or "analytical error" (Chayes and Fairbairn, 1951) and is inversely related to the number of points counted. In this study, we counted 500 points for each slide; 300 points were recommended as sufficient by sedimentologists regularly using point counts (Stuart Jones, 2010, personal communication), which agrees with the 300 or fewer points that are routinely used by other workers in sedimentology (e.g., Purvis, 1992). Therefore 500 points comfortably exceeds the general practise, making conclusions from this test robust. The number of "points" counted by jPOR equals the number of pixels in the image, therefore dramatically reduces the analytical error as described above. The maximum image size encountered in our test samples was 3,983,252 pixels and the minimum was 957,269 pixels, which can be considered as the number of points analysed in comparison to the 500 used for point counting. (2) The error encountered when using a 2D slice to estimate volume percentage in the hand sample, generally termed "specimen error." It exists because of hand sample heterogeneity often not sampled in the section (Murphy, 1983) and stereological considerations in converting 2D–3D data where variations in the pore size distribution can affect the reproducibility of true 3D from 2D data (e.g., Jerram et al., 2009; Mock and Jerram, 2005; Morgan and Jerram, 2006). Specimen error is equal for both point counting and PIA using jPOR in this case as the same specimens are being tested. (3) The user introduced variability commonly termed as "operator error" (Demirmen, 1971) or "interoperator differences" (Chayes and Fairbairn, 1951). Results obtained by multiple operators may disagree due to misidentification of feature classes (mineral phases, including porosity), skill of researcher, experience, degree of fatigue, psychological state, and physical conditions (Griffiths and Rosenfeld, 1954; Demirmen, 1972). Data depicting the interoperator variability in

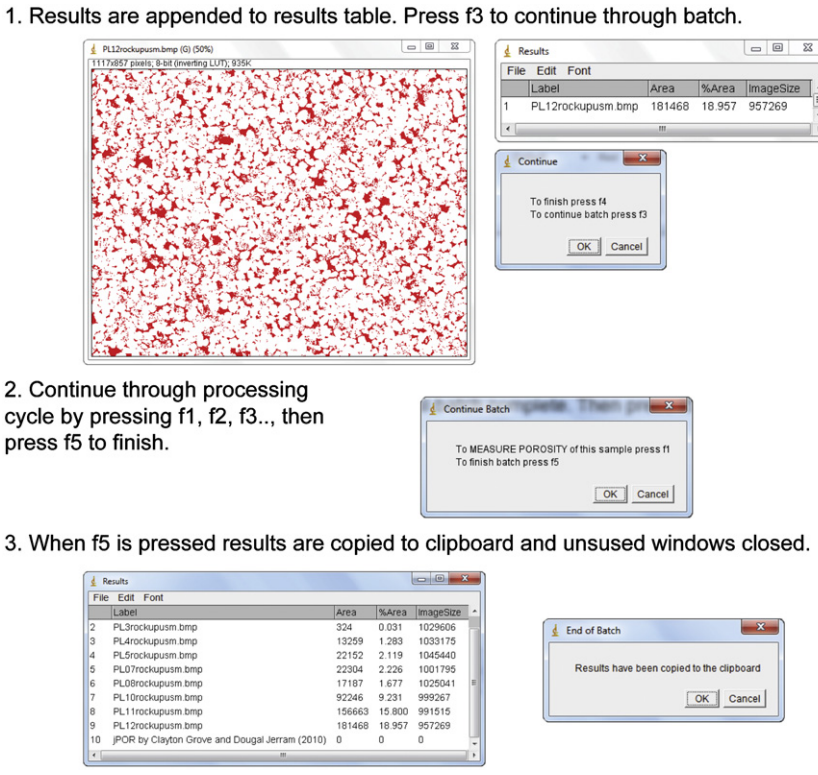

Fig. 5. jPOR workflow after thresholding. 1. Results window and option to finish or continue batch. 2. Porosity measurement of second sample. 3. Results output.

Table 2
jPOR test results.

Sample	Point counting (porosity%)		He injection (porosity%)	jPOR (porosity%)	
	Point count	2σ counting error		jPOR60 (default)	2σ counting error
PL1	0.00	0.00	–	0.01	0.00
PL3	0.10	0.28	–	0.03	0.00
PL4	2.60	1.42	–	1.28	0.02
PL5	3.00	1.53	–	2.12	0.03
PL07	2.90	1.50	–	2.23	0.03
PL08	2.30	1.34	–	1.68	0.03
PL10	9.10	2.57	–	9.23	0.06
PL11	13.60	3.07	–	15.80	0.07
PL12	15.00	3.19	–	18.96	0.08
FellSst13A-139	20.00	3.58	20.65	22.79	0.04
FellSst1A-3	16.00	3.28	15.57	14.09	0.05
FellSst286	21.10	3.65	17.39	21.76	0.05
FellSst9A-84	16.30	3.30	18.80	15.34	0.04
FellSstA	22.80	3.75	19.92	19.74	0.05

Sample	jPOR 10 tested with 10 researchers (porosity%)											
	1	2	3	4	5	6	7	8	9	10	Mean	SD
PL1	0.01	0.01	0.01	0.00	0.01	0.01	0.01	0.01	0.00	0.00	0.01	0.01
PL3	1.76	0.03	0.03	0.00	0.00	0.03	0.03	0.03	0.03	0.03	0.18	0.55
PL4	7.90	1.07	1.28	6.32	1.04	1.28	1.28	1.03	1.28	1.43	2.27	2.52
PL5	1.32	2.12	2.12	2.12	1.65	2.12	2.12	1.65	2.46	2.12	1.95	0.33
PL07	1.59	2.23	2.23	0.54	1.44	2.23	2.15	1.44	1.71	2.23	1.75	0.55
PL08	1.68	1.79	1.68	1.41	1.68	1.68	1.68	1.26	1.68	1.68	1.63	0.16
PL10	9.23	8.28	9.23	6.28	9.23	9.23	9.23	7.68	7.14	9.23	8.54	1.09
PL11	13.83	15.80	15.80	15.80	14.47	15.80	15.80	14.31	16.18	15.80	15.28	0.82
PL12	16.29	18.96	18.96	18.96	19.66	16.78	17.53	16.78	16.78	18.96	18.12	1.25
FellSst13A-139	22.79	19.20	22.79	21.82	22.72	22.79	21.82	22.79	25.62	22.79	22.53	1.56
FellSst1A-3	18.10	14.09	14.09	10.34	14.02	14.09	15.51	14.09	14.09	14.09	14.23	1.88
FellSst286	20.77	17.70	21.76	21.76	21.76	21.76	21.76	21.76	20.77	21.76	21.21	1.29
FellSst9A-84	15.34	19.63	15.34	15.34	19.63	15.34	15.34	15.34	14.65	15.34	16.45	1.86
FellSstA	23.59	19.74	19.74	19.74	17.82	19.74	17.82	19.74	19.74	19.74	19.57	1.57

point counting have been sourced from the literature (Chayes and Fairbairn, 1951; Griffiths and Rosenfeld, 1954; Demirmen, 1972). The interoperator variability for the jPOR method has been tested in the present study by 10 different operators (termed Researcher 1, 2,…,10). Results are presented in Table 2 and Fig. 6.

Counting errors were calculated at the 95.4% confidence level (2σ) using the equations in Galehouse (1971, p. 396). Five hundred points were counted for each thin section which produced counting errors of between $\pm 0\%$ and $\pm 3.8\%$. Using the same equation errors calculated for jPOR were between $\pm 0.002\%$ and $\pm 0.05\%$ (smaller than graph points so not plotted). For point counting the only variable (as 500 points were counted for each sample) was the percentage porosity; hence the counting error reflects that. Where zero porosity was counted the error is zero. jPOR has two variables as the number of "points" counted depends on the image size (here between 3,983,252 and 957,269) and the percentage porosity; the increase from 500 points to the large numbers of pixels within our prepared images

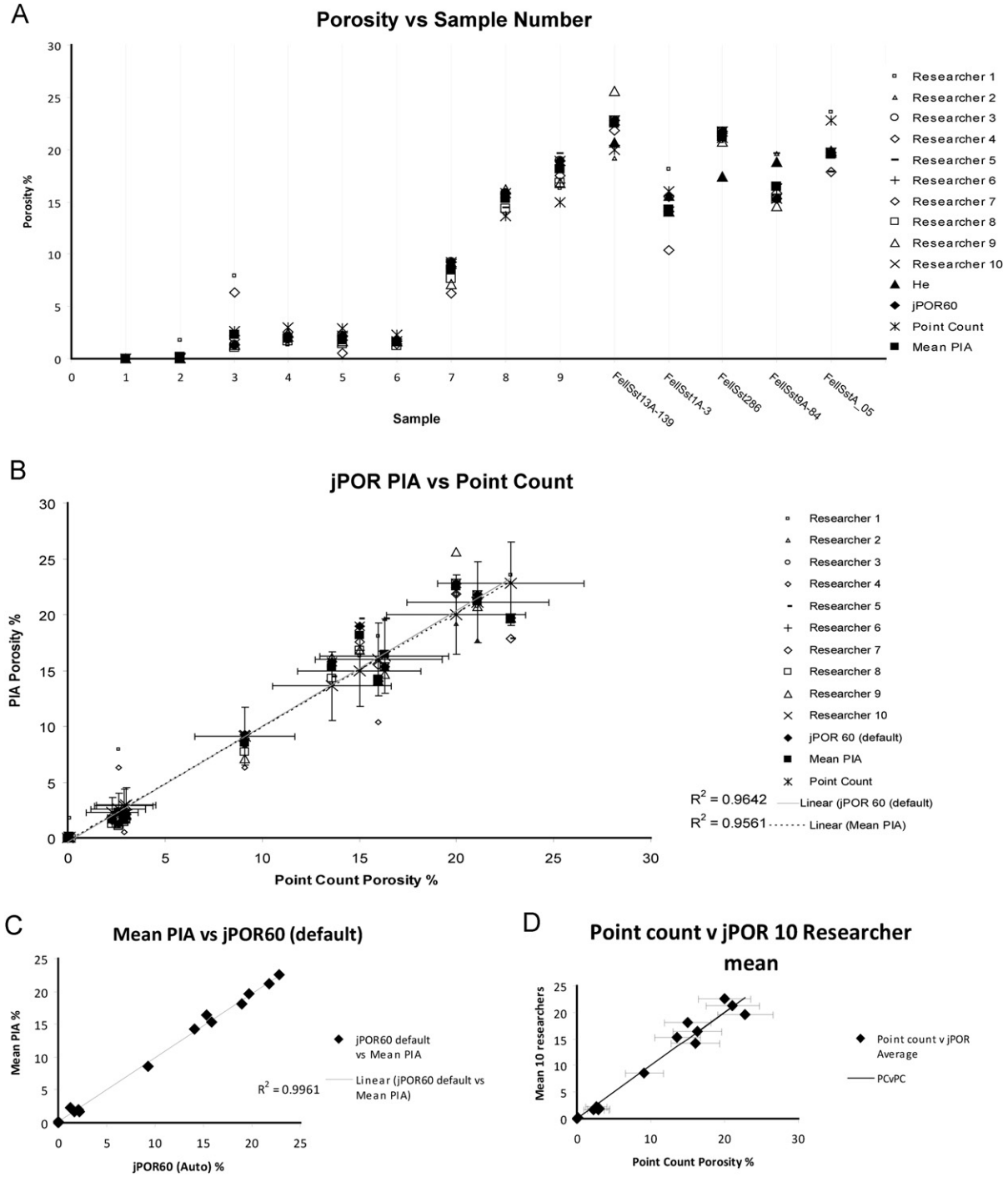

Fig. 6. Compilation of results graphs. (A) Porosity vs. sample for each of the 10 researchers (grey dashed lines with open markers), He injection porosity (solid triangle marker), jPOR60 (solid diamond marker). Point count (double cross marker) and mean PIA (solid square). (B) PIA vs. point count with the same symbology as (A). Counting errors at the 2σ confidence level are for point count data. (C) Mean PIA vs. jPOR60. (D) Point count vs. jPOR 10 researcher average. (For interpretation of the references to colour in this figure legend, the reader is referred to the web version of this article.)

is responsible for the decrease in counting error from a maximum of 3.8% (point count) to 0.1% (jPOR).

Tests between multiple operators showed a mean interoperator variability of 3.5%. The maximum interoperator difference was 7.8%, which was on sample FellSstA; 9/14 samples had differences between researchers less than 3.8% (within the counting error of point counting). In this study the mean standard deviation between operators over the 14 sections was 1.2%. For point counting the interoperator variability is generally considerably higher than between operators using jPOR. In the three studies we have used from the literature (Chayes and Fairbairn, 1951; Griffiths and Rosenfeld, 1954; Demirmen, 1972) the mean interoperator variability was 6.4% with a maximum of 12.2%. The mean standard deviation between operators in the three studies was 2.3% (Chayes and Fairbairn, 1951; Griffiths and Rosenfeld, 1954; Demirmen, 1972). Errors in porosity measurement using point counting and jPOR are listed in Table 3. The interoperator error is rarely identified in geological studies using point counting and is often assumed to be negligible despite its magnitude exceeding the often used "counting error." Indeed errors are often not quoted at all in published point counts, with common counting values between 200 and 400 (e.g., Purvis, 1992; Stokkendal et al., 2009; Khidir and Catuneanu, 2010).

Most jPOR results fall within the 95.4% counting error bars for those from point counting in the same samples. The mean jPOR value was always within the point count counting error and the jPOR 60 (default) value was within the point count counting error for 13/14 samples. The difference between jPOR 60 (default) and point counting was between 0.0% and 4.0% over the 14 sample thin sections with a mean difference of 1.4% with a standard deviation of 1.2%. The difference between the mean jPOR porosity value (10 researchers) and point counting ranged from 0.0% to 3.3% with a mean difference of 1.2% and a standard deviation of 1.1%. The comparison of jPOR 60 (default) with mean porosity values of the 10 test researchers produced a good correlation ($R^2=0.9923$) with a mean difference of 0.6%. The porosity measurements achieved by using jPOR can be considered as providing the most statistically robust compared to point counting, and considering its speed and ease of use, a vast improvement to the way in which we routinely measure porosity from blue-stained thin sections.

Table 3
Comparison of errors between jPOR and point counting.

	Point counting (area %)	jPOR (area%)	Reason for error
Counting error (2σ)	2.5[a] 2.6[b]	0.039[a]	Result of counting observations being an estimate of the true area and not the true fraction
Operator error (σ)	3.1[c] 1.2[b] 2.9[d]	1.2[a]	Misidentification, inconsistent identification, mistakes

Data sourced from this study and Chayes and Fairbairn (1951), Griffiths and Rosenfeld (1954), Demirmen (1972).

[a] This study (10 operators, 14 thin sections, porosity).
[b] Chayes and Fairbairn (1951) (5 operators, 10 thin sections, quartz area).
[c] Griffiths and Rosenfeld (1954) (5 operators, 3 thin sections, quartz area).
[d] Demirmen (1972) (8 operators, 5 thin sections, limestone constituent).

5. Conclusions

Porosity measurements using jPOR combined with the jPOR 60 custom palette make an effective, accurate, and easy method of measuring total optical porosity. The use of the custom 8-bit palette makes it possible to accurately threshold pore space from rock based on hue rather than a single RGB greyscale channel. The calculated counting errors at the 95.4% confidence level for point counting were higher than jPOR, as expected due to the vastly superior number of points counted with jPOR (whole image). Both methods (jPOR and point counting) have an inherent element of operator error defining porosity. The interoperator variability using the jPOR method was less than point counting, probably due to the fact that the whole slide can be viewed in our process, making comparison within the slide possible before a threshold decision is made; this is impossible while point counting.

PIA calculated porosities generally agreed with point counting (within (2σ) point count counting errors), even with user variability among the 10 researchers. The mean value of the 10 researchers agreed well with the point counting values, suggesting that the actual porosity of the rock was well defined by both methods. The fully default jPOR 60 values also produced good results compared with point counting. The similarity between jPOR 60 (default) and the mean value of the 10 test researchers leads to the conclusion that running jPOR 60 without user action at the thresholding stage will produce results as good as point counting but with a smaller counting error and if run automatically with the default setting no operator variability (by definition). Even if operator error is introduced by manual adjustment during thresholding we have shown that to be less than the operator error routinely encountered while point counting.

6. jPOR in the future

jPOR will be continually improved by adding functionality and responding to user reviews. In addition to the appendix attached to this paper the latest jPOR version, palettes, and test files are also available to download from www.geoanalysis.org and clicking on the jPOR tab.

Acknowledgements

We thank the anonymous researchers for testing the macro and giving helpful feedback to refine the interface. Tim Watton is gratefully acknowledged for the loan of hyaloclastite samples. We thank Brian Turner for the Fell Sandstone samples and He injection data. Christopher Hamilton is thanked for his thorough review. We finally thank Ciaran Beggan and Christopher Hamilton for hosting jPOR on www.geoanalysis.org. The lead author was funded by OneNortheast and the Volcanic Margins Research Consortia.

Appendix A. Supporting information

Supplementary data associated with this article can be found in the online version at doi:10.1016/j.cageo.2011.03.002.

References

Andriani, G., Walsh, N., 2002. Physical properties and textural parameters of calcarenitic rocks: qualitative and quantitative evaluations. Engineering Geology 67 (1–2), 5–15.

Beggan, C., Hamilton, C., 2010. New image processing software for analyzing object size-frequency distributions, geometry, orientation, and spatial distribution. Computers & Geosciences 36 (4), 539–549.

Chayes, F., 1949. A simple point counter for thin-section analysis. American Mineralogist 34, 1–11.
Chayes, F., Fairbairn, H., 1951. A test of the precision of thin section analysis by point counter. American Mineralogist 36, 704–712.
Corel Help, 2005. Corel Photopaint X3. Corel Inc., Mountain View, CA.
Crawford, E.C., Mortensen, J.K., 2009. An ImageJ plugin for the rapid morphological characterization of separated particles and an initial application to placer gold analysis. Computers & Geosciences 35 (2), 347–359.
Curtis, B.F., 1971. Measurement of porosity and permeability. In: Carver, R.E. (Ed.), Procedures in Sedimentary Petrology. Wiley Interscience, New York, pp. 653.
DeKeyser, T., 1999. Digital scanning of thin sections and peels. Journal of Sedimentary Research 69 (4), 962.
Demirmen, F., 1971. Counting error in petrographic point-count analysis: a theoretical and experimental study. Mathematical Geology 3 (1), 15–41.
Demirmen, F., 1972. Operator error in petrographic point-count analysis: a theoretical approach. Mathematical Geology 4 (1), 35–43.
Dey, S., Ghosh, S., Debbarma, C., Sarkar, P., Marfai, M., Maiti, S., 2009. Some observations from radiometric '8-bit' data of sediment thin sections based on alternative petrographic image analysis method. Journal of Earth System Science 118 (2), 163–173.
Dickinson, W., Milliken, K., 1995. The diagenetic role of brittle deformation in compaction and pressure solution, Etjo sandstone, Nambia. The Journal of Earth System Science 118 (2), 163–173.
Ehrlich, R., Kennedy, S.K., Crabtree, S.J., Cannon, R.L., 1984. Petrographic image analysis: analysis of reservoir pore complexes. Journal of Sedimentary Petrology 54, 1365–1378.
Fischer, R.V., Schmincke, H.-U., 1984. Pyroclastic Rocks. Springer-Verlag, Berlin, pp. 472.
Galehouse, J., 1971. Point counting. In: Carver, R.E. (Ed.), Procedures in Sedimentary Petrology. Wiley Interscience, New York, pp. 653.
Griffiths, J.C., Rosenfeld, M.A., 1954. Operator variation in experimental research. The Journal of Geology 62, 74–91.
Hersum, T.G., Marsh, B.D., 2007. Igneous textures: on the kinetics behind the words. Elements 3, 247–252.
Higgins, M., 2006. Quantitative Textural Measurements in Igneous and Metamorphic Petrology. Cambridge University Press, .
Higgins, M.D., Roberge, J., 2007. Three magmatic components in the 1793 eruption of Eldfell volcano, Iceland: evidence from plagioclase crystal size distribution (CSD) and geochemistry. Journal of Volcanology and Geothermal Research 161, 247–260.
Jerram, D.A., 2001. Visual comparators for degree of sorting in 2-D and 3-D. Computers & Geosciences 27, 485–492.
Jerram, D.A., Cheadle, M.J., 2000. On the cluster analysis of rocks. American Mineralogist 85, 47–67.
Jerram, D.A., Higgins, M., 2007. 3D analysis of rock textures: quantifying igneous microstructures. Elements 3, 239–245.
Jerram, D.A., Mock, A., Davis, G.R., Field, M., Brown, R.J., 2009. 3D crystal size distributions: a case study on quantifying olivine populations in kimberlites. Lithos 112S, 223–235.
Jerram, D.A., Mountney, N., Holzförster, F., Stollhofen, H., 1999. Internal stratigraphic relationships in the Etendeka Group in the Huab Basin, NW Namibia: understanding the onset of flood volcanism. Journal of Geodynamics 28, 393–418.
Jerram, D.A., Mountney, N., Howell, J., Stollhofen, H., Long, D., 2000. Death of a sand sea: an active aeolian erg systematically buried by the Etendeka Flood Basalts of NW Namibia. Journal of the Geological Society 157, 513–516.
Kang, H.R., 1997. Colour Technology for Electronic Imaging Devices. SPIE- International Society for Optical Engineering, Washington, pp. 5.
Khidir, A., Catuneanu, O., 2010. Reservoir characterization of Scollard-age fluvial sandstones, Alberta foredeep. Marine and Petroleum Geology 27, 2037–2050.
Lamoureux, S.F., Bollmann, J., 2004. Image acquisition. In: Francus, P. (Ed.), Image Analysis, Sediments and Palaeoenvironments. Kluwer Academic Publishers, The Netherlands.
Mock, A., Jerram, D.A., 2005. Crystal size distributions in three dimensions: insights from the 3D reconstruction of a highly porphyritic rock texture. Journal of Petrology 46, 1525–1541.
Morgan, D., Jerram, D.A., 2006. On estimating crystal shape for crystal size distribution analysis. Journal of Volcanology and Geothermal Research 154, 1–7.
Mountney, N., Howell, J., Flint, S., Jerram, D.A., 1999. Climate, sediment supply and tectonics as controls on the deposition and preservation of the Aeolian-fluvial Etjo SandstoneFormation, Namibia. Journal of the Geological Society 156, 771–777.
Murphy, C., 1983. Point counting pores and illuvial clay in thin section. Geoderma 31, 133–150.
Purvis, K., 1992. Lower Permian rotliegend sandstones, southern north sea: a case study of sandstone diagenesis in evaporite-associated sequences. Sedimentary Geology 77, 155–171.
Rasband, W.S., ImageJ, US National Institutes of Health, Bethesda, Maryland, USA, http://rsb.info.nih.gov/ij/, 1997–2009.
Stokkendal, J.H., Friis, H., Svendsen, J.B., Poulsen, M.L.K., Hamberg, L., 2009. Predictive permeability variations in a Hermod sand reservoir, Stine Segments, Siri Field, Danish North Sea. Marine and Petroleum Geology 26, 397–415.
Tovey, N.K., Hounslow, M.W., 1995. Quantitative micro-porosity and orientation analysis in soils and sediments. Journal of the Geological Society 152, 119–129.
Tucker, M.E., 2001. Sedimentary Petrology, 3rd ed. Blackwell Science, Oxford, 262 pp.

References

A

Aarnes, I., Fristad, K., Planke, S. and Svensen, H. (2011a) The impact of host-rock composition on devolatilization of sedimentary rocks during contact metamorphism around mafic sheet intrusions. *Geochemistry, Geophysics, Geosystems*, **121,** 10019.

Aarnes, I., Svensen, H., Polteau, S. and Planke, S. (2011b) Contact metamorphic devolatilization of shales in the Karoo Basin, South Africa, and the effects of multiple sill intrusions. *Chemical Geology*.

Ackermann, P.B. and Walker, F. (1960) Vitrification of arkose by Karroo dolerite near Heilbron, Orange free state. *Quarterly Journal of the Geological Society*, **116,** 239-253.

Andriani, G. and Walsh, N. (2002) Physical properties and textural parameters of calcarenitic rocks: qualitative and quantitative evaluations. *Engineering Geology*, **67,** 5-15.

Ahmed, W. (2003) Effects of heat-flow and hydrothermal fluids from volcanic intrusions on authigenic mineralization in sandstone formations. *Bulletin of the Chemical Society of Ethiopia*, **16,** 37.

Allman, M., Lawrence, D.F. and Kirkaldy, J.F. (1972) *Geological laboratory techniques*. Blandford Press London.

Andersen, M. (1988) Late Cretaceous and early Tertiary extension and volcanism around the Faeroe Islands. *Geological Society, London, Special Publications*, **39,** 115-122.

Archer, S.G., Bergman, S.C., Iliffe, J., Murphy, C.M. and Thornton, M. (2005) Palaeogene igneous rocks reveal new insights into the geodynamic evolution and petroleum potential of the Rockall Trough, NE Atlantic Margin. *Basin Research*, **17,** 171-201.

Arnórsson, S. (1986) Chemistry of gases associated with geothermal activity and volcanism in Iceland: A review. *Journal of Geophysical Research: Solid Earth*, **91,** 12261-12268.

B

Bailey, S., Bell, R. and Peng, C. (1958) PLASTIC DEFORMATION OF QUARTZ IN NATURE. *Geological Society of America Bulletin*, **69,** 1443-1466.

Ballance, P.F. and Waiters, W. (2002) Hydrothermal alteration, contact metamorphism, and authigenesis in Ferrar Supergroup and Beacon Supergroup rocks, Carapace Nunatak, Allan Hills, and Coombs Hills, Victoria Land, Antarctica. *New Zealand Journal of Geology and Geophysics*, **45,** 71-84.

Bamford, M.K. (2000) Fossil woods of Karoo age deposits in South Africa and Namibia as an aid to biostratigraphical correlation. *Journal of African Earth Sciences*, **31,** 119-132.

Barker, C.E., Bone, Y. and Lewan, M.D. (1998) Fluid inclusion and vitrinite-reflectance geothermometry compared to heat-flow models of maximum paleotemperature next to dikes, western onshore Gippsland Basin, Australia. *International Journal of Coal Geology*, **37,** 73-111.

Barker, D. (2007) Origin of cementing calcite in" carbonatite" tuffs. *Geology*, **35,** 371.

Beitler, B., Chan, M. and Parry, W. (2003) Bleaching of Jurassic Navajo sandstone on Colorado Plateau Laramide highs: Evidence of exhumed hydrocarbon supergiants? *Geology*, **31,** 1041.

Beitler, B., Parry, W. and Chan, M. (2005) Fingerprints of fluid flow: chemical diagenetic history of the Jurassic Navajo Sandstone, southern Utah, USA. *Journal of Sedimentary Research*, **75,** 547.

Bell, B. and Butcher, H. (2002) On the emplacement of sill complexes: evidence from the Faroe-Shetland Basin. *Geological Society, London, Special Publications*, **197,** 307-329.

Bermúdez, A. and Delpino, D.H. (2008) Concentric and radial joint systems within basic sills and their associated porosity enhancement, Neuquén Basin, Argentina. *Geological Society, London, Special Publications*, **302,** 185-198.

Bloch, S., Lander, R.H. and Bonnell, L. (2002) Anomalously high porosity and permeability in deeply buried sandstone reservoirs: Origin and predictability. *AAPG Bulletin*, **86,** 301-328.

Bonnichsen, B. and Godchaux, M. (2002) Late Miocene, Pliocene, and Pleistocene geology of southwestern Idaho with emphasis on basalts in the Bruneau-Jarbidge, Twin Falls, and western Snake River Plain regions. *Tectonic and magmatic evolution of the Snake River Plain Volcanic Province. Idaho Geol Surv Bull*, **30,** 387-434.

Bowen, G. and Revenaugh, J. (2003) Interpolating the isotopic composition of modern meteoric precipitation. *Water Resources Research*, **39,** 1299.

Branney, M.J., Bonnichsen, B., Andrews, G.D.M., Ellis, B., Barry, T.L. and McCurry, M. (2008) 'Snake River (SR)-type' volcanism at the Yellowstone hotspot track: distinctive products from unusual, high-temperature silicic super-eruptions. *Bulletin of Volcanology*, **70,** 293-314.

Brauckmann, F.J. and Füchtbauer, H. (1983) Alterations of cretaceous siltstones and sandstones near basalt contacts (Nûgssuaq, Greenland). *Sedimentary Geology*, **35,** 193-213.

Brey, G.P. and Kohler, T. (1990) Geothermobarometry in Four-phase Lherzolites II. New Thermobarometers, and Practical Assessment of Existing Thermobarometers. *Journal of Petrology*, **31,** 1353-1378.

Brown, D.J. and Bell, B.R. (2007) How do you grade peperites? *Journal of Volcanology and Geothermal Research*, **159,** 409-420.

Brownlow, A.H. (1996) *Geochemistry*. Prentice Hall Englewood Cliffs.

Burley, S. (1984) Patterns of diagenesis in the Sherwood Sandstone Group (Triassic), United Kingdom. *Clay Minerals*, **19,** 403-440.

Bucher, K. and Grapes, R.H. (2011) *Petrogenesis of metamorphic rocks*. Springerverlag Berlin Heidelberg.

Bryan, S.E., Peate, I.U., Peate, D.W., Self, S., Jerram, D.A., Mawby, M.R., Marsh, J. and Miller, J.A. (2010) The largest volcanic eruptions on Earth. *Earth-Science Reviews*, **102,** 207-229.

C

Carter, N.L., Christie, J.M. and Griggs, D.T. (1964) Experimental deformation and recrystallization of quartz. *The Journal of Geology***,** 687-733.

Chayes, F. (1949) A simple point counter for thin-section analysis. *American Mineralogist*, **34,** 1-11.

Clemson, J., Cartwright, J. and Booth, J. (1997) Structural segmentation and the influence of basement structure on the Namibian passive margin. *Journal of the Geological Society*, **154,** 477-482.

Cooper, R.F., Fanselow, J.B. and Poker, D.B. (1996) The mechanism of oxidation of a basaltic glass: Chemical diffusion of network-modifying cations. *Geochimica et Cosmochimica Acta*, **60,** 3253-3265.

Cooper, J.R., Crelling, J.C., Rimmer, S.M. and Whittington, A.G. (2007) Coal metamorphism by igneous intrusion in the Raton Basin, CO and NM: implications for generation of volatiles. *International journal of coal geology*, **71,** 15-27.

Cooper, F.J., van Soest, M.C. and Hodges, K.V. (2011) Detrital zircon and apatite (U-Th)/He geochronology of intercalated baked sediments: A new approach to dating young basalt flows. *Geochemistry, Geophysics, Geosystems*, **12,** Q07003.

Correa-Gomes, L., Souza Filho, C., Martins, C. and Oliveira, E. (2001) Development of symmetrical and asymmetrical fabrics in sheet-like igneous bodies: the role of magma flow and wall-rock displacements in theoretical and natural cases. *Journal of Structural Geology*, **23,** 1415-1428.

Crawford, E.C. and Mortensen, J.K. (2009) An ImageJ plugin for the rapid morphological characterization of separated particles and an initial application to placer gold analysis. *Computers & Geosciences*, **35,** 347-359.

Crisp, J., Cashman, K., Bonini, J., Hougen, S. and Pieri, D. (1993) Crystallization history of the 1984 Mauna Loa lava flow.

Crisp, J. and Baloga, S. (1994) Influence of crystallization and entrainment of cooler material on the emplacement of basaltic aa lava flows. *Journal of geophysical research*, **99,** 11819-11,831.

Curtis, B.F. (1971) Measurement of porosity and permeability. *Procedures in Sedimentary Petrology: New York, Wiley***,** 335-363.

D

David, J.M., Simões, M.G., Anelli, L.E., Rohn, R. and Holzfoerster, F. (2011) Permian bivalve molluscs from the Gai-As Formation, northern Namibia: systematics, taphonomy and biostratigraphy. *Alcheringa: An Australasian Journal of Palaeontology*, **35,** 497-516.

Davison, I. (1999) Tectonics and hydrocarbon distribution along the Brazilian South Atlantic margin. *Geological Society, London, Special Publications*, **153,** 133-151.

Deer, W.A., Howie, R.A., Zussman. (1966) *An introduction to the rock-forming minerals*. Longman.

De Keyser, T. (1999) Digital scanning of thin sections and peels. *Journal of Sedimentary Research*, **69,** 962.

Delaney, P.T. and Pollard, D.D. (1982) Solidification of basaltic magma during flow in a dike. *American Journal of Science*, **282,** 856-885.

Delmelle, P. and Stix. (2000) Volcanic gases. In: Sigurdsson, H. et al., (Eds), Encyclopedia of Volcanoes.

Academic press, 803-145.

Demirmen, F. (1971) Counting error in petrographic point-count analysis: A theoretical and experimental study. *Mathematical Geology*, **3,** 15-41.

Dey, S., Ghosh, S., Debbarma, C., Sarkar, P., Marfai, M. and Maiti, S. (2009) Some observations from radiometric '8 bit' data of sediment thin sections based on alternative petrographic image analysis method. *Journal of Earth System Science*, **118,** 163-173.

Dickinson, W. and Milliken, K. (1995) The diagenetic role of brittle deformation in compaction and pressure solution, Etjo sandstone, Namibia. *The Journal of Geology*, **103,** 339-347.

Duarte, L.C., Hartmann, L.A., Vasconcellos, M.A.Z., Medeiros, J.T.N. and Theye, T. (2009) Epigenetic formation of amethyst-bearing geodes from Los Catalanes gemological district, Artigas, Uruguay, southern Paraná Magmatic Province. *Journal of volcanology and geothermal research*, **184,** 427-436.

Duncan, A., Newton, S., Van den Berg, C. and Reid, D. (1989) Geochemistry and petrology of dolerite sills in the Huab River valley, Damaraland, north western Namibia. *Communications of the Geological Survey of Namibia*, **5,** 5-17.

Duncan, L., Helland-Hansen, D. & Dennehy, C. (2009). The Rosebank discovery: A new play type in intra basalt reservoirs of the North Atlantic volcanic province. DEVEX 2009. 6th European Production & Development Conference - Crossing the Boundaries in Pursuit of Ultimate Recovery, 12-13 May, Aberdeen Exhibition & Conference Centre.

Dutrow, B.L., Travis, B.J., Gable, C.W. and Henry, D.J. (2001) Coupled heat and silica transport associated with dike intrusion into sedimentary rock: effects on isotherm location and permeability evolution. *Geochimica et Cosmochimica Acta*, **65,** 3749-3767.

E

Eckardt, F., Soderberg, K., Coop, L., Muller, A., Vickery, K., Grandin, R., Jack, C., Kapalanga, T. and Henschel, J. (2012) The nature of moisture at Gobabeb, in the central Namib Desert. *Journal of Arid Environments*.

Edwards, B., Magnússon, E., Thordarson, T., Guđmundsson, M.T., Höskuldsson, A., Oddsson, B. and Haklar, J. (2012) Interactions between lava and snow/ice during the 2010 Fimmvörðuháls eruption, south-central Iceland. *Journal of Geophysical Research: Solid Earth*, **117,** B04302.

Ehrlich, R., Kennedy, S., Crabtree, S. and Cannon, R. (1984) Petrographic image analysis: I, Analysis of reservoir pore complexes.

Eklund, O. and Lindberg, B. (1992) Interaction between basaltic melts and their wallrock in dykes and sills in Åland, southwestern Finland. *GFF*, **114,** 93-102.

Ellefsen, M., Boldreel, L. and Larsen, M. (2010) Intra-basalt units and base of the volcanic succession east of the Faroe Islands exemplified by interpretation of offshore 3D seismic data, **7**, pp. 1033-1042. Geological Society of London.

Ellis, D., Bell, B.R., Jolley, D.W. and O'Callaghan, M. (2002) The stratigraphy, environment of eruption and age of the Faroes Lava Group, NE Atlantic Ocean. *Geological Society, London, Special Publications*, **197,** 253-269.

Emery, D. and Robinson, A. (1993) Porosity and Permeability Prediction. *Inorganic Geochemistry: Applications to Petroleum Geology***,** 129-169.

Erlank, A., Marsh, J., Duncan, A., Miller, R., Hawkesworth, C., Betton, P. and Rex, D. (1984) Geochemistry and petrogenesis of the Etendeka volcanic rocks from SWA/Namibia. *Special Publication of Geological Society of South Africa*, **13,** 195-245.

Ernesto, M., Raposo, M., Marques, L., Renne, P., Diogo, L. and De Min, A. (1999) Paleomagnetism, geochemistry and 40Ar/39Ar dating of the North-eastern Paraná Magmatic Province: tectonic implications. *Journal of Geodynamics*, **28,** 321-340.

Ernst, R.E. and Bell, K. (2010) Large igneous provinces (LIPs) and carbonatites. *Mineralogy and Petrology*, **98,** 55-76.

EWART, A., MARSH, J.S., MILNER, S.C., DUNCAN, A.R., KAMBER, B.S. and ARMSTRONG, R.A. (2004a) Petrology and Geochemistry of Early Cretaceous Bimodal Continental Flood Volcanism of the NW Etendeka, Namibia. Part 1: Introduction, Mafic Lavas and Re-evaluation of Mantle Source Components. *Journal of Petrology*, **45,** 59-105.

EWART, A., MARSH, J.S., MILNER, S.C., DUNCAN, A.R., KAMBER, B.S. and ARMSTRONG, R.A. (2004b) Petrology and Geochemistry of Early Cretaceous Bimodal Continental Flood Volcanism of the NW Etendeka, Namibia. Part 2: Characteristics and Petrogenesis of the High-Ti Latite and High-Ti and Low-Ti Voluminous Quartz Latite Eruptives. *Journal of Petrology*, **45,** 107-138.

Ewart, A., Milner, S., Armstrong, R. and Dungan, A. (1998a) Etendeka volcanism of the Goboboseb Mountains and Messum Igneous Complex, Namibia. Part I: Geochemical evidence of early Cretaceous Tristan plume melts and the role of crustal contamination in the Parana-Etendeka CFB. *Journal of Petrology*, **39,** 191.

Ewart, A., Milner, S., Armstrong, R. and Duncan, A. (1998b) Etendeka volcanism of the Goboboseb Mountains and Messum Igneous Complex, Namibia. Part II: Voluminous quartz latite volcanism of the Awahab magma system. *Journal of Petrology*, **39,** 227.

Ewart, A., Milner, S., Duncan, A. and Bailey, M. (2002) The Cretaceous Messum igneous complex, SW Etendeka, Namibia: reinterpretation in terms of a downsag-cauldron subsidence model. *Journal of volcanology and geothermal research*, **114,** 251-273.

F

Faure, K. and Cole, D. (1999) Geochemical evidence for lacustrine microbial blooms in the vast Permian Main Karoo, Paraná, Falkland Islands and Huab basins of southwestern Gondwana. *Palaeogeography, Palaeoclimatology, Palaeoecology*, **152,** 189-213.

Folk, R.L. (1976) Reddening of desert sands: Simpson Desert, NT, Australia. *Journal of Sedimentary Research*, **46**.

Franke, D. (2012) Rifting, lithosphere breakup and volcanism: Comparison of magma-poor and volcanic rifted margins. *Marine and Petroleum Geology*.

Frankel, J. (1949) A note on the vitrification of Karroo sediment by dolerite intrusions. *Transactions of the Royal Society of South Africa*, **32,** 287-293.

Fu, Q., Lu, P., Konishi, H., Dilmore, R., Xu, H., Seyfried Jr, W.E. and Zhu, C. (2009) Coupled alkali-feldspar dissolution and secondary mineral precipitation in batch systems: 1. New experiments at 200 °C and 300 bars. *Chemical Geology*, **258,** 125-135.

Galehouse, J. (1971) Point counting. *Procedures in sedimentary petrology: New York, Wiley-Interscience*, **653,** 385-407.

Galland, O., Planke, S., Neumann, E.-R. and Malthe-Sørenssen, A. (2009) Experimental modelling of shallow magma emplacement: Application to saucer-shaped intrusions. *Earth and Planetary Science Letters*, **277,** 373-383.

Ghosh, P., Sayeed, M.R.G., Islam, R. and Hundekari, S.M. (2006) Inter-basaltic clay (bole bed) horizons from Deccan traps of India: Implications for palaeo-weathering and palaeo-climate during Deccan volcanism. *Palaeogeography, Palaeoclimatology, Palaeoecology*, **242,** 90-109.

Gibbs, R. (1971) X-ray diffraction mounts. *Procedures in Sedimentary Petrology. Wiley-Interscience, New York***,** 531-539.

Gilg, H., Morteani, G., Kostitsyn, Y., Preinfalk, C., Gatter, I. and Strieder, A. (2003) Genesis of amethyst geodes in basaltic rocks of the Serra Geral Formation (Ametista do Sul, Rio Grande do Sul, Brazil): a fluid inclusion, REE, oxygen, carbon, and Sr isotope study on basalt, quartz, and calcite. *Mineralium Deposita*, **38,** 1009-1025.

Gladczenko, T.P., Skogseid, J. and Eldhom, O. (1998) Namibia volcanic margin. *Marine Geophysical Research*, **20,** 313-341.

Glen, J., Renne, P., Milner, S. and Coe, R. (1997) Magma flow inferred from anisotropy of magnetic susceptibility in the coastal Parana-Etendeka igneous province: Evidence for rifting before flood volcanism. *Geology*, **25,** 1131.

Gluyas, J. and Cade, C.A. (1998) Prediction of porosity in compacted sands. *MEMOIRS-AMERICAN ASSOCIATION OF PETROLEUM GEOLOGISTS***,** 19-28.

Godchaux, M. and Bonnichsen, B. (2002) Syneruptive magma-water and posteruptive lava-water interactions in the Western Snake River Plain, Idaho, during the past 12 million years. *Tectonic and magmatic evolution of the Snake River Plain Volcanic Province. Idaho Geol Surv Bull*, **30,** 387-434.
Govindaraju, K. (1994) 1994 compilation of working values and sample description for 383 geostandards. *Geostandards newsletter*, **18,** 1-158.

Grapes, R. (2010) *Pyrometamorphism*. Springer.

Gray, D., Foster, D.A., Meert, J.G., Goscombe, B.D., Armstrong, R., Trouw, R.A.J. and Passchier, C.W. (2008) A Damara orogen perspective on the assembly of southwestern Gondwana. *Geological Society, London, Special Publications*, **294,** 257-278.

Griffiths, J.C. and Rosenfeld, M.A. (1954) Operator Variation in Experimental Research. *The Journal of Geology*, **62,** 74-91.

Grove, C. and Jerram, D.A. (2011) jPOR: An ImageJ macro to quantify total optical porosity from blue-stained thin sections. *Computers & Geosciences*.
Grove, C. (2013) Submarine hydrothermal vent complexes in the Paleocene of the Faroe-Shetland Basin: Insights from three-dimensional seismic and petrographical data. *Geology*, **41,** 71-74.

Hangx, S.J.T. and Spiers, C.J. (2009) Reaction of plagioclase feldspars with CO2 under hydrothermal conditions. *Chemical Geology*, **265,** 88-98.

Hawkesworth, C., Kelley, S., Turner, S., Le Roex, A. and Storey, B. (1999) Mantle processes during Gondwana break-up and dispersal. *Journal of African Earth Sciences*, **28,** 239-261.

Hawkesworth, C., Gallagher, K., Kelley, S., Mantovani, M., Peate, D., Regelous, M. and Rogers, N. (1992) Paraná magmatism and the opening of the South Atlantic. *Geological Society, London, Special Publications*, **68,** 221-240.

Heiri, O., Lotter, A.F. and Lemcke, G. (2001) Loss on ignition as a method for estimating organic and carbonate content in sediments: reproducibility and comparability of results. *Journal of paleolimnology*, **25,** 101-110.

Helland-Hansen, D. (2009) Rosebank - Challenges to development from a subsurface perspective. In:

Varming, T. & Ziska, H. (eds). Faroe Islands Exploration Conference: Proceedings of the 2nd Conference.

Annales Societatis Scientiarum Færoensis, Tórshavn**, 50**, 241-245.

Henley, R.W. and Ellis, A.J. (1983) Geothermal systems ancient and modern: a geochemical review. *Earth-Science Reviews*, **19,** 1-50.

Hiscock, K. (2005) Hydrogeology, Blackwell, Oxford.

Holford, S., Schofield, N., MacDonald, J., Duddy, I. and Green, P. SEISMIC ANALYSIS OF IGNEOUS SYSTEMS IN SEDIMENTARY BASINS AND THEIR IMPACTS ON HYDROCARBON PROSPECTIVITY: EXAMPLES FROM THE SOUTHERN AUSTRALIAN MARGIN.

Holness, M. (1999) Contact metamorphism and anatexis of Torridonian arkose by minor intrusions of the Rum Igneous Complex, Inner Hebrides, Scotland. *Geological Magazine*, **136,** 527-542.

Holness, M. and Watt, G. (2002) The aureole of the Traigh Bhan na Sgurra sill, Isle of Mull: reaction-driven micro-cracking during pyrometamorphism. *Journal of Petrology*, **43,** 511-534.

Holness, M.B. and Humphreys, M.C.S. (2003) The Traigh Bhàn na Sgùrra Sill, Isle of Mull: Flow Localization in a Major Magma Conduit. *Journal of Petrology*, **44,** 1961-1976.

Holness, M.B., Dane, K., Sides, R., Richardson, C. and Caddick, M. (2005) Melting and melt segregation in the aureole of the Glenmore Plug, Ardnamurchan. *Journal of Metamorphic Geology*, **23,** 29-43.

Holness, M.B., Sides, R., Prior, D.J., Cheadle, M.J. and Upton, B.G.J. (2012) The peridotite plugs of Rum: Crystal settling and fabric development in magma conduits. *Lithos*, **134–135,** 23-40.

Hooper, P.R. (1997) The Columbia River flood basalt province: Current status. In: *Large Igneous Provinces: Continental, Oceanic, and Planetary Flood Volcanism*, *Geophys. Monogr. Ser.*, **100**, pp. 1-27. AGU, Washington, DC.

Horsthemke, E., Ledendecker, S., Paroda. (1990) Depositional environments and stratigraphic correlations of the Karoo Sequence in North-Western Damaraland. Communications of the Geological Survey of Namibia, **6,** 63-75.

Houseknecht, D.W. (1984) Influence of grain size and temperature on intergranular pressure solution, quartz cementation, and porosity in a quartzose sandstone. *Journal of Sedimentary Research*, **54**.

Houseknecht, D.W. (1988) Intergranular pressure solution in four quartzose sandstones. *Journal of Sedimentary Research*, **58**.

Howell, J. and Mountney, N. (2001) Aeolian grain flow architecture: hard data for reservoir models and implications for red bed sequence stratigraphy. *Petroleum Geoscience*, **7,** 51.

Hudson, J. and Andrews, J. (1987) The diagenesis of the Great Estuarine Group, Middle Jurassic, Inner Hebrides, Scotland. *Geological Society, London, Special Publications*, **36,** 259-276.

Hutton, D. (2009) Insights into magmatism in volcanic margins: bridge structures and a new mechanism of basic sill emplacement–Theron Mountains, Antarctica. *Petroleum Geoscience*, **15,** 269-278.

I

Ibrahim, K.M. and Al-Malabeh, A. (2006) Geochemistry and volcanic features of Harrat El Fahda: A young volcanic field in northwest Arabia, Jordan. *Journal of Asian Earth Sciences*, **27,** 147-154.

J

Jakobsson, S. and Íslands, N. (1978) *Environmental factors controlling the palagonitization of the Surtsey tephra, Iceland*. Museum of Natural History, Dept. of Geology and Geography.

Jerram, D., Mountney, N., Holzförster, F. and Stollhofen, H. (1999a) Internal stratigraphic relationships in the Etendeka Group in the Huab Basin, NW Namibia: understanding the onset of flood volcanism. *Journal of Geodynamics*, **28,** 393-418.

Jerram, D.A., Mountney, N. and Stollhofen, H. (1999b) Facies architecture of the Etjo Sandstone Formation and its interaction with the Basal Etendeka Flood Basalts of northwest Namibia: implications for offshore prospectivity. *Geological Society, London, Special Publications*, **153,** 367-380.

Jerram, D., Mountney, N., Howell, J., Long, D. and Stollhofen, H. (2000a) Death of a sand sea: an active aeolian erg systematically buried by the Etendeka flood basalts of NW Namibia, **157**, pp. 513-516. Geological Soc London.

Jerram, D. and Robbe, O. (2001) Building a 3-D model of a flood basalt: an example from the Etendeka, NW Namibia. *Visual Geosciences*, **6,** 1-8.

Jerram, D. and Stollhofen, H. (2002a) Lava–sediment interaction in desert settings; are all peperite-like textures the result of magma–water interaction? *Journal of volcanology and geothermal research*, **114,** 231-249.

Jerram, D.A. (2002b) Volcanology and fades architecture of flood basalts. *Volcanic Rifted Margins***,** 119.

Jungslager, E.H.A. (1999) Petroleum habitats of the Atlantic margin of South Africa. *Geological Society, London, Special Publications*, **153,** 153-168.

Jerram, D.A., Mock, A., Davis, G.R., Field, M. and Brown, R.J. (2009) 3D crystal size distributions: A case study on quantifying olivine populations in kimberlites. *Lithos*, **112,** 223-235.

K

Keszthelyi, L. (1995) Measurements of the cooling at the base of pahoehoe flows. *Geophysical research letters*, **22,** 2195-2198.

Khidir, A. and Catuneanu, O. (2010) Reservoir characterization of Scollard-age fluvial sandstones, Alberta foredeep. *Marine and Petroleum Geology*, **27,** 2037-2050.

Kille, I., Thompson, R., Morrison, M. and Thompson, R. (1986) Field evidence for turbulence during flow of basalt magma through conduits from southwest Mull. *Geological Magazine*, **123,** 693-697.

King, D.W. (1998) Role of Carbonate Speciation on the Oxidation Rate of Fe(II) in Aquatic Systems. *Environmental Science & Technology*, **32,** 2997-3003.

Kirkland, D.W., Denison, R.E. and Rooney, M.A. (1995) Diagenetic alteration of Permian strata at oil fields of south central Oklahoma, USA. *Marine and Petroleum Geology*, **12,** 629-644.

Kitchen, D. (1984) Pyrometamorphism and the contamination of basaltic magma at Tieveragh, Co. Antrim. *Journal of the Geological Society*, **141,** 733-745.

Krynauw, J., Hunter, D. and Wilson, A. (1988) Emplacement of sills into wet sediments at Grunehogna, western Dronning Maud Land, Antarctica. *Journal of the Geological Society*, **145,** 1019-1032.

L

Lamers, E. and Carmichael, S. (1999) The Paleocene deepwater sandstone play West of Shetland. In: *Geological Society, London, Petroleum Geology Conference series*, **5**, pp. 645-659. Geological Society of London.

Lamoureux, S.F.,Bollmann,J.,(2004) Imageacquisition.In:Francus,P.(Ed.),Image Analysis, SedimentsandPalaeoenvironments.KluwerAcademicPublishers, The Netherlands.

Lin, T.C. and Qun, P. (1987) On the formation of regmaglypts on meteorites. *Fluid Dynamics Research*, **1,** 191-199.

Long, P.E. and Wood, B.J. (1986) Structures, textures, and cooling histories of Columbia River basalt flows. *Geological Society of America Bulletin*, **97,** 1144-1155.

Lundegard, P.D. (1992) Sandstone porosity loss; a" big picture" view of the importance of compaction. *Journal of Sedimentary Research*, **62,** 250-260.

M

Ma, Y., Liu, C., Zhao, J., Huang, L., Yu, L. and Wang, J. (2007) Characteristics of bleaching of sandstone in northeast of Ordos Basin and its relationship with natural gas leakage. *Science in China Series D: Earth Sciences*, **50,** 153-164.

Mainprice, D., Bouchez, J.-L., Blumenfeld, P. and Tubià, J.M. (1986) Dominant c slip in naturally deformed quartz: implications for dramatic plastic softening at high temperature. *Geology*, **14,** 819-822.

Malde, H.E. (1989) Geologic map of the Breuneau Formation in the C.J Strike Dam and Breneau quadrangles, southwestern Idaho. USGS, Reston, Virginia.

Marsh, J., Erlank, A. and Duncan, A. (1991) Preliminary geochemical data for dolerite dykes and sills of the southern part of the Etendeka Igneous Province. *Communications of the Geological Survey of Namibia*, **7,** 71-73.

Marsh, J., Ewart, A., Milner, S., Duncan, A. and Miller, R. (2001) The Etendeka Igneous Province: magma types and their stratigraphic distribution with implications for the evolution of the Parana-Etendeka flood basalt province. *Bulletin of Volcanology*, **62,** 464-486.

Marsh, J., Swart, R. and Phillips, D. (2003) Implications of a new 40Ar/39Ar age for a basalt flow interbedded with the Etjo Formation, northeast Namibia. *South African Journal of Geology*, **106,** 281-286.

Marsh, J. and Milner, S. (2007) Stratigraphic correlation of the Awahab and Tafelberg Formations, Etendeka Group, Namibia, and location of an eruptive site for flood basalt volcanism. *Journal of African Earth Sciences*, **48,** 329-340.

MATSUI, E., SALATI, E. and MARINI, O. (1974) D/H and 18O/16O Ratios in Waters Contained in Geodes from the Basaltic Province of Rio Grande do Sul, Brazil. *Geological Society of America Bulletin*, **85,** 577-580.

Magee, C., Stevenson, C., O'Driscoll, B., Schofield, N. and McDermott, K. (2012) An alternative emplacement model for the classic Ardnamurchan cone sheet swarm, NW Scotland, involving lateral magma supply via regional dykes. *Journal of Structural Geology*.

Magee, C., Jackson, C.A.-L. and Schofield, N. (2013) The influence of normal fault geometry on igneous sill emplacement and morphology. *Geology*, **41,** 407-410.

Mckinley, J., Worden, R. and Ruffell, A. (2001) Contact diagenesis: The effect of an intrusion on reservoir quality in the Triassic Sherwood sandstone group, northern Ireland. *Journal of Sedimentary Research*, **71,** 484-495.

McMillian, I.K. (1990) Foraminiferal biostratigraphy of the Barremian to Miocene rocks of the Kudu 9A-1, 9A-2 and 9A-3 boreholes. *Communications of the Geological Survey of Namibia,* **6,** 23-31.

Merguerian, C. and Sanders, J.E. (1995) Late syn-intrusive clastic dikes at the base of the Palisades intrusive sheet, Fort Lee, NJ, imply a shallow (~ 3 to 4 km) depth of intrusion. *Geology of Long Island and metropolitan New York. State University of New York, Stony Brook, NY***,** 54-63.

Milner, S.C., Duncan, A.R. (1987) Geochemical characterization of quartz latite units in the Etendeka Formation. *Communications of the Geological Survey of Namibia*, **3,** 83-90.

Milner, S., Duncan, A. and Ewart, A. (1992) Quartz latite rheoignimbrite flows of the Etendeka Formation, north-western Namibia. *Bulletin of Volcanology*, **54,** 200-219.

Milner, S.C., Duncan, A.R., Ewart, A., Marsh, J.S. (1994). Promotion of the Etendeka Formation to Group status: A new integrated stratigraphy. *Communications of the Geological Survey of Namibia*. **9,** 5-11.

Milner, S., Duncan, A., Whittingham, A. and Ewart, A. (1995a) Trans-Atlantic correlation of eruptive sequences and individual silicic volcanic units within the Paraná-Etendeka igneous province. *Journal of volcanology and geothermal research*, **69,** 137-157.

MILNER, S. and LE, R. (1995b) Age of Mesozoic igneous rocks in northwesternNamibia, and their relationship to continental breakup. *Journal of Geological Society*, **152,** 97.

Milner, S.C. and Ewart, A. (1989) The geology of the Goboboseb Mountain volcanics and their relationship to the Messum Complex, Namibia. Communications of the Geological Survey of Namibia, **5**, 31-40.

Mock, A. and Jerram, D. (2005) Crystal size distributions (CSD) in three dimensions: insights from the 3D reconstruction of a highly porphyritic rhyolite. *Journal of Petrology*, **46,** 1525-1541.

Moore, D.M. and Reynolds Jr, R.C. (1989) *X-ray diffraction and the identification and analysis of clay minerals*. Oxford University Press (OUP).

Morgan, D. and Jerram, D. (2006) On estimating crystal shape for crystal size distribution analysis. *Journal of volcanology and geothermal research*, **154,** 1-7.

Moulton, G.F. (1926) Some features of redbed bleaching. *AAPG bulletin*, **10,** 304-311.

Mountney, N., Howell, J., Flint, S. and Jerram, D. (1998) Aeolian and alluvial deposition within the Mesozoic Etjo Sandstone Formation, northwest Namibia. *Journal of African Earth Sciences*, **27,** 175-192.

Mountney, N., Howell, J., Flint, S. and Jerram, D. (1999a) Climate, sediment supply and tectonics as controls on the deposition and preservation of the aeolian-fluvial Etjo Sandstone Formation, Namibia. *Journal of the Geological Society*, **156,** 771-777.

Mountney, N., Howell, J., Flint, S. and Jerram, D. (1999b) Relating eolian bounding-surface geometries to the bed forms that generated them: Etjo Formation, Cretaceous, Namibia. *Geology*, **27,** 159.

Milner, S.C., Duncan, A.R., Ewart, A., Marsj, J.S. (1994). Promotion of the Etendeka Formation to group status: a new integrated stratigraphy. Communictions of the Geological Survey of Namibia **9**, 5-11.

Muirhead, J.D., Airoldi, G., Rowland, J.V. and White, J.D. (2012) Interconnected sills and inclined sheet intrusions control shallow magma transport in the Ferrar large igneous province, Antarctica. *Geological Society of America Bulletin*, **124,** 162-180.

Murphy, C. (1983) Point counting pores and illuvial clay in thin section. *Geoderma*, **31,** 133-150.

N

Nawaz, R. (1977) Pyrometamorphic Rocks at the Contact of a Dolerite Plug near Bunowen, Co Galway, Ireland. *The Irish Naturalists' Journal*, **19,** 101-104.

Nelson, C., Jerram, D. and Hobbs, R. (2009) Flood basalt facies from borehole data: implications for prospectivity and volcanology in volcanic rifted margins. *Petroleum Geoscience*, **15,** 313.

Newcomb, R.C. (1961) *Storage of ground water behind subsurface dams in the Columbia River Basalt, Washington, Oregon, and Idaho*. US Government Printing Office.

Norrish, K. and Hutton, J. (1969) An accurate X-ray spectrographic method for the analysis of a wide range of geological samples. *Geochimica et cosmochimica acta*, **33,** 431-453.

O

O'Connor, J.M. and Duncan, R.A. (1990) Evolution of the Walvis Ridge-Rio Grande Rise Hot Spot System: Implications for African and South American Plate motions over plumes. *Journal of Geophysical Research: Solid Earth (1978–2012)*, **95,** 17475-17502.

O'Neil, J.R., Clayton, R.N. and Mayeda, T.K. (1969) Oxygen isotope fractionation in divalent metal carbonates. *The Journal of Chemical Physics*, **51,** 5547.

Owen-Smith, T., Ashwal, L., Torsvik, T. and Harris, C. (2012) Petrogenesis of the Doros Gabbroic Complex, Namibia: Multiple mingling magma mushes? In: *EGU General Assembly Conference Abstracts*, **14**, pp. 3299.

P

Passchier, C.W., Trouw, R.A.J., Goscombe, B., Gray, D. and Kröner, A. (2007) Intrusion mechanisms in a turbidite sequence: the Voetspoor and Doros plutons in NW Namibia. *Journal of structural geology*, **29,** 481-496.

Passey, S.R. (2004). The volcanic and sedimentary evolution of the Faeroe plateau lava group, Faroe Islands and Faroe-Shetland Basin, NE Atlantic. *PhD Thesis*, University of Glasgow.

Passey, S.R. and Bell, B.R. (2007) Morphologies and emplacement mechanisms of the lava flows of the Faroe Islands Basalt Group, Faroe Islands, NE Atlantic Ocean. *Bulletin of Volcanology*, **70,** 139-156.

Parmentier, E.M. and Schedl, A. (1981) Thermal Aureoles of Igneous Intrusions: Some Possible Indications of Hydrothermal Convective Cooling. *The Journal of Geology*, **89,** 1-22.

Parry, W., Chan, M. and Beitler, B. (2004) Chemical bleaching indicates episodes of fluid flow in deformation bands in sandstone. *AAPG bulletin*, **88,** 175.

Peate, D. (1997) The Paraná-Etendeka Province. *GEOPHYSICAL MONOGRAPH-AMERICAN GEOPHYSICAL UNION*, **100,** 217-246.

Peck, D.L., Hamilton, M.S. and Shaw, H.R. (1977) Numerical analysis of lava lake cooling models; Part II, Application to Alae lava lake, Hawaii. *American Journal of Science*, **277,** 415-437.

Petford, N. (2003) Controls on primary porosity and permeability development in igneous rocks. *Geological Society, London, Special Publications*, **214,** 93-107.

Pettijohn, F., Potter, P. and Siever, R. (1973) Sand and Sandstone, 618 pp. *New York/Heidelberg/Berlin*.

Petry, K., Jerram, D., de Almeida, D. and Zerfass, H. (2007) Volcanic-sedimentary features in the Serra Geral Fm., Parana Basin, southern Brazil: Examples of dynamic lava-sediment interactions in an arid setting. *Journal of volcanology and geothermal research*, **159,** 313-325.

Philpotts, A.R. and Asher, P.M. (1993) Wallrock Melting and Reaction Effects along the Higganum Diabase Dike in Connecticut: Contamination of a Continental Flood Basalt Feeder. *Journal of Petrology*, **34,** 1029-1058.

Pryor, W.A. (1973) Permeability-Porosity Patterns and Variations in Some Holocene Sand Bodies. *AAPG Bulletin,* **57,** 162-189.

Purvis, K. (1992) Lower permian rotliegend sandstones, southern north sea: a case study of sandstone diagenesis in evaporite-associated sequences. *Sedimentary Geology*, **77,** 155-171.

Q

No references with leading authors going by surnames beginning with the letter Q

R

Raab, M., Brown, R., Gallagher, K., Weber, K. and Gleadow, A. (2005) Denudational and thermal history of the Early Cretaceous Brandberg and Okenyenya igneous complexes on Namibia's Atlantic passive margin. *Tectonics*, **24,** TC3006.

Rasband, W.S.,ImageJ,USNationalInstitutesofHealth,Bethesda,Maryland,USA, http://rsb.info.nih.gov/ij/, 1997–2009.

Renne, P., Glen, J., Milner, S. and Duncan, A. (1996) Age of Etendeka flood volcanism and associated intrusions in southwestern Africa. *Geology*, **24,** 659.

Renne, P., Ernesto, M. and Milner, S. (1997) Geochronology of the Paraná–Etendeka magmatic province. *EOS Transactions, American Geophysical Union*, **78**.

Renton, J., Heald, M. and Cecil, C. (1969) Experimental investigation of pressure solution of quartz. *Journal of Sedimentary Research*, **39**.

Reynolds, D.L. (1940) Contact metamorphism by a tertiary dyke at Waterfoot, Co. Antrim. *Geological Magazine*, **77,** 461-469.

Rijswijck, P.G., Steyn, A. van C. (1990) A short note on the results of geophysical logging and testing at the Kudu 9A-2 and (a-3 boreholes. *Communications of the Geological Survey of Namibia,* **6,** 7-9.

Rollinson, H.R. (1993) Using geochemical data: evaluation, presentation, interpretation.

Rutter, E.H. (1983) Pressure solution in nature, theory and experiment. *Journal of the Geological Society*, **140,** 725-740.

Rye, R.O. (2005) A review of the stable-isotope geochemistry of sulfate minerals in selected igneous environments and related hydrothermal systems. *Chemical Geology*, **215,** 5-36.

S

Saar, M. and Manga, M. (1999) Permeability-porosity relationship in vesicular basalts. *Geophys. Res. Lett*, **26,** 111-114.

Saemundsson, K., (1979), Outline of the geology of Iceland: *Jökull* **29**, 7-28.

Sawyer, E. (1999) Criteria for the recognition of partial melting. *Physics and Chemistry of the Earth, Part A: Solid Earth and Geodesy*, **24,** 269-279.

Scherer, C. (2000) Eolian dunes of the Botucatu Formation (Cretaceous) in southernmost Brazil: morphology and origin. *Sedimentary Geology*, **137,** 63-84.

Scherer, C. (2002) Preservation of aeolian genetic units by lava flows in the Lower Cretaceous of the Paraná Basin, southern Brazil. *Sedimentology*, **49,** 97-116.

Scherer, C.M.S. and Goldberg, K. (2007) Palaeowind patterns during the latest Jurassic–earliest Cretaceous in Gondwana: Evidence from aeolian cross-strata of the Botucatu Formation, Brazil. *Palaeogeography, Palaeoclimatology, Palaeoecology*, **250,** 89-100.

Scherer, C.M.S. and Goldberg, K. (2007) Palaeowind patterns during the latest Jurassic–earliest Cretaceous in Gondwana: Evidence from aeolian cross-strata of the Botucatu Formation, Brazil. *Palaeogeography, Palaeoclimatology, Palaeoecology*, **250,** 89-100.

Schofield, N., Stevenson, C. and Reston, T. (2010) Magma fingers and host rock fluidization in the emplacement of sills. *Geology*, **38,** 63-66.

Schofield, N.J., Brown, D.J., Magee, C. and Stevenson, C.T. (2012) Sill morphology and comparison of brittle and non-brittle emplacement mechanisms. *Journal of the Geological Society*, **169,** 127-141.

Schöner, R. and Gaupp, R. (2005) Contrasting red bed diagenesis: the southern and northern margin of the Central European Basin. *International Journal of Earth Sciences*, **94,** 897-916.

Schutter, S.R. (2003a) Occurrences of hydrocarbons in and around igneous rocks. *Geological Society, London, Special Publications*, **214,** 35-68.

Schutter, S.R. (2003b) Hydrocarbon occurrence and exploration in and around igneous rocks. *Geological Society, London, Special Publications*, **214,** 7-33.

Scotchman, I., Griffith, C., Holmes, A. and Jones, D. (1998) The Jurassic petroleum system north and west of Britain: a geochemical oil-source correlation study. *Organic Geochemistry*, **29,** 671-700.

Shaw, H.R. (1963) The four-phase curve sanidine-quartz-liquid-gas between 500 and 4000 bars. *American Mineralogist*, **48,** 883-896.

Sheldon, N.D. (2003) Pedogenesis and geochemical alteration of the Picture Gorge subgroup, Columbia River basalt, Oregon. *Geological Society of America Bulletin*, **115,** 1377-1387.

Sigurgeirsson, M.Á., 1995, The Younger-Stampar eruption at Reykjanes, SW-Iceland (in Icelandic with English Summary), Náttúrufræðingurinn 64, p.211-230

Simmons, S. and Christenson, B. (1994) Origins of calcite in a boiling geothermal system. *American Journal of Science*, **294,** 361.

Sircar, A. (2004) Hydrocarbon production from fractured basement formations. *CURRENT SCIENCE-BANGALORE-*, **87,** 147-151.

Skinner, D. and Ricker, J. (1968) The geology of the region between the Mawson and Priestley glaciers, north Victoria Land, Antarctica. *New Zealand journal of geology and geophysics*, **11,** 1041-1075.

Smallwood, J.R., Prescott, D. and Kirk, W. (2004) Alternatives in Paleocene exploration West of Shetland: a case study. *Scottish Journal of Geology*, **40,** 131-143.

Smallwood, J. and Kirk, W. (2005) Paleocene exploration in the Faroe–Shetland Channel: disappointments and discoveries. In: *Geological Society, London, Petroleum Geology Conference series*, **6**, pp. 977-991. Geological Society of London.

Smith, D.G.W. (1969) Pyrometamorphism of Phyllites by a Dolerite Plug. *Journal of Petrology*, **10,** 20-55.

Smith, B.J. and McAlister, J.J. (1995) Mineralogy, chemistry and palaeoenvironmental significance of an Early Tertiary Terra Rossa from Northern Ireland: A preliminary review. *Geomorphology*, **12,** 63-73.

Smith, R.P. (2004) Geologic setting of the Snake River Plain aquifer and vadose zone. *Vadose Zone Journal*, **3,** 47-58.

Spry, A.H. and Solomon, M. (1964) Columnar buchites at Apsley, Tasmania. *Quarterly Journal of the Geological Society*, **120,** 519-544.

Stollhofen, H., Stanistreet, I.G., Bangert, B. and Grill, H. (2000a) Tuffs, tectonism and glacially related sea-level changes, Carboniferous–Permian, southern Namibia. *Palaeogeography, Palaeoclimatology, Palaeoecology*, **161,** 127-150.

Stollhofen, H., Stanistreet, I.G., Rohn, R., Holzförster, F. and Wanke, A. (2000b) AAPG Studies in Geology# 46, Chapter 6: The Gai-As Lake System, Northern Namibia and Brazil.

Stanistreet, I. and Stollhofen, H. (1999) Onshore equivalents of the main Kudu gas reservoir in Namibia. *Geological Society, London, Special Publications*, **153,** 345-365.

Stewart, A., Massey, M., Padgett, P., Rimmer, S. and Hower, J. (2005) Influence of a basic intrusion on the vitrinite reflectance and chemistry of the Springfield (No. 5) coal, Harrisburg, Illinois. *International journal of coal geology*, **63,** 58-67.

Stevens, T.O. and McKinley, J.P. (2000) Abiotic controls on H2 production from basalt-water reactions and implications for aquifer biogeochemistry. *Environmental science & technology*, **34,** 826-831.

Stokkendal, J., Friis, H., Svendsen, J.B., Poulsen, M.L.K. and Hamberg, L. (2009) Predictive permeability variations in a Hermod sand reservoir, Stine Segments, Siri Field, Danish North Sea. *Marine and Petroleum Geology*, **26,** 397-415.

Stroncik, N. and Schmincke, H. (2002) Palagonite-a review. *International Journal of Earth Sciences*, **91,** 680-697.

Suchý, V., Šafanda, J., Sýkorová, I., Stejskal, M., Machovič, V. and Melka, K. (2004) Contact metamorphism of Silurian black shales by a basalt sill: geological evidence and thermal modeling in the Barrandian Basin. *Bulletin of Geosciences*, **79,** 133-145.

Summer, N. and Ayalon, A. (1995) Dike intrusion into unconsolidated sandstone and the development of quartzite contact zones. *Journal of Structural Geology*, **17,** 997-1010.

Summer, N.S. and Verosub, K.L. (1992) Diagenesis and organic maturation of sedimentary rocks under volcanic strata, Oregon. *AAPG bulletin*, **76,** 1190-1199.

Surdam, R.C., Jiao, Z.S. and MacGowan, D.B. (1993) Redox reactions involving hydrocarbons and mineral oxidants: A mechanism for significant porosity enhancement in sandstones. *AAPG bulletin*, **77,** 1509-1518.

T

Tada, R. and Siever, R. (1989) Pressure solution during diagenesis. *Annual Review of Earth and Planetary Sciences*, **17,** 89.

Taylor, T.R., Giles, M.R., Hathon, L.A., Diggs, T.N., Braunsdorf, N.R., Birbiglia, G.V., Kittridge, M.G., Macaulay, C.I. and Espejo, I.S. (2010) Sandstone diagenesis and reservoir quality prediction: Models, myths, and reality. *AAPG bulletin*, **94,** 1093-1132.

Thompson, G. and Jerram, D. (2003) Quantifying diagenetic alteration at hot lava/sediment contacts: an example from NW Namibia. In: *EGS-AGU-EUG Joint Assembly*, **1**, pp. 6232.

Thomson, K. and Schofield, N. (2008) Lithological and structural controls on the emplacement and morphology of sills in sedimentary basins. *Geological Society, London, Special Publications*, **302,** 31-44.

Thompson, R., Gibson, S., Dickin, A. and Smith, P. (2001) Early Cretaceous basalt and picrite dykes of the southern Etendeka region, NW Namibia: windows into the role of the Tristan mantle plume in Paraná-Etendeka magmatism. *Journal of Petrology*, **42,** 2049.

Thordarson, T. and Self, S. (1993) The Laki (Skaftár Fires) and Grímsvötn eruptions in 1783–1785. *Bulletin of Volcanology*, **55,** 233-263.

Tolan, T.L., Martin, B.S., Reidel, S.P., Kauffman, J.D., Garwood, D.L. and Anderson, J.L. (2009) Stratigraphy and tectonics of the central and eastern portions of the Columbia River Flood-Basalt Province: An overview of our current state of knowledge. *Field Guides*, **15,** 645-672.

TOVEY, N.K. and HOUNSLOW, M.W. (1995) Quantitative micro-porosity and orientation analysis in soils and sediments. *Journal of the Geological Society*, **152,** 119-129.

Trumbull, R.B., Vietor, T., Hahne, K., Wackerle, R. and Ledru, P. (2004) Aeromagnetic mapping and reconnaissance geochemistry of the Early Cretaceous Henties Bay-Outjo dike swarm, Etendeka Igneous Province, Namibia. *Journal of African Earth Sciences*, **40,** 17-29.

Trumbull, R., Bühn, B., Romer, R. and Volker, F. (2003) The petrology of basanite–tephrite intrusions in the Erongo Complex and implications for a plume origin of Cretaceous alkaline complexes in Namibia. *Journal of Petrology*, **44,** 93-112.

Tucker, M.E. (2001) Sedimentology. Springer, Berlin

U

Underhill, J.R. (2003) The tectonic and stratigraphic framework of the United Kingdom's oil and gas fields. *Geological Society, London, Memoirs*, **20,** 17-59.

V

Varga, R.J., Gee, J.S., Staudigel, H. and Tauxe, L. (1998) Dike surface lineations as magma flow indicators within the sheeted dike complex of the Troodos ophiolite, Cyprus. *Journal of Geophysical Research: Solid Earth (1978–2012)*, **103,** 5241-5256.

Visser, J. (1989) The Permo-Carboniferous Dwyka Formation of southern Africa: deposition by a predominantly subpolar marine ice sheet. *Palaeogeography, Palaeoclimatology, Palaeoecology*, **70,** 377-391.

Waichel, B.L., de Lima, E.F., Viana, A.R., Scherer, C.M., Bueno, G.V. and Dutra, G. (2011) Stratigraphy and volcanic facies architecture of the Torres Syncline, Southern Brazil, and its role in understanding the Paraná-Etendeka Continental Flood Basalt Province. *Journal of volcanology and geothermal research*.

Waichel, B.L., Scherer, C. and Frank, H.T. (2008) Basaltic lava flows covering active aeolian dunes in the Paraná Basin in southern Brazil: Features and emplacement aspects. *Journal of volcanology and geothermal research*, **171,** 59-72.

Waichel, B., de Lima, E., Lubachesky, R. and Sommer, C. (2006) Pahoehoe flows from the central Parana continental flood basalts. *Bulletin of Volcanology*, **68,** 599-610.

Wang, D., Song, Y., Xu, H., Ma, X. and Zhao, M. (2012) Numerical modeling of thermal evolution in the contact aureole of a 0.9 m thick dolerite dike in the Jurassic siltstone section from Isle of Skye, Scotland. *Journal of Applied Geophysics*.

Wanke, A., Stollhofen, H., Stanistreet, I.G. and Lorenz, V. (2000) Karoo unconformities in NW-Namibia and their tectonic implications. *Communications of the geological Survey of Namibia,* **12,** 259-268.

Warren, A., Rubidge, B., Stanistreet, I., Stollhofen, H., Wanke, A., Latimer, E., Marsicano, C. and Damiani, R. (2001) Oldest known stereospondylous amphibian from the Early Permian of Namibia. *Journal of Vertebrate Paleontology*, **21,** 34-39.

Wartho, J.A., Kelley, S.P. and Blake, S. (2001) Magma flow regimes in sills deduced from Ar isotope systematics of host rocks. *Journal of Geophysical Research*, **106,** 4017-4035.

Watkins, R., McDougall, I. and Le Roex, A. (1994) K-Ar ages of the Brandberg and Okenyenya igneous complexes, north-western Namibia. *Geologische Rundschau*, **83,** 348-356.

Watton, T.J., Wright. K.A., Jerram, D.A., Brown, R.J. (2013) The Petrophysical Properties of Hyaloclastite Deposits: Implications for Petroleum Exploration. *AAPG Bulletin,* **20.**

Walderhaug, H.J., Eide, E.A., Scott, R.A., Inger, S. and Golionko, E.G. (2005) Palaeomagnetism and 40Ar/39Ar geochronology from the South Taimyr igneous complex, Arctic Russia: a Middle–Late Triassic magmatic pulse after Siberian flood-basalt volcanism. *Geophysical Journal International*, **163,** 501-517.

Walderhaug, O. (1994) Temperatures of quartz cementation in Jurassic sandstones from the Norwegian continental shelf--evidence from fluid inclusions. *Journal of Sedimentary Research*, **64**.

Walker, G.P.L. (1959) Some Observations on the Antrim Basalts and associated Dolerite Intrusions. *Proceedings of the Geologists Association,* **70,** 179-205.

Walker, G.P.L. (1971) Compound and simple lava flows and flood basalts. *Bulletin of Volcanology*, **35,** 579-590.

White, J., McPhie, J. and Skilling, I. (2000) Peperite: a useful genetic term. *Bulletin of Volcanology*, **62,** 65-66.

White, D. (1957) Thermal waters of volcanic origin. *Geological Society of America Bulletin*, **68,** 1637.

White, R. (1988) A hot-spot model for early Tertiary volcanism in the N Atlantic. *Geological Society, London, Special Publications*, **39,** 3-13.

Wickens, H. de V., McLachlan, I.R. (1990) The stratigraphy and sedimentology of the reservoir interval of the Kudu9A-2 and 9A-3 boreholes. *Communications of the Geological Survey of Namibia,* **6,** 9-23.

Wigand, M., Schmitt, A.K., Trumbull, R.B., Villa, I.M. and Emmermann, R. (2004) Short-lived magmatic activity in an anorogenic subvolcanic complex:< sup> 40</sup> Ar/< sup> 39</sup> Ar and ion microprobe U–Pb zircon dating of the Erongo, Damaraland, Namibia. *Journal of volcanology and geothermal research*, **130,** 285-305.

Williams, D.A., Fagents, S.A. and Greeley, R. (2000) A reassessment of the emplacement and erosional potential of turbulent, low-viscosity lavas on the. *Journal of geophysical research*, **105,** 20,189-20,205.

Wilson, R.L. (1964) The Tertiary Dykes of Magho Mountain Co. Fermanagh. *The Irish Naturalists' Journal*, **14,** 254-257.

Wilson, M.D. and Sedeora, S.S. (1979) An improved thin section stain for potash feldspar. *Journal of Sedimentary Research*, **49,** 637-638.

Wright, K.A., Davies, R.J., Jerram, D.A., Morris, J., Fletcher, R. (2011) Application of seismic and sequence stratigraphic concepts to a lava-fed delta system in the Faroe-Shetland Basin, UK and Faroes. *Basin Research*, 1-16.

Wyllie, P. (1961) Fusion of Torridonian sandstone by a picrite sill in Soay (Hebrides). *Journal of Petrology*, **2,** 1-37.

X

Xiong, Y. and Zhai, Y. (1992) Oxygen isotope studies of epithermal systems: A review. *Chinese Journal of Geochemistry*, **11,** 329-343.

Y

Young, G.M. (2008) Origin of Enigmatic Structures: Field and Geochemical Investigation of Columnar Joints in Sandstones, Island of Bute, Scotland. *The Journal of Geology*, **116,** 527-536.

Z

Zheng, Y.F. (1990) Carbon-oxygen isotopic covariation in hydrothermal calcite during degassing of CO 2. *Mineralium Deposita*, **25,** 246-250.

Zheng, Y. and Hoefs, J. (1993) Carbon and oxygen isotopic covariations in hydrothermal calcites. *Mineralium Deposita*, **28,** 79-89.